196
HBB
8.10.76

GA-278

GENERAL ATOMIC

GA-A13941
UC-77

HTGR FUELS AND CORE DEVELOPMENT PROGRAM

QUARTERLY PROGRESS REPORT FOR THE PERIOD ENDING MAY 31, 1976

Prepared under
Contract E(04-3)-167
Project Agreement No. 17
for the San Francisco Operations Office
U.S. Energy Research and Development Administration

DATE PUBLISHED: JUNE 30, 1976

Printed in the United States of America
Available from
National Technical Information Service
U.S. Department of Commerce
5285 Port Royal Road
Springfield, Virginia 22161
Price: Printed Copy $10.75 Microfiche $2.25

DISCLAIMER

GENERAL ATOMIC

GA-A13941
UC-77

HTGR FUELS AND CORE DEVELOPMENT PROGRAM

QUARTERLY PROGRESS REPORT FOR THE PERIOD ENDING MAY 31, 1976

Prepared under
Contract E(04-3)-167
Project Agreement No. 17
for the San Francisco Operations Office
U.S. Energy Research and Development Administration

GENERAL ATOMIC PROJECT 3224

DATE PUBLISHED: JUNE 30, 1976

QUARTERLY REPORT SERIES

GA-4072-December, 1962, through February, 1963
GA-4350-March, 1963, through May, 1963
GA-4569-June, 1963, through August, 1963
GA-4937-September, 1963, through November, 1963
GA-5104-December, 1963, through February, 1964
GA-5366-March, 1964, through May, 1964
GA-5618-June, 1964, through August, 1964
GA-5866-September, 1964, through November, 1964
GA-6113-December, 1964, through February, 1965
GA-6418-March, 1965, through May, 1965
GA-6671-June, 1965, through August, 1965
GA-6869-September, 1965, through November, 1965
GA-7010-December, 1965, through February, 1966
GA-7181-March, 1966, through May, 1966
GA-7396-June, 1966, through August, 1966
GA-7553-September, 1966, through November, 1966
GA-7801-December, 1966, through February, 1967
GA-7981-March, 1967, through May, 1967
GA-8200-June, 1967, through August, 1967
GA-8356-September, 1967, through November, 1967
GA-8530-December, 1967, through February, 1968
GA-8662-March, 1968, through May, 1968
GA-8860-June, 1968, through August, 1968
GA-9090-September, 1968, through November, 1968
GA-9227-December, 1968, through February, 1969
GA-9372-March, 1969, through May, 1969
GA-9660-June, 1969, through August, 1969
GA-9815-September, 1969, through November, 1969
GA-9944-December, 1969, through February, 1970
GA-10088-March, 1970, through May, 1970
GA-10288-June, 1970, through August, 1970
GA-10399-September, 1970, through November, 1970
GA-10501-December, 1970, through February, 1971
GA-10661-March, 1971, through May, 1971
Gulf-GA-A10784-June, 1971, through August, 1971
Gulf-GA-A10930-September, 1971, through November, 1971
Gulf-GA-A10999-December, 1971, through February, 1972
Gulf-GA-A12150-March, 1972, through May, 1972
Gulf-GA-A12222-June, 1972, through August, 1972
Gulf-GA-A12422-September, 1972, through November, 1972
Gulf-GA-A12515-December, 1972, through February, 1973
Gulf-GA-12599-March, 1973, through May, 1973
Gulf-GA-A12725-June, 1973, through August, 1973
Gulf-GA-A12818-September, 1973, through November, 1973
GA-A12916-December, 1973, through February, 1974
GA-A13030-March, 1974, through May, 1974
GA-A13126-June, 1974, through August, 1974
GA-A13253-September, 1974, through November, 1974
GA-A13353-December, 1974, through February, 1975
GA-A13444-March, 1975, through May, 1975
GA-A13592-June, 1975, through August, 1975
GA-A13737-September, 1975, through November, 1975
GA-A13804-December, 1975, through February, 1976

ABSTRACT

This publication continues the quarterly report series on the HTGR Fuels and Core Development Program. The Program covers items of the base technology of the High-Temperature Gas-Cooled Reactor (HTGR) system. The development of the HTGR system will, in part, meet the greater national objective of more effective and efficient utilization of our national resources. The work reported here includes studies of reactions between core materials and coolant impurities, basic fission product transport mechanisms, core graphite development and testing, the development and testing of recyclable fuel systems, and physics and fuel management studies. Materials studies include irradiation capsule tests of both fuel and graphite. Experimental procedures and results are discussed and, where appropriate, the data are presented in tables, graphs, and photographs. More detailed descriptions of experimental work are presented in topical reports; these are listed at the end of the report.

INTRODUCTION

This report covers the work performed by the General Atomic Company under U.S. Energy Research and Development Administration Contract E(04-3)-167, Project Agreement No. 17. This Project Agreement calls for support of basic technology associated with the fuels and core of the gas-cooled, nuclear power reactor systems. The program is based on the concept of the High-Temperature Gas-Cooled Reactor (HTGR) developed by the General Atomic Company.

Characteristics of advanced large HTGR designs include:

1. A single-phase gas coolant allowing generation of high-temperature, high-pressure steam with consequent high-efficiency energy conversion and low thermal discharge.

2. A prestressed concrete reactor vessel (PCRV) offering advantages in field construction, primary system integrity, and stressed member inspectability.

3. Graphite core material assuring high-temperature structural strength, large temperature safety margins, and good neutron economy.

4. Thorium fuel cycle leading to U-233 fuel which allows good utilization of nuclear resources and minimum demands on separative work.

These basic features are incorporated into the 330-MW(e) prototype Fort St. Vrain reactor which is currently undergoing prestartup testing.

CONTENTS

ABSTRACT iii

INTRODUCTION v

4. HTGR FISSION PRODUCT MECHANISMS, 189a NO. SU001 4-1

Task 100: Fission Product Transport 4-1
Subtask 140: Diffusion of Fission Product Metals in Graphite 4-1
Task 200: Fission Product Transport Code Development and Validation 4-3
Subtask 210: Code Development 4-3
Subtask 220: Code Validation 4-4
Task 500: Fission Product Plateout and Liftoff 4-24
Subtask 510: Fission Product Plateout 4-24
References 4-44

6. HTGR ALTERNATIVE FUEL SYSTEMS STUDIES, 189a NO. SU047 6-1

Summary 6-1
Fuel Development Plans 6-1
Introduction 6-1
High Conversion Ratio with Standard HTGR Fuel Element . 6-5
Evaluation of Alternate Strategies for U-235 Recycle 6-34
References 6-39

8. HTGR PHYSICS, 189a NO. SU002 8-1

Cross-Section Evaluation 8-1
Multidimensional Reactor Kinetics 8-1
Xenon Stability and Control Study 8-1
FSV Operating Data Analysis 8-2
References 8-2

9. HTGR FUEL DEVELOPMENT AND ENGINEERING, 189a NO. SU003 9-1

Task 200: Accelerated Irradiation Tests 9-1
Subtask 210: Fresh Fuel Qualification 9-1
Task 300: Integral Fuel System Testing 9-24
Subtask 310: Peach Bottom Fuel Test Elements 9-24
Task 500: Fuel Rod Test and Evaluation 9-58
Subtask 520: Fuel Rod Thermal Expansivity 9-58
Subtask 530: Fuel Rod Mechanical Properties 9-59

Task 600: Fuel Design and Performance Models 9-63
Subtask 610: Fuel Design Models 9-63
References 9-83

11. GRAPHITE DEVELOPMENT, 189a NO. SU004 11-1

Task 100: Fabrication and Operation of Irradiation Capsules in the ORR 11-1
Capsule OG-3 11-1
Capsule OG-4 11-1
Capsule OG-5 11-1
Task 200: Graphite Specimen Preparation and Property Measurement for Capsule Irradiations 11-2
Capsule OG-3 11-2
Capsule OG-5 11-2
Task 300: Characterization of Candidate Graphites for Properties and Purity 11-2
Fuel Element and Reflector Graphites 11-2
Side Reflector Graphites 11-5
Core Support Post and Seat Graphites 11-5
Task 400: Statistical Study of Graphite Strength 11-6
Introduction 11-6
Experimental 11-7
Results 11-7
Task 500: Fatigue Behavior of Graphite 11-9
Introduction 11-9
Material 11-9
Test Conditions 11-10
Test Data 11-10
Statistical Analysis of Test Data 11-11
Task 600: Structural Integrity of Graphite Blocks 11-13
Residual Stress Analysis 11-13
Task 700: Program Plan 11-13
References 11-15
11-16

APPENDIX: PROJECT REPORTS PUBLISHED DURING THE QUARTER A-1

FIGURES

4-1. Cross section of heat exchanger - recuperator 4-9

4-2. Comparison of calculated and observed Cs-137 plateout profiles for tube 5 4-10

4-3. Comparison of calculated and observed I-131 plateout profiles for tube 5 4-11

4-4. Comparison of calculated and observed Cs-137 plateout profiles for tube A-11 4-13

4-5. Comparison of calculated and observed I-131 plateout profiles for tube A-11 4-14

4-6. Comparison of calculated and observed Cs-137 plateout profiles for tube B-31 4-16

4-7. Comparison of calculated and observed I-131 plateout profiles for tube B-31 4-17

4-8. Comparison of GA-calculated and observed I-131 plateout profiles for tube A-11 4-18

4-9. Fuel element. 4-22

4-10. New design of pseudo-isopiestic adsorption assembly 4-28

4-11. Cesium adsorption on Incoloy 800 (as-received) at 873 K (600°C) 4-36

4-12. Cesium adsorption isotherm at 873 K for as-received Incoloy 800 4-37

4-13. Cesium adsorption isotherms for as-received Incoloy 800 . . 4-38

4-14. Arrhenius plot for cesium adsorption on as-received Incoloy 800 4-39

6-1. Attainable C/Th ratio for increasing fuel rod diameter at reduced power density 6-8

9-1. Operating history for cell 1 of capsule P13T 9-85

9-2. Operating history for cell 2 of capsule P13T 9-86

9-3. Revised schematic layout showing temperature-fluence conditions for capsules P13U and P13V 9-87

9-4. Coating porosity versus mercury intrusion 9-88

9-5. R/B Kr-85m versus mercury intrusion 9-89

9-6. Phosgene gas leaching at 1100°C, BISO ThO_2 particles, batch 6779-65 9-90

FIGURES (Continued)

9-7. Phosgene gas leaching at 1100°C, BISO ThO_2 particles, batch 6779-65, R/B Kr-85m = 1.7 x 10^{-3} at 1100°C 9-91

9-8. Phosgene gas leaching at 1100°C, BISO ThO_2 particles, batch 6779-67, R/B Kr-85m = 3.2 x 10^{-6} at 1100°C 9-92

9-9. Typical fuel test element assembly 9-93

9-10. Graphite fuel body for Peach Bottom fuel test elements . . 9-94

9-11. FTE-6 cross section 9-95

9-12. Visual examination of fuel rod 2-1-7 from FTE-6 9-96

9-13. Visual examination of fuel rod 2-2-7 from FTE-6 9-97

9-14. Visual examination of fuel rod 2-3-7 from FTE-6 9-98

9-15. Visual examination of fuel rod 2-4-7 from FTE-6 9-99

9-16. Visual examination of fuel rod 2-5-7 from FTE-6 9-100

9-17. Visual examination of fuel rod 2-6-7 from FTE-6 9-101

9-18. Visual examination of fuel rod 2-7-8 from FTE-6 9-102

9-19. Visual examination of fuel rod 2-8-7 from FTE-6 9-103

9-20. Photomicrographs of fuel rod 2-1-7 9-105

9-21. Photomicrographs of fuel rod 2-2-7 9-107

9-22. Photomicrographs of fuel rod 2-3-7 9-109

9-23. Photomicrographs of fuel rod 2-6-7 9-111

9-24. Photomicrographs of fuel rod 2-8-7 9-113

9-25. Photomicrographs of representative fuel particles from fuel rod 2-1-7 9-115

9-26. Photomicrographs of UO_2 TRISO particle showing SiC attack from fuel rod 2-1-7 9-116

9-27. Photomicrographs of representative fuel particles from fuel rod 2-2-7 9-117

9-28. Photomicrographs of representative fuel particles from fuel rod 2-3-7 9-118

9-29. Photomicrographs of $(Th,U)C_2$ TRISO particle from fuel rod 2-3-7 from FTE-6 showing matrix-particle interaction . . . 9-119

9-30. Photomicrographs of ThC_2 TRISO particle in fuel rod 2-6-7 9-120

9-31. Photomicrographs of representative fissile $(Th,U)C_2$ particle from fuel rod 2-6-7 9-121

9-32. Photomicrographs of representative fuel particles from fuel rod 2-8-7 9-122

FIGURES (Continued)

9-33. Photomicrographs of UC_2 TRISO particle from fuel rod 2-8-7 of FTE-6 showing apparent contamination attack . . . 9-123

9-34. Single-channel gamma scans of fuel rods used in fuel examination 9-124

9-35. FTE-6 single-channel gamma scan comparison of fuel rods . 9-125

9-36. Total FIMA in fuel stacks 1 and 2 measured by gamma spectroscopy 9-126

9-37. Total FIMA in fuel stacks 3 and 4 measured by gamma spectroscopy 9-127

9-38. Total FIMA in fuel stacks 5 and 6 measured by gamma spectroscopy 9-128

9-39. Total FIMA in fuel stacks 7 and 8 measured by gamma spectroscopy 9-129

9-40. Cs-137/Zr-95 ratio for fuel rods in stacks 1 and 2 9-130

9-41. Cs-137/Zr-95 ratio for fuel rods in stacks 3 and 4 9-131

9-42. Cs-137/Zr-95 ratio for fuel rods in stacks 5 and 6 9-132

9-43. Cs-137/Zr-95 ratio for fuel rods in stacks 7 and 8 9-133

9-44. Cs-137 loss from fuel rods in stacks 1 and 2 9-134

9-45. Design of type II thermal stability crucibles 9-135

9-46. Stereophotographs of thermal stability spine samples from FTE-6 9-136

9-47. Photomicrographs of typical microstructure of ThC_2 TRISO particle from spine sample TS 18-3 9-137

9-48. Photomicrographs of typical microstructure of UC_2 120-μm (VSM) particles from spine sample TS 4-5 9-138

9-49. GA hot cell gamma scan of body 1 spine samples 9-139

9-50. GA hot cell gamma scan of body 2 spine samples 9-140

9-51. GA hot cell gamma scan of body 3 spine samples 9-141

9-52. FTE-6 graphite fuel body 2 gamma scanned areas 9-142

9-53. FTE-6 fuel body 2 (holes 1 and 2) single-channel gamma scans of cesium 9-143

9-54. FTE-6 fuel body 2 (holes 5 and 6) single-channel gamma scans of cesium 9-144

9-55. Fuel rod mechanical properties test specimen geometry . . 9-145

9-56. Compressive stress-strain curves for HTGR fuel rods . . . 9-146

9-57. Fracture surfaces of LHTGR fuel rods 9-147

FIGURES (Continued)

9-58. Variation of the preferred orientation of carbon crystallites with coating rate 9-148

9-59. Irradiation-induced dimensional changes of intermediate-density carbons 9-149

9-60. Irradiation-induced dimensional changes of high-density carbons 9-150

9-61. Irradiation-induced dimensional changes of an intermediate-density carbon as a function of fast neutron fluence . . . 9-151

9-62. Preferred orientation changes of restrained and unrestrained intermediate-density carbons during irradiation 9-152

9-63. Variation of preferred orientation with apparent creep strain 9-153

9-64. Agreement between predicted and calculated irradiation-induced strains 9-154

9-65. Young's modulus of carbons before and after irradiation . 9-156

9-66. Flow diagram for the BISO stress analysis model 9-157

9-67. Comparison of calculated and measured diametral changes of BISO particles irradiated in position 40 using dimensional changes for a coating with a density of 1.83 Mg/m^3 9-158

9-68. Comparison of calculated and measured diametral changes of BISO particles irradiated in position 40 using dimensional changes for a coating with a density of 1.75 Mg/m^3 9-159

9-69. Comparison of calculated and measured diametral changes of BISO particles irradiated in position 27 using dimensional changes for a coating with a density of 1.75 Mg/m^3 9-160

9-70. Mean fracture strength of pyrocarbon strips measured in three-point bending 9-161

9-71. Behavior of coatings irradiated restrained on sapphire spheres 9-162

9-72. Dimensional changes of pyrocarbons 9-166

9-73. Preferred orientation changes of restrained high-density carbons during irradiation 9-170

9-74. Preferred orientation changes of restrained intermediate-density carbons during irradiation 9-171

9-75. Preferred orientation changes of restrained low-density carbons during irradiation 9-172

9-76. Calculated stresses and failure probability of a low-coating-rate intermediate-density carbon using a constant value of K 9-173

FIGURES (Continued)

9-77. Calculated stresses and failure probability of a low-coating-rate intermediate-density carbon using the determined variation of K 9-174

11-1. Log 5651-90 of H-451 graphite showing locations of slabs used in statistical strength study and fatigue study . . . 11-80

11-2. Map of local variations in density in edge zone of slab 1 . 11-81

11-3. Map of local variations in strength in edge zone of slab 1 11-82

11-4. Map of local variations in density in center zone of slab 1 11-83

11-5. Map of local variations in strength in center zone of slab 1 11-84

11-6. Map of local variations in density in edge zone of slab 2 . 11-85

11-7. Map of local variations in strength in edge zone of slab 2 11-86

11-8. Map of local variations in density in center zone of slab 2 11-87

11-9. Map of local variations in strength in center zone of slab 2 11-88

11-10. Map of local variations in density in edge zone of slab 3 . 11-89

11-11. Map of local variations in strength in edge zone of slab 3 11-90

11-12. Map of local variations in density in center zone of slab 3 11-91

11-13. Map of local variations in strength in center zone of slab 3 11-92

11-14. Map of local variations in density in edge zone of slab 4 . 11-93

11-15. Map of local variations in strength in edge zone of slab 4 11-94

11-16. Map of local variations in density in center zone of slab 4 11-95

11-17. Map of local variations in strength in center zone of slab 4 11-96

11-18. Mean flexural strength of 6.4-mm-diameter specimens versus mean tensile strength of 6.4-mm-diameter companion specimens 11-97

11-19. Mean flexural strength of 6.4-mm-diameter specimens versus mean tensile strength of 12.8-mm-diameter companion specimens 11-98

11-20. Location of the cores for fatigue specimens in slab 5B . . 11-99

11-21. Fatigue test data on H-451 graphite, axial orientation, quarter-length edge location, in air at ambient temperature, R = -1.0 11-100

FIGURES (Continued)

11-22. Fatigue test data on H-451 graphite, axial orientation, quarter-length edge location, in air at ambient temperature, R = -0.5 11-101

11-23. Fatigue test data on H-451 graphite, axial orientation, quarter-length edge location, in air at ambient temperature, R = 0 11-102

11-24. Fatigue test data on H-451 graphite, axial orientation, quarter-length edge location, in air at ambient temperature, R = 0.5 11-103

11-25. Constant life fatigue diagram for H-451 graphite 11-104

11-26. Finite element model for residual stress analysis 11-105

11-27. Finite element model for thermal analysis 11-106

11-28. Finite element model for primary loading analysis 11-107

11-29. Residual stress, σ_{max}, for FTE-4 at axial position 23 . . 11-108

11-30. Residual stress, σ_{xy}, for FTE-4 at axial position 23 . . 11-109

11-31. Residual stress, σ_{yy}, for FTE-4 at axial position 23 . . 11-110

11-32. Residual stress, σ_{zz}, for FTE-4 at axial position 23 . . 11-111

11-33. x-stress contour under 25.4 kN/m compression load 11-112

11-34. xy-stress contour under 25.4 kN/m compression load . . . 11-113

11-35. y-stress contour under 25.4 kN/m compression load 11-114

11-36. x-stress contour under 100 kPa pressure load 11-115

11-37. xy-stress contour under 100 kPa pressure load 11-116

11-38. y-stress contour under 100 kPa pressure load 11-117

TABLES

4-1. Cesium-137 release from CPL-2/1 fuel element 4-23

4-2. Typical primary circuit component materials and in-service surface temperatures for 3000-MW(t) HTGR 4-27

4-3. Cesium sorption on as-received Incoloy-800 specimen (experiment 2) 4-32

4-4. Cesium sorption on as-received Incoloy-800 specimens (experiments 10 and 11) 4-33

4-5. Cesium sorption on as-received Incoloy-800 specimens (experiments 14 and 15) 4-34

4-6. Data for cesium adsorption on empty Inconel-625 specimen tube in terms of relative in-situ cesium count rate . . . 4-41

6-1. Advanced BISO fertile particle description 6-9

6-2. High conversion parameters for different fuel particle systems, 6 MW/m^3 power density 6-11

6-3. High conversion parameters for different fuel particle systems, 8.4 MW/m^3 power density 6-12

6-4. High conversion parameters for equal pressure drop fuel elements, 6 MW/m^3 power density 6-13

6-5. Costs for fuel cycle evaluation plan - standard element . 6-16

6-6. Costs for the development of silicon-alloyed-pyrocarbon coated fertile particles for high conversion HTGR application 6-25

6-7. Characteristics of silicon-alloyed-pyrocarbon coated fertile particles under irradiation 6-26

6-8. Comparison of fuel cycle costs for alternative U-235 recycle plans 6-37

6-9. Projected cost changes for recycle and waste 6-38

9-1. Control temperatures for capsule P13V 9-10

9-2. OPyC density and porosity determination 9-12

9-3. OPyC densities of recent capsule particle batches 9-14

9-4. Buffer porosity loss during OPyC coating 9-16

9-5. Comparison of optical anisotropy calculation techniques . 9-23

9-6. FTE-6 drawing and parts list 9-28

9-7. Graphite materials used in Peach Bottom fuel elements . . 9-30

TABLES (Continued)

9-8. FTE-6 preirradiation fuel rod quality control attributes . . 9-32
9-9. FTE-6 composition and location of bonded fuel rods 9-33
9-10. FTE-6 spine sample irradiation conditions 9-34
9-11. FTE-6 fuel rod bow 9-36
9-12. Summary of postirradiation examination of FTE-6 fuel rods . 9-37
9-13. FTE-6 fuel rod gamma scan summary 9-43
9-14. FTE-6 comparison between gamma spectroscopy and GAUGE/FEVER-calculated fuel rod burnups 9-52
9-15. Comparison of Cs-137 loss and fuel failure fractions 9-53
9-16. Preirradiation data for FTE-6 type II thermal stability spine samples 9-55
9-17. Postirradiation data for FTE-6 type II thermal stability spine samples 9-55
9-18. Mechanical properties of HTGR fuel rods 9-61
9-19. Dimensions and coating properties of BISO particles 9-72
9-20. Irradiation conditions and diametral changes 9-72
9-21. Young's modulus, Poisson's ratio, and Poisson's ratio in creep used in calculation 9-74
9-22. Weibull parameters of pyrocarbon determined from three-point bend tests 9-78
9-23. Creep constants from sapphire spheres in capsules HT-20 through HT-23 9-81
11-1. Thermal conductivity of H-451 graphite, log 6484-41 11-17
11-2. Flexural strength of H-451 graphite, logs 6484-40 and -41 . 11-18
11-3. Thermal conductivity of H-451 graphite, log 6484-55 11-26
11-4. Flexural strength of H-451 graphite, log 6484-54 11-27
11-5. Flexural strength of H-451 graphite, log 6484-55 11-31
11-6. Flexural strength of H-451 graphite, log 6484-56 11-35
11-7. Impurity content of H-451 graphite 11-39
11-8. Ash and sulfur content of H-451 graphite 11-43
11-9. Thermal conductivity of SO818 graphite 11-44
11-10. Flexural strength of SO818 graphite 11-45
11-11. Impurity content of SO818 graphite, log 6484-59 11-53
11-12. Impurity content of SO818 graphite, log 6484-60 11-57

TABLES (Continued)

11-13. Impurity content of S0818 graphite, log 6484-61 11-61

11-14. Impurity content of S0818 graphite, log 6484-62 11-65

11-15. Ash and sulfur content of S0818 graphite 11-69

11-16. Summary of statistical study of the strength of H-451 graphite, slab 1 11-70

11-17. Summary of statistical study of the strength of H-451 graphite, slab 2 11-71

11-18. Summary of statistical study of the strength of H-451 graphite, slab 3 11-72

11-19. Summary of statistical study of the strength of H-451 graphite, slab 4 11-73

11-20. Fatigue tests on H-451 graphite, control tensile tests . . 11-74

11-21. Fatigue tests on H-451 graphite, R = -1.0 11-75

11-22. Fatigue tests on H-451 graphite, R = -0.5 11-76

11-23. Fatigue tests on H-451 graphite, R = 0 11-77

11-24. Fatigue tests on H-451 graphite, R = 0.5 11-78

11-25. Data for axial position 23 11-79

4. HTGR FISSION PRODUCT MECHANISMS
189a NO. SU001

TASK 100: FISSION PRODUCT TRANSPORT

Subtask 140: Diffusion of Fission Product Metals in Graphite

Cesium Transport Through Graphite

Introduction and Summary. A laboratory study of the transport of cesium through graphite utilizing a method described in Ref. 4-1 is continuing. A diffusion assembly used in this study was irradiated in GA capsule HB-2. Preliminary results from postirradiation examination of the assembly have been obtained. The most striking result is that more than two-thirds of the cesium that left the source was found within the graphite sleeve barrier and less than one-third crossed this barrier and was found in the sink. This is in contrast to laboratory (out-of-pile) experiments in which the amount crossing the graphite barrier is always much larger than that taken up by it. Although there are other differences, in particular the amount lost by the source is larger than that observed in any laboratory experiments thus far, the indication is clear that in-pile transport is quite different from out-of-pile transport, and the expected reactor release is lower than would be estimated from laboratory experiments alone.

Description of Assembly. The basic diffusion assembly, described in Ref. 4-1, consisted of a source which was a rod of highly sorptive char-loaded graphite containing 62 μCi of Cs-134, surrounded by a sleeve and end plugs of H-451 graphite (containing about 0.4 μCi of Cs-134 from previous experiments), and in turn surrounded completely by a sink and caps of char-loaded graphite. This assembly was placed in a tightly fitting graphite cylinder (spacer) which also fitted tightly into a crucible of char-loaded

graphite closed at both ends with screw caps. For use in the irradiation test capsule, the crucible was fitted snugly into a sealed niobium can. The parts were baked out in hydrogen and handled under a hydrogen-helium mixture prior to sealing.

Results and Discussion. The diffusion assembly was exposed in capsule HB-2 to a design fluence of 4.6×10^{25} n/m^2 $(E > 29\ fJ)_{HTGR}$ during 104 days of irradiation. The irradiation temperatures, calculated on the basis of design data and actual control rod positions, varied from 1123 to 913 K. The irradiation conditions were equivalent to 45.5 days at 1123 K (if the activation energy for the transport is taken as 110.9 kJ/mol (26,500 cal/mol) on the basis of the data given in Ref. 4-1.

There was no evidence of contamination of the source but contaminants, mainly Co-60, Nb-95, and Sb-124, increased with distance outward towards the crucible. Antimony-124 was particularly deleterious as it obscured the 9.67×10^{-14} J (604.7 KeV) emission of the Cs-134. Thus, there is some uncertainty in the cesium determinations, and better values should be obtained after further radioactive decay of the contaminants.

A total of approximately 92 μCi of Cs-134 was found in the various parts of the assembly, some of it produced by irradiation of originally stable cesium. About 63% of this total was in the source, 25.5% in the graphite sleeve and plugs, 9.5% in the sink and caps, and 2% in the spacer and crucible.

The striking result is the small amount of cesium in the sink compared to that in the sleeve. This is in marked contrast to out-of-pile experiments in which the cesium appeared to simply pass through the graphite sleeve after an initial superficial adsorption of a small amount. For 9.5% of cesium in the sink, only about 1% would be expected in the sleeve. In fact, 25 times more is found. This is consistent with the idea that irradiation increases the sorptive capacity of graphite (or produces traps)

which immobilizes the cesium. This result is independent of any temperature uncertainty involved in the capsule experiment.

The amount in the sleeve is also small compared to that expected for 45 days at 1123 K from laboratory experiments by a factor of the order of four. This would correspond to a temperature uncertainty of about 100 K which is unlikely. Thus it seems very likely that transport of cesium through graphite is slower in-pile than out-of-pile.

Experiments and calculations are in progress to refine and buttress these conclusions but the first results demonstrate both the feasibility of meaningful in-pile measurements and their importance, since clearly cesium transport through matrix and graphite in a reactor is likely to be less than predicted from simple laboratory experiments.

TASK 200: FISSION PRODUCT TRANSPORT CODE DEVELOPMENT AND VALIDATION

Subtask 210: Code Development

COPAR (Coated Particle Release Model)

Development of COPAR, the new model for predicting diffusive release from multilayered coated particles, is complete. Documentation of the code is now in progress.

The release of metallic fission products from coated fuel particles in an HTGR is dependent on a number of physical phenomena including fission birth, recoil, trapped fraction, transient diffusion, interlayer discontinuities, and failure of the coatings. COPAR considers all these effects, yet maintains good calculational efficiency.

The basic method for COPAR is to evaluate an analytic solution for each independent layer and then to combine the layers numerically through

interface and boundary conditions. In its design application, the COPAR algorithm is applied in two phases. In the first phase, composite analytic solutions are obtained for a discrete birth impulse, considering in turn various particle geometries in both the intact and failed states. These solutions are tabulated as functions of dimensionless time. In the second phase, the release from a continuous irradiation history is obtained by superimposing the release from all unique birth histories. This procedure accounts for temperature and birth rate variations as well as the transition from the intact to the failed state. The numerical evaluation is accomplished efficiently by linear interpolation of the tabulated functions. Additional information on the method is given in Ref. 4-2.

COPAR is in the form of three computer programs. One of these is a stand-alone program for analysis of a single particle. This version employs an "exact" solution procedure for a continuous irradiation history. The other two programs are core design codes in which COPAR serves as a modular source subroutine. This routine employs the previously mentioned superposition principle to enhance calculational efficiency. The stand-alone code is used for experimental correlations and to validate the superposition principle. The design codes are used to survey and integrate metallic fission product release for the entire core.

Subtask 220: Code Validation

Code Validation with CPL-2/1 Data

Introduction and Summary. As part of the code validation effort (Ref. 4-3), an analysis of the release of metallic and gaseous fission products from the fuel element and the deposition of condensable species on coolant circuit surfaces in the CPL-2/1 loop experiment was performed using GA reference design methods. The loop experiment was carried out in the French Cadarache Pegase Loop. A description of the loop and the CPL-2/1 experiment is given in Ref. 4-2. This effort was an initial attempt to

apply fission product transport design (calculational) methods to test loop data for the purpose of design method validation (comparing calculated and observed fission product release and plateout behavior). It should be emphasized that the conclusions concerning the adequacy of design methods presented here are not final, but rather are contingent on the findings of the remaining CPL-2 tests, as well as other fission product code validation tests (Ref. 4-3).

The observed data for use in this study were generously provided by the Commissariat a l'Energie Atomic (CEA). The data are CEA private data and are not final. Therefore, it was not appropriate to publish the data in this report. Accordingly, the results of this study are presented in the form of simple comparisons of calculated and observed data.

On completion of the flow analysis of the CPL-2/1 heat exchanger - recuperator (Ref. 4-4), the GA reference design method [Plateout Activity Distribution (PAD) code (Ref. 4-5)] for determining plateout distribution in the primary coolant circuit of an HTGR was used to calculate (predict) iodine and cesium plateout behavior in the heat exchanger - recuperator. Recently derived sorption isotherms for alloy materials used in the heat exchanger - recuperator (measured under the CEA program) were used as input. Results show good agreement between calculated and observed shapes of iodine plateout profiles; however, calculated levels of deposited iodine activity are lower than observed values. For cesium, calculated and observed plateout profile shapes and levels of deposition are in good agreement. The results indicate that the reference GA method for calculating plateout distribution is acceptable, provided accurate surface temperatures and the appropriate sorption isotherms are utilized as input for the calculations.

The release of Cs-137 from the CPL-2/1 fuel element was calculated using the FIPER Q code. Input data included sorption and diffusion data derived from CEA measurements on fuel rod matrix and graphite materials

used in the CPL-2/1 experiment. The calculated release of Cs-137 is approximately three times greater than the observed release. This is satisfactory agreement considering the complexities involved. For strontium, not enough data from CPL-2/1 are available at this time to afford a meaningful comparison of calculated and observed releases.

The release of iodine from the fuel element was calculated using the GA reference design method. Input data included measured fractional releases (R/B values) obtained from TRIGA reactor irradiation of a CPL-2 fuel rod. Very satisfactory agreement between calculated and observed iodine release values was obtained. (The ratio of calculated to observed release was 0.8.) The release of krypton and xenon was not treated since the circulating activity in the loop has not yet been evaluated by CEA.

Plateout Analysis. The reference design method for computing the distribution of plated-out fission products on the surfaces of a reactor circuit utilizes the PAD computer code (Ref. 4-5). Given a release rate of fission products into the coolant stream (both radioactive and stable species), the code performs a mass balance between the concentration in the coolant and on the surface for a predetermined length of circuit. The amount of fission products which reaches the surface is established by the mass transfer coefficient, which is a function of the flow conditions and coolant diffusion properties. Once the coolant-borne fission products reach the surface, the code is capable of treating three different deposition conditions:

1. No sorption - no deposition on the surfaces.

2. No desorption - zero vapor pressure above the deposition surface.

3. Desorption - level of deposition determined by the sorption isotherm for the surface material and depositing element. Given the surface temperature and vapor pressure above the surface, the

allowable surface concentration is calculated via the appropriate sorption isotherm, with any excess desorbing back into the coolant stream.

Input Data for the Plateout Analysis. In the plateout analysis, the deposition of Cs-137 and I-131 was investigated. The total release of both these nuclides from the fuel element was estimated from analysis of gamma scans performed on the diffusion probe and filter located at the tube-side inlet of the heat exchanger - recuperator (Ref. 4-2). The tube wall and gas temperature distributions used in the analysis were those calculated at GA (Ref. 4-4). Four different sets of sorption isotherm data, two for iodine and two for cesium, were employed in the PAD calculations. One set of iodine sorption isotherm data, labeled CEA iodine data, was derived from preliminary measurements under the CEA program on materials (Hastelloy-X, Incoloy 800, and SS347) actually used in the heat exchanger - recuperator. One set of cesium sorption data, labeled CEA cesium data, is actually a composite of early GA data and recent data derived from preliminary CEA measurements on materials used in the heat exchanger - recuperator. The CEA data were informally transmitted to GA. The other two sets of data consist of current GA reference sorption data for iodine and cesium.* It is important to note that the GA reference data for iodine were determined mainly from measurements (Ref. 4-6) made on 1% Cr - 1/4% Mo steel, a low-alloy material. The GA reference data for cesium were deduced from deposition experiments on SS304 which was preoxidized in air at 1123 K for 18 hr (Ref. 4-7). All plateout calcualtions were carried out using the "desorption" option of the PAD code. New GA data for cesium sorption on Incoloy 800 reported below (see Subtask 510) were not available for use in this analysis.

Plateout Analysis Results. As discussed in Ref. 4-2, the heat exchanger - recuperator contained a number of tubes fabricated in two sections: the lower (upstream) half, at the higher temperature helium inlet region, was Incoloy 800; the upper half was either T-22 (2-1/2% Cr - 1% Mo), SS347, or SS410. Two tubes made entirely of Hastelloy-X were also

*The GA reference sorption isotherm data are being revised.

included. A number of tubes of each material type were preoxidized for the purpose of studying the effect that an oxide film has on the deposition of fission products.

Three tubes were chosen for this preliminary analysis on the basis that they represented the tube wall temperature distributions, material compositions, and plateout profiles (for nonpreoxidized tubes) found in the heat exchanger - recuperator. Figure 4-1 shows a cross-sectional view of the heat exchanger - recuperator and the location of the three tubes studied (tubes 5, A-11, and B-31). The two nuclides studied, Cs-137 and I-131, are important species from the perspective of radiological consequences. The results obtained for each tube studied, using the CEA sorption isotherm data, are presented below.

Tube 5 was an Incoloy 800 tube located in the center of the tube bundle, as shown in Fig. 4-1. As described in Ref. 4-4, the calculated wall temperatures for this tube are possibly ∿100 K lower than the actual operating values. This is primarily due to uncertainty in the degree of flow starvation that occurred in the center of the tube bundle. As a consequence, the calculated temperature distribution at the entrance of this tube is highly uncertain.

Figures 4-2 and 4-3 show the measured and calculated plateout profiles for tube 5 for Cs-137 and I-131, respectively. It can be seen that the calculated curves exhibit good qualitative agreement with the observed profiles for the last ∿750 mm of tube (from ∿500 mm to the end at 1.25 m). A parametric study confirmed that increasing the magnitude of the wall temperature would cause a decrease in the amount of deposited activity without changing the shape of the profile. Therefore, an increase of the tube wall temperature by ∿100 K would bring the calculated and observed cesium profiles into reasonable agreement for this exit section of the tube. In the case of iodine (Fig. 4-3), an increase in the wall temperature by ∿100 K would cause the calculated profile to be between two and three orders of magnitude less than the observed profile.

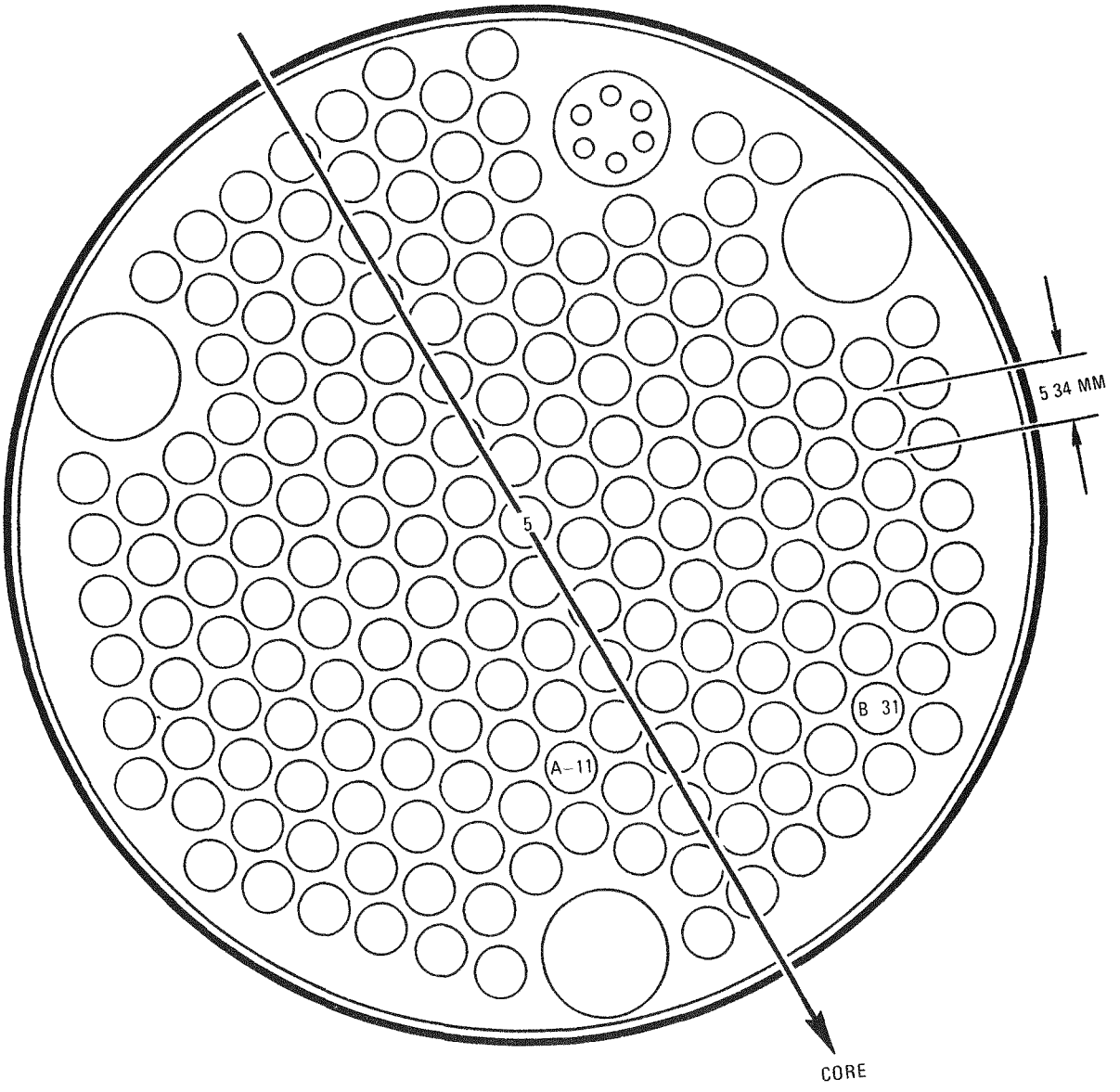

Fig. 4-1. Cross section of heat exchanger - recuperator, No. 5 central tube

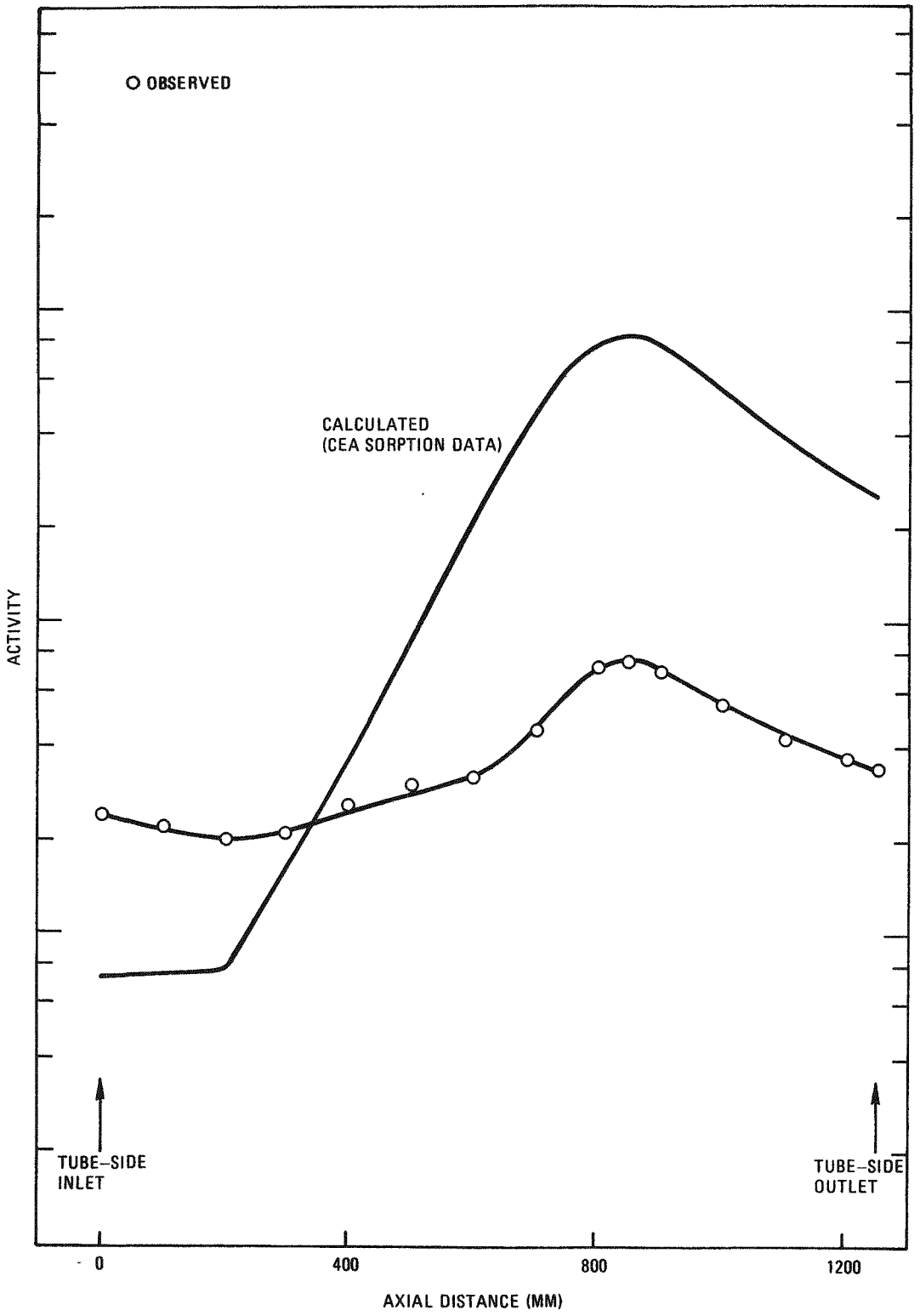

Fig. 4-2. Comparison of calculated and observed Cs-137 plateout profiles for tube 5 (Incoloy 800)

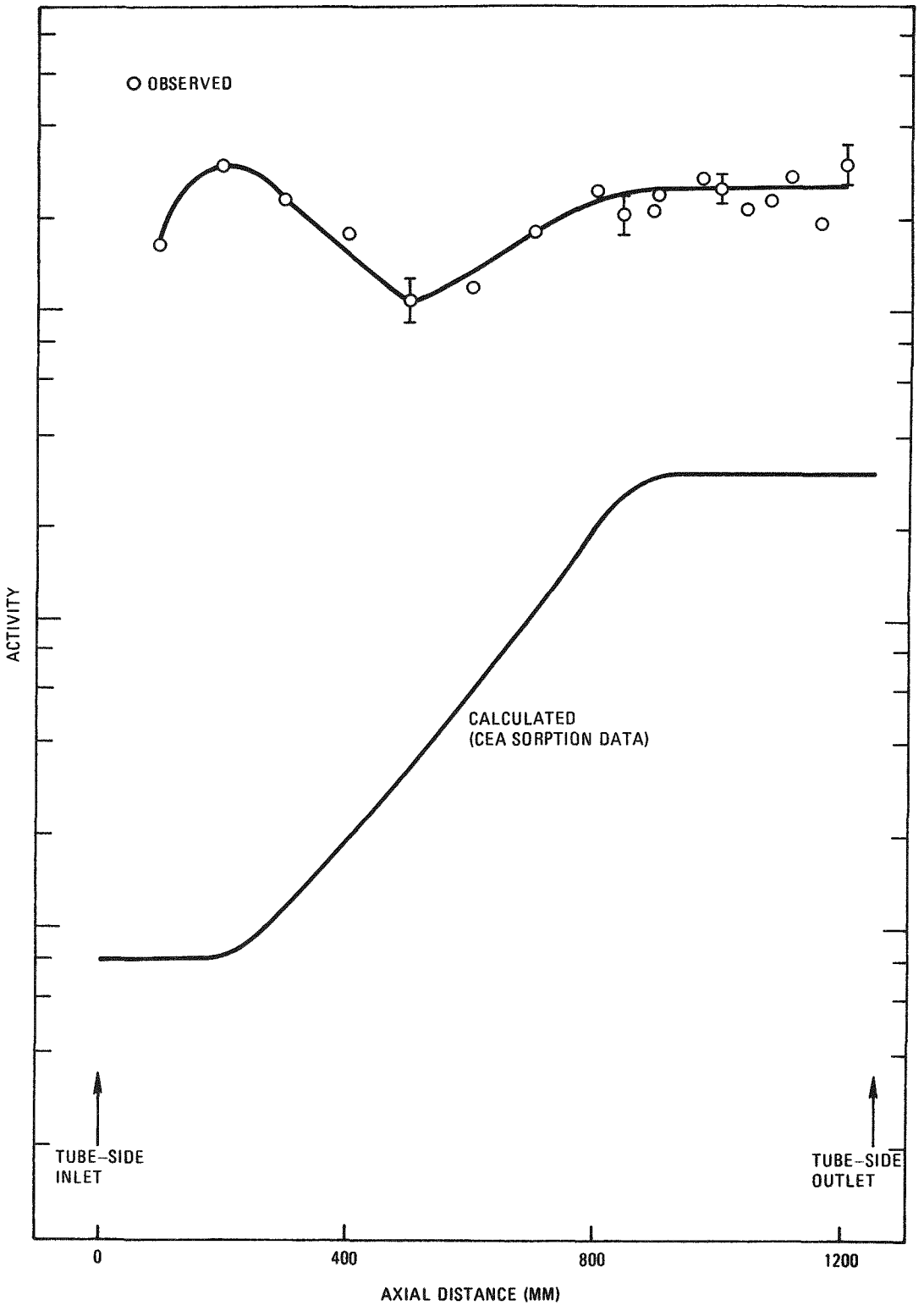

Fig. 4-3. Comparison of calculated and observed I-131 plateout profiles for tube 5 (Incoloy 800)

With regard to the first ∿500 mm (entrance region) of tube 5, the discord between the calculated and observed profiles for both nuclides suggests a degree of uncertainty in the calculated wall temperature for this section. However, the agreement obtained for the exit region of the tube indicates that the temperature dependence is relatively accurate in this region. This analysis illustrates the importance of accurate surface temperatures in predicting plateout distributions.

Tube A-11 was fabricated from a section of high-alloy Incoloy 800 steel (0 to 625 mm) and a section of low-alloy T-22 (625 mm to 1.250 m) in order to determine the difference, if any, between deposition of activity on high- and low-alloy surfaces. From Fig. 4-1 it can be seen that this tube is located approximately midway between the center and the periphery of the tube bundle where the flow distribution, and thus the tube wall temperature distribution, was known with more certainty over the entire length of tube than for the central tube. Although the CEA data sorption isotherms apply to high-alloy steels, they were used in the PAD calculations for both the Incoloy 800 and T-22 sections of the tube.

The results for tube A-11 are shown in Figs. 4-4 and 4-5 for Cs-137 and I-131, respectively. In the case of cesium (Fig. 4-4), the calculated profile coincides reasonably well in shape and magnitude with the observed profile; however, toward the end of the tube the calculated plateout activity is somewhat greater than the observed value. In addition, the calculated profile appears to indicate the onset of a transition to mass-transfer-controlled deposition (as indicated by the curl in the calculated profile at the tube exit), which is not evident from the observed data.

A comparison of the observed and calculated I-131 profiles for tube A-11 in Fig. 4-5 reveals that the shapes of the two curves are nearly identical, indicating that the temperature dependence of the CEA (high-alloy) sorption data adequately describes iodine deposition behavior on a low-alloy surface as in the case of cesium. However, the calculated profile is displaced approximately two to three orders of magnitude below the measured profile, indicating discord between calculated and observed equilibrium specific activities on the surface.

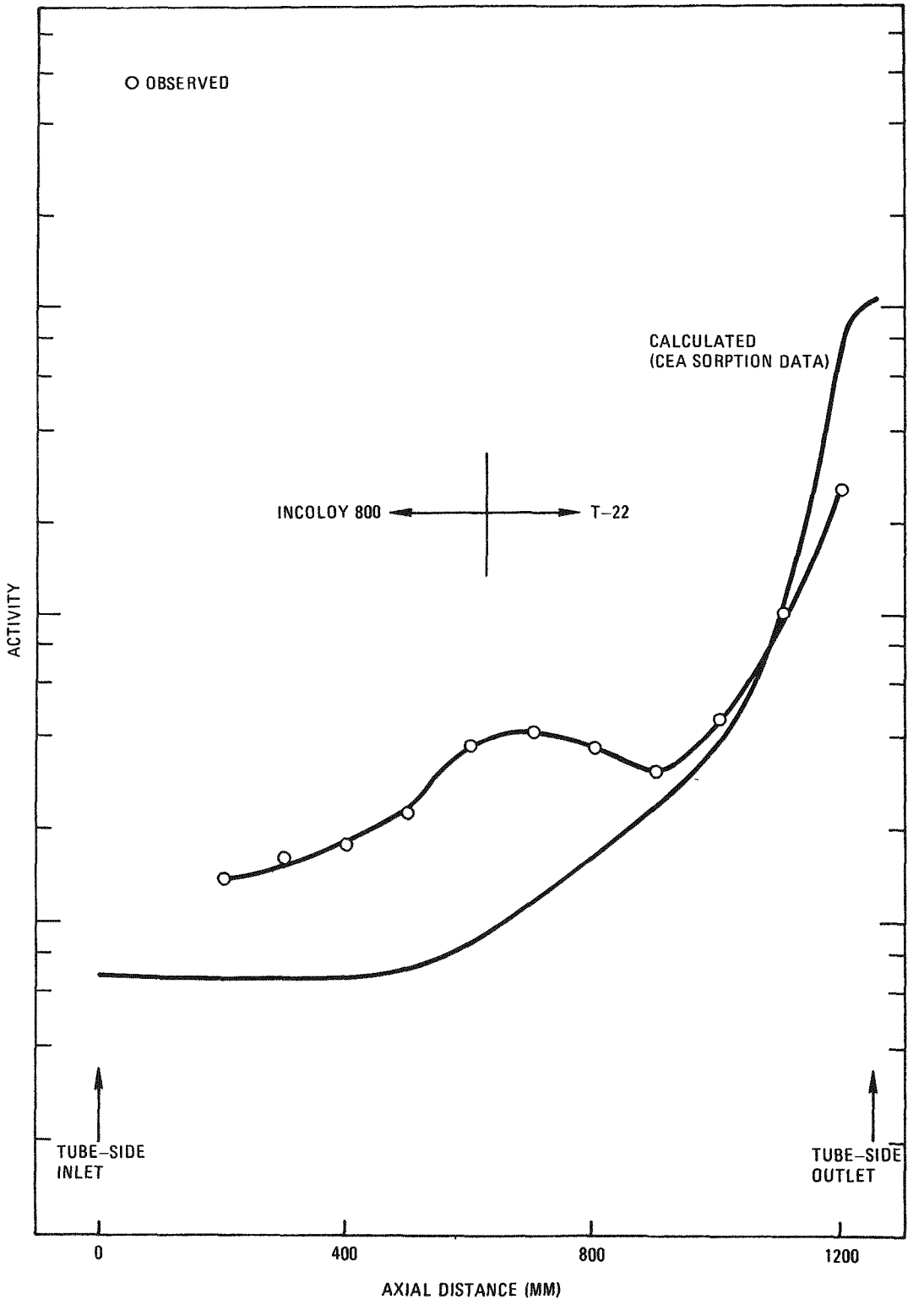

Fig. 4-4. Comparison of calculated and observed Cs-137 plateout profiles for tube A-11

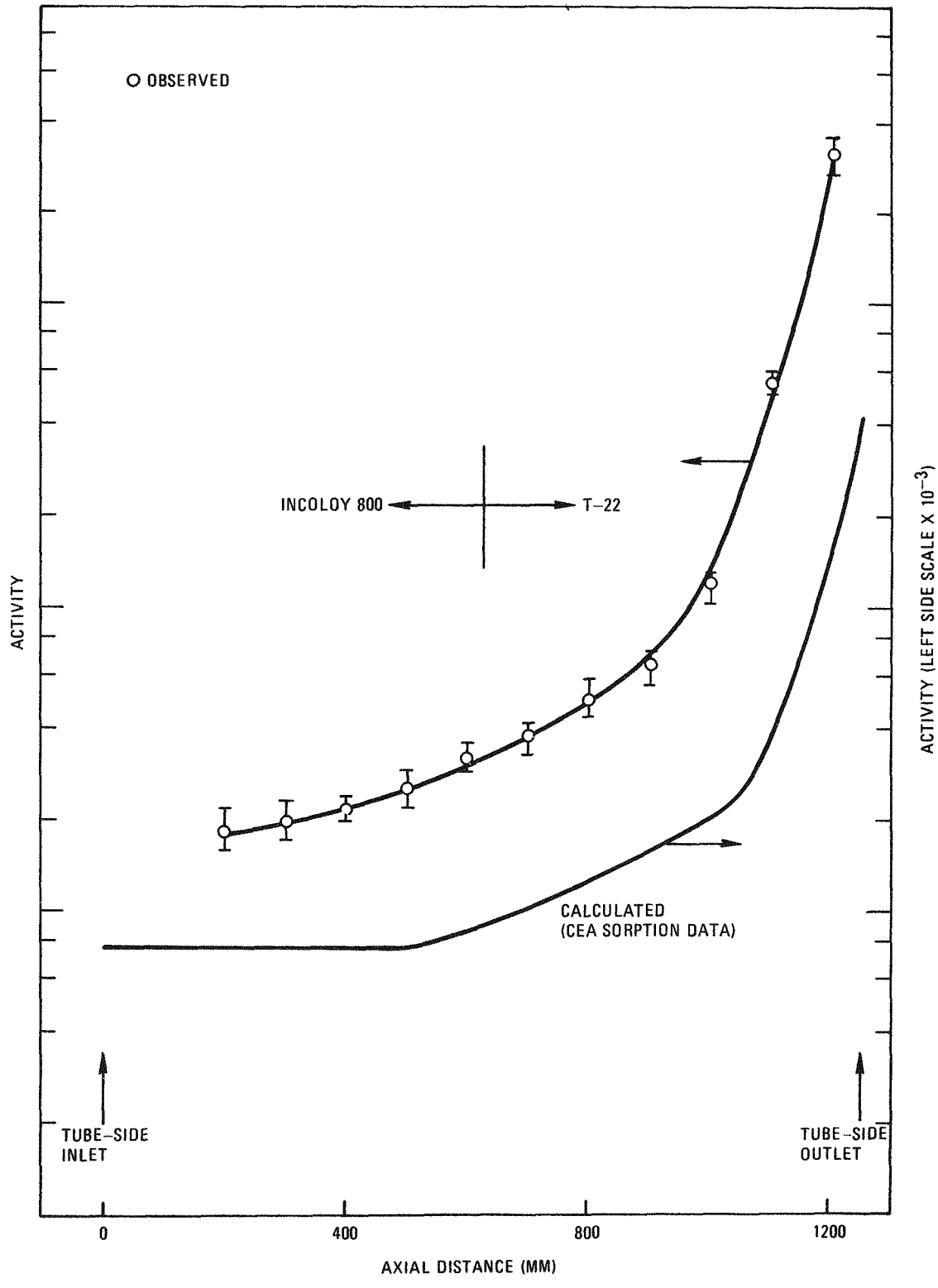

Fig. 4-5. Comparison of calculated and observed I-131 plateout profiles for tube A-11

Incoloy 800 and SS347, both high-alloy steels, comprise the two sections of tube B-31, located one tube row in from the periphery (Fig. 4-1). The results of the PAD calculations along with the corresponding observed profiles are shown in Figs. 4-6 and 4-7 for Cs-137 and I-131, respectively. The agreement between the observed and calculated deposition profiles for cesium is good both in shape and magnitude (Fig. 4-6). As with tube A-11, the calculated activity of deposited Cs-137 at the end of the tube is somewhat higher than the observed activity. Unlike tube A-11, however, both the observed and calculated profiles indicate a transition to mass-transfer-limited deposition, as evidenced by the onset of a curl in the profile at the heat exchanger - recuperator exit. For the iodine profiles (Fig. 4-7), it is again clear that the calculated and observed profiles agree in general shape, but the calculated profile is between two and three orders of magnitude lower than the observed profile.

Plateout Results Using GA Data. Calculated profiles obtained using the GA reference cesium and iodine sorption isotherm data do not agree with the observed profiles for both high- and low-alloy tube sections. This lack of agreement is exemplified by the curves shown in Fig. 4-8 for the plateout of iodine on tube A-11, fabricated from a section of Incoloy 800 (high alloy) and a section of T-22 (low alloy). CEA data were used for the high-alloy section as shown in Fig. 4-5, and GA data were used for the low-alloy section.

As shown in Fig. 4-8, use of the GA data yielded (1) a high calculated level of deposited iodine on the low-alloy section compared to the calculated and observed amounts deposited on the high-alloy surface, and (2) a "no desorption" or perfect sink behavior over the length of the T-22 section. (Perfect sink behavior of any condensable fission product from the coolant stream is typified, on a semilog plot, by a straight line of negative slope.) In discord with the calculated profile, the observed profile shows a smooth and continuous transition from the high-alloy to the low-alloy surface and a constant increase of deposited activity on the T-22 section.

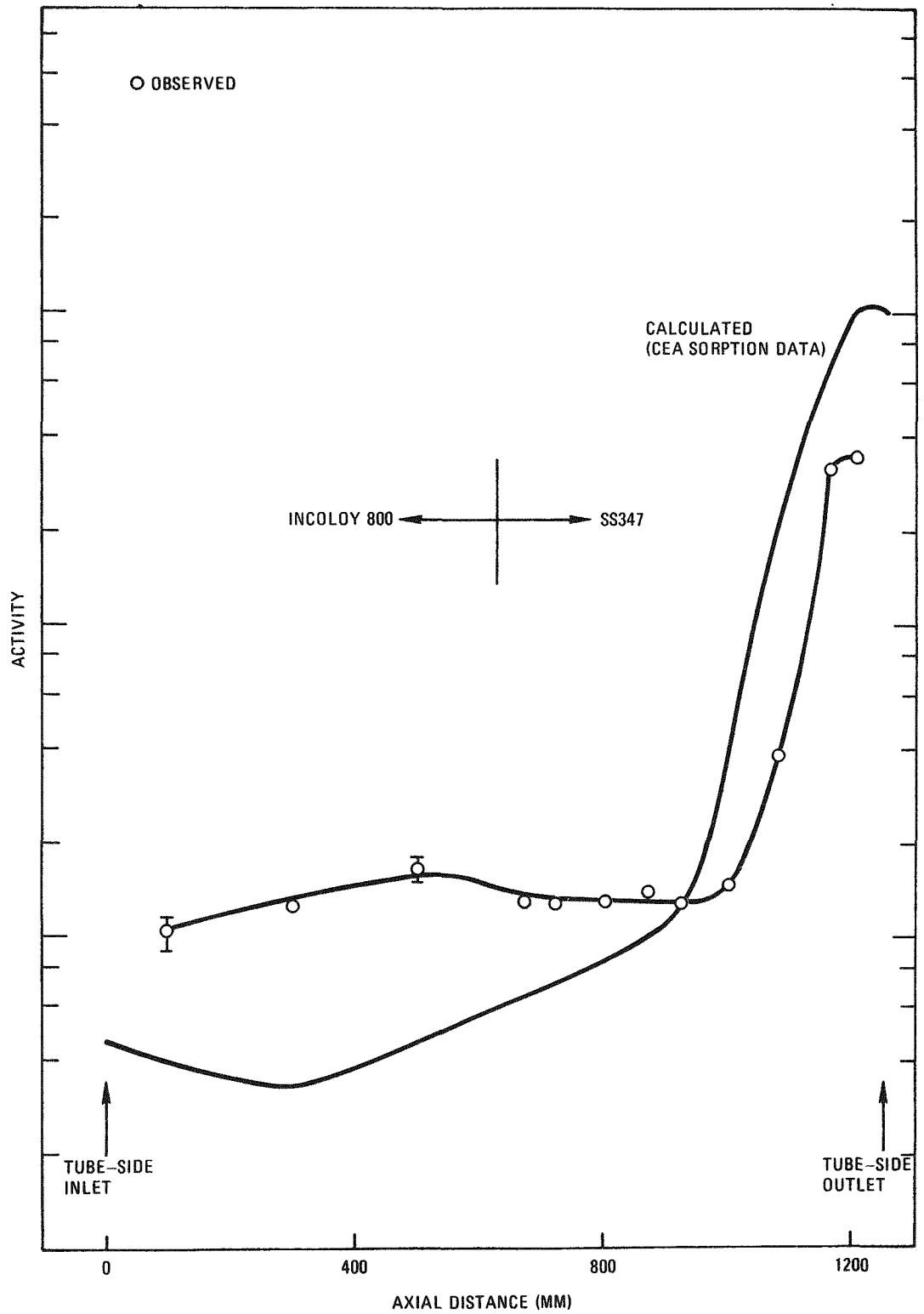

Fig. 4-6. Comparison of calculated and observed Cs-137 plateout profiles for tube B-31

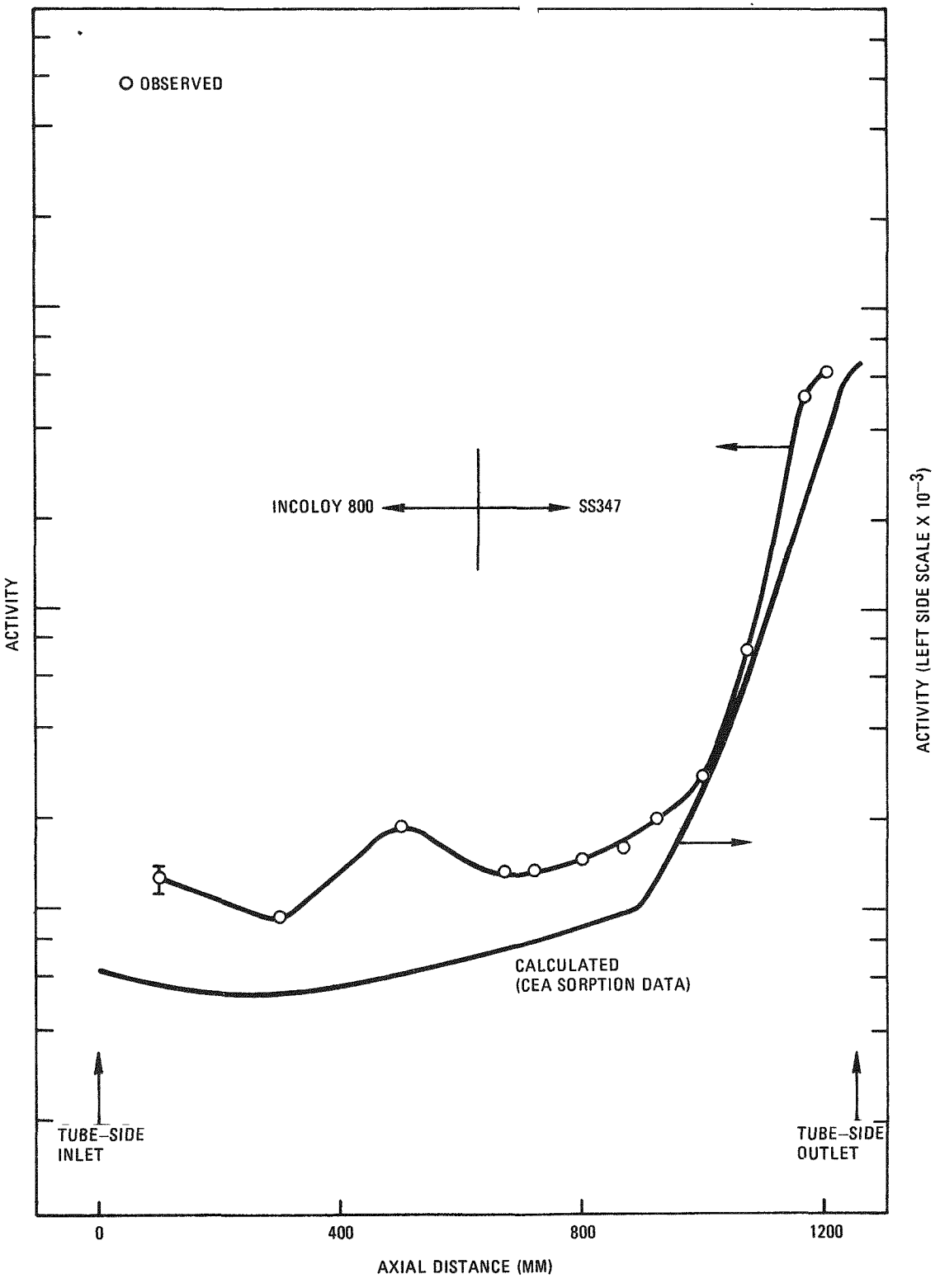

Fig. 4-7. Comparison of calculated and observed I-131 plateout profiles for tube B-31

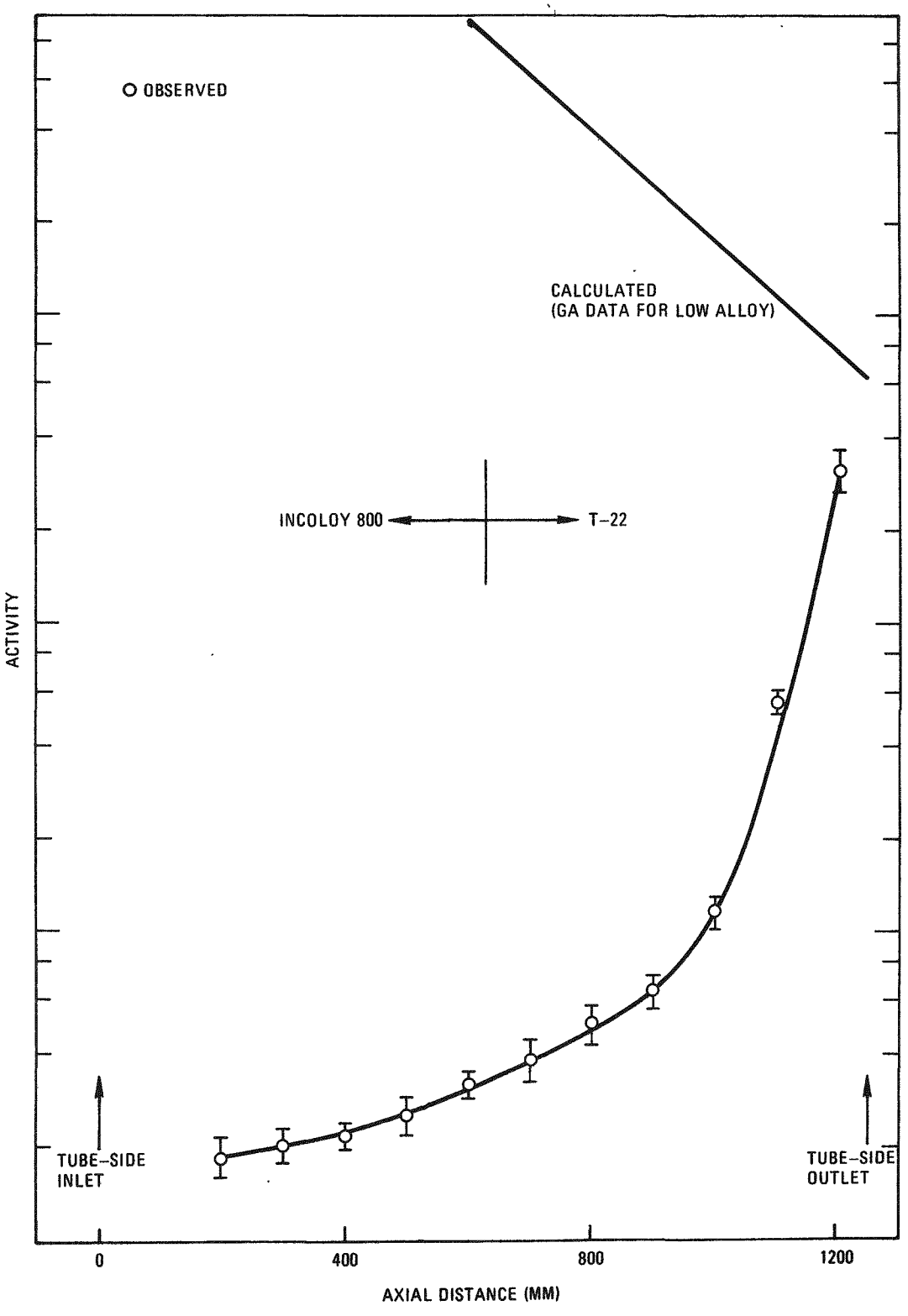

Fig. 4-8. Comparison of GA-calculated and observed I-131 plateout profiles for tube A-11

A similar substantial difference between calculated and observed Cs-137 plateout on tube A-11 resulted from use of GA Cs-137 isotherm data for calculating deposition on low-alloy surfaces. It appears, therefore, that the GA isotherm data are not satisfactory for use in calculating the deposition behavior of iodine and cesium in the CPL-2/1 heat exchanger - recuperator. Apparently, the GA reference data do not represent the tube materials. However, when sorption isotherm data representative of the actual materials studied (CEA measured data) are used, the PAD calculational technique is capable of describing the plateout of these nuclides relatively well.

Discussion and Conclusions of Plateout Analysis. The calculated wall temperatures used in the PAD calculations were based on the results of flow analyses performed for both the tube and shell side of the heat exchanger - recuperator (Ref. 4-4). Results of the plateout analysis indicate that the calculated wall temperatures and temperature distributions are representative of the actual operating values.

Perturbations in the wall temperature distributions were apparently caused by collars welded to all tubes. (These collars were used to join two alloy types to form a single tube and to lend structural support to the tube bundle since there were no baffles.) It is reasonable to assume that these collars caused localized discontinuities in the tube wall temperature distributions by causing flow disturbances and enhancement of the heat transfer. These temperature perturbations apparently caused perturbations, or "humps," in the plateout profiles (as indicated by the observed data shown in Figs. 4-1 through 4-7). These plateout perturbations were not accounted for in the calculations.

Examination of all the plateout measurements leads to a number of observations. For the tube surface conditions and temperatures, coolant impurity levels, and fission product vapor pressures existing in the CPL-2/1 loop during the deposition process, cesium and iodine appear to

plateout almost identically in shape and magnitude. It is also clear that the transition from high- to low-alloy steels did not drastically affect the deposition profiles. Rather, the curves were smooth and continuous as exemplified by the profiles for tube A-11. However, a comparison of the experimentally determined plateout proifles for tubes B-31 and A-11 indicates that the deposited iodine activity reached a higher maximum value on the low alloy (tube A-11) than on the high alloy (tube B-31), whereas the maximum cesium activity deposited on both tubes was about equal. Furthermore, it is evident that the CEA sorption isotherm data for high alloy steels, although still preliminary, described the temperature dependence of deposition on both low- and high-alloy steels quite adequately for this analysis, whereas the GA isotherms for low-alloy steels predicted behavior which is significantly different from that which was observed. Finally, the predicted amount of deposited iodine activity was consistently two or three orders of magnitude lower than the measured value, but the shapes of the calculated profiles were in close agreement with the observed curves.

Based on these initial results, it can be concluded that the PAD calculational method yields plateout predictions which closely reflect the observed deposition behavior when the proper surface temperatures and appropriate sorption isotherms are used for input data. These observations and conclusions are preliminary and apply specifically to the CPL-2/1 results. Final conclusions can be reached only after analyzing the data from the remaining CPL-2 tests, as well as from the Peach Bottom end-of-life program and obtaining consistent findings.

Metallic Fission Product Release From Fuel. The reference GA method, described in Ref. 4-8, was used for analysis of the release of metallic fission products. For calculating release from the CPL-2/1 fuel element, the FIPER Q computer code was used (Ref. 4-9). Given a source of fission products in the fuel rod, the FIPER Q code employs a finite-difference solution of the diffusion equation in order to determine the release from the fuel into the bulk coolant stream.

The release of Cs-137 was calculated and compared to the total release estimated from measurements taken on the heat exchanger - recuperator inlet diffusion probe and filter. Not enough data from CPL-2/1 were available to analyze the release of Sr-90.

As described in Ref. 4-2, the CPL-2/1 fuel element was loaded with fuel rods containing Dragon-design TRISO coated UO_2 particles. The rods located in the highest temperature region of the fuel element were seeded with a known amount (4%) of bare UO_2 kernels. A small number of rods seeded with bare kernels were also placed in cooler sections of the element in order to study the effect of temperature on release. By seeding the rods with a fixed amount of bare kernels, the fraction of releasing fuel was known exactly, thereby greatly reducing the uncertainties of the release analysis.

A schematic of the fuel element and the location of seeded rods is shown in Fig. 4-9. The maximum fuel centerline temperature, approximately 1573 K, occurred in layers 10 and 11; fission product release was dominated by the contribution from these two layers. For completeness, calculations were performed for each rod containing bare kernels.

Input Data for Release Calculations. In all calculations, the fuel, graphite, and coolant temperatures, as well as the fuel rod power densities used, were preliminary estimates made by CEA. The calculations were performed using sorption and diffusion data measured under the CEA program for the actual fuel rod matrix and graphite materials used in the CPL-2/1 experiment. It was assumed that none of the coated particles failed during irradiation. It was also assumed that additional release due to uranium contamination in the fuel rod was negligible on the basis of the fuel fabrication specifications which required the amount of contamination in a fuel rod to be less than 10^{-2} fraction by weight of the amount of uranium contained in the bare kernels of the same fuel rod. All FIPER Q calculations were performed in slab geometry by modeling the equivalent volumes and surface areas of the actual configuration.

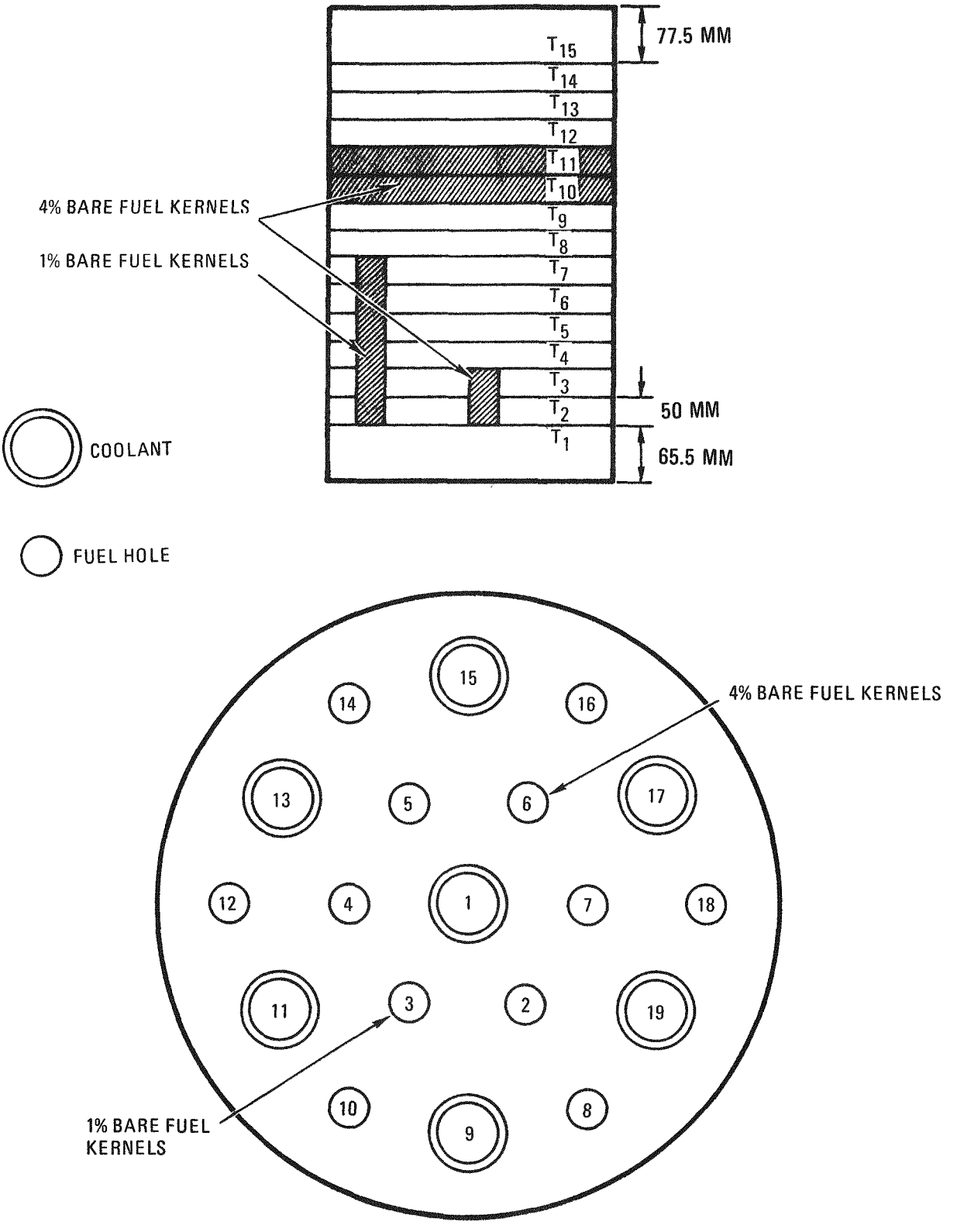

Fig. 4-9. Fuel element

Results and Discussion of Cesium-137 Release. Two different cases were calculated for the release of cesium. Case 1, which is the reference calculation, utilized the current GA design method assumptions (Ref. 4-8). Case 2 was identical to case 1 but with a modification of the amount released from the bare kernels based on the trapped fraction data given in Ref. 4-10. The results, given in Table 4-1, show that the calculated releases are about three times greater than the observed releases. This is satisfactory agreement considering the complexities involved. The fact that the calculated releases are larger than the observed releases suggests that the calculations are conservative.

TABLE 4-1
CESIUM-137 RELEASE FROM CPL-2/1 FUEL ELEMENT

	$\frac{\text{Calculated Release}}{\text{Observed Release}}$
Case 1 (no trapped fractions)	3.3
Case 2 (trapped fractions)	2.5

Case 1, the reference case calculation, included the present reference design modeling assumption: 100% release of cesium from fuel particles with failed coatings, in this case the bare UO_2 kernels. The second case was identical to the first case except that trapped fractions for cesium, as a function of fuel temperature, were included. The trapped fraction is the fraction of cesium inventory in a kernel that is essentially unavailable for release. Figure 6-1 in Ref. 4-10 shows the experimentally measured trapped fraction data as a function of fuel temperature and gives the recommended curve which was used for the calculation. The trapped fraction was assumed to apply to the bare kernels. Because of the high temperature in fuel layers 10 and 11 where most of the release occurred and because of the conservative nature of the recommended trapped fraction curve, use of the trapped fraction in the calculations yielded only a small decrease in the release.

Gaseous Release. A comparison of calculated and observed noble gas (krypton and xenon) radioactivity levels cannot be made at this time because the loop operational circulating activity data have not yet been reduced. However, the release of iodine from the fuel element was measured by means of diffusion probe gamma scans, permitting a comparison of calculated and observed iodine release values. In order to provide fission gas release data for use in this calculation, a CPL-2 fuel rod containing 4% bare kernels was irradiated in the TRIGA King furnace facility at GA, and fractional release (R/B) values for four isotopes of krypton and two of xenon were measured at 1173, 1273, 1373, and 1573 K. The iodine release calculation was carried out in accordance with the method described in Ref. 4-11. In this method, iodine release is treated like xenon release and R/B depends on the square root of half-life. The xenon R/B values measured in the TRIGA tests were used as input to the calculation.

Very satisfactory agreement between calculated and observed iodine releases was found. The calculated release/observed release ratio is 0.8. This good agreement tends to confirm the method used and the assumption that the release of iodine is like the release of xenon. However, further confirmation is needed, such as can be provided by more detailed CPL-2/1 data and particularly Fort St. Vrain data.

TASK 500: FISSION PRODUCT PLATEOUT AND LIFTOFF

Subtask 510: Fission Product Plateout

Cesium Sorption on Incoloy 800

Summary. The results of five cesium adsorption experiments on as-received Incoloy 800 employing a pseudo-isopiestic technique are reported. The experimental temperatures ranged from 673 to 1090 K and the cesium vapor pressure ranged from 10^{-5} to 1 Pa (10^{-11} to 10^{-5} atm). In summary, the results indicate that:

1. Cesium adsorption on Incoloy 800 at constant cesium vapor pressure varies only by a factor of about 10 in the temperature range 673 to 1090 K, with highest loadings obtained at the lower temperatures. This phenomenon is consistent with a physical adsorption mechanism.

2. Clausius-Clapeyron isosteric heats of adsorption, $q = -R[d\ln P/d(1/T)]$, are estimated to be 34 and 18 kcal/mole for cesium loadings of 0.2 and 0.8 $\mu g/cm^2$, respectively.

3. At constant temperature, the amount of cesium adsorbed varies only by a factor of 2 or 3 over the cesium vapor pressure range 10^{-6} to 1 Pa (10^{-11} to 10^{-5} atm). At lower temperatures (<725 K) the surface appears to saturate (i.e., approaches one monolayer surface coverage) in this vapor pressure range.

4. Cesium adsorption is sensitive to surface conditions (i.e., roughness and/or oxidation state) of the alloy. It is believed that this phenomenon contributed to appreciable differences in sorption data from different experiments. Because of these differences, a conclusive set of isotherms cannot be derived from the sorption data.

Introduction. Calculational methods, such as the PAD code (Ref. 4-12) used for predicting plateout distribution in the primary circuit of an HTGR, require as input the adsorption characteristics of condensable fission products on the various alloy components in the primary circuit. The distribution of plateout activity is quite complex and involves circuit geometry, prevailing fluid dynamics, physical and chemical properties of the fission products, and temperature, surface chemistry, and nature of the alloy substrates. The dynamics of plateout depend upon whether contact with the surfaces leads to reversible or irreversible deposition. The fission product plateout studies are aimed at providing the necessary experimental input data in terms of equilibrium adsorption isotherms.

It is generally recognized that, from the view point of shielding design criteria, maintenance, and safety, the most important condensable fission products are the isotopes of cesium and iodine. Other fission products of relatively decreasing significance are the isotopes of tellurium, silver, and strontium. The potential plateout surfaces in terms of various components, fabrication material, and typical surface temperatures during normal operation of a LHTGR are summarized in Table 4-2.

The adsorption characteristics of the important condensable fission products on alloys of HTGR interest are not yet fully understood. In particular, very little is known about the deposition of cesium. A systematic investigation has now begun. The first experiments have been made to study cesium adsorption characteristics on as-received (degreased) Incoloy 800 using a pseudo-isopiestic adsorption technique. Subsequent experiments must then be planned to study the effect of surface alteration by long-term exposures to HTGR helium (with representative impurity levels).

Five experiments on cesium adsorption on Incoloy 800 have been completed. The adsorption temperatures (673 to 1090 K) span the entire range of service temperatures for this material. One experiment on an empty specimen tube made of Inconel 625 is also reported.

Experimental. The pseudo-isopiestic method was described earlier (Ref. 4-13). However, a number of design improvements have been made. The new design incorporates several adsorption furnaces mounted on a rack with a single traveling detector on rails. The detector has a 19 by 19 mm slit and can be positioned under the specimen at each adsorption furnace at any desired time for the measurement of in-situ Cs (tagged with Cs-137) loadings. An isometric view of the adsorption equipment is shown in Fig. 4-10. The reproducibility of the detector position as measured by a standard Cs-137 source was found to be very good. The small slit size over the detector produces a solid angle that includes only the length of the

TABLE 4-2
TYPICAL PRIMARY CIRCUIT COMPONENT (EXCLUDING GRAPHITE)
MATERIALS AND IN-SERVICE SURFACE TEMPERATURES
FOR 3000-MW(t) HTGR

Component	In-Service Surface Temp		Material	Surface Area (m^2)
	Kelvin	°C		
Inlet ducts	∿1048	∿775	Incoloy-800	60
Reheater	913-828	640-555	Incoloy-800	2,580
Central duct to main steam bundle	∿963	∿690	Incoloy-800	1,460
Superheater-2	877-774	604-501	Incoloy-800	3,500
Superheater-1	764-714	491-441	Alloy steel T-22	2,200
Evaporator-2	696-672	423-399	Alloy steel T-22	6,300
Evaporator-1	672-664	399-391	Alloy steel T-22	
Economizer-2	655-604	382-331	Alloy steel T-22	10,200
Economizer-1	604-491	331-218	Carbon steel SA-210-A1	
Circulators	∿623	∿350	Various 400-series steels	520
Upper plenum duct	∿608	∿335	Carbon steel	1,760

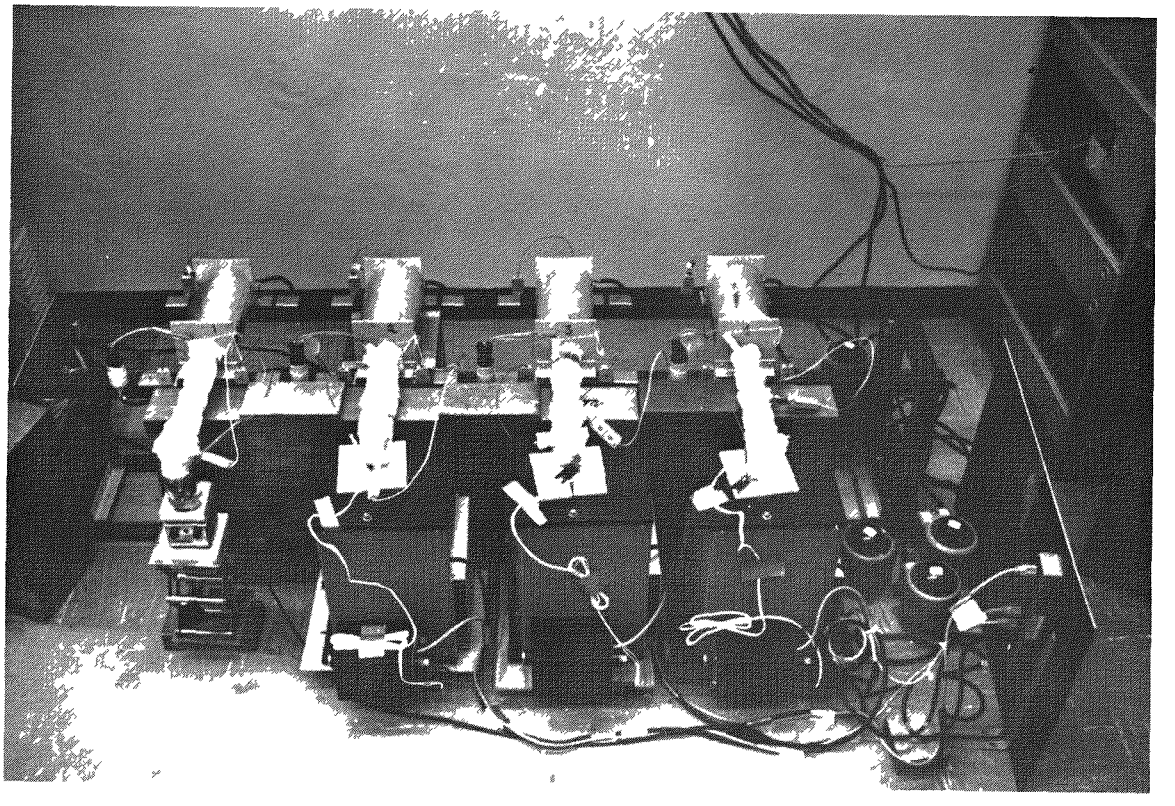

Fig. 4-10. New design of pseudo-isopiestic adsorption assembly

specimen when positioned under the furnace. The adsorption furnaces are mounted more than 380 mm apart so that no cross-interference from specimens in adjacent furnaces during simultaneous runs is produced. The moveable detector system allows easy calibration checks using a standard source of Cs-137. It also avoids overheating the detector [NaI (Tl)] crystal due to extended exposures to radiating furnace heat. Of most importance, the moving detector has increased our experimental capability for simultaneous experiments fourfold. This is significant realizing that one adsorption experiment on the average takes from 3 to 5 months to complete.

The furnaces used for isothermal heating of the specimen are made at our laboratories. These are small in size and yet designed to give at least a 60-mm-long isothermal zone at temperatures to 1273 K. The small size produces the least attenuation of gamma activity.

During an experiment, precautions are taken to clamp the adsorption tube on a small extended portion of the furnace ceramic tube. This avoids any tube movement, and hence specimen movement, during an experiment.

The adsorption tube is made of Inconel 625 with a heli-arc welded cap of the same alloy at the closed end. At the other end the metal portion joins a glass part through a glass - stainless steel seal which is also heli-arc welded. The heli-arc welding provides a clean joint and is done prior to the degreasing and cleaning operation.

Since the adsorption phenomena are very sensitive to surface characteristics of the adsorber (tube and specimen), there was a need to standardize sample pretreatment. The following degreasing and cleaning procedure was rigidly adhered to. The specimen so cleaned was termed "as-received."

Step 1 Two half-hour ultrasonic cleanings with inhibited 30% Vertan-675 (Dow Chemical) solution at ∿333 K (60°C) followed by distilled water rinses.

Step 2 One half-hour ultrasonic degreasing with benzene solvent followed by acetone rinse to dryness.

Step 3 One half-hour ultrasonic mild acid-etching with 50% concentrated HNO_3 at room temperature.

Step 4 Distilled water and acetone rinse to dryness.

The degreased and clean specimen is subsequently handled with care (never with bare hands) and used immediately. Both the specimen and the specimen tube are given the same treatment.

The specimen is then positioned in the specimen tube that already has a glass-metal seal welded at one end. The glass end is then attached to another glass assembly having cesium generator and cesium collector arms (Ref. 4-13, p. 31). Known amounts of calcium metal chips and tracer (Cs-137) tagged cesium chloride are introduced in the generator side and the arm is sealed. The entire assembly is then attached to a high-vacuum system with the tube (containing the specimen) positioned in a furnace. The tube is then evacuated and outgassed at the desired temperature. The completion of the outgassing is indicated by a stable vacuum of $<10^{-5}$ torr. The cesium metal is than generated by carefully heating the (CsCl + Ca) mixture under vacuum, and the cesium is distilled off to the collector arm (Ref. 4-14). After completion of cesium metal collection (∿80% yield), the glass generator arm is removed by melting with a gas torch. The adsorption tube is given a final outgassing to a stable vacuum of 3 to 4 x 10^{-6} torr; it is then sealed from the vacuum system and moved to an adsorption furnace.

At the adsorption furnace, the cesium pool temperature is controlled by a constant-temperature oil bath for obtaining cesium vapor pressures above 4×10^{-4} Pa (4×10^{-9} atm) and by an automatic refrigeration unit for lower vapor pressures (Fig. 4-10). Temperatures of the specimen, the heating tape, and the cesium pool are monitored independently by calibrated Chromel/Alumel thermocouples.

The cesium vapor pressure over the specimen is calculated by first calculating the cesium vapor pressure over cesium from the published data (Ref. 4-14) at the temperature of the cesium pool and then correcting for Knudsen flow characteristics for the difference between the specimen and the cesium pool temperatures (Ref. 4-15).

The Incoloy 800 material used is in the form of a 0.01 mm (0.002 in.) thick metal foil with a roughness factor of $\sim$4.0, which is the ratio of the actual available surface area to the measured geometric surface area. The roughness factor was determined by a Surfanalyzer unit with a fine-point diamond stylus that scanned the sample surface at various positions. The maximum sensitivity of the NBS calibrated Surfanalyzer stylus is 25 nm (1 μin.) of surface deformations.

The Incoloy 800 specimen was received from Ulbrich of California and has a nominal composition of C (0.05), Mn (0.75), Si (0.50), Cr (21.0), Ni (32.5), Ti (0.38), Al (0.38), and the balance Fe in weight percent. The cesium chloride is analytical grade (99.9 to 100% pure) from BDH, and the calcium metal is 99.5% pure from Atomerg Chemetal Company. The radioactive Cs-137 chloride stock solution was obtained from Oak Ridge National Laboratory.

Results and Discussion. The adsorption data for cesium on as-received Incoloy 800 obtained in five different experiments are summarized in Tables 4-3 through 4-5. The data for each experiment are presented in the order in which the conditions (of vapor pressure and specimen temperature) were

TABLE 4-3
CESIUM SORPTION ON AS-RECEIVED (DEGREASED) INCOLOY-800 (FOIL) SPECIMEN WITH SURFACE AREA (GEOMETRIC) OF 464.52 CM^2. SPECIMENS OUTGASSED AT 900 K FOR 48 HOURS. RESULTS FROM EXPERIMENT NO. 2.

Specimen Temp		Cesium Vapor Pressure		Cesium Loading[a] [$\mu g/cm^2$(geom. area)][b]
Kelvin	°C	Pascal	Atm	
673	400	1.3×10^{-2}	1.3×10^{-7}	1.28
773	500	1.4×10^{-2}	1.4×10^{-7}	1.15
873	600	1.4×10^{-2}	1.4×10^{-7}	0.83
988	715	1.5×10^{-2}	1.5×10^{-7}	0.434
1091	818	1.6×10^{-3}	1.6×10^{-8}	0.144
1091	818	3.1×10^{-4}	3.1×10^{-9}	0.091
1091	818	2.8×10^{-2}	2.8×10^{-7}	0.120

[a] Corrected data from Ref. 4-16. See text for details.

[b] Divide by roughness factor of four to convert to absolute area basis.

TABLE 4-4
CESIUM SORPTION ON AS-RECEIVED (DEGREASED) INCOLOY-800 (FOIL) SPECIMENS OUTGASSED AT 900 K FOR 48 HOURS. RESULTS FROM EXPERIMENTS NO. 10 AND 11.

Experiment No.	Specimen Temp		Cesium Vapor Pressure		Cesium Loading [$\mu g/cm^2$(geom. area)](a)
	Kelvin	°C	Pascal	Atm	
10	873	600	3.8×10^{-4}	3.8×10^{-9}	0.490
Surface area (geom.) of 154.84 cm^2	873	600	2.0×10^{-5}	2.0×10^{-10}	0.432
	873	600	1.7×10^{-6}	1.7×10^{-11}	0.361
	873	600	1.1×10^{-2}	1.1×10^{-7}	0.747
	873	600	3.0×10^{-2}	3.0×10^{-7}	0.957
11	973	700	3.6×10^{-4}	3.6×10^{-9}	1.02
Surface area (geom.) of 129.03 cm^2	973	700	2.1×10^{-5}	2.1×10^{-10}	0.437
	973	700	1.7×10^{-6}	1.7×10^{-11}	0.274
	973	700	1.5×10^{-3}	1.5×10^{-8}	0.345
	973	700	8.4×10^{-3}	8.4×10^{-8}	0.368
	973	700	6.4×10^{-2}	6.4×10^{-7}	0.400

(a) Divide by roughness factor of four to convert to absolute area basis.

TABLE 4-5
CESIUM SORPTION ON AS-RECEIVED (DEGREASED) INCOLOY-800 (FOIL) SPECIMENS OUTGASSED AT 600 K FOR 48 HOURS. RESULTS FROM EXPERIMENTS NO. 14 AND 15. BOTH SPECIMENS HAD GEOMETRIC AREAS OF 129.03 CM^2.

Experiment No.	Specimen Temp		Cesium Vapor Pressure		Cesium Loading [$\mu g/cm^2$(geom. area)](a)
	Kelvin	°C	Pascal	Atm	
14	673	400	2.6×10^{-4}	2.6×10^{-9}	0.442
	673	400	1.7×10^{-5}	1.7×10^{-10}	0.384
	773	500	1.9×10^{-5}	1.9×10^{-10}	0.271
	873	600	2.0×10^{-5}	2.0×10^{-10}	0.181
	973	700	2.1×10^{-5}	2.1×10^{-10}	0.074
15	873	600	4.3×10^{-4}	4.3×10^{-9}	0.227
	973	700	4.0×10^{-4}	4.0×10^{-9}	0.091
	873	600	3.1×10^{-4}	3.1×10^{-9}	0.105
	873	600	2.0×10^{-5}	2.0×10^{-10}	0.098

(a) Divide by roughness factor of four to convert to absolute area basis.

changed. Specimens were given 48 hr outgassing under vacuum either at 900 K (experiments 2, 10, and 11) or at 600 K (experiments 14 and 15), as noted. The cesium loadings are given in micrograms per unit geometric area. However, the specimens had a surface roughness factor of 4.0 based on measurements described above on a spare sample of foil. To obtain cesium loadings in $\mu g/cm^2$ (true, or absolute, area), the data presented in Tables 4-3 through 4-5 should be divided by the roughness factor.

A typical adsorption profile showing the rate of in-situ cesium loading on the specimen is shown in Fig. 4-11. The rate of adsorption, i.e., attainment of equilibrium, was generally slow, taking from 15 to 60 days for attainment of steady state at each condition.

The data for an empty Inconel 625 tube are presented in Table 4-6. The equilibrium cesium loadings are given in terms of relative in-situ count rate, and the temperatures relate to the isothermal specimen zone.

The results in general indicate that cesium adsorption on Incoloy 800 involves Freundlich behavior, i.e., a linear relationship between log C (cesium surface concentration) and log P_{Cs} (vapor pressure). This is particularly true for the data from individual experiments (Fig. 4-12). However, the data from different experiments under similar conditions differ appreciably. This is evidenced by the 873 K isotherm data points plotted in Fig. 4-12. The selected data for various adsorption isotherms are plotted in Fig. 4-13.

The dependence of cesium loading on surface temperature [i.e., log C (cesium concentration) versus 1/T] at various constant cesium vapor pressures is shown in Fig. 4-14. The data exhibit a linear relationship in the low surface coverage region and an onset of saturation effect to monolayer coverage at temperatures below 725 K in the experimental vapor pressure range. Theoretical monolayer coverage for our experimental surface is calculated to be $\sim$0.36 $\mu g/cm^2$ (geom.) (assuming 4×10^{14} cesium atoms/cm^2/ monolayer as discussed in Ref. 4-7). Clausius-Clapeyron isosteric heats

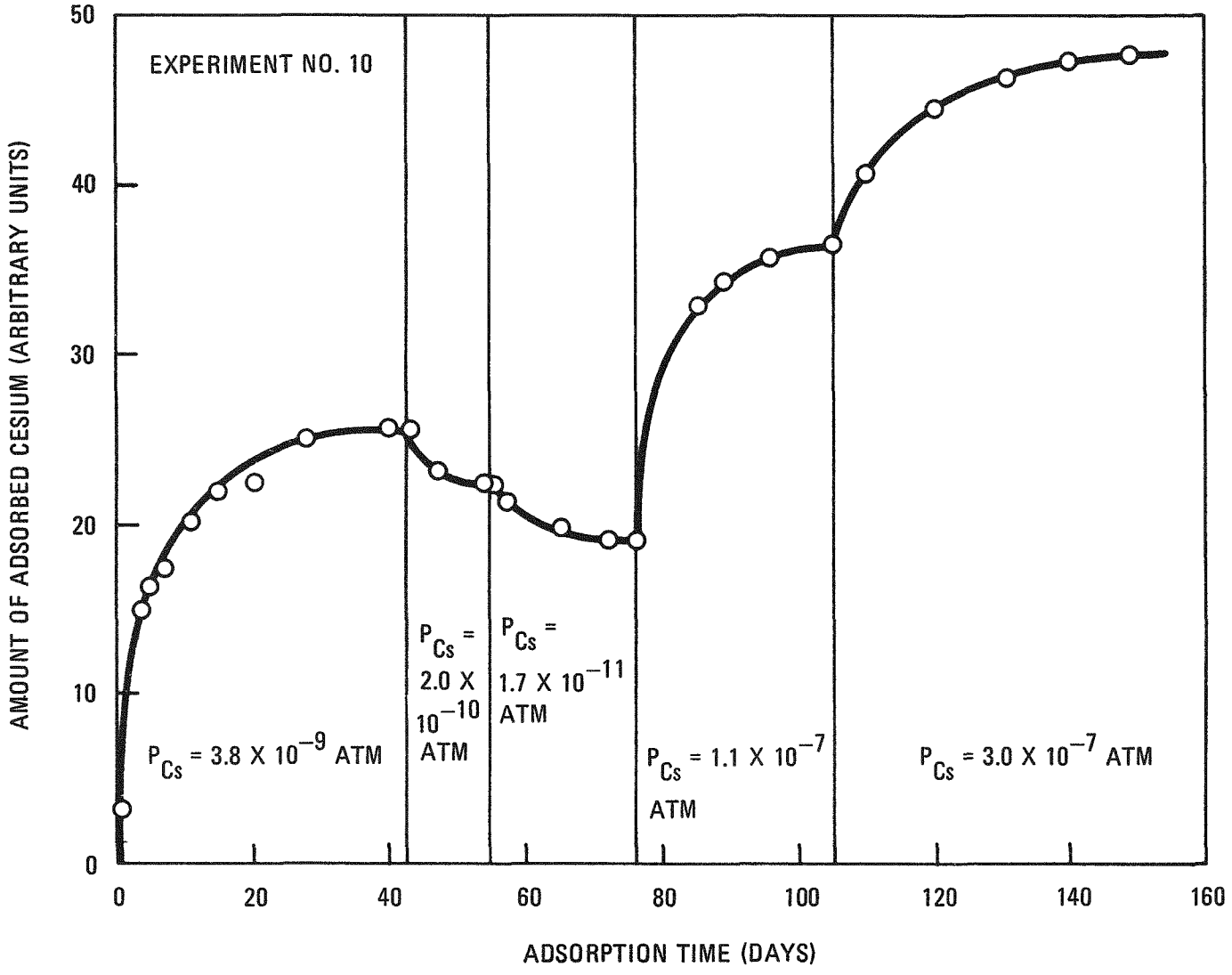

Fig. 4-11. Cesium adsorption on Incoloy 800 (as-received) at 873 K (600°C)

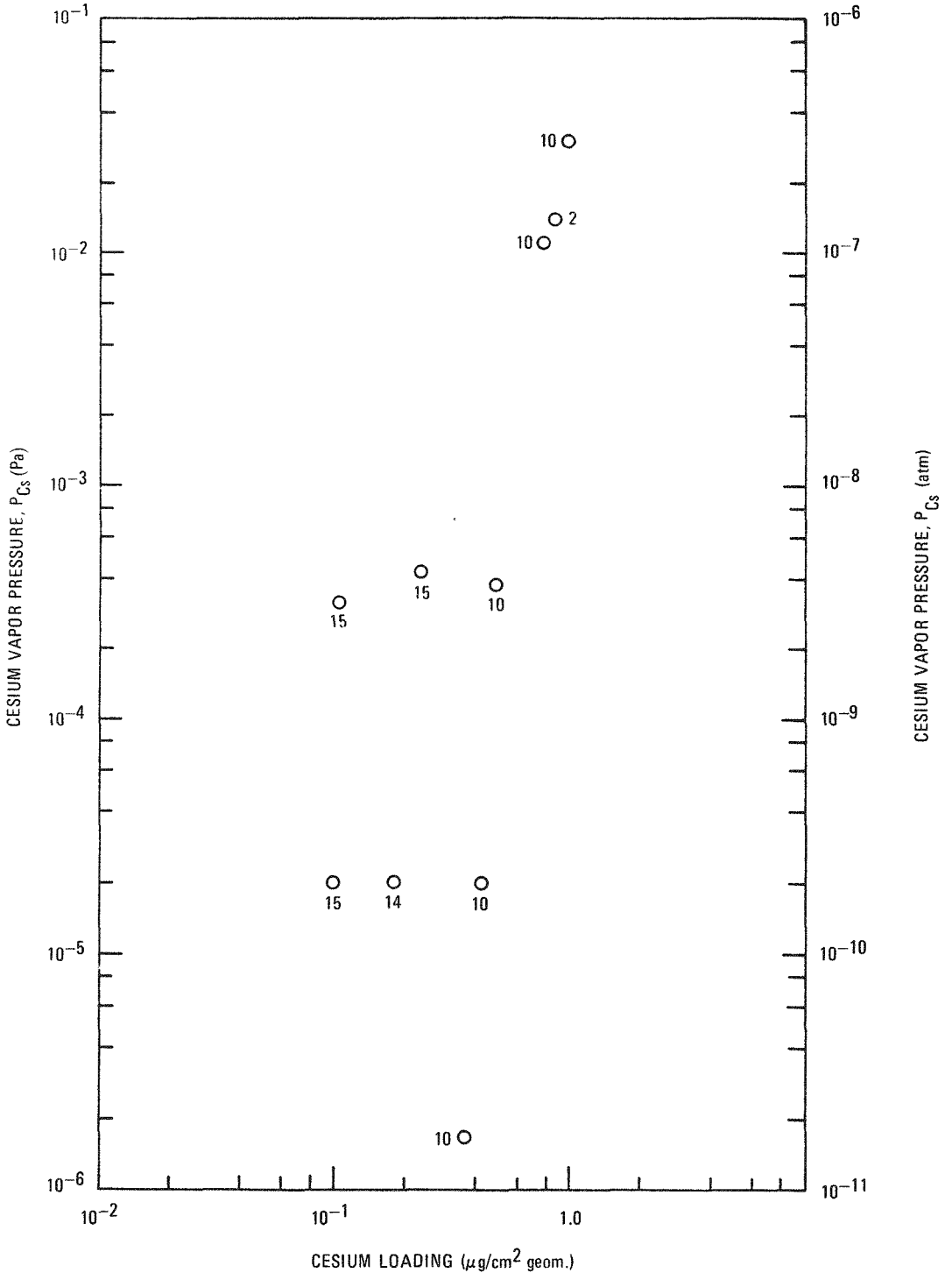

Fig. 4-12. Cesium adsorption isotherm at 873 K for as-received Incoloy 800 in terms of geometric area of a surface with a roughness factor of ∿4.0. The data are derived from four experiments, as indicated by the experiment number by each data point.

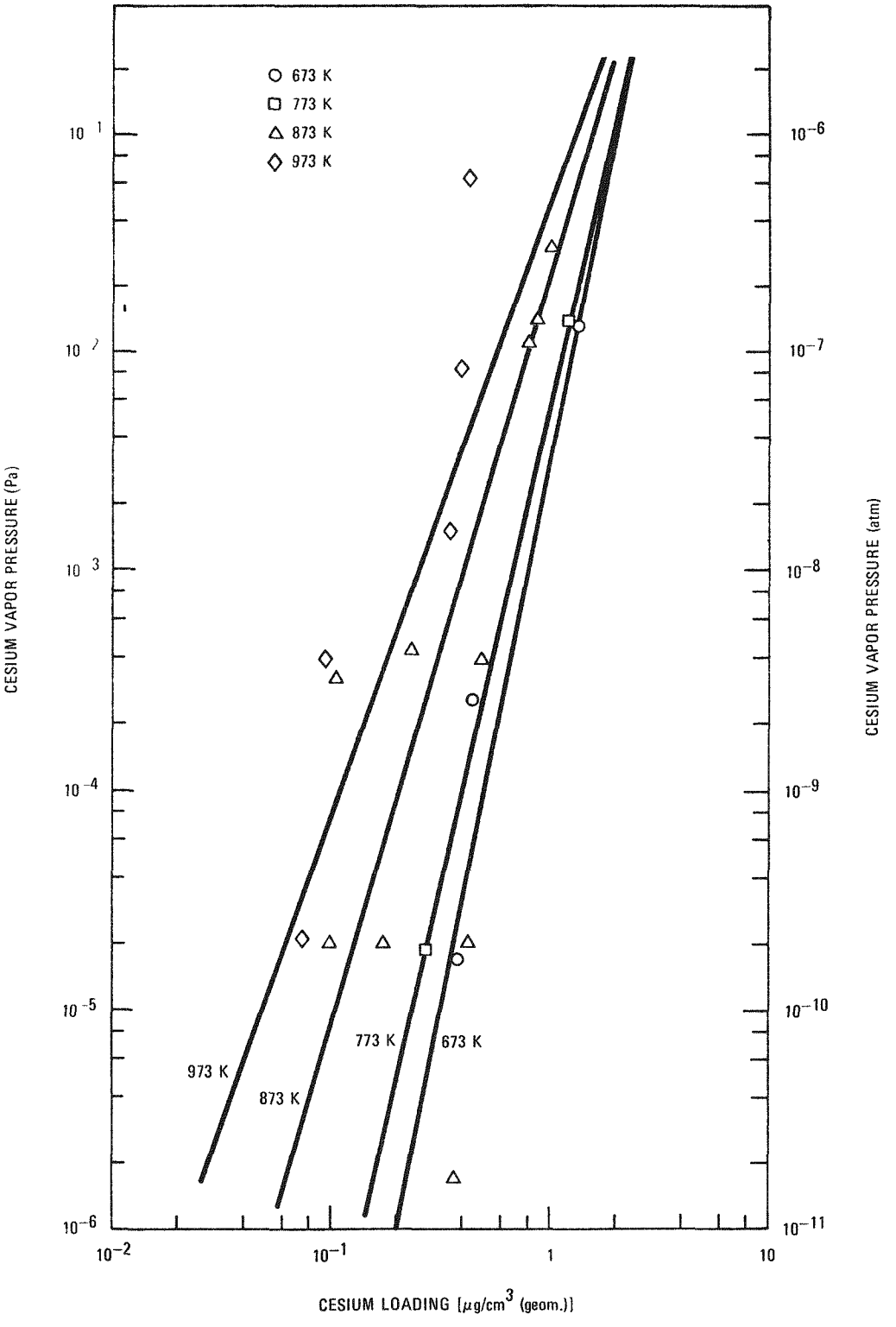

Fig. 4-13. Cesium adsorption isotherms for as-received Incoloy 800. The geometric surface area was used. Data are derived from different experiments.

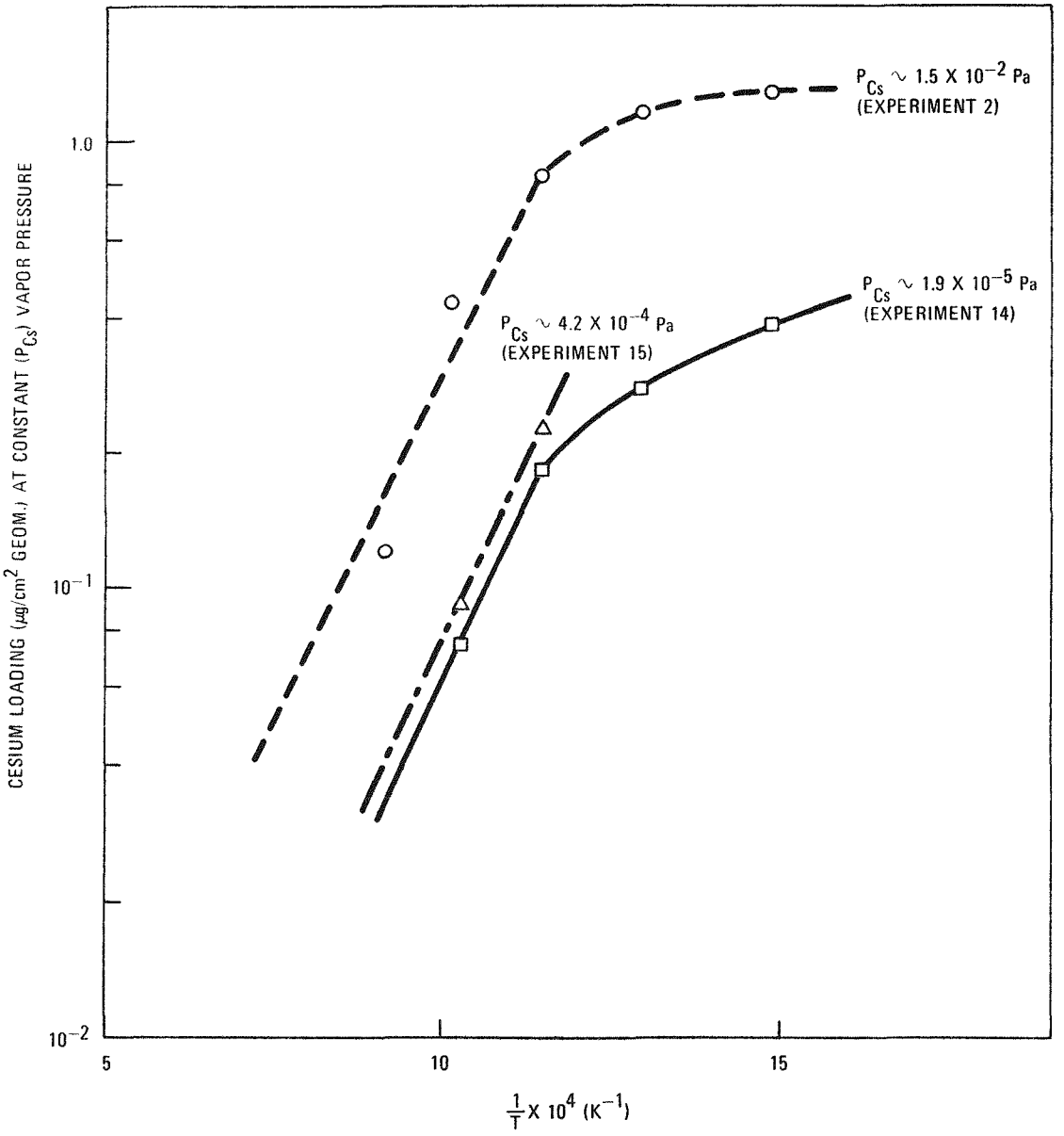

Fig. 4-14. Arrhenius plot for cesium adsorption on as-received Incoloy 800. Data obtained from various experiments as indicated.

of adsorption, $q = -R[d\ln P/d(1/T)]$, using the data for various isotherms in Fig. 4-13 are estimated to be 34 and 18 kcal/mole for cesium loadings of 0.2 and 0.8 $\mu g/cm^2$, respectively.

The data indicate that the overall variation of cesium loadings at any pressure studied lies within a factor of 10 when temperatures are changed from 673 to 1090 K. On the other hand, at a constant temperature in a given experiment, the change in cesium vapor pressure by several orders of magnitude (10^{-5} to 1 Pa) produces only a factor of three change in cesium loadings. These results are significant in that they represent the maximum variation in cesium deposition for plateout calculations under reactor conditions using adsorption isotherms.

The adsorption data need to be verified, primarily because some yet unexplained effects were observed in these experiments. For example, the reasons are not known for the hysteresis effect observed in experiment 11 where the specimen (in a vacuum sealed tube) showed a decrease in adsorption after prolonged heating at high temperatures. This effect was also evident in the empty tube experiment (Table 4-6).

The sorption data appeared to be affected by the vacuum baking conditions prior to sealing the system. Lower cesium loadings were found for lower baking temperatures. This behavior is evident in the comparison of data in Tables 4-3 and 4-4 with those in Table 4-5 and is contrary to the effect of vacuum baking observed by Milstead and Zumwalt (Ref. 4-7) for cesium adsorption on 304 stainless steel using the same technique. However, it should be noted that the outgassing temperatures in our experiments are believed to be too low to cause a significant "baking" effect.

The scatter in cesium adsorption data, in particular, differences in data from different experiments, reflect the difficulty of typical adsorption experiments in reproducing a representative surface. Since, the

TABLE 4-6
DATA FOR CESIUM ADSORPTION ON EMPTY INCONEL-625 SPECIMEN TUBE IN TERMS OF RELATIVE IN-SITU CESIUM COUNT RATE. RESULTS FROM EXPERIMENT NO. 9. THE TEMPERATURES GIVEN ARE FOR ISOTHERMAL SPECIMEN PORTION OF THE TUBE. CESIUM SPECIFIC ACTIVITY EQUIVALENT TO THAT FOR EXPERIMENTS NO. 2, 10, AND 11. TUBE OUTGASSED AT 900 K FOR 48 HOURS.

Specimen Temp		Cesium Vapor Pressure		Relative Cs Activity (counts/10 min)
Kelvin	°C	Pascal	Atm	
573	300	1.1×10^{-3}	1.1×10^{-8}	14,148
773	500	1.2×10^{-3}	1.2×10^{-8}	14,850
1098	825	1.5×10^{-3}	1.5×10^{-8}	1,720
1098	825	5.2×10^{-4}	5.2×10^{-9}	1,473
1098	825	2.5×10^{-2}	2.5×10^{-7}	1,961
1098	825	4.2×10^{-4}	4.2×10^{-9}	1,408
973	700	3.6×10^{-4}	3.6×10^{-9}	1,688
873	600	4.3×10^{-4}	4.3×10^{-9}	1,778
773	500	4.0×10^{-4}	4.0×10^{-9}	2,001
1098	825	3.9×10^{-3}	3.9×10^{-8}	1,532
973	700	3.6×10^{-3}	3.6×10^{-8}	1,626
1098	825	1.8×10^{-2}	1.8×10^{-7}	1,698

degreasing and cleaning procedure was strictly adhered to, the scatter could be due to varying effects on in-situ surface baking in prolonged experiments. Another reason for the scatter could be in the method used for estimating in-situ activity due to cesium adsorbed on the specimen relative to that on the specimen tube. The roughness factor of the Inconel tube material has not been measured but is estimated to be $\sim$40, so that a small tube portion could contribute significantly to in-situ cesium loadings.

Early in this work it was felt adequate to conduct a simultaneous empty tube experiment so that the tube contribution could be directly subtracted from the tube plus specimen data. This approach was used in reporting the data from experiment 2 in Ref. 4-16. However, later a number of inadequacies of this approach were discovered, examples being the irreproducibility of important parameters such as the tube surface conditions due to welding effects, the detection geometry and hence in-situ counting efficiency, and the cesium metal specific activity. As a result the method of calculating in-situ activity due only to the specimen had to be changed. In the current method, which was used to obtain the reported data, the natural background count rate is subtracted first from all equilibrium count rates to give the tube plus specimen contribution. At the end of the experiment the in-situ count rate is measured with and without the specimen (the tube is cut and the specimen removed). The ever-constant laboratory background is subtracted, and from the data so obtained, a fraction indicating the ratio of count rate due to specimen and that due to specimen plus tube is calculated. The equilibrium count rate due to the specimen plus tube at various conditions is multiplied by this ratio to obtain the in-situ count rate due only to the specimen. This method, although more appropriate than the earlier method, is not yet adequate. It inherently assumes that the specimen and the tube material have the same adsorption characteristics under all conditions of the experiment. To make the tube effect less significant would require a specimen with relatively large surface area. Large surface area specimens

were tried in the earlier experiments. However, these experiments showed very slow adsorption rates and were thus unusually long. Subsequently small specimens were used. In the experiments reported, depending upon the available surface area of the specimen, contributions due to the tube ranging from 15 to 40% were observed.

Due to the difficulties mentioned above, including scatter in the data and differences in data from one experiment to another, a set of conclusive isotherms cannot yet be developed for cesium adsorption on as-received Incoloy 800. More experiments are needed, and the data need to be compared with the CEA data derived from measurements associated with the code validation work on CPL-2/1 (see Subtask 220). The data derived from experiments 14 and 15 should be the most reliable since they were taken at a point when the equipment design and its performance were best.

Conclusions. Conclusions based on the present data are as follows:

1. The adsorption of cesium on as-received Incoloy 800 appears to follow an adsorption mechanism of the Freundlich type. Clausius-Clapeyron isosteric heats of adsorption are estimated to be 34 and 18 kcal/mole for cesium surface loadings of 0.2 and 0.8 $\mu g/cm^2$ (geom.), respectively.

2. At constant pressure (within 10^{-6} to 1 Pa) the cesium loadings change within a factor of 10 in the temperature range 673 to 1090 K.

3. At constant temperature (within 673 to 1090 K) the cesium loadings vary little with changes in cesium vapor pressure.

4. This effect in (3) appears to be due to surface saturation, i.e., at or near monolayer coverage in the ranges studies. This is particularly true at temperatures <725 K.

5. The adsorption characteristics are sensitive to changes in surface conditions which would also explain the hysteresis effect noticed in a few experiments.

6. More experiments are needed to conclusively define cesium adsorption characteristics on Incoloy 800.

The reproducibility of the data can be improved by adequately characterizing the surface and by conducting short-duration single-point tests (i.e., one data point for each experiment). This, however, would require several-fold more experiments.

It would be appropriate to conclude that future adsorption experiments should be selectively done on specimens that have been given long-term exposures to helium containing representative impurity levels. The exposures should be done at actual service temperatures. The pretreated specimen so prepared may be less sensitive to further changes in surface characteristics, and the data would be more directly applicable to HTGR plateout distribution calculations.

REFERENCES

4-1. "HTGR Fuels and Core Development Program Quarterly Progress Report for the Period Ending May 31, 1975," ERDA Report GA-A13444, General Atomic, June 30, 1975.

4-2. "HTGR Fuels and Core Development Program Quarterly Progress Report for the Period Ending August 31, 1975," ERDA Report GA-A13592, General Atomic, September 30, 1975.

4-3. Jensen, D. D., et al., "Planning Guide for Validation of Fission Product Transport Codes," ERDA Report GA-A13386, General Atomic, April 15, 1975.

4-4. "HTGR Fuels and Core Development Program Quarterly Progress Report for the Period Ending February 29, 1976," ERDA Report GA-A13804, General Atomic, March 31, 1976.

4-5. Vanslager, F. E., and L. D. Mears, "PAD, A Computer Code for Calculating the Plateout Activity Distribution in a Reactor Circuit," Gulf General Atomic Report GA-10460, January 1971.

4-6. Milstead, C. E., W. E. Bell, and J. H. Norman, "Deposition of Iodine on Low Chromium-Alloy Steel," Nucl. Appl. Technol. 7, 361 (1969).

4-7. Milstead, C. E., and L. R. Zumwalt, "Cesium Deposition on Stainless Steel," General Atomic Division of General Dynamics Report GA-7433, September 1, 1966.

4-8. Alberstein, D., P. D. Smith, and M. J. Haire, "Metallic Fission Product Release from the HTGR Core," General Atomic Report GA-A13258 (GA-LTR-20), May 15, 1975.

4-9. Forutanpour, B., and B. Roos, "FIPERX, A Fortran Program for the Solution of One-Dimensional Linear and Non-Linear Diffusion Problems," USAEC Report GA-9704, Gulf General Atomic, September 1969.

4-10. "HTGR Accident Initiation and Progression Analysis Status Report - AIPA Fission Product Source Terms," ERDA Report GA-A13617, Volume V, General Atomic, February 1976.

4-11. Haire, M. J., and D. W. McEachern, "Gaseous Radioactivity Levels in the Primary Coolant of an HTGR," General Atomic Report GA-A12946 (GA-LTR-14), October 1, 1974.

4-12. Hansen, D. L., "Results of the General Atomic Deposition Loop Program," ERDA Report GA-A13140, General Atomic, April 1, 1976.

4-13. "GCR Safety Program Quarterly Progress Report for the Period Ending December 31, 1974," USAEC Report GA-A13280, General Atomic, February 14, 1975.

4-14. Hultgren, R. (ed.), Selected Values of the Thermodynamic Properties of Elements, American Society for Metals, Metals Park, Ohio (1973), p. 146.

4-15. Rapp, R. A. (ed.), Techniques of Metals Research, Volume IV, Physico-chemical Measurements in Metals Research, Part I, Interscience Publishers, New York (1970), Chapter 2C, p. 146.

4-16. "GCR Safety Program Quarterly Progress Report for the Period Ending June 30, 1975," ERDA Report GA-A13513, General Atomic, July 31, 1975.

6. HTGR ALTERNATIVE FUEL SYSTEMS STUDIES
189a NO. SU047

SUMMARY

The primary effort under Task 6 in this reporting period was related to the preparation and publication of the Fuel Development Plans for Alternate Fuel Systems (Ref. 6-1). Other analysis efforts involved the completion of preliminary calculations of fuel temperatures, core pressure drop, and fuel element stresses for alternative fuel block designs considered for high conversion applications. The results of these calculations will be included in the final topical report on high conversion HTGR designs. In addition, the evaluation of alternate strategies for U-235 recycle was expanded to include estimates of waste storage and ultimate waste disposal cost tradeoffs for the various strategies considered. The effects of throughput changes on the reprocessing and refabrication unit costs have been considered in this newer evaluation.

FUEL DEVELOPMENT PLANS

Introduction

An alternate fuel systems study was funded by ERDA in FY-76 under Task 6 of the HTGR Fuel and Core Development Program. The major emphasis of Task 6 is to evaluate high conversion HTGRs both with the standard fuel element and with modified fuel elements capable of containing significantly higher thorium loadings. In addition, studies have been performed under this task to evaluate plutonium-fueled HTGRs and to evaluate recycle strategies which would allow simplifications and cost reductions in the reprocessing and refabrication plant designs. Specifically, fuel development plans for the following were prepared:

1. Achieving higher conversion ratio with the standard HTGR fuel element.

2. Achieving still higher conversion ratio with modified fuel elements.

3. Plutonium-fueled HTGRs.

4. Simplifying the reprocessing-refabrication plant design.

Significant results obtained from Task 6 studies to date, as well as other events occurring in FY-76, have affected the relative importance, and thus the scope, of the various development plans prepared. The significant study conclusions and events which have had a bearing on these plans are:

1. The extremely rapid increase in the price of U_3O_8 and the resultant fuel cycle cost benefit to be gained by increasing conversion ratio to reduce U_3O_8 requirements.

2. The potential performance benefits that accrue to higher conversion ratio designs.

3. The realization that very significant conversion ratio increases are possible with the standard HTGR fuel element if thinner coated fertile particles are developed.

4. The change in the HTGR commercial stance and the resultant timing requirements for certain developments.

5. The cancellation by EPRI of the contract for core design studies of plutonium-fueled HTGRs.

As a result of the above, and other conclusions discussed in Ref. 6-1, the major emphasis has been on the development plan for achieving high

conversion in the standard HTGR fuel block design. This development is clearly realizable and yields large benefits for minimum development time and costs. This development, in addition to further conserving resources, would improve both the performance and the fuel cycle costs of the HTGR.

In the longer range, the development of alternate block designs is also important for further increasing the HTGR conversion ratio. Many alternate fuel rod and/or block designs have been investigated. Three alternate fuel block concepts have been singled out as having good long-term potential for significantly enhancing the conversion ratio. These elements offer substantially higher fuel volumes per block than the standard eight-row block design.

However, the additional available fuel volume in these blocks, if loaded with reference fuel particles, is less than that which could be loaded into the standard block if silicon-alloyed BISO particles were developed. Thus, these elements would only be developed and used in conjunction with the silicon-alloyed BISO fertile particles. Much detailed fuel management and core performance analysis work remains to be done before the reasonable choice of element could be made on which to base a large-scale fuel development program. The development program prepared emphasizes the analysis effort over the next few years that would be required before a final choice of fuel element configuration should be pursued to final development.

The rapidly rising costs of enriched uranium have also altered the relative potential attractiveness of alternate U-235 recycle strategies utilizing simplifications in reprocessing/refabrication plant design. The most promising such strategy involves recycle of U-235 from only the first two initial core segments along with the U-233 produced in those segments. In this strategy, the U-235 from the third and subsequent segments was not recycled, but retired. Even though potentially large plant cost savings

would result from this strategy, they are increasingly overshadowed by the fuel cycle cost increase resulting from not recycling the U-235 from the third and subsequent segments.

Two additional considerations affect the desirability of choosing alternate U-235 recycle strategies. First, there is an increasing necessity to recycle the residual U-235 from higher conversion ratio designs. Second, the total U-236 penalty is lower in high conversion designs and thus there is less incentive to purge out the U-236. These two considerations result in the conclusion that single particle fuel systems, with continuous or long-term U-235 recycle, should be evaluated as a potential means for obtaining reprocessing/refabrication plant cost savings. Analytical studies of this concept makes up the bulk of the development program outlined.

The EPRI-supported core design studies of plutonium-fueled HTGRs was terminated by EPRI in January 1976. This work was about one-fourth completed at the time of cessation. The plutonium development program prepared is for the completion of the analysis work scope that was left unfinished from the EPRI study. The final conclusion from that work would be required well in advance of starting the large-scale fuel materials development that would be required for the commercialization of plutonium-burning HTGRs.

In summary, the development plans prepared emphasize the near-term benefits of gaining higher conversion ratio (0.80 to 0.90) with the standard HTGR fuel element. An important part of this strategy is the development of silicon-alloyed BISO fertile particles. The other three development plans contain the near-term, i.e., 2 to 3 year supportive developments, required for analyzing alternate elements, Pu feed, and simplified processing. A summary of the plan for achieving high conversion in the standard element is given in the following section.

High Conversion Ratio with Standard HTGR Fuel Element

Resource Utilization and Fuel Cycle Cost Savings

The primary benefit in developing higher conversion ratio HTGRs is the national resource savings that results. Studies performed to date under Task 6 on about fifteen different designs show that significant reductions in both U_3O_8 and enrichment are possible if higher conversion HTGR designs are developed.

The secondary benefits for developing higher conversion HTGR designs lie in the areas of improved fuel cycle costs and improved HTGR performance characteristics. The rapidly escalating costs of U_3O_8 feed uranium have significantly increased the economic incentive to develop higher conversion designs. In the 7-month interval since the Task 6 studies were started, the commercial price of uranium has increased from \$55/kg (\$25/lb) of U_3O_8 to more than \$77/kg (\$35/lb).

A very important consideration for determining the optimum conversion design is the assumed rate of marginal U_3O_8 cost (price) increase due to future scarcity of this resource. To quantify this effect, escalated 30-year levelized fuel cycle costs have been calculated for PWRs and a variety of alternate high gain HTGR designs. The relative escalated fuel cycle cost results from this study were shown in Fig. 6-5 of Ref. 6-2. From these results it was seen that the minimum cost HTGR design and conversion ratio is significantly modified by the assumed rate of U_3O_8 scarcity related cost escalation. At 6%/year, typical of current estimates, the optimum HTGR design is characterized by a reduced power density (6.5 to 7.5 MW/m^3) and a heavy thorium loading (C/Th = 150).

At very heavy thorium loadings e.g., C/Th = 100, the initial core inventory requirements are very high, and such cycles result in relatively poor initial core fuel utilization which is reflected in the fuel cycle

cost. Preliminary investigations of these cycles show that the initial core and early reload performance can be significantly improved by increasing the initial core effective C/Th ratio as well as the initial core cycle length.

Performance Improvement

Potentially significant core performance benefits result from increasing the thorium loading and reducing the power density. Both changes result in reduced fuel temperatures, reduced fuel burnup, and reduced core pressure drop, i.e., higher plant thermal efficiency. Such performance improvements may be required to achieve reliable process heat HTGR systems. This potential optimum design characteristic has commonality between steam cycle and process heat HTGRs which needs further study and evaluation.

An increased thorium loading reduces the reload region peaking factor (RPF) in freshly loaded fuel. Thus, for a specified power density, the highest powered refueling region, i.e., the region of maximum RPF, determines the core pressure drop since the flow orifice valve is wide open in that region and partially closed in all other regions. For a given RPF, the core pressure drop is approximately proportional to the square of the average core power density. Thus, increasing the thorium loading and/or reducing the core power density lead to reduced core pressure drop, reduced fuel temperatures, and higher thermal efficiency.

For designs utilizing lower average core power density, an attractive potential design modification may be to increase the thorium loading by increasing the fuel rod diameter at the expense of the coolant hole diameter while maintaining a constant fuel-coolant graphite web thickness. Thus, potential conversion ratio increases can be traded off against fuel temperature and core pressure drop to determine overall optimum designs for different performance limits and/or fuel cycle economic parameters.

Figure 6-1 shows a typical result in which it was assumed that the fuel pin diameter was allowed to increase in designs of 6 and 7 MW/m^3 power density until the core pressure drop at the lower power density equals the reference pressure drop for the reference power density (8.4 MW/m^3). The reference particle design packing characteristics were assumed in obtaining these results.

Thorium Loading

The maximum attainable thorium loading per fuel element is a strong function of the overall coating thickness required on the fertile particle. The advanced Si-alloyed coatings display higher strength than the pyrocarbon coatings used in the reference fertile particle design. Thus, thinner coatings could be used in such advanced particle designs which would allow higher thorium loadings to be achieved. The required coating thickness is not now known, but would be determined in the materials development program.

For purposes of analysis, three such designs have been considered. These designs, designated as advanced BISO-I, -II, and -III, have total coating thicknesses of 125, 100, and 75 μm, respectively. The thinnest coating design, i.e., the BISO-III particle, is calculated to have about the same coating strength as the reference pyrocarbon coated fertile particle. Table 6-1 lists the particle parameters for the reference particle design and the three advanced designs considered.

Single mixed-oxide particle systems having the same coating thicknesses as the advanced designs given above have also been evaluated. Such single particle designs allow even higher thorium loadings which would further increase the attainable conversion ratio by about 0.05 to 0.10 over and above the resultant U-236 neutronic penalty associated with the single particle systems.

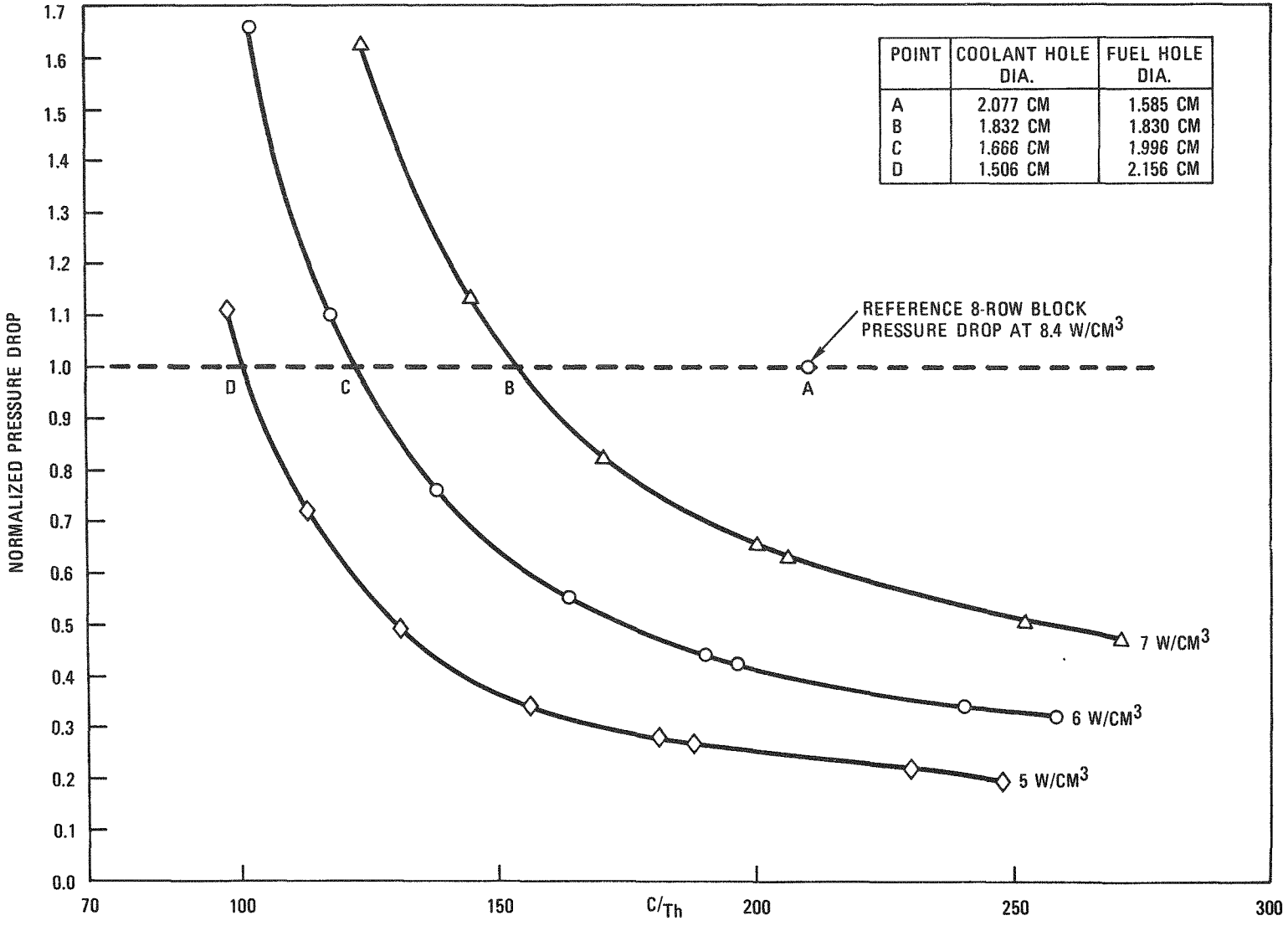

Fig. 6-1. Attainable C/Th ratio for increasing fuel rod diameter at reduced power density

TABLE 6-1
ADVANCED BISO FERTILE PARTICLE DESCRIPTION

Particle System	Particle Parameters				
	Kernel Diameter (μm)	Buffer Thickness (μm)	Outer Coating Thickness (μm)	Total Coating Thickness (μm)	Kernel Volume Fraction[a]
Reference TRISO-BISO	305 (TRISO) 500 (BISO)	50 85	100 75	150 160	0.128 0.227
Advanced BISO-I	500	60	65 (Si-PyC)	125	0.274
Advanced BISO-II	500	50	50 (Si-PyC)	100	0.364
Advanced BISO-III	500	40	35 (Si-PyC)	75	0.477

[a] The fraction of total particle volume taken up by the kernel volume.

At relatively high conversion ratios, there is less incentive to limit U-236 buildup and a single particle design would look promising, particularly for its potential for allowing reprocessing/refabrication plant design simplifications. The conversion ratio above which a single particle design would look attractive needs to be determined.

The attainable thorium loading and conversion ratio for 4-year annual designs at power densities of 6, and 8.4 MW/m^3 is shown in Tables 6-2 and 6-3 for the advanced particle designs described above. The reference HTGR fuel rod and fuel element configurations were assumed. A particle packing fraction limit of 60% was assumed. The relative core pressure drop for each case is also given. Table 6-4 shows the same information except that it has been assumed that the fuel rod diameter is allowed to increase to the indicated values until the core pressure drop is the same for each design considered. The economic, conversion ratio, and performance tradeoffs between the various design alternatives indicated from these results need to be determined and this is included as a separate task in the development program.

From the results shown in Tables 6-2 through 6-4, it is seen that very significant conversion ratio increases are possible with the standard eight-row fuel block design. This is particularly true for the combination of increasing the fuel rod diameter at reduced power density coupled with the packing characteristics of the BISO-III fertile particle.

The results shown are for 4-year, annually refueled HTGRs. The corresponding conversion ratios for semiannual refueling would be 0.03 to 0.05 higher than the indicated values for annual refueling.

Objectives and Work Scope Description

The overall development plan for achieving high conversion ratio with the standard HTGR fuel block design has been divided into two major categories: the Fuel Cycle Evaluation Plan and the Materials Development Plan.

TABLE 6-2
HIGH CONVERSION PARAMETERS FOR DIFFERENT FUEL PARTICLE SYSTEMS, 6 MW/m^3 POWER DENSITY
(Reference Fuel Rod and Fuel Block Design)

Particle System	Thorium Loading [MT/MW(e)]	C/Th Limit	Effective Conversion Ratio[a]	Region Peaking Factor, RPF	Normalized At-Power Pressure Drop[b]
Present Reference TRISO-BISO	0.052	192	0.78	1.34	0.44
Present TRISO BISO-I	0.065	151	0.80	1.26	0.38
Present TRISO BISO-II	0.075	131	0.84	1.22	0.37
Present TRISO BISO-III	0.088	113	0.87	1.18	0.34
Mixed Th/U All BISO-I	0.088	115	0.84	1.19	0.35
Mixed Th/U All BISO-II	0.111	90	0.89	1.14	0.32
Mixed Th/U All BISO-III	0.143	70	0.93	1.10	0.30

[a] Including the negative neutronic effect on conversion ratio of absorption by Si and the mixing of U-236 with bred U-233 and recycle U-235 in the mixed Th/U all-BISO systems.

[b] Pressure drop normalized to the case of 8.4 MW/m^3, C/Th = 210 at equilibrium reload. Effect of region peaking factor (RPF) included.

TABLE 6-3
HIGH CONVERSION PARAMETERS FOR DIFFERENT FUEL PARTICLE SYSTEMS
8.4 MW/m^3 POWER DENSITY
(Reference Fuel Rod and Fuel Block Design)

Particle System	Thorium Loading [MT/MW(e)]	C/Th Limit	Effective Conversion Ratio[a]	Normalized At-Power Pressure Drop[b]
Present reference TRISO-BISO	0.0328	210	0.69	1.00
Present TRISO BISO-I	0.0414	170	0.70	0.89
Present TRISO BISO-II	0.0466	150	0.74	0.84
Present TRISO BISO-III	0.0517	135	0.77	0.80
Mixed Th/U All BISO I	0.0535	130	0.75	0.79
Mixed Th/U All BISO II	0.0690	100	0.82	0.72
Mixed Th/U All BISO III	0.0862	80	0.87	0.67

(a) Including the negative neutronic effect on conversion ratio of absorption by Si and the mixing of U-236 with bred U-233 and recycle U-235 in the mixed Th/U BISO systems.

(b) Pressure drop normalized to the case of 8.4 MW/m^3, C/Th = 210 at equilibrium reload. Effect of region power peaking (RPF) is included.

TABLE 6-4
HIGH CONVERSION PARAMETERS FOR EQUAL PRESSURE DROP FUEL ELEMENTS
6 MW/m^3 POWER DENSITY
(Coolant Hole Diameter = 17 mm, Fuel Hole Diameter = 19.92 mm, Modified 8-Row Block)

Particle System	Thorium Loading [MT/MW(e)]	C/Th Limit	Effective Conversion Ratio	Region Peaking Factor	Normalized At-Power Pressure Drop
Present reference TRISO-BISO	0.076	130	0.86	1.22	1.00[(a)]
Present TRISO BISO-I	0.093	105	0.86	1.17	0.92
Present TRISO BISO-II	0.103	95	0.89	1.15	0.89
Present TRISO BISO-III	0.117	85	0.91	1.13	0.86
All BISO-I	0.126	80	0.89	1.12	0.84
All BISO-II	0.154	65	0.93	1.09	0.80
All BISO-III	0.200	50	0.95	1.06	0.75

(a) Based on increasing fuel rod diameter while decreasing coolant hole diameter until the pressure drop at 6 MW/m^3 equals the reference pressure drop at 8.4 MW/m^3 and C/Th = 210.

The former plan includes five major tasks and the latter six. The major tasks described for each plan are:

Fuel Cycle Evaluation Plan

Task I Resource optimization and initial core inventory reduction strategy studies.

Task II Evaluation of core performance and fuel cycle economic tradeoffs with increasing conversion ratio.

Task III Evaluation of optimum conversion ratio for varying economic and resource availability assumptions.

Task IV Determination of core physics characteristics and control requirements for high conversion designs.

Task V Cost-benefit evaluations of high conversion designs at the Hanford Engineering Development Laboratory (HEDL).

Materials Development Plan

Task I Postirradiation evaluation of the performance of silicon-alloyed-pyrocarbon coated fertile particles irradiated in capsule HB-2.

Task II Silicon-alloyed-pyrocarbon coating process development.

Task III Scaleup of the silicon-alloyed-pyrocarbon coater the production size.

Task IV Full fluence irradiation qualification test for silicon-alloyed-pyrocarbon coated fertile particle designs selected on the basis of HB-2 results.

Task V Irradiation proof test of the optimum coating design selected on the basis of results obtained under Task IV.

Task VI Reprocessing study of silicon-alloyed-pyrocarbon coated fertile particles.

Fuel Cycle Evaluation Plan. The objectives and work scope for the five tasks of the Fuel Cycle Evaluation Plan are given below. The manpower and cost estimates for these tasks are given in Table 6-5.

Task I - Resource Optimization and Initial Core Inventory Reduction Strategy Studies

1. Objectives: Develop fuel management and core design strategies which optimize the resource savings, fuel utilization, and fuel cycle flexibilities of high conversion HTGRs. Determine promising fuel management strategies for reducing the initial core inventory requirements for high conversion ratio designs. Determine the optimum initial core and approach to equilibrium reload refueling frequency which yields the minimum cumulative U_3O_8 requirements and minimum fuel cycle costs for selected performance limits. Define the potential short- and long-term resource saving strategies which appear to be possible by varying the reload interval C/Th ratio and refueling frequency, i.e., converting from annual to semiannual refueling. Determine the 5 to 10 year makeup fuel requirement reductions possible by successively reducing the reload segment thorium loading in order to "burn out" the high U-233 inventory built into, and recovered from, earlier high conversion designed cycles.

2. Work Scope: Zero-dimensional, and where necessary, two-dimensional diffusion and fuel depletion calculations will be

TABLE 6-5
COSTS FOR FUEL CYCLE EVALUATION PLAN - STANDARD ELEMENT

Task	Allocation	CY-76	CY-77	CY-78
I	Manpower (man-years)	0.1	1.25[a]	
	Computer ($ x 10^3)	1.0	10.00	
II	Manpower (man-years)		0.50	0.50
	Computer ($ x 10^3)		5.00	5.00
III	Manpower (man-years)		0.70	0.10
	Computer ($ x 10^3)		5.00	0
IV	Manpower (man-years)		0.50	
	Computer ($ x 10^3)		4.00	
V	Manpower (man-years)	0.2	0.70[b]	0.70
	Computer ($ x 10^3)	2.0	5.00	5.00

[a] Includes 5 man-months under Task 8 in FY-77.

[b] Under Task 8 in FY-77

performed to determine fuel loading and core physics characteristics, as well as fuel cycle costs, for the following high conversion design strategy studies:

a. For initial core and transition reload optimization, determine the benefits and design modifications needed for minimizing initial core inventory requirements. For selected equilibrium thorium loadings and conversion ratio, determine the allowable reduction in the average initial core thorium loading to yield minimum initial core inventories consistent with acceptable early reload peaking factor limits. Evaluate combinations of initial core thorium reductions and initial core and transition reload interval variations to minimize cumulative U_3O_8 requirements and reload power peaking factors. From two-dimensional depletion calculations, determine the benefits of varying the C/Th and C/U ratios in the four initial core segments for achieving the above benefits.

b. Define the fuel segment distributions, the optimum C/Th ratio, and the fuel resource requirements and savings for converting from annual to semiannual refueling following several annual reloads. Determine the short- and long-term resource savings and fuel cycle cost improvements for such a strategy.

c. Quantify the cycle flexibility limits and potential short- and long-term resource savings possible by converting from high conversion designs to designs of lower conversion ratio by successively lowering the reload interval thorium loading. Such a strategy involves "burnout out" the high U-233 inventories recovered after reprocessing of earlier high thorium and high conversion cycles. The preliminary

analysis of one such strategy shows this scheme to have great promise; i.e., the average U-235 makeup requirement was reduced by 40% per year for the 8-year period over which it was assumed the thorium loading had been reduced.

Task II - Evaluation of Core Performance and Fuel Cycle Economic Tradeoffs with Increasing Conversion Ratio

1. Objectives: Determine the maximum conversion ratio, and the resultant fuel cycle and total power costs, for selected fuel performance limits, e.g., at constant core pressure drop and/or constant peak fuel element temperature. Quantify the most promising design alternatives and tradeoffs for obtaining maximum resource savings for minimum fuel development and fuel cycle costs within performance constraints. Define the most fruitful design approach or approaches for obtaining high conversion for minimum risk and development costs.

2. Work Scope: The following evaluations will be conducted to determine performance tradeoffs and achievable conversion ratio increases. The results will be based on evaluations of selected 4-year, annually refueled high conversion designs for which the C/Th ratio will vary from C/Th = 100 to C/Th = 240 and the power density will vary from 6.0 to 8.4 MW/m^3.

   For the reference fuel rod diameter,

   a. Determine the maximum conversion ratio, the expected region peaking factor and peak fuel temperature, core pressure drop, thermal efficiency, and resultant fuel cycle costs for each design considered. Develop estimates of plant cost effects due to changing power density (core size) and also determine expected total power costs for each design considered.

b. Repeat (a) with the assumption that the fuel rod diameter in the standard eight-row HTGR block design can increase at power densities below 8.4 MW/m^3 until

(1) The reference (8.4 MW/m^3) core pressure drop is achieved, or

(2) The reference peak fuel element temperature is reached.

c. Determine from the results of (a) and (b) which combination of possible design modifications shows the greatest promise for maximizing resource utilization for minimum fuel developments and power costs within selected performance constraints.

Task III - Evaluation of Optimum Conversion Ratio for Varying Economic and Resource Availability Assumptions

1. Objectives: The economic benefit of high conversion HTGR designs varies appreciably depending on the projected rate of U_3O_8 scarcity and certain fuel cycle economic parameters, particularly the working capital rate for fuel investments. The objective of this task is to determine the optimum conversion ratio, i.e., optimum benefit, as a function of variations in the principal resource and economic assumptions. The results of such evaluations are needed for Tasks I and II, as well as for the cost-benefit studies described in Task V.

2. Work Scope:

a. For installed nuclear capacities of 700 GW(e) and 900 GW(e) (through year 2000), determine the expected cumulative U_3O_8 consumed and on order. Utilizing current ERDA estimates of

marginal U_3O_8 price versus cumulative consumption, determine the expected future price due to scarcity for small, base, and large assumed uranium reserves. Determine the range of U_3O_8 prices due to scarcity by year for (1) price determined by actual consumption and (2) price determined when order placed to reflect expected future consumption.

b. For promising resource and/or performance optimized high conversion designs identified in Tasks I and II, determine the levelized fuel cycle costs of each design for the range of U_3O_8 price schedules determined from (a) above. The results will be calculated both with and without inflation assumptions and will be based on an internally consistent set of economic assumptions as described by Stauffer, Palmer, and Wyckoff.*

c. From (b) determine the optimum benefit conversion ratio and/or resource utilization design strategies to be evaluated in the Task V cost-benefit studies.

Task IV - Determination of Core Physics Characteristics and Control Requirements for High Conversion Designs

1. Objectives: Determine the important core physics characteristics for potential high conversion ratio designs. Determine what, if any, changes would be required in the core design components and/or reactor operating procedures as a result of achieving higher conversion ratio.

2. Work Scope:

a. Define the core temperature coefficient of reactivity and total reactivity defect due to temperature from room

*ERDA Authorizing Legislation Fiscal Year 1976. Hearings before the Subcommittee on Legislation of the Joint Committee on Atomic Energy, March 11 and 13, 1975 - Part 4.

temperature to operating temperature for the range of power density and C/Th ratio of interest.

b. Utilizing the results of (a), determine the adequacy of the current control rod design and configuration for achieving adequate shutdown margins for the various high conversion designs studied. Define what, if any, are the limits of C/Th ratio and/or power density changes for which the reference control system is not adequate. Recommend design changes required to extend the conversion ratio potential if that is indicated.

c. Perform preliminary evaluations of the stability of high conversion designs to xenon transients. Identify potential operational problems, if any, of high conversion designs.

Task V - Cost-Benefit Evaluations of High Conversion Designs at HEDL

1. Objectives: Determine the national benefit for developing HTGRs of higher conversion ratio compared with standard thermal reactors. Evaluate various HTGR high conversion design concepts and fuel cycle strategies for minimizing and extending the availability of uranium resources. Determine the sensitivity of the HTGR cost benefit to economic and resource cost assumptions and its timing relative to fast breeder reactor (FBR) introduction. Evaluate the potential of high conversion HTGR designs for relaxing the performance requirements necessary in FBRs.

2. Work Scope: An important portion of the overall evaluation of high conversion HTGR designs is the determination of the expected national benefit to be gained from developing such designs. These calculations are performed at HEDL. The following work scope at GA is proposed for providing input, case identification, and results evaluation in support of the HEDL studies.

a. Prepare case description data, mass flows, and recommended input variables for FY-76 benefit studies to be performed under Task 6 work scope.

b. Perform technical evaluation of FY-76 studies to better understand the interrelationships and interdependence of the important input variables and resultant sensitivities.

c. Define new input assumptions, including the U_3O_8 cost-scarcity relationships, for the FY-77 studies.

d.* Prepare case description and required input data for HEDL evaluations to determine:

(1) An optimum resource solution for competing reactor types in which only fuel costs are input.

(2) The extent to which high gain HTGR increases the FBR benefit by relaxing the requirements upon the nuclear performance of the FBR.

(3) The economic and resource consumption advantages of direct cycle and high conversion HTGRs over LWRs.

(4) The benefit of utilizing thorium blankets on FBRs in symbiosis with U-233 burning HTGRs.

e. Perform technical evaluation of the results and conclusions obtained from the benefit runs performed in (d).

f. Prepare mass flows and case input assumptions required to evaluate the resource savings and benefits for optimized

*Proposed for inclusion under Task 8 in FY-77.

high conversion designs and reload strategies determined from Tasks I and II study results.

g. Issue final report on significant conclusions determined from technical evaluation of the results obtained from above.

Materials Development Plan

An increase in the thorium loading of the HTGR core raises the conversion ratio, reduces the overall uranium requirements over the plant lifetime, and improves the HTGR performance by reducing age-peaking which lowers the pumping power requirement and thus improves the plant efficiency. Moreover, an increased thorium loading is now expected to yield appreciable fuel cycle cost savings due to the reduced U_3O_8 requirement that results from increasing the thorium loading.

Since a major portion of the fuel rod volume is occupied by the fertile particles, the obvious approach for achieving a high conversion core is to reduce the fertile particle volume by thinning the coating. The pyrocarbon coating used in the reference fertile particle design has low coating strength and exhibits large shrinkage under irradiation; therefore, a relatively thick coating and buffer layer are required to meet the fuel performance requirement. To overcome these difficulties, it is necessary to develop coating materials of better strength and dimensional stability under irradiation.

General Atomic has been working on the development of such coating materials since 1970. It has been observed that the incorporation of 20 to 40 wt % silicon in the pyrocarbon coating by codeposition improves the dimensional stability by a factor of 3 at 1000°C to full HTGR fuel design fast neutron fluence, and increases the mechanical strength by about 50%.

Preliminary estimates indicate that if such a silicon-alloyed-pyrocarbon coating is used to replace the reference pyrocarbon coating, the thicknesses of the coating and the buffer layer can be greatly reduced and that an increase in the thorium loading by 50 to 75% should be possible. A capsule (designated as HB-2) containing silicon-alloyed-pyrocarbon coated fertile particles of various coating and buffer thicknesses has been irradiated in GETR at 1000° to 1050°C to about 5 x 10^{25} n/m^2 fast neutron fluence for a screening study of the coating design limits. The irradiation was completed in January of CY-76.

To continue the development of improved fertile particle coating materials for high conversion HTGR application, it is proposed that a program composed of the tasks described below be initiated. The overall program is expected to take a period of 5-1/2 years to complete and to cost about $5 million.

The objectives and work scope for the six tasks of the Materials Development Plan are listed below. The manpower and cost estimates are given in Table 6-6.

Task I - Postirradiation Evaluation of the Performance of Silicon-Alloyed-Pyrocarbon Coated Fertile Particles Irradiated in Capsule HB-2

1. Objectives: Capsule HB-2 containing silicon-alloyed-pyrocarbon coated $10ThO_2$ - $1UO_2$* of various coating designs (Table 6-7) has been irradiated in the GETR at 1000° to 1050°C. Unalloyed pyrocarbon coated $10ThO_2$ - $1UO_2$ fuel particles of similar coating designs are included in the same capsule as references. The irradiation produced an integrated fast neutron fluence of 5 x 10^{25} n/m^2 and a fission density corresponding to that in fertile particles at full burnup (7% FIMA). In addition, the Si-BISO fuel particles will also be irradiated in two GA-French joint

*Due to the difference in GETR and HTGR neutron energy spectra and the accelerated nature of the test, uranium is added to the ThO_2 to simulate the bred U-233.

TABLE 6-6
COSTS FOR THE DEVELOPMENT OF SILICON-ALLOYED-PYROCARBON COATED FERTILE PARTICLES FOR HIGH CONVERSION HTGR APPLICATION

Task	Allocation	CY-77	CY-78	CY-79	CY-80	CY-81	CY-82	CY-83
I	Manpower (man-years)	4.0	3.0					
	Materials and hot cell service ($ x 10^3)	70.0	30.0					
II	Manpower (man-years)	2.0	2.0	2.0				
	Materials and services ($ x 10^3)	20.0	20.0	20.0				
III	Manpower (man-years)	0.5	4.0	4.0	2.0	2.0		
	Materials and services ($ x 10^3)			20.0	20.0			
	Equipment[a] ($ x 10^3)			450.0				
IV	Manpower (man-years)		5.0	7.0	5.0	3.5		
	Materials, hot cell services, and irradiation units ($ x 10^3)		100.0	430.0	315.0	85.0		
V	Manpower (man-years)				3.0	3.5	2.0	3.6
	Materials, hot cell services, and irradiation units ($ x 10^3)				40.0	115.0	95.0	65.0
VI	Manpower (man-years)	1.0	1.0		1.0	1.0	1.0	1.0
	Materials and hot cell services ($ x 10^3)	30.0	30.0		30.0	30.0	30.0	30.0

[a] Power supply, temperature control system, coater components, effluent control system, gas control valves, flow meters and manifolds.

TABLE 6-7
CHARACTERISTICS OF SILICON-ALLOYED-PYROCARBON COATED FERTILE PARTICLES UNDER IRRADIATION

Sample Batch Designation	Buffer Thickness (μm)	Pyrocarbon Coating Thickness (μm)			Si Concentration in Alloyed Coating (wt %)
		Unalloyed Portion	Si-Alloyed Portion	Total	
6832-119	16	10	39	49	30
6832-129	16	10	40	50	25
7021-11	16	50	--	50	0 (control)
6832-127	35	15	43	58	35
6832-117	35	15	34	49	25
7021-13	35	50	--	50	0 (control)
6832-125	50	20	40	60	30
6832-115	50	20	42	62	20
6832-133	50	5	64	69	25
7021-15	50	49	--	49	0 (control)
6832-121	57	15	34	49	30
6832-123	57	5	62	67	25
6832-131	57	15	56	71	25
7021-7	57	61	--	61	0 (control)

capsules (GF-3 and GF-4) at 1250°C to full HTGR fast fluence. Postirradiation evaluation of the performance of such irradiated fuel particles should provide valuable information for establishing an optimum fuel particle design for further qualification tests in full fluence capsules at high temperatures for high conversion HTGR application.

2. Work Scope: The HB-2 capsule will be disassembled in the GA hot cell, and the irradiated fuel particles will be subjected to the following investigations:

   a. Comparison of the dimensional changes, microstructures, and failure fractions of the irradiated fuel particle coatings as a function of coating composition and design.

   b. Determination of the high-temperature fission gas release rates of irradiated fuel particles selected on the basis of the results obtained in (a).

   c. Measurement of the high-temperature cesium release rates and the kernel thermal stability (amoeba effect) of irradiated fuel particles selected on the basis of the results obtained in (a) and (b).

   The experimental results obtained will be used to define the coating designs for further qualification tests at high temperatures and full fast neutron fluence.

Task II - Silicon-Alloyed-Pyrocarbon Coating Process Development

1. Objectives: In previous studies and irradiation tests, silicon-alloyed-pyrocarbon coated fuel particles were prepared in laboratory-size 50.8-mm-diameter coaters. Much remains to be

studied on the optimization of the coating process variables and effluent control problems. A 127-mm-diameter coater is currently under construction for these purposes. The information generated will be needed for the scale-up of the coater to production size and control of the quality of the coating in production coaters.

2. Work Scope: The following work will be carried out using the 127-mm-diameter coater completed in CY-76:

   a. Determination of the temperature and gas flow rates necessary for the deposition of silicon-alloyed-pyrocarbon coatings on fertile kernels.

   b. Evaluation of the effect of various coating gas inlet geometries on the deposition of silicon-alloyed-pyrocarbon coatings on fertile kernels.

   c. Determination of the effect of deposition conditions on the structure and mechanical properties of the silicon-alloyed-pyrocarbon coatings and comparison of the results with those of similar coatings produced in laboratory-size 50.8-mm-diameter coaters.

   d. Study of the operation of the effluent control system.

   The information will be used to define the conditions for the preparation of samples for a full fluence irradiation qualification test and to plan the scale-up of the coater to the 254-mm-diameter production size.

Task III - Scale-up of the Silicon-Alloyed-Pyrocarbon Coater to Production Size

1. Objectives: The 127-mm-diameter coater is convenient for the study of process parameter optimization and for the preparation

of samples for irradiation qualification tests, but the throughput is too small from the point of view of production. For irradiation proof tests for fuel particle licensing, the test samples must be prepared in a production coater. It is therefore necessary to design and assembly a 254-mm-diameter coater, which is of the same size as that used for the production of reference HTGR fuel particles at GA. It is expected that the information gained in Task II on process parameter optimization and effluent control will also be applicable to the design and operation of the 254-mm-diameter coater.

2. Work Scope: After the 127-mm-diameter coater has generated enough operating experience, work should be initiated in the following areas:

   a. Design of a 254-mm-diameter production-size coater and its associated effluent control system and instrumentation.

   b. Procurement of components and assembly of the coater system.

   c. Preparation of samples and comparison of structures and properties of the deposits with that obtained in the 127-mm-diameter coater under similar conditions.

   d. Determination of the optimum deposition conditions for silicon-alloyed-pyrocarbon coating in the 254-mm-diameter coater.

   The 254-mm-diameter coater will be used for the preparation of samples for the irradiation proof test and for coating fertile particles for the high conversion HTGR core if the irradiation proof test is successful.

Task IV - Full Fluence Irradiation Qualification Test for Silicon-Alloyed-Pyrocarbon Coated Fertile Particle Designs Selected on the Basis of HB-2 Results

1. Objectives: On the basis of the postirradiation evaluation results obtained from the samples irradiated in the HB-2 capsule, it should be possible to establish the promising coating design ranges. The next step is to arrive at the optimum coating design by studying the in-pile performance of selected samples irradiated to full fluence and burnup at temperatures of HTGR interest. This step will be accomplished by the irradiation of two multicelled irradiation capsules (HF-1 and HF-2) in the GETR.

2. Work Scope: Selected silicon-alloyed-pyrocarbon coated fertile particles* and fuel rods containing such particles will be included in this study. The work can be divided into the following areas:

   a. Sample preparation. The fertile* kernels will be coated with buffer and silicon-alloyed-pyrocarbon coatings in the 127-mm-diameter coater. The fuel rod samples will be prepared by the reference HTGR process, using pitch binder, TRISO coated WAR UC_2 fissile particles, and selected silicon-alloyed-pyrocarbon coated fertile* particles.

   b. Capsule design, assembly, and irradiation. The different test samples will be located in individual cells instrumented with thermocouples and equipped with controlled gas gaps for temperature monitoring and control. The samples will be irradiated in the temperature range 1100° to 1350°C in a test reactor facility (e.g., GETR) capable of

*$10ThO_2$ - $1UO_2$ instead of ThO_2 will be used in order to simulate the bred U-233.

providing an integrated fast neutron fluence of 9×10^{25} n/m^2 and full high conversion HTGR burnup in about 10 to 12 months. The fission gas release characteristics of each individual cell will be monitored during the irradiation. Selected cells will be thermal cycled for the study of the effect of thermal cycling on irradiation performance.

c. Postirradiation examinations (PIEs). The irradiated samples will be examined in the hot cell for their macroscopic appearances, dimensional changes, structural integrity, microstructures, and heavy metal and fission product distributions.

d. Postirradiation annealing studies (PIAs). Based on the results obtained in (c), samples will be selected for the study of fission gas release characteristics, metallic fission product release rates, and thermal stability of the fuel particle kernels in a temperature gradient.

The results obtained in (c) and (d) will be used to define the optimum fertile particle coating design for irradiation proof test.

Task V - Irradiation Proof Test of the Optimum Coating Design Selected on the Basis of Results Obtained Under Task IV

1. Objective: The objective of this task is to proof test the in-pile performance of the optimum coating design selected. The results are needed for licensing the improved fuel particle for manufacturing. For this task a large-diameter capsule (HF-3) will be irradiated at ORR.

2. Work Scope: Fuel rods containing fertile particles of the selected optimum coating design will be subjected to irradiation proof test. The work can be divided into the following areas:

   a. Sample preparation. Fertile particles of the optimum coating design will be prepared by coating fertile kernels ($10ThO_2$ - $1UO_2$ used to simulate ThO_2 containing bred U-233) in the 254-mm-diameter coater with the buffer layer and the silicon-alloyed-pyrocarbon coating required. Fuel rod samples containing such fertile particles will be prepared by the reference HTGR fuel rod fabrication techniques, using pitch binder and TRISO coated WAR UC_2 fertile particles.

   b. Capsule design, assembly, and irradiation. The design of the capsule, the irradiation procedures, and the test facility required are similar to that for the irradiation qualification test described under Task IV. The samples will be irradiated in the temperature range 1100° to 1350°C to an integrated fast neutron fluence of 9×10^{25} n/m^2 and full high conversion HTGR burnup in about 10 to 12 months. The fission gas release characteristics of each individual cell will be monitored during the irradiation. Selected cells will be thermal cycled for the study of the effect of thermal cycling on irradiation performance.

   c. Postirradiation examinations (PIEs). The irradiated samples will be examined in the hot cell for their macroscopie appearances, dimensional changes, structural integrity, microstructures, and heavy metal and fission product distributions.

   d. Postirradiation annealing studies (PIAs). Selected samples will be studied for their fission gas release characteristics and metallic fission product release rates.

The results will be used for the preparation of specifications for licensing the improved fertile particles for manufacturing.

Task VI - Reprocessing Study of Silicon-Alloyed-Pyrocarbon Coated Fertile Particles

1. Objective: To close the fuel cycle, it is necessary to find out whether the presence of silicon in the pyrocarbon coating of the fertile particles would affect the reprocessing of the used graphite fuel blocks so that the total fuel cycle cost can be assessed.

2. Work Scope: The work included in this task is as follows:

   a. Using unirradiated fuel particles* and fuel rods,* the effect of the presence of silicon in the pyrocarbon coating on the burning, Thorex leaching, and solvent extraction processes will be studied. The results should indicate how the silicon additive affects the coating burning rate at various temperatures and the Thorex leaching rate of the burned particles. The amount of silicon dissolved in the Thorex solution will be measured as a function of leaching time and temperature. The effect of the presence of silica, if any, in the Thorex solution on the solvent extraction process will also be investigated. The results should indicate the potential problem areas which should be studied further with irradiated particles and fuel rods.

   b. Similar studies should be carried out on the irradiated particles and fuel rods in capsules HF-1, HF-2, and HF-3.

The results should be taken into consideration in fuel cycle cost evaluation and in reprocessing plant design.

*$10ThO_2$ - $1UO_2$ instead of ThO_2 will be used in order to simulate the bred U-233.

EVALUATION OF ALTERNATE STRATEGIES FOR U-235 RECYCLE

Work has continued on the evaluation of alternate strategies for U-235 recycle. The objectives still include minimization of:

1. Resource requirements.
2. Recycle plant design and cost.
3. Total fuel cycle cost.

In evaluating the alternate strategies, the following features of the fuel cycle and its evaluation are being allowed to vary:

1. Fuel cycle design, including design of the recycle plant.
2. Economic projection and assumption.

The results reported here have also been applied in a detailed study of the recycle plant being done under the Thorium Utilization Program.

Basically the procedure is to calculate fuel cycle costs, including depletion costs representing resource utilization, for various HTGR fuel cycle designs and to determine the difference relative to the reference fuel cycle design, which includes U-235 recycle in specially dedicated fuel elements. Besides the changes in depletion costs and in distribution between fabrication and refabrication, the changes in reprocessing and refabrication prices and in waste repository fees are also reflected in the fuel cycle cost calculation. These price changes in turn result from capital and operating cost changes within the recycle plant and in waste disposal as a result of the modifications in the fuel cycle design regarding U-235 recycle. All of these comparisons are done for various sets of economic ground rules and assumptions. In particular, costs are computed both with and without general escalation and for an assumption on U_3O_8 ore scarcity.

Preliminary results have now been obtained for all of the fuel cycle designs under consideration. Furthermore, these results include the following effects for each alternative:

1. Changes in prices of reprocessing and refabrication that result from changes in the costs to build and operate the recycle plant.

2. Estimates of the price of the ultimate waste handling and disposal.

The fuel cycle alternatives are as follows:

Case 1. Reference fuel cycle - all U-235 is recycled once in specially dedicated fuel elements prior to retirement at zero value.

Case 2. No U-235 recycle - all U-235 is retired at zero value upon discharge after its first residence period in the reactor (as fresh, fully enriched U-235 material).

Case 3. Full recycle - all discharged U-235 is mixed with all discharge recycle material (U-233 + U-235) for continuous recycle.

Case 4. Mixed recycle - discharged U-235 is mixed with discharged bred U-233 for one recycle in specially dedicated fuel elements prior to retiring the mixture at zero value.

Case 5. Partial mixed recycle, first variation - same as Case 4 for segments 1 and 2; same as Case 2 for segments 3 on.

Case 6. Partial mixed recycle, second variation - same as Case 5, except for segments 3 on, discharged bred U-233 is recycled only once prior to retirement at zero value.

Table 6-8 reflects the fuel cycle cost changes that would result from shifting to the alternative cycles (Cases 2 through 6) from the reference cycle (Case 1). The table includes results for two sets of economic evaluation conditions. The first is unescalated, i.e., without inflation, but includes a "scarcity-escalation" of U_3O_8 ore price to reflect a projection of excess demand for this basic resource. This scarcity rate remains at 6% per year through 2000 A.D. and then drops to 3% thereon. (An alternative, reported in Ref. 6-2, with a lower scarcity rate has now been dropped from consideration in view of the recent, steadily using predictions of uranium costs.) The other set of economic conditions in Table 6-8 includes, in addition to U_3O_8 ore scarcity rates, predictions of escalation on all components of the fuel cycle. For the noninflation set of conditions, the working capital and discount rates are 9.1 and 4.3%, respectively; for the inflation (escalation) conditions, they are 15.6 and 7.4%, respectively.

All the depletion results of Table 6-8 employ the assumption of \$57/kg (\$26/lb) of U_3O_8 and \$75/SWU in the 1975 base year. These are considerably lower than the 1976 current prices of uranium, which are about \$84/kg (\$38/lb) U_3O_8 and \$103/SWU estimated for private uranium enrichment. In most cases in Table 6-8, the adoption of the newer uranium costs would only serve to increase the dominance of the already dominant depletion component of the fuel cycle cost (FCC). Only Case 4 (mixed recycle) would be significantly affected such that the very small fuel cycle cost difference from the reference would be made smaller.

Table 6-9 summarizes the projected cost changes in the recycle facility and waste depository that might be expected from the adoption of the alternative fuel cycle plans.

TABLE 6-8
COMPARISON OF FUEL CYCLE COSTS FOR ALTERNATIVE U-235 RECYCLE PLANS

Case	Cost Components	Level (0 to 15 year) Fuel Cycle Cost Changes [m/kWh(e)]	
		No Inflation, 6 to 3% Core Scarcity	General Escalation
1	Reference		
	Depletion	--	--
	Handling	--	--
	Total	--	--
2	No U-235 recycle		
	Depletion	+0.25	+0.48
	Handling	-0.05	-0.12
	Total	+0.20	+0.36
3	Full recycle		
	Depletion	+0.16	+0.32
	Handling	+0.01	+0.02
	Total	+0.17	+0.34
4	Mixed recycle		
	Depletion	+0.01	+0.02
	Handling	-0.01	-0.04
	Total	--	-0.02
5	Partial mixed, No. 1		
	Depletion	+0.15	+0.27
	Handling	-0.04	-0.10
	Total	+0.11	+0.17
6	Partial mixed, No. 2		
	Depletion	+0.23	+0.46
	Handling	-0.04	-0.23
	Total	+0.19	+0.23

TABLE 6-9
PROJECTED COST CHANGES FOR RECYCLE AND WASTE
(1975 $)

Case	Recycle Plant		Waste Fees (10^6/yr)
	Capital (10^6)	Operating (10^6/yr)	
1. Reference	--	--	--
2. No U-235 recycle	-26	-14	-1.3
3. Full recycle	0	0	-1.0
4. Mixed recycle	-10	-5	+0.7
5. Partial mixed recycle, No. 1	-26	-14	-1.3
6. Partial mixed recycle, No. 2	-26	-14	-1.5

REFERENCES

6-1. Lane, R. K., and L. Yang, "HTGR Fuel Development Plans for Alternate Fuel Systems," ERDA Report GA-A13879, General Atomic, April 19, 1976.

6-2. "HTGR Fuels and Core Development Program Quarterly Progress Report for the Period Ending February 28, 1976," ERDA Report GA-A13804, General Atomic, March 31, 1976.

8. HTGR PHYSICS
189a NO. SU002

CROSS-SECTION EVALUATION

A preliminary study of the effect that the latest ENDF/B actinide data would have upon predictions of the neutron source in spent HTGR fuel has been completed. The results indicate that the use of the new data, in conjunction with an explicit treatment of the actinide chain through Cf-252, will significantly reduce the discrepancy between calculated and measured neutron source strengths. Consequently, detailed processing of the cross-section data has been initiated.

MULTIDIMENSIONAL REACTOR KINETICS

After discussions with Savannah River Laboratory personnel, the decision was made to acquire the TRIMHEX (Ref. 8-1) computer code for use in the study of multidimensional kinetics effects in HTGRs. Coordination with the Argonne Code Center is under way.

XENON STABILITY AND CONTROL STUDY

During this quarter an approximate temperature feedback option was added to the GAUGE (Ref. 8-2) computer program. This option will be used to confirm past calculations of the stabilizing effect that temperature feedback has upon xenon oscillations.

A brief study of the validity of bang-bang control procedures for use in damping azimuthal xenon oscillations in HTGRs was completed. The results of the study indicate that this mode of control could be an effective technique for HTGR applications.

FSV OPERATING DATA ANALYSIS

A draft report describing a comparison of calculational results with the experimental data obtained during the initial stages of the FSV rise-to-power program has been completed. All comparisons were consistent within the experimental uncertainties present.

REFERENCES

8-1. Buckner, M. R., and J. W. Stewart, "Multidimensional Space-Time Kinetics Studies - Part I - Theoretical," Nucl. Sci. Eng. 59, 289 (1976).

8-2. Wagner, M. R., "GAUGE - A Two-Dimensional Few Group Neutron Diffusion-Depletion Program for a Uniform Triangular Mesh," USAEC Report GA-8307, Gulf General Atomic, March 15, 1968.

9. HTGR FUEL DEVELOPMENT AND ENGINEERING
189a NO. SU003

TASK 200: ACCELERATED IRRADIATION TESTS

Subtask 210: Fresh Fuel Qualification

Summary and Conclusions

An incorrect capsule purge gas mixture composition was used in initial P13R and P13S thermal analysis. Upon discovery of the error, revised thermal analysis computer runs were required with consequent delay in the final report of P13R and P13S. Completion of draft review is now scheduled for June 30.

Capsule P13T has now reached a peak fast fluence of 7.8×10^{25} n/m^2 $(E > 29\ fJ)_{HTGR}$. The fission gas release remains relatively low. A small leak in the secondary gas system has increased about a factor of six and has been determined to be a result of a breach in the primary containment of cell 1.

Capsules P13U and P13V were inserted into the ORR reactor on March 3, 1976. Four days later the majority of the tungsten/rhenium thermocouples failed in the P13U capsule and it was permanently discharged. The cause of loss of thermocouples was water leaking into the capsule through a crack in the secondary containment. The containment failed by a fatigue crack at a standoff pin weldment which, through an assembly error, was not annealed after welding. A second P13U capsule is being prepared for insertion.

In a separate problem area, GETR measured the reactivity of the P13V capsule to be higher than the specification limit and the capsule was moved to a lower flux position. The fuel temperatures are now below design in

some cells. The design of the replacement capsule P13U(R) is being modified to provide a high-temperature cell which was previously planned for P13V.

Work in the area of development of test techniques is summarized as follows:

1. The Hg porosimetry technique has been shown to give a screening test for out-of-specification (fission gas release as a result of porosity) BISO ThO_2 particles and to give a necessary, but not sufficient, value for in-specification particles used in irradiation capsules.

2. Phosgene leaching at 1100°C has progressed to the stage where there is confidence that this test can be substituted for TRIGA fission gas release measurements (for both contamination and porosity) used to qualify BISO ThO_2 particles for capsule tests. However, leaching times are excessively long (9 to 18 hr), and higher test temperatures will be investigated.

3. Development of methods of analysis and sample preparation has been initiated for LECO analyzers to be used for measurement of carbon, hydrogen, oxygen, and nitrogen in WAR kernels which are undergoing qualification tests.

4. A measurement technique for the bulk density of PyC has been developed using a combination of liquid gradient and Hg density measurements.

5. The determination of void volume in the buffer, after OPyC deposition, of BISO ThO_2 has been developed utilizing Hg particle density and burnback techniques.

6. The procedure for measuring BAF_o via the Seibersdorf OAF unit has been modified to make a 24-μm circle measurement standard rather than the 4 by 24 μm scanning technique.

Capsules P13R and P13S

During the thermal analyses of capsules P13R and P13S, it was discovered that the capsules had been purged with 100% neon rather than a mixture of 90% neon and 10% helium, as had been originally intended. A detailed gas specification has been transmitted to GETR to clarify operation of future capsules. This discrepancy required a revised CAPTEM computer run, which delayed completion of the capsule thermal analyses until April 1976.

Capsule P13T

Capsule P13T is the ninth in a GA series of LHTGR fuel irradiation tests conducted under the HTGR Fuels and Core Development Program. P13T is a large-diameter capsule containing two cells. Cell 1 is a qualification test of reference fresh fuel [TRISO UC_2 (VSM) and BISO ThO_2 particles] irradiated at 1300°C. Cell 2 is an evaluation test of reference fresh fuel and recycle fissile fuel [TRISO UC_xO_y (WAR) particles] irradiated at 1100°C. The capsule was inserted in the ORR reactor in May 1975 and will be irradiated to a peak fast fluence of 8.5×10^{25} n/m^2 $(E > 29\ fJ)_{HTGR}$. The capsule is scheduled to be discharged from the core in July 1976. A detailed description of the capsule is given in Ref. 9-1.

The capsule has reached an estimated peak fast fluence of 7.8×10^{25} n/m^2 $(E > 29\ fJ)_{HTGR}$. The latest fission gas release of the fuel is still relatively low: 1×10^{-5} and 1×10^{-6} (R/B Kr-85m) for cells 1 and 2, respectively. The results show that all fuel is performing well. The irradiation conditions as a function of time for the two cells are presented in Figs. 9-1 and 9-2.*

Two significant problems have occurred in cell 1 of capsule P13T. One problem is thermocouple failure. Two additional thermocouples have failed in-pile since the failures reported last quarter (Ref. 9-2). A total of

*Figures appear at the end of Section 9.

eight tungsten/rhenium thermocouples and one Chromel/Alumel thermocouple have become inoperative in this cell, and only two Chromel/Alumel thermocouples and one tungsten/rhenium thermocouple remain. These failures will make the thermal analysis more difficult. Fortunately, the Chromel/Alumel thermocouple which has been the control thermocouple since the beginning of the irradiation is still functioning.

The other problem is that a small leak in the secondary gas system detected in November 1975 increased about a factor of six over the subsequent 4 months. This system was originally pressurized with He gas to 70 psi and then closed off. The leak was detected by a small drop in pressure and was originally thought to be in the hardware outside of the core. During each subsequent normal reactor shutdown, an attempt was made to find the leak; however, because of its small size, the leak could not be located. Helium gas was occasionally added to keep the pressure near 70 psi. When the leak rate became noticeably higher, a major effort was undertaken to determine its location. In late March 1976 it was discovered that the gas was leaking into cell 1 and, therefore, the primary containment was breached. The increase in the leak rate indicated the crack was enlarging. A purification system and a 3-liter tank were installed in the secondary gas system to reduce the effects of the problem. During April and up to the present time the leak rate has leveled off. The ORR operations personnel feel there is no hazard to the reactor operation at present and will allow the irradiation to continue unless the leak rate becomes excessive, in which case the capsule would be immediately discharged. To date, the leak has had only a slight effect on the fission gas release and the temperatures in cell 1. Therefore, it now appears that the P13T capsule will complete the scheduled irradiation time.

Capsules P13U and P13V

Introduction. Capsules P13U and P13V are the tenth and eleventh in a GA series of LHTGR fuel irradiations. Primarily, these capsules will test TRISO WAR U·C_x·O_y and BISO ThO_2 BISO particles under normal and thermal cycling conditions to peak LHTGR temperatures and fluences. Each capsule

will be 31.75 mm in diameter and similar in design to capsules P13R and P13S. Five fuel rod cells and one unbonded particle cell will be tested in each irradiation test vehicle.

Capsules P13U and P13V were successfully installed in GETR core position E7 on March 1, 1976 and brought on-test without significant difficulty on March 2 and March 3, 1976.

P13U Failure. On March 7, 1976 GETR personnel notified the cognizant engineer at GA for capsule P13U and P13V operation that during a period of several hours 16 of the 27 W/Re thermocouples had failed in capsule P13U. The sudden failure of these thermocouples indicated that there was a leak (air or water) in the secondary gas system. The capsule primary and secondary systems were placed on helium gas to reduce fuel temperature. On March 8, the GA cognizant engineer conducted a review of current operational data at the GETR site. The review indicated that there was a momentary change in all thermocouple temperatures on March 7. Shortly thereafter the W/Re thermocouples began to fail; the failures appeared to progress from the hottest to the coolest thermocouples. By March 8 when the GA engineer arrived at GETR, all but two of the W/Re thermocouples had failed. All the Chromel/Alumel (C/A) thermocouples were still operative. Fuel cells 1, 3, 4, and 5 and the thermocouple cell were thus without any operating thermocouples inside the primary containment. No change in gaseous activity was observed in the primary circuits during this time period. This sequence of events lead to the conclusion that a leak in the secondary gas circuit had suddenly occurred, admitting either water or air into the capsule.

Because of the lack of instrumentation, the capsule was immediately discharged from the GETR and planning was begun to determine the cause of the failure. An Unusual Occurrence report was submitted to ERDA on March 9, 1976.

Failure analysis of P13U began during the month of April 1976. On April 11, the lead tube was cut, the gas lines were crimped, and the

capsule was sealed in an aluminum can for neutron radiography at the Vallecitos Nuclear Center. Completion of the neutron radiography on April 12 revealed water in the capsule up to the bottom of cell 3. Significant damage to the capsule thermocouples was also indicated. This damage appeared to be caused by a steam reaction resulting from a breach in the secondary containment. The source of the leak was not revealed in the neutron radiograph. Plans were then made for a hot cell examination of P13U at Vallecitos to determine the exact cause of the leak.

A pressure check made on May 3 in the GETR Vallecitos hot cell revealed a crack in the secondary containment around the periphery of an upper standoff weldment. These standoff weldments are used to center the capsule within the filler piece of reactor core position E7. The evidence indicated that a fatigue crack formed and propagated through the action of cyclic loads on the 304L stainless steel (1/2 hard condition) secondary containment. A similiar failure had been observed on the F-24 capsule, and changes were made at that time to the capsule design and construction procedures to eliminate this problem in the future. One of these changes was to anneal the welds which attach the standoff pins to the secondary containment. However, the requirement to anneal the secondary containment tube only appeared on the P13U assembly drawing and not on the QA checkoff list. It now appears that the secondary containment for capsule P13U was not annealed after welding of the standoff pin and this, coupled with the in-pile capsule fatigue loads, caused the P13U failure.

Investigations have shown that the secondary containment for capsule P13V was annealed, so that this type of failure is not expected to occur in capsule P13V.

Action has been taken to prevent this type of containment failure in the future. The standoff pin welding procedure has been identified as the source of this problem. This operation is also a difficult and time-consuming step in the capsule assembly and involves some risk, i.e., it could cause warpage of the containment tube. Therefore, an alternative

procedure will be used in the future. The standoff pins will be machined onto the tubing. This procedure was recently employed on a GA privately sponsored capsule, and the capsule performed satisfactorily in the GETR.

Revised Capsule Plans. P13U and P13V were companion irradiation capsules designed to complement each other. Following the loss of P13U, a proposal was made to ERDA to remake the capsule using funds already committed for GETR irradiation charges. The proposal was accepted and reconstruction has begun. The replacement capsule will be identified as P13U(R). The new schedule calls for completion of construction by early July 1976 and insertion and startup during the first part of August. This short schedule is possible because there are spare parts of many items, including all of the fuel rod types and most of the coated fuel particle batches. The PIE of capsules P13V and P13U(R) will begin in December 1976 and May 1977, respectively.

The sample description and/or the temperatures of the original P13V capsule and the remake P13U capsule have been changed. The original description of the capsules was presented in Ref. 9-3. The temperatures of the fuel cells will be higher in some cells, as shown in the revised capsule layout in Fig. 9-3. The peak temperature of cell 1 of P13U(R) and P13V will now be 1250°C instead of 1200°C. Cells 3, 4, and 6 in both capsules will operate at 1250°C rather than 1200°, 1100°, and 1200°C, respectively. The temperature in cell 5 will be 1500°C for P13U(R) and 1350°C for P13V (see "P13V Operation" for explanation). Cells 3 and 6 of P13U(R) rather than P13V will be thermal cycled. There are no previous tests with all fertile particle rods (cell 3) and all fissile particle rods (cell 6), and it is prudent to obtain the constant temperature data in P13V before the thermal cycling data which will now come from P13U(R). The last significant change in the fuel is that the unbonded particle crucibles (cell 4) of P13U(R) will contain two batches of ThO_2 BISO particles made in the 24-cm-diameter coater.

P13U(R) Capsule Preparation. The preparation of the fuel for P13U(R) is nearing completion. Since historical rods of all fuel rod types were

available, the time involved in fabricating the fuel rod bodies was significantly shortened. After fuel rods were selected and the graphite bodies loaded, the fuel bodies were fired under the same conditions as the original P13U firings. The bodies were measured for fission gas release and all were found to be acceptable [$\leq 3 \times 10^{-5}$ R/B (Kr-85m)]. All of the unbonded particle trays have been loaded, x-radiographed, and photographed, except the trays for the ThO_2 BISO particles, which are presently being fabricated in the 24-cm-diameter coater.

Reactivity Test on P13U and P13V. During April, significant reactivity discrepancies between calculated and measured values for both P13U and P13V were discovered. GETR measured the reactivity to be -0.9% $\Delta k/k$ for each capsule, whereas calculated values using GA materials data were only -0.2% $\Delta k/k$. Reactor licensing requirements limit capsule experiments to reactivities of $\leq$-0.8% $\Delta k/k$; therefore, it was necessary to move P13V to a lower flux position (E7C) in the same filler piece. In addition, a stainless steel tube was inserted in the filler piece to reduce the worth of the capsule to $\leq$-0.6% $\Delta k/k$. This depression in both fast and thermal flux levels increased the irradiation time by $\sim$15% to achieve full fluence and lowered peak burnups by about 30%.

Neutron radiography and chemical analysis of components did not detect any high neutron poison levels. An independent calculation of capsule reactivity worth was performed at GA and revealed that the reactivity problem is associated with the large amounts of tantalum in the thermocouple sheaths. When the tantalum cross section in the eipthermal region is properly treated, a reactivity value of -0.7% $\Delta k/k$ results.

With capsule P13V in the new core position (E7C), only two of the six cells were able to reach design temperature. Because of this unsatisfactory mode of capsule operation, and because of the GA calculated reactivity value of -0.7% $\Delta k/k$, it was requested that provisions be made to increase the flux level. In early May, this was accomplished by removing the stainless steel plug from the E7B core position. It was expected that this

would achieve a 20% increase in the thermal flux in P13V. Capsule P13V will not be permitted to return to its design core position (E7B). It is expected that capsule P13U(R) will be placed in core position E7D rather than the original E7A position so that irradiation conditions will be the same as P13V.

P13V Operation. Initial R/B results for P13V were in the mid-to-low 10^{-6} range for the 1250°C cells, except for the all-fertile fuel cell which was releasing around 10^{-5}. Since the number of fissions occurring in this latter cell is very low, considerable uncertainty exists in the data. Confidence in the R/B data from the all-fertile fuel cell should increase as the fuel begins to breed U-233 and the fission rate increases. The R/B for the fuel originally operating at 1500°C was around 10^{-5}. These figures indicate that the WAR $UC_3O_{0.5}$ TRISO/ThO_2 BISO fuel within P13V is performing very well to date.

Currently, even with the stainless steel plug removed from the E7B core position, only two of the six cells are operating at their design temperature, as shown in Table 9-1. It is expected that at slightly higher rod bank positions, cell 4 will be able to achieve its design temperature. In addition, an argon-helium rather than a neon-helium gas mixture will be used in cells 3 and 6 after the GETR shutdown on May 20. It is expected that the decreased thermal conductivity of this mixture in the primary containment temperature gap will permit these two cells to achieve their design temperatures. During the May 20 GETR shutdown, a shutoff valve will be installed in the gas control system for cells 3 and 6 to permit positive shutoff of the argon gas during periods in which fission gas samples are being taken from these cells. Cell 5 was originally designed to operate at 1500°C; however, the temperature has been changed to 1350°C because of the new lower flux position. Capsule P13U(R) will operate at 1500°C by using argon purge gas.

TABLE 9-1
CONTROL TEMPERATURES FOR CAPSULE P13V[a]

Cell No.	Control Temperature[b] (°C)	
	Actual (5/9/76)	Design
1	1260	1250
2	1160	1150[c]
3	1140	1250
4	1180	1250
5	1260	1350
6	1110	1250

[a] GETR rod bank position: 280 in.

[b] Same as fuel temperature except cell 2.

[c] Fuel estimated to be 50°C lower.

Test Technique Development

Bulk Density Measurement on PyC Coatings. A study was conducted to determine the relationship between PyC density determined by a liquid gradient column, bulk density, and high-pressure Hg intrusion in PyC coatings. The objective was to develop a technique for measuring the bulk density in capsule fuel samples by using porosimetry data to correct liquid gradient density for the effect of penetration of the liquid into coating pores.

The bulk density of the OPyC coating was measured directly on a series of reference TRISO particle batches by a Hg pycnometry and burnback procedure. The bulk density D_B (Mg/m^3) was calculated from the formula

$$D_B = \frac{W_C D_P D_S}{D_S - D_P (1 - W_C)} \quad , \tag{9-1}$$

where D_P = intact particle density, Mg/m^3; Hg at 1.7 MPa (250 psi),

D_S = particle density after burnback to SiC coating, Mg/m^3; Hg at 1.7 MPa (250 psi),

W_C = carbon loss in burnback (weight fraction).

Both densities were determined by Hg pycnometry.

The coating porosity penetrated by the liquid gradient was then calculated by

$$P_{LG}\ (m^3/Mg \text{ of coating}) = 1/D_B - 1/D_{LG}) \quad , \tag{9-2}$$

where D_{LG} is the density in Mg/m^3 of OPyC coating taken from the particle as measured with a liquid gradient column.

This was then correlated with P_{Hg}, the porosity (m^3/Mg of coating) penetrated by Hg at 69 MPa (10,000 psi) as measured with an AMINCO porosimeter. The data for the correlation are given in Table 9-2. A good linear fit was obtained, as shown in Fig. 9-4, with the least-squares equation

$$P_{LG} = 1.162\ P_{Hg} - 0.0031 \quad . \tag{9-3}$$

The non-zero y-intercept was attributed to the filling of particle interstices rather than coating pores for the first 1.7 MPa (250 psi) of applied pressure.

This same relationship was then assumed to hold for OPyC coatings on BISO coated ThO_2 particles. This resulted in the bulk density formula

$$D_B = \frac{1}{1.162\ P_{Hg} + 1/D_{LG}} \quad , \tag{9-4}$$

where P_{Hg} = Hg instrusion (m^3/Mg of coating) from 1.7 MPa (250 psi) to 69 MPa (10,000 psi).

TABLE 9-2
OPyC DENSITY AND POROSITY DETERMINATION

Batch No.	D_{LG} (a)	D_B (b)	P_{Hg} (c)	P_{LG} (d)
6151-00-01	1.80	1.74	0.0129	0.0191
6151-00-02	1.88	1.85	0.0149	0.0086
6151-00-03	1.85	1.76	0.0286	0.0276
6151-00-04	1.81	1.72	0.0311	0.0289
6151-01-01	1.90	1.87	0.0114	0.0084
6151-03-01	1.77	1.73	0.0138	0.0131
6151-04-01	1.82	1.76	0.0153	0.0187
6151-09-01	1.94	1.81	0.0282	0.0370
6151-09-02	1.95	1.86	0.0241	0.0248
6155-00-02	1.76	1.72	0.0130	0.0132
6155-01-01	1.78	1.74	0.0166	0.0129
6155-01-02	1.81	1.77	0.0153	0.0125
6155-02-02	1.82	1.79	0.0138	0.0092
6252-03-01	1.82	1.61	0.0654	0.0716
6252-04-01	1.82	1.59	0.0716	0.0794
6252-05-01	1.84	1.70	0.0361	0.0447

(a) D_{LG} = liquid gradient density (Mg/m^3) of PyC taken from coatings.

(b) D_B = bulk density (Mg/m^3).

(c) P_{Hg} = Hg intrusion (0 to 10,000 psi) (m^3/Mg).

(d) $P_{LG} = 1/D_B - 1/D_{LG}$ (m^3/Mg).

Since the porosimeter can only measure the OPyC porosity on a particle weight basis, the value obtained has to be divided by the weight fraction of OPyC coating relative to the complete particle. This was approximated from geometrical considerations using the mean kernel diameter, buffer thickness, and OPyC thickness (determined from radiographic measurements of 100 particles) assuming sphericity, and the kernel density, buffer density, and liquid gradient OPyC density.

Results of qualification tests on capsule material are given in Table 9-3. This measurement is now in routine use for coating development and evaluation.

Buffer Porosity Measurement. The purpose of the upper limit on buffer density in the HTGR fuel specifications for BISO coated ThO_2 particles is to ensure sufficient void volume for fission gas containment. Buffer density measurements made before application of the OPyC coating may not be indicative of the true buffer void volume in the finished particle due to intrusion of the OPyC coating into the buffer. Thus, a direct measurement of buffer porosity in the completed particle is necessary in order to reduce uncertainties in the correlation of pressure vessel model calculations and predictions of fuel performance.

The following procedure was devised for this measurement. First, the combined density of the buffer and OPyC coatings is measured by a Hg pycnometry and burnback technique using the formula

$$D_C = \frac{W_C \cdot D_P D_K}{D_K - D_P (1 - W_C)} \quad , \tag{9-5}$$

where D_C = combined buffer-OPyC carbon density , Mg/m^3,

D_P = completed particle density, Mg/m^3; from Hg pycnometry at 1.7 MPa (250 psi),

D_K = ThO_2 kernel density, Mg/m^3; from Hg pycnometry at 1.7 MPa (250 psi),

TABLE 9-3
OPyC DENSITIES OF RECENT CAPSULE PARTICLE BATCHES

Batch No.	D_{LG} (a)	D_B (b)
6542-09-010	1.93	1.83
6542-22-010	1.80	1.70
6542-18-010	1.84	1.73
6542-02-025	1.91	1.82
4252-06-010	1.82	1.74
6542-23-020	1.89	1.77
6542-24-010	1.94	1.84
4252-02-010	1.83	1.76
6542-21-010	1.73	1.59
6542-01-020	1.82	1.76
4252-06-018	1.82	1.74
6542-01-010	1.80	1.71

(a) D_{LG} = liquid gradient density (Mg/m^3) of PyC taken from coatings.

(b) D_B = bulk density (Mg/m^3).

W_C = weight fraction of carbon in completed particle as measured by burnback to kernel.

The bulk density D_B of the OPyC coating is then determined by the procedure outlined in the previous section. A theoretical carbon density of 2.2 Mg/m^3 is assumed for both buffer and OPyC. The buffer void volume per gram of particles is then calculated by subtracting the OPyC void volume from the total carbon void volume:

$$P = W_C \left(\frac{1}{D_C} - \frac{1}{2.2} \right) - W_O \left(\frac{1}{D_B} - \frac{1}{2.2} \right) \quad , \tag{9-6}$$

where P = buffer porosity, m^3/Mg of particles,

W_O = weight fraction of OPyC in completed particle; determined from geometrical relationships using the mean kernel diameter, buffer thickness, OPyC coating thickness (radiographs of 100 particles), assuming sphericity, and the kernel density, buffer density, and liquid gradient OPyC density.

Finally, the buffer porosity (m^3 void/Mg ThO_2) is expressed as P^1:

$$P^1 = P/(1 - W_C) \quad . \tag{9-7}$$

Experimental results are shown in Table 9-4 for a group of particle batches for which the buffer density, as measured before application of the OPyC coating, was close to the nominal fuel specification value of 1.05 Mg/m^3. An average 10.6% loss in buffer porosity was measured after application of the OPyC coating.

As a basis for comparison, the buffer porosity of a nominal particle (all thickness and density values equal to the specification targets) is 0.0868 m^3/Mg ThO_2, while the minimal allowable average buffer porosity (maximum allowable buffer density, minimum average thickness, all other values nominal) is 0.0603 m^3/Mg ThO_2.

TABLE 9-4
BUFFER POROSITY LOSS DURING OPyC COATING

Batch No.	Pre-OPyC Buffer Density (Mg/m^3)	Pre-OPyC Porosity ($m^3/Mg\ ThO_2$)	Post-OPyC Porosity ($m^3/Mg\ ThO_2$)	Porosity Loss (%)
3804-59-2	1.06	0.0812	0.0688	15.3
3804-59-3	1.10	0.0875	0.0734	16.0
3804-59-4	1.10	0.0854	0.0774	9.4
3804-59-5	1.10	0.0824	0.0694	15.8
3804-65-1	1.125	0.0766	0.0657	14.2
3804-65-2	1.133	0.0779	0.0715	8.2
3804-65-3	1.127	0.0826	0.0750	9.2
3804-65-4	1.128	0.0694	0.0673	3.0
3804-65-1	1.115	0.0766	0.0704	8.1
3804-65-6	1.060	0.0780	0.0725	7.0
3804-65-7	1.126	0.0836	0.0736	12.0
3804-65-8	1.10	0.0845	0.0772	8.7
Nominal	1.05		0.0868	
Minimal	1.2		0.0603	

Determination of OPyC Porosity by High-Pressure Hg Intrusion. Fission gas retention is a necessary attribute of LTI carbon coatings on BISO fuel particles. A method was sought to measure this quality in a less expensive and faster fashion than the accepted irradiation/fission gas collection (Kr-85m R/B) method. High-pressure Hg intrusion seemed to offer some potential for meeting the testing requirements.

The essence of the high-pressure Hg intrusion method is pressurizing a BISO particle sample to 69 MPa (10,000 psi) in a Hg-filled tube. The high pressure forces Hg into pores in the particle surface, with increasingly smaller pores filled at higher pressures. By measuring the volume of Hg which is forced into these open pores, an indication of the porosity of the sample is obtained. The data show that low values of open porosity are necessary, but not sufficient, for low fission gas release values.

The Hg intrusion method is useful as a screening device to reject obviously bad particle batches. As shown in Fig. 9-5, Hg intrusion values above 40 μℓ/g LTI always show excess fission gas release. Mercury intrusion values below 40 μℓ/g LTI, and even Hg intrusion values as low as 16 μℓ/g LTI, may or may not have excess fission gas release. Thus, particle batches having Hg intrusion values below 40 μℓ/g LTI required the TRIGA fission gas release or gas leaching test to determine if they meet the $\leq 3 \times 10^{-5}$ R/B Kr-85m specification for LHTGR fuel irradiation samples.

Phosgene Gas Leaching. The purpose of this work is to develop a QC test to replace TRIGA and LINAC activation of fuel for determination of as-manufactured defects, i.e., contamination and defective coatings. Previous work has involved gas leaching of BISO coated ThO_2 fuel particles with phosgene for 200 min at 960° and 1100°C in an attempt to relate fuel quality with the rate at which heavy metal was leached from the particles under these conditions. During this quarter, work was carried out with BISO ThO_2 particles at much longer leach times to: (1) determine the extent of leaching required to prove whether a batch of particles meets the fission gas release specification and (2) determine whether the particles

with impermeable coatings are attacked or modified under these required leaching conditions.

The procedure is based on the volatilization of exposed thorium by a suitable chlorinating agent with subsequent collection and spectrophotometric measurement of the separated chloride, according to the following overall reactions:

$$ThO_2 + 2COCl_2 \xrightarrow{1100°C} ThCl_4 + 2CO_2$$

$$Th^{+4} + \text{Arsenazo-III in } HNO_3 \rightarrow \text{blue complex} \quad .$$

The specific procedure employed in this study involves reacting a split sample of 9 to 10 g of particles with phosgene at 1100°C in a quartz furnace tube. After a 20-min leaching period, the sample is cooled for 3 min under phosgene, and the volatilized thorium chloride is rinsed from the condenser tube into an evaporation flask using 0.5M HNO_3. The sample can then be replaced in the furnace tube for another leaching cycle if desired. The nitric acid solution of the leached thorium is evaporated to near dryness to remove volatile ions such as Cl^- which interfere with the spectrophotometric determination.

The concentrated solution is then made up to 25 ml of approximately 0.5M HNO_3. The thorium content of an aliquot of this solution is determined spectrophotometrically using Arsenazo-III as the complexing agent at a wavelength of 660 μm in 0.5M HNO_3.

Initially, a study was carried out to determine the effectiveness of short versus long cycles in leaching thorium from BISO ThO_2 particles. The results are shown in Fig. 9-6. These results indicate that thorium can be leached at a much greater rate using short (20-min) cycles than cycles of several hours each. Although 20 min may not be an optimum cycle time, a 20-min leach cycle was chosen for these studies in order to eliminate cycle time as a variable.

In order to determine the extent of phosgene leaching required at 1100°C to remove exposed thorium, a split sample of BISO ThO_2 particles from batch 6779-65 having a photofission R/B Kr-85m value of 1.7×10^{-3} was leached until the total fraction of thorium leached reached 3×10^{-3}. The results (Fig. 9-7) indicate that not all of the exposed thorium was removed after 18 hr of leaching since the rate of removal was not decreasing.

Microscopic examination of these particles both before and after leaching using the stereomicroscope, metallography, and radiography indicated that the thorium was leached from the kernels through existing PyC coating porosity, i.e., no "new" porosity (coating damage) was formed.

In order to determine whether these required leaching conditions attack particles with impermeable coatings, a split sample of BISO ThO_2 particle batch 6779-67 having a photofission R/B Kr-85m value of 3.2×10^{-6} was leached with phosgene under identical conditions of 1100°C for 18 hr using 20-min cycles. This test involved a total of 54 thermal cycles. The leach results are shown in Fig. 9-8.

The results indicate negligible attack of the coating since the total fraction of thorium leached was 2.44×10^{-5}. The thorium leached from the particles was surface contamination. This conclusion is supported by the lack of further leaching of thorium from the sample over the last 8 hr of the test. Surface contamination releases gas at a rate of about 3×10^{-2} releases per fission so that the amount of leached material would produce about 7×10^{-6} R/B Kr-85m at 1100°C, which is in fair agreement with the measured value of 3.2×10^{-6} R/B Kr-85m.

The leached particles from this experiment were compared with unleached particles from the same batch by microscopic examination using the stereomicroscope, metallography, and radiography. No evidence of coating damage was observed, and there appeared to be no difference between the leached and unleached particles. Also, the radiographs were examined for total coating thickness; there was no significant difference between the coating thicknesses of the leached and unleached samples.

An attempt was made in previous work to relate fuel quality with the rate at which heavy metal was leached over the first 200 min in order to devise a short leach test. Examination of Figs. 9-7 and 9-8 indicates that no conclusion on fuel quality can be derived until after about 600 min of leaching. In fact, both plots show similar plateaus in the early stages of leaching, which suggests the stepwise leaching of contamination from the particle surface and coatings and then a breakthrough to recovery of thorium from exposed kernels. However, the mechanisms probably overlap, preventing a simple interpretation of the slopes.

Higher heating temperatures would accelerate permeation and reaction rates. Therefore, in order to shorten the leaching time, higher heating temperatures will be investigated.

Seibersdorf Bacon Anisotropy Factor (BAF_o) Measurement. The optical anisotropy of PyC is a critical material property which is specified for irradiation samples. Several changes have recently been instituted in the optical anisotropy measurement on the Seibersdorf instrument. The most significant of these is the change from a scanning 4 by 24 μm window to a fixed 24-μm diameter circle and the change from a tabulated conversion of the optical anisotropy factor (OAF) to BAF to a calculated conversion. The current method, which is intended to become standard for the Seibersdorf equipment, is briefly described in this section.

One effect of anisotropy in PyC coatings is a reflectivity for polarized light that varies with polarization direction. The Seibersdorf unit measures the OAF, which is defined by

$$OAF = R_A/R_B \quad , \tag{9-8}$$

where R_A and R_B are the reflectivities for directions A and B, respectively. Directions A and B are perpendicular to each other, with A being vertical as viewed through the eyepieces of the microscope. The reflectivity for direction A is defined by

$$R_A = I_A / I'_A \quad , \tag{9-9}$$

where I_A = intensity of reflected A-polarized beam as measured by a photomultiplier,

I'_A = intensity of the same reflected A-polarized beam when a reference surface (an isotropic mirror) is substituted for the sample.

The analogous definition holds for R_B.

The following measurement conditions are now standard:

1. The 32/0.55 oil immersion objective is used with Reichert immersion oil (n_D = 1.516).

2. The measurement is made on a 24-μm-diameter circular spot at the 3 o'clock position of a metallographic cross section of a particle coating. The center of the spot is placed over the approximate centerline of the coating.

3. Three OAF readings are taken on each spot. The reported value is the average.

4. Each OAF value is converted to a BAF_o value by BAF_o = 0.71777 x OAF + 0.28299. This formula is based on a linear fit to the tabulated values supplied by the manufacturer and is valid for OAF values from 1.000 to 1.750.

5. Ten particles selected at random are read per batch. The average of the ten readings is reported.

6. The reference surface for the reflectivity measurement is the mirrored surface on the Reichert stage micrometer.

The main reason for the use of a scanning window rather than a fixed window is the increased speed of the measurement and consequent increased number of coatings per batch that can be measured. Also, the change to the calculation procedure from the tabulated values eliminates a significant roundoff error since the table only yields values to the nearest 0.005 BAF_o unit. Overall, there appears to be no significant systematical bias introduced by the change in procedure. Table 9-5 shows comparative values using the old and the new procedures on typical samples from a current interlaboratory round-robin anisotropy measurement program.

Fuel Analysis for Carbon, Hydrogen, Nitrogen, and Oxygen. Three analyzers (carbon, hydrogen, and nitrogen/oxygen) from LECO Corporation were recently installed. Calibration of these analyzers using metallic standard materials has been accomplished.

The carbon analyzer utilizes an induction furnace for sample combustion in an oxygen atmosphere. The evolved CO_2 combustion product is selectively measured by an infrared detector. Carbon content is displayed directly as percent carbon on an electronic digital voltmeter. Analysis time is on the order of 1 min.

The hydrogen analyzer releases hydrogen from the sample by fusion in an inert argon atmosphere. An impulse furnace which delivers currents up to 900 amp raises the sample temperature to nearly 2000°C, fusing the sample. The hydrogen gas evolved is detected in a thermal conductivity cell and the results are displayed on an electronic digital voltmeter. The sample analysis time is about 3 min.

The nitrogen/oxygen analyzer is also based on inert gas fusion techniques. An impulse furnace fuses the sample material at temperatures up to 2700°C in a helium atmosphere. The nitrogen and oxygen evolved are separated chromatographically and measured sequentially in a thermal conductivity cell. The measured values of nitrogen and oxygen are displayed separately on identical digital voltmeter readouts. The sample analysis time is approximately 4 min.

TABLE 9-5
COMPARISON OF OPTICAL ANISOTROPY CALCULATION TECHNIQUES

Sample No.	BAF_o Scanning Window Table Look-Up	BAF_o Fixed Window Calculation
4674-23	1.110	1.103
4483-107	1.035	1.031
6155-01-20	1.020	1.021
6151-00-010	1.045	1.041
6151-01-015	1.075	1.077
6151-00-035	1.065	1.071

Applications of these instruments include carbon analysis of kernels and coated particles and hydrogen, nitrogen, and oxygen analysis of WAR particles and HTGR fuel rods for irradiation capsule samples.

TASK 300: INTEGRAL FUEL SYSTEM TESTING

Subtask 310: Peach Bottom Fuel Test Elements

Fuel Test Element FTE-6

Conclusion. The fuel rods and loose particle spine samples in FTE-6 behaved satisfactorily at peak exposures of 2.88×10^{25} n/m^2 $(E > 29\ fJ)_{HTGR}$ and 1250°C. The current HTGR fuel performance codes were all substantiated at the peak irradiation conditions of FTE-6. No significant SiC attack, kernel migration, or matrix-coating interactions were observed except for the UO_2 TRISO fuel. This particular fuel had kernel migration extending up to the SiC inner surface, which caused SiC attack and subsequent pressure vessel failure exceeding 20% in some of the fuel rods. The poor performance of the UO_2 fuel has also been observed in the accelerated testing of P13N and P13P (Ref. 9-9) and the UO_2 is no longer a candidate HTGR fuel type.

Specific fuel examination conclusions are as follows:

1. The appearance of the fuel rods in FTE-6 was satisfactory. Matrix end cap cracking and small surface cracks were found on the majority of the fuel rods.

2. Fuel rods from stacks 1 and 2 containing the UO_2-ThO_2 fuel blend were bowed up to 0.58 mm on their length (48.3 mm). This was apparently caused by nonhomogeneity of the fuel particle loadings.

3. Fission gas release measurements of the UO_2-ThO_2 fuel rods show fuel failure fractions of ∿20%, which correlates well with

metallographically measured fuel failure fractions of the UO_2 TRISO particles.

4. Using 5×10^{-3} as the release from fuel in a constrained geometry, the calculated fuel failure fractions of all the fuel blends except the UO_2-ThO_2 were between 0.5% and 5%. In some cases this did not compare well with fuel failure measured during metallography. This discrepancy is believed to be caused by the hydrolysis of the thorium-bearing fuel, which would cause a higher R/B_f.

5. Metallography showed little thermochemical effects of SiC attack, kernel migration, or matrix-coating interactions in the fuels tested except for the UO_2 TRISO particles.

6. Kernel migration of the UO_2 kernels caused SiC attack and up to 20% pressure vessel failure.

7. Gamma scanning indicates insignificant cesium release from any fuel rods except for the UO_2-ThO_2 fuel blend. Release from these fuel rods was ∿70% from the failed fuel fraction. Approximately 40% of the released cesium was found absorbed on the graphite fuel body. Ongoing graphite sleeve scanning will hopefully aid in the completion of the cesium inventory balance in the test element.

8. Gamma-scan-measured total FIMA values for the fuel rods using Cs-137 as a burnup monitor indicate a systematic 10 to 20% higher burnup than that calculated by GAUGE.

9. Spine sample batches 4000-242 (ThC_2 TRISO) and 4000-320 (UC_2 TRISO) showed good irradiation behavior at 2.0×10^{25} n/m^2 $(E > 29\ fJ)_{HTGR}$ and ∿1050°C.

Experiment Description. FTE-6 was the third of a series of nearly identical fuel test elements irradiated in Core 2 of the Peach Bottom reactor. FTE-3, -4, -6, and -5 were irradiated for 133, 449, 645, and 897 EFPD,* respectively. The results of the postirradiation examinations (PIEs) of FTE-3 and FTE-4 are reported in Refs. 9-4 and 9-5; FTE-5 is presently being examined in the GA hot cell on a privately funded program.

The major objectives of these test elements was to evaluate HTGR fuel types and materials in a representative HTGR environment. The postirradiation data are a direct comparison and verification source for the following HTGR design codes: (1) fluence and depletion, (2) thermal performance, (3) thermal and Wigner strain and stress, and (4) fission product behavior.

Under Phase II of the Peach Bottom test element program, FTE-6 was inserted in core position CO2-01 on July 11, 1971, with beginning-of-life (BOL) at 252 EFPD of Core 2 operation and end-of-life (EOL) occurring at 897.3 EFPD (October 31, 1974) of Core 2 operation. The total irradiation of FTE-6 was 645 EFPD of Core 2 operation. The average radial power factor for FTE-6 in Core 2 was 0.98, and energy production was 9.04×10^4 KW/days. The maximum EOL fuel temperature was $\sim$1463°C and the peak fluence was 2.8×10^{25} n/m^2 $(E > 29\ fJ)_{HTGR}$.

All fuel and fuel rods in FTE-6 showed satisfactory irradiation performance except for the UO_2 TRISO particles in one fuel blend. This particular fuel had previously been eliminated as a candidate HTGR fuel after its poor performance in P13N and P13P (Ref. 9-6). Completed fuel gamma scanning and in-progress graphite gamma scanning will allow the determination of fuel rod fission product inventories and burnups and the distribution of volatile fission products in the test element. Gamma scanning measured burnups agreed to within ±20% of the GAUGE-calculated values.

*EFPD = equivalent full power days of reactor operation at 115 MW(t) from 804 elements.

The design of FTE-6 was that of three identical teledial fuel bodies in a standard Peach Bottom driver containment; 336 fuel rods and 34 centrally located spine samples were tested in the element. FTE-6 was assembled with two thermocouples at 1917.7 mm (75.5 in.) total core height [i.e., 1257.3 mm (49.5 in.) active core height]. Thermocouple A was a W/Re type thermocouple located near the spine samples and thermocouple B was a C/A type thermocouple located near the outer sleeve.

The assembly of FTE-6 is shown in Fig. 9-9. A list of the detailed drawings for all the test element components is given in Table 9-6. The sleeve and upper and lower reflectors were standard Peach Bottom driver element designs; the materials used in these components are listed in Table 9-7. The purge flow in this element was down the center of the top reflector, through the upper porous plug, down the gap between the sleeve inside diameter and the fuel body outside diameter, through the internal trap in the bottom reflector and the standoff pin, and into the main manifold of the Peach Bottom reactor. No individual fission gas release measurements were taken.

The fuel zone consisted of three teledial 787.4 mm (31 in.) long fuel bodies (Fig. 9-10) stacked one on top of another. Bodies 1 and 2 were radially oriented to one another by means of two thermocouples, which are shown in the cross section of the fuel body in Fig. 9-11. Body 3 was not positioned via any thermocouples and therefore was subject to azimuthal movement. Fourteen fuel rods were loaded into each of the eight teledial holes. Spine samples were loaded into the 25.4 mm (1 in.) diameter hole in the center of the bodies.

FTE-6 contained 336 fuel rods that were carbonized in Al_2O_3 beds. These rods consisted of a closely packed bed of blended fissile and fertile coated fuel particles bonded together in a carbonaceous matrix. The matrix was a blend of 27 to 30% natural-flake graphite flour and 70 to 73% coal tar pitch. The matrix was prepared by hot-mixing the ingredients to form a homogeneous blend, followed by cooling to room temperature and then

TABLE 9-6
FTE-6 DRAWING AND PARTS LIST

Drawing/Part No.	Issue	Title
11497-1, 2	B	Assembly
11666-1	B	Sleeve
11668-1	B	Brazing Ring
11669-6	B	Upper Reflector
11670-2	B	Bottom Connector
11671-1	B	Screen
11672-1, 2	B	W/Re, C/A Thermocouples
11673-1	B	Upper Contact
11541-1	B	Spacer
11542-1	B	Internal Trap Assembly
11543-1	B	Lower Reflector
11510-1	B	Fuel Body Assembly, 6-1
11503-3	B	Fuel Body
11503-4	B	Fuel Hole Plug
11503-5	B	Compact Pusher
11503-6	B	Sample Hole Plug
11503-7	B	Sample Hole Plug
11400-1	A	Fuel Stack Assembly
11704-1	A	Fuel Stack Assembly
11410-1	A	Fuel Stack Assembly
11411-1	A	Fuel Stack Assembly
11510-15	B	Graphite Cement (P-511)
11510-16	B	Polystyrene Solution
11510-17	B	Graphite Spacer
11510-18	B	Boronated Graphite Sample
11510-19, 20, 21, 22, 23	B	Diffusion Sample
11510-24, 25	B	Fission Product Release Sample
11510-26, 27	B	Boronated Graphite Sample
11510-28, 29, 30, 31	B	Diffusion Sample

TABLE 9-6 (Continued)

Drawing/Part No.	Issue	Title
11510-32	B	Graphite Spacer
11511-1	B	Fuel Body Assembly 6-2
11511-2	B	Fuel Body
11511-3	B	Fuel Hole Plug
11511-4	B	Compact Pusher
11511-5	B	Sample Hole Plug
11511-6	B	Sample Hole Plug
11511-7, 8, 9, 10	B	Fuel Stack Assembly
11511-15	B	Graphite Cement (P-511)
11511-16	B	Polystyrene Solution
11511-17	B	Graphite Spacer
11511-18, 19	B	Fission Product Release Sample
11511-20, 21, 22	B	Advanced Fuel Rod Samples
11511-24, 25, 26, 27, 28, 29, 30	B	Fission Product Release Sample
11511-31	B	Graphite Spacer
11512-1	B	Fuel Body Assembly 6-3
11512-2	B	Fuel Body
11512-3	B	Fuel Hole Plug
11512-4	B	Compact Pusher
11512-5	B	Sample Hole Plug
11512-6	B	Sample Hole Plug
11512-7, 8, 9, 10	B	Fuel Stack Assembly
11512-14	B	Polystyrene Solution
11512-15	B	Graphite Cement (P-511)
11512-16	B	Graphite Spacer
11512-17, 18	B	Thermal Stability Sample, Type 1
11512-19, 20, 21, 22, 23	B	Thermal Stability Sample, Type 2
11512-24, 25	B	Boronated Graphite Sample
11512-26	B	Graphite Spacer

TABLE 9-7
GRAPHITE MATERIALS USED IN PEACH BOTTOM FUEL ELEMENTS

Fuel Element Component	Core 1 Driver Graphite Type		Core 2 Driver Graphite Type		FTE-3, -4, -5, -6 Graphite Type	
	Base Stock	Manufacturer	Base Stock	Manufacturer	Base Stock	Manufacturer
Top reflector	H-253[a]	GLCC	H-381[b]	GLCC	H-381[b]	GLCC
Top spine	711-GSXY	Speer	711-T	Speer	H-327	GLCC
Lower two spines (with T/L slots)	711-GSXY	Speer	711-GSXY	Speer	H-327	GLCC
Fuel compact or rod						
Filler	GP-38 flour	UCC	GP-38 flour	UCC	6353	Ashbury
Binder	Barrett No. 30	Allied Chemical	Barrett No. 30	Allied Chemical	15V	Allied Chemical
Graphite fuel body	NA[c]		NA		H-327	GLCC
Sleeve	H-253[a]	GLCC	H-382[b]	GLCC	H-382[b]	GLCC
Internal trap	806 RL	Speer	580	Speer	580	Speer
Lower reflector	806 RL	Speer	580	Speer	H-327	GLCC
Bottom connector	H-253[a]	GLCC	H-381	GLCC	H-253[a]	GLCC

[a] Also referred to as HLM-85-10, made with Texas Lockport coke.

[b] Also referred to as HLM-85-10, made with "Y" coke. Discrimination into H-381 and H-382 lacks explanation. It should be noted that most of the Core 1 and all Core 2 HLM-85-10 material was graphitized in a standard Acheson-type furnace for about 28 days with temperatures up to 2800°C. However, some of the Core 1 material went through a rapid graphitization process in a tube furnace for about 1 hr at 2800°C (which also has been used for impregnation purposes of Core 1 and 2 sleeves after machining). About 40 elements in Core 2 were made out of leftover Core 1 rapid graphitized material. This material happened to shrink more than the Core 2 standard material, as realized during the Core 2 unloading exercise.

[c] NA = not applicable.

grinding the solid matrix into granules suitable for use in the fuel rod injection equipment. The impurities in the matrix were kept in the low ppm range.

Both the fuel particles and the fuel rods were made in production equipment using the then-available production processes and quality control techniques. The hot matrix was injected into the particle bed with a prototype injection machine similar to that built for manufacturing of Fort St. Vrain fuel. After cooling, the fuel rods were removed from the injection die; at this point, the rods were referred to as "green" rods. The green rods were then packed into Al_2O_3 beds and subjected to a carbonization treatment.

The carbonization cycle consisted of heating the fuel rods in a flowing nitrogen atmosphere for 2 hr to 750°C and holding at that temperature for 0.5 hr. The fuel rods were then heat treated by passing them through a furnace, which had a hot zone 1814.4 mm (72 in.) long, at 1800°C and at a rate of 25.4 mm (1 in.) per min. The atmosphere in the furnace was argon. The cured rods were measured for length and diameter and loaded into the three graphite fuel bodies.

The eight teledial holes contained four different kinds of fuel rods:

Holes 1 and 2	UO_2 TRISO, ThO_2 BISO
Holes 3 and 4	(2.75 Th:U)C_2 TRISO, ThC_2 BISO
Holes 5 and 6	(2.75 Th:U)C_2 TRISO, ThC_2 TRISO
Holes 7 and 8	UC_2 TRISO, ThC_2 BISO

Preirradiation fuel particle and fuel rod attributes are shown in Tables 9-8 and 9-9.

The spine samples and their location in the test element are listed in Table 9-10. A detailed description of all the spine samples is given in Ref. 9-7.

TABLE 9-8
FTE-6 PREIRRADIATION FUEL ROD QUALITY CONTROL ATTRIBUTES[a]

Body	Hole	Fuel Blend	Preirradiation Fission Gas Release Kr-85m at 1100°C	Exposed Heavy Metal[b] (kg Th/kg Th)	Heavy Metal Loadings[c]		Impurities						
					Th ($\times 10^{-3}$ kg)	U ($\times 10^{-3}$ kg)	Fe (ppm)	S (ppm)	Ti (ppm)	V (ppm)	Residual Hydrogen (ppm)	Residual Ash (ppm)	H_2O (ppm)
1, 2, 3	1, 2	UO_2 - ThO_2	2.0×10^{-5}	5.0×10^{-6}	4.973	0.6556	400	80	20	4	10	2000	250
1, 2, 3	3, 4	$(Th,U)O_2$ - ThC_2	3.4×10^{-6}	1.5×10^{-4}	1.950	0.6557	400	80	20	4	10	2000	250
1, 2, 3	5, 6	$(Th,U)C_2$ - ThC_2	6.7×10^{-7}	3.7×10^{-5}	1.892	0.6557	400	80	20	4	10	2000	250
1, 2, 3	7, 8	UC_2 - ThC_2	1.7×10^{-6}	2.5×10^{-5}	1.133	0.6557	400	80	20	4	10	2000	250

[a] Representative rod attributes.

[b] Determined by hydrolysis technique.

[c] Design loadings.

TABLE 9-9
FTE-6 COMPOSITION AND LOCATION OF BONDED FUEL RODS[a]

Body	Hole	FOD Number	FMB Number	Kernel			Coating Type	As-Manufactured Coating Parameters								Total Particle Parameters			
								Nominal Thickness (μm)					OPyC Density (Mg/m^3)	OPyC OPTAF	SiC Density (Mg/m^3)	Density (Mg/m^3)	Diameter (μm)	Heavy Metal Content	
				Type	Density (Mg/m^3)	Nominal Diameter (μm)		Buffer	IPyC	SiC	OPyC	Total						wt % U	wt % Th
Fissile Particle																			
1,2,3	1,2	ED1258BIL(A)SL	4000-355	UO_2	10.23	201	TRISO	53	27	23	37	140	1.80	1.07	3.20	2.62	472	25.70	--
	3,4	ET1272BIL(A)SL	4000-357	$(Th,U)C_2$[b]	9.07	211	TRISO	56	28	27	44	147	1.80	1.06	3.19	2.47	509	7.70	17.75
	5,6	ET1272BIL(A)SL	4000-357	$(Th,U)C_2$	9.07	211	TRISO	56	28	27	44	147	1.80	1.06	3.19	2.47	509	7.70	17.75
	7,8	ET1274BIL(A)SL	4000-358	UC_2	12.50	99	TRISO	57	27	27	33	137	1.79	1.11	3.20	2.26	382	9.85	--
Fertile Particle																			
1,2,3	1,2	T01236BL	4000-339	ThO_2	9.95	410	BISO	62	--	--	81	142	1.78	1.09	--	3.42	690	--	53.40
	3,4	T1254BL	4000-345	ThC_2	8.78	351	BISO	63	--	--	69	135	1.81	1.15	--	3.04	629	--	51.23
	5,6	CT6A56L	4000-335	ThC_2	8.80	360	TRISO	56	26	28	41	145	1.79	1.13	3.20	3.15	663	--	44.15
	7,8	T1254BL	4000-345	ThC_2	8.78	351	BISO	63	--	--	69	145	1.81	1.15	--	3.04	629	--	51.23

[a] All values are from data retrieval (Fuel Materials Branch).

[b] Th/U ratio = 2.75.

TABLE 9-10
FTE-6 SPINE SAMPLE IRRADIATION CONDITIONS[a]

Position	Pre-Irrad. Length (mm)	Pre-Irrad. Weight (kg)	Mean Core Height[b] (mm)	Sample Type	Ident. Number	Composite Spine Length (mm) Pre-Irrad.	Composite Spine Length (mm) Post-Irrad.
Body 1							
Δ	9.652						
1	45.720	0.04090	663.702	Graphite spacer	12		
2	96.520	0.07721	734.822	Boronated graphite	4465-57-1		
3	32.004	0.02453	799.084	Diffusion	23		
4	32.004	0.02469	831.088	Diffusion	40		
5	32.004	0.02471	863.092	Diffusion	51		
6	32.004	0.02513	895.096	Diffusion	60		
7	32.004	0.02448	927.100	Diffusion	13		
8	32.004	0.02475	959.104	Fission product release	73-P	28.530	28.3230
9	32.004	0.02501	991.108	Fission product release	56-P		
10	45.720	0.07853	1055.370	Boronated graphite	4465-57-2	$\frac{\Delta L}{L}$ = -0.7255%	
11	45.720	0.07899	1151.890	Boronated graphite	4465-57-3		
12	32.004	0.02472	1216.152	Diffusion	17		
13	32.004	0.02455	1248.156	Diffusion	33		
14	32.004	0.02452	1280.160	Diffusion	19		
15	32.004	0.02463	1312.164	Diffusion	26		
16	37.338	0.03358	1346.835	Graphite spacer	13		
d	52.857						
Σ	787.171						
Body 2							
Δ	9.652						
1	63.500	0.05738	1459.763	Graphite spacer	14		
2	31.496	0.02494	1507.388	Fission product release	122-P		
3	31.750	0.02500	1539.138	Fission product release	168-P		
4	101.854	0.09358	1605.940	Advanced fuel rods	3c		
5	101.600	0.09108	1707.667	Advanced fuel rods	3b		
6	101.600	0.09257	1809.267	Advanced fuel rods	3a		
7	31.750	0.10158	1875.942	Fission product release	NB-4		
8	31.750	0.02455	1907.692	Fission product release	12-P	28.480	28.3852
9	31.750	0.10144	1939.442	Fission product release	NB-7		
10	31.750	0.02506	1971.192	Fission product release	29-P	$\frac{\Delta L}{L}$ = -0.3329%	
11	31.750	0.10158	2002.942	Fission product release	NB-11		
12	31.750	0.02467	2034.692	Fission product release	44-P		
13	31.750	0.10167	2066.442	Fission product release	NB-15		
14	31.750	0.02460	2098.192	Fission product release	148-P		
15	37.338	0.03367	2132.736	Graphite spacer	15		
d	52.400						
Σ	785.444						
Body 3							
Δ	9.652						
1	63.500	0.05725	2245.208	Graphite spacer	16		
2	146.050	0.13749	2349.983	Thermal stability - 1	M		
3	146.050	0.13741	2496.033	Thermal stability - 1	N		
4	31.750	0.02603	2584.933	Thermal stability - 2	18		
5	31.750	0.02383	2616.683	Thermal stability - 2	24	28.550	28.4100
6	31.750	0.02390	2648.433	Thermal stability - 2	30		
7	31.750	0.02463	2680.183	Thermal stability - 2	6	$\frac{\Delta L}{L}$ = 0.4904%	
8	31.750	0.02479	2711.933	Thermal stability - 2	12		
9	96.520	0.07988	2776.068	Boronated graphite	4465-57-4		
10	96.520	0.07855	2872.588	Boronated graphite	4465-57-5		
11	17.780	0.01598	2929.738	Graphite spacer	17		
d[b]	52.654						
Σ	787.476						

[a] Irradiation temperature, EOL fast fluence, and FIMA not available at this time.

[b] Ref. 0 in Drawing 1151C is beginning of mean core height.

Visual Examination. After unloading the fuel rods from the graphite fuel bodies, composite Kollmorgan photographs of 12 complete fuel stacks were taken of various fuel blends from all three fuel bodies. These are shown in Ref. 9-7. Random matrix end cap cracking and debonding were evident in all the fuel blends and in all three fuel bodies. Surface cracks and soot "pock" marks (surface fuel failure) were more evident in the center region of the fuel element, which correlates with the higher temperatures and neutron fluences in this region. The majority of the soot marks caused by surface fuel failure were seen in rods from stacks 1 and 2, which contained the UO_2 TRISO particles which had high fuel failure (see section on fuel rod metallography). Unloading damage was also evident on some rods. This was caused by debonded fuel particles caught between the fuel rod and fuel hole periphery during unloading, which causes long striations and damaged fuel particles at the surface.

Fuel rods from stacks 1 and 2 also showed significant bow of up to ∿0.5 mm (0.020 in.) in their length (see Table 9-11). This was felt to be caused by nonhomogeneous fuel loadings in the TRISO UO_2 - BISO ThO_2 blend which would cause nonhomogeneous fuel rod shrinkage.

Several representative fuel rods from body 2 which were chosen for fission gas release analysis were examined and photographed with the stereomicroscope. Stereophotographs confirm the Kollmorgan photography results. Eight fuel rods are shown in Figs. 9-12 through 9-19 and a summary of the amount of surface fuel failure is shown in Table 9-12. In all cases there was cracking of the matrix end cap region of the rods and some small surface crazing. The soot marks left by the surface failed fuel is obvious in the stereoexamination of rods 2-1-7 and 2-2-7 (Figs. 9-12 and 9-13).

Fuel Rod Fission Gas Release Measurements. Eight fuel rods were measured for Kr-85m fission gas release at 1100°C in the TRIGA irradiation facility. Results are presented in Table 9-12; the preirradiation results are shown in Table 9-8. Except for the fuel rods containing UO_2

TABLE 9-11
FTE-6 FUEL ROD BOW

Rod	Mean Core Height (mm)	Bow (mm)
2-1-10	1925	0.53
2-1-11	1974	0.45
2-2-5	1677	0.39
2-2-10	1925	0.42
2-2-13	2073	0.42
3-1-1	2269	0.55
3-1-2	2318	0.46
3-1-3	2368	0.45
3-1-4	2418	0.57
3-1-5	2467	0.59
3-1-6	2517	0.53
3-1-7	2566	0.44
3-1-12	2814	0.54
3-1-13	2863	0.50
3-2-3	2368	0.40
3-2-7	2318	0.28
3-2-13	2863	0.45

TABLE 9-12
SUMMARY OF POSTIRRADIATION EXAMINATION OF FTE-6 FUEL RODS

Fuel Rod Ident. No.[a]	Fuel Types		Irradiation Conditions			Fission Gas Release[d] R/B Kr-85m	Dimensional Change		Broken Particles on Surface from Stereo-Examination	Metallographic Examination											
										Fissile Particle						Fertile Particle					
	Fissile Particle	Fertile Particle	Avg Fuel Temp[b] (°C)	Fast Fluence[c] (x 10^{25} n/m^2)	FIMA Fissile[c] (%)		Diameter (%)	Length (%)		OPyC Failure (%)	95% Confidence Limits P (%)	SiC Failure (%)	95% Confidence Limits P (%)	Pressure Vessel Failure (%)	95% Confidence Limits P (%)	OPyC Failure (%)	95% Confidence Limits P (%)	SiC Failure (%)	95% Confidence Limits P (%)	Pressure Vessel Failure (%)	95% Confidence Limits P (%)
2-1-7	201-μm UO_2 TRISO	410-μm ThO_2 BISO		2.84	45.4	1.1 X 10^{-3}	-2.28	-3.03	43	22.8	$16.1 \leq P \leq 31.3$	22.8	$16.1 \leq P \leq 31.3$	21.1	$14.6 \leq P \leq 29.4$	0.4[f]	$0.1 \leq P \leq 2.1$			0.4	$0.1 \leq P \leq 2.1$
2-2-7	201-μm UO_2 TRISO	410-μm ThO_2 BISO		2.84	45.4	1.2 X 10^{-3}	-2.42	-3.43	43	13.2	$8.5 \leq P \leq 20.0$	19.9	$14.0 \leq P \leq 27.3$	8.1	$4.6 \leq P \leq 13.9$	0.0	$0.0 \leq P \leq 1.8$			0.0	$0.0 \leq P \leq 1.8$
2-3-7	211-μm $(Th,U)C_2$ TRISO	351-μm ThC_2 BISO		2.84	45.4	1.8 X 10^{-4}	-1.82	-1.78	5	0.7	$0.3 \leq P \leq 1.7$	0.0	$0.0 \leq P \leq 0.6$	0.0	$0.0 \leq P \leq 0.6$	0.0	$0.0 \leq P \leq 5.7$			0.0	$0.0 \leq P \leq 5.7$
2-4-7	211-μm $(Th,U)C_2$ TRISO	351-μm ThC_2 BISO		2.84	45.4	1.1 X 10^{-4}	-1.73	-2.37	0												
2-5-7	211-μm $(Th,U)C_2$ TRISO	360-μm ThC_2 TRISO		2.84	45.4	2.3 X 10^{-5}	-1.62	-1.86	4												
2-6-7	211-μm $(Th,U)C_2$ TRISO	360-μm ThC_2 TRISO		2.84	45.4	1.1 X 10^{-4}	-1.55	-1.70	4	1.4	$0.7 \leq P \leq 2.7$	0.3	$0.1 \leq P \leq 1.2$	0.2	$0.0 \leq P \leq 1.0$	8.7	$2.5 \leq P \leq 21.0$	0.0	$0.0 \leq P \leq 7.5$	0.0	$0.0 \leq P \leq 7.5$
2-7-8	99-μm UC_2 TRISO	351-μm ThC_2 BISO		2.83	45.2	1.7 X 10^{-4}	-2.01	-2.22	3	1.7	$0.8 \leq P \leq 3.5$	2.2	$1.2 \leq P \leq 4.1$	0.7	$0.2 \leq P \leq 2.1$	0.0	$0.0 \leq P \leq 2.2$			0.0	$0.0 \leq P \leq 2.2$
2-8-7	99-μm UC_2 TRISO	351-μm ThC_2 BISO		2.84	45.4	2.6 X 10^{-4}	-1.84	-2.37	1												

[a] Fuel body - hole no. - fuel rod no. (No. 11 is at top of the fuel body.)
[b] Calculated by TREVER code.
[c] Calculated by GAUGE/FEVER code.
[d] Measured in TRIGA at 1100°C.
[e] Failure of all structural coatings.
[f] Two of the failures were cross-contaminated ThC_2 TRISO particles. Run also contained 11 ThO_2 TRISO and 4 ThC_2 TRISO intact particles.

TRISO/ThO_2 BISO particles, the fission gas release measurements indicate between 0.5 and 5% fuel failure, if the release of Kr-85m at 1100°C (R/B_b) is assumed to be 5×10^{-3} (Ref. 9-8). In rods 2-3-7, 2-6-7, and 2-7-8 the magnitude of fuel failure did not correlate well with the metallographically measured fuel failure, which was lower. It is believed that the calculated failure is higher than actual because the thorium-bearing fuel in these fuel rods hydrolyzes upon failure producing an R/B_f much higher than 5×10^{-3} per failed particle (Ref. 9-8).

Fuel rods 2-1-7 and 2-2-7 (UO_2 TRISO/ThO_2 BISO) had fuel failures measured by fission gas release of ∿20% assuming an R/B_f of 5×10^{-3}. This correlates well with the ∿20% fuel failure measured by metallography on these fuel rods.

A detailed fission gas release analysis will be made using nominal thorium contamination and preirradiation fission gas release measurements as soon as the nuclear analysis is complete on the element.

Fuel Rod Metallography. Four fuel rods from the center of body 2, which had the highest fast neutron fluence and temperature, i.e., 2.84×10^{25} n/m^2 $(E > 29 \text{ fJ})_{HTGR}$ and 1250°C, were chosen for metallography. These fuel rods represented each fuel blend tested in FTE-6 (Table 9-9). A summary of the postirradiation examination of these fuel rods is given in Table 9-12. A radial metallographic cross section and a representative photomicrograph of the matrix of each of these fuel rods are shown in Figs. 9-20 through 9-24. Representative photomicrography of the fuel particles in each of these fuel rods are shown in Figs. 9-25 through 9-33. A single-channel gamma scan plot of most of the fuel rods examined is shown in Fig. 9-34.

All of the fuel particles examined in these fuel rods had <1% pressure vessel failure except for the UO_2 TRISO fissile particles in rods 2-1-7. These particles had ∿20 to 30% pressure vessel failure due to migration of the UO_2 kernels through the IPyC to the SiC inner surface and subsequent

mixed fission product attack and failure of the SiC coating (Figs. 9-25 and 9-26). In FTE-3, which had a low peak thermal neutron exposure [$\sim$0.6 x 10^{25} n/m^2 $(E > 29\ fJ)_{HTGR}$], the UO_2 kernel had not really begun to deform plastically or to migrate (Ref. 9-4). FTE-4, which had a intermediate peak exposure of 1.9 x 10^{25} n/m^2 $(E > 25\ fJ)_{HTGR}$, showed significant UO_2 kernel plasticity and migration up to the IPyC inner surface. FTE-6, with a peak exposure of 2.8 x 10^{25} n/m^2 $(E > 29\ fJ)_{HTGR}$, reveals the final effect of the UO_2 migration in the pressure vessel failure of the fuel particles. UO_2 fissile particles have been previously rejected as candidate HTGR fuel based on similar poor irradiation performance observed in P13N and P13P (Ref. 9-9).

OPyC failure was low in most cases and was attributed mainly to polishing damage. The ThC_2 TRISO fuel in rod 2-6-7 showed the highest OPyC failure of $\sim$9% (Fig. 9-30). This is consistent with the $\sim$5% failure observed in FTE-4 (Ref. 9-6). Because of incomplete preirradiation data on this particular fuel particle, it is difficult to assess the reason for the OPyC failure. One possible explanation for this high failure is that this is the largest diameter TRISO coated particle examined in FTE-6. Evidence discussed in Ref. 9-9 has shown that the larger the particle, the higher the probability of failure. This is explained by Weibull statistics where the probability of finding a critical flaw in a stressed region is proportional to the area or volume under stress.

The only significant thermochemical effect in the fuel rods in FTE-6 was the UO_2 kernel migration. All of the UC_2 TRISO particles in rod 2-8-7 had mixed fission products in the IPyC. One isolated UC_2 particle showed what appeared to be contamination attack of the fuel particle (Fig. 9-33). All the fissile particles in FTE-6 had buffer densification and debonding and, in some cases, IPyC debonding and IPyC failure. One isolated case of matrix-coating interaction was seen in rod 2-3-7 on a $(Th,U)C_2$ TRISO particle (Fig. 9-29). The OPyC coating on this particle had been torn off by the differential shrinkage of the bonded matrix and the OPyC coating.

Homogeneity of the fuel loadings was a further significant metallographic observation. Rods 2-1-7, 2-3-7, and 2-8-7 all showed various forms of fuel nonhomogeneity. Rods 2-3-7 and 2-8-7 had significant skewing of the fertile particles toward the matrix end cap portion of the fuel rod. The single-channel gamma scan Zr-95 profile in Fig. 9-34 shows that this fertile nonhomogeneity has little effect on the overall power profile in the fuel rod. On the other hand, rod 2-1-7, which showed a fissile particle nonhomogeneity in metallography, had an equally great nonhomogeneity in the power profile in Fig. 9-34. Comparison of rods 2-1-7 and 2-2-7, which showed good and bad fuel homogeneity, respectively, shows that the nonuniform fuel loadings had little effect on the UO_2 TRISO and ThO_2 BISO fuel performance. In both cases the extent of the fuel failure and the degree of kernel migration and SiC attack were similar for the fissile fuel. This nonhomogeneity may have caused bowing of the fuel rods, which was discussed previously in the section on the visual examination.

Fuel Rod Gamma Scan Results. Fuel rods from all four fuel blends and from different axial locations in the element were gamma scanned with a high resolution Ge(Li) gamma spectrometer. The scanning geometry and calibration calculations are described in Ref. 9-6. These gamma scans give the following information:

1. Relative axial homogeneity of each fuel rod.

2. Fission product inventory of the most significant isotopes in each fuel rod.

3. Total burnup of each fuel rod.

The axial fuel homogeneity is shown in Fig. 9-34 for fuel rods used in the detailed examination and in Fig. 9-35 for a representative cross section of fuel rods in the element. In general, the fuel homogeneity was good except for several cases in holes 1, 2, 7, and 8.

The fission product inventories and burnup of each fuel rod are presented in Table 9-13. The gamma-scan-calculated total burnup from the Cs-137 inventory is compared to the GAUGE/FEVER-calculated values in Table 9-14 and plotted against the axial core location in Figs. 9-36 through 9-39. The shape of the total FIMA plots of the various fuel stacks is a direct comparison to the thermal neutron fluence and power profile of the test element. For fuel stacks from holes 3 through 8, the curve is smooth and shows only a few anomalous points. Rods from stacks 1 and 2 show a large deviation from a smooth FIMA plot in Fig. 9-36. This was caused by the high failure of the UO_2 fissile particles in these fuel rods which allowed Cs-137 release, which in turn lowered the total FIMA value calculated from the Cs-137 inventory. Table 9-14 shows that in stacks 3 through 8 the gamma-spectroscopy-measured mean total FIMA was systematically 10 to 20% higher than the GAUGE-calculated mean total FIMA. In stacks 1 and 2 the mean total FIMA was $\sim$5% lower than the GAUGE value, which is directly related to the Cs-137 loss from the UO_2 particle.

Using the measured and deduced theoretical Cs-137/Zr-95 ratios, the percent Cs-137 loss from the various fuel rods can be calculated. Figures 9-40 through 9-43 show the Cs-137/Zr-95 ratio for fuel rods from different stacks along the axial length of the element. If there is no particle failure or diffusive loss of the volatile Cs-137, the Cs-137/Zr-95 ratio should be nearly the same for all fuel rods in FTE-6. The mean deduced theoretical Cs-137/Zr-95 ratio was calculated by averaging the measured ratio in fuel rods from stacks 3 through 6 which showed essentially no fuel failure. In rods from stacks 7 and 8 (Fig. 9-43), the deduced theoretical Cs-137/Zr-95 ratio is within the 2σ confidence level on the Cs-137/Zr-95 ratio measured on individual fuel rods, indicating no Cs-137 loss.

Stacks 1 and 2 show a definite correlation of Cs-137 loss with temperature and thermal neutron exposure. A plot of the Cs-137 loss for these fuel stacks at various core locations is shown in Fig. 9-44. The Cs-137 loss was the lowest in body 1, which had the lowest temperature and fluence exposure, and the highest ($\sim$30%) in the center of body 2, which had the

TABLE 9-13

FTE-6 FUEL ROD GAMMA SCAN SUMMARY

FUEL ROD I.D.	MEAN CORE HT (MM)	PA-233 (311.9KEV) (CI)	RU-103 (497.1KEV) (CI)	RU-106 (511.9KEV) (CI)	CS-134 (604.7KEV) (CI)	CS-137 (661.6KEV) (CI)	CE-144 (695.6KEV) (CI)	ZR-95 (724.2KEV) (CI)	CS-137 /ZR-95 (CT/MIN)	TOTAL FIMA %
1-1-2	738.00	0.00000	0.00000	4.82959-01	3.21043-01	5.87629-01	7.40963+00	7.01076+00	.17816	3.38143
	2SIG ERR	0.00000	0.00000	1.19644-01	6.58544-02	1.18869-01	2.04234+00	3.46936+00	.08067	.69204
1-1-4	837.00	0.00000	0.00000	5.37624-01	5.10875-01	6.83811-01	7.74154+00	1.38666+01	.10482	3.93490
	2SIG ERR	0.00000	0.00000	1.37788-01	1.23265-01	1.38272-01	2.15514+00	3.55991+00	.01690	.80503
1-1-6	936.00	0.00000	0.00000	6.98969-01	8.42291-01	9.15300-01	1.00664+01	1.88455+01	.10324	5.26698
	2SIG ERR	0.00000	0.00000	1.70343-01	1.70580-01	1.84718-01	2.52411+00	4.65763+00	.01496	1.07565
1-1-8	1035.00	0.00000	0.00000	7.04546-01	8.45449-01	9.04059-01	1.09078+01	1.69716+01	.11323	37.53512
	2SIG ERR	0.00000	0.00000	1.68732-01	1.70966-01	1.82334-01	2.72665+00	4.34335+00	.01803	1.06182
1-1-12	1232.00	0.00000	0.00000	6.30133-01	1.00667+00	1.07647+00	1.16066+01	1.88174+01	.12160	6.19440
	2SIG ERR	0.00000	0.00000	1.86157-01	2.03149-01	2.17054-01	2.82861+00	4.76721+00	.01885	1.26405
1-1-14	1331.00	0.00000	0.00000	9.75185-01	1.54032+00	1.23927+00	1.38736+01	2.03752+01	.12929	7.13124
	2SIG ERR	0.00000	0.00000	2.33867-01	3.10522-01	2.49733-01	3.27372+00	4.88857+00	.01704	1.45444
2-1-2	1528.00	0.00000	0.00000	9.26793-01	1.33977+00	1.05214+00	1.29755+01	2.25532+01	.09916	6.05440
	2SIG ERR	0.00000	0.00000	2.21106-01	2.70478-01	2.12343-01	3.01002+00	5.54268+00	.01414	1.23651
2-1-4	1627.00	0.00000	0.00000	1.02647+00	1.23916+00	9.88492-01	1.36601+01	2.38249+01	.08819	5.68815
	2SIG ERR	0.00000	0.00000	2.29906-01	2.50110-01	1.99379-01	3.20982+00	5.46490+00	.00986	1.16108
2-1-7	1775.00	0.00000	0.00000	1.01070+00	1.30778+00	1.01625+00	1.48831+01	2.35662+01	.09166	5.84790
	2SIG ERR	0.00000	0.00000	2.32173-01	2.64073-01	2.05101-01	3.50883+00	5.41125+00	.01031	1.19433
2-1-8	1824.00	0.00000	0.00000	9.53600-01	1.09283+00	8.84058-01	1.29967+01	2.20453+01	.08524	5.08720
	2SIG ERR	0.00000	0.00000	2.19381-01	2.20839-01	1.78470-01	3.07776+00	5.38007+00	.01190	1.03923
2-1-10	1923.00	0.00000	0.00000	1.05767+00	1.39103+00	1.11710+00	1.39902+01	2.35111+01	.10100	6.42820
	2SIG ERR	0.00000	0.00000	2.34119-01	2.80630-01	2.25264-01	3.23292+00	5.78080+00	.01439	1.31185
2-1-12	2022.00	0.00000	0.00000	9.56416-01	1.18707+00	9.52504-01	1.34815+01	2.39936+01	.08438	5.48106
	2SIG ERR	0.00000	0.00000	2.18330-01	2.39825-01	1.92305-01	3.18829+00	5.80300+00	.01146	1.11978
2-1-14	2121.00	0.00000	0.00000	9.38723-01	1.37392+00	1.09629+00	1.37440+01	2.24040+01	.10401	6.30846
	2SIG ERR	0.00000	0.00000	2.17203-01	2.77311-01	2.21196-01	3.14465+00	5.36799+00	.01368	1.28809
3-1-2	2318.00	0.00000	0.00000	9.05713-01	9.48819-01	8.22088-01	1.26129+01	2.12098+01	.08239	4.73060
	2SIG ERR	0.00000	0.00000	2.13475-01	1.91964-01	1.66137-01	3.12389+00	5.36687+00	.01278	.96732
3-1-4	2417.00	0.00000	0.00000	8.97980-01	8.22396-01	7.65790-01	1.34695+01	2.14688+01	.07582	4.40664
	2SIG ERR	0.00000	0.00000	2.15205-01	1.66760-01	1.54791-01	3.19945+00	5.40384+00	.01160	.90124
3-1-6	2516.00	0.00000	0.00000	7.75027-01	7.69452-01	7.89776-01	1.11033+01	1.90754+01	.08790	4.53891
	2SIG ERR	0.00000	0.00000	1.89627-01	1.56014-01	1.59446-01	2.72364+00	4.96066+00	.01462	.92834
3-1-8	2615.00	0.00000	0.00000	7.65165-01	7.89808-01	7.85582-01	1.10185+01	1.79149+01	.09321	4.52053
	2SIG ERR	0.00000	0.00000	1.77083-01	1.59942-01	1.58642-01	2.66674+00	4.79341+00	.01656	.92374

TABLE 9-13 (Continued)

FUEL ROD I.D.	MEAN CORE HT (PM)	PA-233 (311.9KEV) (CI)	RU-103 (497.1KEV) (CI)	RU-106 (511.9KEV) (CI)	CS-134 (604.7KEV) (CI)	CS-137 (661.6KEV) (CI)	CE-144 (695.6KEV) (CI)	ZR-95 (724.2KEV) (CI)	CS-137 /ZR-95 (CT/MIN)	TOTAL FIMA %
3-1-10	2713.06	0.00000	0.00000	6.09078-01	6.68511-01	7.62821-01	9.02207+00	1.55432+01	.10432	4.38956
	2SIG ERR	0.00000	0.00000	1.47990-01	1.35512-01	1.54031-01	2.37221+00	4.24193+00	.01936	.89690
3-1-12	2817.00	0.00000	0.00000	5.93801-01	4.73929-01	6.70677-01	7.95108+00	1.38225+01	.10314	3.85933
	2SIG ERR	0.00000	0.00000	1.46999-01	9.68382-02	1.35683-01	2.15816+00	4.06229+00	.02224	.78993
3-1-14	2911.00	0.00000	0.00000	5.69211-01	3.98388-01	6.58904-01	7.12663+00	1.60804+01	.08710	3.79158
	2SIG ERR	0.00000	0.00000	1.45005-01	8.14752-02	1.33159-01	1.95171+00	4.58586+00	.01771	.77531
1-2-6	936.00	0.00000	0.00000	7.10639-01	7.71765-01	8.51057-01	9.19035+00	1.62303+01	.11146	4.71893
	2SIG ERR	0.00000	0.00000	1.63383-01	1.56433-01	1.71897-01	2.42120+00	4.48140+00	.02121	1.00091
2-2-1	1479.00	0.00000	0.00000	9.19277-01	1.40023+00	1.09873+00	1.27330+01	2.06258+01	.11323	6.32249
	2SIG ERR	0.00000	0.00000	2.26877-01	2.83048-01	2.21965-01	2.87764+00	4.19621+00	.00423	1.29242
2-2-2	1528.00	0.00000	0.00000	9.65850-01	1.39526+00	1.11271+00	1.28018+01	2.17925+01	.10853	6.40295
	2SIG ERR	0.00000	0.00000	2.30946-01	2.82098-01	2.24869-01	2.88503+00	4.43157+00	.00404	1.30928
2-2-3	1578.00	0.00000	0.00000	9.77174-01	1.35904+00	1.06542+00	1.32526+01	2.20311+01	.10279	6.13080
	2SIG ERR	0.00000	0.00000	2.36498-01	2.74780-01	2.15401-01	2.96652+00	4.48247+00	.00393	1.25411
2-2-4	1627.00	0.00000	0.00000	9.70538-01	1.18307+00	9.53754-01	1.24082+01	2.07211+01	.09784	5.48826
	2SIG ERR	0.00000	0.00000	2.30813-01	2.39309-01	1.92898-01	2.82725+00	4.21247+00	.00369	1.12305
2-2-5	1676.00	0.00000	0.00000	9.47650-01	1.08213+00	8.79309-01	1.29988+01	2.11818+01	.08824	5.05987
	2SIG ERR	0.00000	0.00000	2.23268-01	2.19259-01	1.77941-01	2.94067+00	4.30901+00	.00345	1.03592
2-2-6	1726.00	0.00000	0.00000	1.01626+00	1.26335+00	1.00931+00	1.47567+01	2.36945+01	.09054	5.80792
	2SIG ERR	0.00000	0.00000	2.36207-01	2.55614-01	2.04123-01	3.28017+00	4.81310+00	.00333	1.18841
2-2-7	1775.00	0.00000	0.00000	1.00941+00	1.33756+00	1.04002+00	1.40816+01	2.20034+01	.10047	5.76669
	2SIG ERR	0.00000	0.00000	2.29524-01	2.70070-01	2.09888-01	3.30305+00	4.98891+00	.01069	1.22222
2-2-8	1824.00	0.00000	0.00000	9.92807-01	1.13696+00	9.03436-01	1.26480+01	2.41225+01	.07961	5.00936
	2SIG ERR	0.00000	0.00000	2.27109-01	2.29817-01	1.82468-01	3.03184+00	5.93947+00	.01143	1.06246
2-2-9	1874.00	0.00000	0.00000	9.49149-01	1.12794+00	9.21972-01	1.30194+01	2.19915+01	.08911	5.30537
	2SIG ERR	0.00000	0.00000	2.23820-01	2.28512-01	1.86629-01	2.94175+00	4.47072+00	.00345	1.08646
2-2-10	1923.00	0.00000	0.00000	9.49848-01	1.28130+00	1.02206+00	1.28059+01	2.17651+01	.09982	5.88130
	2SIG ERR	0.00000	0.00000	2.26504-01	2.59217-01	2.06646-01	2.97553+00	4.42568+00	.00376	1.20313
3-2-6	2516.00	0.00000	0.00000	9.45274-01	8.65731-01	8.13717-01	1.14166+01	2.14577+01	.08061	4.68235
	2SIG ERR	0.00000	0.00000	2.13242-01	1.75079-01	1.64247-01	2.69456+00	5.16121+00	.01075	.95641

TABLE 9-13 (Continued)

FUEL ROD I.D.	MEAN CORE HT (MM)	PA-233 (311.9KEV) (CI)	RU-103 (497.1KEV) (CI)	RU-106 (511.9KEV) (CI)	CS-134 (604.7KEV) (CI)	CS-137 (661.6KEV) (CI)	CE-144 (695.6KEV) (CI)	ZR-95 (724.2KEV) (CI)	CS-137 /ZR-95 (CT/MIN)	TOTAL FIMA %
1-3-2	738.00	0.00000	0.00000	9.76238-01	3.65173-01	6.08894-01	6.28011+00	1.29517+01	.09993	7.58170
	2SIG ERR	0.00000	0.00000	2.42171-01	7.47713-02	1.23110-01	1.77590+00	3.55315+00	.01878	1.55097
1-3-4	837.00	1.89428+05	0.00000	6.31562-01	5.82511-01	7.52788-01	1.80723+00	1.37232+01	.11660	9.37341
	2SIG ERR	3.80765+04	0.00000	1.55467-01	1.18582-01	1.52171-01	1.43435+00	3.78257+00	.02213	1.91713
1-3-6	936.00	0.00000	0.00000	7.18956-01	8.33769-01	8.90473-01	1.01305+01	1.65239+01	.11455	11.08780
	2SIG ERR	0.00000	0.00000	1.77064-01	1.69072-01	1.79841-01	2.55296+00	4.49619+00	.02113	2.26592
1-3-8	1034.00	0.00000	0.00000	8.52703-01	9.33016-01	9.59010-01	1.06600+01	1.76158+01	.11572	11.94120
	2SIG ERR	0.00000	0.00000	2.04030-01	1.88821-01	1.93523-01	2.68383+00	4.58446+00	.01924	2.43849
1-3-10	1133.00	0.00000	0.00000	7.64550-01	1.01181+00	9.59966-01	9.26806+00	1.78440+01	.11435	11.95311
	2SIG ERR	0.00000	0.00000	1.99263-01	2.04685-01	1.93830-01	2.09371+00	4.60665+00	.01865	2.44223
1-3-12	1232.00	0.00000	0.00000	9.14201-01	1.41715+00	1.15218+00	1.15128+01	2.06951+01	.11834	14.34653
	2SIG ERR	0.00000	0.00000	2.07918-01	2.86181-01	2.32474-01	2.95491+00	5.27456+00	.01866	2.92934
1-3-14	1331.00	0.00000	0.00000	1.07091+00	1.64125+00	1.24615+00	1.42540+01	2.22429+01	.11909	15.51651
	2SIG ERR	0.00000	0.00000	2.52757-01	3.31151-01	2.51327-01	3.34570+00	5.47411+00	.01702	3.16703
2-3-2	1528.00	0.00000	0.00000	1.04853+00	1.68307+00	1.22832+00	1.34753+01	2.27419+01	.11481	15.29454
	2SIG ERR	0.00000	0.00000	2.41989-01	3.39572-01	2.47692-01	3.22284+00	5.46885+00	.01527	3.12127
2-3-4	1627.00	0.00000	0.00000	1.02027+00	1.71589+00	1.22676+00	1.37855+01	2.29014+01	.11386	15.27517
	2SIG ERR	0.00000	0.00000	2.31235-01	3.46053-01	2.47459-01	3.17952+00	5.64013+00	.01632	3.11823
2-3-7	1775.00	0.00000	0.00000	1.07117+00	1.70895+00	1.24276+00	1.31420+01	2.22317+01	.11882	15.47438
	2SIG ERR	0.00000	0.00000	2.44222-01	3.44694-01	2.50615-01	3.06253+00	5.06662+00	.01291	3.15808
2-3-9	1824.00	0.00000	0.00000	1.07378+00	1.63463+00	1.19048+00	1.20210+01	2.04571+01	.12370	14.82337
	2SIG ERR	0.00000	0.00000	2.47712-01	3.29787-01	2.40140-01	2.90468+00	5.29798+00	.02031	3.02600
2-3-10	1923.00	0.00000	0.00000	1.05998+00	1.58065+00	1.16497+00	1.32324+01	2.10058+01	.11789	14.50569
	2SIG ERR	0.00000	0.00000	2.45975-01	3.18965-01	2.35063-01	3.12799+00	5.35892+00	.01864	2.96195
2-3-12	2022.00	0.00000	0.00000	1.02178+00	1.59975+00	1.18752+00	1.32862+01	2.26104+01	.11164	14.78651
	2SIG ERR	0.00000	0.00000	2.33834-01	3.72310-01	2.39542-01	3.16542+00	5.71441+00	.01721	3.01848
2-3-14	2121.00	0.00000	0.00000	1.10754+00	1.63767+00	1.18559+00	1.21449+01	2.25475+01	.11177	14.76252
	2SIG ERR	0.00000	0.00000	2.50658-01	3.30161-01	2.38985-01	2.87155+00	5.54127+00	.01589	3.01165
3-3-2	2319.00	0.00000	0.00000	9.82577-01	1.38015+00	1.08670+00	1.27440+01	2.16242+01	.10682	13.53114
	2SIG ERR	0.00000	0.00000	2.31539-01	2.78697-01	2.19289-01	3.04725+00	5.46778+00	.01650	2.76317
3-3-4	2417.00	0.00000	0.00000	9.06672-01	1.30406+00	1.01219+00	1.11111+01	2.25074+01	.09559	12.60341
	2SIG ERR	0.00000	0.00000	2.08102-01	2.63307-01	2.04263-01	2.68790+00	5.43105+00	.01288	2.57382
3-3-6	2516.00	0.00000	0.00000	8.84761-01	1.10406+00	9.62238-01	1.17428+01	1.83258+01	.11161	11.98139
	2SIG ERR	0.00000	0.00000	2.04063-01	2.27133-01	1.94234-01	2.67595+00	4.68087+00	.01771	2.44739

TABLE 9-13 (Continued)

FUEL ROD I.D.	MEAN CORE HT (MM)	PA-233 (311.9KEV) (CI)	RU-103 (497.1KEV) (CI)	RU-106 (511.9KEV) (CI)	CS-134 (604.7KEV) (CI)	CS-137 (661.6KEV) (CI)	CE-144 (695.6KEV) (CI)	ZR-95 (724.2KEV) (CI)	CS-137 /ZR-95 (CT/MIN)	TOTAL FIMA %
3-3-8	2615.00	0.00000	0.00000	8.34849-01	9.56897-01	9.16391-01	1.10367+01	1.75924+01	.11072	11.41053
	2SIG ERR	0.00000	0.00000	1.95612-01	1.93511-01	1.85040-01	2.74191+00	4.60191+00	.01866	2.33147
3-3-10	2713.00	0.00000	0.00000	7.85096-01	8.03258-01	8.51076-01	1.01596+01	1.76807+01	.10231	10.59675
	2SIG ERR	0.00000	0.00000	1.82478-01	1.62685-01	1.71868-01	2.51448+00	4.52703+00	.01635	2.16547
3-3-12	2816.00	0.00000	0.00000	5.66603-01	4.80261-01	6.43238-01	7.82223+00	1.28931+01	.10605	8.00934
	2SIG ERR	0.00000	0.00000	1.39723-01	9.78873-02	1.30089-01	2.01794+00	3.66048+00	.02139	1.63886
3-3-14	2911.00	0.00000	0.00000	5.32058-01	4.05193-01	6.38501-01	8.27438+00	1.03747+01	.13082	7.95036
	2SIG ERR	0.00000	0.00000	1.36329-01	8.32390-02	1.29188-01	2.21996+00	3.12707+00	.02954	1.62744
1-4-6	936.02	0.00000	0.00000	7.90571-01	8.19272-01	8.82381-01	9.37366+00	1.56165+01	.12010	10.98705
	2SIG ERR	0.00000	0.00000	1.83031-01	1.65979-01	1.78198-01	2.29347+00	4.27992+00	.02250	2.24523
2-4-7	1775.00	0.00000	0.00000	1.07888+00	1.69173+00	1.21266+00	1.37321+01	2.09612+01	.12297	15.09953
	2SIG ERR	0.00000	0.00000	2.40142-01	3.41099-01	2.44553-01	3.60180+00	4.82225+00	.01391	3.08169
7-4-8	1824.00	0.00000	0.00000	1.02177+00	1.59763+00	1.15894+00	1.17687+01	2.04895+01	.12023	14.43070
	2SIG ERR	0.00000	0.00000	2.46780-01	3.21760-01	2.33970-01	3.08979+00	5.51351+00	.02162	2.94758
3-4-6	2516.00	0.00000	0.00000	8.88527-01	1.20921+00	1.02421+00	1.15808+01	1.90359+01	.11437	12.75302
	2SIG ERR	0.00000	0.00000	1.97848-01	2.44032-01	2.06533-01	2.74614+00	4.55583+00	.01497	2.60260

TABLE 9-13 (Continued)

FUEL ROD I.D.	MEAN CORE HT (MM)	PA-233 (311.9KEV) (CI)	RU-103 (497.1KEV) (CI)	RU-106 (511.9KEV) (CI)	CS-134 (604.7KEV) (CI)	CS-137 (661.6KEV) (CI)	CE-144 (695.6KEV) (CI)	ZR-95 (724.2KEV) (CI)	CS-137 /ZR-95 (CI/MIN)	TOTAL FIMA %
1-5-2	738.00	0.00000	0.00000	4.95754-01	3.63268-01	6.00887-01	6.78274+00	1.23623+01	.10332	7.65289
	2SIG ERR	0.00000	0.00000	1.25988-01	7.45596-02	1.23330-01	1.82561+00	3.87769+00	.02525	1.58704
1-5-4	837.00	0.00000	0.00000	5.99480-01	6.31576-01	7.82511-01	7.89183+00	1.04506+01	.15916	9.96606
	2SIG ERR	0.00000	0.00000	1.49462-01	1.28310-01	1.58139-01	2.34304+00	3.23492+00	.03761	2.03787
1-5-6	936.00	0.00000	0.00000	7.42280-01	8.08980-01	8.59683-01	9.61399+00	1.76353+01	.10362	10.94892
	2SIG ERR	0.00000	0.00000	1.86169-01	1.63914-01	1.73673-01	2.43269+00	4.50666+00	.01648	2.23813
1-5-8	1034.00	0.00000	0.00000	7.72570-01	8.67118-01	8.79975-01	9.47057+00	1.65808+01	.11281	11.20735
	2SIG ERR	0.00000	0.00000	1.87541-01	1.75651-01	1.77712-01	2.41454+00	4.51728+00	.02086	2.29025
1-5-10	1133.00	0.00000	0.00000	7.38034-01	9.65442-01	9.09684-01	1.02770+01	1.66499+01	.11613	11.58573
	2SIG ERR	0.00000	0.00000	1.80408-01	1.95378-01	1.83712-01	2.66674+00	4.49362+00	.02104	2.36757
1-5-12	1232.00	0.00000	0.00000	9.74795-01	1.35982+00	1.09900+00	1.13897+01	2.14343+01	.10899	13.99688
	2SIG ERR	0.00000	0.00000	2.32874-01	2.74539-01	2.21753-01	2.84508+00	5.50807+00	.01755	2.85805
1-5-14	1331.00	0.00000	0.00000	9.64805-01	1.55759+00	1.19993+00	1.33012+01	2.24607+01	.11356	15.28228
	2SIG ERR	0.00000	0.00000	2.25666-01	3.14354-01	2.42035-01	3.24536+00	5.70803+00	.01776	3.11957
2-5-2	1528.00	0.00000	0.00000	1.02323+00	1.61439+00	1.19455+00	1.32769+01	2.16535+01	.11726	15.21373
	2SIG ERR	0.00000	0.00000	2.26839-01	3.25480-01	2.40816-01	3.15823+00	5.26609+00	.01615	3.10401
2-5-4	1627.00	0.00000	0.00000	1.03201+00	1.67025+00	1.20606+00	1.40299+01	2.14566+01	.11948	15.36040
	2SIG ERR	0.00000	0.00000	2.29174-01	3.36642-01	2.47684-01	3.27794+00	5.20979+00	.01637	3.13330
2-5-7	1775.00	0.00000	0.00000	1.05098+00	1.72150+00	1.23836+00	1.31403+01	2.08203+01	.12643	15.77169
	2SIG ERR	0.00000	0.00000	2.38977-01	3.47213-01	2.49726-01	3.06946+00	4.88264+00	.01541	3.21876
2-5-8	1824.00	0.00000	0.00000	9.01728-01	1.61498+00	1.17346+00	1.26225+01	1.90947+01	.13063	14.94515
	2SIG ERR	0.00000	0.00000	2.16300-01	3.25975-01	2.36839-01	3.24917+00	5.16621+00	.02378	3.05241
2-5-10	1923.00	0.00000	0.00000	1.05028+00	1.62601+00	1.15767+00	1.28230+01	2.05397+01	.11980	14.74404
	2SIG ERR	0.00000	0.00000	2.41777-01	3.28063-01	2.33521-01	3.07239+00	5.33627+00	.01982	3.00981
2-5-12	2022.00	0.00000	0.00000	1.07183+00	1.66468+00	1.20691+00	1.32540+01	2.35874+01	.10876	15.37115
	2SIG ERR	0.00000	0.00000	2.36674-01	3.35555-01	2.43210-01	3.05303+00	5.80092+00	.01549	3.13499
2-5-14	2121.00	0.00000	0.00000	9.99139-01	1.66296+00	1.20664+00	1.28183+01	2.15456+01	.11904	15.36774
	2SIG ERR	0.00000	0.00000	2.30935-01	3.35406-01	2.43339-01	3.15540+00	5.43096+00	.01821	3.13643
3-5-2	2318.00	0.00000	0.00000	9.08700-01	1.39784+00	1.08810+00	1.35587+01	2.14005+01	.10808	13.85807
	2SIG ERR	0.00000	0.00000	2.17084-01	2.82216-01	2.19554-01	3.29898+00	5.34190+00	.01611	2.82971
3-5-4	2417.00	0.00000	0.00000	9.21305-01	1.28250+00	1.05306+00	1.27447+01	1.98715+01	.11265	13.41203
	2SIG ERR	0.00000	0.00000	2.22874-01	2.59026-01	2.12533-01	3.06758+00	5.10525+00	.01814	2.73918
3-5-6	2516.00	0.00000	0.00000	8.14352-01	1.06261+00	9.31575-01	1.07654+01	1.74520+01	.11346	11.86454
	2SIG ERR	0.00000	0.00000	1.97546-01	2.14845-01	1.88115-01	2.58921+00	4.58310+00	.01930	2.42434

TABLE 9-13 (Continued)

FUEL ROD I.D.	MEAN CORE HT (MM)		PA-233 (311.9KEV) (CI)	RU-103 (497.1KEV) (CI)	RU-106 (511.9KEV) (CI)	CS-134 (604.7KEV) (CI)	CS-137 (661.6KEV) (CI)	CE-144 (695.6KEV) (CI)	ZR-95 (724.2KEV) (CI)	CS-137 /ZR-95 (CT/MIN)	TOTAL FIMA %
3-5-8	2615.00		0.00000	0.00000	8.09800-01	9.80508-01	9.21447-01	1.02065+01	1.80398+01	.10857	11.73554
		2SIG ERR	0.00000	0.00000	1.88751-01	1.98299-01	1.85975-01	2.55498+00	4.75375+00	.01861	2.39688
3-5-10	2713.00		0.00000	0.00000	6.72150-01	7.26791-01	7.91770-01	9.37556+00	1.70319+01	.09881	10.08398
		2SIG ERR	0.00000	0.00000	1.66828-01	1.47412-01	1.60018-01	2.43282+00	4.51248+00	.01718	2.06208
3-5-12	2817.00		0.00000	0.00000	6.47322-01	4.91650-01	6.72582-01	7.71294+00	1.70257+01	.08397	8.56600
		2SIG ERR	0.00000	0.00000	1.59834-01	1.00270-01	1.36038-01	2.01660+00	4.51083+00	.01462	1.75293
3-5-14	2911.00		0.00000	0.00000	5.16054-01	3.97838-01	6.23500-01	7.11110+00	1.26273+01	.10496	7.94089
		2SIG ERR	0.00000	0.00000	1.27392-01	8.15912-02	1.26211-01	1.96689+00	3.71103+00	.02264	1.62618
1-6-6	936.00		0.00000	0.00000	6.64951-01	7.90111-01	8.39251-01	9.41873+00	1.38896+01	.12844	10.68870
		2SIG ERR	0.00000	0.00000	1.62771-01	1.60061-01	1.69512-01	2.34216+00	3.89756+00	.02528	2.18455
2-6-7	1775.00		0.00000	0.00000	1.04557+00	1.62618+00	1.17958+00	1.44344+01	1.99446+01	..2571	15.02310
		2SIG ERR	0.00000	0.00000	2.41926-01	3.28027-01	2.37931-01	3.31722+00	4.81266+00	.01692	3.06666
2-6-8	1824.00		0.00000	0.00000	1.07978+00	1.60504+00	1.16741+00	1.40836+01	2.17409+01	.11414	14.86817
		2SIG ERR	0.00000	0.00000	2.45879-01	3.27710-01	2.35487-01	3.34185+00	5.44626+00	.01717	3.03515
3-6-6	2516.00		0.00000	0.00000	8.79236-01	1.10118+00	9.49440-01	1.17273+01	1.80453+01	.11184	12.09207
		2SIG ERR	0.00000	0.00000	2.05293-01	2.22561-01	1.91660-01	2.88479+00	4.61145+00	.01777	2.47010

TABLE 9-13 (Continued)

FUEL ROD I.D.	MEAN CORE HT (MM)	PA-233 (311.9KEV) (CI)	RU-103 (497.1KEV) (CI)	RU-106 (511.9KEV) (CI)	CS-134 (604.7KEV) (CI)	CS-137 (661.6KEV) (CI)	CE-144 (695.6KEV) (CI)	ZR-95 (724.2KEV) (CI)	CS-137 /ZR-95 (CI/MIN)	TOTAL FIMA %
1-7-2	738.00	0.00000	0.00000	4.21219-01	3.07788-01	5.33762-01	0.00000	1.06671+01	.10636	9.69615
	2SIG ERR	0.00000	0.00000	1.21567-01	6.37307-02	1.08363-01	0.00000	3.48204+00	.02752	1.99092
1-7-4	837.00	0.00000	0.00000	5.35116-01	5.20369-01	6.61613-01	8.69541+00	1.20605+01	.11661	12.01865
	2SIG ERR	0.00000	0.00000	1.43958-01	1.06432-01	1.34038-01	2.36487+00	3.79970+00	.02844	2.46312
1-7-6	936.00	0.00000	0.00000	6.32310-01	7.84585-01	8.33760-01	8.62268+00	1.42370+01	.12448	15.14582
	2SIG ERR	0.00000	0.00000	1.57647-01	1.58952-01	1.69428-01	2.38735+00	4.02196+00	.02484	3.09590
1-7-8	1034.00	0.00000	0.00000	7.24861-01	8.35673-01	8.74131-01	1.01750+01	1.35341+01	.13729	15.87918
	2SIG ERR	0.00000	0.00000	1.79402-01	1.69323-01	1.76566-01	2.63321+00	3.90507+00	.02855	3.24552
1-7-10	1133.00	0.00000	0.00000	8.20067-01	9.34100-01	8.57580-01	8.55061+00	1.01057+01	.18038	15.57853
	2SIG ERR	0.00000	0.00000	2.11351-01	1.89410-01	1.74009-01	2.47514+00	4.54747+00	.07279	3.19718
1-7-12	1232.00	0.00000	0.00000	7.65533-01	1.22269+00	1.00667+00	1.10674+01	1.94121+01	.11023	18.28693
	2SIG ERR	0.00000	0.00000	2.04780-01	2.47264-01	2.03368-01	2.86905+00	5.29780+00	.02047	3.73813
1-7-14	1331.00	0.00000	0.00000	9.75539-01	1.43401+00	1.09592+00	1.22927+01	1.74706+01	.13334	19.90820
	2SIG ERR	0.00000	0.00000	2.39580-01	2.89671-01	2.21302-01	3.08088+00	4.73146+00	.02434	4.06794
2-7-1	1479.00	0.00000	0.00000	9.79325-01	1.62947+00	1.16631+00	1.17708+01	1.95957+01	.12651	21.18686
	2SIG ERR	0.00000	0.00000	2.19736-01	3.28610-01	2.35407-01	2.75076+00	4.55164+00	.01491	4.32740
2-7-2	1528.00	0.00000	0.00000	9.71147-01	1.59231+00	1.13823+00	1.27107+01	2.16360+01	.11182	20.67664
	2SIG ERR	0.00000	0.00000	2.24417-01	3.21168-01	2.29618-01	3.05450+00	5.20647+00	.01492	4.22119
2-7-3	1578.00	0.00000	0.00000	9.69059-01	1.59161+00	1.13788+00	1.30853+01	2.04442+01	.11831	20.67036
	2SIG ERR	0.00000	0.00000	2.24945-01	3.21015-01	2.29473-01	3.01929+00	4.79233+00	.01440	4.21866
2-7-4	1627.00	0.00000	0.00000	9.78745-01	1.53519+00	1.09526+00	1.16500+01	2.05600+01	.11323	19.89622
	2SIG ERR	0.00000	0.00000	2.24361-01	3.09751-01	2.20980-01	2.86916+00	4.96570+00	.01529	4.06234
2-7-5	1676.00	0.00000	0.00000	8.99872-01	1.51300+00	1.10206+00	1.22222+01	1.98721+01	.11788	20.01965
	2SIG ERR	0.00000	0.00000	2.05979-01	3.05329-01	2.22351-01	2.87894+00	4.54868+00	.01307	4.08754
2-7-6	1726.00	0.00000	0.00000	8.75620-01	1.47211+00	1.05007+00	1.14469+01	1.85869+01	.12009	19.07528
	2SIG ERR	0.00000	0.00000	2.02689-01	2.97142-01	2.11671-01	2.74704+00	4.56044+00	.01703	3.89487
2-7-8	1824.00	0.00000	0.00000	9.62078-01	1.56041+00	1.10472+00	1.20404+01	1.99694+01	.11759	20.06803
	2SIG ERR	0.00000	0.00000	2.24800-01	3.14641-01	2.22897-01	2.87508+00	4.61364+00	.01355	4.09758
2-7-9	1874.00	0.00000	0.00000	1.00779+00	1.61936+00	1.16142+00	1.37270+01	1.97676+01	.12489	21.09797
	2SIG ERR	0.00000	0.00000	2.28733-01	3.26626-01	2.34458-01	3.19468+00	4.54962+00	.01414	4.30656
2-7-10	1923.00	0.00000	0.00000	8.51562-01	1.37156+00	9.77942-01	1.06139+01	1.72890+01	.11974	17.69231
	2SIG ERR	0.00000	0.00000	1.95907-01	2.76897-01	1.96597-01	2.55412+00	4.32588+00	.01798	3.61394
2-7-11	1973.00	0.00000	0.00000	7.57849-01	1.16901+00	8.28410-01	8.91925+00	1.49511+01	.11778	15.04863
	2SIG ERR	0.00000	0.00000	1.76796-01	2.36105-01	1.67380-01	2.20802+00	3.58962+00	.01565	3.07659

TABLE 9-13 (Continued)

FUEL ROD I.D.	MEAN CORE HT (MM)	PA-233 (311.9KEV) (CI)	RU-103 (497.1KEV) (CI)	RU-106 (511.9KEV) (CI)	CS-134 (604.7KEV) (CI)	CS-137 (661.6KEV) (CI)	CE-144 (695.6KEV) (CI)	ZR-95 (724.2KEV) (CI)	CS-137 /ZR-95 (CT/MIN)	TOTAL FIMA %
2-7-12	2022.00	0.00000	0.00000	9.63120-01	1.48817+00	1.11804+00	1.15041+01	1.89046+01	.12571	20.30993
	2SIG ERR	0.00000	0.00000	2.18954-01	3.00265-01	2.25673-01	2.75637+00	4.84978+00	.02017	4.14779
2-7-13	2071.00	0.00000	0.00000	9.52588-01	1.48123+00	1.06975+00	1.12971+01	2.08073+01	.10928	19.43268
	2SIG ERR	0.00000	0.00000	2.23493-01	2.98827-01	2.15831-01	2.64063+00	4.71963+00	.01164	3.96769
2-7-14	2121.00	0.00000	0.00000	1.00620+00	1.54209+00	1.09490+00	7.50150+01	1.94664+01	.11956	19.88958
	2SIG ERR	0.00000	0.00000	2.35658-01	3.11213-01	2.20906-01	1.51848+01	4.82359+00	.01745	4.06098
3-7-2	2318.00	0.00000	0.00000	9.49548-01	1.30813+00	1.00424+00	1.32033+01	1.89037+01	.11292	18.24268
	2SIG ERR	0.00000	0.00000	2.32544-01	2.64294-01	2.02907-01	3.25857+00	5.17955+00	.02115	3.72959
3-7-6	2516.00	0.00000	0.00000	8.16800-01	1.05613+00	9.03832-01	9.54209+00	9.32642+00	.20599	16.41872
	2SIG ERR	0.00000	0.00000	2.03210-01	2.13811-01	1.82742-01	2.56577+00	5.32931+00	.11028	3.35875
3-7-9	2664.00	0.00000	0.00000	6.55988-01	7.70446-01	7.64041-01	8.87465+00	1.54225+01	.10530	13.87931
	2SIG ERR	0.00000	0.00000	1.67880-01	1.56350-01	1.54546-01	2.35243+00	4.15620+00	.01905	2.84038
3-7-11	2763.00	0.00000	0.00000	6.24821-01	5.53545-01	6.50806-01	8.07211+00	1.43167+01	.09663	11.82234
	2SIG ERR	0.00000	0.00000	1.61110-01	1.12931-01	1.31849-01	2.39894+00	4.00542+00	.01896	2.42289
3-7-13	2861.00	0.00000	0.00000	5.04493-01	4.08325-01	5.75210-01	7.64562+00	9.96477+00	.12270	10.44907
	2SIG ERR	0.00000	0.00000	1.31421-01	8.38074-02	1.16599-01	3.17379+00	3.36781+00	.03349	2.14255
1-8-6	936.00	0.00000	0.00000	6.32817-01	7.25787-01	7.72985-01	8.87653+00	1.52884+01	.10747	14.04180
	2SIG ERR	0.00000	0.00000	1.50227-01	1.47199-01	1.56198-01	2.30053+00	4.20460+00	.02029	2.87101
2-8-1	1479.80	0.00000	0.00000	1.01645+00	1.65074+00	1.18649+00	1.31974+01	1.99314+01	.12654	21.55348
	2SIG ERR	0.00000	0.00000	2.33496-01	3.32887-01	2.39376-01	3.13660+00	5.12310+00	.02038	4.39987
2-8-2	1528.60	0.00000	0.00000	9.88384-01	1.63420+00	1.18492+00	1.27220+01	2.01554+01	.12496	21.52492
	2SIG ERR	0.00000	0.00000	2.28791-01	3.29605-01	2.38979-01	3.02695+00	5.04790+00	.01878	4.39339
2-8-3	1578.40	0.00000	0.00000	9.24710-01	1.62690+00	1.17219+00	1.27779+01	2.21787+01	.11234	21.29361
	2SIG ERR	0.00000	0.00000	2.15022-01	3.28187-01	2.36421-01	2.95167+00	5.48014+00	.01625	4.34633
2-8-4	1627.20	0.00000	0.00000	1.03351+00	1.56053+00	1.11616+00	1.21409+01	1.87815+01	.12632	20.27589
	2SIG ERR	0.00000	0.00000	2.40477-01	3.14851-01	2.25177-01	2.95334+00	4.64730+00	.01836	4.13954
2-8-5	1676.00	0.00000	0.00000	9.28650-01	1.55370+00	1.10083+00	1.23137+01	1.84178+01	.12705	19.99728
	2SIG ERR	0.00000	0.00000	2.15612-01	3.13500-01	2.22093-01	2.92581+00	4.79902+00	.02118	4.08281
2-8-6	1726.00	0.00000	0.00000	9.40003-01	1.57398+00	1.11837+00	1.25428+01	1.81485+01	.13099	20.31602
	2SIG ERR	0.00000	0.00000	2.16299-01	3.17375-01	2.25549-01	2.90153+00	4.55629+00	.01984	4.14649
2-8-8	1824.60	0.00000	0.00000	8.87415-01	1.57827+00	1.11938+00	1.25777+01	1.98396+01	.11993	20.33437
	2SIG ERR	0.00000	0.00000	2.07519-01	3.18443-01	2.25836-01	2.99595+00	4.80716+00	.01636	4.15164
2-8-9	1874.00	0.00000	0.00000	1.01368+00	1.61734+00	1.16399+00	1.37176+01	2.00118+01	.12364	21.14465
	2SIG ERR	0.00000	0.00000	2.33006-01	3.26257-01	2.34796-01	3.24411+00	5.21689+00	.02063	4.31641

TABLE 9-13 (Continued)

FUEL ROD I.D.	MEAN CORE HT (MM)	PA-233 (311.9KEV) (CI)	RU-103 (497.1KEV) (CI)	RU-106 (511.9KEV) (CI)	CS-134 (604.7KEV) (CI)	CS-137 (661.6KEV) (CI)	CE-144 (695.6KEV) (CI)	ZR-95 (724.2KEV) (CI)	CS-137 /ZR-95 (CT/MIN)	TOTAL FIMA %
2-8-10	1923.00	0.00000	0.00000	9.10384-01	1.49161+00	1.05533+00	1.14199+01	1.71019+01	.13117	19.17079
	2SIG ERR	0.00000	0.00000	2.07263-01	3.00895-01	2.12887-01	2.81117+00	4.28826+00	.01979	3.91362
2-8-11	1973.00	0.00000	0.00000	9.77219-01	1.59107+00	1.14489+00	1.23261+01	2.21897+01	.10967	20.79765
	2SIG ERR	0.00000	0.00000	2.26547-01	3.21040-01	2.30952-01	2.97497+00	5.51661+00	.01615	4.24574
2-8-12	2022.00	0.00000	0.00000	8.67417-01	1.48581+00	1.08388+00	1.17611+01	2.00659+01	.11482	19.68937
	2SIG ERR	0.00000	0.00000	1.96672-01	2.99828-01	2.18682-01	2.72948+00	4.83529+00	.01539	4.02010
2-8-13	2071.00	0.00000	0.00000	7.09553-01	7.57472-01	7.94795-01	1.00872+01	1.88724+01	.08952	14.43799
	2SIG ERR	0.00000	0.00000	1.71847-01	1.53605-01	1.60597-01	2.46404+00	4.86270+00	.01455	2.95188
2-8-14	2121.00	0.00000	0.00000	6.79137-01	1.49473+00	1.06506+00	1.15978+01	1.90236+01	.11900	19.34745
	2SIG ERR	0.00000	0.00000	1.58814-01	3.01525-01	2.14885-01	2.78517+00	4.56947+00	.01579	3.95029
3-8-6	2516.00	0.00000	0.00000	7.91693-01	1.03179+00	8.87182-01	1.04967+01	1.57299+01	.11989	16.11626
	2SIG ERR	0.00000	0.00000	1.84933-01	2.08505-01	1.79084-01	2.59607+00	4.03241+00	.01920	3.29201

TABLE 9-14
FTE-6 COMPARISON BETWEEN GAMMA SPECTROSCOPY AND GAUGE/FEVER-CALCULATED FUEL ROD BURNUPS

Fuel Body	Fuel Rod	Total FIMA (%)											
		Stacks 1 and 2			Stacks 3 and 4			Stacks 5 and 6			Stacks 7 and 8		
		Gamma Scan F_G	1σ Error S_G	Gauge/ Fever[a] F_C	Gamma Scan F_G	1σ Error S_G	Gauge/ Fever F_C	Gamma Scan F_G	1σ Error S_G	Gauge/ Fever F_C	Gamma Scan F_G	1σ Error S_G	Gauge/ Fever F_C
1	2	3.38	0.35	3.04	7.58	0.79	6.30	7.65	1.59	6.32	9.70	1.99	9.09
1	4	3.93	0.41	4.13	9.37	0.98	8.34	9.92	2.04	8.27	12.02	2.46	11.93
1	6	5.27	0.55	4.90	11.09	1.16	9.68	10.95	2.24	9.51	15.15	3.10	13.77
1	8	5.20	0.54	5.46	11.94	1.24	10.61	11.21	2.29	10.90	15.88	3.25	15.01
1	10	5.70[b]	0.59[b]	5.89	11.95	1.24	11.33	11.59	2.37	11.56	17.07[b]	3.50[b]	15.98
1	12	6.19	0.64	6.23	14.35	1.49	11.89	14.00	2.86	12.12	18.29	3.74	16.72
1	14	7.13	0.74	6.42	15.52	1.92	12.21	15.28	3.12	12.45	19.91	4.07	17.14
Body 1 mean		5.26		5.15	11.69		10.05	11.52		10.16	15.43		14.23
S.D. (1σ)[c]		±1.28		±1.22	±2.72		±2.13	±2.52		±2.25	±3.55		±2.89
$\frac{F_C - F_G}{F_G} \times 100$			-2.1%			-13.7%			-11.8%			-7.8%	
2	2	6.05	0.63	6.59	15.59	1.59	12.45	15.21	3.10	12.70	20.68	4.22	17.49
2	4	5.69	0.59	6.67	15.28	1.59	12.60	15.36	3.13	12.85	19.90	4.06	17.66
2	6	5.85[d]	0.60	6.69	15.47	1.61	12.65	15.77[d]	3.09	12.90	19.08	3.89	17.71
2	8	5.09	0.53	6.61	14.82	1.55	12.51	14.95	3.05	12.76	20.07	4.10	17.56
2	10	6.43	0.67	6.47	14.51	1.51	12.29	14.74	3.01	12.54	17.69	3.61	17.26
2	12	5.48	0.57	6.30	14.79	1.69	12.00	15.37	3.13	12.24	20.31	4.15	16.86
2	14	6.31	0.66	6.08	14.76	1.54	11.66	15.37	3.14	11.90	19.89	4.06	16.43
Body 2 mean		5.84		6.49	15.03		12.31	15.34		12.56	19.66		17.28
S.D. (1σ)		±0.47		±0.22	±0.41		±0.36	±0.27		±0.36	±1.00		±0.47
$\frac{F_C - F_G}{F_G} \times 100$			+10.0%			-18.1%			-18.1%			+12.1%	
3	2	4.73	0.49	5.80	13.53	1.41	10.30	13.86	2.83	11.39	18.24	3.73	15.76
3	4	4.41	0.46	5.43	12.60	1.31	9.80	13.41	2.74	10.78	17.33[b]	3.55[b]	14.94
3	6	4.54	0.47	5.00	11.98	1.25	9.17	11.86	2.42	10.02	16.42	3.36	13.92
3	8	4.52	0.47	4.52	11.41	1.19	8.45	11.74	2.40	9.15	14.11[b]	3.40	12.76
3	10	4.39	0.46	4.03	10.60	1.11	7.71	10.08	2.06	8.27	12.85[b]	3.09	11.58
3	12	3.86	0.40	3.51	8.01	0.84	6.92	8.57	1.76	7.34	11.14[b]	2.68	10.32
3	14	3.79	0.39	3.05	7.95	0.83	6.24	7.94	1.63	6.52	9.76[b]	2.34	9.28
Body 3 mean		4.32		4.48	10.87		8.37	11.07		9.07	14.34		12.65
S.D. (1σ)		±0.36		±1.01	±2.17		±1.50	±2.29		±1.80	±3.32		±2.40
$\frac{F_C - F_G}{F_G} \times 100$			-3.6%			-23.0%			-18.1%			-11.8%	
Total mean		5.14		5.37	12.53		10.27	12.61		10.59	16.45		14.72
S.D. (1σ)		±1.11		±1.23	±2.66		±2.19	±2.68		±2.18	±3.58		±2.86
$\frac{F_C - F_G}{F_G} \times 100$			+4.5%			-18.3%			-16.0%			-10.5%	

[a] 1σ error not available for GAUGE/FEVER.

[b] Interpolated from neighboring rods.

[c] $S_W^2 = \frac{1}{n-1} \Sigma [(F - \bar{F})^2]$.

[d] Rod 7 substituted in this case.

highest temperature and fluences. The Cs-137 loss can also be compared with fuel failure fractions determined by metallographic and fission gas release measurements. A comparison between rods 2-1-7 and 2-2-7 is given in Table 9-15.

TABLE 9-15
COMPARISON OF Cs-137 LOSS AND FUEL FAILURE FRACTIONS

Rod	Failure Measured by Fission Gas Release (%)	SiC Failure[a] (%)	Pressure Vessel Failure[a] (%)	Cs-137 Loss From Fuel Rod (%)
2-1-7	22	18	17	20
2-2-7	24	20	8	12

[a]Determined by metallography.

The following assumptions have been made:

1. Kr-85m at 1100°C $R/B_f = 5 \times 10^{-3}$ for failed fuel particles in a constrained geometry.

2. Pressure vessel failure is failure of all structural coatings in the particle.

3. Cs-137 loss is calculated from Cs-137/Zr-95 ratios.

Using the average failure from fission gas release measurements and the average fuel rod Cs-137 loss in rods 2-1-7 and 2-2-7, the loss from a UO_2 fuel failure in the constrained state (i.e., fuel rod) is calculated to be approximately 70%. This is consistent with the ∿70% Cs-137 loss per fuel failure measured in P13R and P13S fuel rods and particles (Ref. 9-10).

Thermal Stability Samples. The two thermal stability spine samples that were examined from FTE-6 were located in type II crucibles. A

description of these crucibles is given in Fig. 9-45. This particular design guaranteed a relatively isothermal environment for each batch of particles in any particular hole.

The visual examination of samples TS18-3 and TS6-5 are summarized in Table 9-16 and a stereophotograph of each batch is shown in Fig. 9-46. Preirradiation data on batches 4000-302 (TS6-5) and 4000-242 (TS18-3) are also given in Table 9-16. There was no observable fuel failure in any of the particles in batch 4000-302. The appearance of the 4000-242 batch was also good, with the exception of one doublet with a cracked OPyC coating and four OPyC coating fragments.

Metallographic examination results on spine samples TS18-3 and TS6-5 are shown in Table 9-17. Representative microphotographs of each of the fuel types are shown in Figs. 9-47 and 9-48. Batch 4000-242 (ThC_2 TRISO) showed very good fuel performance. There were no thermochemical effects and only one hairline SiC failure was observed. Hydrolysis of the kernels during the examination caused IPyC and buffer cracking. The UC_2 (VSM) TRISO particles of batch 4000-302 showed no failure or kernel migration. All the particles observed had buffer densification and debonding and mixed fission products in the IPyC. In ∿4% of the particles, the mixed fission products had attacked the SiC. In no case did this attack extend more than ∿5 μm into the surface of the particle.

Figures 9-49 through 9-51 show the relative activity of Cs-144, Cs-134, and Cs-137 in the spine samples from the three fuel bodies as determined by gamma scans. The activity of some of the fueled spine samples indicates significant heat sources that could be used in a detailed thermal analysis.

Graphite Fuel Body Gamma Scans. The graphite fuel bodies were gamma scanned using the same scanning geometry as was used for the fuel rods. Quantitative isotope inventories were calculated using the fuel rod detector calibration to approximate quantitative result. The error in this

TABLE 9-16
PREIRRADIATION DATA FOR FTE-6 TYPE II THERMAL STABILITY SPINE SAMPLES

FMB No.(a)	Kernel			Coating Type	As-Manufactured Coating Parameters								Total Particle Parameters			
					Nominal Thickness (μm)					OPyC Density (Mg/m^3)	OPyC OPTAF(b)	SiC Density (Mg/m^3)	Density(c) (Mg/m^3)	Diameter (μm)	Heavy Metal Content	
	Type	Density (Mg/m^3)	Nominal Diameter (μm)		Buffer	IPyC	SiC	OPyC	Total						U (wt %)	Th (wt %)
4000-242	ThC_2	8.86	384	TRISO	46	28	23	42	133	1.71	1.04	3.19	3.30	650	--	48.71
4000-302	UC_2	10.43	100	TRISO	50	18	20	36	122	1.71	1.05	3.19	2.05	344	11.57	--

(a) Fuel Materials Branch data retrieval number.

(b) BAF disc OPTAF.

(c) Density in air.

TABLE 9-17
POSTIRRADIATION DATA FOR FTE-6 TYPE II THERMAL STABILITY SPINE SAMPLES(a)

FMB Number(b)	Particle Type	Location(c)	EOL Avg Fuel Temp(d) (°C)	Number of Particles in Sample		Stereo Examination		Metallography Examination(e)									
				Stereo Exam.	Metallography	OPyC Failure (%)	SiC Failure (%)	OPyC Failure (%)	95% Confidence Limits P (%)	SiC Failure (%)	95% Confidence Limits P (%)	Pressure Vessel Failure (%)	95% Confidence Limits P (%)	Mixed Fission Product in IPyC (%)	95% Confidence Limits P (%)	SiC Attack (%)	95% Confidence Limits (%)
4000-242	TRISO ThC_2	TS 18-3	1140	962	63	<1%(f)		0	$0 \le P \le 5.7$	1.6	$0 \le P \le 5.7$	0	$0 \le P \le 5.7$	0	$0 \le P \le 5.7$	0	$0 \le P \le 5.7$
400-302	TRISO UC_2	TS 6-5	1090	4053	185	0	--	0	$0 \le P \le 2.0$	0	$0 \le P \le 2.0$	0	$0 \le P \le 2.0$	100	$97.9 \le P \le 100$	2.7	$1.2 \le P \le 6.2$

(a) Fluence, FIMA, and fission gas release not yet available.

(b) Fuel Materials Branch data retrieval number.

(c) TS 15-6 (thermal stability type II crucible No. 15, hole 6).

(d) Calculated by TREVER

(e) Approximately 10 to 20% of the sample is examined.

(f) One cracked doublet and four coated fragments.

method is that the fuel rod has higher attenuation effects than the graphite fuel bodies, which gives higher reported graphite results in relation to the fuel rod isotope inventories. The purpose of the exercise is to determine the isotope distribution in the element.

Preliminary graphite gamma scanning showed the majority of the cesium plateout to be around fuel holes 1 and 2, which contained UO_2 TRISO particles with high failure. It was therefore decided to scan holes 1 and 2 together and then rotate the body 180° and scan holes 5 and 6 as a comparison. The area scanned in each case is shown in Fig. 9-52. Figures 9-53 and 9-54 give a single-channel trace of the Cs-137 and Cs-134 inventories in the two axial scans. Only Cs-137 and Cs-134 were detected in these scans. The single-channel scans show a smooth profile of both Cs-137 and Cs-134 across the fuel body, with a drop in activity near the unfueled zone at the bottom of the body. The top of the body has been cut off [102 mm (4 in.) from the top end] for radial graphite sectioning purposes. Results of this analysis will be compared to the gamma scanning results when they become available.

The average cesium activity across the fuel body was determined and from this value the total Curies of cesium were calculated for the two scans. The results were as follows:

	Holes 1 and 2	Holes 5 and 6
Cs-137	2.48 ± 0.52 Ci	0.10 ± 0.02 Ci
Cs-134	3.60 ± 0.72 Ci	0.22 ± 0.04 Ci

Using the Cs-137/Zr-95 theoretical and measured ratios for the fuel rods in holes 1 and 2, a theoretical Cs-137 inventory was determined and compared to the measured Cs-137 inventory. The results show an average Cs-137 loss of ∿17% per fuel rod, which corresponds to a total cesium loss of 5.8 Curies from all 28 fuel rods in holes 1 and 2 of body 2. The fact that only ∿40% of the lost Cs-134 plated out on the fuel body suggests that some of the Cs-137 escaped from the fuel body and traveled to the sleeve or was

removed by the purge gas flow. Future scanning of the fuel element sleeves will give an indication of the magnitude of this plateout. Quantitative analysis of the cesium concentration in the graphite slice from this fuel body will aid in correcting the gamma detector calibration used in the above analysis.

Apparatus for Structural Examination of Peach Bottom Test Elements

Equipment is being developed for use in structural measurements on irradiated graphite fuel bodies from the Peach Bottom test elements. This equipment will be used in performing experimental portions of the program described in Ref. 9-2. This work has been done partially with GA funds to speed development of the equipment.

Strip Cutting Apparatus. Equipment has been developed to cut samples from irradiated graphite fuel bodies. The elements to be cut are six-hole and eight-hole teledial bodies designated as FTE-1 through -6 and FTE-14 and -15. A number of cuts will be made perpendicular to the extrusion axis producing 20-mm-thick "wafers," which will be used for pressure burst tests of the fuel holes as well as ring compression tests. The remainder of each fuel body, $\sim$0.45 m long, will be used for strip cutting.

A double-bladed saw will be used to "straddle cut" strips 8.9 mm wide by 0.45 m long from the outer edge of each of the fuel bodies. The strips taken will be from the graphite web between each fuel hole and the outer edge of the body. It is planned to cut six strips from each six-hole element and eight strips from each eight-hole body. The strips will be measured for bow and the results compared with predictions derived from detailed stress analyses.

Strip Measuring Equipment. The curvature of the strips will be measured before and after cutting. The initial bow of the fuel bodies will be measured using a dial gage mounted on a travelling bridge that traverses a granite surface plate. Since the graphite body is several centimeters in

diameter, its bow will not be affected by the measuring forces applied by the dial gage.

The measurement of strips after cutting is made more difficult by the flexibility of the thin strips. After study of a variety of measuring techniques, an optical method was selected to avoid applying any measuring forces to the strips that could cause deflection. The measurements will be made through the magnification system of the hot cell periscope. The strips will be photographed while resting on a precision grid with lines spaced 0.1 mm from one another. The grid, on a Mylar film, will be mounted on a vacuum chuck, which consists of a flat plate with small holes drilled through it. The holes connect to a cavity below the plate that is evacuated by means of a vacuum pump. Preliminary tests with a vacuum chuck have indicated that this method should be adequate to hold the strip flush against the grid and assure a sharp, unshadowed image that will allow an accurate measurement.

Pressure Burst Apparatus. An apparatus has been developed for applying a hydrostatic pressure to the inside surface of fuel holes in the test elements. The pressure is applied by a hydraulic fluid acting through a length of Tygon tubing. The tubing is sealed at both ends to metal fittings. The fittings are connected to a rod that prevents axial growth of the tubing and allows high-pressure forces to be developed in the radial direction. The apparatus will be used to pressurize the fuel holes of the 20-mm-thick "wafers" to be cut from the fuel bodies. The pressure at failure of the fuel holes will be measured by a transducer connected to a recording instrument located outside of the hot cell.

TASK 500: FUEL ROD TEST AND EVALUATION

Subtask 520: Fuel Rod Thermal Expansivity

Final assembly and calibration of equipment for measurement of fuel rod thermal expansivity was delayed pending delivery of programmer parts which were received in May. Assembly is now nearing completion.

Subtask 530: Fuel Rod Mechanical Properties

Conclusions

The mechanical properties of HTGR fuel rods have been determined on prototype unirradiated rods. Unshimmed rods have a mean tensile strength of approximately 0.86×10^6 Pa (125 psi) and a mean compressive strength of 6.54×10^6 Pa (950 psi). Rods containing 23 and 36 vol % shim were significantly weaker, exhibiting an ultimate tensile strength of 0.6×10^6 Pa (87 psi) and an ultimate compressive strength of 4.75×10^6 Pa (690 psi). The shimmed rods were also significantly softer with a modulus of 3.85×10^8 Pa compared to 8.13×10^8 Pa for unshimmed rods.

The decrease in strength and modulus of shimmed rods may be due to a weakened fuel rod matrix caused by absorption of matrix pitch binder by the shim particles.

Failure of HTGR fuel rods under compressive loads is not typical brittle fracture, but rather a slow crumbling of the rod at the fracture surface.

Description of Tests

Prototype HTGR fuel rods were cut into cylinders by a diamond circular saw. The compression specimens were approximately 0.25 mm (1 in.) long sections of the fuel rod and the tension specimens were cylinders approximately 0.5 mm (2 in.) long taken from the prototype fuel rod. The surfaces of the cylinder ends were generally uniform but quite rough due to the high concentration of particles.

In order to achieve specimens with parallel ends, metal end caps were carefully aligned with and then epoxied to the cylindrical fuel rod specimens. The end caps served as tensile grips and compression plates, as illustrated in Fig. 9-55. As shown in this figure, the tensile test followed exactly the method used for testing of nuclear graphites under Task

11. The fuel rod cylinder and metal end caps were pulled by a self-aligning chain - universal joint load train on an Instron model 1102 tensile tester.

In the compression tests, the fuel rod specimen and steel end caps were placed between two compression plates of the Instron 1102. The specimen was compressed at a crosshead speed of 2.12×10^{-6} m/sec (0.005 in./min) to compressive failure, defined by load reduction to at least 30% of peak compressive load. The crosshead travel was measured and labeled as compression at failure in Table 9-18.

Results

Table 9-18 contains the results of the mechanical properties tests on 11 prototype HTGR rods according to the test matrix presented earlier (Ref. 9-7).

Two typical compression stress-strain curves are shown in Fig. 9-56. The large difference between a shimmed rod and an unshimmed rod is evident in the curves.

Discussion

As shown in Fig. 9-56, the reduction in compressive load-bearing ability was quite gradual in these tests. Nuclear graphites show a sharp drop in load immediately after failure, whereas the fuel rods continued to support loads at 40% of ultimate compressive strain to compressive strains 2 to 3 times the strain at failure. At the loading rates applied (2.1×10^{-6} m/sec), the failure appears to be piecemeal as a slow crumbling of the fuel rod, rather than a catastrophic break. The specimens failed from 1 to 5 min after the test was initiated.

Compressive strain was calculated from the test machine crosshead travel. The arrangement of the compression load train (Fig. 9-55) was such

TABLE 9-18
MECHANICAL PROPERTIES OF HTGR FUEL RODS

Fuel Rod			Tensile Properties				Compressive Properties							
			Failure Load		Ultimate Strength		Ultimate Strength		Modulus[a]		Failure Load		Compression at Failure	Length
Type	Shim Vol. (Vol %)	Specimen	(N)	(lb)	(10^6 Pa)	(psi)	(10^6 Pa)	(psi)	(10^8 Pa)	(10^5 psi)	(10^3 N)	(lb)	(10^{-4} m)	(10^{-2} m)
A3	0	4003-3	173.5	39	0.89	130	6.44	934	8.09	1.17	1.25	282	1.7	2.143
		4004-1	142.3	32	0.73	106	5.30	768	--	--	1.03	232	--	2.170
		4004-3	129.0	29	0.66	96	7.24	1050	8.77	1.27	1.41	317	2.0	2.423
		4005-2	222.4	50	1.44	166	7.19	1043	7.52	1.09	1.40	315	2.0	2.092
		Mean			0.86 ± 0.21	124 ± 31	6.54 ±0.91		8.13 ± 0.63					
C3	23	4021-3	146.8	33	0.75	109	6.01	871	5.79	0.84	1.17	263	3.2	3.082
		4021-4	111.2	25	0.57	83	2.12	308	--	--	0.41	93	--	3.019
		4022-1	142.3	32	0.73	106	5.21	755	4.55	0.66	1.01	228	3.5	3.074
		4022-2	120.1	27	0.62	89	4.00	580	2.81	0.41	0.78	175	4.3	3.018
		Mean			0.67 ± 0.09	97 ± 13	4.32 ± 1.70		4.38 ± 1.5					
D2	36	4025-3	133.4	30	0.68	99	6.12	888	3.97	0.58	1.19	268	3.5	2.275
		4026-1	115.7	26	0.59	86	4.52	656	3.60	0.52	0.88	198	3.3	2.627
		4026-2	53.4	12	0.27	40	5.28	765	2.37	0.34	1.03	231	6.0	2.693
		Mean			0.52 ± 0.22	75 ± 31	5.31 ± 0.80		3.31 ± 0.84					

[a]Modulus measured as compressive stress at failure divided by compressive strain at failure.

that all components except the specimen itself were at least 100 times stiffer than the stiffest specimen. The very thin eopxy glue joint did not show a significant effect on modulus, as evidenced by the standard deviation in modulus presented in Table 9-18. The coefficients of variance in the modulus measurements (standard deviation/mean) were equal to or less than the coefficients of variance in the strength measurements. The modulus values measured compare to predicted values extrapolated from other graphite-particle composites (Ref. 9-11).

The observed tensile strengths indicate that the fuel rods have low tensile strength and that the strength of the rods is decreased by shim particle addition. Similarly, the strength of fuel rods in compression is also reduced by the presence of shim particles. In both cases, the difference in mean strengths between shimmed and unshimmed rods has been shown to be statistically significant at the 95% confidence level.

The modulus of the rods also shows a strong effect of shim addition to the fuel rod. The modulus values of shimmed rods were approximately half those of unshimmed rods. The stress-strain curves of Fig. 9-56 illustrate the significant differences between the shimmed rod specimens and the unshimmed rods.

Two possible mechanisms may explain the effects of shim on fuel rod mechanical properties. Either the impregnated shim is not wet by the matrix pitch, producing poor bond strength, or the shim absorbs additional pitch binder within the particle which could significantly weaken the matrix and matrix-particle interfaces. Although the shim is impregnated with pitch binder before incorporation in the fuel rod blend, the degree of previous impregnation may not be sufficient to preclude further absorption of pitch by shim during the fuel rod fabrication and cure-in-place processes.

Figure 9-57 shows photographs of typical compressive fracture surfaces in an unshimmed and a shimmed rod. The unshimmed rod exhibits a characteristic 45° fracture surface which is made up of well bonded particles on

a fairly smooth plane. The fracture surface of the shimmed rod does not lie along any one plane and is composed of large shim particles as well as fuel particles. If the shim had not been wet by the pitch binder (first alternative above), one would expect fracture to proceed through the matrix guided by poorly bonded shim particles. The existence of bonded shim particles in the fracture surface would support the hypothesis of a weak matrix caused by absorption of binder by the shim.

TASK 600: FUEL DESIGN AND PERFORMANCE MODELS

Subtask 610: Fuel Design Models

Summary

Coated particle stress analysis models can be used to predict either diametral changes of BISO particles or coating failure of BISO or TRISO particles. Modeling efforts have been made in both these areas. The key to accurate modeling of coated particles is data on the irradiation behavior of pyrocarbon coatings. Recent results obtained from piggyback irradiation in the OG-capsules and the HT-20, -21, -22, and -23 capsules have greatly improved the modeling capability in this respect.

In the effort on modeling the diametral changes of BISO particles, a general stress analysis model for the outer coating on a BISO coated particle has been developed. This model incorporates irradiation-induced dimensional changes of the coating, irradiation-induced creep of the coating, changes in preferred orientation of the carbon crystallites in the coating due to creep and the effect of these changes on subsequent dimensional changes, and pressure buildup inside the coating due to generation of fission product gases and carbon monoxide. The model has been used to predict diametral changes of BISO particles irradiated in capsules HT-17, -18, and -19. These predictions have been compared with measured diametral changes; good agreement is observed if the dimensional changes of a carbon slightly lower in density than that reportedly on the particles is used and

with proper selection of the creep constant which is the one adjustable parameter in the model.

The effort on modeling coating failure has initially concentrated on analyzing the results of a series of carbon coatings irradiated restrained on small sapphire spheres in capsules HT-20, -21, -22, and -23. These coatings experience stress histories which are virtually identical to those experienced by the outer coatings on TRISO particles. Coating properties were varied by including in the irradiation experiment spheres with carbon coatings deposited at a number of deposition rates for each of three densities (1.65, 1.85, and 1.95 Mg/m^3). Coating failure with increasing fast neutron fluence was observed as follows: first the low-density high-coating-rate carbon broke; then the low-density low-coating-rate carbon broke; then the intermediate-density low-coating-rate carbon broke; and finally, the intermediate-density highest-coating-rate carbon broke. The high-density carbons and the intermediate-density intermediate-coating-rate carbons survived the irradiation. The BISO stress analysis model was altered so the coatings restrained on the sapphire spheres could be analyzed, and a routine for calculation of coating failure probability using a Weibull analysis which included the effects of the stress distribution through the coating and the coating volume under stress was added. The observed pattern of coating failure during irradiation could only be explained if the adjustable creep parameter (the creep constant) was allowed to vary during irradiation. The experimental results were used to obtain bounds on the creep constant at different fluences, and it was shown that these results were not inconsistent with the values of the creep constant needed to simulate the BISO particle behavior.

Diametral Changes of BISO Coated Particles

BISO Coating Stress Analysis. The complete derivation of the expressions describing the stresses developed in the outer coating of a BISO particle is lengthy and is not presented here. The derivation follows that described by Stevens in Ref. 9-12 except that the solution has been

generalized to include variation of the creep parameters during irradiation, variation of Young's modulus during irradiation, and variable dimensional changes of the carbon across the coating thickness.

The radial and tangential stresses in the coating are given by:

$$\sigma_r = -P \frac{a^3}{r^3} \frac{(b^3 - r^3)}{(b^3 - a^3)} + \frac{2}{3r^3} \frac{(r^3 - a^3)}{(b^3 - a^3)} \int_a^b r^2 f \, dr$$

$$- \frac{2}{3} \frac{b^3(r^3 - a^3)}{r^3(b^3 - a^3)} \int_a^b \frac{f}{r} \, dr - \frac{2}{3} \frac{1}{r^3} \int_a^r r^2 f \, dr$$

$$+ \frac{2}{3} \int_a^r \frac{f}{r} \, dr \qquad (9\text{-}10)$$

$$\sigma_t = -P \frac{a^3}{2r^3} \frac{(2r^3 + b^3)}{(b^3 - a^3)} + \frac{2r^3 + a^3}{3r^3(b^3 - a^3)} \int_a^b r^2 f \, dr$$

$$- \frac{b^3(2r^3 + a^3)}{3r^3(b^3 - a^3)} \int_a^b \frac{f}{r} \, dr + \frac{1}{3r^3} \int_a^r r^2 f \, dr$$

$$+ \frac{2}{3} \int_a^r \frac{f}{r} \, dr \quad . \qquad (9\text{-}11)$$

P is the internal pressure generated by the fission gas and CO, a, and b are the inner and outer radii of the coating, r is the radius in the coating for which stresses are being calculated, and f is given by

$$f = e^{-Q} \int_o^{\gamma} e^{Q} \dot{\eta} \frac{E}{1 - \mu} d\gamma \quad , \tag{9-12}$$

where

$$Q = \int_o^{\gamma} KE \frac{(1 - \mu_c)}{(1 - \mu)} d\gamma \quad . \tag{9-13}$$

E is Young's modulus, μ is Poisson's ratio, γ is the fast neutron fluence, and K and μ_c are creep parameters in the expression which is assumed to describe irradiation-induced creep in pyrocarbon. This expression is $\dot{\varepsilon}_{c1} = K(\sigma_1 - \mu_c\sigma_2 - \mu_c\sigma_3)$, where 1, 2, and 3 are principal directions. $\dot{\eta}$ in Eq. 9-12 is given by:

$$\dot{\eta} = \frac{d}{d\gamma} \left(\eta_r - \eta_t - r \frac{d\eta_t}{dr} \right) \quad , \tag{9-14}$$

where η_r and η_t are the irradiation-induced dimensional strains of the pyrocarbon in the radial and tangential directions, respectively. The deflection of the coating at any given position is given by:

$$\delta = re_t = r(e_{et} + e_{ct} + \eta_t) \quad . \tag{9-15}$$

e_t is the total tangential strain and e_{et} is the tangential elastic strain, which is:

$$e_{et} = \int_o^{\gamma} \frac{1 - \mu}{E} \frac{d\sigma_t}{d\gamma} d\gamma - \int_o^{\gamma} \frac{\mu}{E} \frac{d\sigma_r}{d\gamma} d\gamma \quad . \tag{9-16}$$

e_{ct} is the tangential creep strain, which is:

$$e_{ct} = \int_o^\gamma K(1 - \mu_c)\, \sigma_t\, d\gamma - \int_o^\gamma \mu_c K \sigma_r\, d\gamma \quad . \tag{9-17}$$

The expressions for σ_r and σ_t (Eq. 9-10 and Eq. 9-11, respectively) can be substituted into Eq. 16 and 9-17 to produce expressions for the elastic and creep strains in terms of known parameters.

Internal Pressure. The development of internal pressure inside of the coating has been taken to be governed by the expressions determined by Lindemer and reported in Ref. 9-13. These are that fractional release of fission gases from the kernel is given by:

$$\begin{aligned} FR &= 10.0(FIMA) && 0.0 < FIMA \leq 0.06 \\ FR &= 0.45 + 2.5(FIMA) && 0.06 \leq FIMA \leq 0.22 \end{aligned} \tag{9-18}$$

and that the number of moles of CO released per mole of metal present follows the expression:

$$CO = [0.234(FIMA) + 26.5(FIMA)^2]\, e^{-10,900/RT} \quad . \tag{9-19}$$

The volume available to the gases is assumed to be that in the porosity of the buffer coating, i.e., the difference between the volume of the buffer coating and the volume that would be occupied if the weight of carbon in the coating had the theoretical density of 2.2 Mg/m^3. Solid and condensed fission products are considered to occupy this volume along with the fission product gases and the CO.

Irradiation-Induced Dimensional Changes of Pyrocarbon. The irradiation-induced dimensional changes of pyrocarbon depend on both the density (measured in this case using a sink-float technique) and on the degree of preferred orientation of the carbon crystallites or anisotropy.

Data on the dimensional changes of pyrocarbon have been determined by irradiating small flat pieces in piggyback positions in fuel capsules in the graphite capsules OG-1, OG-2, and OG-3 and in capsules HT-20, -21, -22, and -23. The flat pieces of pyrocarbon have been taken from coatings on small graphite discs, which have been included along with particles during deposition runs. For a given deposition run, the coatings on the discs do not necessarily have the same density and anisotropy as the coatings on the particles, but it is possible to vary the density and anisotropy of the disc coatings by varying the deposition conditions. If the disc coatings have the same density and preferred orientation as the particle coatings, it is assumed they behave in the same fashion as the particle coatings. For the most part, rather than characterize the coatings by their anisotropy, a more convenient parameter, the coating rate, was used. The variation of anisotropy with coating rate is shown in Fig. 9-58. The degrees of preferred orientation have been measured in terms of the Bacon anisotropy factor (BAF) on the optical microscope developed by Stevens (Ref. 9-14).

The irradiation-induced dimensional changes of each small flat piece of carbon were determined by measuring the density and the distance between two small holes before and after irradiation. From these values, the dimensional strains parallel and perpendicular to the deposition plane were determined. Data typical of the results obtained are shown in Figs. 9-59 and 9-60 for carbons of two different densities. Note the similar shapes of the curves for dimensional change versus coating rate and preferred orientation versus coating rate, indicating the effect of preferred orientation on the dimensional changes. By selecting data for a given carbon from curves similar to those of Figs. 9-59 and 9-60, it is possible to determine the dimensional changes as a function of the fast neutron fluence, a typical example of which is shown in Fig. 9-61.

Changes in Preferred Orientation During Irradiation. It has been observed that restraint of the irradiation-induced dimensional changes and the resulting irradiation-induced creep of pyrocarbon coatings causes a

strong increase in the preferred orientation of the coatings (Ref. 9-15). Since the dimensional changes increase strongly with preferred orientation, the dimensional changes which must be accommodated by a combination of creep and elastic strains in a restrained coating will be larger than those of a similar unrestrained coating. It is imperative that this effect be included in the stress analysis models if reasonable agreement with experiment is to be expected.

To date, accurate data on changes in preferred orientation during irradiation have only been obtained on carbons irradiated at about 950°C in capsules HT-20, -21, -22, and -23. The data were obtained by examining cross sections of unrestrained discs and of coatings restrained on small stable sapphire spheres in the optical anisotropy microscope. The results from both the restrained and unrestrained carbons are shown in Fig. 9-62 as a function of fast neutron fluence. A more fundamental way of showing the preferred orientation of restrained carbons is shown in Fig. 9-63 where the BAF is plotted versus the apparent creep strain.

Effect of Restraint-Induced Changes in Preferred Orientation on Irradiation-Induced Dimensional Changes. In order to account for the increases in preferred orientation caused by restraint in the stress analysis model, it is necessary to know the effect of these increases on the irradiation-induced dimensional changes. To make this determination, specimens were first irradiated restrained on a graphite substrate to introduce some creep strain, then were removed from the graphite substrate, and subsequently were irradiated unrestrained. The dimensional changes of the previously restrained specimens were measured after the second irradiation and were compared with those of totally unrestrained control specimens.

The various dimensional changes were analyzed to determine if they were consistent with crystallite-averaging expressions which assume that the macroscopic dimensional changes are an average of the dimensional changes of individual crystallites. These expressions are:

$$\Delta L/\Delta L_o(\parallel) = RX_a + (1 - R)X_c \qquad (9\text{-}20)$$

$$\Delta L/L_o(\perp) = (1 - R/2)X_a + R/2\ X_c \quad , \qquad (9\text{-}21)$$

$\Delta L/L_o(\parallel)$ and $\Delta L/L_o(\perp)$ are the macroscopic dimensional changes parallel and perpendicular to the deposition plane, respectively; X_a and X_c are the dimensional changes of the crystallites in the a and c directions (within and perpendicular to the layer planes); and R is a preferred orientation parameter given by:

$$R = 2/(2 + BAF) \quad . \qquad (9\text{-}22)$$

These expressions do not account for density changes which must result from the crystallite dimensional changes. In fact, the density changes obviously are due to accommodation of the crystallite dimensional changes by pores. To account for density changes, they are assumed to add an isotropic component to the dimensional change given by:

$$\ell n(1 + \Delta L/L_o) = -1/3\ \ell n(1 + \Delta\rho/\rho_o) \quad . \qquad (9\text{-}23)$$

Using the above expressions and knowing the macroscopic dimensional changes and the preferred orientation of the totally unrestrained specimens of the experiment described above, it should be possible to predict the macroscopic dimensional changes of the previously restrained specimens from their preferred orientations. The results of such calculations are shown in Figs. 9-64a and 9-64b for one particular experiment. There is fairly good agreement between the predicted and measured dimensional changes parallel to the deposition plane, but agreement between the predicted and observed dimensional changes perpendicular to the deposition plane is poor. The results of similar comparisons for carbons irradiated under different conditions were about the same as those shown above. Since the parallel dimensional changes are much more important than the perpendicular dimensional changes in the stress calculations for coated particles, the poor agreement in the perpendicular direction will not introduce large errors.

Therefore, the crystallite-averaging expressions were adopted for use in the stress analysis models.

Changes in Young's Modulus During Irradiation. It has been observed that the Young's modulus of pyrocarbon increases strongly during irradiation (Ref. 9-16). The effect is shown in Fig. 9-65. These increases were factored into the stress model. However, it should be noted that there is a paradox in that if the Young's modulus gradually increases while the stress is increasing, the total elastic strain is not recovered when the stress is released. This effect is not large, so it does not appreciably affect the results.

Method of Solution. A block diagram of the computer program written to do the stress analysis of the BISO coating is shown in Fig. 9-66. Two iterative loops are involved. The first ensures that the strain at the outer surface does not change appreciable when the new position of the outer surface is employed in the calculation; this is not a large effect. The second ensures that the strain at the inner surface does not change appreciably when the new position of the inner surface is employed in the calculation. This is a larger effect since it changes the volume available to the gases and thus the internal pressure.

Comparison with Experiment. The BISO stress analysis model has been used to predict diametral changes of one set of particles irradiated in capsules HT-17, -18, and -19. The dimensions and coating properties of these particles are given in Table 9-19 and the irradiation conditions and measured diametral changes are given in Table 9-20. This particular batch of particles was chosen for the initial comparison with the model because the anisotropy of the coating was in a range where dimensional changes have been well established. (The other particles irradiated in the diametral change experiments had coatings with higher anisotropies.) Note that these particles have been coated in a larger coater than the discs and sapphire spheres used to determine the fundamental properties of coatings, so that structure and coating rate for the coatings on the particles might not

TABLE 9-19
DIMENSIONS AND COATING PROPERTIES OF BISO PARTICLES

	Kernel		Buffer Coating		Outer Coating		
Batch No.	Diameter (μm)	Density (Mg/m^3)	Thickness (μm)	Density (Mg/m^3)	Thickness (μm)	Density (Mg/m^3)	BAF
6542-01-013	509	10.04	79	1.08	89	1.82	1.012

TABLE 9-20
IRRADIATION CONDITIONS AND DIAMETRAL CHANGES

Capsule	Capsule Position	Average Irradiation Temperature (°C)	Fast Neutron Fluence ($\times 10^{25}$ n/m^2) $(E > 29\ fJ)_{HTGR}$	Kernel Burnup (FIMA)	Measured Diametral Change, $\Delta D/D_o$
HT-17	40	1175	3.3	0.020	-0.057
HT-18	40	1256	6.7	0.066	-0.057
HT-19	40	1290	10.0	0.117	-0.037
HT-17	27	1426	4.2	0.024	-0.043
HT-18	27	1492	8.5	0.079	-0.042

correlate in exactly the same way as for the coatings on the discs and spheres. For this reason, the anisotropy of the coating on the particles was measured and the BAF was used to pick a coating rate appropriate to the discs and spheres. For these particular particles, the appropriate disc-sphere coating rate was the same as that of the particles. (For other batches of particles irradiated in the diametral change experiment, this was not the case.)

The values of Young's modulus, Poisson's ratio, and Poisson's ratio in creep employed in the calculation are shown in Table 9-21 along with the source from which they were obtained. Values for unrestrained dimensional changes were taken from Fig. 9-61, and changes in preferred orientation were taken from Figs. 9-62 and 9-63. The value of the creep parameter K has not been well established, and it was treated as an adjustable parameter which was used to improve the fit of the predicted and measured values.

The predicted and measured diametral changes for the particles irradiated in position 40 of capsules HT-17, -18, and -19 are shown in Fig. 9-67 for two different values of the creep parameter K. The predicted values at low fluences are smaller in magnitude than the measured values regardless of the value of K. This seems to occur because the pyrocarbon dimensional changes used in the model are not sufficiently large at low fluences. To examine the effect of using the dimensional changes of a pyrocarbon with a lower density in the stress analysis model, the dimensional changes of a carbon with a density of 1.75 Mg/m^3 were interpolated from those of 1.012 BAF carbons with densities of 1.65 and 1.85 Mg/m^3 and were used in the model. The predicted and measured diametral changes for the position 40 particles are shown in Fig. 9-68. The fit is now quite good and the values of the creep parameter K which produce these fits are consistent with earlier estimates of K in this temperature range (Ref. 9-20). The predicted and measured diametral changes of the particles irradiated in position 27 are shown in Fig. 9-69. The fit for the low-fluence data point is not good, but the fit to the high-fluence data point is better. In this

TABLE 9-21
YOUNG'S MODULUS, POISSON'S RATIO, AND POISSON'S RATIO IN CREEP USED IN CALCULATION

Young's modulus	$13.8 \times 10^{6} + 0.7 \times 10^{-15}$ (γ) kPa	Ref. 9-16
Poisson's ratio	0.223	Ref. 9-17
Poisson's ratio in creep	0.4 $0 < \gamma < 2.0 \times 10^{21}$	Ref. 9-18
	0.5 $\gamma > 2.0 \times 10^{21}$	Ref. 9-19

case dimensional changes of a carbon with a slightly higher density would have produced a better fit to the experimental data.

There are a number of ways to rationalize the apparent inconsistency between the particle coating density and the dimensional change density, all being related to penetration of the sink-float fluid into accessible pores in the carbon. Before such rationalizations are made, it would be best to complete the comparison of the model predictions with the measured diametral changes for other particles in the HT-experiments in order to see whether such density differences are consistently observed.

Prediction of Coating Failure

Failure Criterion. Prediction of coating failure involves another step beyond prediction of particle diametral changes. This step is the selection and use of a failure criterion for the coating. A Weibull-type failure criterion is being used in the stress analysis model. The Weibull criterion expresses the likelihood of failure in terms of a probability and incorporates the volume under stress and the stress distribution into the analysis. It has been shown that the Weibull technique accurately predicts the observed difference in mean fracture stresses caused by the different stress distributions in pyrocarbon strips tested in three- and four-point bending (Ref. 9-21). Also, the observed increasing probability of failure of identical coatings on particles with increasing diameters has been shown to agree well with the variations predicted from the Weibull theory due to volume increases (Ref. 9-22). Thus, both elements of the Weibull theory have been verified independently for pyrocarbons.

Mathematical Formulation of the Weibull Failure Criterion. As generally used, the Weibull theory states that the failure probability, F, of a specimen in uniaxial tension is given by:

$$F = 1 - \exp\left[\int_V -\left(\frac{\sigma}{\sigma_o}\right)^M dV\right] \quad . \tag{9-24}$$

σ is the uniaxial stress, V is the volume under stress, and M and σ_o are material properties which will be discussed in more detail later. A fuel particle coating is not in uniaxial tension but is under a triaxial stress state which varies with the radial distance from the center of the particle. The method used to take multiaxial stresses into account is to resolve them into a normal stress and then to integrate the normal stress over all directions where it is positive. The result is normalized with the normal stress due to uniaxial tension integrated over all directions. Normal stresses are used because fracture is due to normal stresses rather than shear stresses. The net result is that Eq. 9-24 becomes:

$$F = 1 - \exp\left\{\frac{4\pi(2M + 1)}{\sigma_o^M} \int_a^b \left[\int_o^{\Phi_I} (\sigma_t \cos^2\phi + \sigma_r \sin^2\phi)^M \, d\phi\right] r^2 \, dr\right\} \quad . \quad (9\text{-}25)$$

σ_t and σ_r are the tangential and radial stresses, respectively, and

$$\Phi_I = \tan^{-1/2}\left(-\frac{\sigma_t}{\sigma_r}\right) \quad . \quad (9\text{-}26)$$

Weibull Parameters of Pyrocarbon. As noted above, M and σ_o are properties of the material under consideration. The mechanical properties of pyrocarbons with a range of structures (sink-float densities and coating rates) have been measured by testing about a dozen specimens from each batch in three-point bending. The specimens were in the form of small strips which were cut from coatings on graphite discs (the same coatings which were used to determine the dimensional changes). The mean fracture stresses determined in the three-point bend tests are shown in Fig. 9-70. The strength of the carbon is strongly dependent on the coating rate and is relatively insensitive to the density. This coating-rate dependence of the strength is used to explain observed coating behavior during irradiation in the subsequent discussion.

The Weibull parameter M describes the scatter of strengths for the material while σ_o locates the strength distribution. The values of M and σ_o determined from the results of the three-point bend tests are shown in

Table 9-22. As might be expected from the well-behaved variation of the mean strength with coating rate, the values of σ_o vary systematically with the coating rate. However, the values of M do not. In order to ensure that small scratches or nicks in the specimens were not responsible for the nonsystematic variation of M, the three-point bend tests should be repeated again with very careful specimen preparation to see if the results change. However, in the absence of such evidence, the above Weibull parameters have been used.

Observed Coating Failure During Irradiation. One-millimeter-diameter sapphire spheres with pyrocarbon coatings have been routinely included as a part of the pyrocarbon irradiation experiments. Under irradiation, the single-crystal sapphire spheres are stable and force the pyrocarbon coatings to accommodate the dimensional changes through creep and elastic strains. Therefore, the stresses generated in the pyrocarbon coatings on the sapphire spheres are virtually identical to those in outer coatings on TRISO particles irradiated under the same conditions.

The results observed in one series of such irradiations (capsules HT-20, -21, -22, and -23) where three spheres of each coating batch were included are shown in Figs. 9-71a through 9-71d. The dimensional changes of the unrestrained pyrocarbons irradiated in these experiments are shown in Figs. 9-72a through 9-72d for carbons with coating rates of 1, 2, 4, and 12 μm/min. The behavior of the coatings on the spheres can be rationalized in the following way from these dimensional changes and from the strengths shown in Fig. 9-70. The stresses generated in the coatings are controlled almost entirely by the rate of dimensional change in the tangential direction. The low-density coatings have the highest rates of tangential dimensional change at low fast neutron fluences, and thus, coating failure first appears in these carbons. At this stage, the dimensional changes do not depend strongly on coating rate. The low-density coating deposited at the lowest coating rate survived longer than the other low-density carbons because it was the strongest. The intermediate-density carbon deposited at the lowest coating rate broke after an intermediate fluence because its

TABLE 9-22
WEIBULL PARAMETERS OF PYROCARBON DETERMINED
FROM THREE-POINT BEND TESTS

Density (Mg/m^3)	Coating Rate ($\mu m/min$)	No. of Specimens Tested	M	σ_o [10^8 $(mPa)^m$ m^3]
1.94	1.50	12	8.9	230.6
1.94	1.61	12	10.2	255.9
1.98	9.20	10	8.1	121.1
1.95	11.90	8	7.6	57.7
1.85	1.22	6	11.9	339.7
1.88	1.51	10	9.8	251.7
1.83	3.36	6	20.2	153.6
1.83	10.40	6	29.0	75.9
1.65	4.50	12	28.9	325.7
1.67	11.15	12	10.0	191.0
1.63	27.60	12	15.5	73.9

high crystalline anisotropy was beginning to cause acceleration in the dimensional changes. Fracture of the intermediate-density carbon deposited at the highest coating rate occurred because of the low strength of this coating. The apparent inconsistency between the two intermediate-density carbons deposited at the lowest rates in Fig. 9-71c is just an indication of the poor statistics obtained using three spheres per sample.

Comparison of Stress Analysis Model with Results. The BISO stress analysis model was modified so that it could be used to analyze the results obtained with the coated sapphire spheres. This involved removing the routine for calculation of an internal pressure due to fission gases and replacing it with expressions for calculating a pressure at the inner coating surface determined from a boundary condition which set the displacement of the sapphire sphere equal to the displacement of the pyrocarbon at the inner surface. In addition, the Weibull failure criterion was added to the model.

The unrestrained dimensional change data shown in Figs. 9-72a through 9-72d were used in analyzing the results. The Young's modulus was varied with the initial density of the coating according to Fig. 9-65, and the change in preferred orientation with apparent creep strain was assumed to follow one of the curves in Figs. 9-73 through 9-75 depending on the initial density and coating rate. (The latter data were obtained by measuring the preferred orientations of the coatings on the spheres after irradiation.) Otherwise, the data used in the calculations were the same as those used in analyzing the diametral changes of the BISO particles.

The tangential stress and failure probability calculated for an intermediate-density low-coating-rate carbon using a constant value of the creep parameter K is shown in Fig. 9-76. It is apparent that this curve is not consistent with the experimentally observed results. This coating and another with a slightly higher coating rate did not break at a low fluence where the calculated stresses and the fracture probability are high; they broke at an intermediate fluence. The same inconsistency was present in

the calculated results for the other intermediate-density carbon which fractured (coating rate of 10 μm/min). Only the low-density carbons broke at low fluences in the region of high calculated stress. Different values of K do not change the shape of the curves in Fig. 9-76, and, therefore, the inconsistency cannot be removed by adjusting the variable parameter.

One way of explaining the above inconsistency is that K varies with fast neutron fluence or with creep strain. If this is the case, the value of K must be high early in the irradiation and decrease with increasing fast neutron fluence. Note that this is not the same as including transient and steady-state creep in the analysis. The stresses in the coatings are continually changing, and therefore they are always in a transient condition; steady-state conditions of a constant stress never apply.

With the particular condition of coatings restrained on an unyielding substrate, the stress state at any given fluence is very nearly independent of the prior stress history. This occurs because the dimensional changes are large compared to the possible elastic strains so that at any given fluence, the dimensional change rate is very nearly balanced by the creep-strain rate. Thus, assuming that K does vary during irradiation, the observation of coating failure or survival at a given fluence can be used to define an upper or lower bound on the value of K. This has been done with the results obtained from the coatings on the sapphire spheres; the values are listed in Table 9-23. Only the value obtained from the intermediate-density, high-coating-rate carbon is inconsistent with K, decreasing from a value of about 0.3×10^{-27} (kPa n/cm^2)$^{-1}$ at a fluence of 1.8×10^{25} n/m^2 to a value of about 0.07×10^{-27} (kPa n/cm^2)$^{-1}$ at a fluence of 3.5×10^{25} n/m^2 and remaining constant thereafter. In this it has been assumed that the value of K does not vary with the carbon structure. There is some evidence in the literature for this. Brockelhurst and Gilchrist (Ref. 9-23) have measured the value of K/E for a low-density and high-density carbon similar to those employed in this study. If values of E from Fig. 9-65 are used to solve for K from their expressions, nearly the same values of K are obtained for each carbon.

TABLE 9-23
CREEP CONSTANTS FROM SAPPHIRE SPHERES IN CAPSULES HT-20 THROUGH HT-23

Density (Mg/m^3)	Rate ($\mu m/min$)	Fluence ($\times 10^{25}$ n/m^2) $(E > 29\ fJ)_{HTGR}$	BAF	Survived (S) or Failed (F)	K $[(10^{-27}\ kPa\ n/cm^2)^{-1}]$
1.65	2.0	1.8	1.142	S	>0.28
1.65	4.0	1.8	1.127	F	<0.29
1.83	1.0	3.5	1.182	F	<0.072
1.83	2.0	3.5	1.144	S	>0.071
1.83	12.0	7.0	1.059	F	<0.011
1.83	8.0	7.0	1.073	S	>0.015
1.83	4.0	7.0	1.103	S	>0.036
1.83	2.0	7.0	1.170	S	>0.070
1.95	1.0	10.4	1.336	S	>0.015
1.95	8.0	10.4	1.120	S	>0.015
1.83	8.0	10.4	1.096	S	>0.023
1.83	4.0	10.4	1.124	S	>0.043
1.83	2.0	10.4	1.201	S	>0.080

To show the effect of variation of K with fast neutron fluence on the calculated stresses and failure probabilities, these values were recalculated from the carbon of Fig. 9-76 with K linearly decreasing with fast neutron fluence through the Table 9-23 value at 1.8×10^{25} n/m^2 to the Table 9-23 value at 3.5×10^{25} n/m^2 and remaining constant thereafter. The results are shown in Fig. 9-77. Needless to say, the inconsistency of high calculated stresses and a high failure probability early in life have been removed.

The high failure probability at low fast neutron fluences could also be explained by a degradation of the strength of the carbon during irradiation. However, there has been no indication of such a strength degradation either in irradiated unrestrained carbons (Ref. 9-16) or irradiated restrained carbons (Ref. 9-15).

Finally, it should be noted that the values of K listed in Table 9-23 are not inconsistent with those used in the former section to obtain agreement between the measured and calculated BISO particle diametral changes. In the BISO particle calculations, an assumed high value of K early in the irradiation would not have greatly changed the calculated diametral changes since there is very little internal pressure early in the irradiation. Also, the value of K is expected to increase strongly with temperature since the value of K for graphite does. Thus, the K of about 0.6×10^{-27} (kPa n/cm^2)$^{-1}$ used for the BISO particle irradiations at a temperature of about 1400°C is not inconsistent with the K of about 0.07×10^{-27} (kPa n/cm^2)$^{-1}$ used for the coated-sapphire-sphere irradiations at a temperature of about 950°C.

REFERENCES

9-1. Young, C. A., and D. P. Harmon, "Preirradiation Report of Fuel Materials for P13T Irradiation Capsule," ERDA Report GA-A13343, General Atomic, April 1976.

9-2. "HTGR Fuels and Core Development Program Quarterly Progress Report for the Period Ending February 29, 1976," ERDA Report GA-A13804, General Atomic, March 31, 1976.

9-3. "HTGR Fuels and Core Development Program Quarterly Progress Report for the Period Ending May 31, 1975," ERDA Report GA-A13444, General Atomic, June 30, 1975.

9-4. Wallroth, C. F., et al., "Postirradiation Examination of Peach Bottom Fuel Test Element FTE-3," ERDA Report GA-A13004, General Atomic, August 15, 1974.

9-5. Wallroth, C. F., J. F. Holzgraf, and D. Jensen, "Postirradiation Examination of Peach Bottom Fuel Test Element FET-4," ERDA Report GA-13452, General Atomic, to be published.

9-6. Steward, K. P., "Spine Samples in the Phase 1 and Phase 2 Peach Bottom Test Elements," General Atomic unpublished data, September 30, 1971.

9-7. "HTGR Fuels and Core Development Program Quarterly Progress Report for the Period Ending November 30, 1975," ERDA Report GA-A13737, General Atomic, December 31, 1975.

9-8. Burnette, R. D., W. E. Bell, and M. L. Baldwin, "Fission Product Retention Characteristics of HTGR Fuel," paper presented at the International Conference on Nuclear Fuel Performance, British Nuclear Energy Society, London, October 15-19, 1973, Paper No. 16.

9-9. Harmon, D. P., and C. B. Scott, "Development and Irradiation Performance of LHTGR Fuel," ERDA Report GA-A13173, General Atomic, October 31, 1975.

9-10. Scott, C. B., D. P. Harmon, and J. F. Holzgraf, "Postirradiation Examination of Capsules P13R and P13S," ERDA Report GA-13827, General Atomic, to be published.

9-11. Beavan, A. L., "Control Materials in LHTGR Design," General Atomic Report GA-A13260, December 31, 1974.

9-12. Stevens, D. W., "An Explicit Solution for Stresses in Pyrocarbon-Coated Fuel Particles," Nucl. Technol. 10, 301 (1971).

9-13. "Base Program Report for the Period January 1, 1975 through June 6, 1975," Oak Ridge National Laboratory, 1975.

9-14. Stevens, D. W., "Optical Anisotropy and Preferred Orientation in Nearly Isotropic Pyrocarbons," General Atomic Report GA-A13307, January 22, 1975.

9-15. Kaae, J. L., "Behavior of Pyrolytic Carbons Irradiated Under Mechanical Restraint," Carbon 12, 577 (1974).

9-16. Kaae, J. L., "Effect of Irradiation on the Mechanical Properties of Isotropic Pyrolytic Carbons," J. Nucl. Mater. 46, 121 (1973).

9-17. Price, R. J., and J. L. Kaaes, "Poisson's Ratio of Pyrolytic Carbon," Carbon 7, 706 (1969).

9-18. Kaae, J. L., "On Irradiation-Induced Creep of Pyrolytic Carbon in a General State of Stress," J. Nucl. Mater. 36, 206 (1970).

9-19. Kaae, J. L., "Calculation of Irradiation Induced Stresses in Restrained Pyrolytic Carbons," in Physical Metallurgy of Reactor Fuel Elements, Metals Society (1973), p. 315.

9-20. Bokros, et al., "Radiation-Induced Dimensional Changes and Creep in Carbonaceous Materials," J. Nucl. Mater. 31, 25 (1969).

9-21. Kaae, J. L., "Application of Weibull Statistics to the Strength of Pyrolytic Carbon," General Atomic Report GA-A13869, March 1976.

9-22. Kaae, J. L., and D. Harmon, General Atomic Company unpublished data.

9-23. Brocklehurst, J. E., and K. E. Gilchrist "Fast Neutron Induced Creep in Pyrocarbon Under Constant Stress," J. Nucl. Mater 59, 1 (1976).

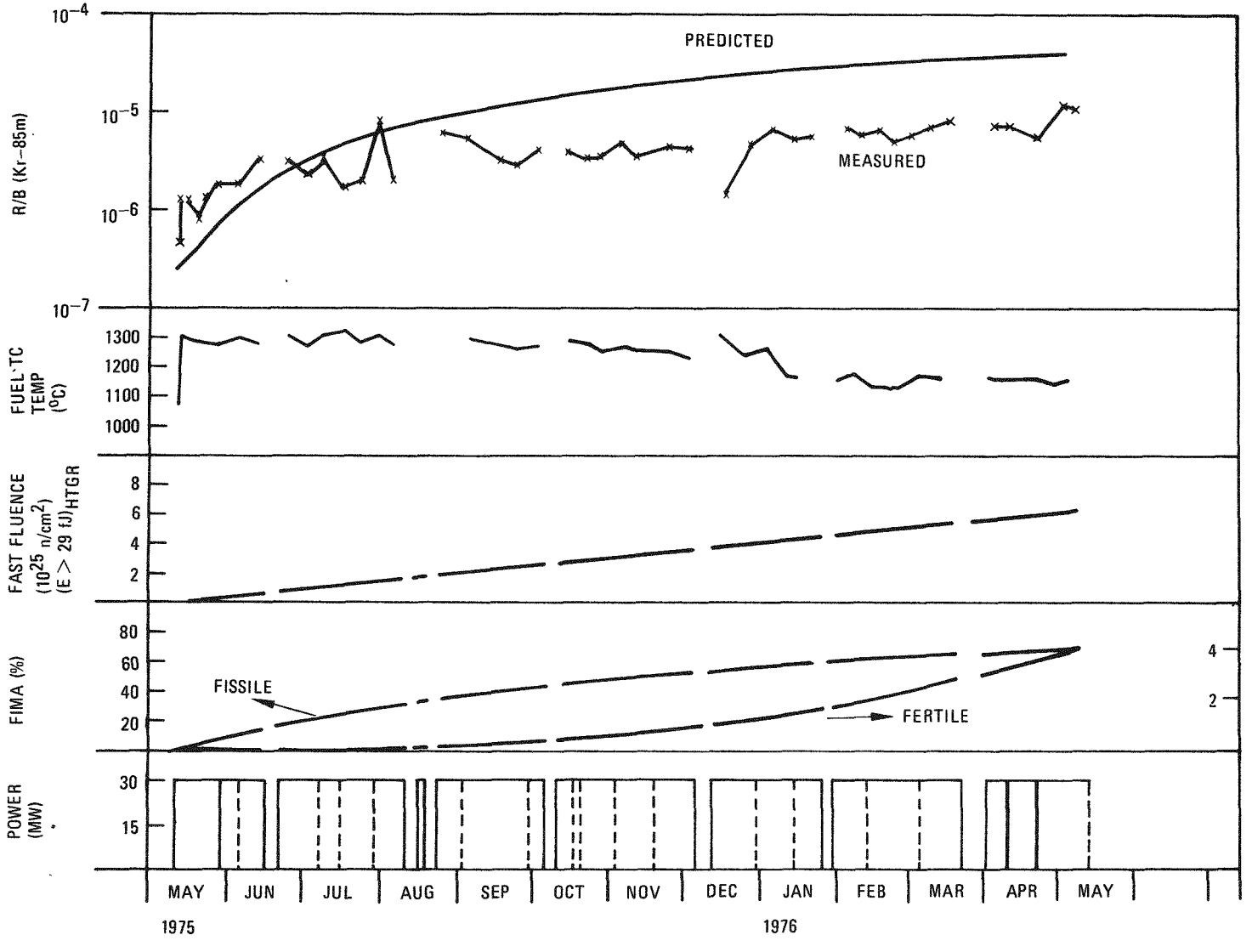

Fig. 9-1. Operating history for cell 1 of capsule P13T (to 5/13/76) containing UC_2 (VSM) TRISO and ThO_2 BISO coated particles

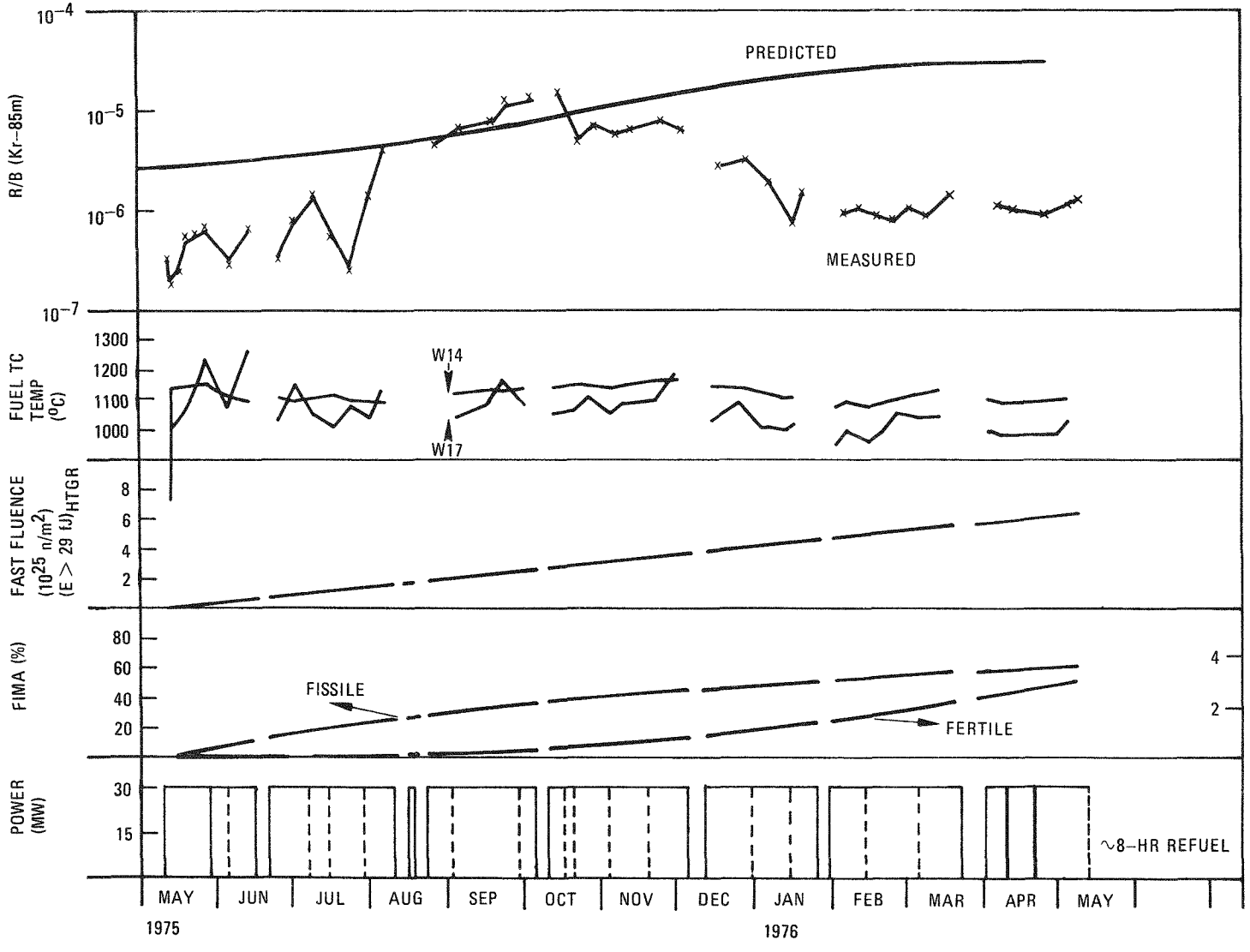

Fig. 9-2. Operating history for cell 2 of capsule P13T (to 5/13/76) containing UC_2 (VSM) and UC_xO_y (WAR) TRISO and ThO_2 BISO coated particles

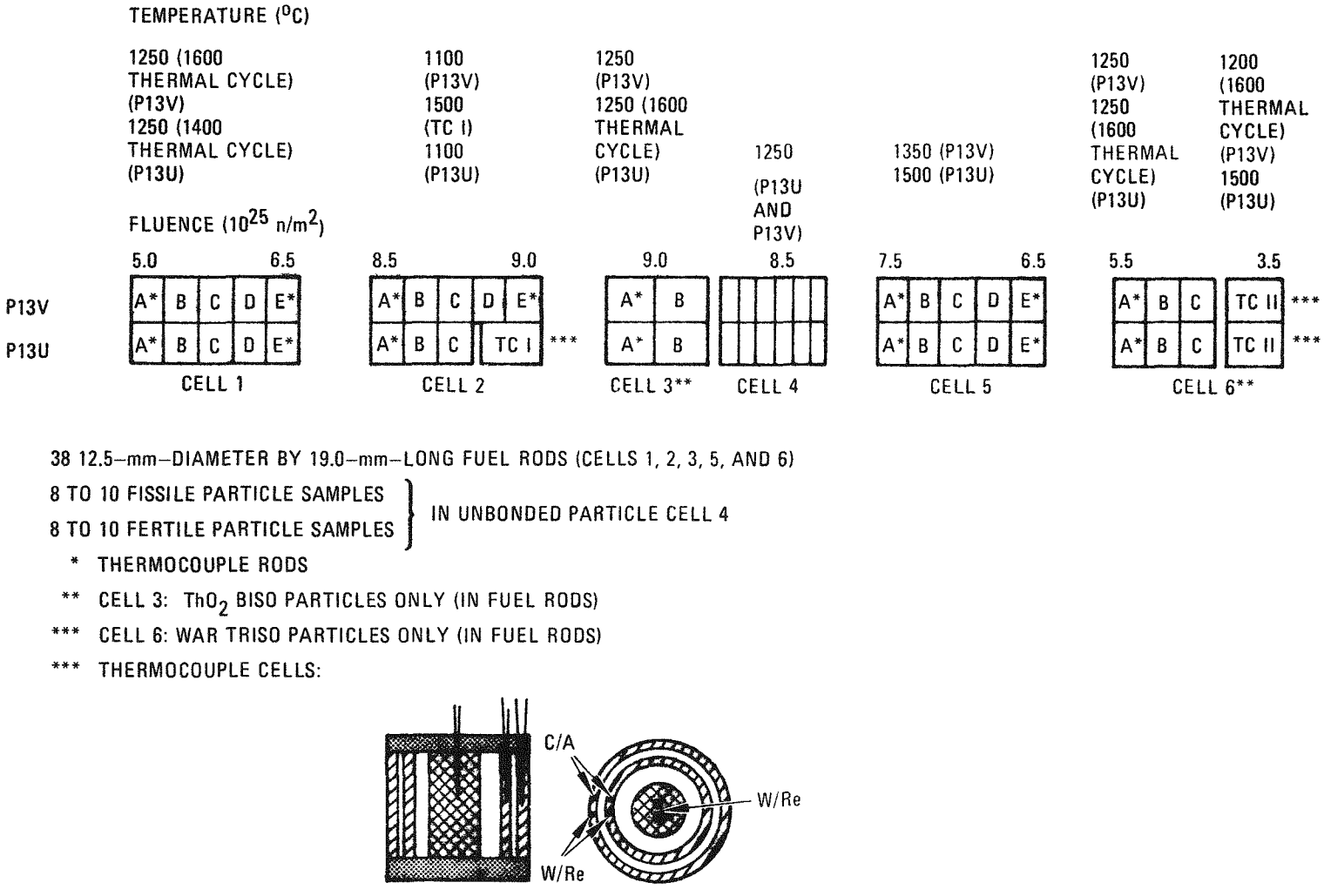

38 12.5–mm–DIAMETER BY 19.0–mm–LONG FUEL RODS (CELLS 1, 2, 3, 5, AND 6)

8 TO 10 FISSILE PARTICLE SAMPLES
8 TO 10 FERTILE PARTICLE SAMPLES
} IN UNBONDED PARTICLE CELL 4

* THERMOCOUPLE RODS

** CELL 3: ThO_2 BISO PARTICLES ONLY (IN FUEL RODS)

*** CELL 6: WAR TRISO PARTICLES ONLY (IN FUEL RODS)

*** THERMOCOUPLE CELLS:

Fig. 9-3. Revised schematic layout showing temperature-fluence conditions for capsules P13U and P13V

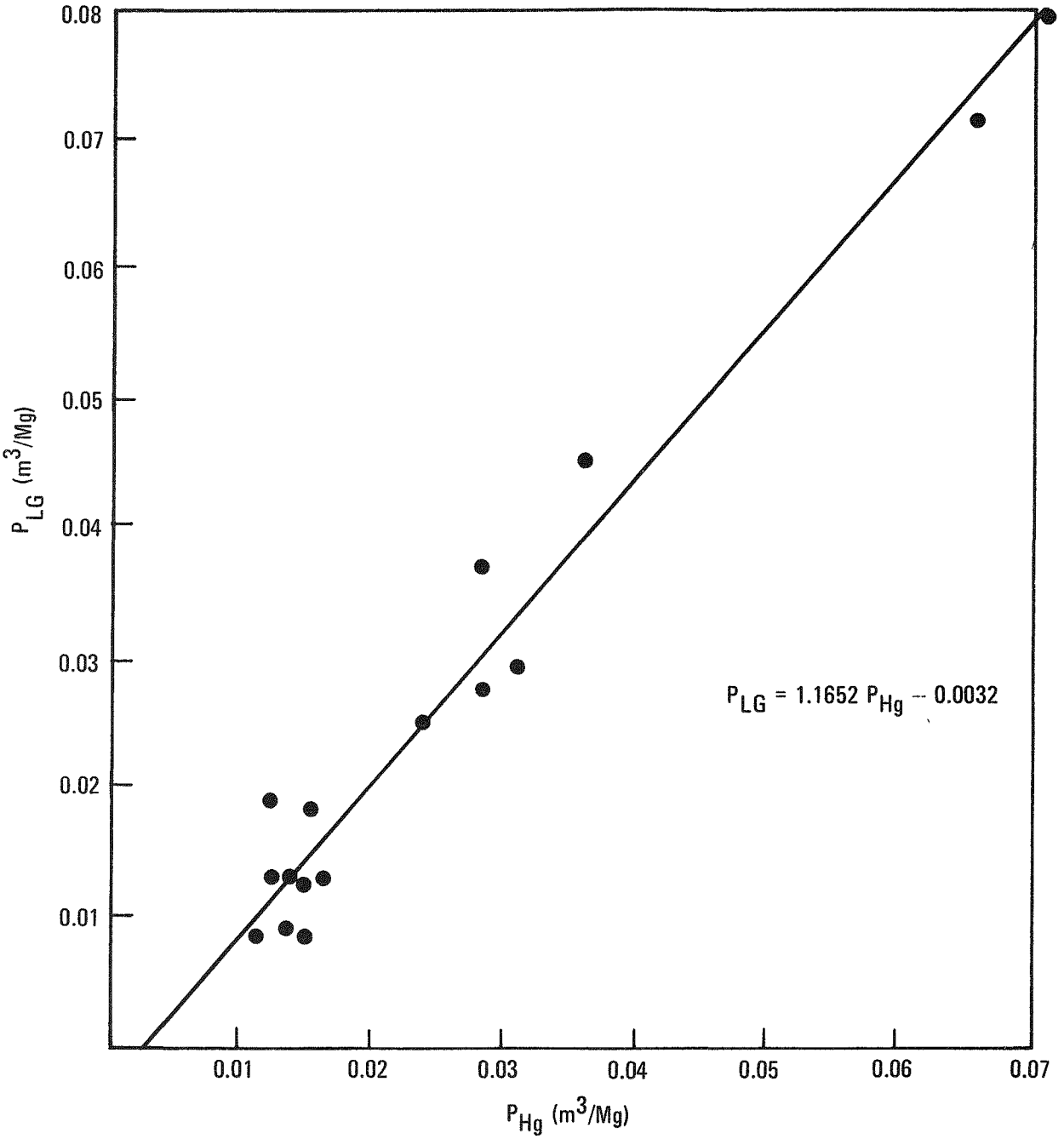

Fig. 9-4. Coating porosity versus mercury intrusion

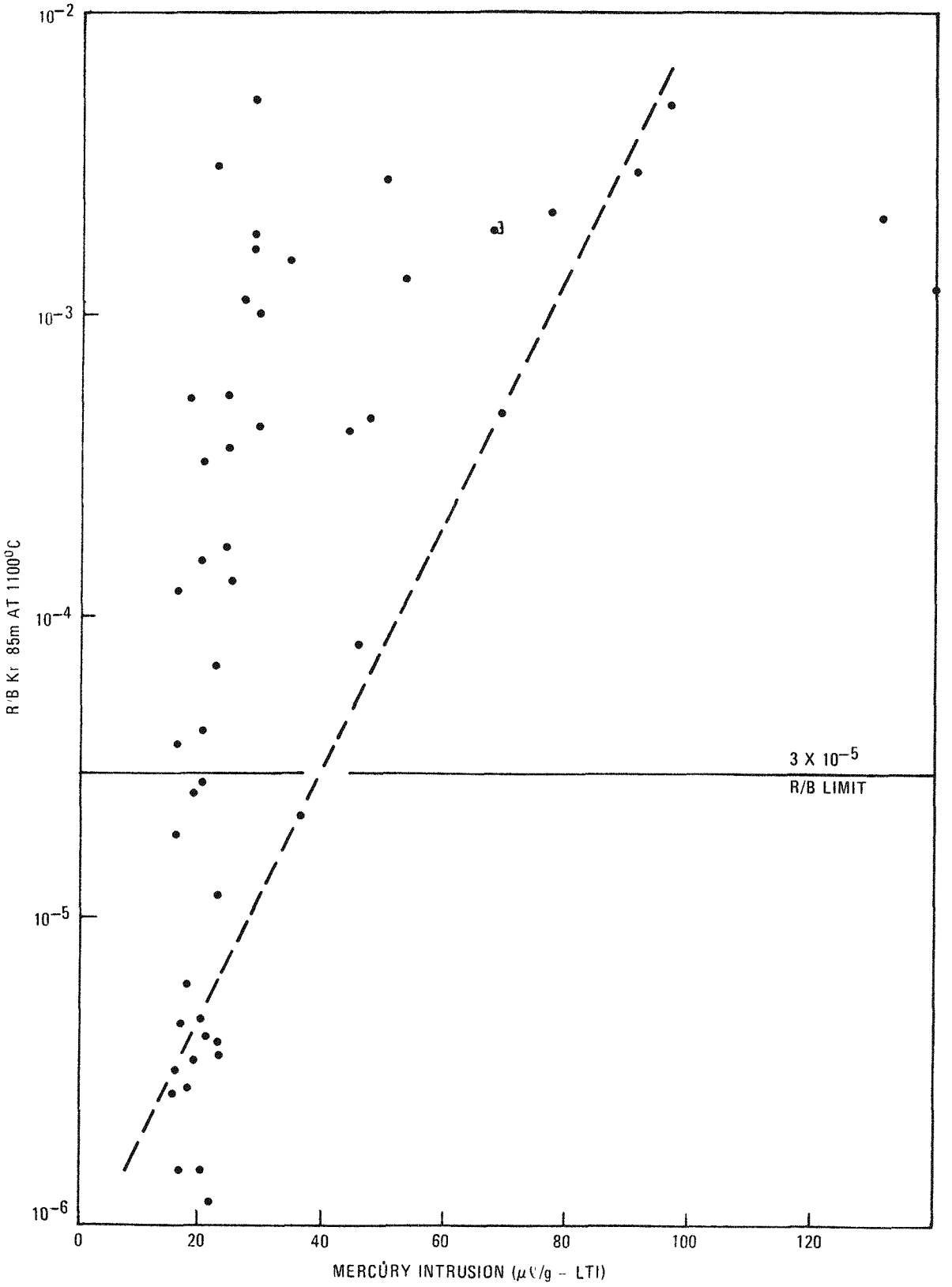

Fig. 9-5. R/B Kr-85m versus mercury intrusion

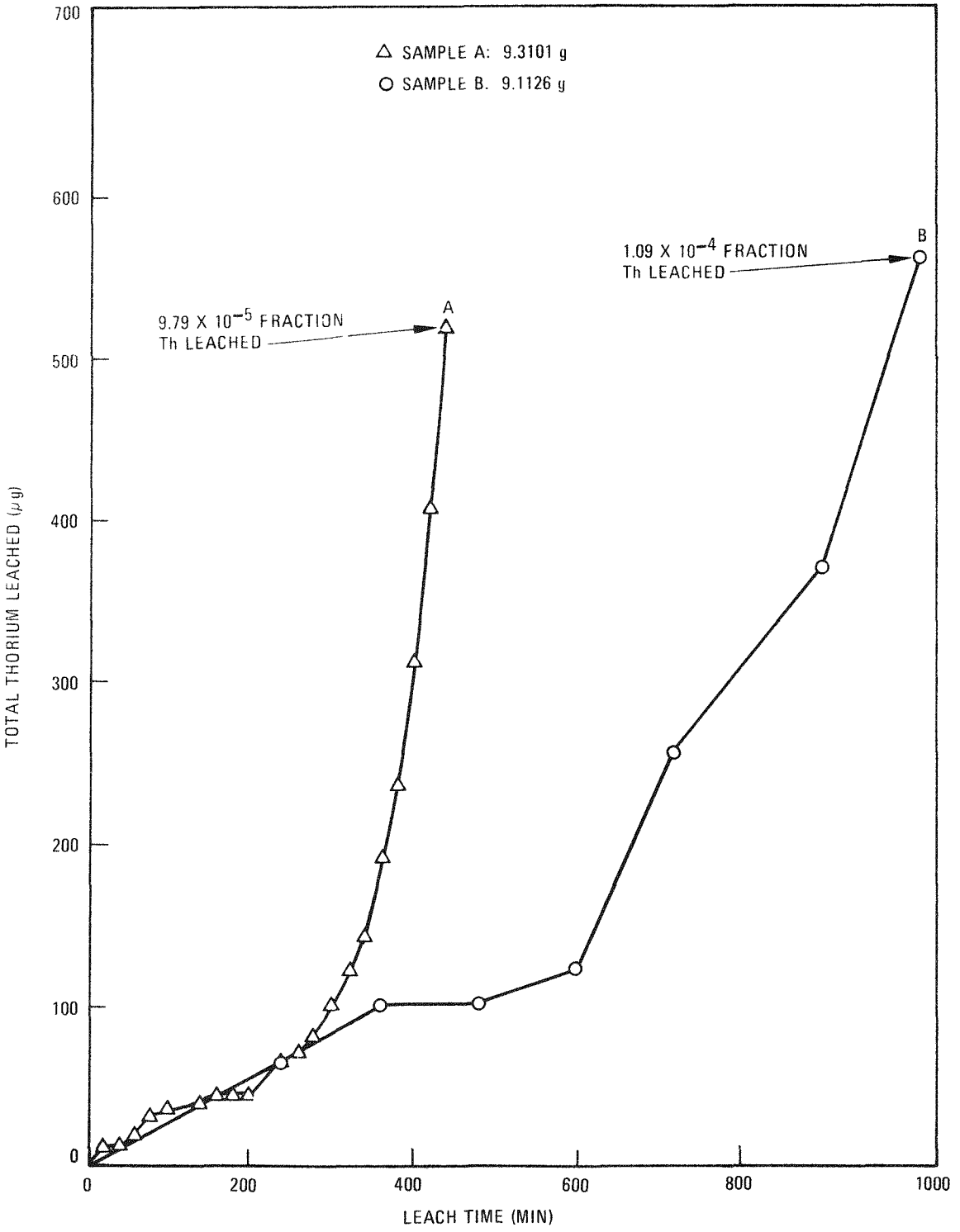

Fig. 9-6. Phosgene gas leaching at 1100°C, BISO ThO_2 particles, batch 6779-65

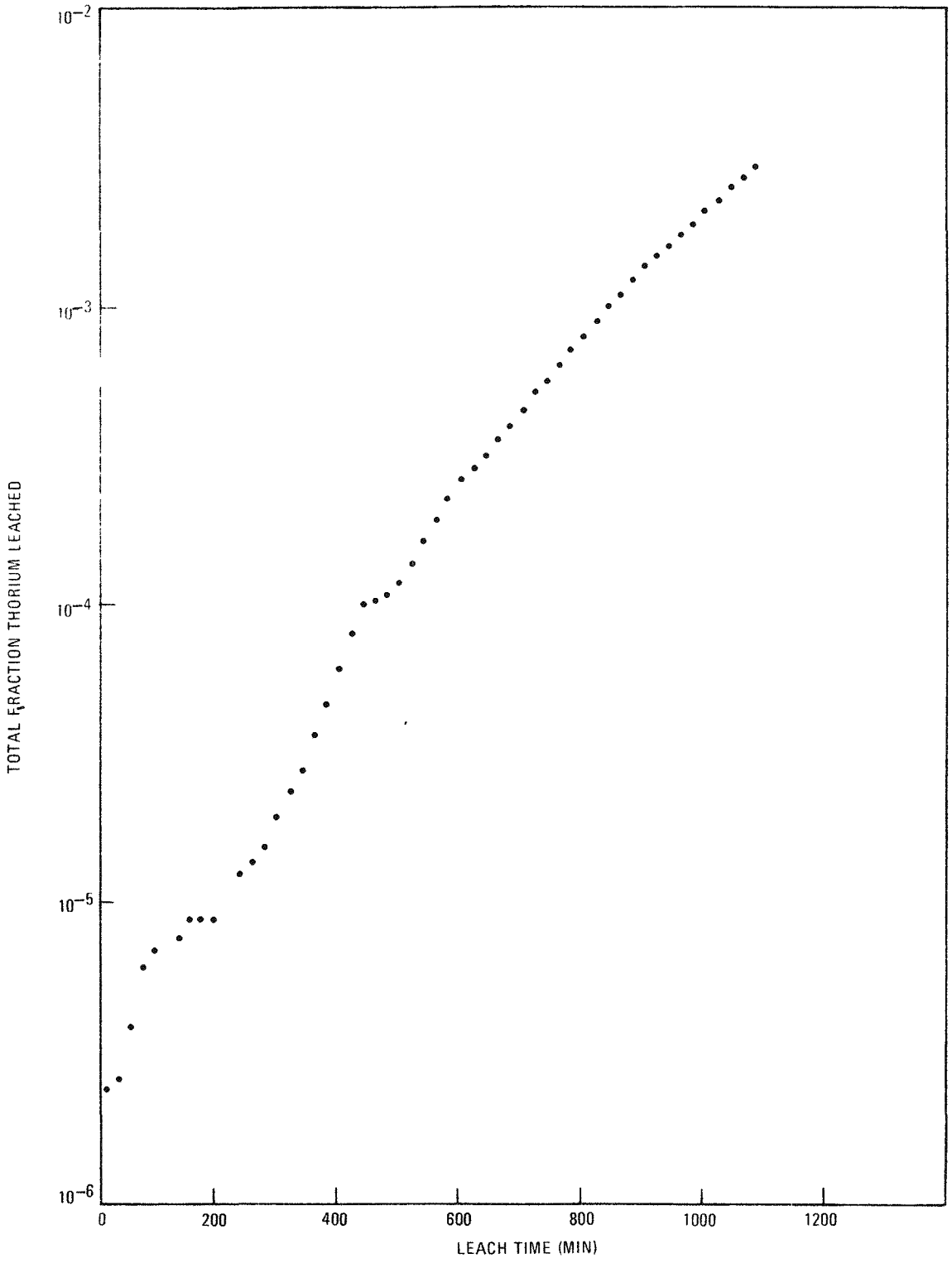

Fig. 9-7. Phosgene gas leaching at 1100°C, BISO ThO_2 particles, batch 6779-65, R/B Kr-85m = 1.7×10^{-3} at 1100°C

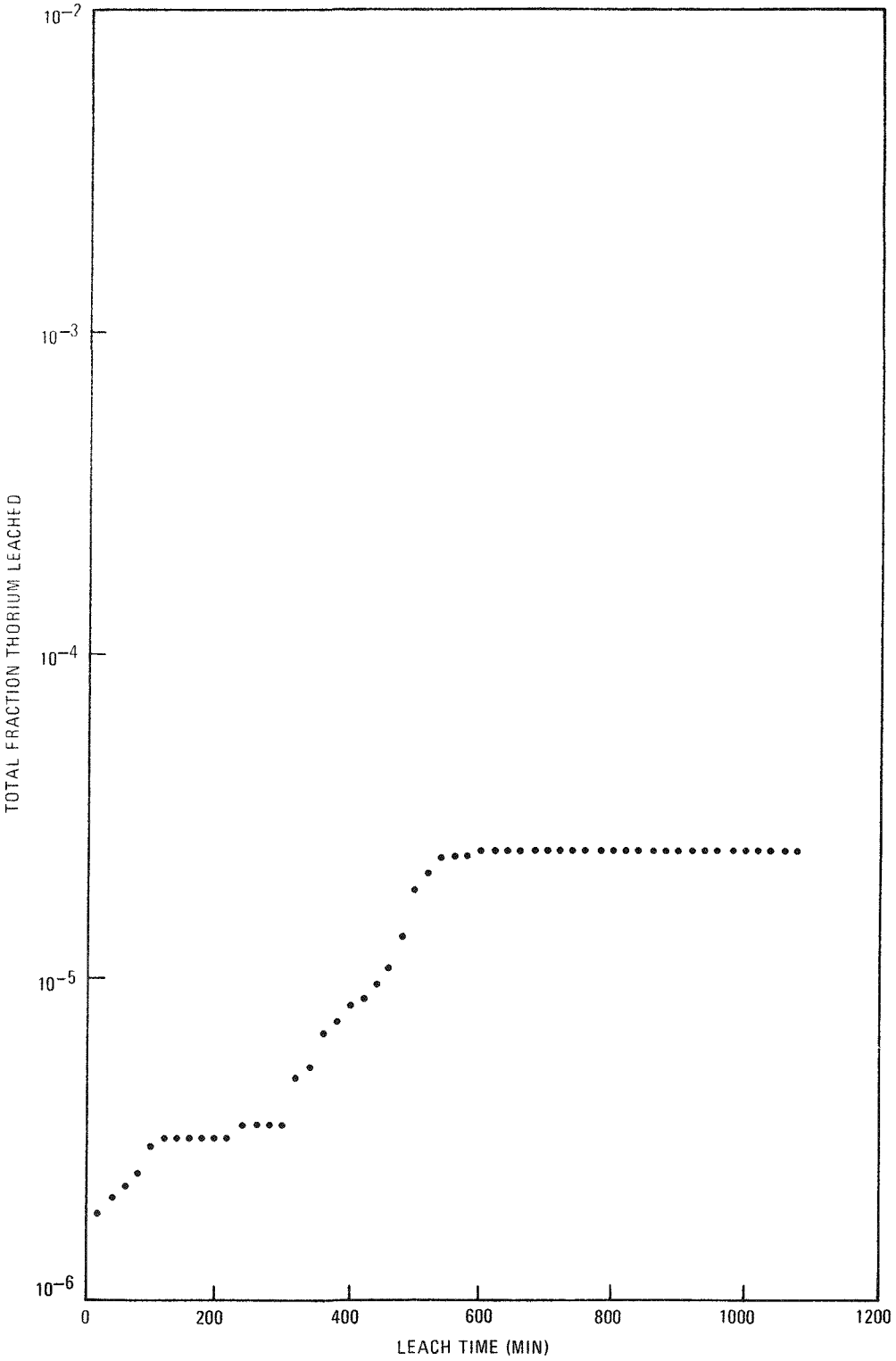

Fig. 9-8. Phosgene gas leaching at 1100°C, BISO ThO_2 particles, batch 6779-67, R/B Kr-85m = 3.2×10^{-6} at 1100°C

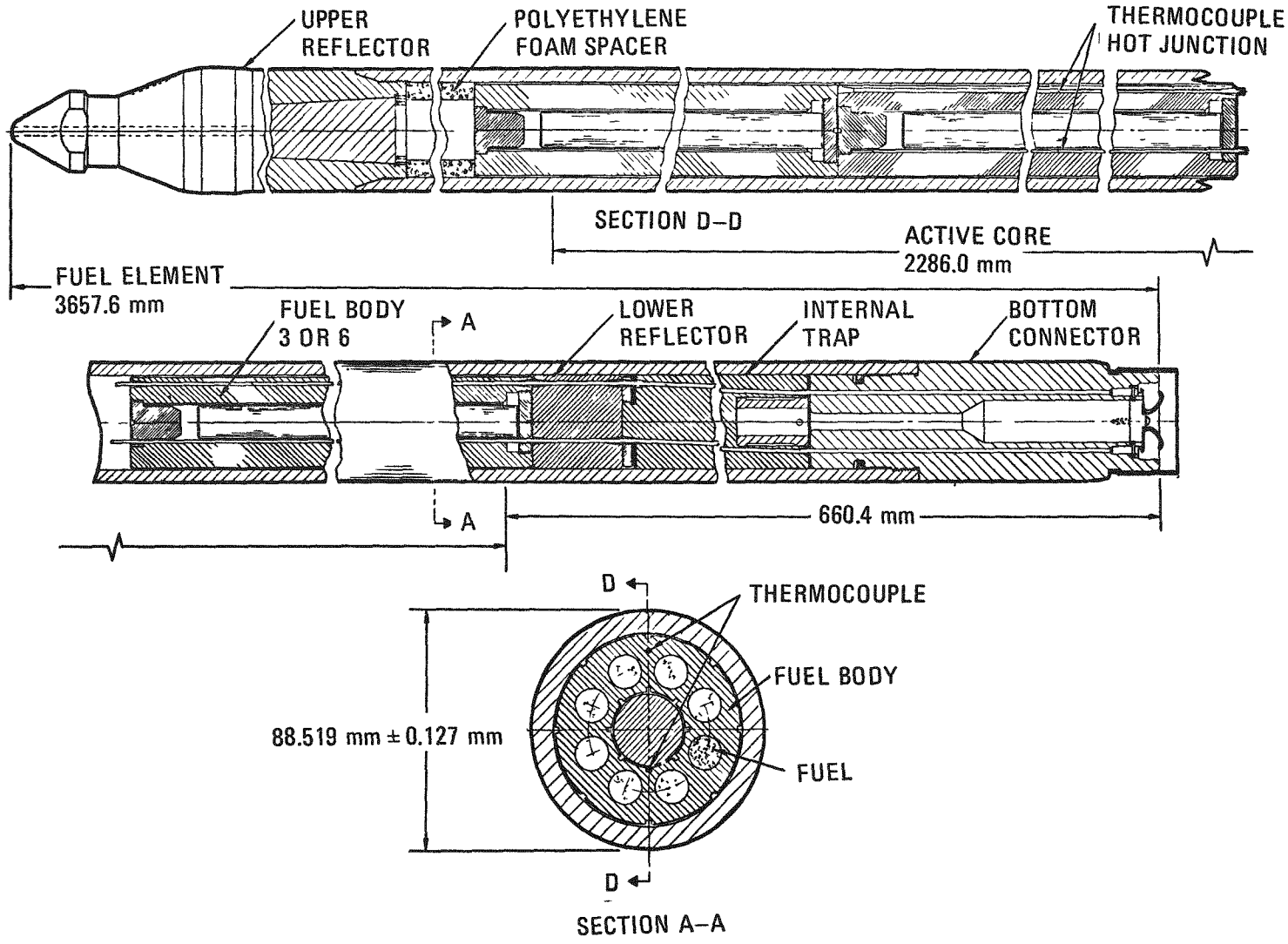

Fig. 9-9. Typical fuel test element assembly

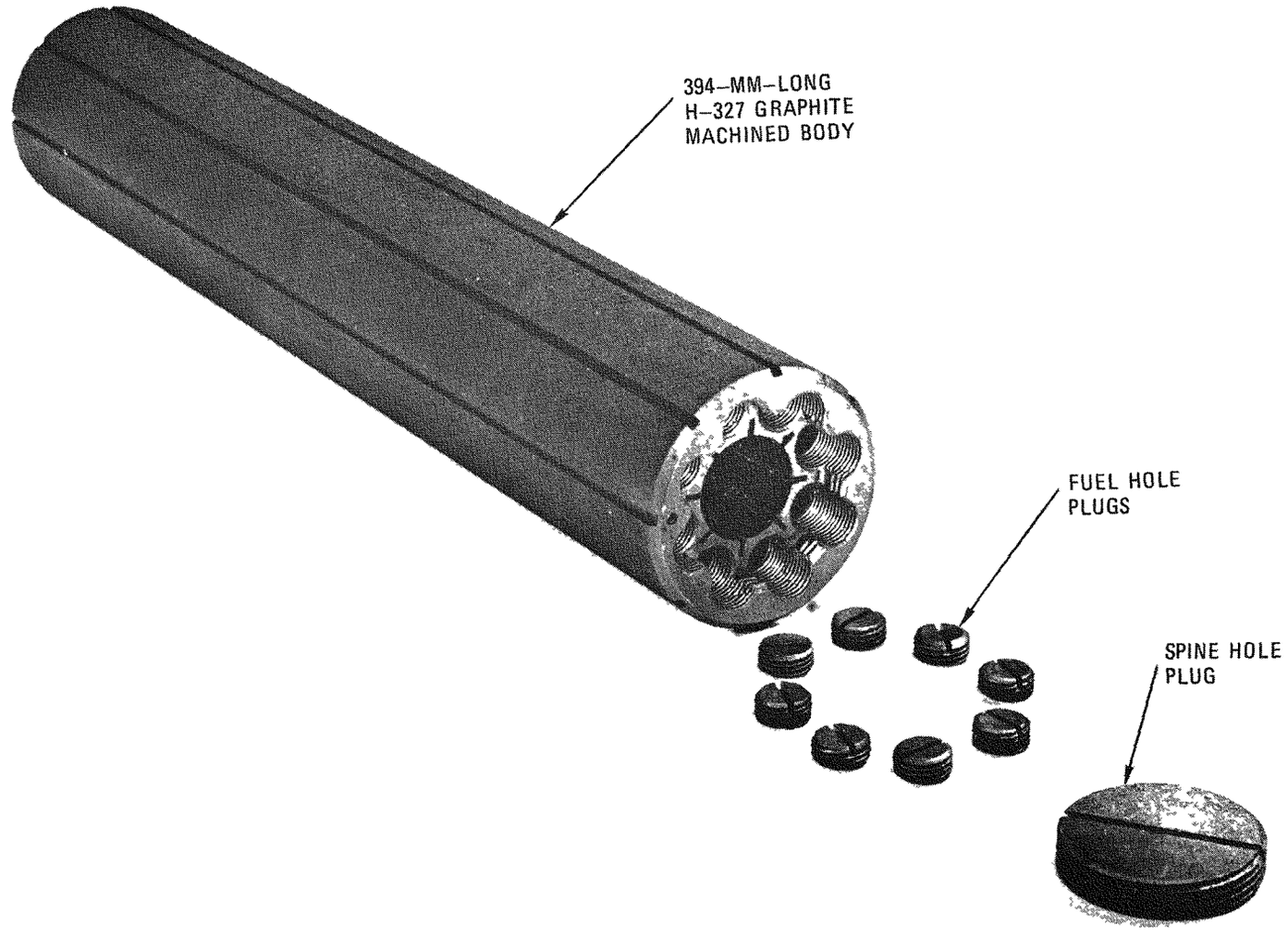

Fig. 9-10. Graphite fuel body for Peach Bottom fuel test elements

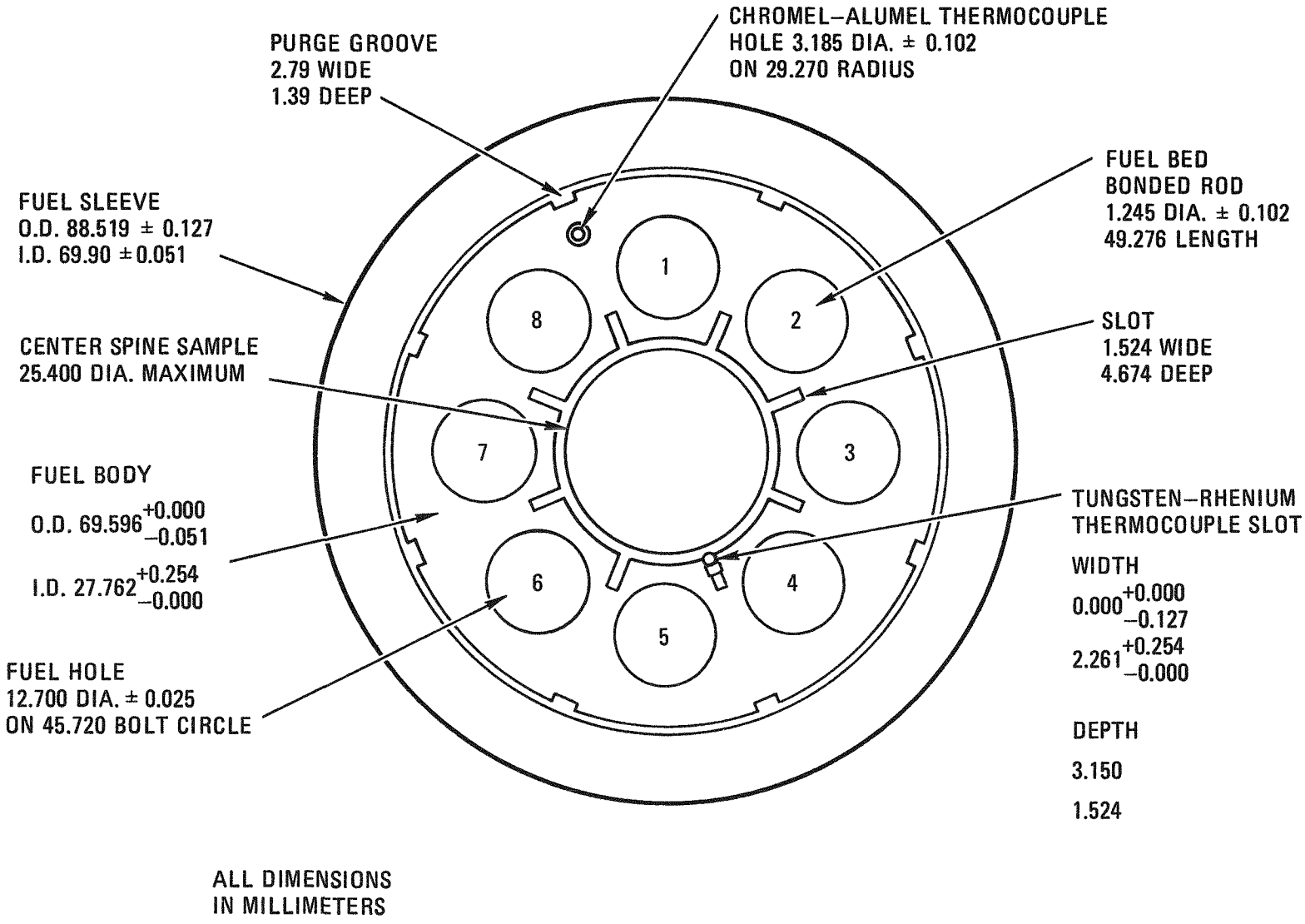

Fig. 9-11. FTE-6 cross section

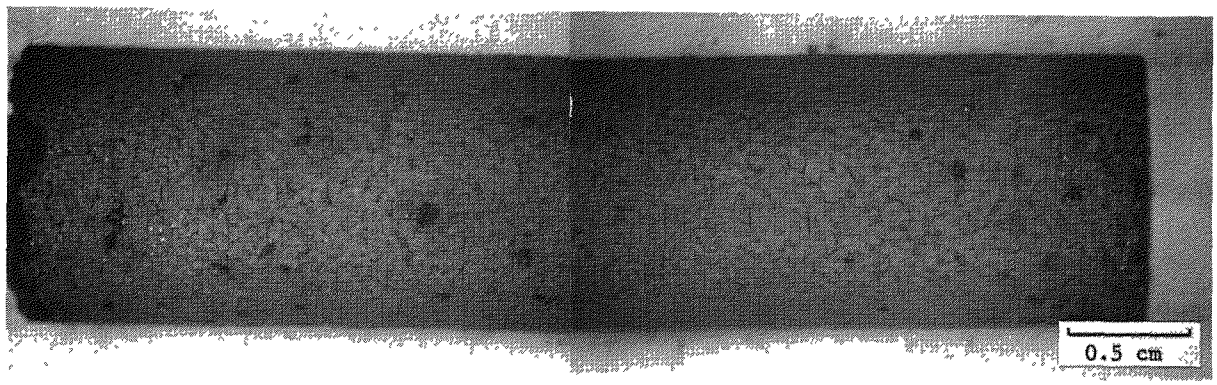

S7519 (3-4)

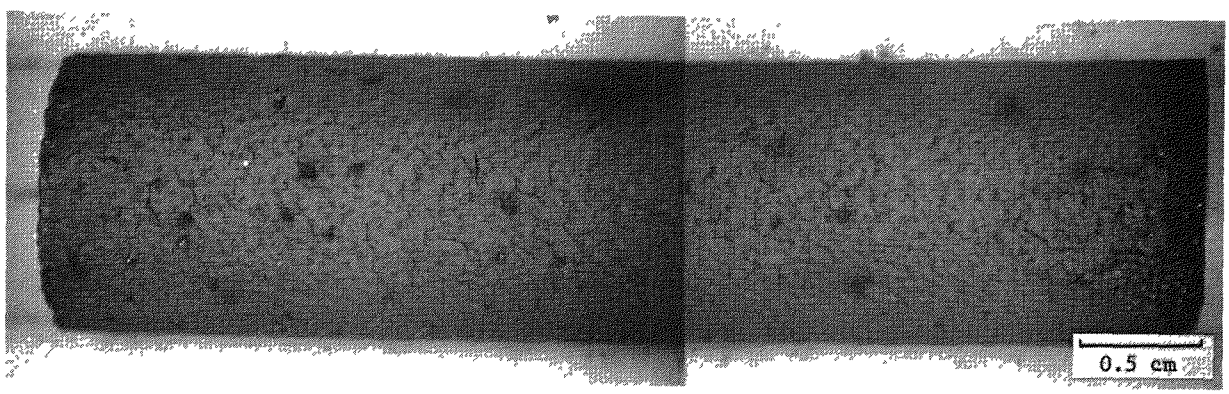

S7519 (5-6)

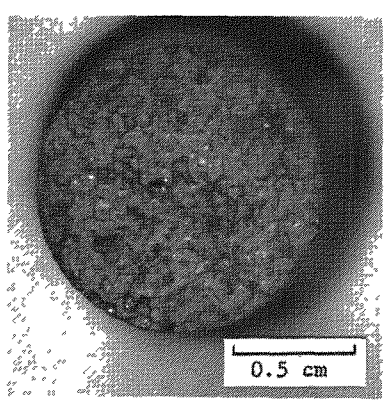

S7519-1

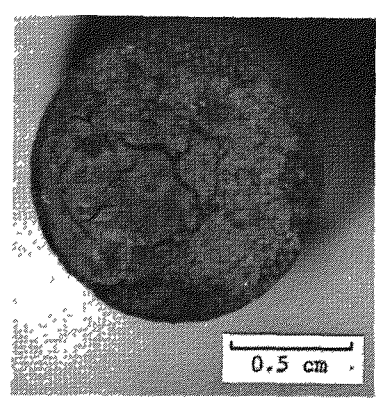

S7519-2

Fig. 9-12. Visual examination of fuel rod 2-1-7 from FTE-6

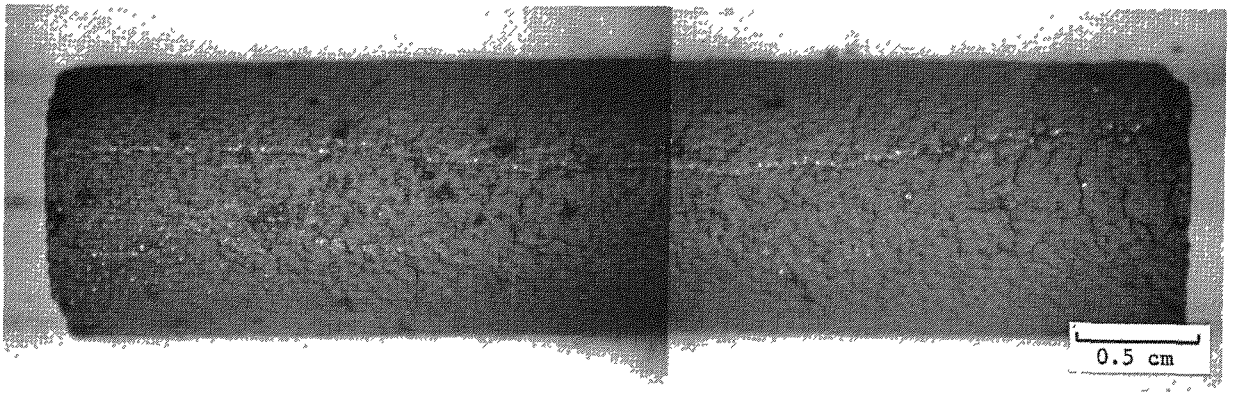

S7519 (9-10)

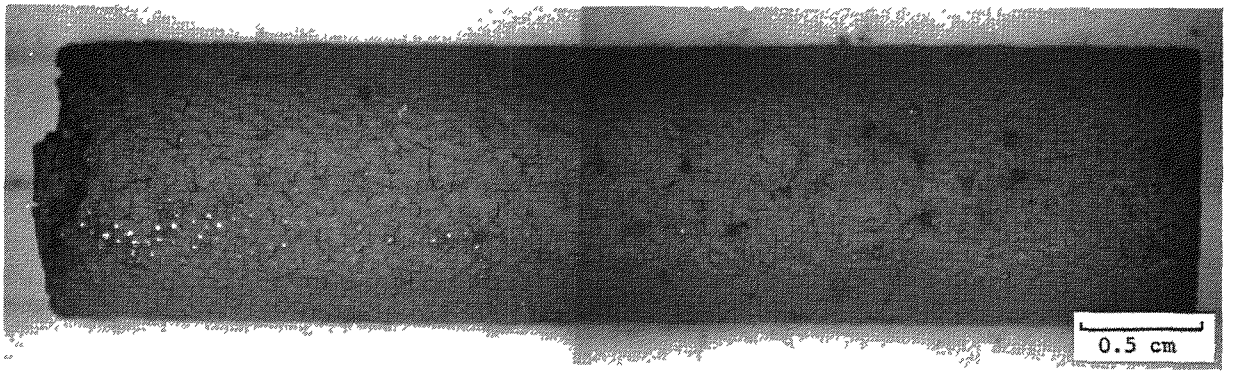

S7519 (11-12)

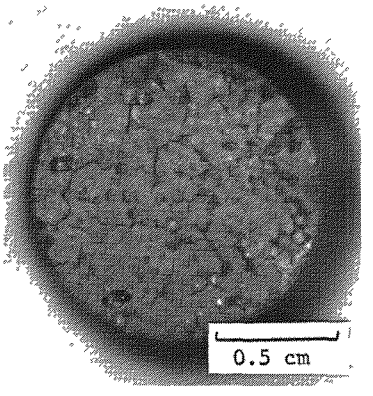

S7519-8

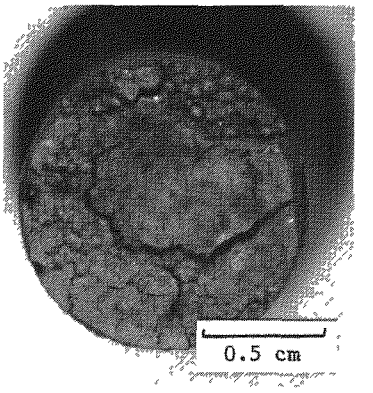

S7519-7

Fig. 9-13. Visual examination of fuel rod 2-2-7 from FTE-6

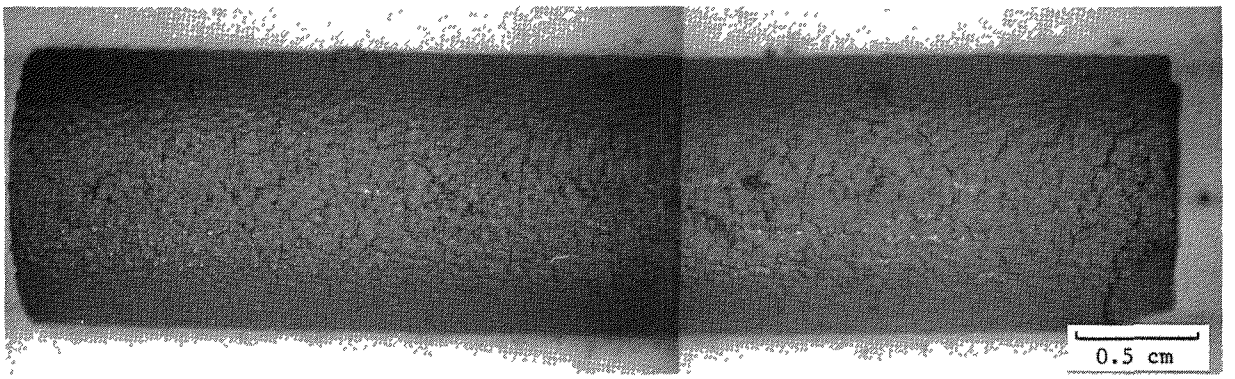

S7519 (15-16)

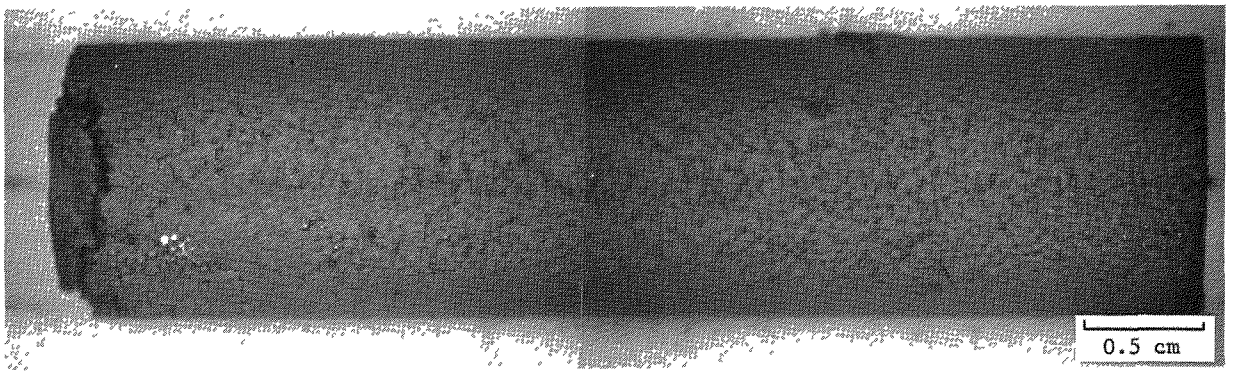

S7519 (17-18)

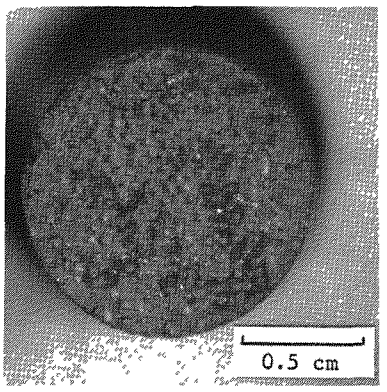

S7519-14

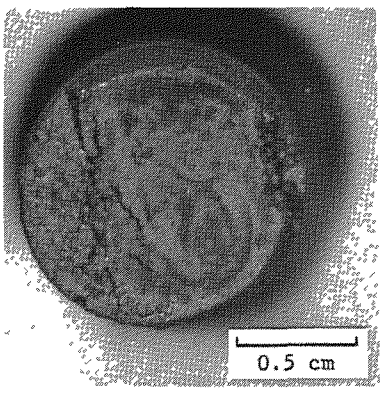

S7519-13

Fig. 9-14. Visual examination of fuel rod 2-3-7 from FTE-6

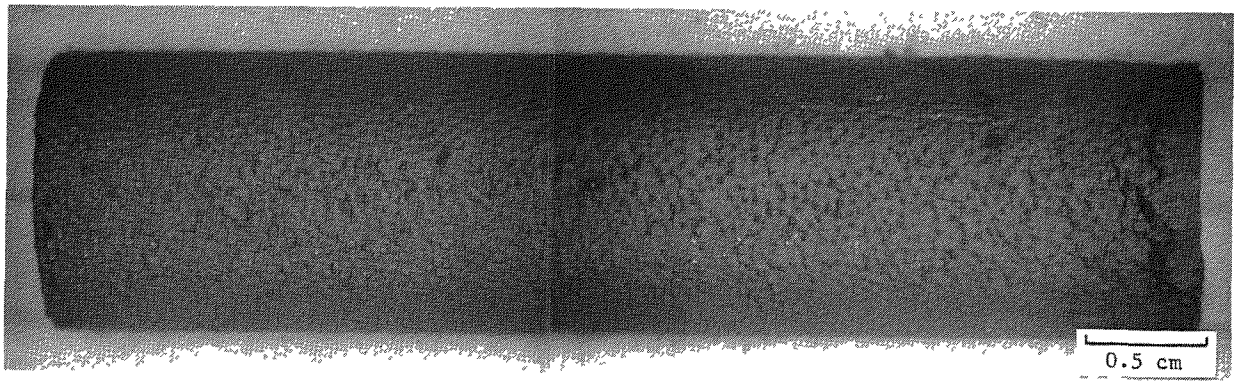

S7519 (21-22)

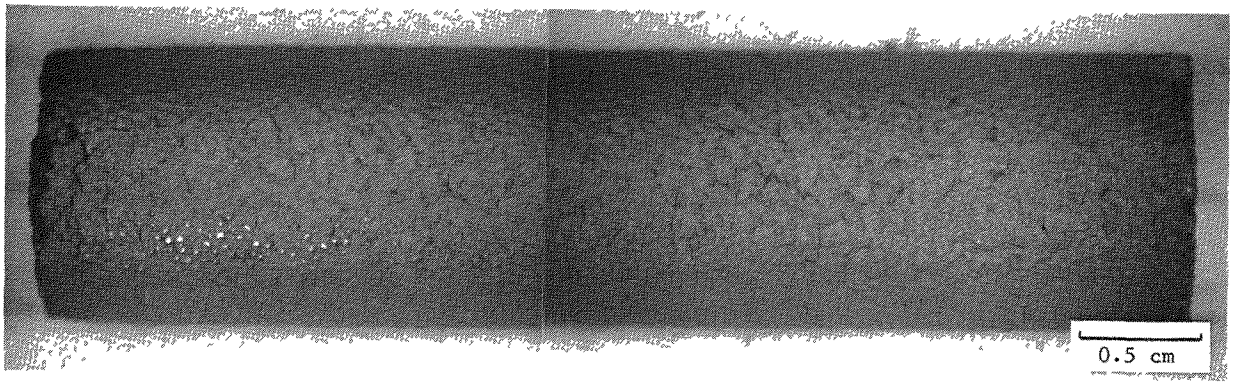

S7519 (23-24)

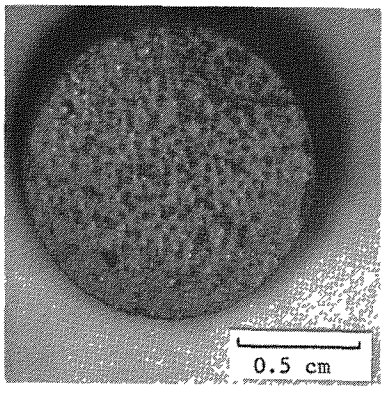

S7519-19

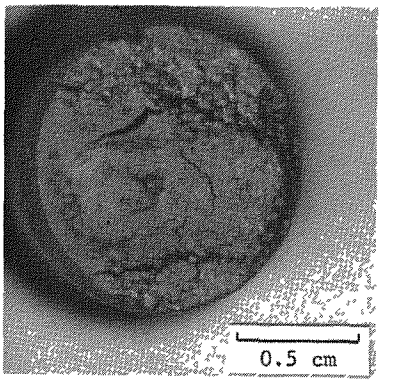

S7519-20B

Fig. 9-15. Visual examination of fuel rod 2-4-7 from FTE-6

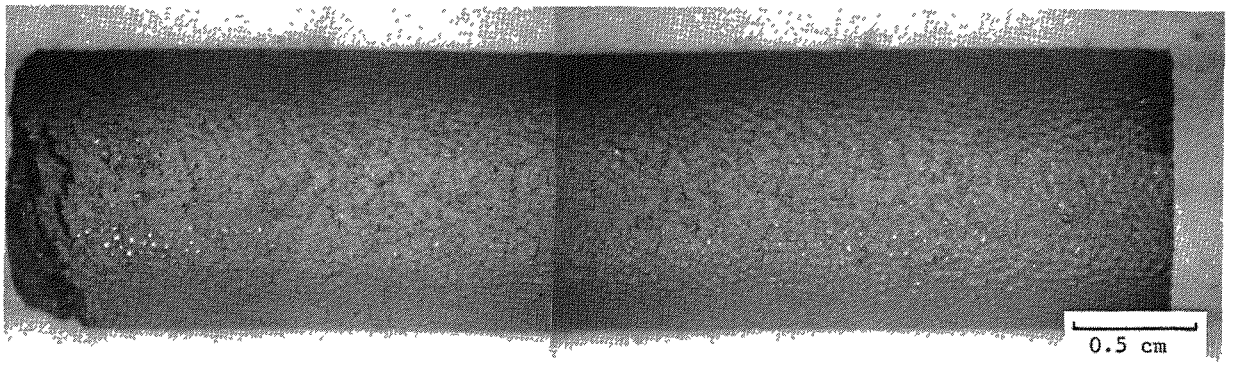

S7519 (27-28)

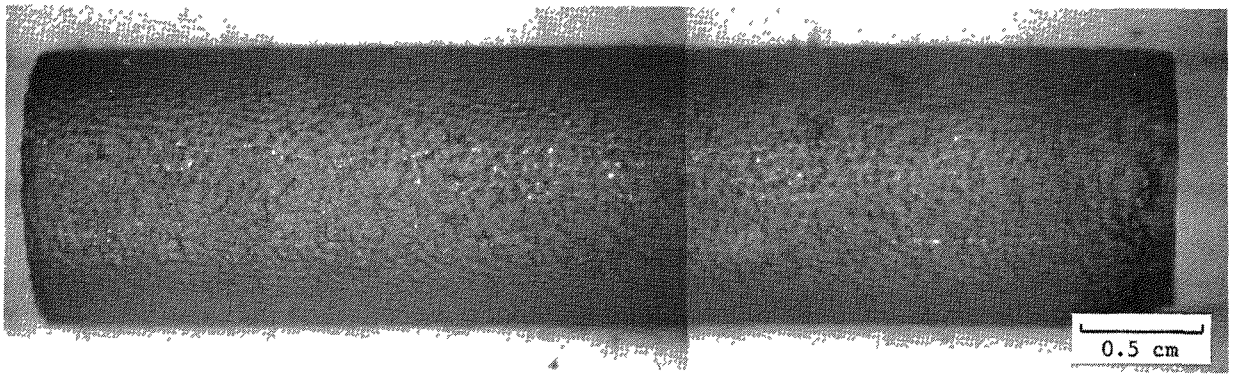

S7519 (29-30)

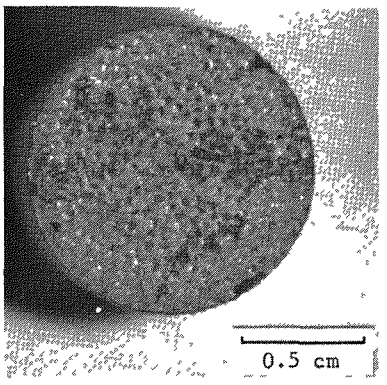

S7519-26

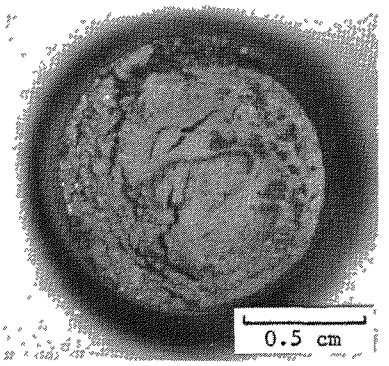

S7519-25

Fig. 9-16. Visual examination of fuel rod 2-5-7 from FTE-6

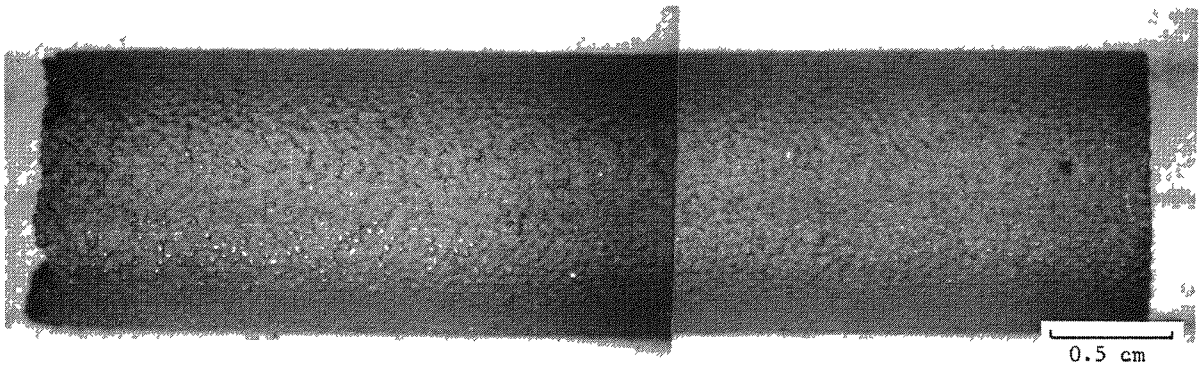

S7519 (33-34)

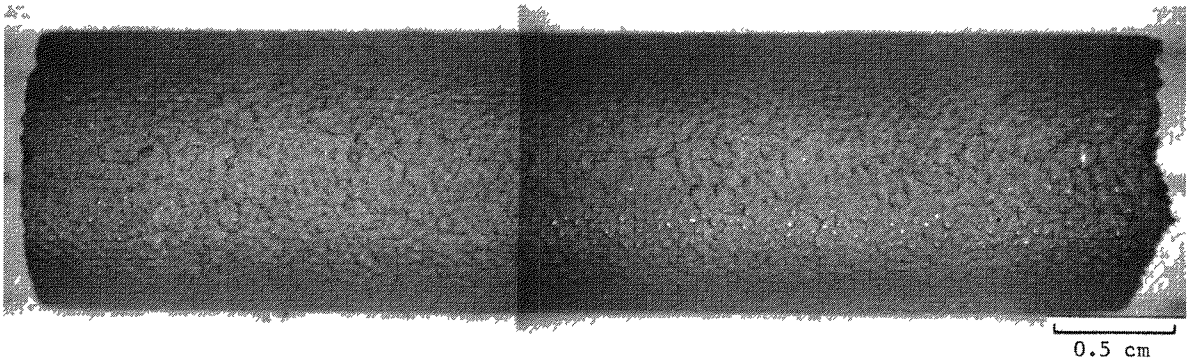

S7519 (35-36)

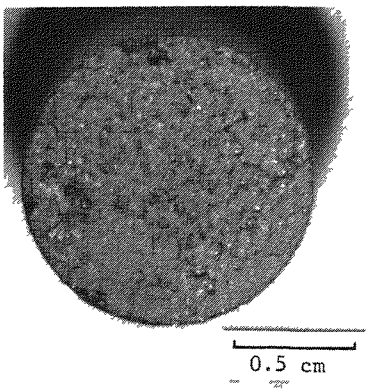

S7519-32

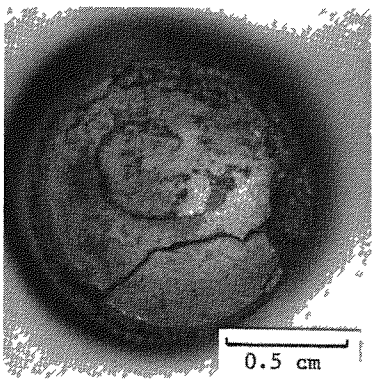

S7519-31

Fig. 9-17. Visual examination of fuel rod 2-6-7 from FTE-6

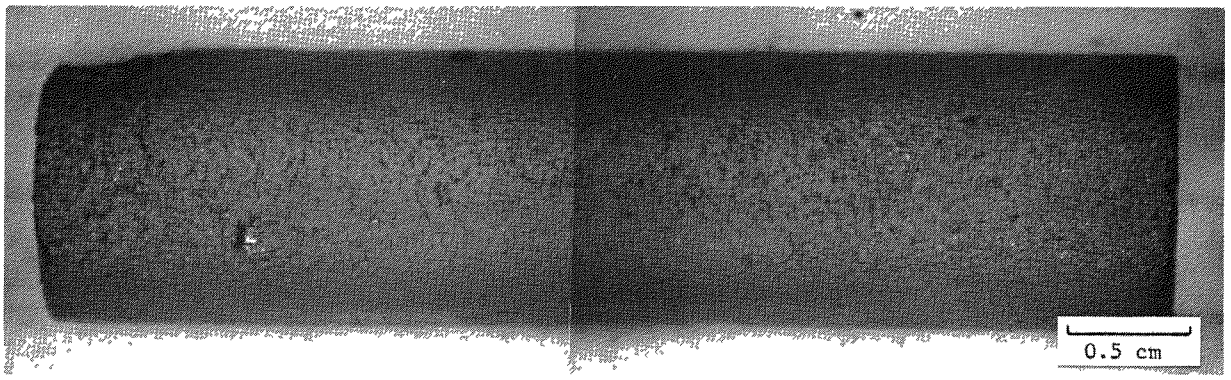

S7519 (45-46)

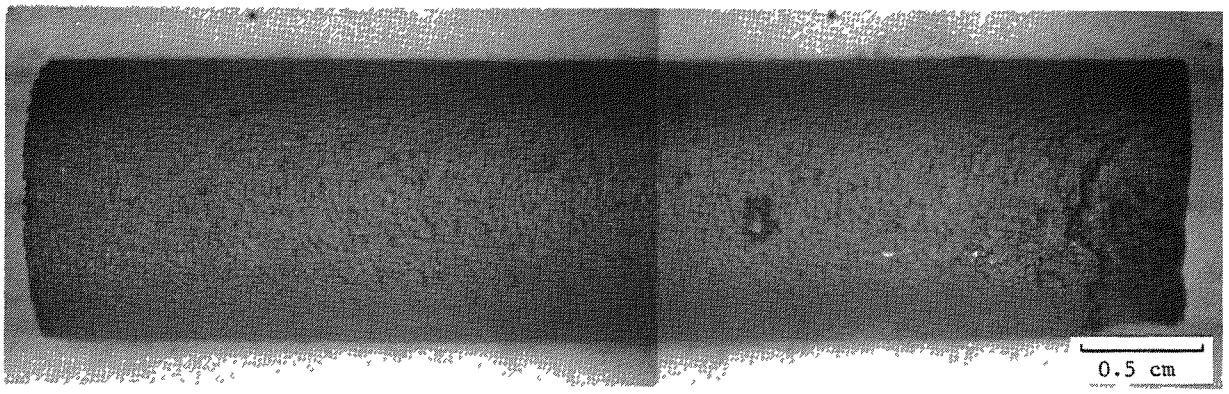

S7519 (47-48)

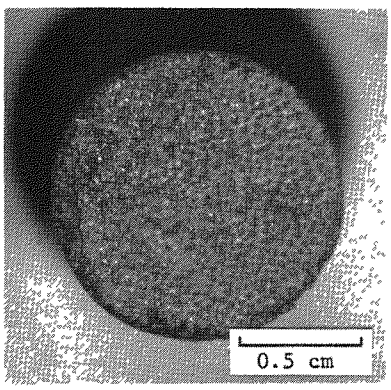

S7519-44

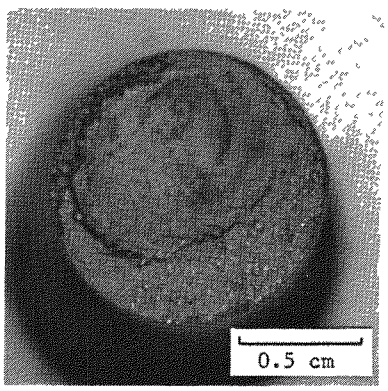

S7519-43

Fig. 9-18. Visual examination of fuel rod 2-7-8 from FTE-6

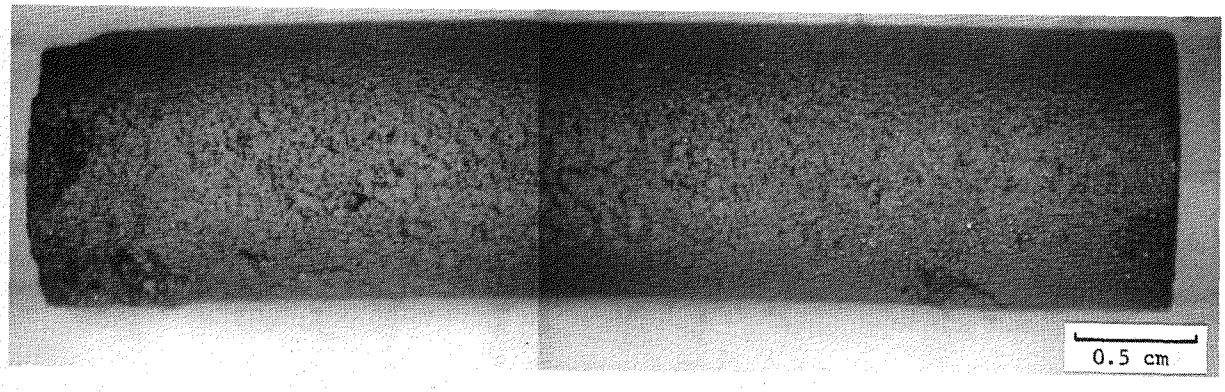

S7519 (39-40)

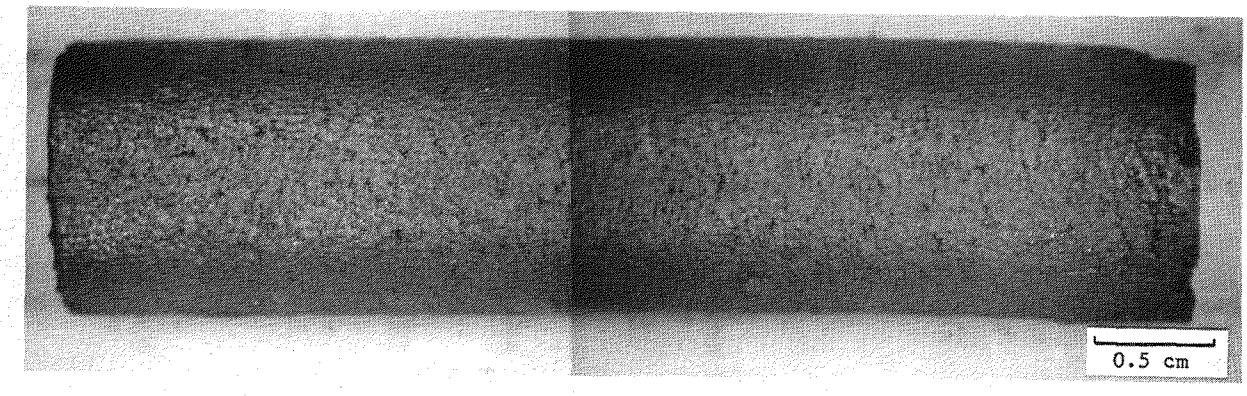

S7519 (41-42)

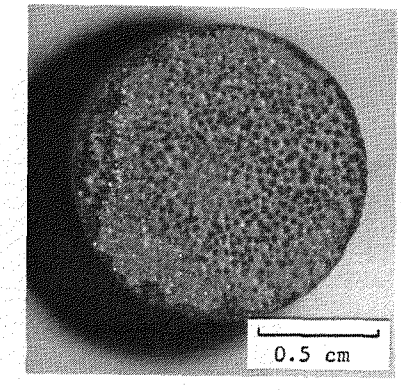

S7519-38

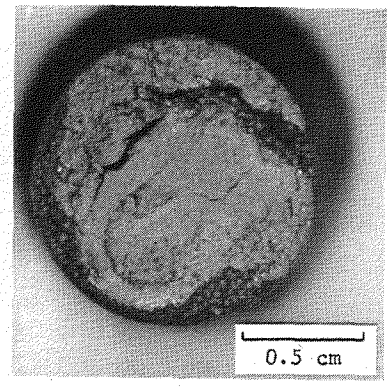

S7519-37

Fig. 9-19. Visual examination of fuel rod 2-8-7 from FTE-6

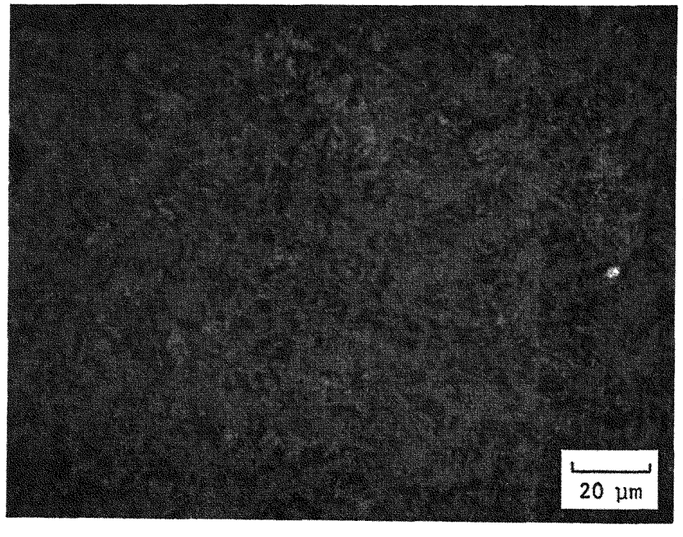

L7519-76 (a)

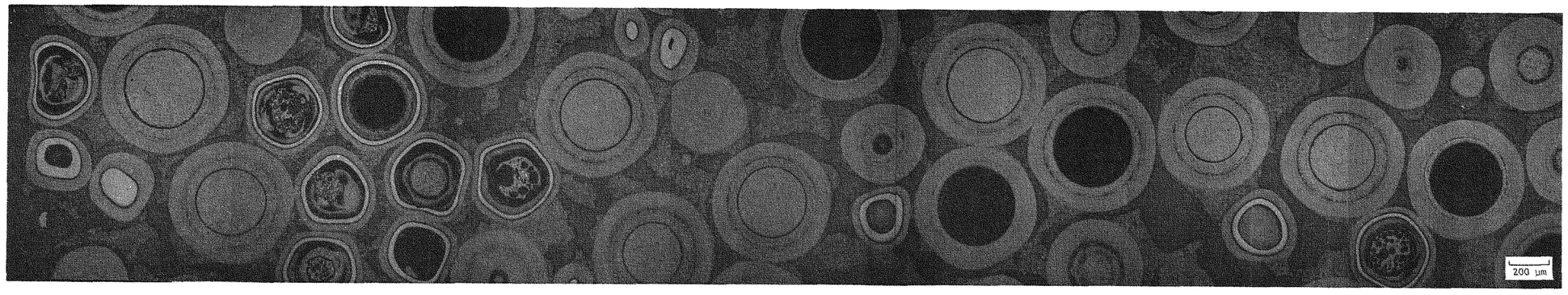

L7519 (68-74) (b)

Fig. 9-20. Photomicrographs of fuel rod 2-1-7 irradiated in FTE-6 to 2.84 x 10^{25} n/m^2 (E > 29 fJ)$_{HTGR}$ at 1250°C: (a) typical graphite matrix and (b) composite radial cross section

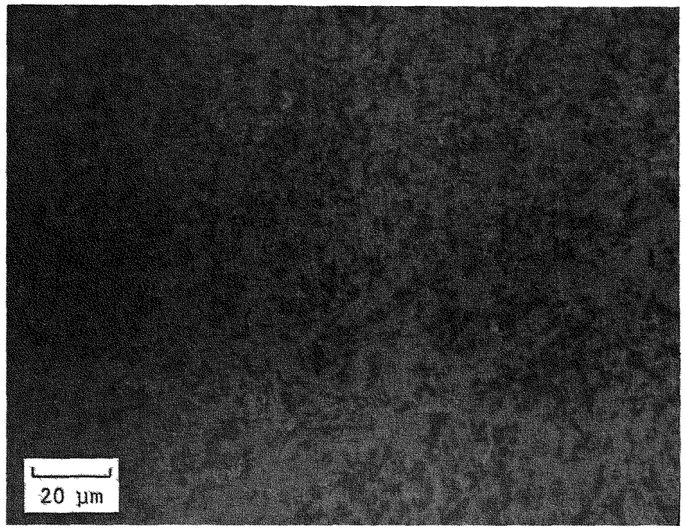

L7519-124 (a)

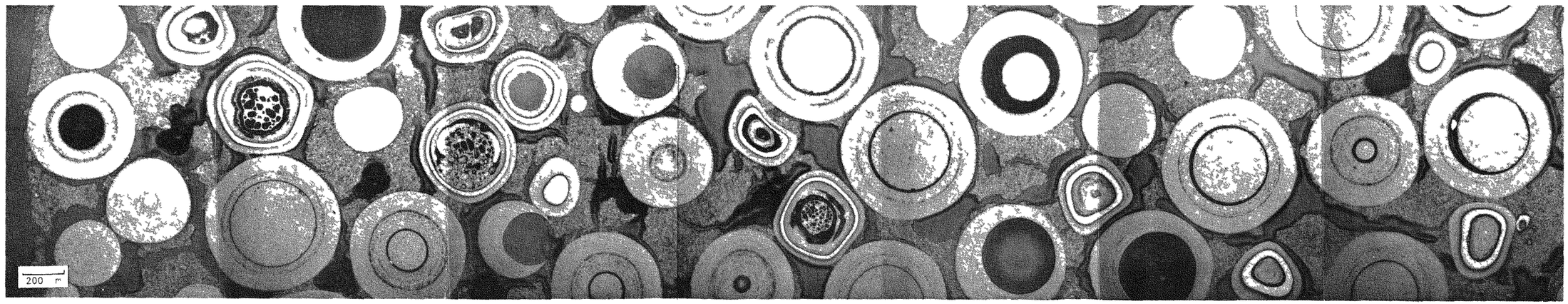

L7519 (147-153) (b)

Fig. 9-21. Photomicrographs of fuel rod 2-2-7 irradiated in FTE-6 to 2.84 x 10^{25} n/cm^2 (E > 29 fJ)$_{HTGR}$ at 1025°C; (a) typical graphite matrix and (b) composite HTGR radial cross section

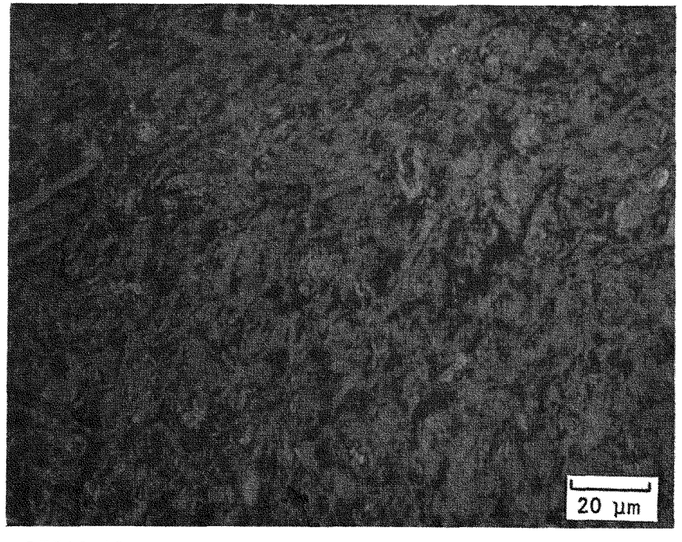

L7519-48 (a)

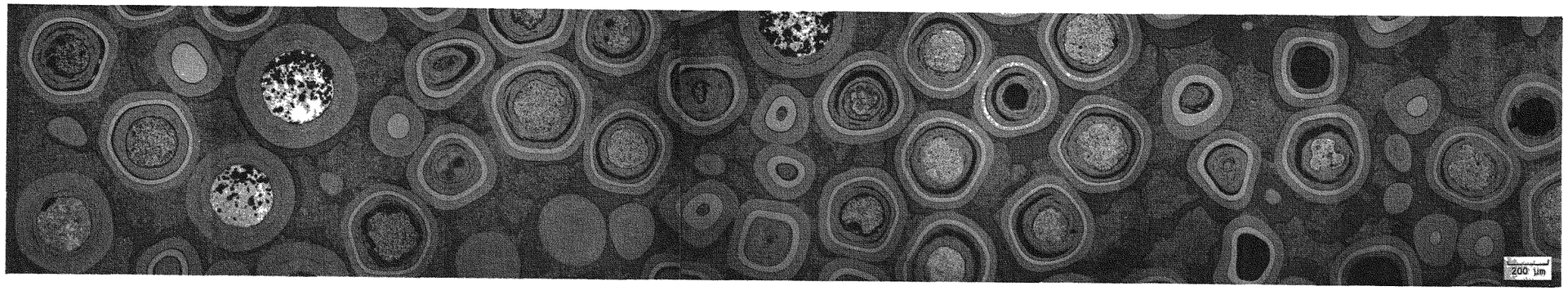

L7519 (40-46) (b)

Fig. 9-22. Photomicrographs of fuel rod 2-3-7 irradiated in FTE-6 to 2.84 x 10^{25} n/m^2 $(E > 29\ fJ)_{HTGR}$ at 1250°C: (a) typical graphite matrix and (b) composite radial cross section

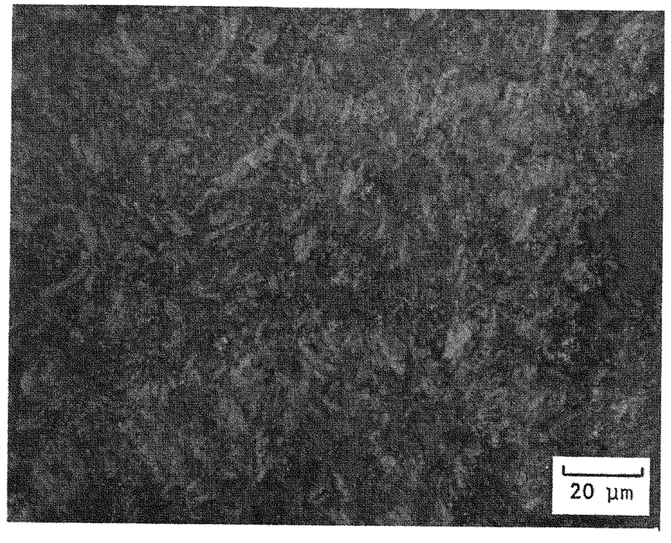

L7519-105 (a)

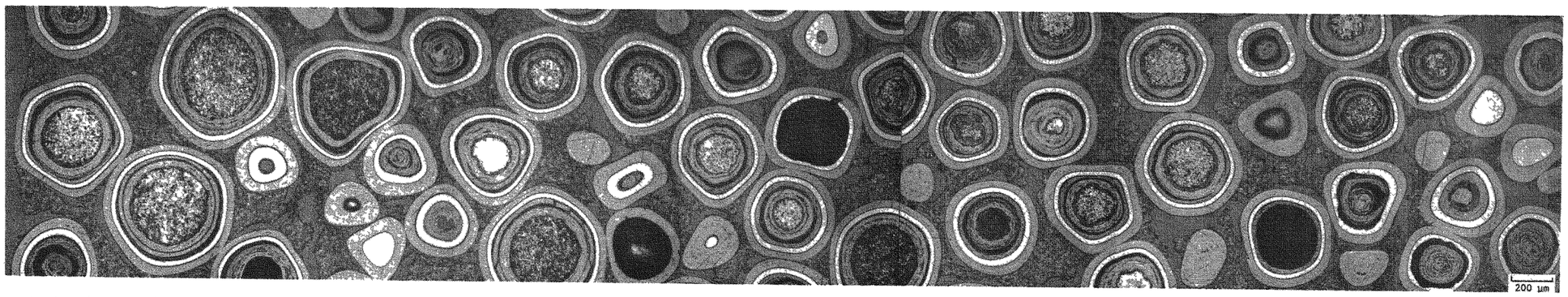

L7519 (97-103) (b)

Fig. 9-23. Photomicrographs of fuel rod 2-6-7 irradiated in FTE-6 to 2.84 x 10^{25} n/m^2 $(E > 29\ fJ)_{HTGR}$ at 1250°C: (a) typical graphite matrix and (b) composite radial cross section

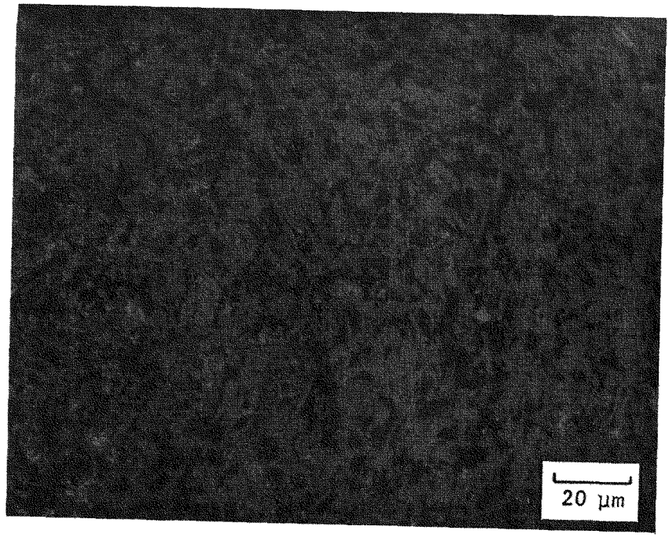

L7519-28 (a)

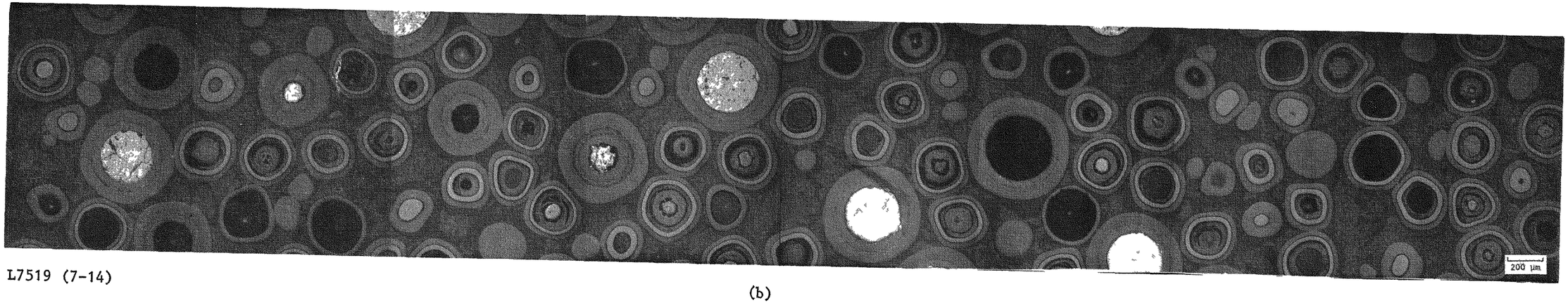

L7519 (7-14) (b)

Fig. 9-24. Photomicrographs of fuel rod 2-8-7 irradiated in FTE-6 to 2.84 x 10^{25} n/m^2 $(E > 29\ fJ)_{HTGR}$ at 1250°C: (a) typical graphite matrix and (b) composite radial cross section

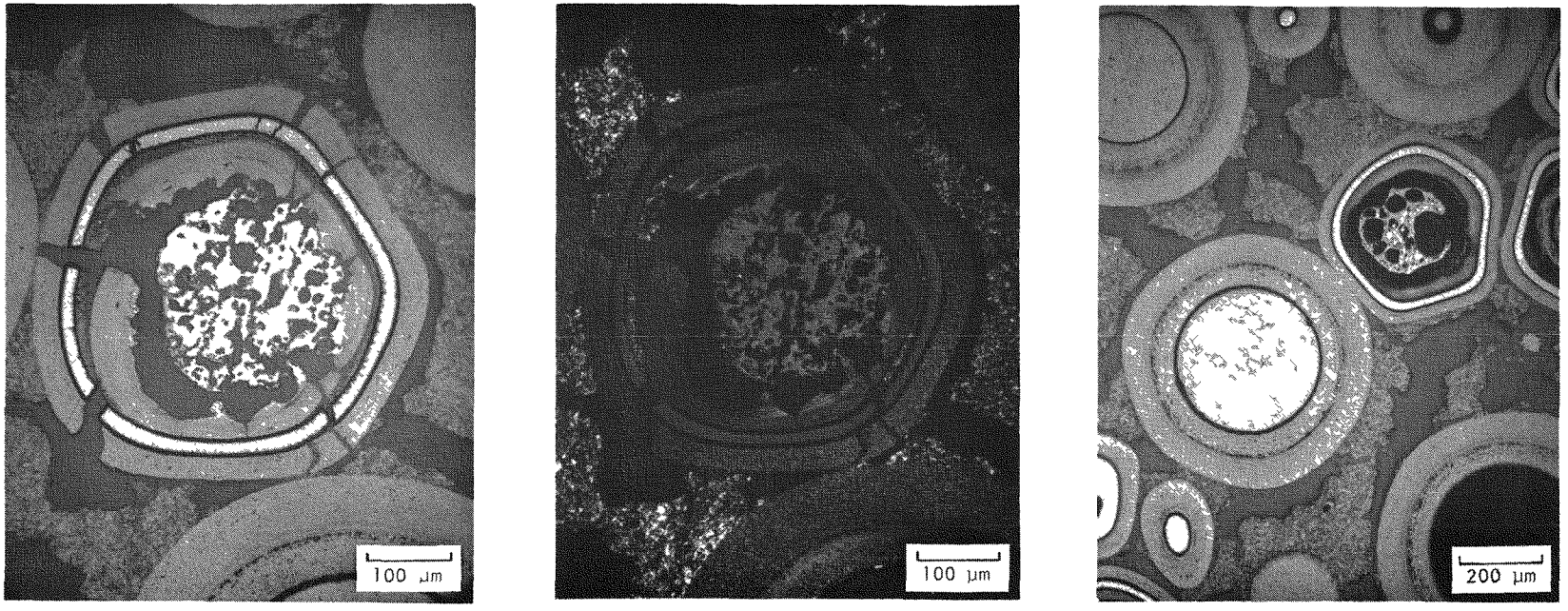

L7519-66 (a) L7519-67 (b) L7519-70 (c)

Fig. 9-25. Photomicrographs of representative fuel particles from fuel rod 2-1-7 irradiated in FTE-6 to 2.84×10^{25} n/m^2 (E > 29 fJ)$_{HTGR}$ at 1250°C: (a) bright field of UO_2 TRISO pressure vessel failure, (b) dark field of (a), (c) ThO_2 BISO - UO_2 TRISO pair

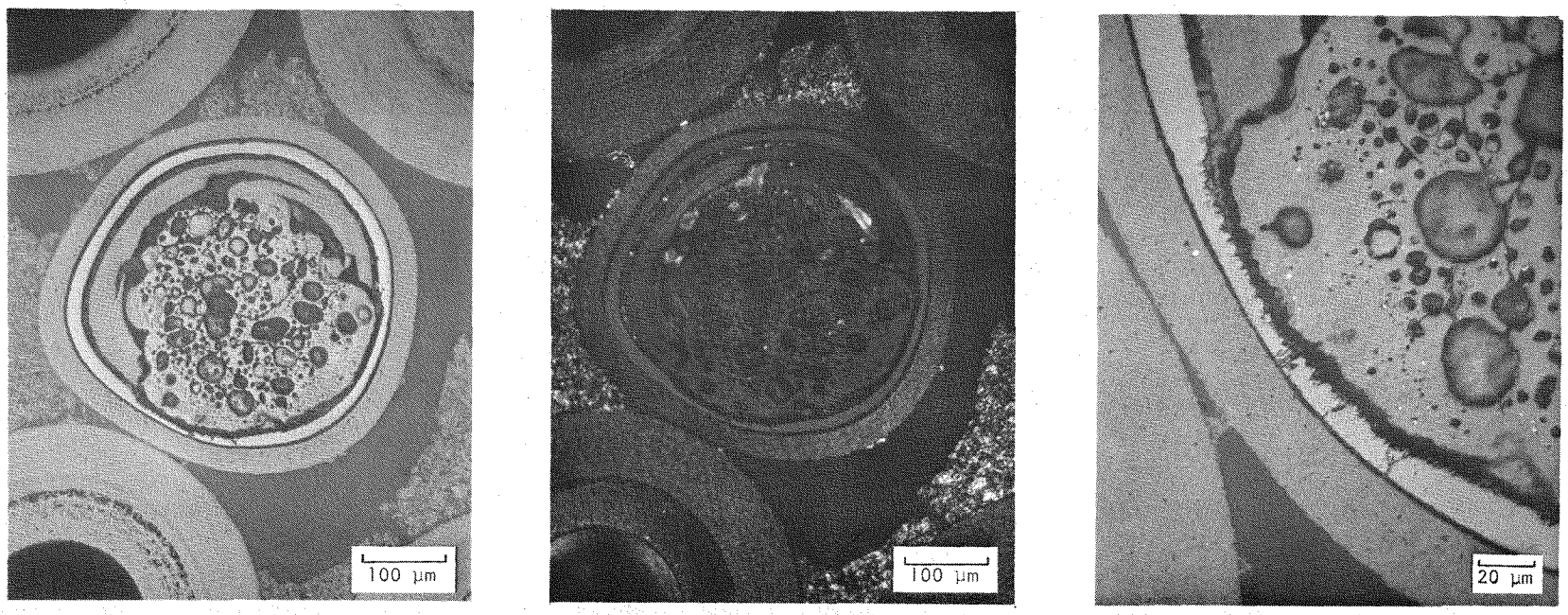

L7519-58 (a) L7519-59 (b) L7519-60 (c)

Fig. 9-26. Photomicrographs of UO_2 TRISO particle showing SiC attack from fuel rod 2-1-7 irradiated in FTE-6 to 2.84 x 10^{25} n/m^2 (E > 29 fJ)$_{HTGR}$ at 1250°C: (a) UO_2 TRISO particle with migrating kernel, (b) dark field of particle in (a), (c) magnification of kernel-SiC interface showing SiC attack

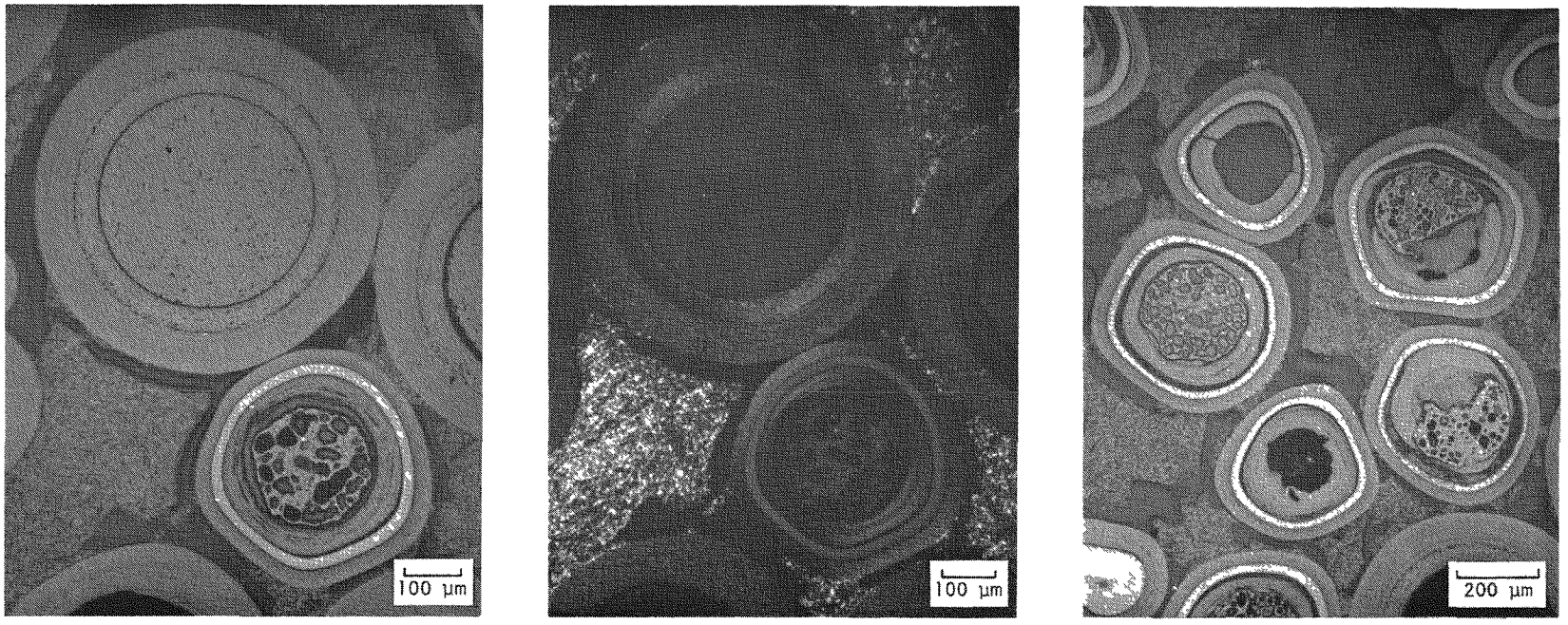

L7519-112 (a) L7519-113 (b) L7519-125 (c)

Fig. 9-27. Photomicrographs of representative fuel particles from fuel rod 2-2-7 irradiated in FTE-6 to 2.84×10^{25} n/m^2 (E > 29 fJ)$_{HTGR}$ at 1250°C: (a) bright field of UO_2 TRISO - ThO_2 BISO pair (b) dark field of (a), (c) randomly migrating UO_2 kernels

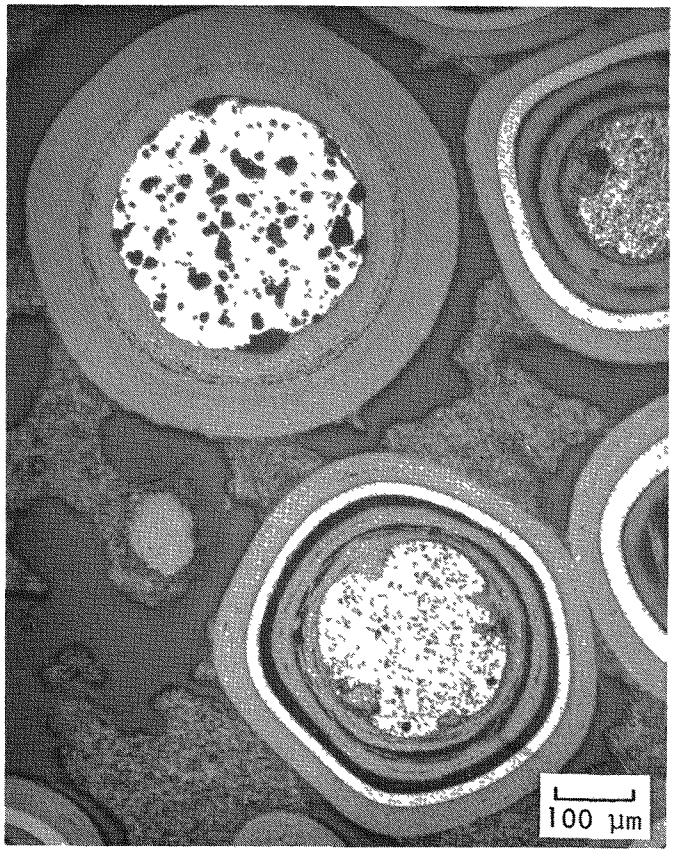

L7519-29 (a)

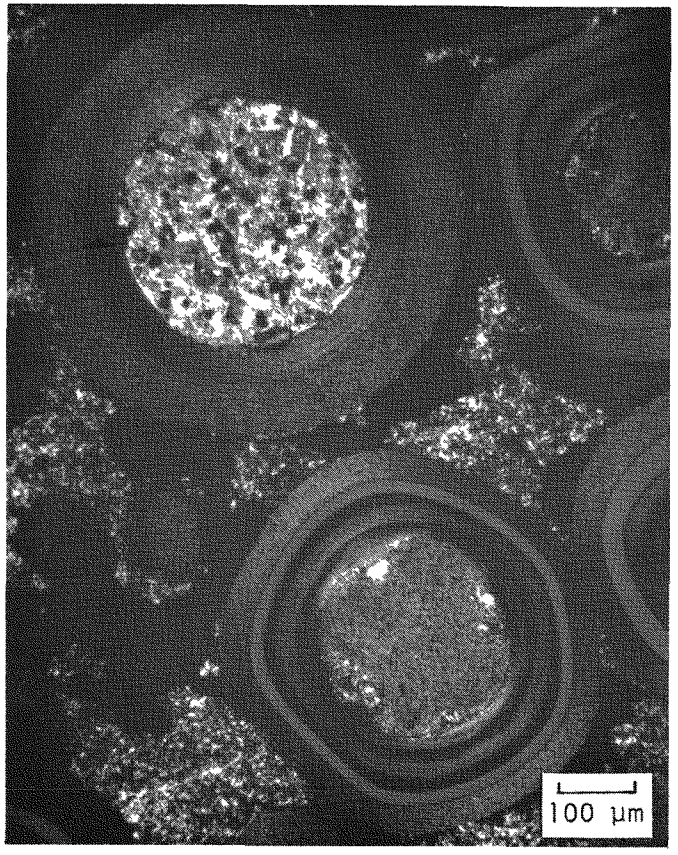

L7519-30 (b)

Fig. 9-28. Photomicrographs of representative fuel particles from fuel rod 2-3-7 irradiated in FTE-6 to 2.84×10^{25} n/m^2 (E > 29 fJ)$_{HTGR}$ at 1250°C: (a) bright field of (Th,U)C_2 TRISO - ThC_2 BISO pair, (b) dark field of (a)

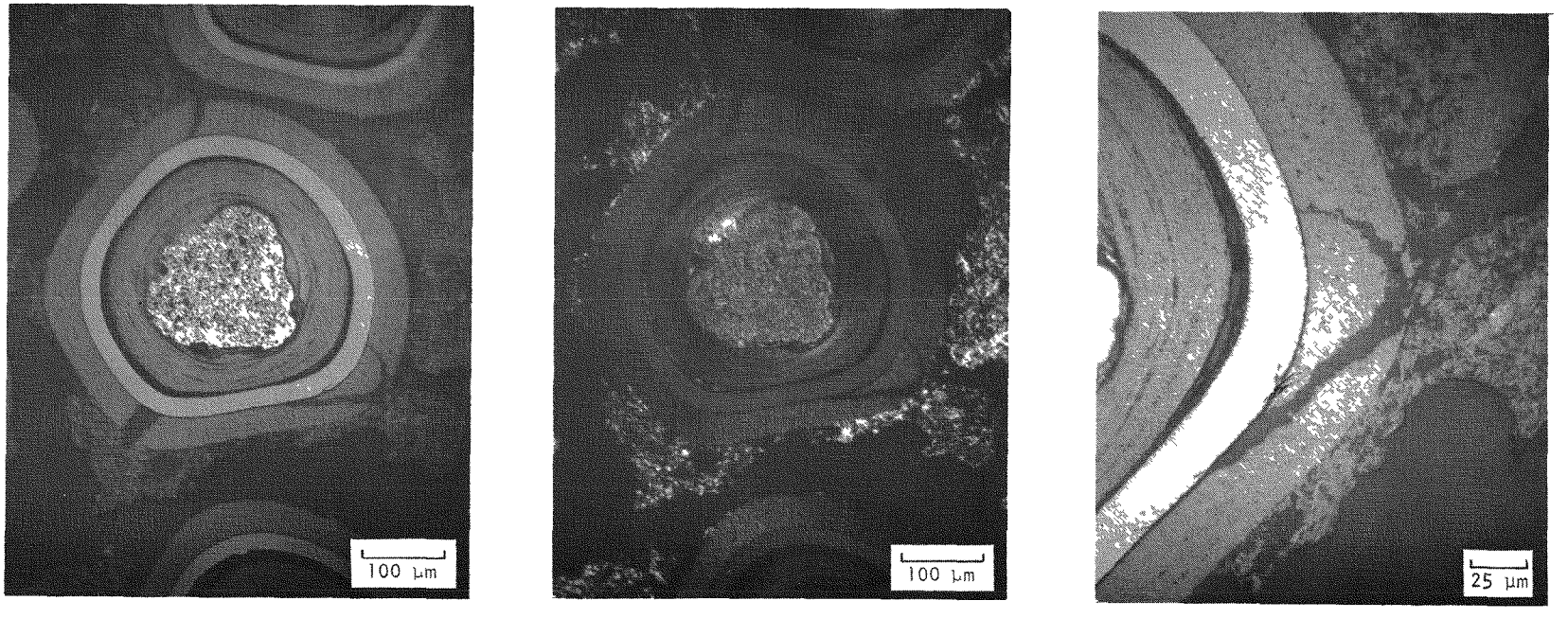

L7519-33 (a) L7519-34 (b) L7519-35 (c)

Fig. 9-29. Photomicrographs of $(Th,U)C_2$ TRISO particle from fuel rod 2-3-7 from FTE-6 showing matrix-particle interaction: (a) light field, (b) dark field, (c) high-magnification interaction area

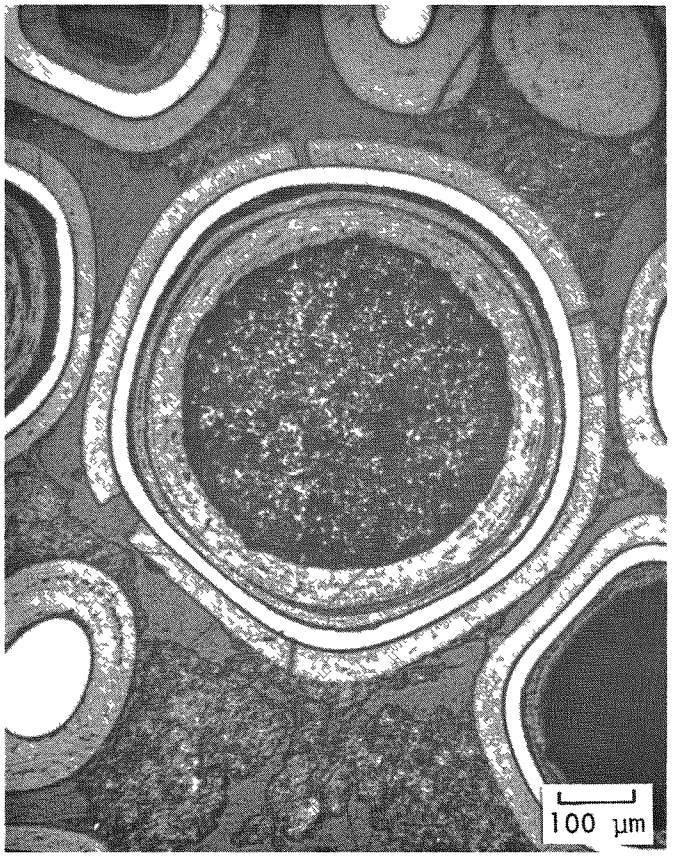

L7519-95 (a)

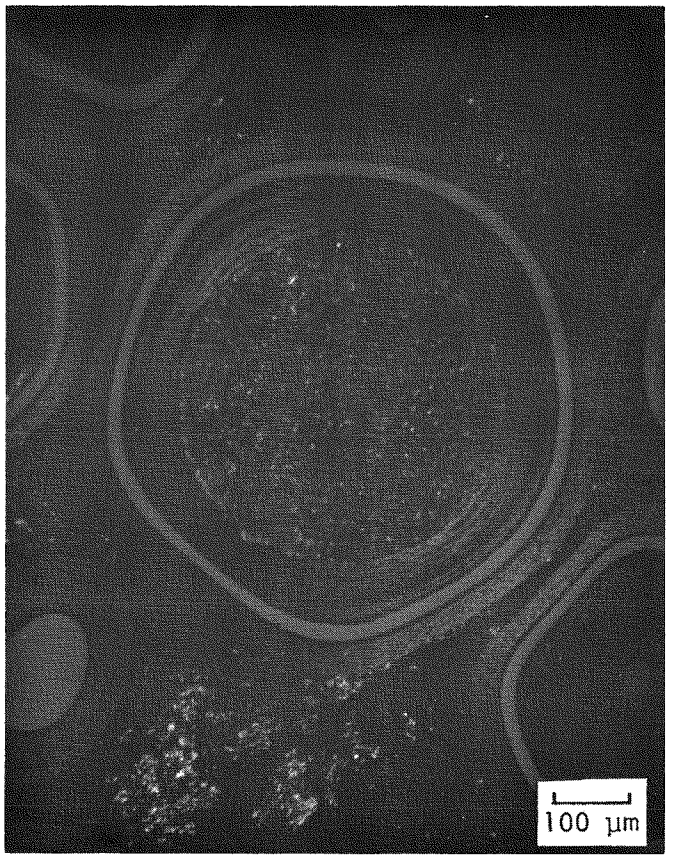

L7519-96 (b)

Fig. 9-30. Photomicrographs of ThC_2 TRISO particle in fuel rod 2-6-7 from FTE-6 with OPyC failure: (a) bright field - kernel hydrolyzed during the examination, (b) dark field

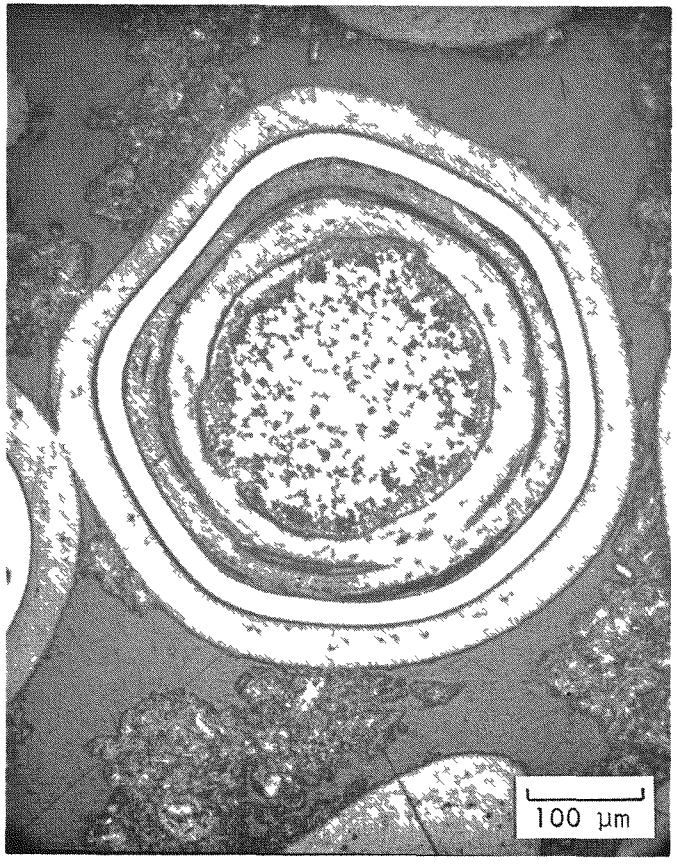

L7519-92 (a)

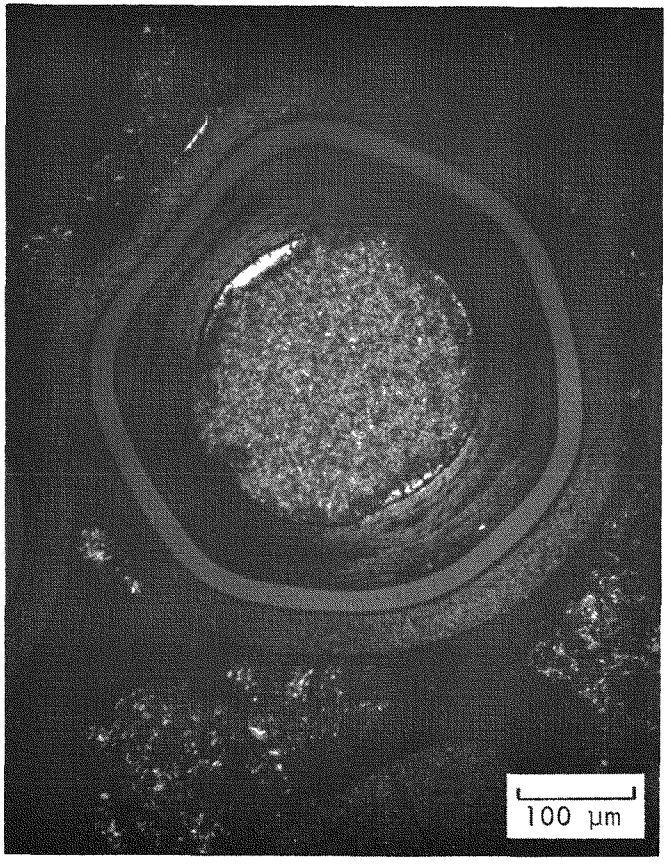

L7519-92A (b)

Fig. 9-31. Photomicrograph of representative fissile $(Th,U)C_2$ particle from fuel rod 2-6-7 irradiated in FTE-6 to 2.84 x 10^{25} n/m^2 $(E > 29\ fJ)_{HTGR}$ at 1250°C: (a) bright field, (b) dark field

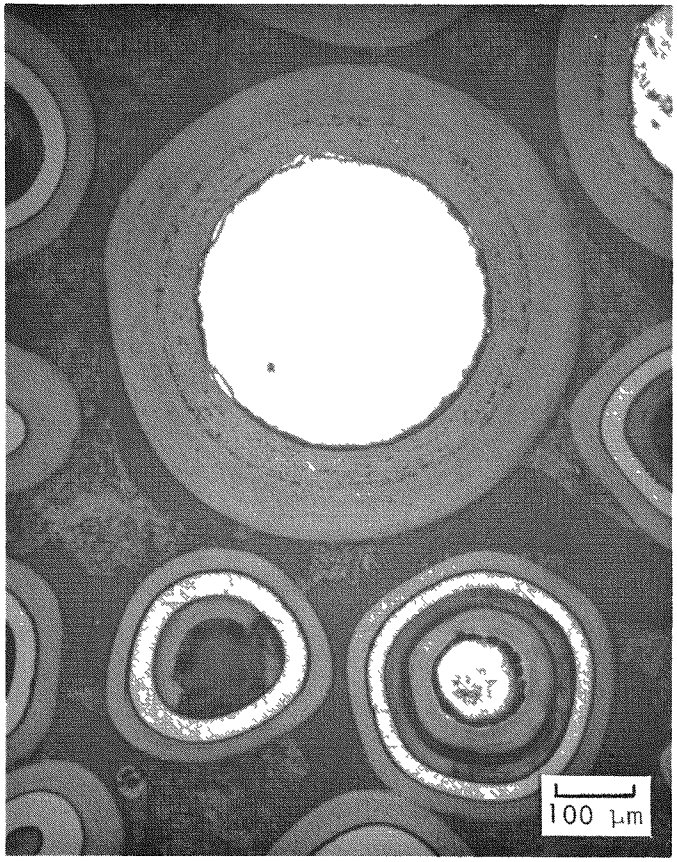

L7519-17 (a)

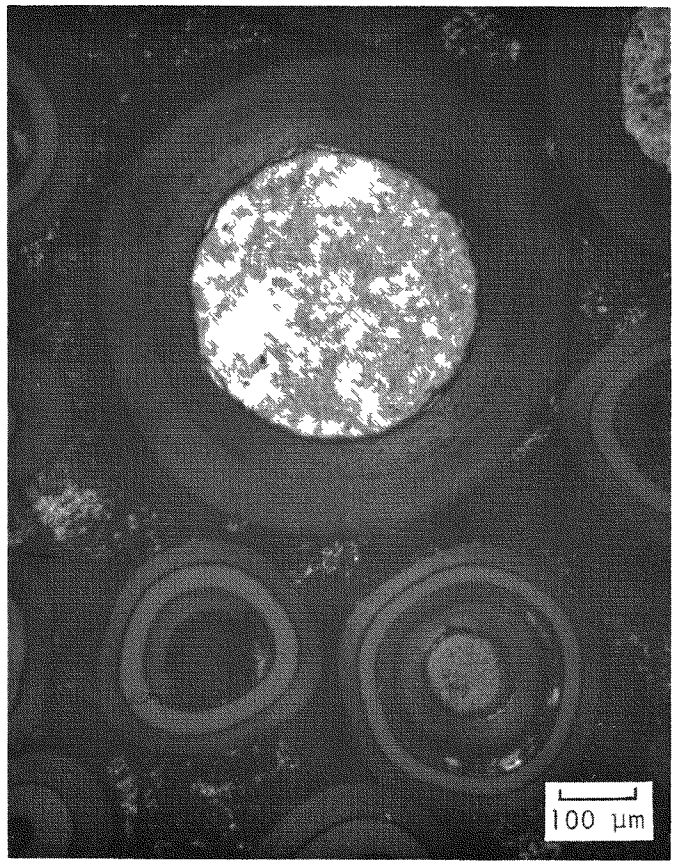

L7519-18 (b)

Fig. 9-32. Photomicrographs of representative fuel particles from fuel rod 2-8-7 irradiated in FTE-6 to 2.84×10^{25} n/m^2 (E > 29 fJ)$_{HTGR}$ at 1250°C: (a) bright field of UC_2 TRISO - ThC_2 BISO pair, (b) dark field of (a)

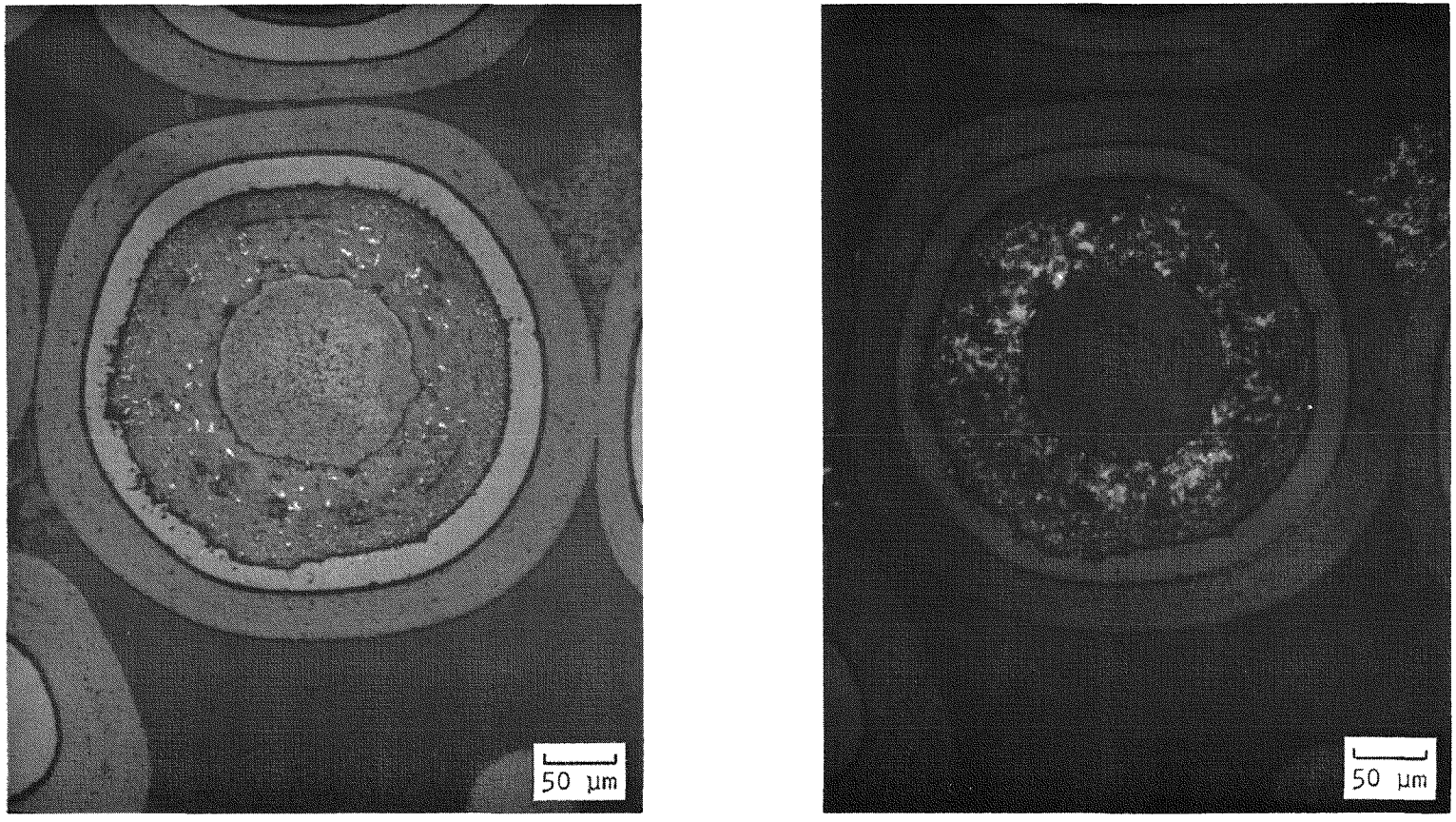

L7519-5 (a) L7519-6 (b)

Fig. 9-33. Photomicrographs of UC_2 TRISO particle from fuel rod 2-8-7 of FTE-6 showing apparent contamination attack: (a) bright field, (b) dark field

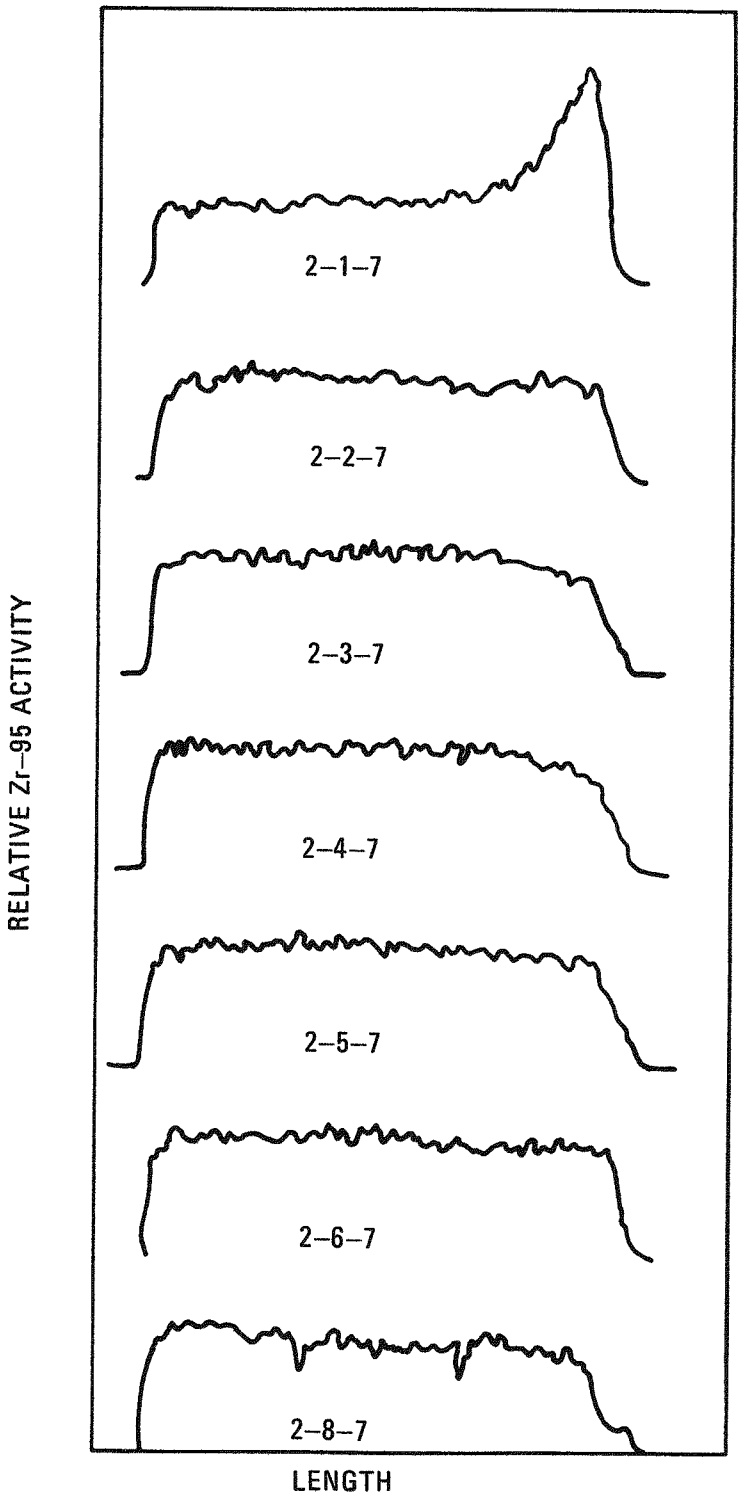

Fig. 9-34. Single-channel gamma scans of fuel rods used in fuel examination

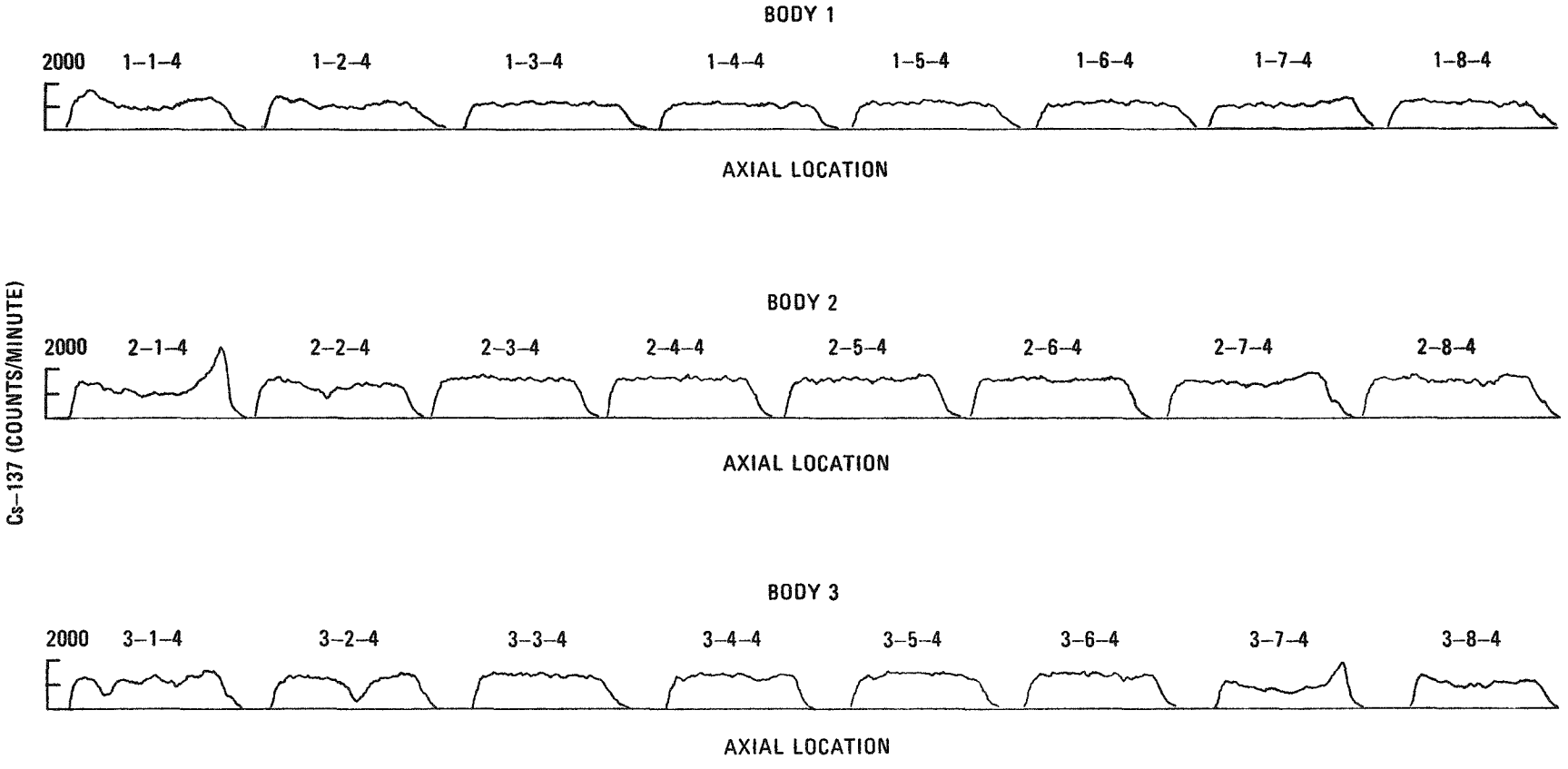

Fig. 9-35. FTE-6 single-channel gamma scan comparison of fuel rods

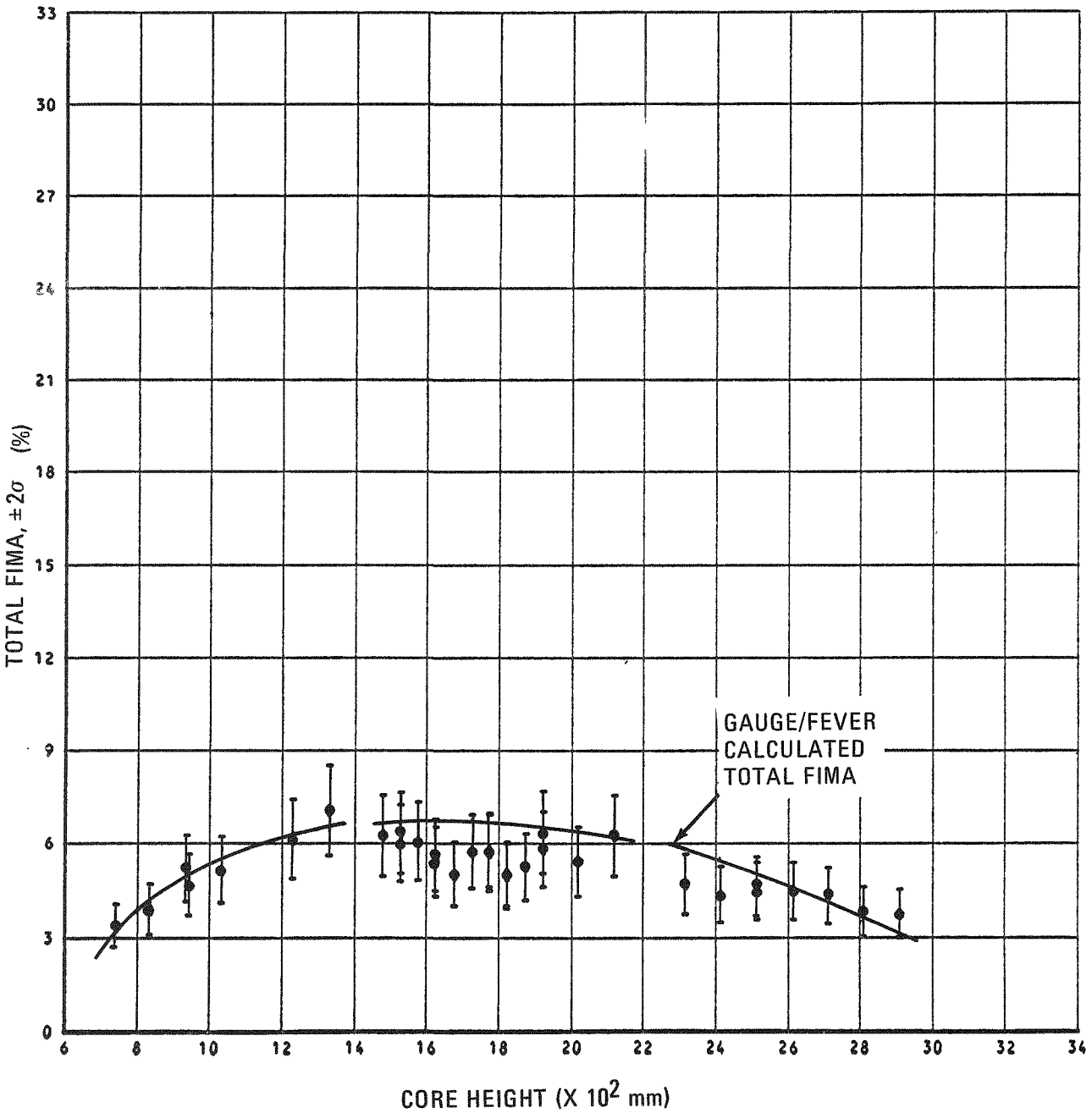

Fig. 9-36. Total FIMA in fuel stacks 1 and 2 measured by gamma spectroscopy

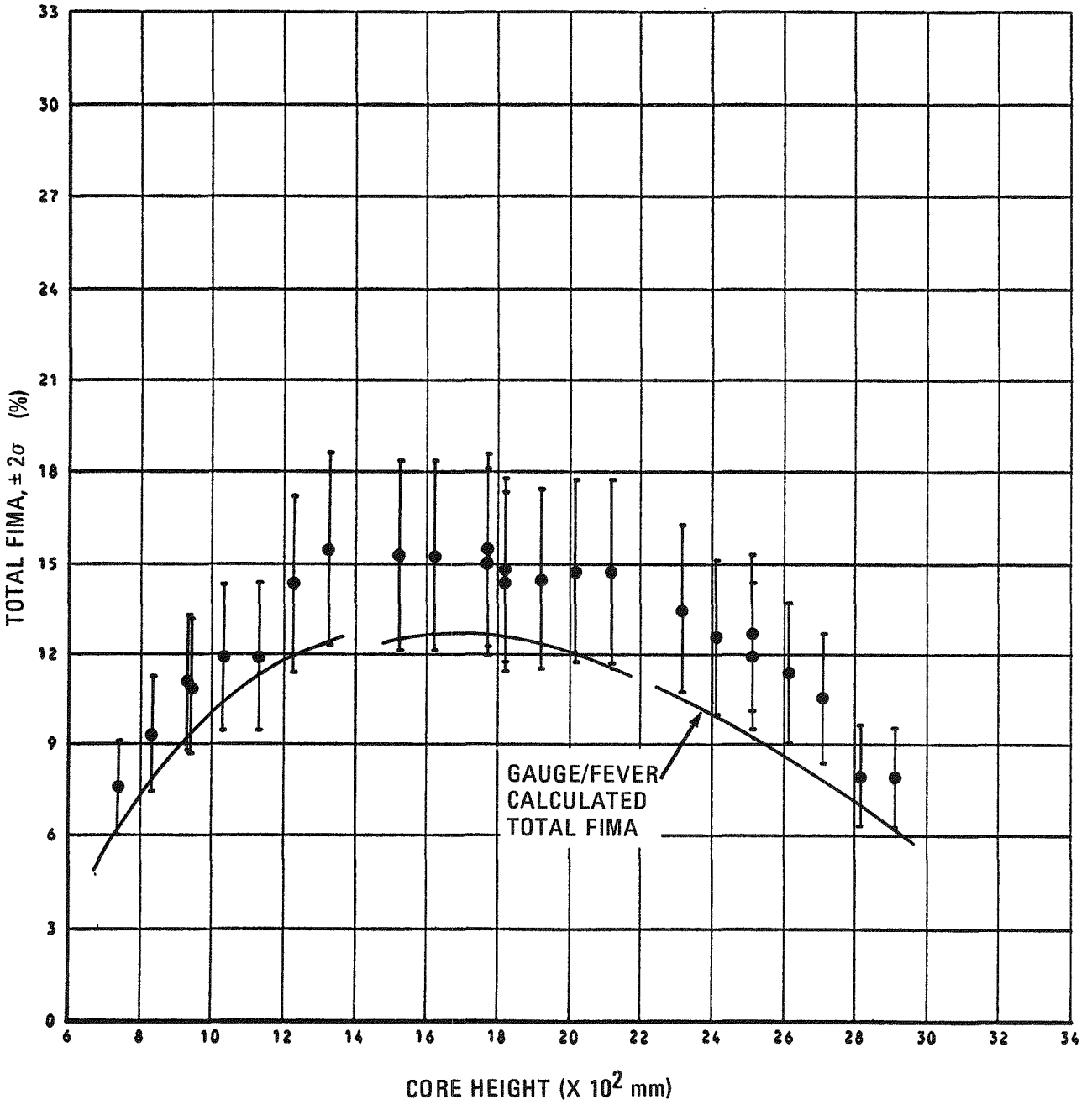

Fig. 9-37. Total FIMA in fuel stacks 3 and 4 measured by gamma spectroscopy

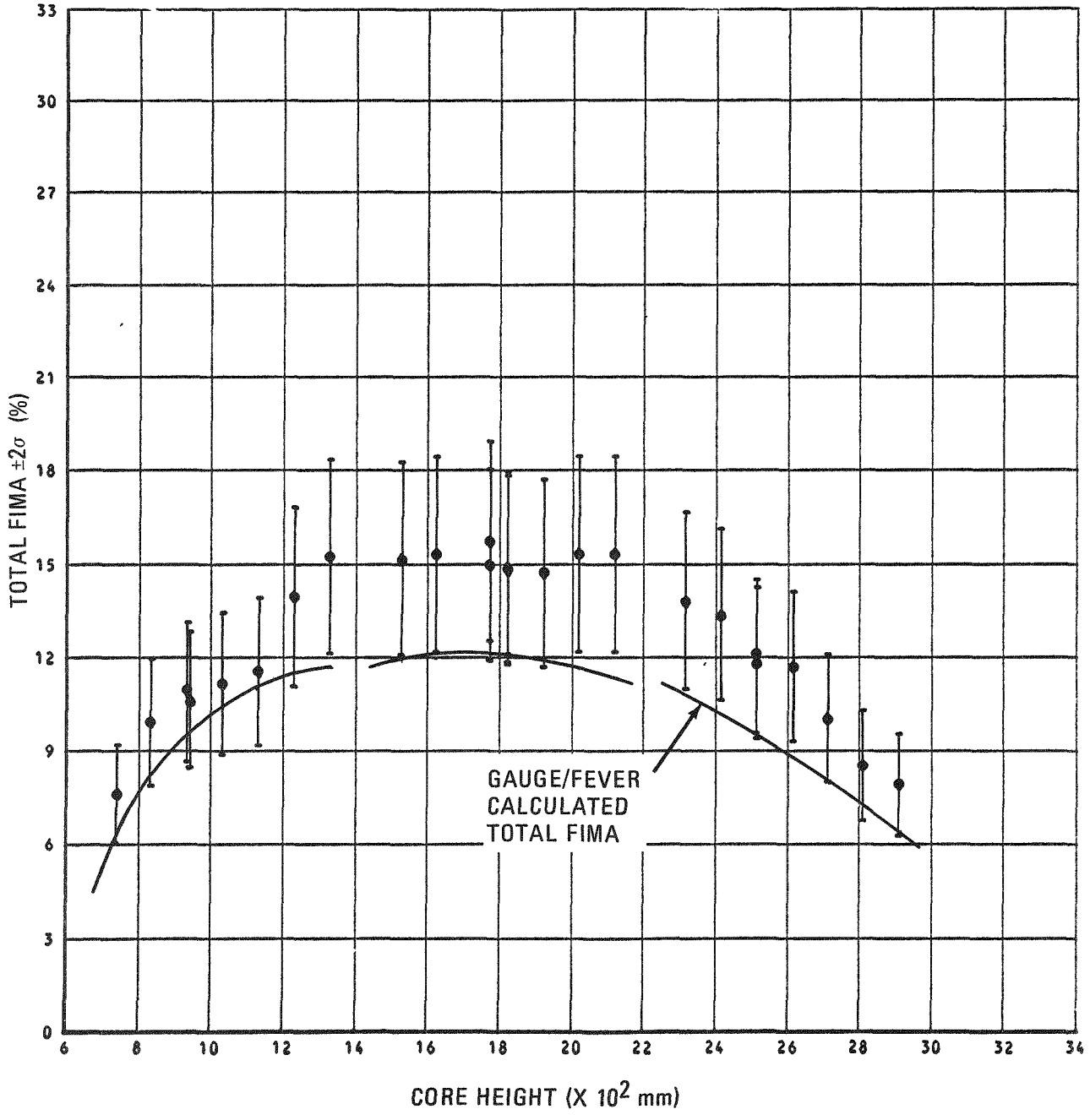

Fig. 9-38. Total FIMA in fuel stacks 5 and 6 measured by gamma spectroscopy

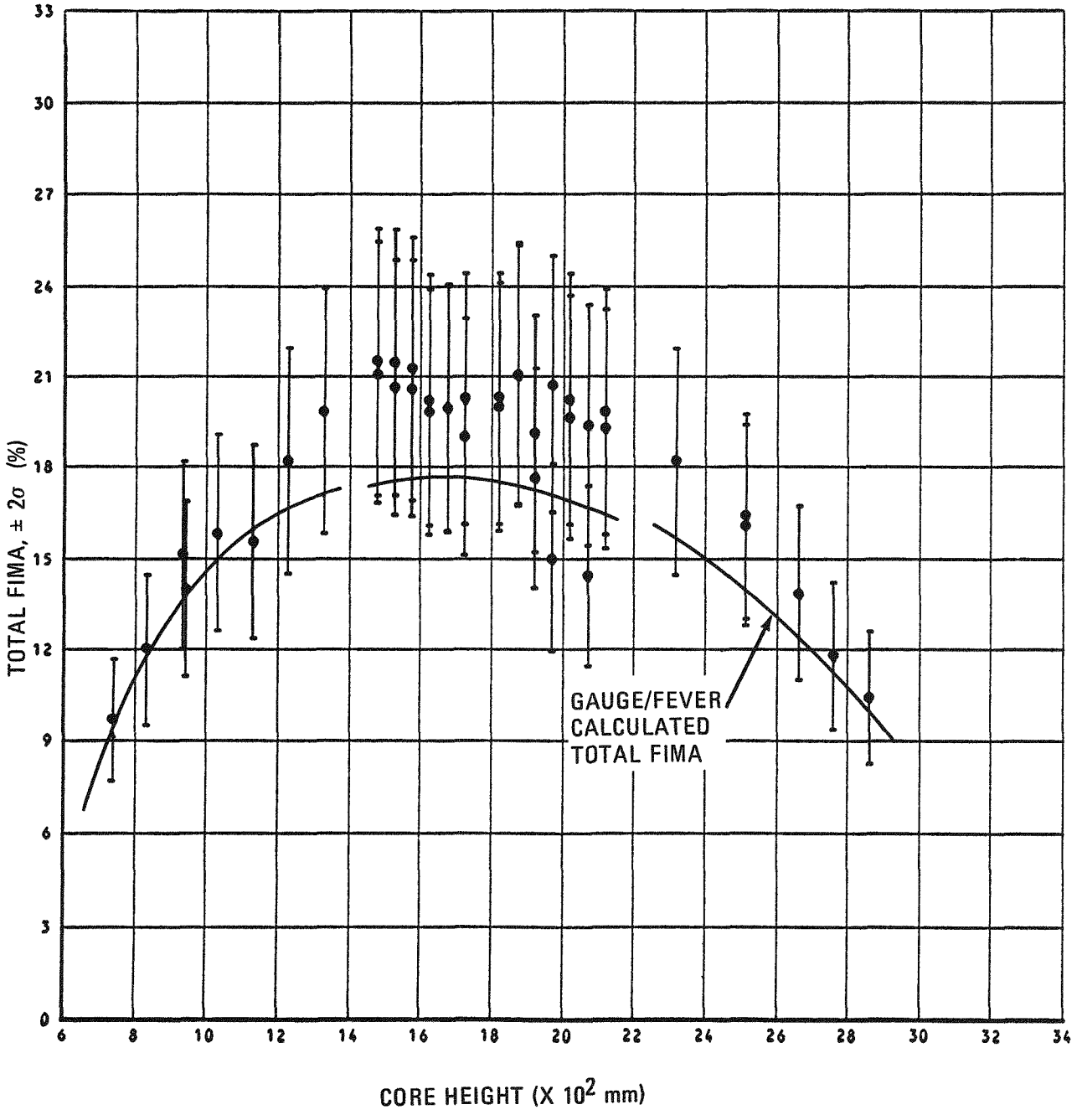

Fig. 9-39. Total FIMA in fuel stacks 7 and 8 measured by gamma spectroscopy

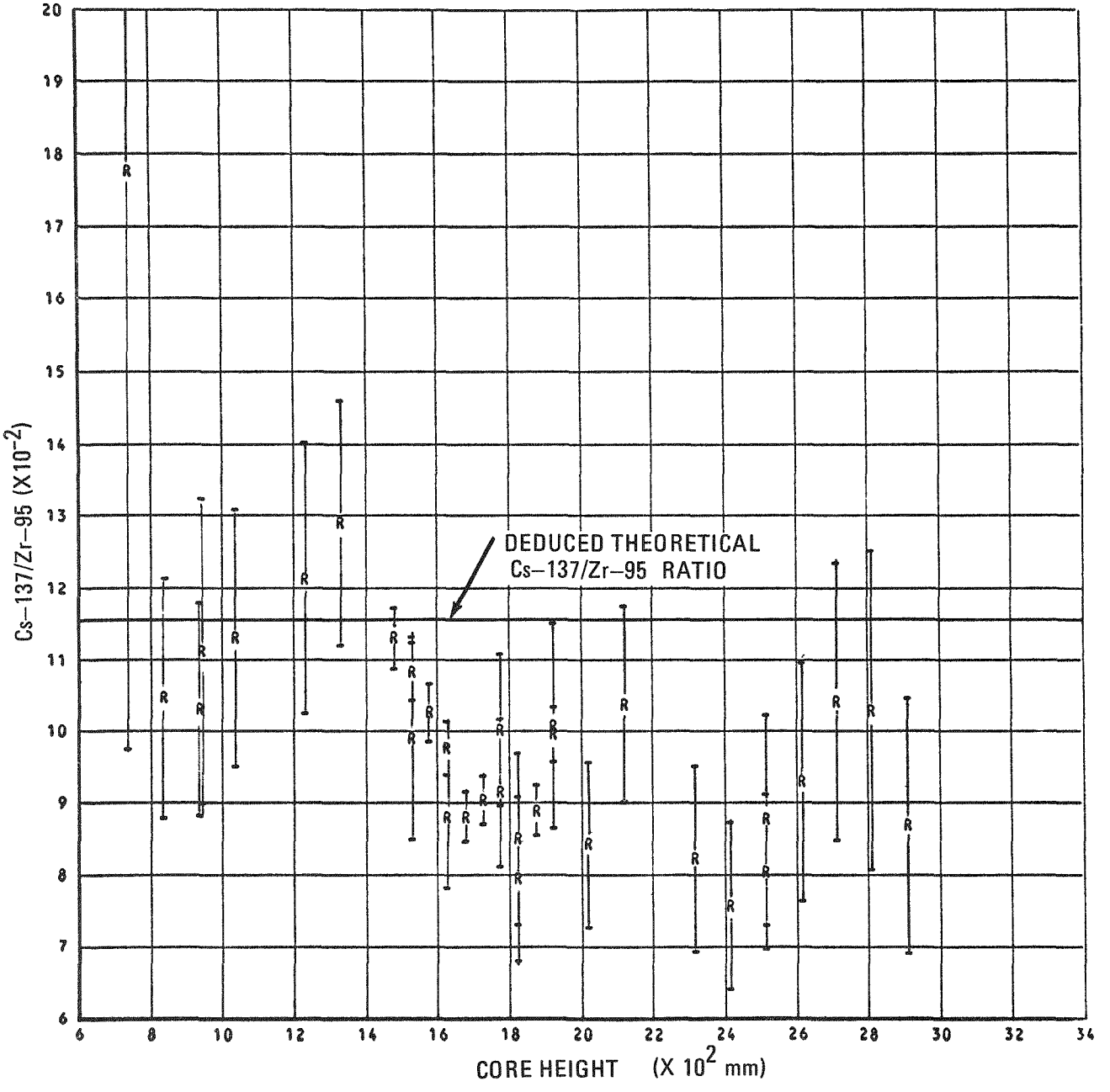

Fig. 9-40. Cs-137/Zr-95 ratio for fuel rods in stacks 1 and 2

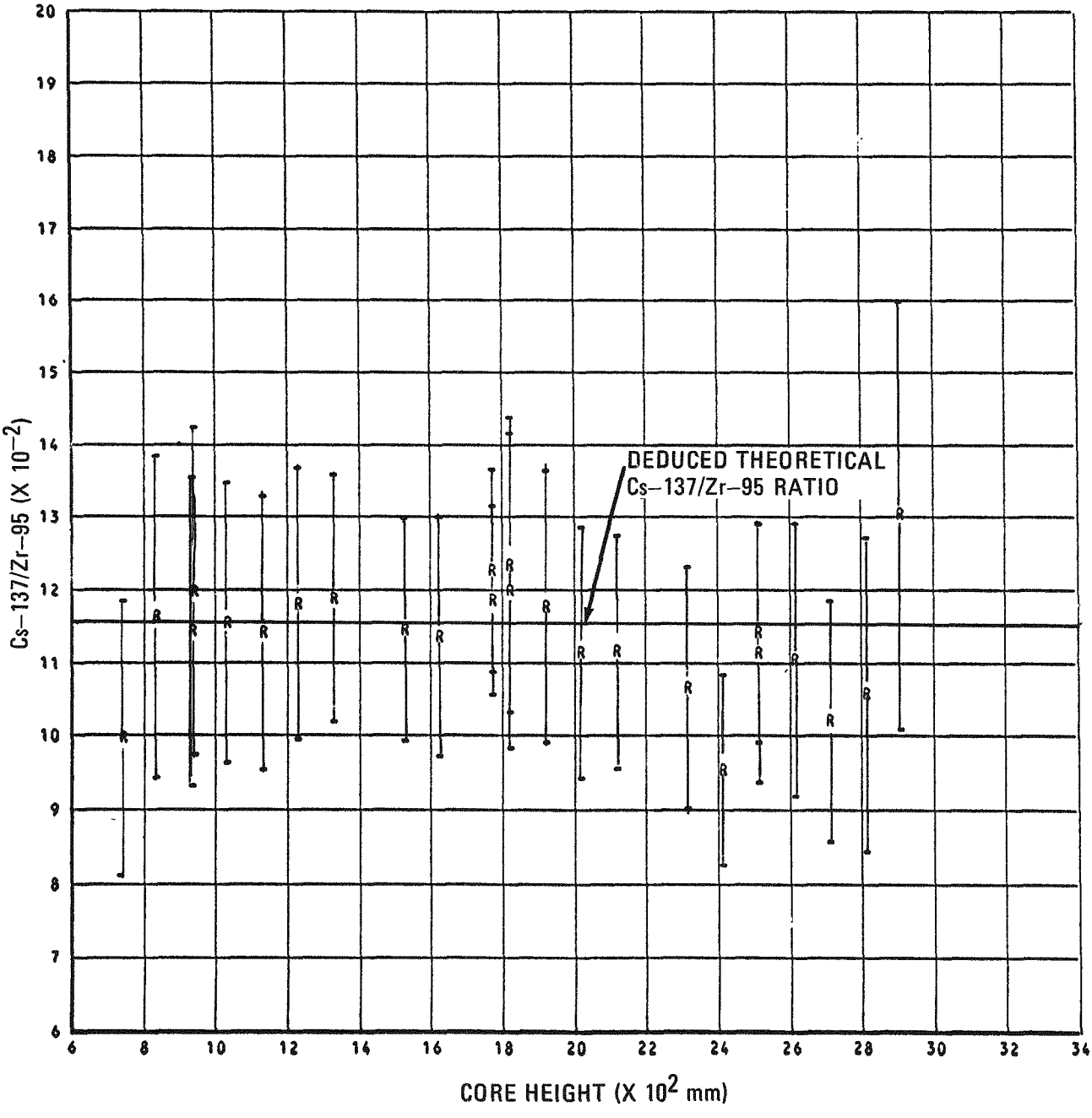

Fig. 9-41. Cs-137/Zr-95 ratio for fuel rods in stacks 3 and 4

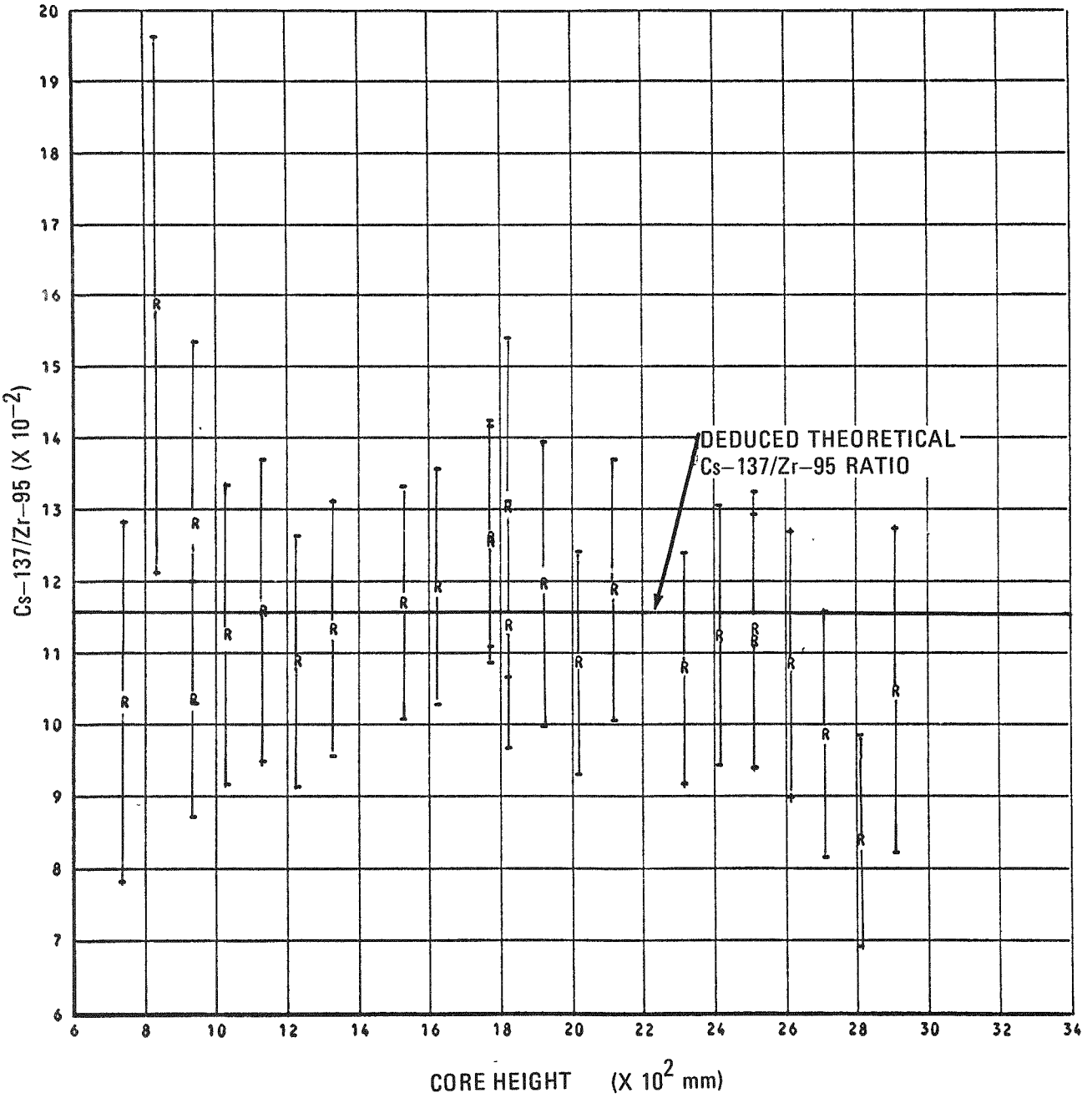

Fig. 9-42. Cs-137/Zr-95 ratio for fuel rods in stacks 5 and 6

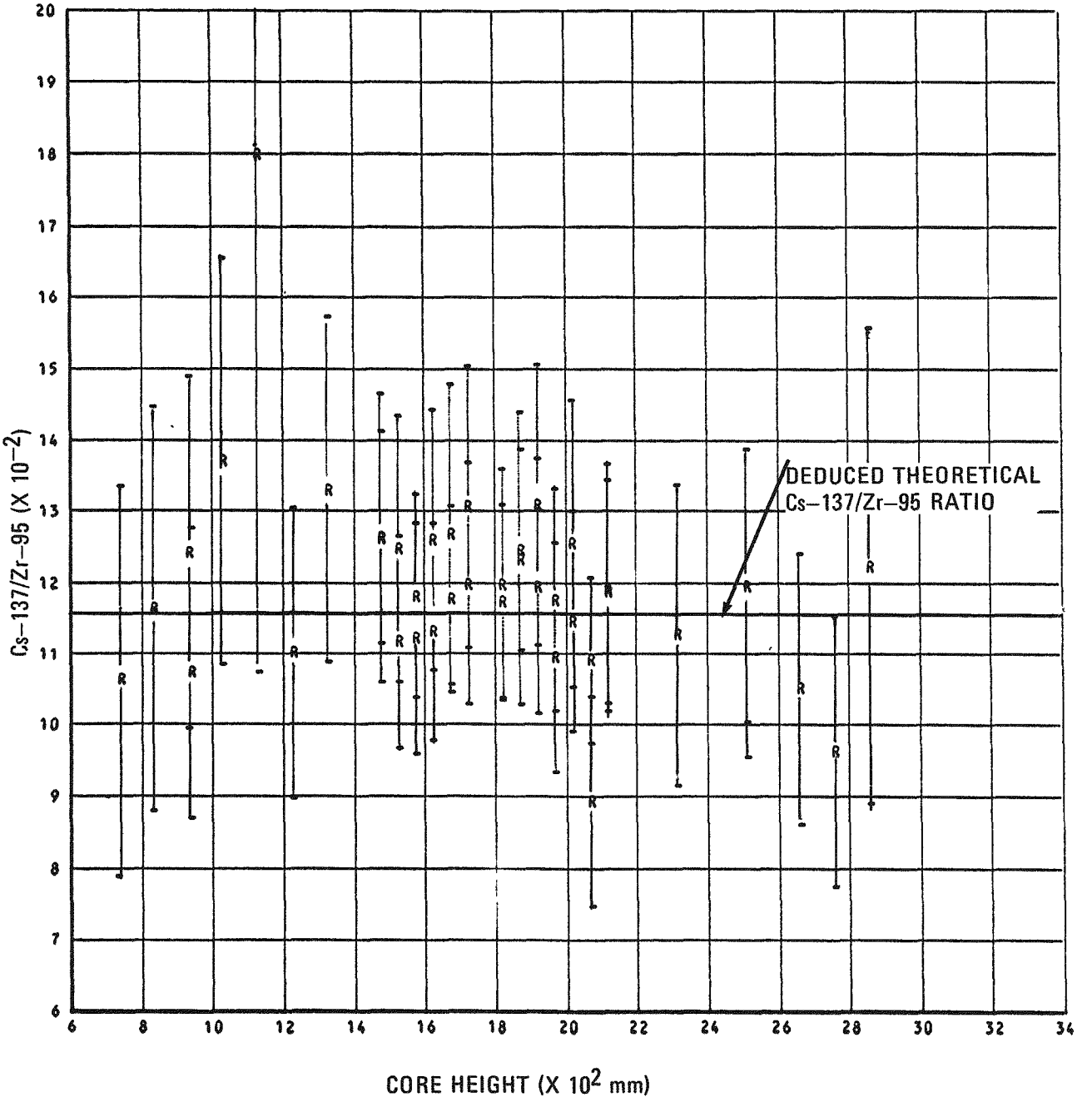

Fig. 9-43. Cs-137/Zr-95 ratio for fuel rods in stacks 7 and 8

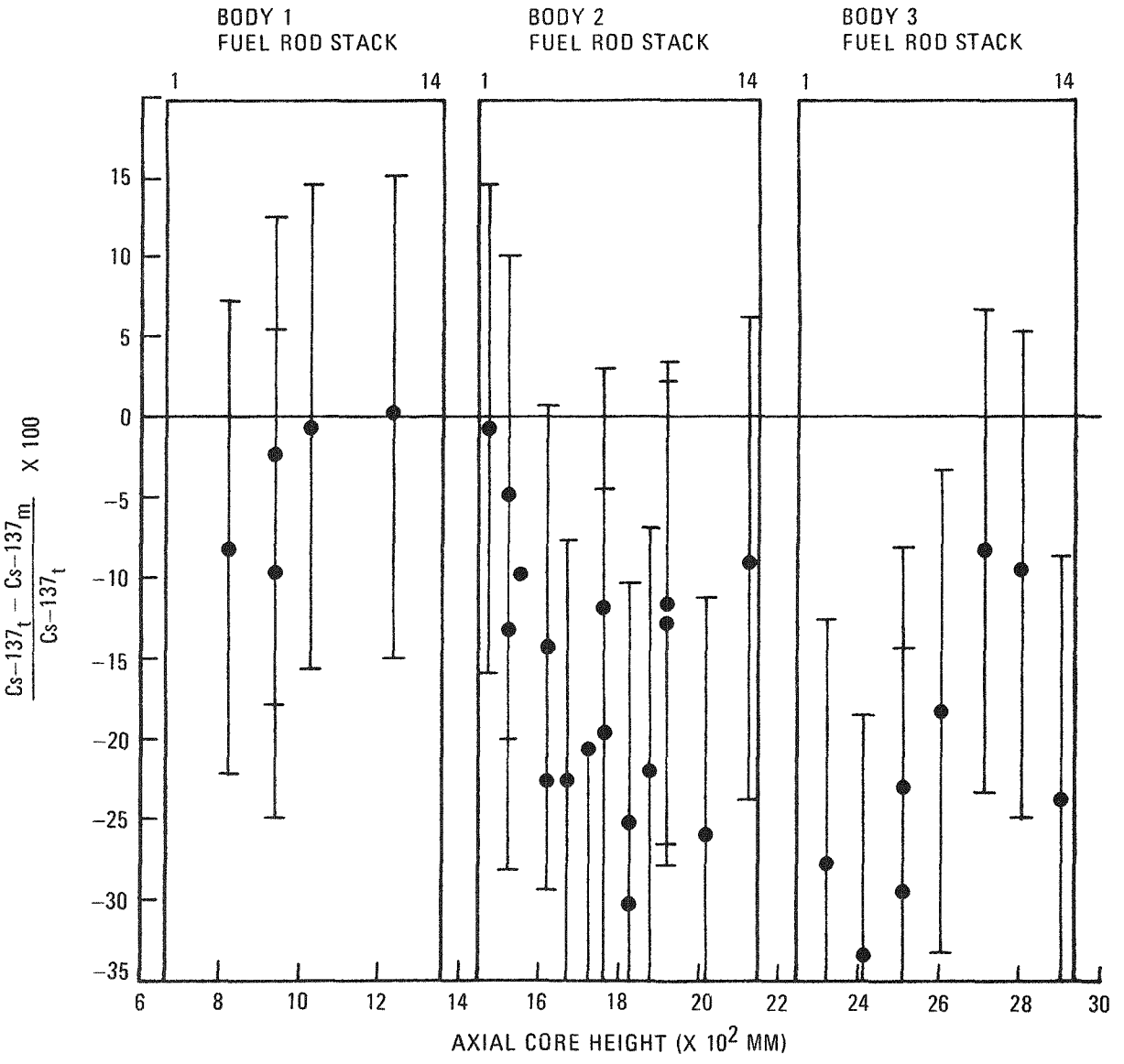

Fig. 9-44. Cs-137 loss from fuel rods in stacks 1 and 2

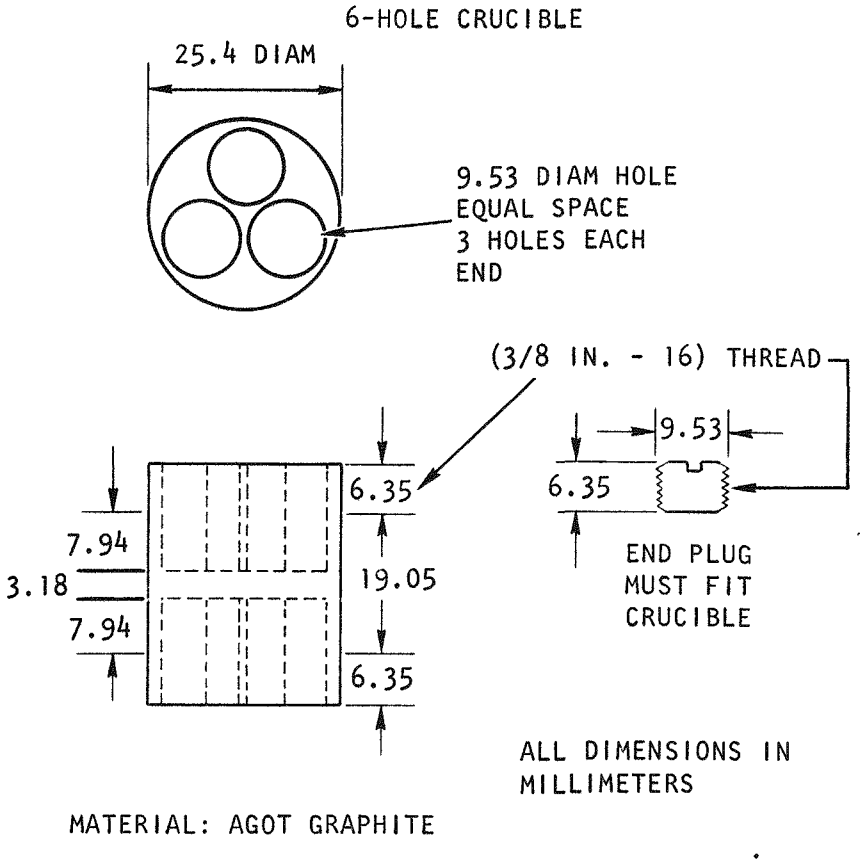

Fig. 9-45. Design of type II thermal stability crucibles

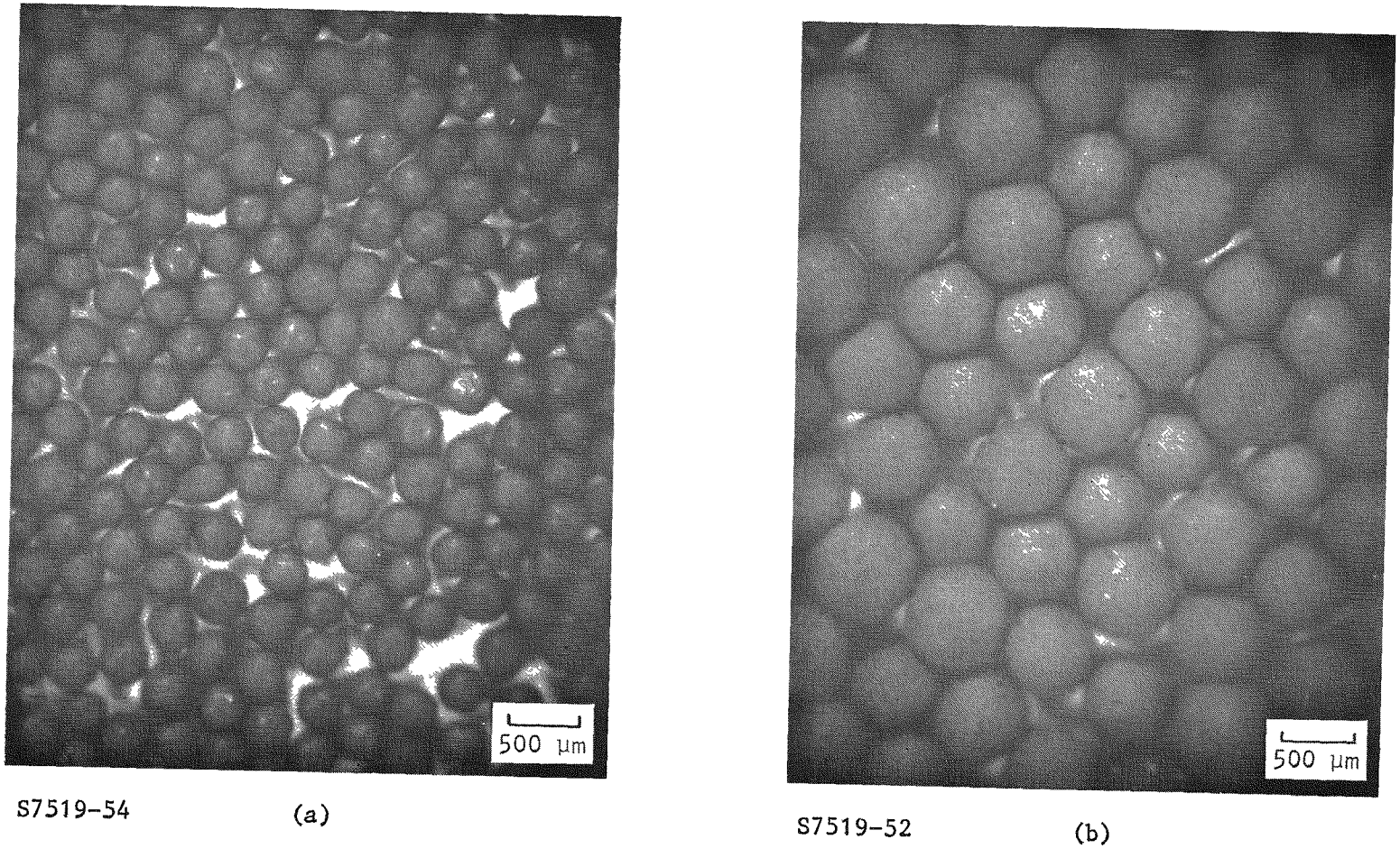

Fig. 9-46. Stereophotographs of thermal stability spine samples from FTE-6; (a) UC_2 TRISO (100 µm) VSM particles from spine sample TS 6-5 irradiated to 2.0 x 10^{25} n/m^2 $(E > 29\ fJ)_{HTGR}$ at 1050°C, (b) ThC_2 TRISO particles from spine sample TS 18-3 irradiated to 2.0 x 10^{25} n/m^2 $(E > 29\ fJ)_{HTGR}$ at 1050°C

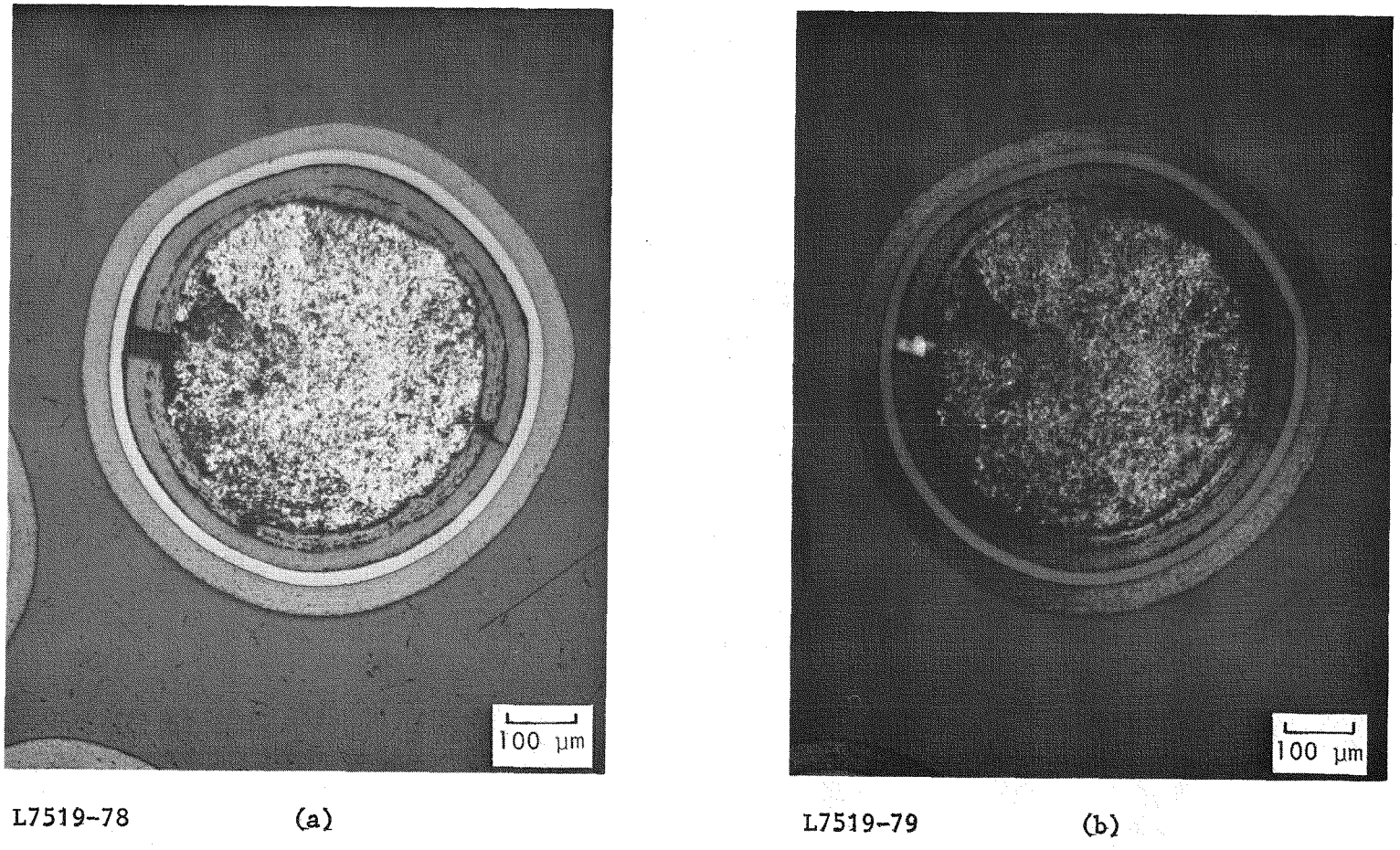

Fig. 9-47. Photomicrographs of typical microstructure of ThC_2 TRISO particle from spine sample TS 18-3 irradiated in FTE-6 to 2.0 x 10^{25} n/m^2 ($E > 29$ fJ)$_{HTGR}$ at 1050°C; dark spots in kernel are due to hydrolysis during sample preparation: (a) bright field, (b) dark field

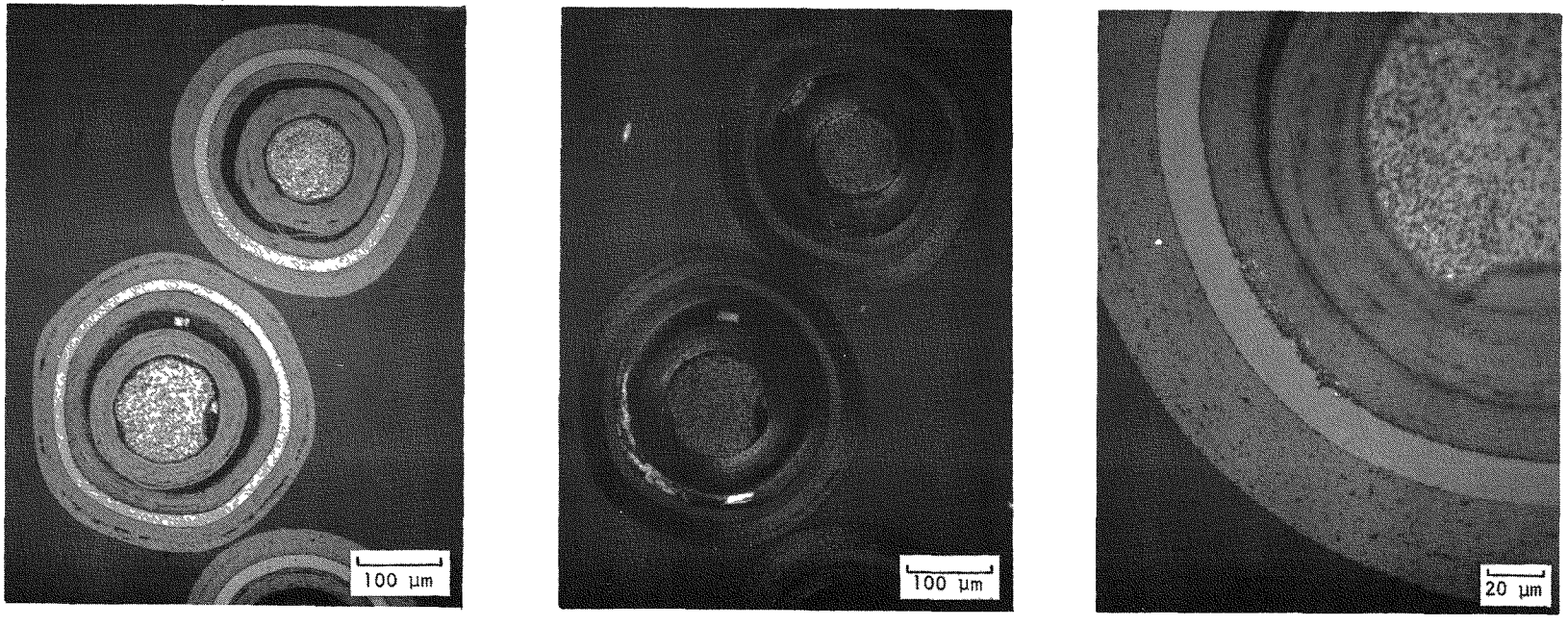

Fig. 9-48. Photomicrographs of typical microstructure of UC_2 120-µm (VSM) particles from spine sample TS 6-5 irradiated in FTE-6 to 2.0 x 10^{25} n/m^2 ($E > 29$ fJ)$_{HTGR}$ at 1050°C: (a) bright field, (b) dark field showing mixed fission products in IPyC, (c) high magnification of SiC attack in particle shown in (a) and (b)

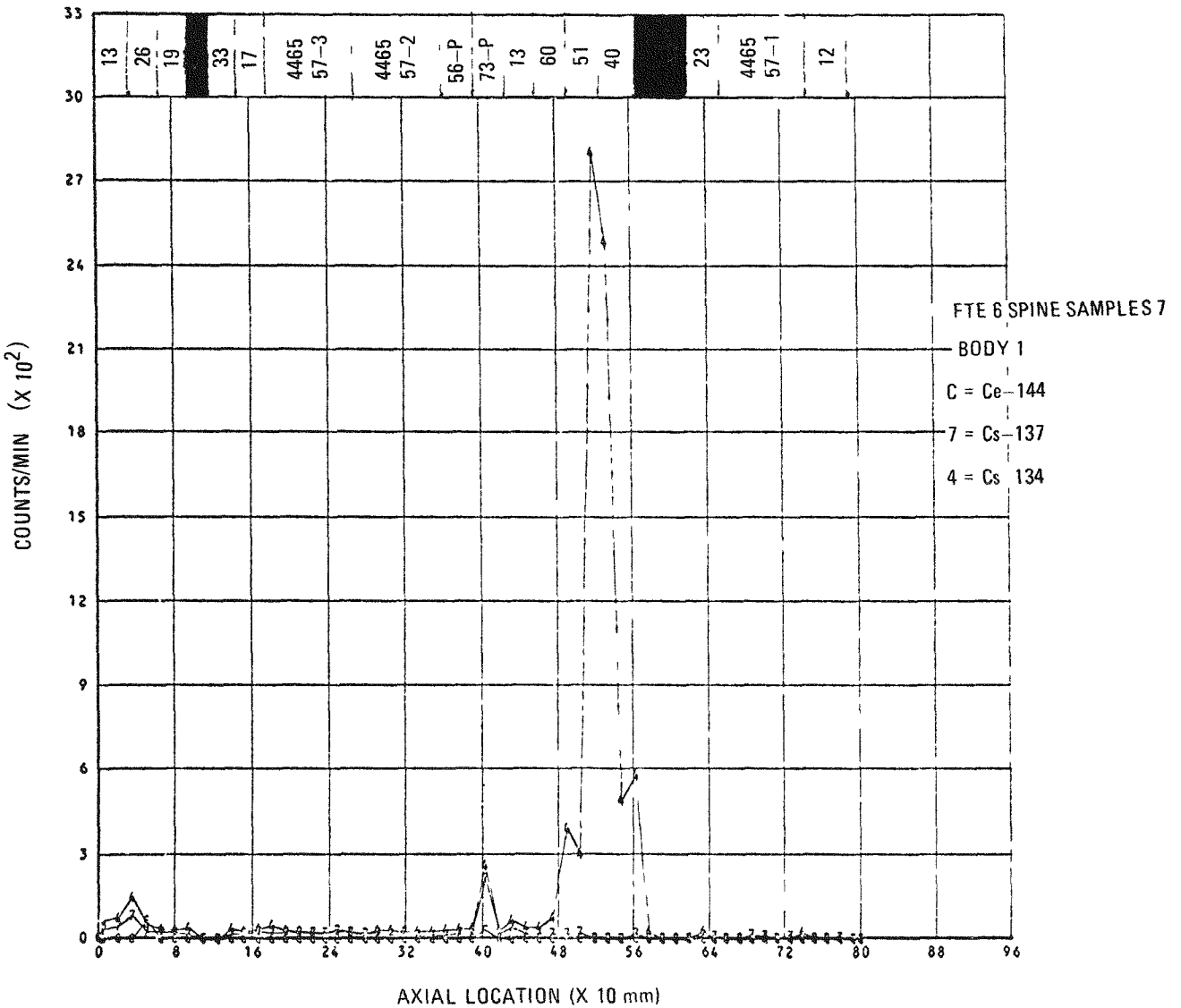

Fig. 9-49. GA hot cell gamma scan of body 1 spine samples

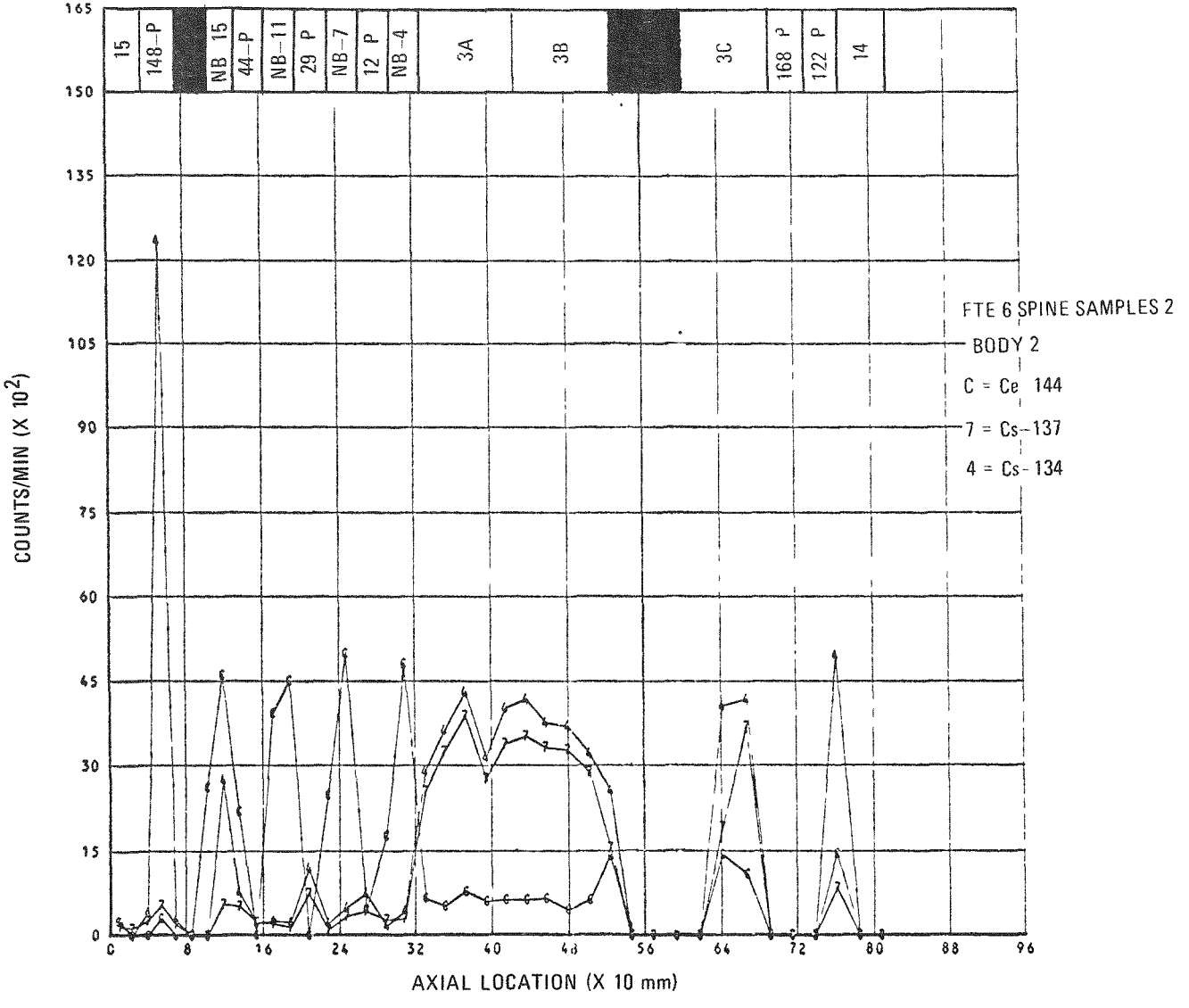

Fig. 9-50. GA hot cell gamma scan of body 2 spine samples

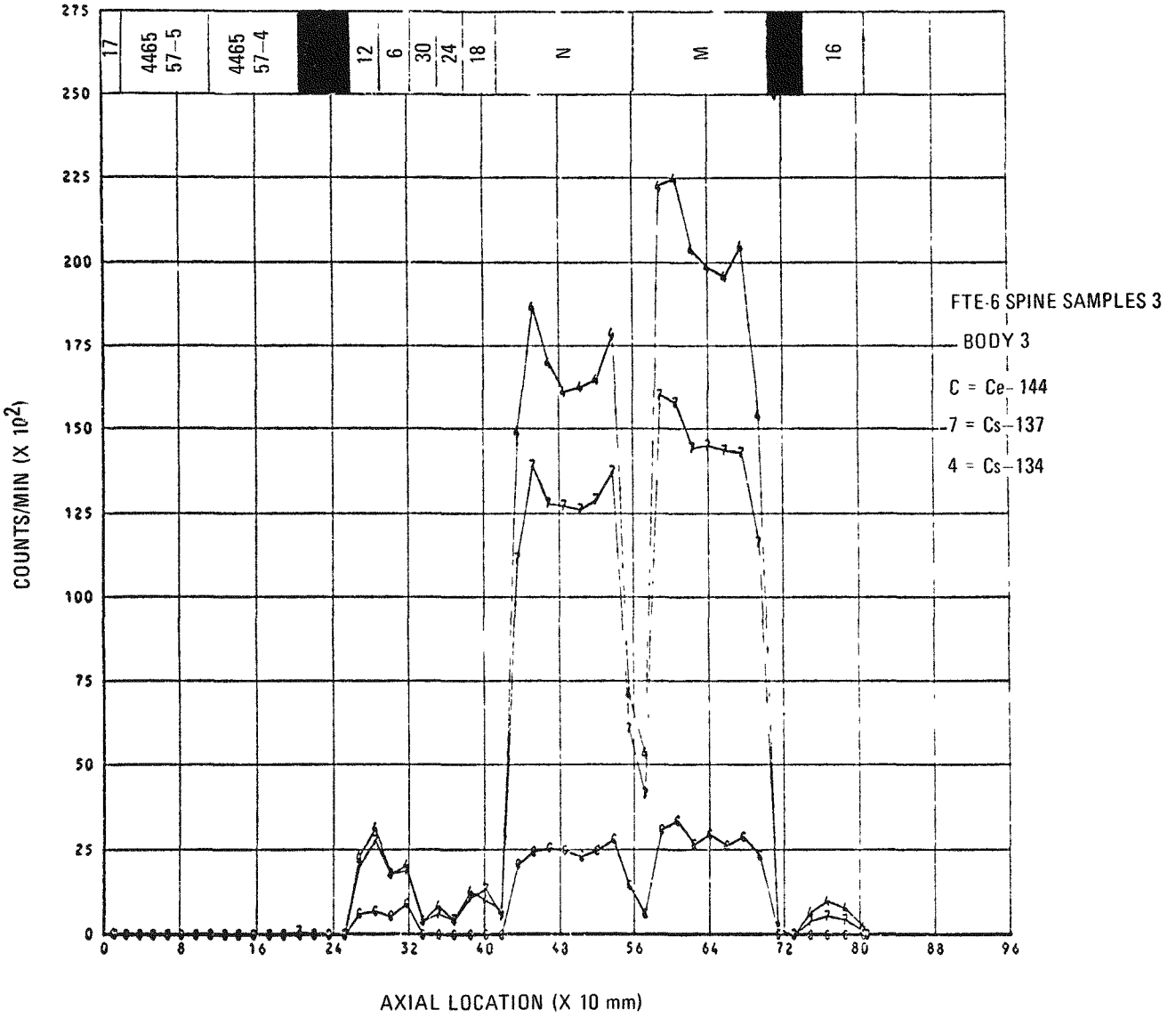

Fig. 9-51. GA hot cell gamma scan of body 3 spine samples

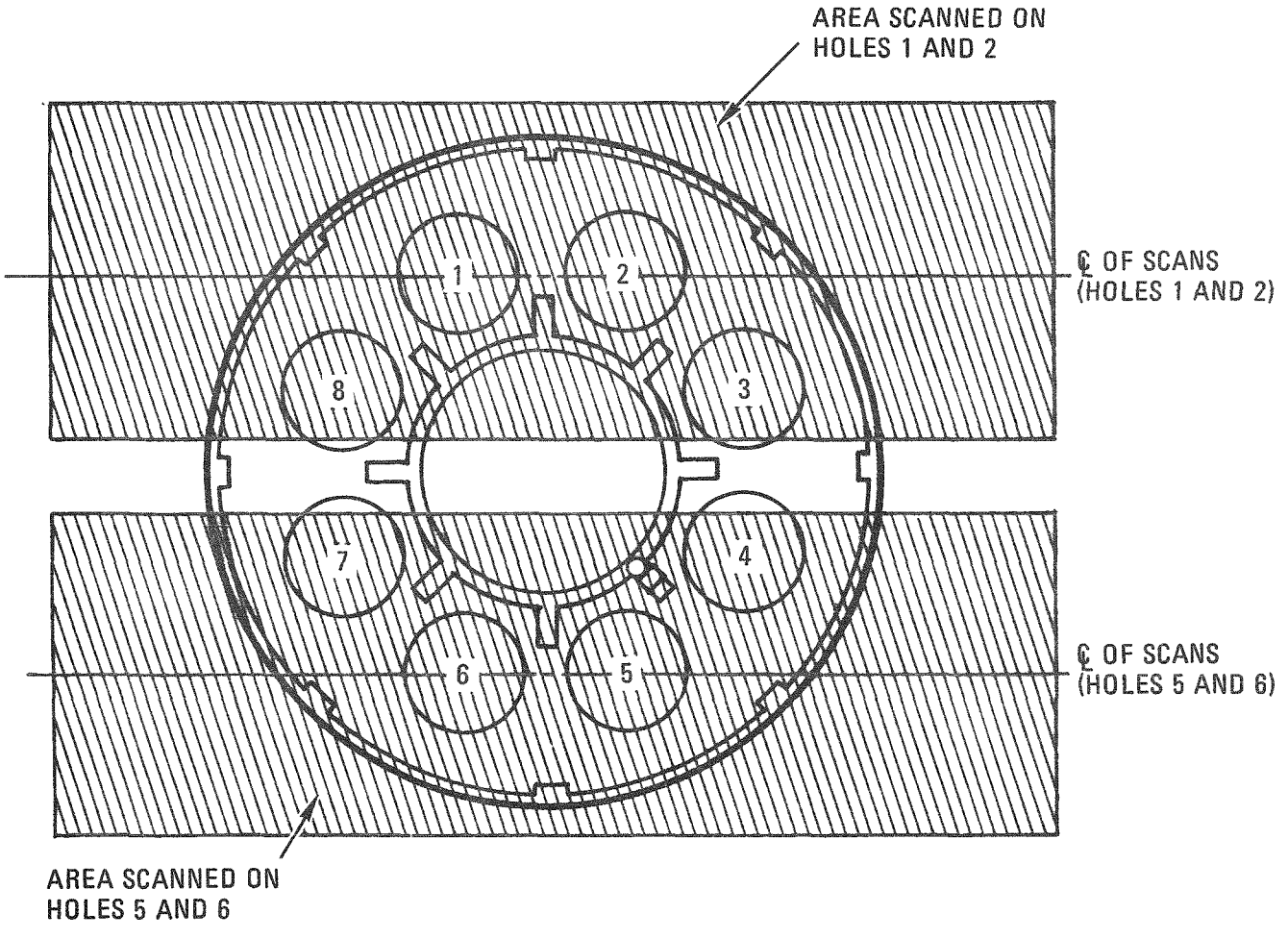

Fig. 9-52. FTE-6 graphite fuel body 2 gamma scanned areas

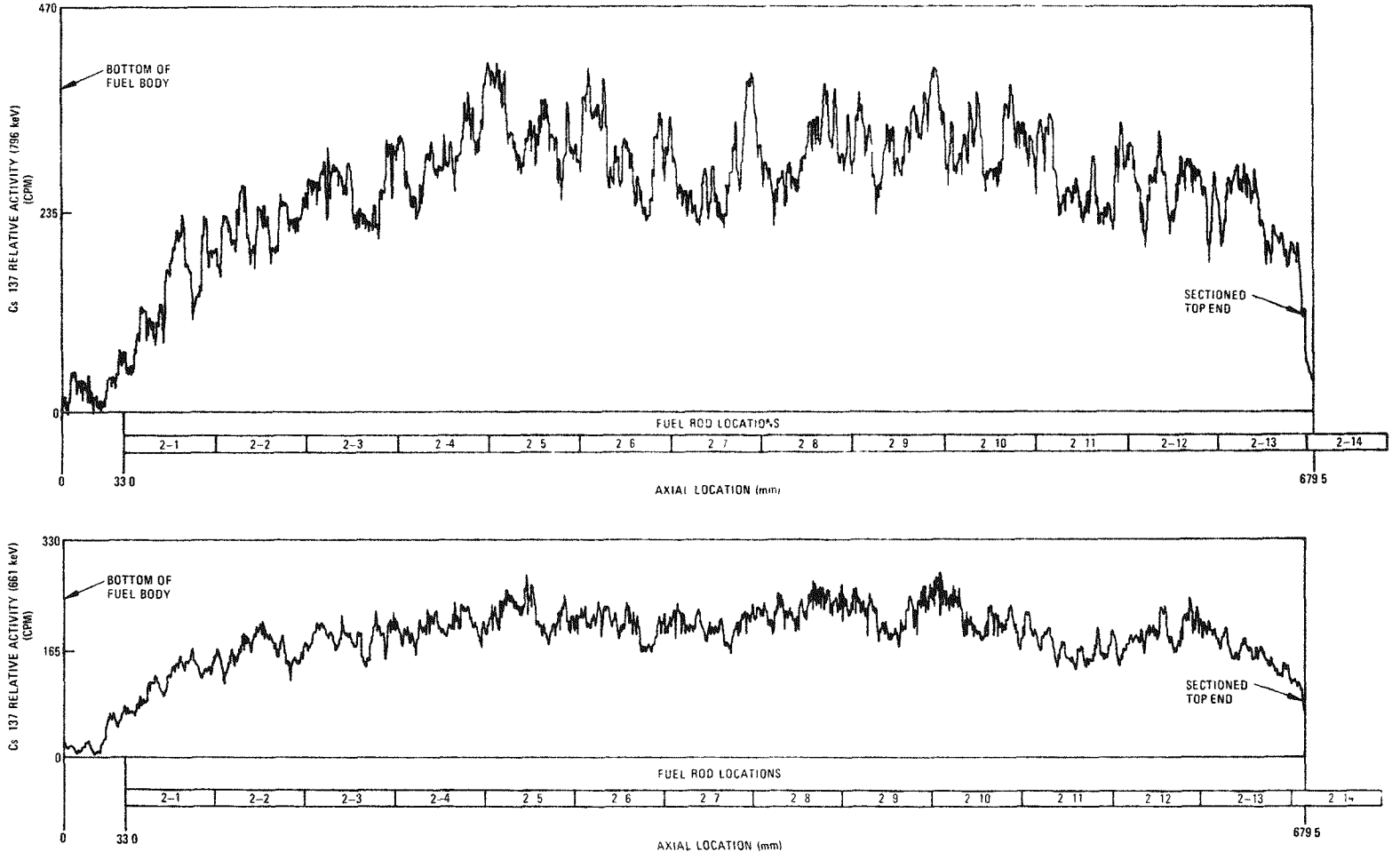

Fig. 9-53. FTE-6 fuel body 2 (holes 1 and 2) single-channel gamma scans of cesium

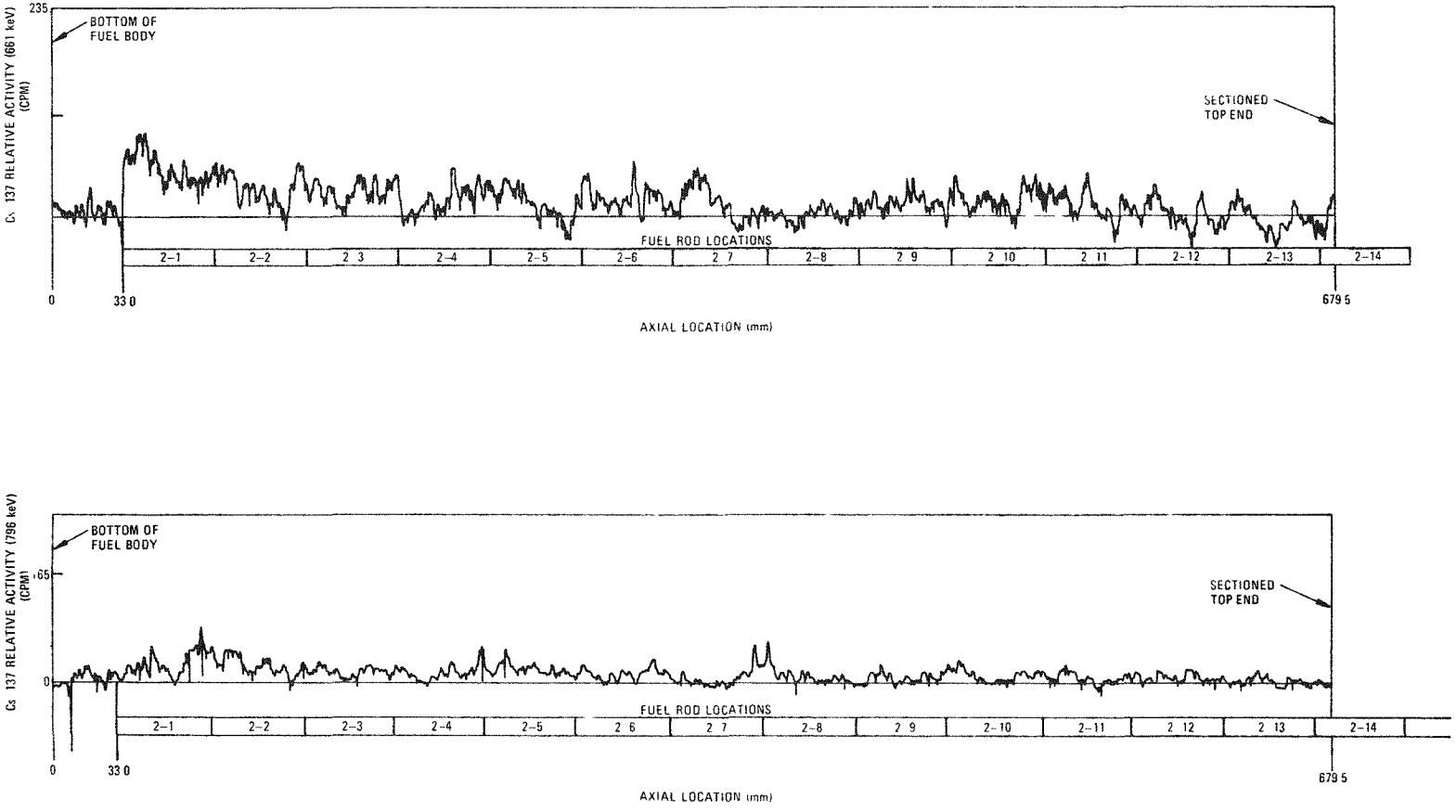

Fig. 9-54. FTE-6 fuel body 2 (holes 5 and 6) single-channel gamma scans of cesium

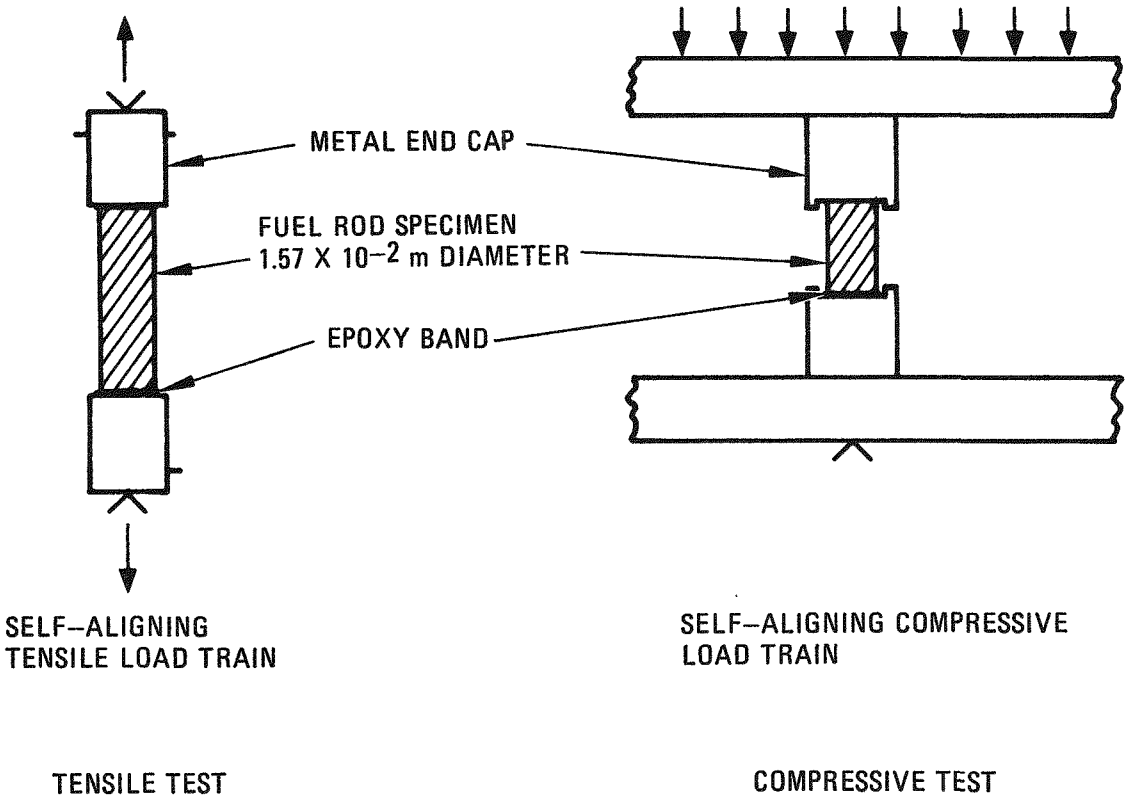

Fig. 9-55. Fuel rod mechanical properties test specimen geometry

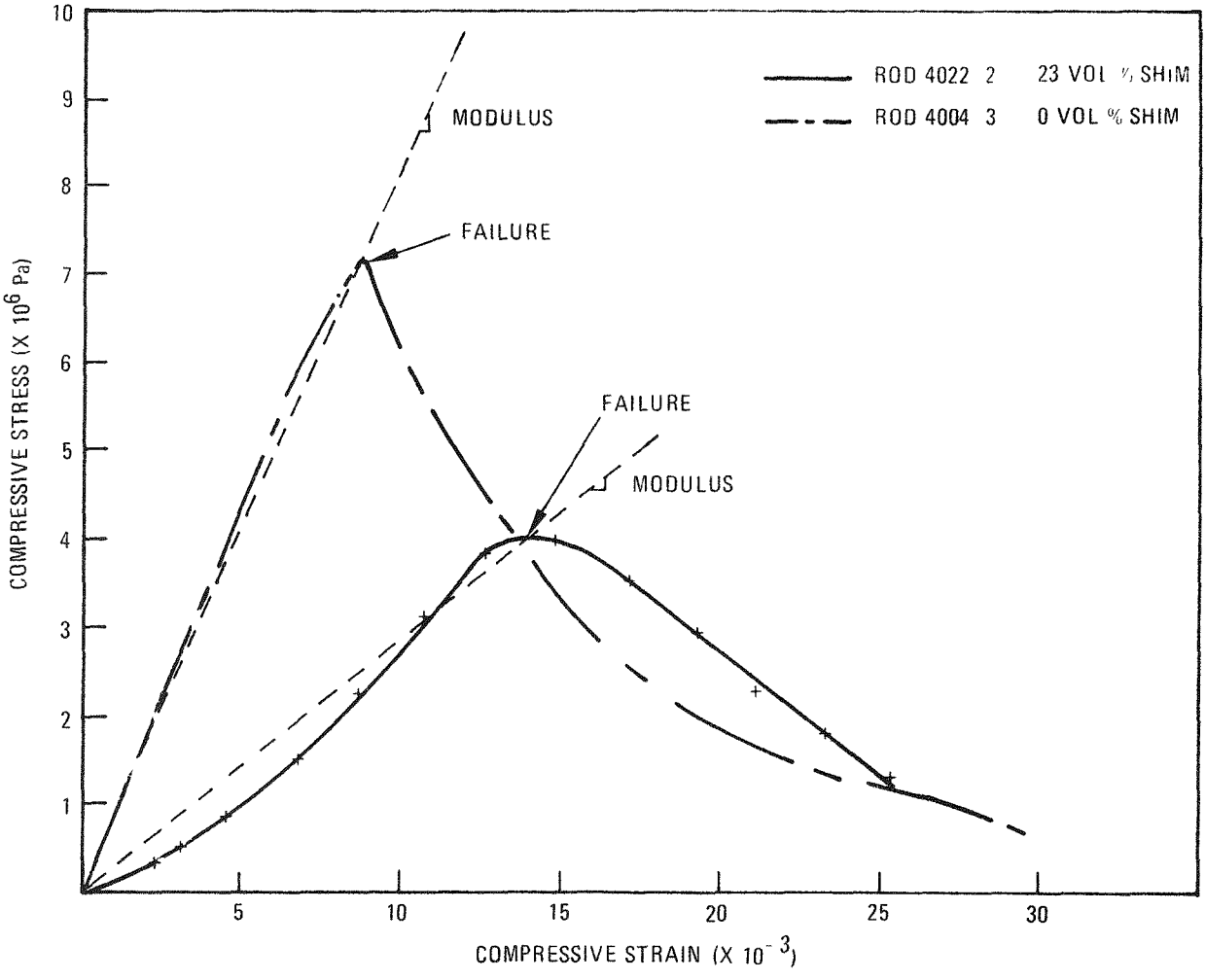

Fig. 9-56. Compressive stress-strain curves for HTGR fuel rods

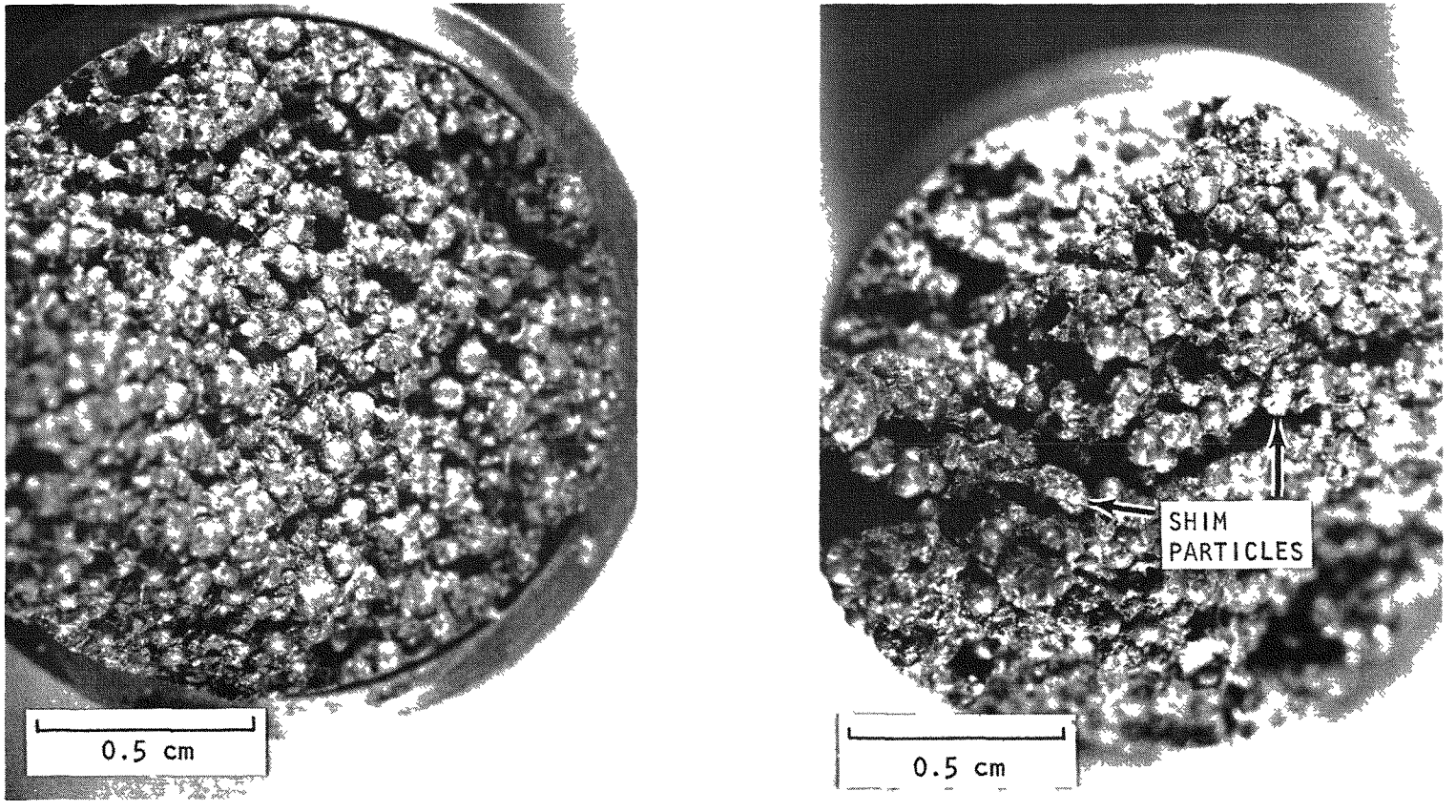

ROD 4005-2-B 0 VOL % SHIM ROD 4022-2-B 23 VOL % SHIM

Fig. 9-57. Fracture surfaces of LHTGR fuel rods

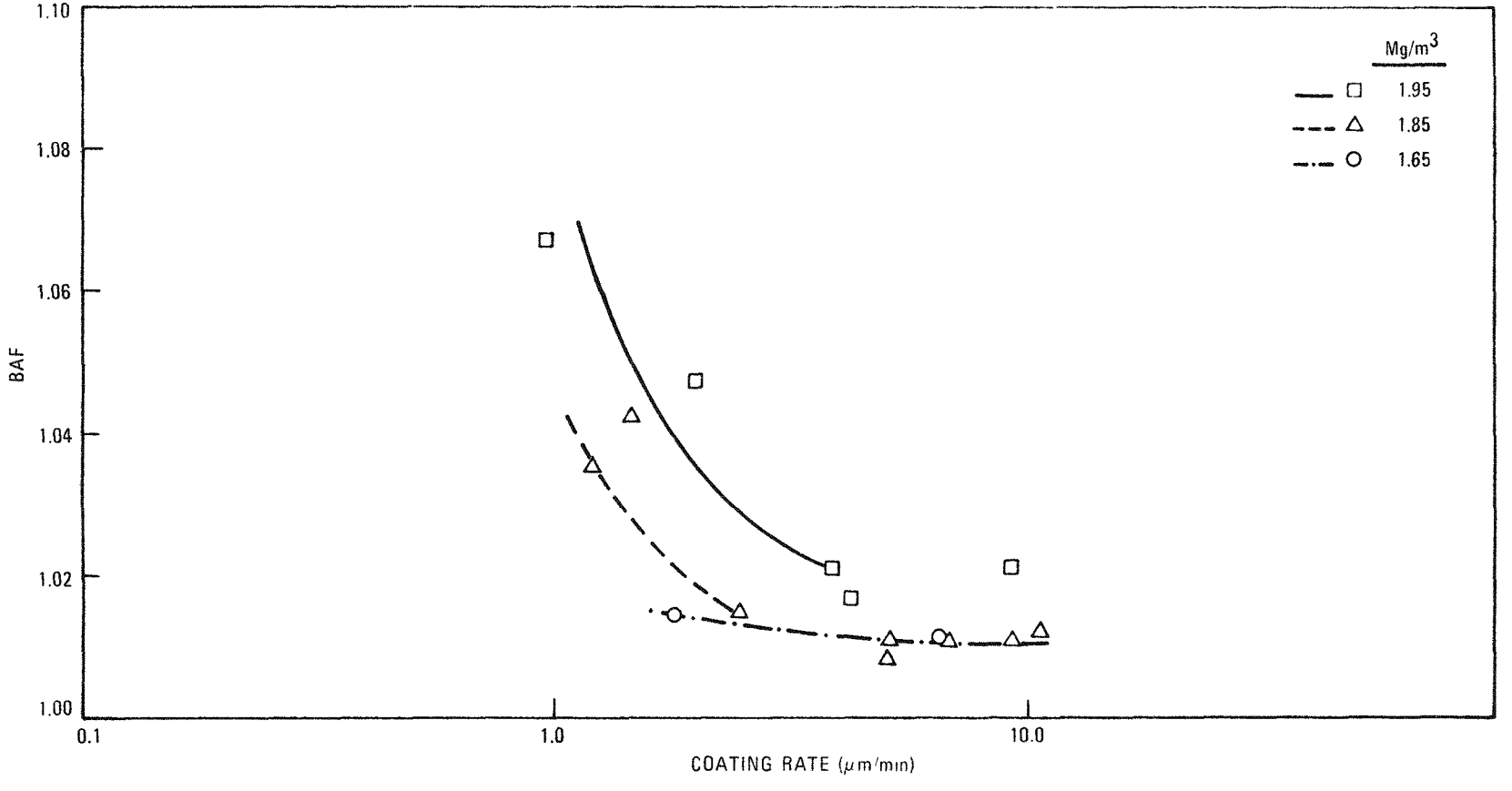

Fig. 9-58. Variation of the preferred orientation of carbon crystallites with coating rate

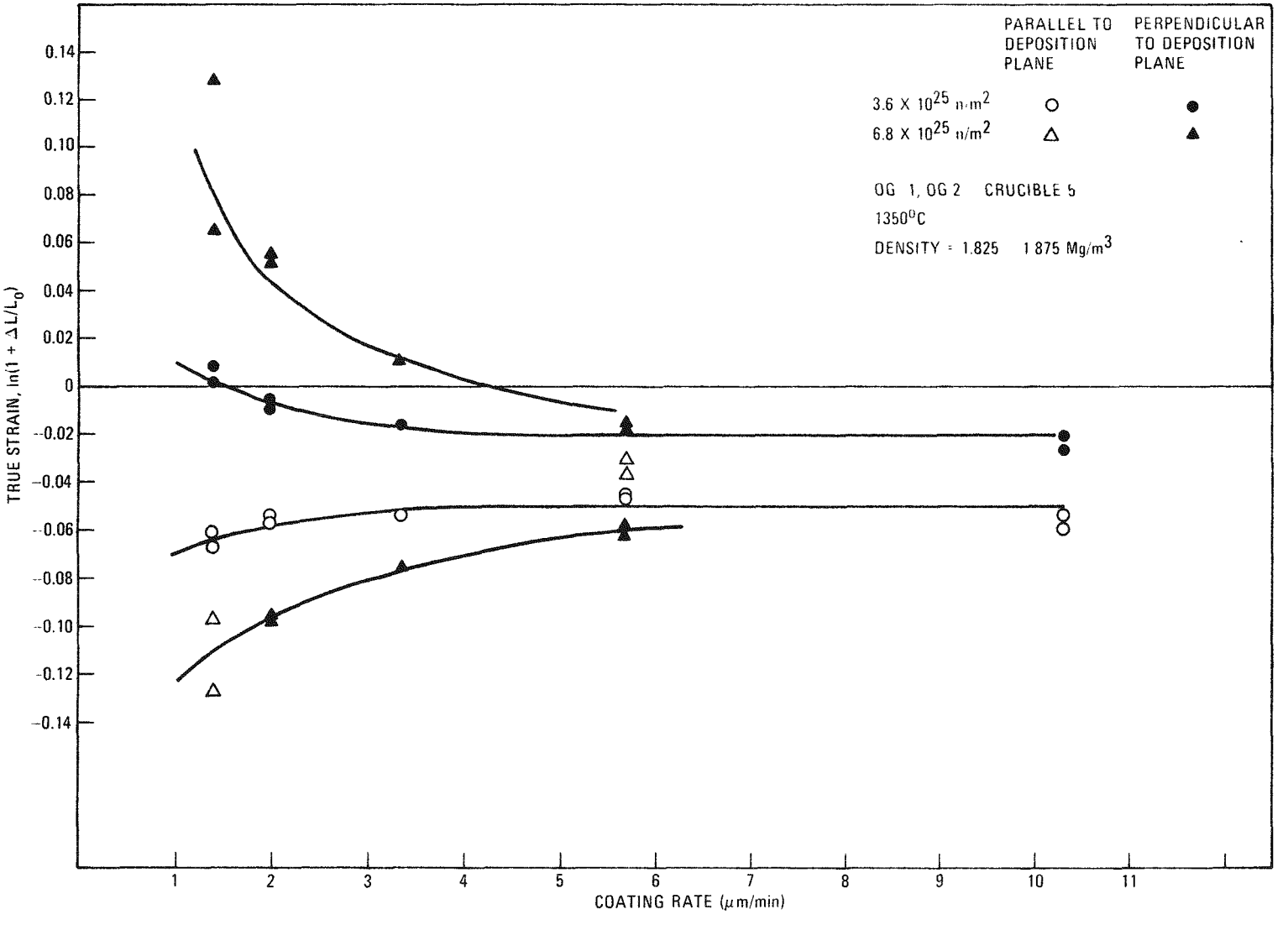

Fig. 9-59. Irradiation-induced dimensional changes of intermediate-density carbons

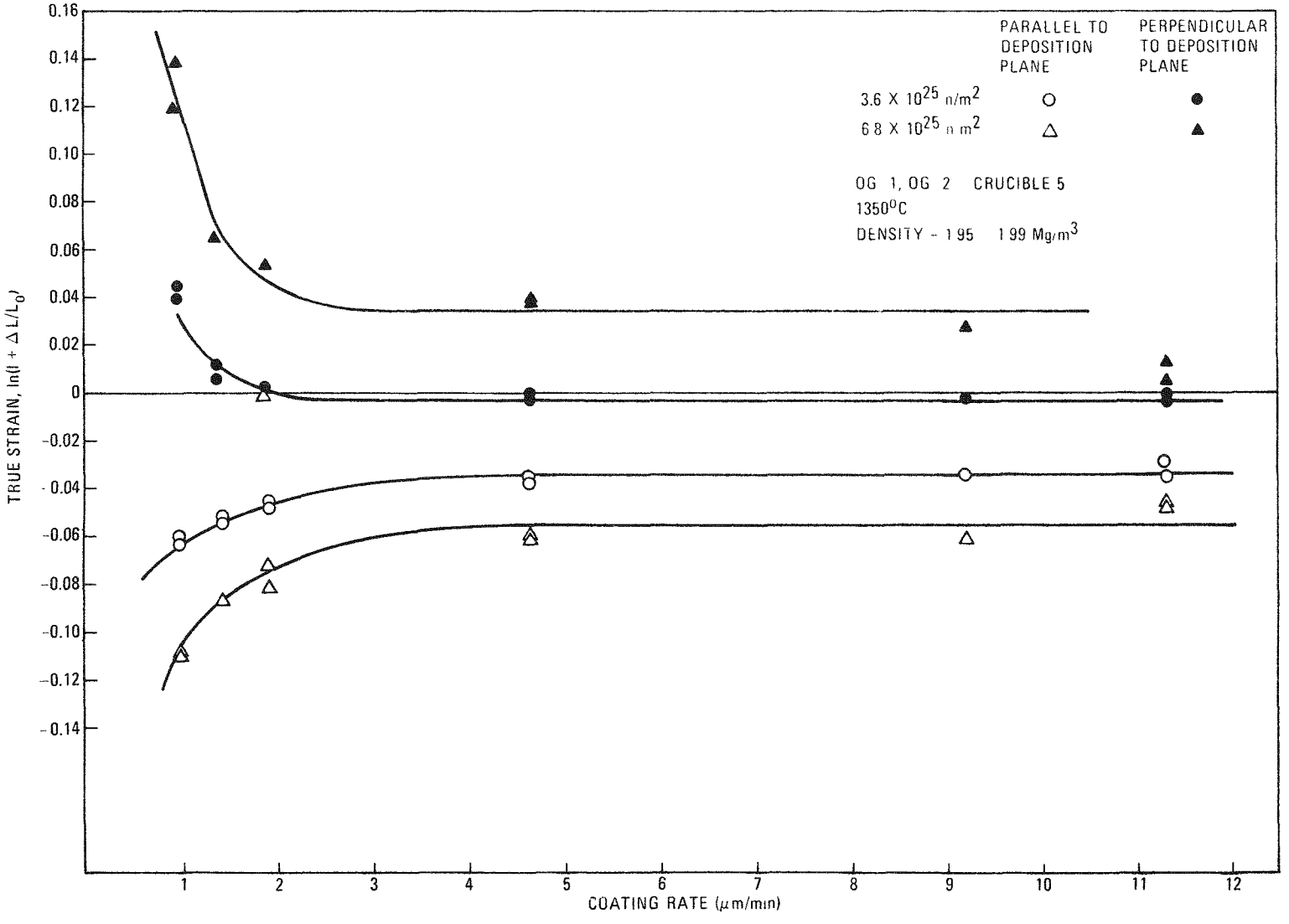

Fig. 9-60. Irradiation-induced dimensional changes of high-density carbons

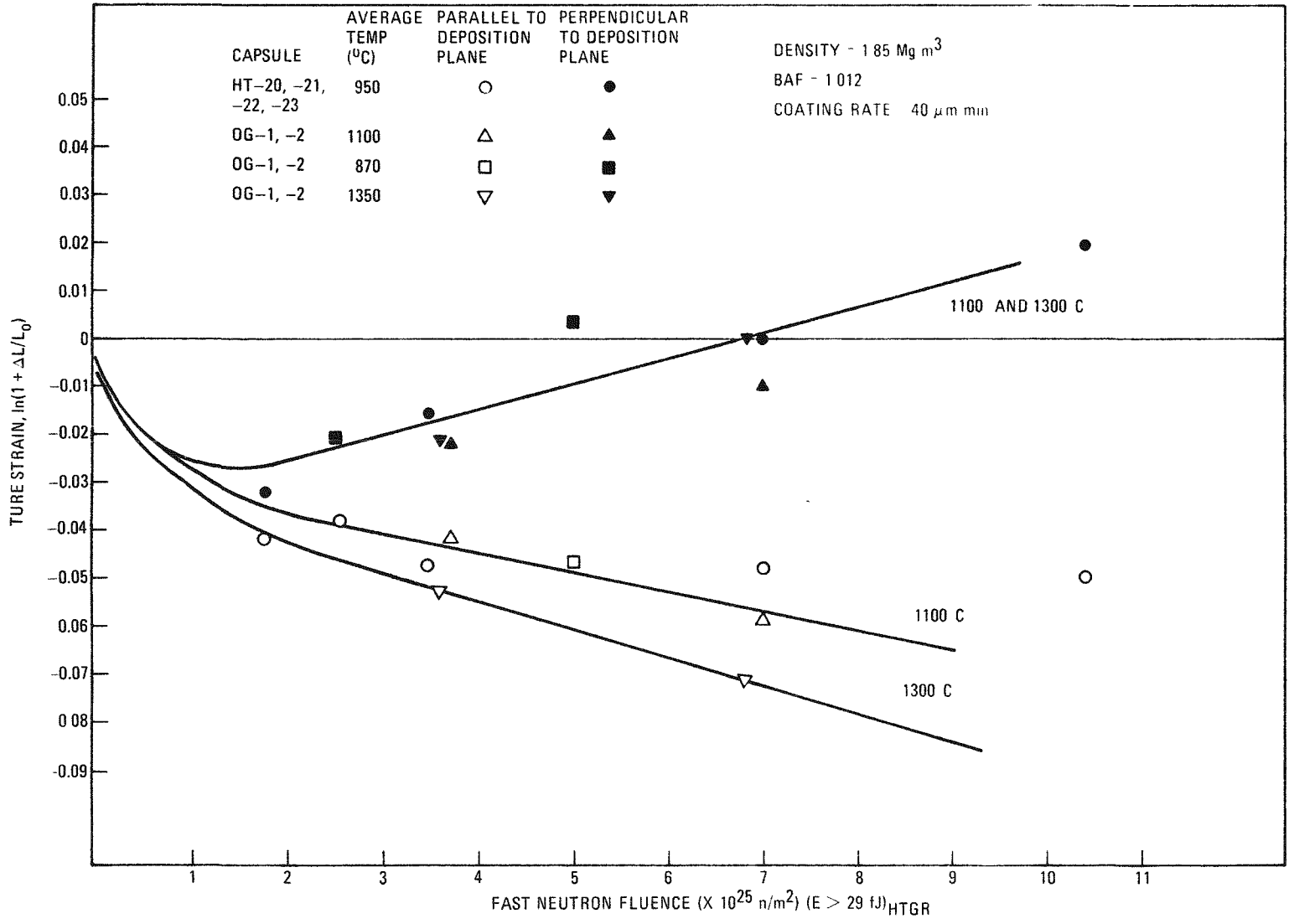

Fig. 9-61. Irradiation-induced dimensional changes of an intermediate-density carbon as a function of fast neutron fluence

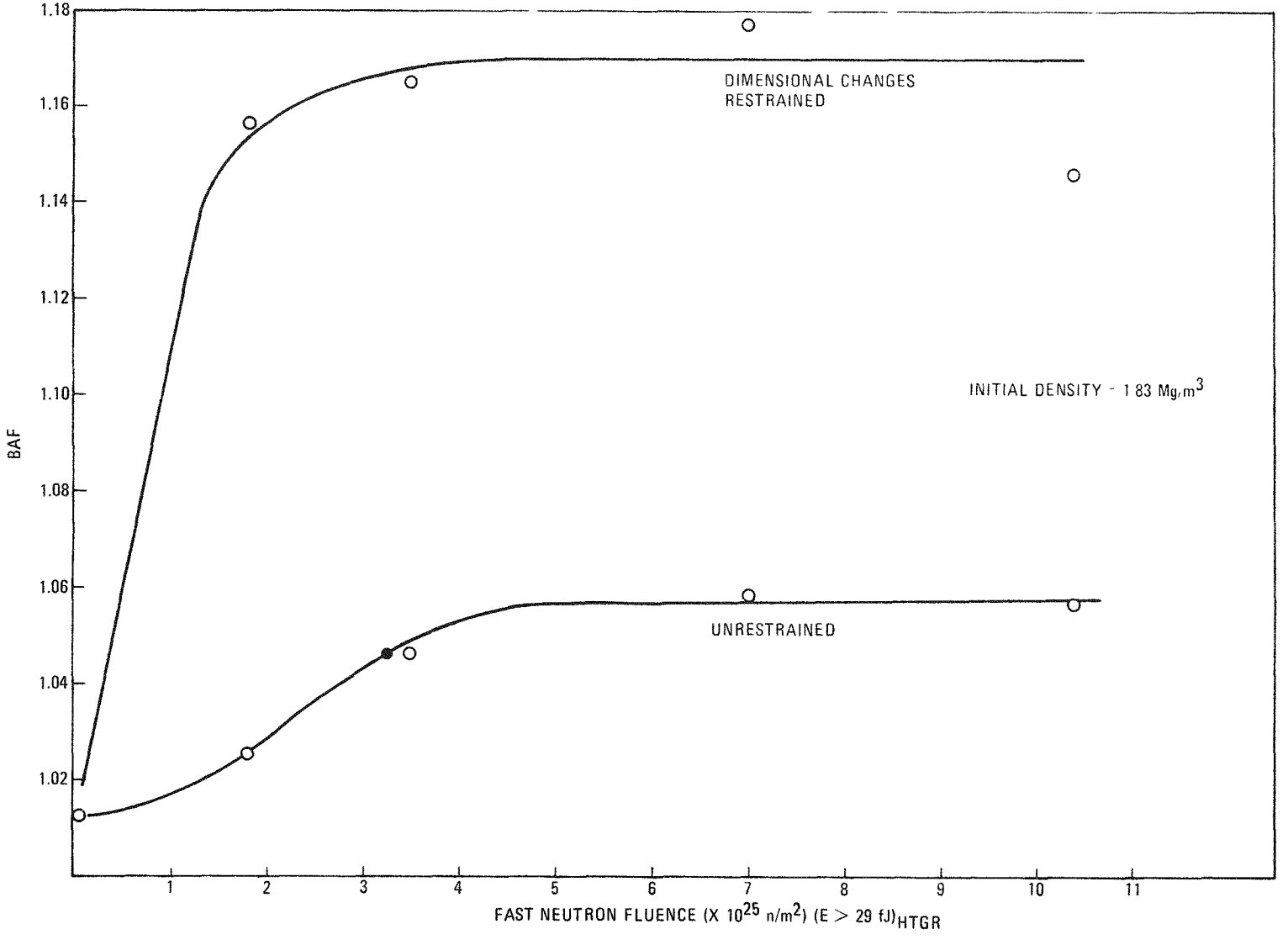

Fig. 9-62. Preferred orientation changes of restrained and unrestrained intermediate-density carbons during irradiation

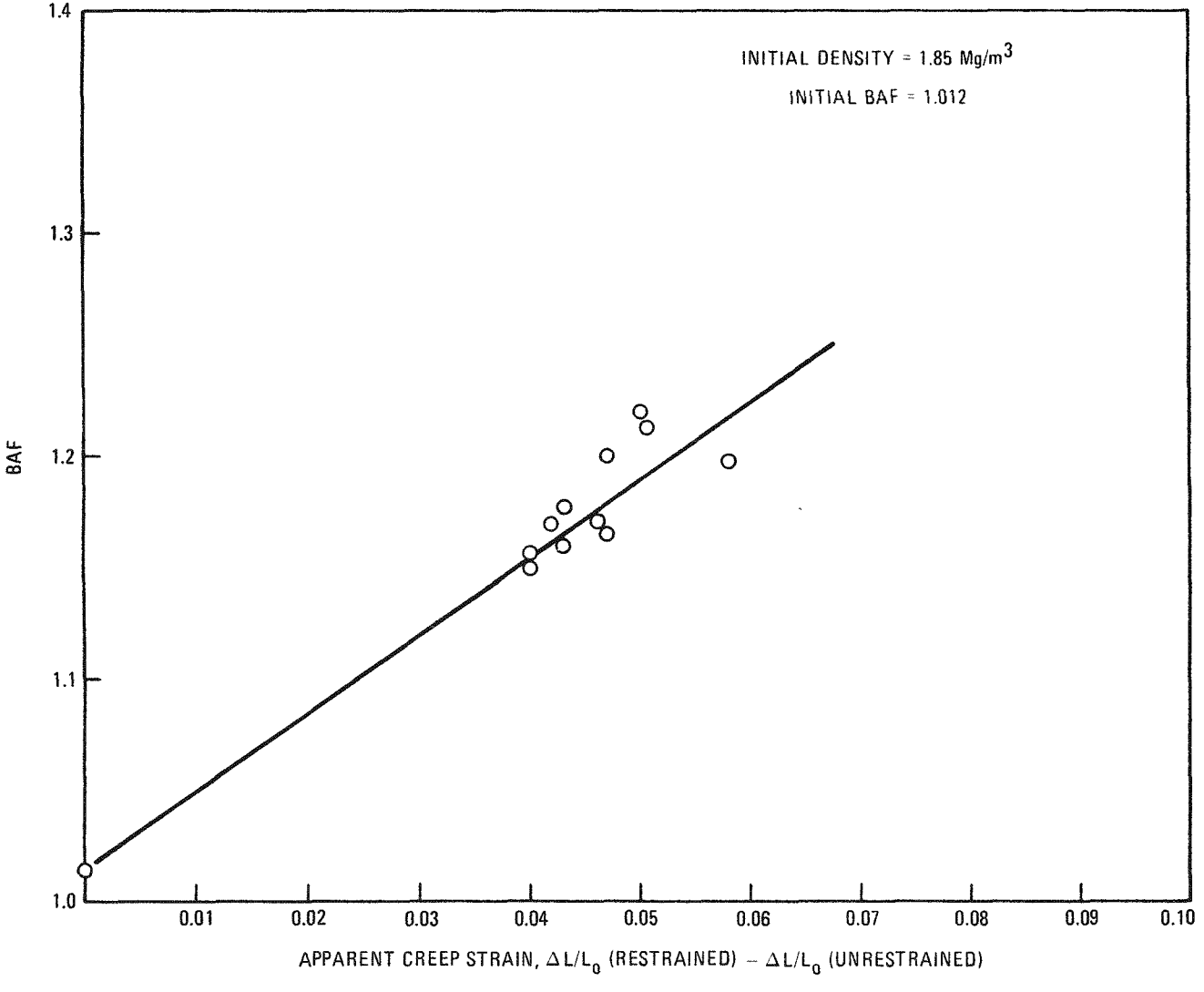

Fig. 9-63. Variation of preferred orientation with apparent creep strain

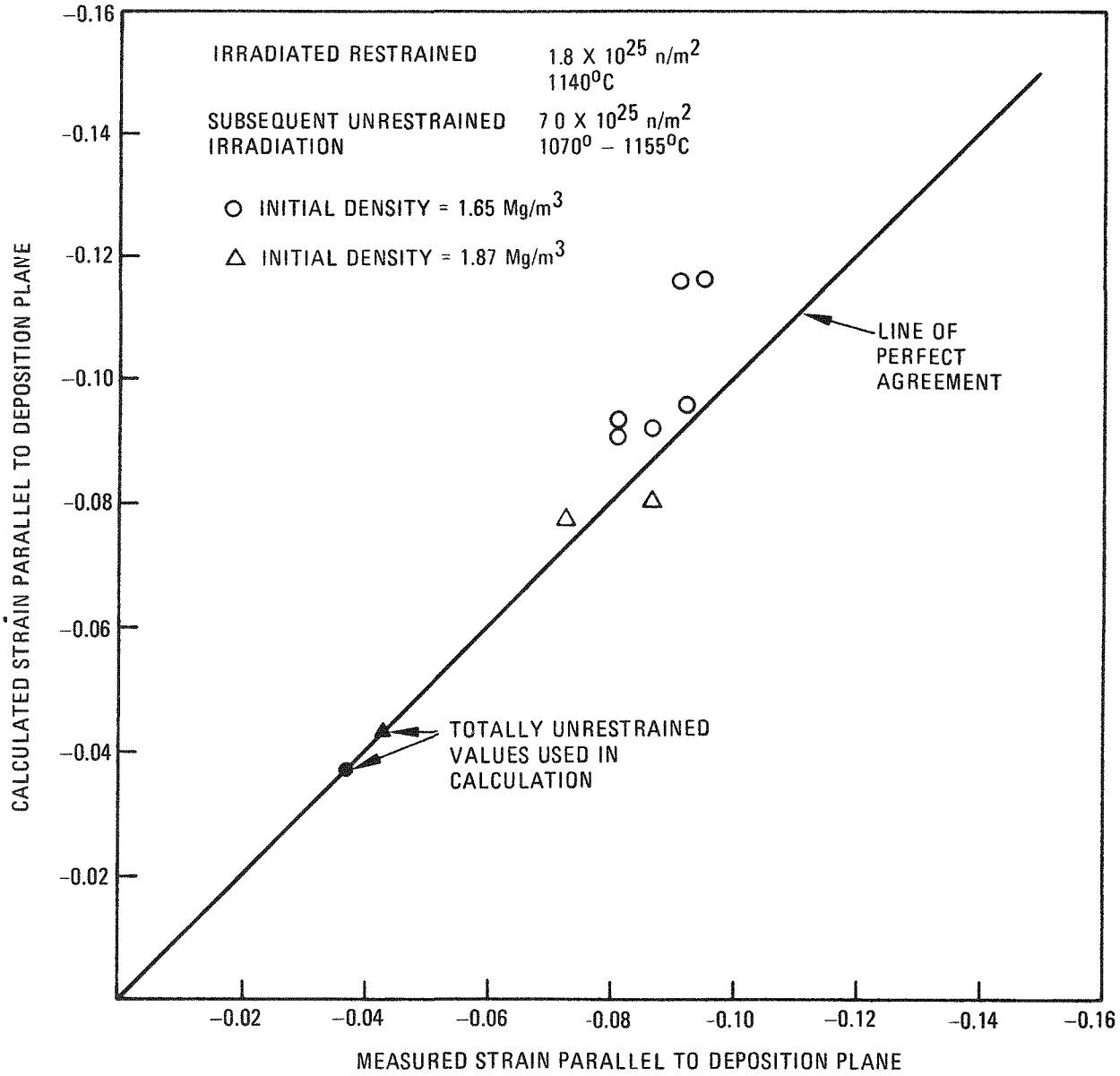

Fig. 9-64. Agreement between predicted and calculated irradiation-induced strains: (a) parallel to the deposition plane for previously restrained carbons

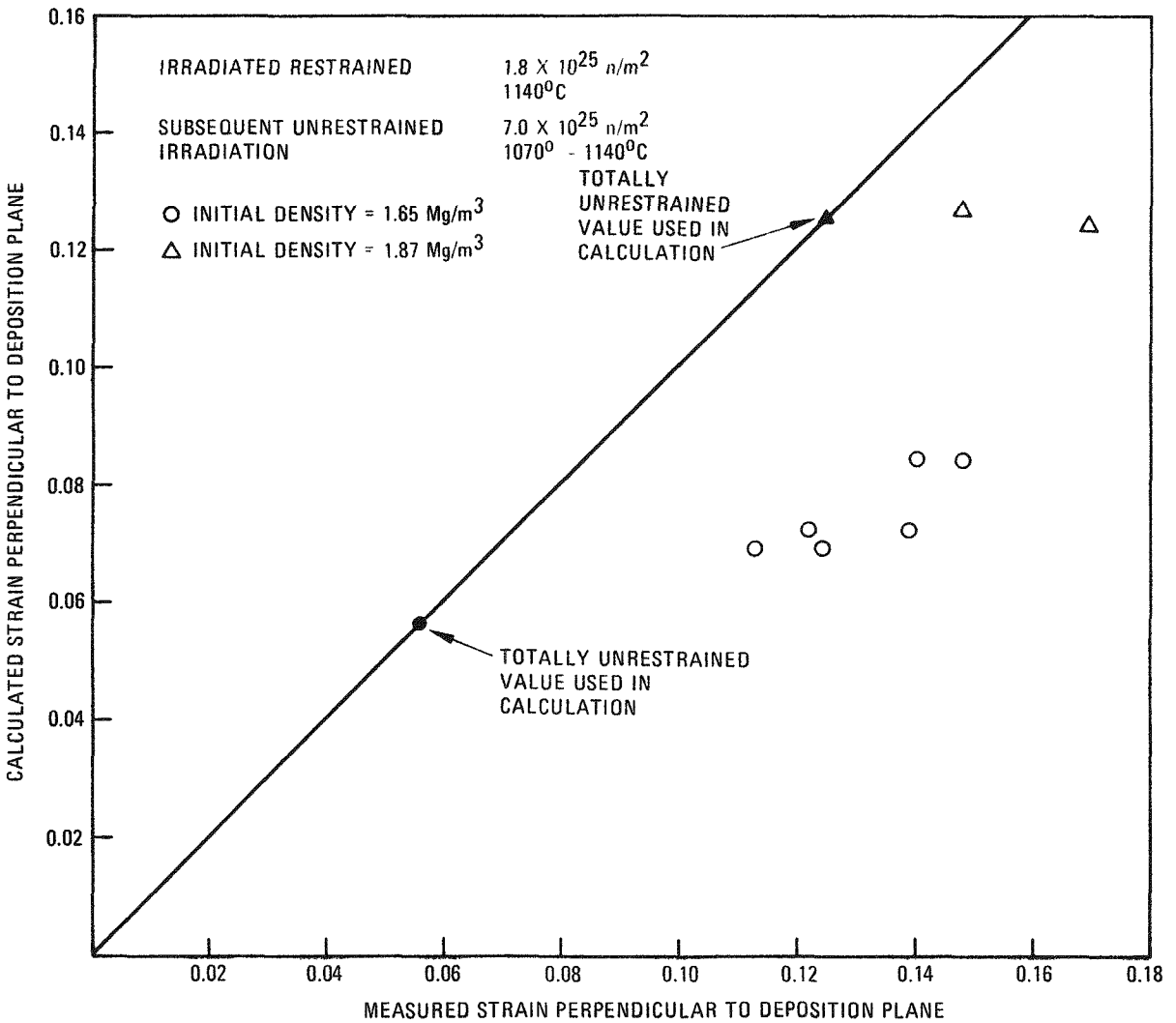

Fig. 9-64. Agreement between predicted and calculated irradiation-induced strains: (b) perpendicular to the deposition plane for previously restrained carbons

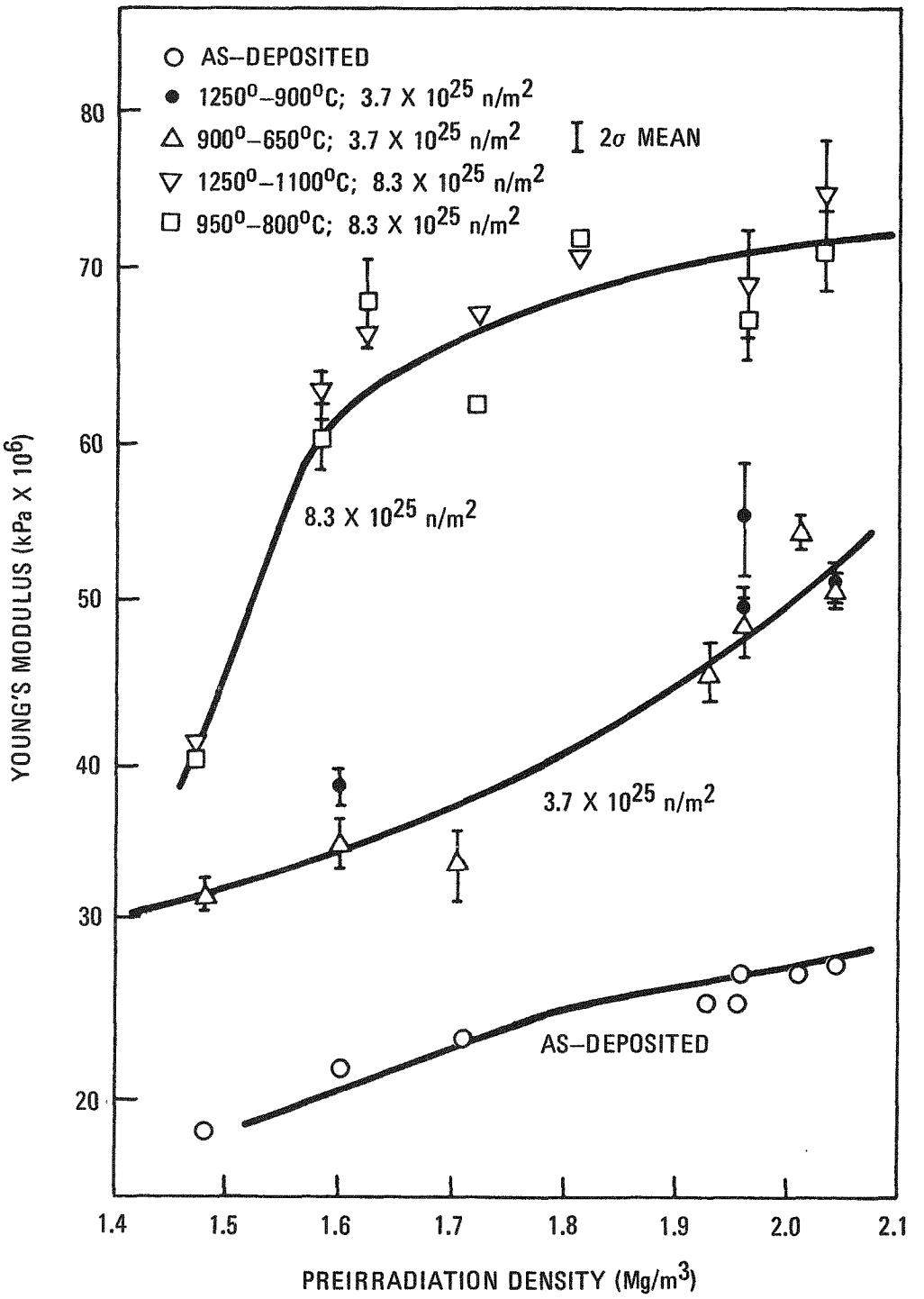

Fig. 9-65. Young's modulus of carbons before and after irradiation

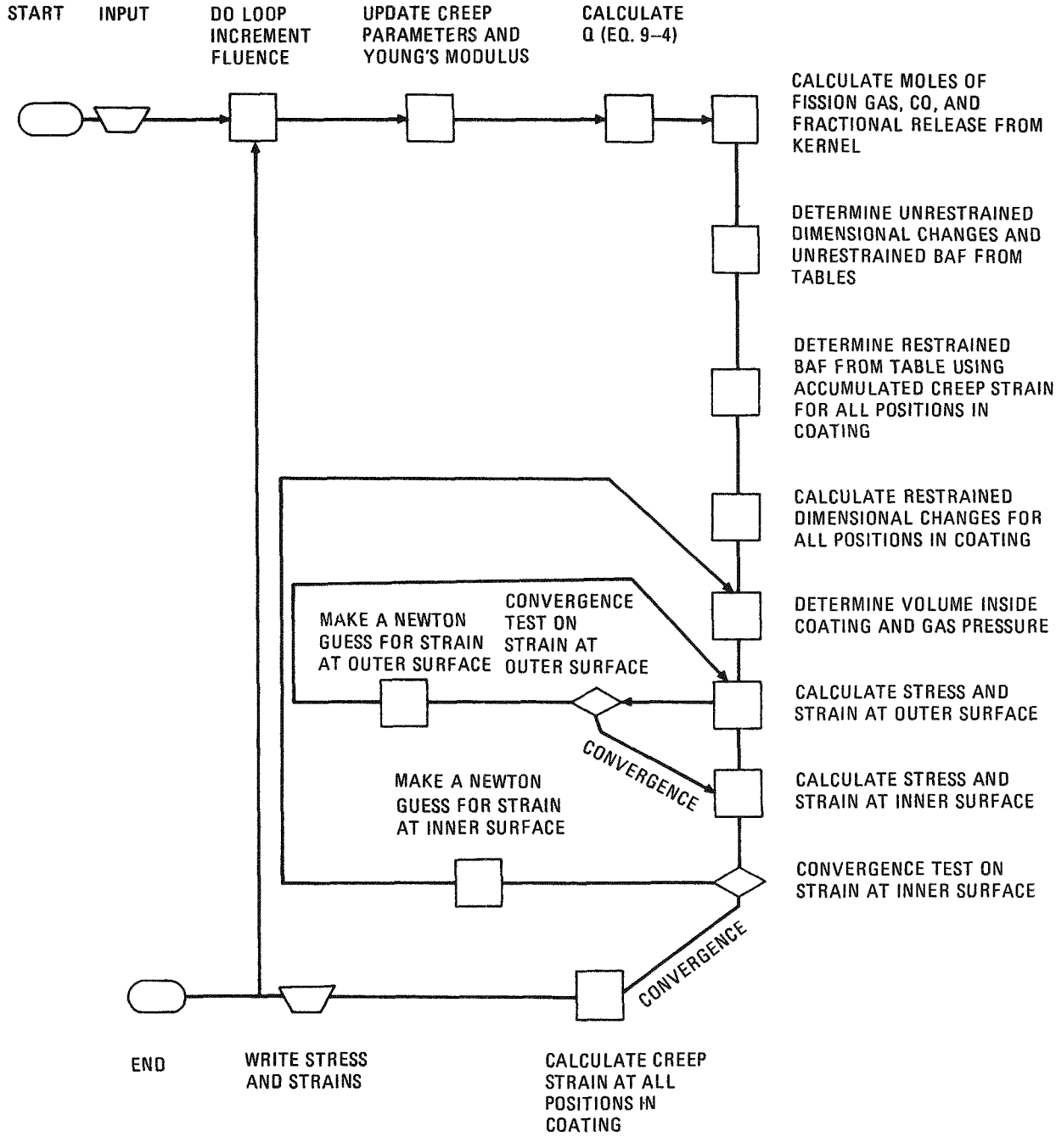

Fig. 9-66. Flow diagram for the BISO stress analysis model

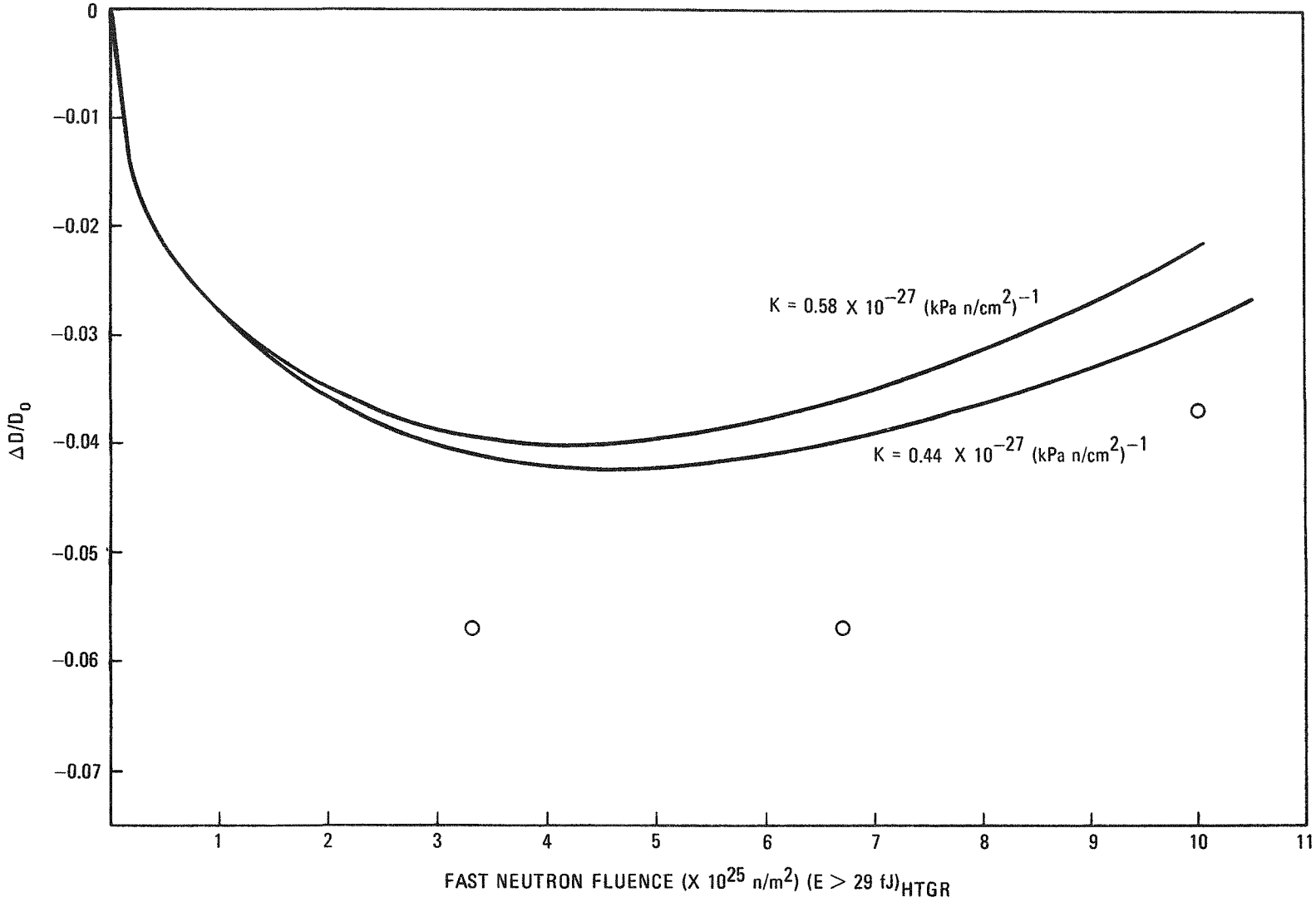

Fig. 9-67. Comparison of calculated and measured diametral changes of BISO particles irradiated in position 40 using dimensional changes for a coating with a density of 1.83 Mg/m^3

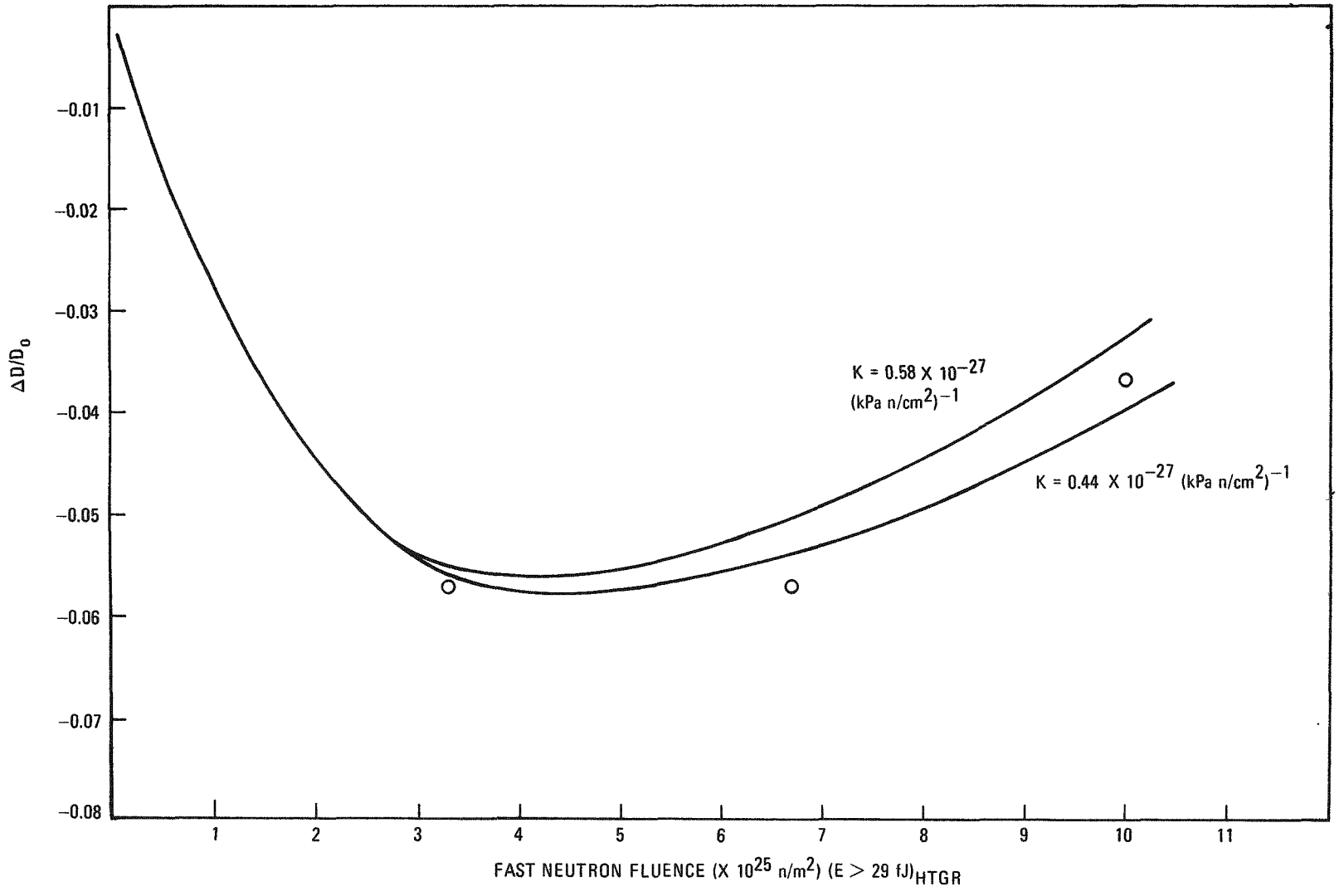

Fig. 9-68. Comparison of calculated and measured diametral changes of BISO particles irradiated in position 40 using dimensional changes for a coating with a density of 1.75 Mg/m^3

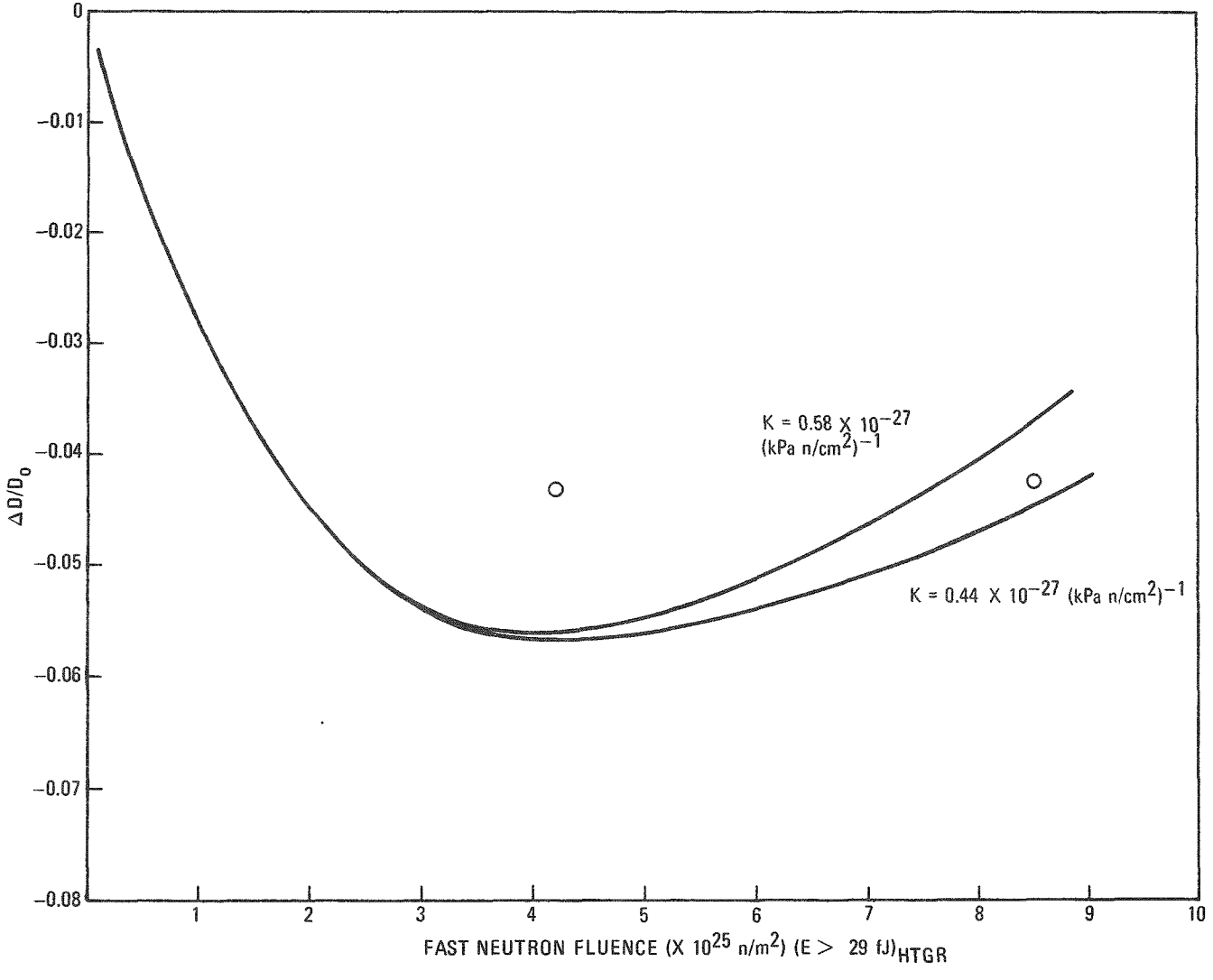

Fig. 9-69. Comparison of calculated and measured diametral changes of BISO particles irradiated in position 27 using dimensional changes for a coating with a density of 1.75 Mg/m^3

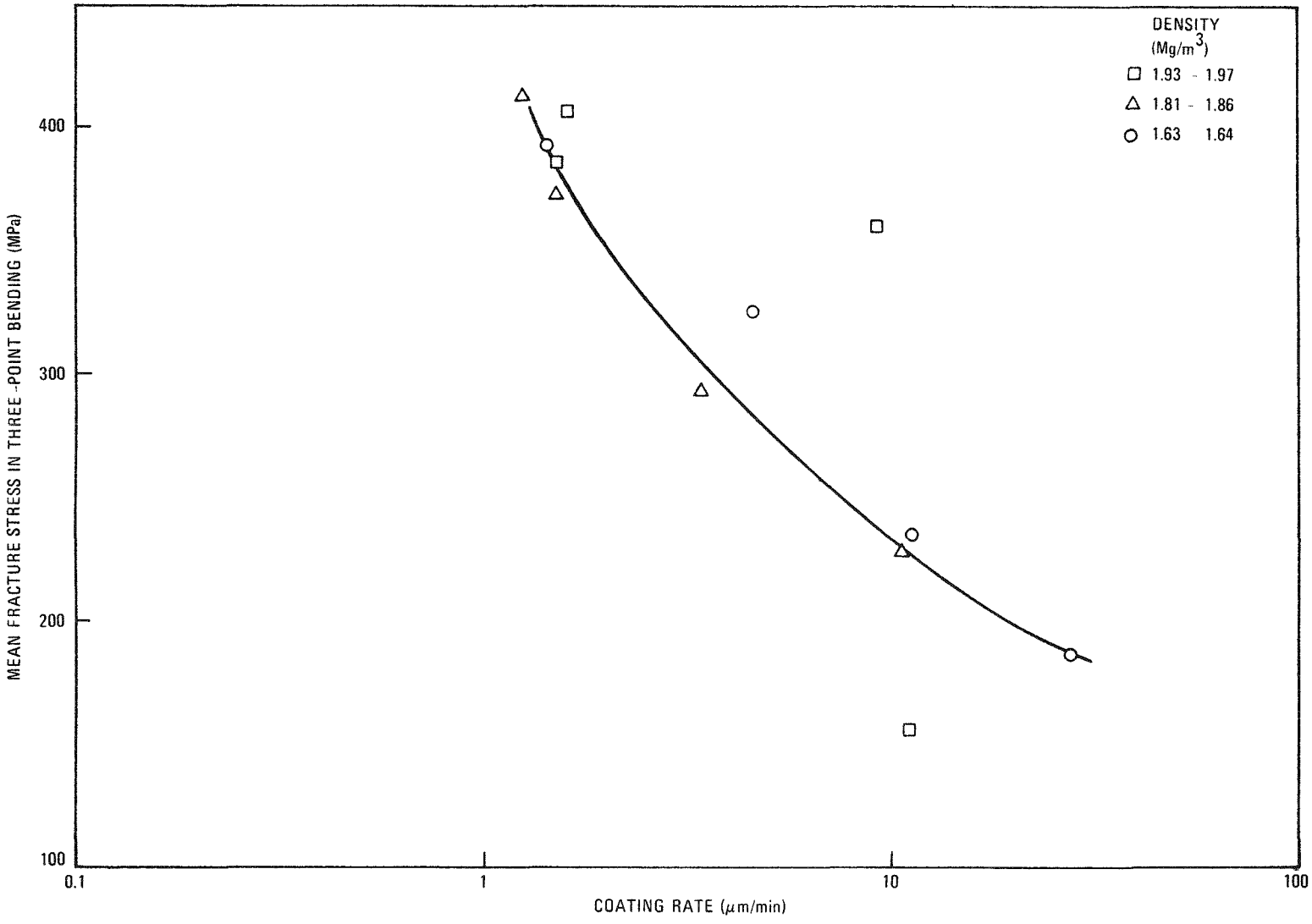

Fig. 9-70. Mean fracture strength of pyrocarbon strips measured in three-point bending

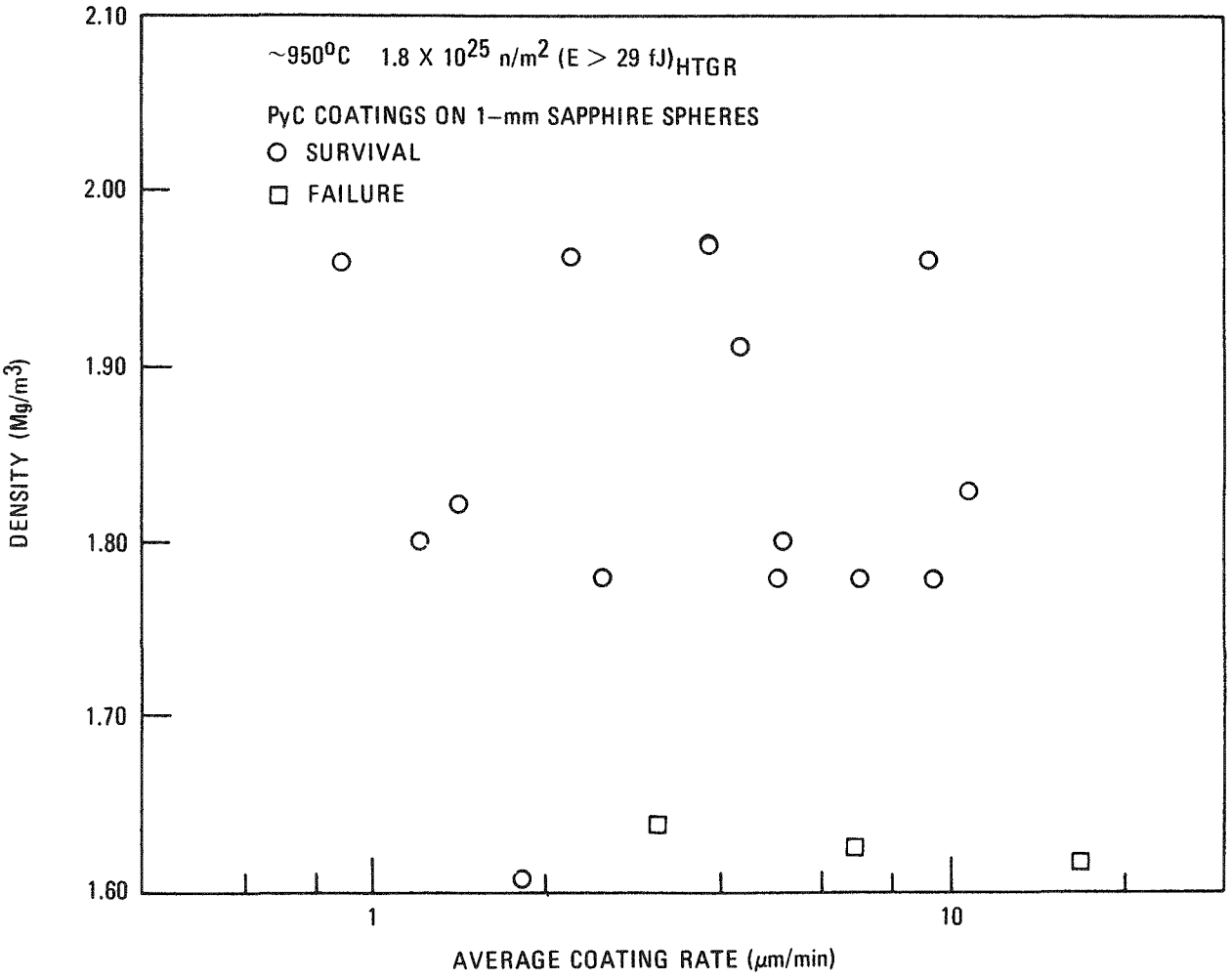

Fig. 9-71. Behavior of coatings irradiated restrained on sapphire spheres (a) capsule HT-20

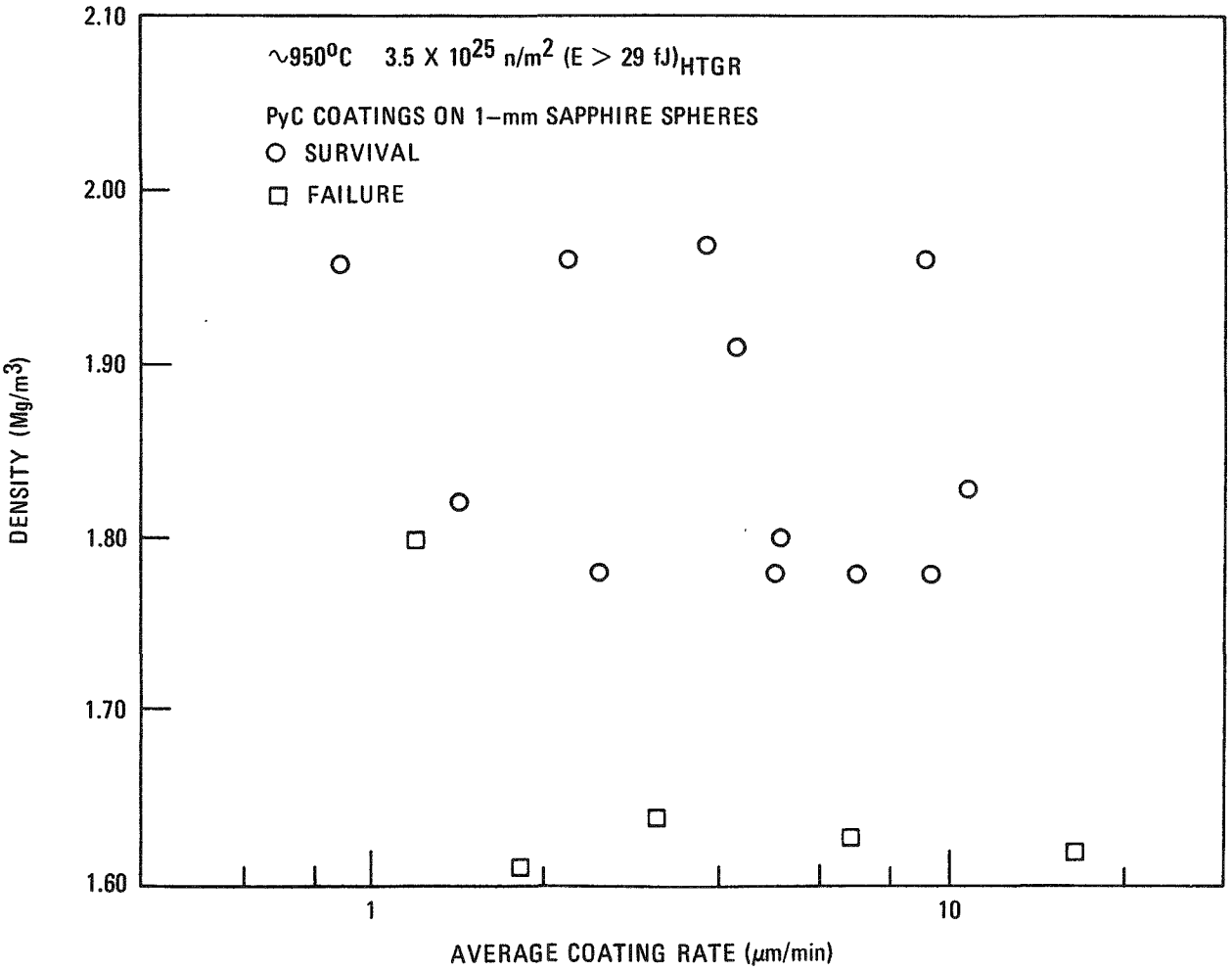

Fig. 9-71. Behavior of coatings irradiated restrained on sapphire spheres (b) capsule HT-23

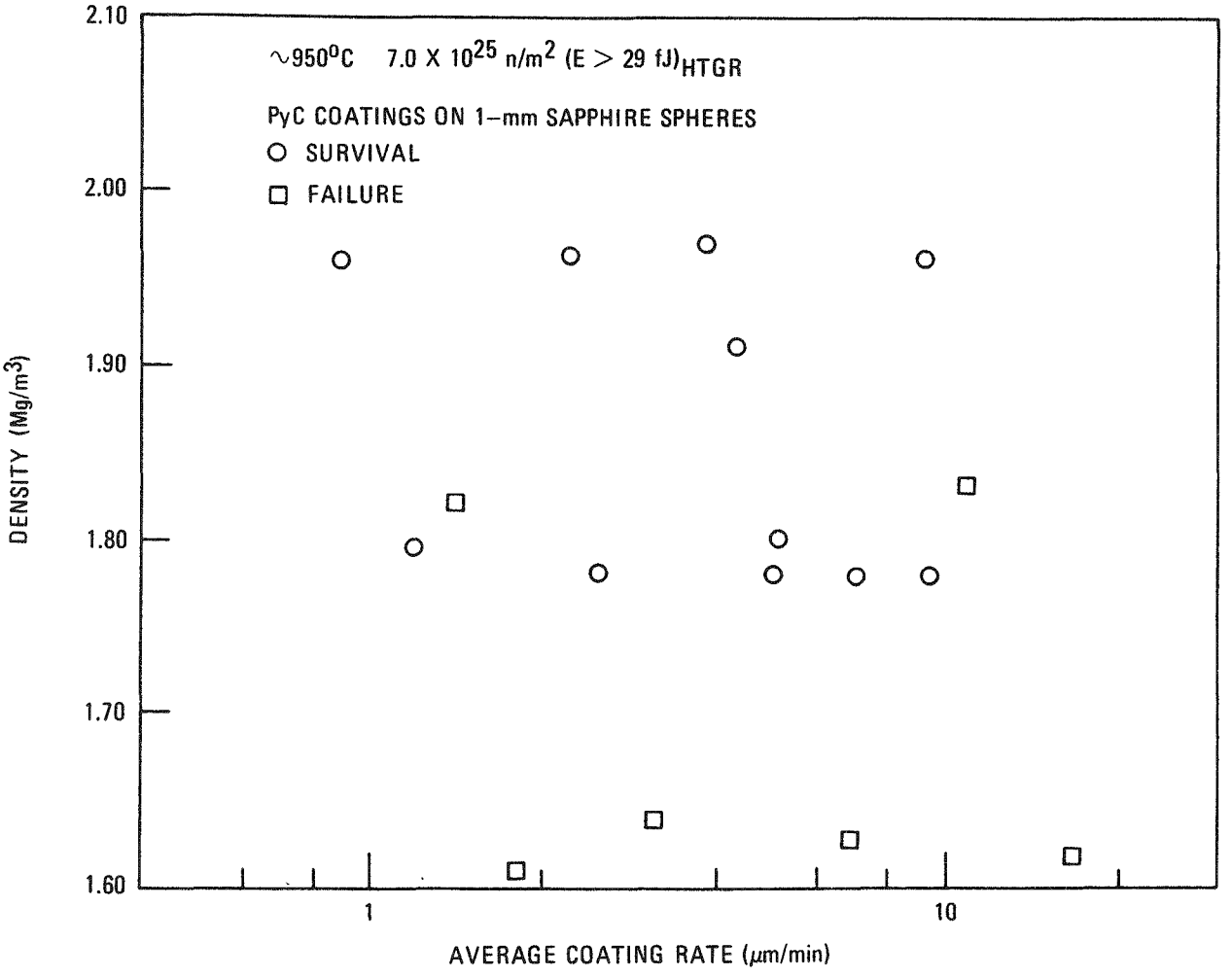

Fig. 9-71. Behavior of coatings irradiated restrained on sapphire spheres (c) capsule HT-22

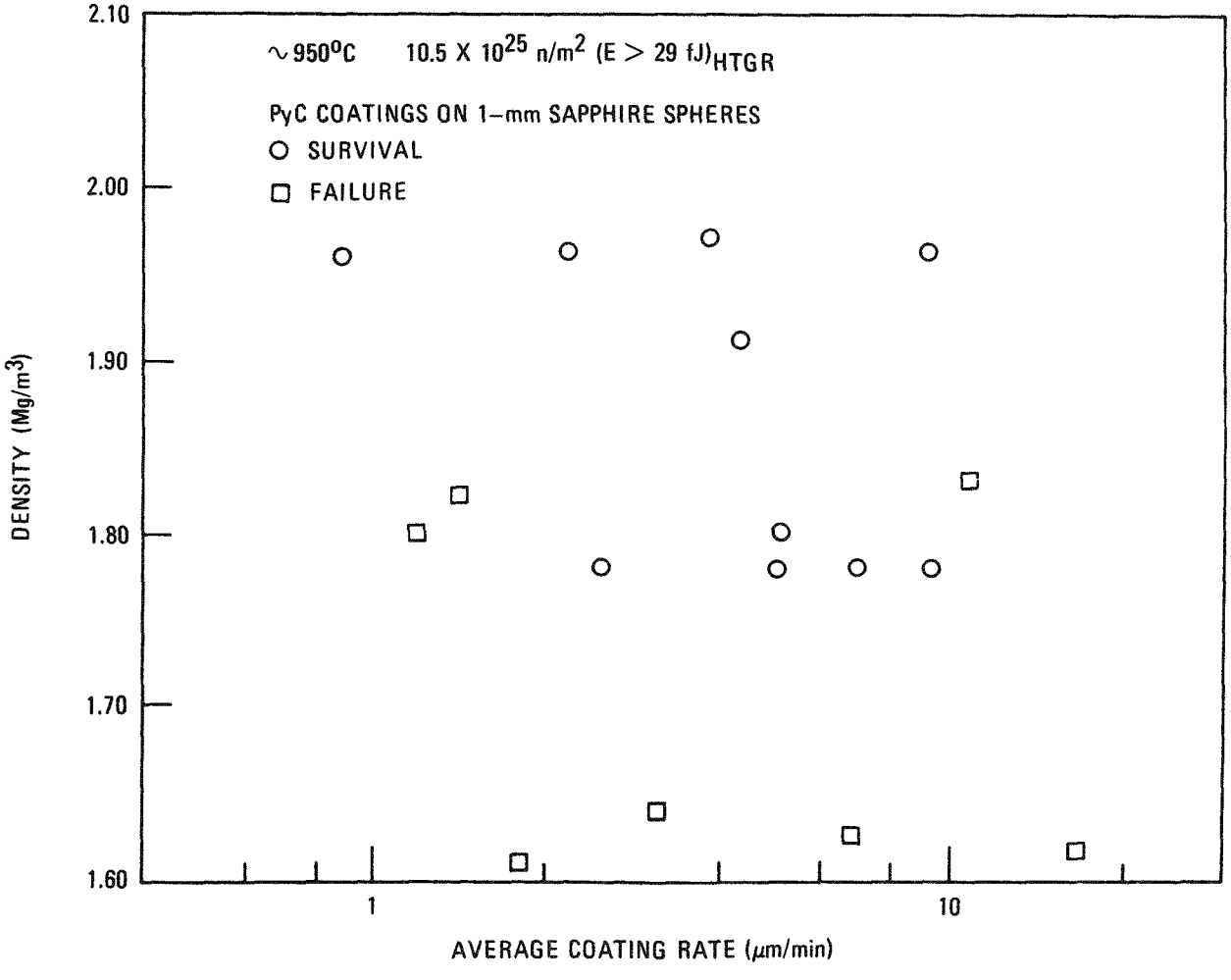

Fig. 9-71. Behavior of coatings irradiated restrained on sapphire spheres (d) capsule HT-21

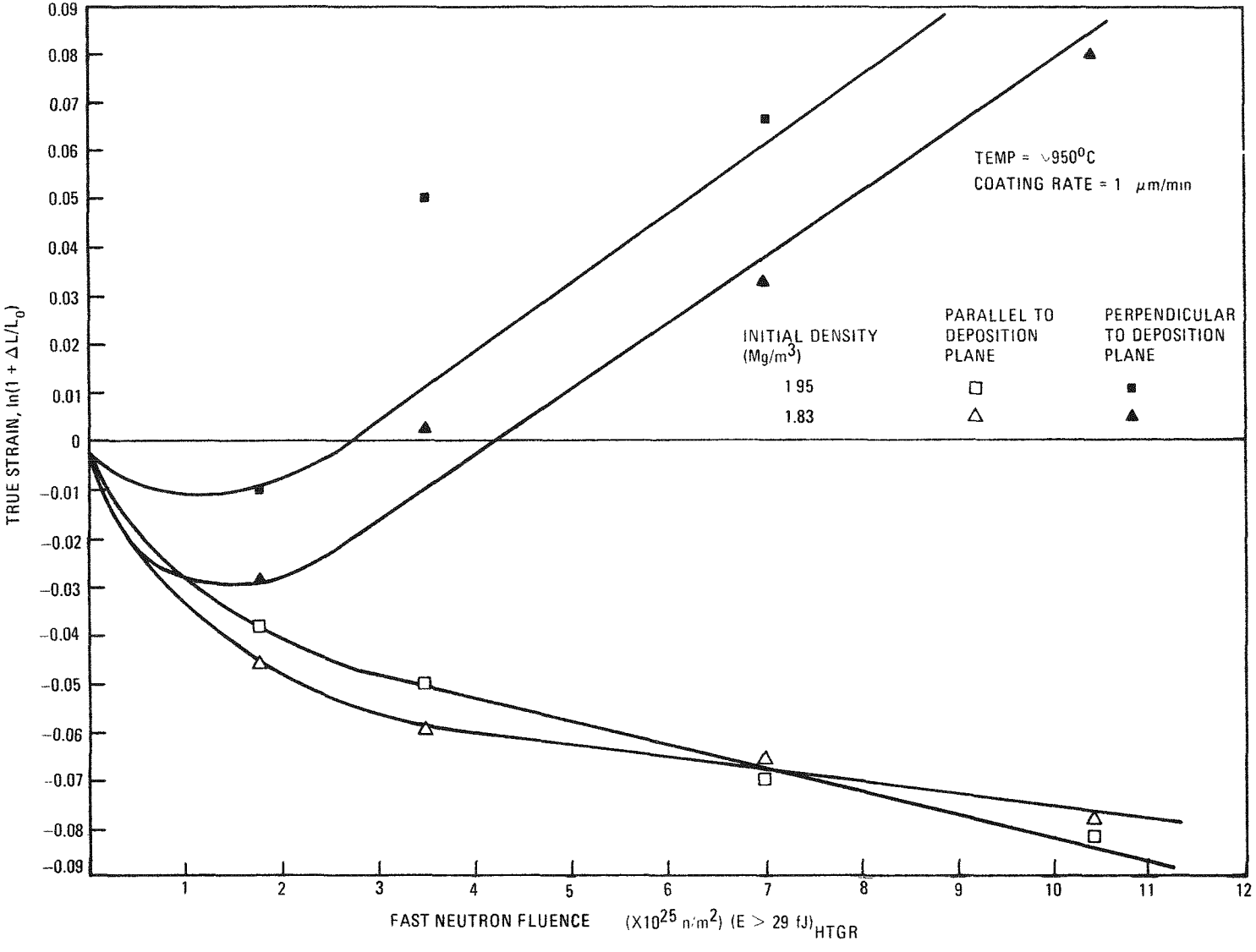

Fig. 9-72. Dimensional changes of pyrocarbons: (a) deposited at a rate of 1.0 μm/min

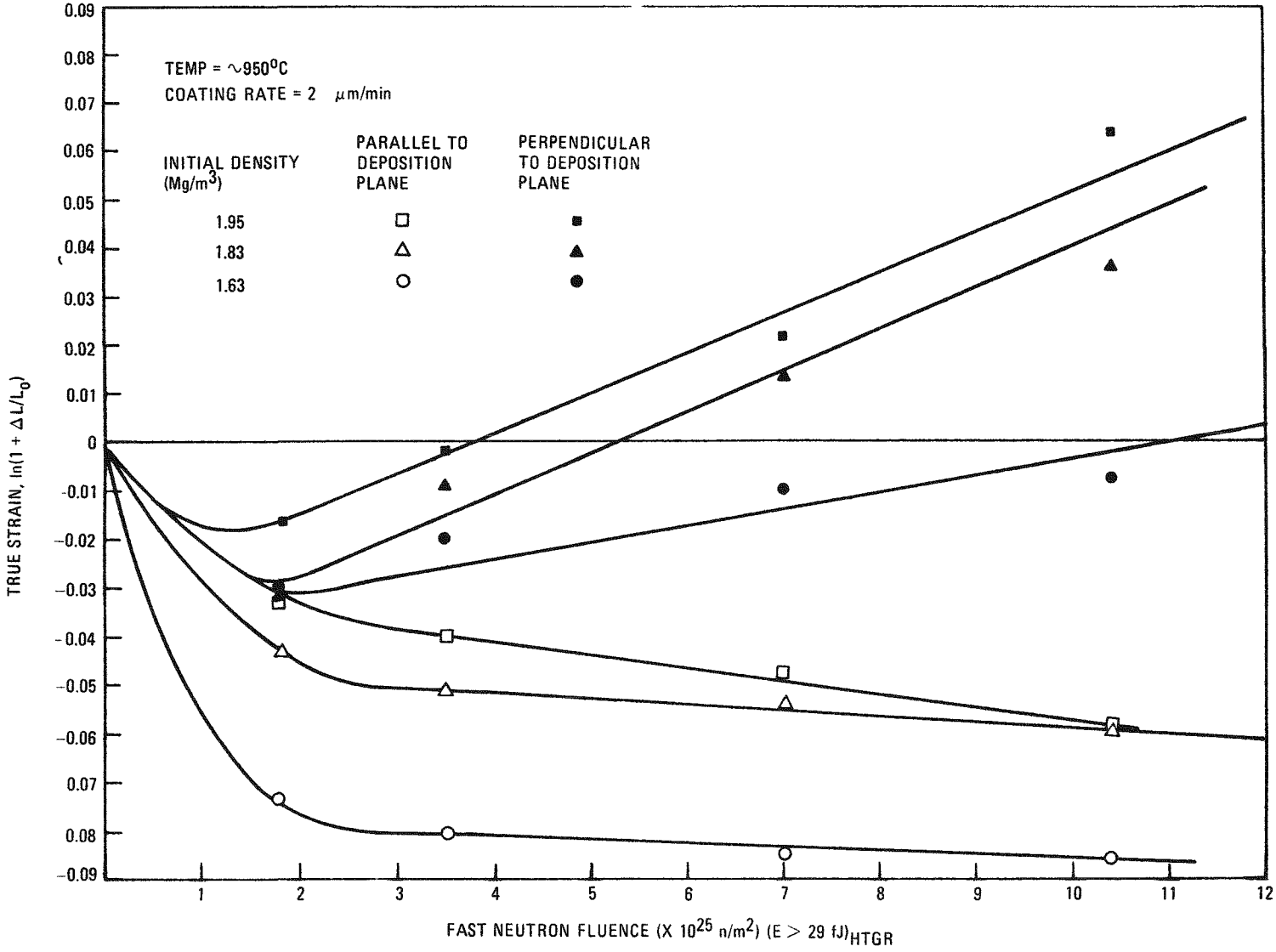

Fig. 9-72. Dimensional changes of pyrocarbons: (b) deposited at a rate of 2.0 μm/min

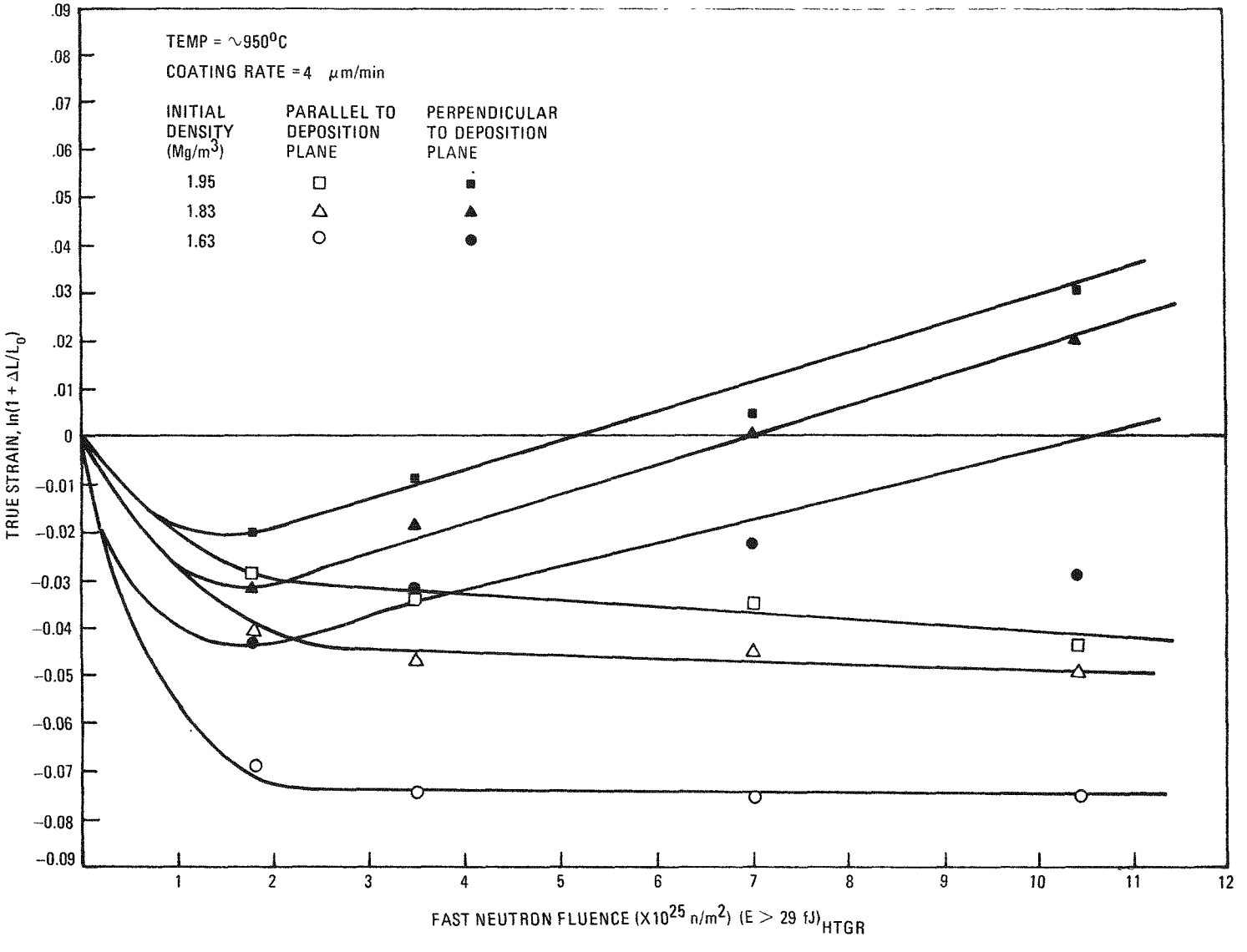

Fig. 9-72. Dimensional changes of pyrocarbons: (c) deposited at a rate of 4.0 μm/min

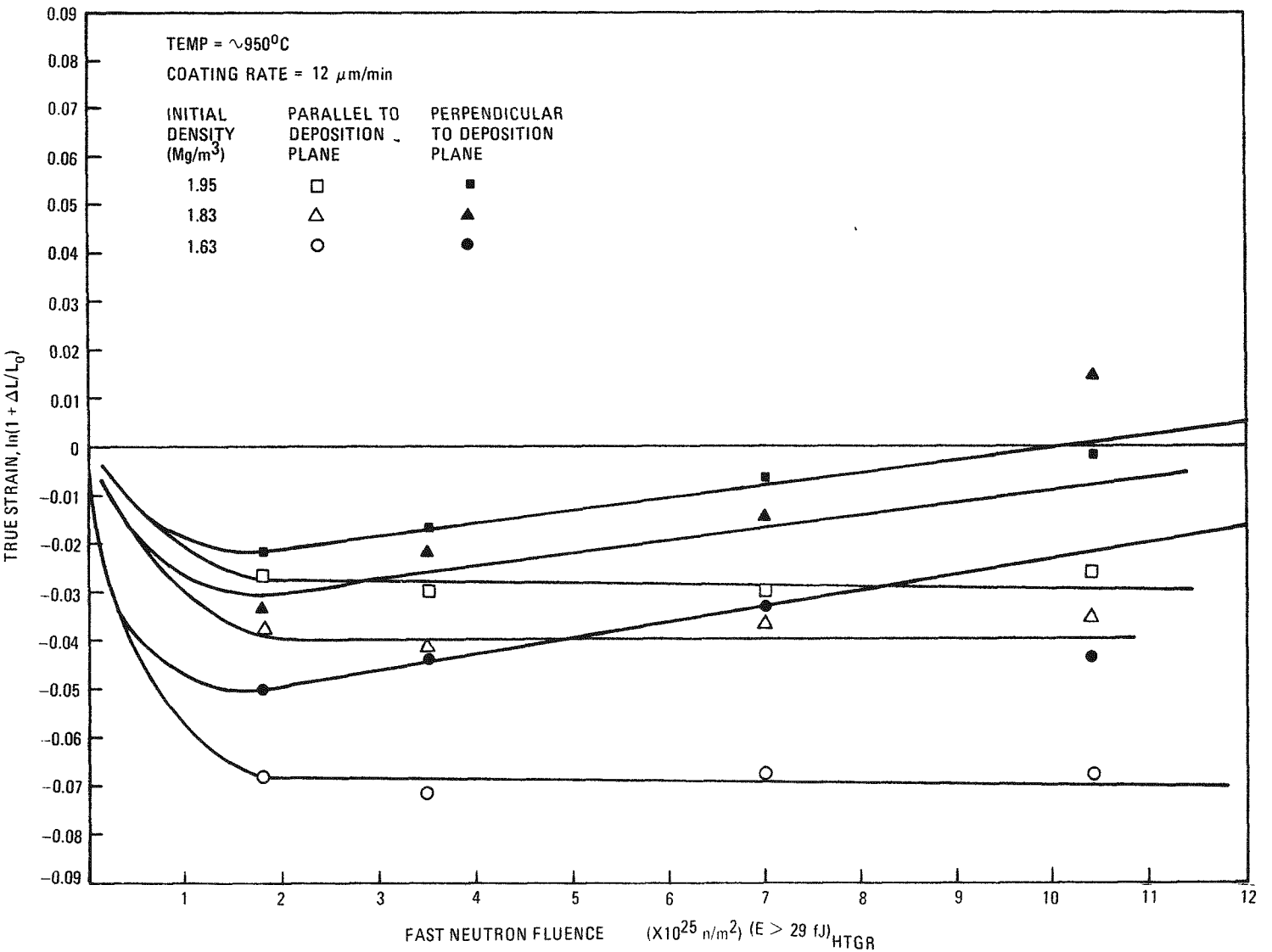

Fig. 9-72. Dimensional changes of pyrocarbons: (d) deposited at a rate of 12.0 μm/min

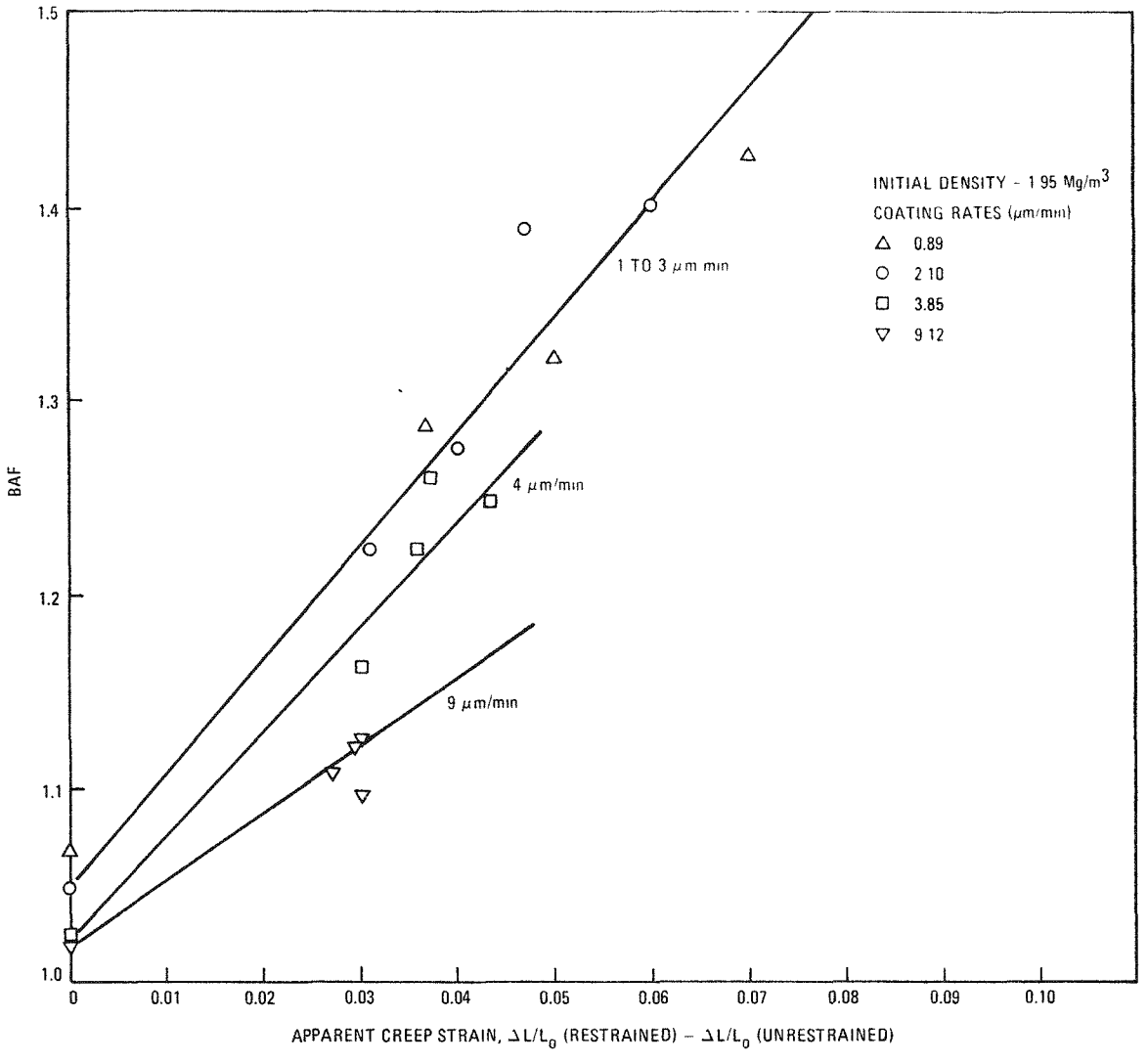

Fig. 9-73. Preferred orientation changes of restrained high-density carbons during irradiation

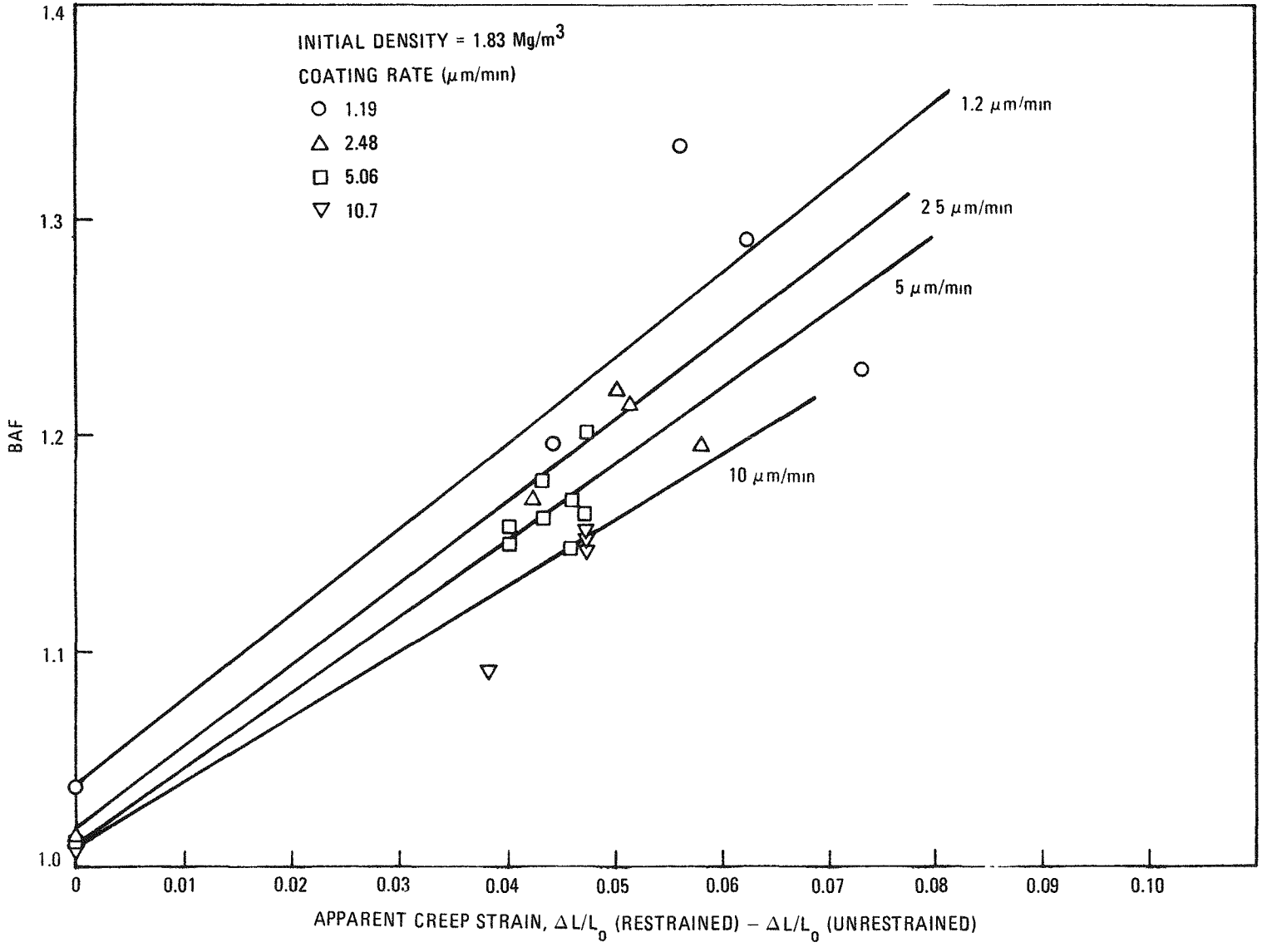

Fig. 9-74. Preferred orientation changes of restrained intermediate-density carbons during irradiation

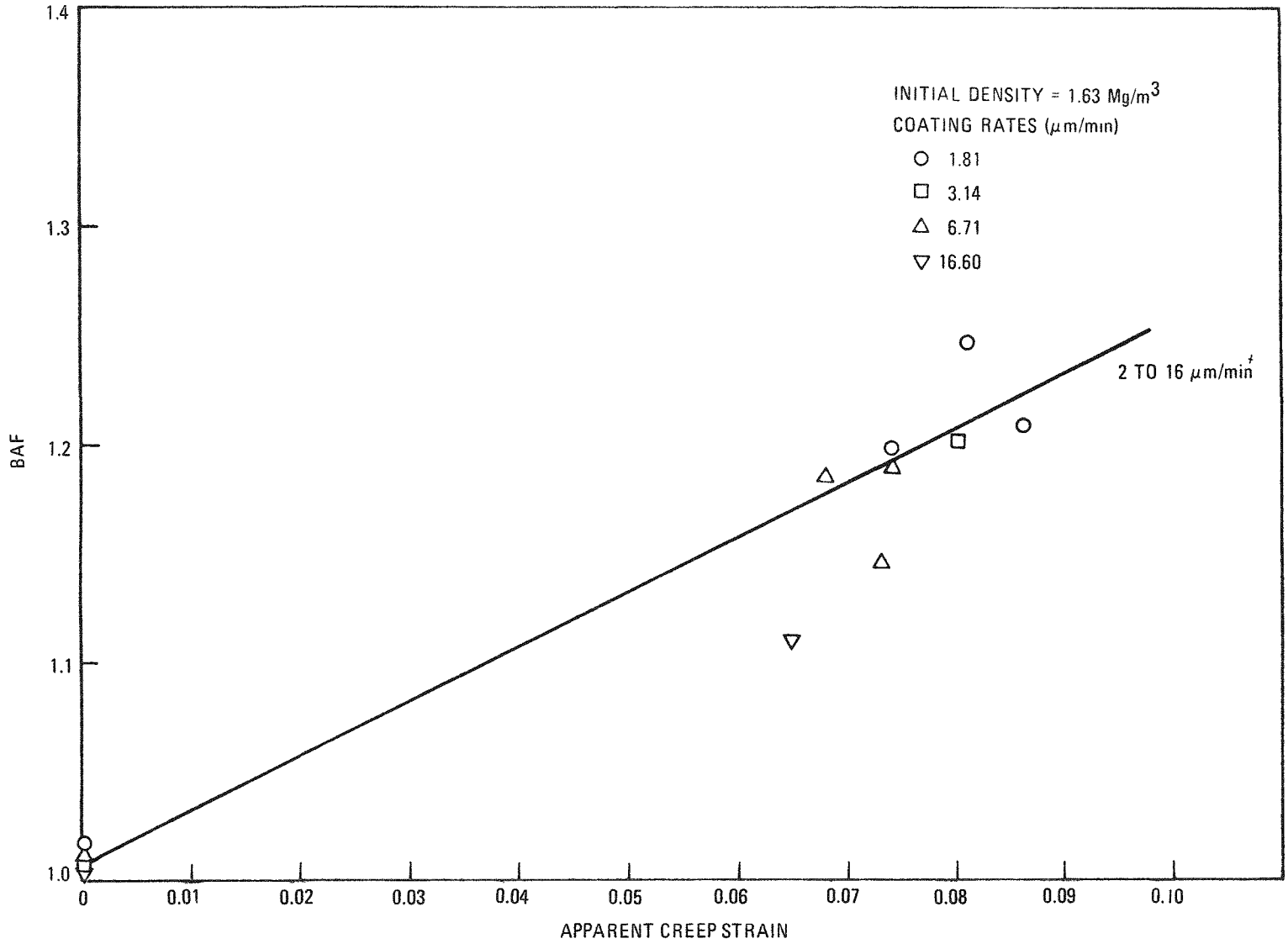

Fig. 9-75. Preferred orientation changes of restrained low-density carbons during irradiation

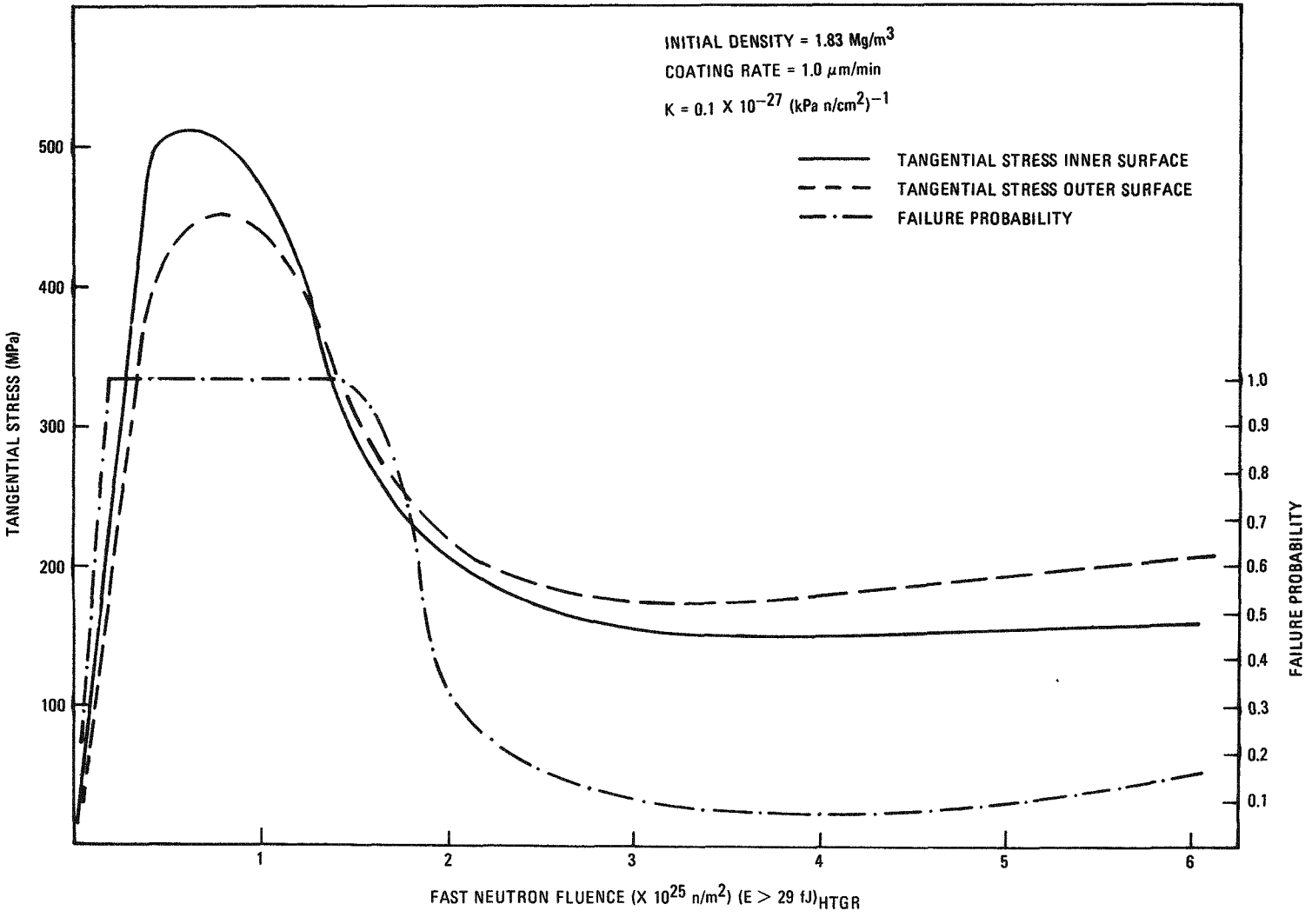

Fig. 9-76. Calculated stresses and failure probability of a low-coating-rate intermediate-density carbon using a constant value of K

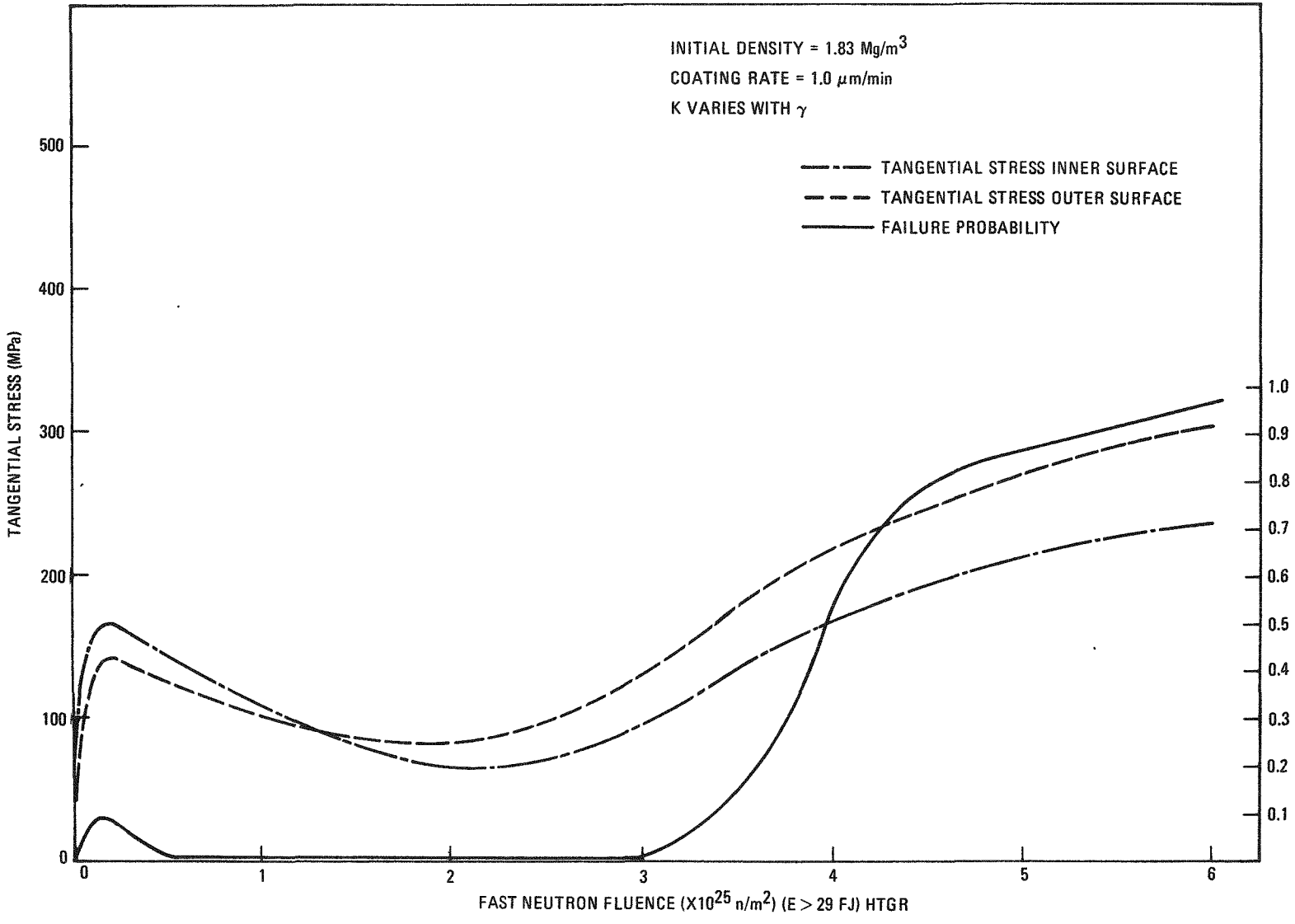

Fig. 9-77. Calculated stresses and failure probability of a low-coating-rate intermediate-density carbon using the determined variation of K

11. GRAPHITE DEVELOPMENT
189a NO. SU004

In the past the graphite development program has been confined to evaluating candidate materials for replaceable fuel and reflector elements. Beginning in the last half of FY-76, the work scope of Task 11 has been broadened to include evaluation of the candidate graphites for the permanent side reflector and core support posts, seats, and floor blocks.

TASK 100: FABRICATION AND OPERATION OF IRRADIATION CAPSULES IN THE ORR

Capsule OG-3

Capsule OG-3 was disassembled in the GA Hot Cell and all specimens were recovered without incident.

Capsule OG-4

Capsule OG-4 was designed to have a different range of operating temperatures than other capsules in the OG-series. Because of program changes, work on this capsule has been suspended. Test plans, drawings, design documents, and some hardware are being retained in case of future re-instatement.

Capsule OG-5

Capsule OG-5 is the successor to capsule OG-3 and has identical thermal design. The combination of a delay in the production schedule of Fort St. Vrain reload segment 9 (FSV-9) material and refueling delays at the Oak Ridge Reactor have caused a postponement of the insertion date for OG-5 from September 1976 until early 1977.

TASK 200: GRAPHITE SPECIMEN PREPARATION AND PROPERTY MEASUREMENT FOR CAPSULE IRRADIATIONS

Capsule OG-3

Postirradiation dimensional measurements of all graphite specimens have been completed and the data are being transferred to magnetic tape for computer storage and analysis. About 30% of the postirradiation measurements of thermal diffusivity and thermal expansivity have been made. Postirradiation measurements of Young's modulus and tensile strength of 215 specimens will start in May.

Analysis of the operating temperatures and fluences in capsule OG-3 is in progress. The physical property measurements will be published when analyses of temperatures and fluences are finalized.

Capsule OG-5

The main objectives of the OG-5 experiment are to compare the irradiation performance of two preproduction lots of Great Lakes Carbon Corporation (GLCC) near-isotropic H-451 graphite (lots 426 and 440, made with coke blends from different sources) and a production-scale lot of H-451 being produced for Fort St. Vrain reload segment 9 (FSV-9). A test plan (TP-325-005) has been written and has received Approval-In-Principle from ERDA.

TASK 300: CHARACTERIZATION OF CANDIDATE GRAPHITES FOR PROPERTIES AND PURITY

Fuel Element and Reflector Graphites

Characterization of Great Lakes Carbon Company (GLCC) grade H-451, Union Carbide Corporation (UCC) grade TS-1240, and AirCo Speer (AS) grade S0818 was continued.

Grade H-451 (GLCC)

Characterization of GLCC grade H-451 lot 440 has been completed, and additional strength, thermal conductivity, and purity measurements have been made on specimens from lot 426. The data are reported herein. This completes the characterization work on selected logs from lots 266, 408, 426, and 440. The previous data for lots 266, 408, and 426 were reported in Refs. 11-1 and 11-2.

Approximately 350 logs of H-451 have been produced for Fort St. Vrain reload segment 9 (FSV-9). This is the first production order of grade H-451. This order is based on the formulation and processing of preproduction lot 426. Approximately 30 logs will be set aside at GA from FSV-9 for experimental work during the next 2 to 3 years. Four logs will be purchased by Brookhaven National Laboratory (BNL) and eight by Oak Ridge National Laboratory (ORNL) for their experimental work. Approximately four of the FSV-9 logs will be selected for characterization studies at GA.

Lot 426. Additional thermal conductivity data on specimens from log 6484-41 (GLCC log 184) are presented in Table 11-1.* Flexural strength data on specimens from logs 6484-40 (GLCC log 155) and 6484-41 (GLCC log 184) are presented in Table 11-2.

A specimen was taken from a H-451 log [lot 426, log 6484-34 (GLCC log 198)] pulverized in a laboratory mill to <44-micron particle size, riffled into six equal and representative samples for GA, BNL, ORNL, GLCC, UCC, and AS for low-temperature ashing and subsequent spectrochemical analyses of the ash. The purpose of this exercise, which is a part of ASTM Nuclear Committee C5:05 on graphite standards, is to establish a procedure for measuring the burnable and nonburnable boron equivalent impurity concentrations in fuel element graphites. The data will be published as an ASTM research report along with the ASTM standard when the latter is published. Results from four laboratories were in excellent agreement. It is apparent

*Tables appear at the end of Section 11.

from this work, which was done on highly concentrated samples thus lowering the detection limits, that it may be possible to eliminate certain elements from consideration for analysis based on evidence that these elements are far below assumed concentrations based on previous analyses where the detection limits were much higher. This concept is being pursued by the ASTM Nuclear Committee task force on analytical techniques to develop an analytical procedure which, if successful, should greatly increase the confidence and accuracy of the boron equivalent values measured on the candidate materials.

Lot 440. Thermal conductivity data for log 6484-55 (GLCC log 63) are presented in Table 11-3. Flexural strength data for logs 6481-54, -55, and -56 (GLCC logs 19, 63, and 65) are presented in Tables 11-4 through 11-6.

Impurity content data, obtained by spectrochemical analyses, for log 6484-57 (GLCC log 68) are presented in Table 11-7. Data on the ash and sulfur content are given in Table 11-8.

Grade SO818 (AS)

The work presented in this quarterly report completes the characterization of the first lot (AS lot 4B) of SO818 graphite logs. The impurity content has been measured on selected logs from a second lot (AS lot 5B), but measurements of additional properties has been suspended while work is concentrated on the candidate materials for core support and side reflector components.

Lot 4B. Thermal conductivity data for log 6484-19 (AS log 13) are presented in Table 11-9. Flexural strength data for logs 6484-19 and -20 (AS logs 13 and 16, respectively) are presented in Table 11-10.

The lithium impurity concentration was found to be <10 ppb when measured on a composite specimen taken from log 6484-19 (AS log 13), prepared by mixing samples from the MLC, MLE, EC, and EE positions.

Lot 5B. Impurity content data obtained by spectrochemical analyses for lot 5B, logs 6484-59, -60, -61, and -62 (AS logs 118, 113, 144, and 161, respectively) are presented in Tables 11-11 through 11-14. Data on the ash and sulfur content are given in Table 11-15.

Side Reflector Graphites

A half log of HLM graphite, which is a candidate material for the side reflector block, was purchased from GLCC. Specimens are being prepared for characterization measurements. Grade HLM is a coarse-grained graphite manufactured by a conventional extrusion process. The full-size HLM log is 1.14 m (45 in.) in diameter by 1.83 m (72 in.) long.

Core Support Post and Seat Graphites

Two logs of commercial grade 2020 have been purchased from the Stackpole Carbon Company (SC) and a half log of preproduction H-440 graphite has been purchased from GLCC for characterization measurements. An additional small sample of H-440P (ash content about 300 ppm) has also been acquired for evaluation. Grades 2020 and H-440 are fine-grained graphites manufactured by an isotstatic molding procedure in 0.254 m (10 in.) diameter by 1.83 m (72 in.) to 2.1 m (83 in.) long logs.

One block of commercial grade ATJ graphite was purchased for characterization measurements. ATJ graphite is a fine-grained graphite manufactured by a conventional molding process. The ATJ block is 0.2 m (8 in.) by 0.43 m (17 in.) by 1.83 m (72 in.).

A block of grade PGX graphite, which is a candidate graphite for the core support floor blocks, was purchased for characterization measurements. PGX is a coarse-grained graphite manufactured by a conventional process. The PGX log is 1.14 m (45 in.) in diameter by 1.83 m (72 in.) long.

TASK 400: STATISTICAL STUDY OF GRAPHITE STRENGTH

Introduction

Work on this task was started in FY-74 and preliminary results were reported in two earlier reports (Refs. 11-3 and 11-4). Work was resumed in FY-76 and the experimental tests were completed in the current quarter. A topical report is in preparation; consequently, only a summary is given here.

A single log of H-451 graphite [lot 408, log 5651-90 (GLCC log 48)] was cut into sections. Tensile specimens of two sizes and flexural specimens were taken in both axial and radial directions from locations covering most of the log. More than 2000 specimens were tested to failure at ambient temperature. The objectives of the experiment were as follows:

1. Provide a map of the systematic variation in strength with location in a typical log.

2. For specimens of a given type, orientation, and location, measure the statistical distribution of strength values and estimate the mean, standard deviation, coefficient of variation, and Weibull modulus of the population.

3. For specimens of a given orientation and location, determine the strength difference between the large and small tensile specimens.

4. For specimens of a given orientation and location, determine the ratio between tensile strength and flexural strength.

5. Compare the strength distribution, specimen size effect, and flexural-to-tensile strength ratio with the predictions of the Weibull theory for the strength of brittle solids.

Experimental

Test specimens were taken from four 127-mm (5-in.) deep slabs transverse to the axis of the original log. Two slabs (1 and 4) were within 25 mm (1 in.) of the two ends of the log, and two slabs (2 and 3) were adjacent to the midlength plane of the log. The slab locations are shown in Fig. 11-1.* Cylindrical cores for test specimens were taken in both axial and radial orientations from a central zone and an edge zone of each slab according to the plan shown in Figs. 11-9 and 11-10 of Ref. 11-3. Large tensile specimens [12.8 mm (0.505 in.) diameter by 76 mm (3.0 in.) long], small tensile specimens [6.4 mm (0.25 in.) diameter by 23 mm (10.9 in.) long], and flexural specimens [6.4 mm (0.25 in.) diameter by 51 mm (2.0 in.) long] were machined from the cores. After cementing metal end pieces to the tensile specimens with epoxy cement, the specimens were tested to failure. The flexural specimens were tested in four-point bending with the loading points spaced 12.7 mm (0.5 in.) apart. The flexural test results were calculated in two ways: (1) uncorrected modulus of rupture from simple beam theory; and (2) corrected flexural strength, representing the outer fiber stress at failure after allowing for the nonlinearity of the stress-strain curve.

Results

The mean strengths, together with standard deviations, coefficients of variation, and Weibull moduli are summarized for slabs 1 through 4 in Tables 11-16 through 11-19. The data showed the usual systematic dependence on orientation and log location, with mean axial strengths consistently higher than mean radial strengths at the same location. Coefficients of variation for radial specimens tended to be higher than for axial specimens. Centerline strengths were lower than edge strengths, with a greater difference apparent in the midlength slabs (2 and 3) than in the end slabs (1 and 4).

---

*Figures appear at the end of Section 11.

In addition to these predictable location effects, some slabs showed a significant second-order variation of strength with location. These local variations in strength, together with the corresponding local variations in density, are illustrated in Figs. 11-2 through 11-17. These figures are maps showing the locations of individual specimens. Open circles or semicircles represent specimens whose strength or density is more than half a standard deviation below the mean for their slab, orientation, and specimen type; half-filled circles or semicircles represent average strength or density (within half a standard deviation); and completely filled circles or semicircles are specimens with high strength or density. For example, in the outer zone of slab 1 (Fig. 11-3) the radial specimens from the upper left-hand quadrant tended to be weaker than their average, while the axial specimens in the lower quadrant tended to be strong. The corresponding map of densities (Fig. 11-2) showed a similar trend in density for the same two specimen groups. The tendency for axial specimens from the lower quadrant of the edge zone to be stronger than average was evident in all four slabs (Figs. 11-3, 11-7, 11-11, and 11-15), suggesting that a zone of higher density and strength material runs through the length of the log.

The small [6.4 mm (0.25 in.) diameter] tensile specimens averaged 5% stronger than the large [12.8 mm (0.505 in.) diameter] tensile specimens. Weibull theory predicts a much greater size effect; for a Weibull modulus of 9, the predicted strength ratio would be 1.34.

Four-point bend strengths (corrected for nonlinearity of the stress-strain curve) averaged 53% higher than the tensile strengths of companion 6.4-mm (0.25 in.) diameter tensile specimens. This is in good agreement with the value of 59% predicted from Weibull theory with a Weibull modulus of 9. Coefficients of variation for bend strengths tended to be smaller than for tensile strengths, which is contrary to the predictions of Weibull theory.

The mean four-point bend strength is plotted against the mean tensile strength of companion 6.4-mm (0.25 in.) diameter specimens in Fig. 11-18. Each data point represents one orientation, slab, and zone (center or

edge). The correlation is good (correlation coefficient = 0.88). When bend strengths are plotted against the mean tensile strength of 12.8-mm (0.505 in.) diameter specimens (Fig. 11-19), the correlation is a little better (correlation coefficient = 0.92).

The cumulative strength distributions for each specimen group was compared with both the Weibull and the Gaussian distribution function. In most cases the data tended to straddle the lines for both distributions, with no clear tendency to conform to one or the other.

It can be concluded that, while the ratio of bend strength to tensile strength for H-451 graphite is about as predicted by Weibull theory, the material does not meet other criteria which would qualify it as a Weibull solid.

TASK 500: FATIGUE BEHAVIOR OF GRAPHITE

Introduction

A series of uniaxial fatigue tests at ambient temperature on axial specimens of H-451 graphite has been completed. Preliminary results were reported in earlier quarterly reports (Refs. 11-2 and 11-5). These earlier results have been reanalyzed and all the data are included in the present report.

Material

H-451 graphite specimens were taken from log 5651-90 (GLCC lot 408, log 48). The parent log was 430 mm (17 in.) in diameter by 860 mm (34 in.) long. The specimens were cored from a localized zone between 25 and 100 mm (1 and 4 in.) from the edge of a transverse slab 150 mm (6 in.) thick, whose faces were 150 and 300 mm (6 and 12 in.) from the end of the log (slab 5B, Fig. 11-1). The location of the individual cores in slab 5B is shown in Fig. 11-20. Each 150-mm (6-in.) long core was machined into five cylindrical test specimens 12.7 mm (0.5 in.) in diameter by 25.4 mm (1 in.)

practice for metals is to deduce the limits from the dispersion of log N values for a single stress setting, treating the data for each stress setting as a sample from a separate population. However, this procedure has several disadvantages when applied to fatigue measurements on graphite. Because of the inherent scatter in the data and the small number of specimens (7 to 10) tested at each stress setting, the tolerance limits calculated by the conventional method are erratic and, in most cases, unreasonably wide. In addition, tolerance limits can be computed only from groups of data containing no runouts, which restricts analysis to the high-stress, low-cycle regime. To avoid these difficulties, the following alternative statistical model was used:

$$\log(S) = \alpha + \beta \log(N) + \varepsilon \quad , \tag{11-1}$$

where S is the maximum stress during a cycle, N is the number of cycles to failure, α and β are constants, and ε (the error term) is a random variable distributed normally with a mean of zero and a variance of σ^2. This model is physically reasonable for graphite because the primary cause of the scatter in the data is the inherent variability in graphite strength.

The data were analyzed according to the statistical model of Eq. 11-1, including the tensile tests at N = 0.25 but omitting the specimens which ran out beyond 10^5 cycles. The mean line through the data and the lower tolerance limits (representing the limits above which at least x% of the data fall, with y% confidence) were constructed using standard statistical methods. The results are shown in Figs. 11-21 through 11-24 for the x/y combinations 90/90, 95/95, and 99/95. The figures support the linear relationship between log(S) and log(N) assumed in the model (Eq. 11-1).

TASK 600: STRUCTURAL INTEGRITY OF GRAPHITE BLOCKS

Residual Stress Analysis

Introduction and Summary

The Phase I stress analysis of Peach Bottom fuel test element FTE-4 has been completed (pp. 11-16 and 11-17 of Ref. 11-2). Residual stresses at the end-of-life and stresses due to primary loadings were calculated. It was calculated that a 0.45-m (18 in.) long strip will bow as much as 3.3 mm (0.13 in.) when the bending moment due to residual stresses is relieved. The analytical results have indicated the experiments that should be performed to verify the calculated effects of the residual stresses.

Analytical Procedure

The GTEPC computer code, a two-dimensional finite element program (Ref. 11-6), was used for temperature and stress computations. In computing residual stresses, a 0.393 rad (22.5 deg) sector of the eight-hole teledial element was idealized by a mesh of triangular elements (Fig. 11-26). A standard solid model (Ref. 11-7) was adopted to account for the irradiation-induced creep in graphite. Material constants were obtained from Ref. 11-8.

The residual stress depends on the thermal and irradiation history. In calculating the thermal boundary conditions and neutron doses at various times during Core 2 operation, a one-dimensional computer program was used (Ref. 11-9). A typical result at axial position 23 [approximately 1.71 m (67.5 in.) from the bottom of the core] is given in Table 11-25. In addition to the finite element model for the graphite, the fuel rod and the graphite sleeve were also included for thermal computations (Fig. 11-27).

The heat transfer across the gap between the fuel rod and the graphite was treated by defining the emissivities (0.89 for fuel and 0.87 for

graphite) and the gas conductivity ($3.32 \times 10^{-3}\ T^{0.674}$ W/m^2-K), where T is the computed gas temperature in K. Because of the small temperature variation along the gap between the graphite and the sleeve, the constant gas conductances given in Table 11-25 were used in the computation. The coolant temperature and the film coefficient were used to define the boundary condition at the outer surface of the sleeve. The thermal computations were carried out using the thermal conductivities and the heat generation rates given in Table 11-25. Assuming the graphite was subjected to no external forces, the operating and the shutdown stress fields resulting from the temperature differential and the neutron dose were computed.

In computing stress under primary loadings, a 1.57 rad (90 deg) sector model with the boundary conditions indicated in Fig. 11-28 was used.

Results and Discussion

The residual stress contours are given in Figs. 11-29 through 11-32. A maximum in-plane stress of 11.0 MPa (1600 psi) was calculated next to the slot cut into the inside of the element (Fig. 11-31). The slot was originally cut to assure that any breakage of graphite due to swelling of fuel rods would be confined to the inside diameter of the element and would not lead to release of fuel particles into the coolant stream. No visible cracks were found during the preliminary examination of the test element in spite of the fact that the mean strength of H-327 graphite in the radial direction is 9.3 MPa (1350 psi) or less. If specimens for pressure burst and compressive loading tests can be cut without cracking the fragile web between the slot and fuel hole, then detailed stress analyses with finer mesh around the slot will be carried out in the Phase II stress analysis to develop a more accurate estimate of the peak stress.

The axial residual stress contours shown in Fig. 11-32, are used to estimate the bow for strip cutting experiments. Since the axial stress varies approximately linearly in the radial direction, strips cut as

indicated in Fig. 11-32 will bow to relieve most of their residual stress. The radius of curvature for the strip is estimated to be 31.8 m (104.3 ft) for strip 1 and 15.4 m (50.5 ft) for strip 2, which gives displacements at the midlength of a 0.45-m (18 in.) long strip of 1.59 mm (0.063 in.) and 3.3 mm (0.13 in.), respectively.

The stress contours under a compression load are given in Figs. 11-33 through 11-35, and the stress contours under a hydrostatic pressure load applied to the walls of the fuel holes are given in Figs. 11-36 through 11-38. A maximum stress of 33 MPa (4787 psi) occurs next to the slot due to the arbitrarily selected compression load of 25.4 kN/m (145 lb/in.) at the outer surface of the graphite. A 100 kPa (14.5 psi) pressure load at the inner surface of a fuel hole produces a maximum stress of 500 kPa (72.5 psi), also next to the slot. The calculations indicate that a cross section adjacent to the slot will be the first to fail under primary loadings since the peak primary stress and the peak residual stress are both found in this location.

The results also suggest that primary loading tests be carried out in such a way that failure across a section with low residual stress, such as section A-A in Fig. 11-31, can also be induced by a measured primary load. This would allow the comparison of the primary stress at failure in the absence of significant residual stress with the primary stress at failure in the presence of high residual stresses, on the order of the strength of the graphite. One possible way to do this would be to place a dowel in the central hole of the teledial element to hold in place the fragment produced by the initial failure and to continue pressurization until section A-A fails. An alternate method would be compressive load testing of the ring left after the material next to the slots has been removed by pressure burst testing all eight of the fuel holes. Tests on unirradiated specimens will be performed to establish the feasibility of these test methods.

TASK 700: PROGRAM PLAN

Executive summaries of a Program Plan "Graphite Development Program for Steam Cycle HTGR" are under review by ERDA-RRD.

REFERENCES

11-1. Johnson, W. R., and G. B. Engle, "Properties of Unirradiated Fuel Element Graphites H-451 and TS-1240," ERDA Report GA-A13752, General Atomic, January 31, 1976.

11-2. "HTGR Fuels and Core Development Program Quarterly Progress Report for the Period Ending February 28, 1976," ERDA Report GA-A13804, General Atomic, March 31, 1976.

11-3. "HTGR Fuels and Core Development Program Quarterly Progress Report for the Period Ending May 31, 1974," USAEC Report GA-A13030, General Atomic, June 28, 1974.

11-4. "HTGR Fuels and Core Development Program Quarterly Progress Report for the Period Ending August 30, 1974," USAEC Report GA-A13126, General Atomic, September 30, 1974.

11-5. "HTGR Fuels and Core Development Program Quarterly Progress Report for the Period Ending November 30, 1975," ERDA Report GA-A13737, General Atomic, December 31, 1975.

11-6. Tzung, F. K., "GTEPC-2D, A Computer Program for Two-Dimensional Graphite Thermal-Elastic-Plastic-Creep Analysis, User's Manual," General Atomic Report GA-A13532, to be published.

11-7. Head, J. L., "The Transient Creep of Graphite in a Reactor Environment," paper presented at the Third International Conference on Structural Mechanics in Reactor Technology, London, September 1-5, 1975.

11-8. Beavan, L. A., "H-327 Graphite - Design Data Package," General Atomic unpublished data, December 1975.

11-9. Saurwein, J. J., "Peach Bottom Test Element Thermal Analysis," General Atomic unpublished data, April 19, 1976.

TABLE 11-1
THERMAL CONDUCTIVITY OF H-451 GRAPHITE
GLCC Lot 426, Log 6484-41 (GLCC Log 184), Density = 1.72 Mg/m^3 (g/cm^3)

ORIENTATION	LOCATION	SPECIMEN NUMBER	THERMAL CONDUCTIVITY (W/M-K) AT: 295K (22C)	473K (200C)	673K (400C)	873K (600C)	1073K (800C)
AXIAL	MLC	3BC-L4B	143.9	116.5	96.0	77.1	69.7
		MEAN:	143.9	116.5	96.0	77.1	69.7
		STD. DEV:					
RADIAL	MLC	3BC-L22B	141.7	114.7	91.5	75.9	64.8
		MEAN:	141.7	114.7	91.5	75.9	64.8
		STD. DEV:					

TABLE 11-2
FLEXURAL STRENGTH OF H-451 GRAPHITE
GLCC Lot 426, Logs 6484-40 and -41 (GLCC Logs 155 and 184, respectively)

LOT NO. 426 SPEC. DIA. 6.4 MM
LOG NO. 6484-40 SPEC. LENGTH 51. MM
LOG DENSITY 1.72 KG/M**3

SPECIMEN NUMBER	ORIENTATION	LOCATION	DENSITY (KG/M**3)	MODULUS OF RUPTURE (MPA) (UNCORRECTED)	FLEXURAL STRENGTH (MPA) (CORRECTED)
3A-3	AX	MLC		24.4	20.7
-5	AX	MLC		29.4	23.8
-6	AX	MLC		27.6	22.8
-10	AX	MLC		27.2	22.5
-12	AX	MLC		26.9	22.3
-13	AX	MLC		25.2	21.2
3A-15	AX	MLC		27.8	22.9
-21	AX	MLC		25.6	21.5
-22	AX	MLC		23.9	20.4
-24	AX	MLC		22.9	19.7
3B-3	AX	MLC		24.8	21.0
-5	AX	MLC		22.8	19.7
-6	AX	MLC		24.7	20.9
-10	AX	MLC		22.7	19.5
-12	AX	MLC		24.6	20.8
-13	AX	MLC		23.8	20.3
-15	AX	MLC		19.7	17.4
-21	AX	MLC		24.1	20.5
-22	AX	MLC		21.1	18.4
-24	AX	MLC		25.7	21.6
	MEAN			24.7 MPA (3588. PSI)	20.9 MPA (3031. PSI)
	STD. DEV.			2.3 MPA (339. PSI)	1.5 MPA (224. PSI)
3A-32	RAD	MLC		20.1	17.4
-33	RAD	MLC		22.2	18.9
-34	RAD	MLC		22.7	19.2
-35	RAD	MLC		21.3	18.3
-36	RAD	MLC		21.1	18.1
-39	RAD	MLC		23.0	19.4
-40	RAD	MLC		27.2	21.9
-41	RAD	MLC		29.7	23.2
-42	RAD	MLC		26.6	21.6
-43	RAD	MLC		28.5	22.6
3B-32	RAD	MLC		23.2	19.5
-33	RAD	MLC		22.8	19.2
-34	RAD	MLC		15.9	14.3
-35	RAD	MLC		15.9	14.3
-36	RAD	MLC		22.4	19.0
3B-39	RAD	MLC		10.4	9.7
-40	RAD	MLC		13.0	12.0
-41	RAD	MLC		11.4	10.6
-42	RAD	MLC		11.3	10.5
-43	RAD	MLC		14.4	13.1
	MEAN			20.2 MPA (2923. PSI)	17.1 MPA (2483. PSI)
	STD. DEV.			5.9 MPA (857. PSI)	4.2 MPA (611. PSI)

TABLE 11-2 (Continued)

LOT NO. 426 SPEC. DIA. 6.4 MM
LOG NO. 6484-40 SPEC. LENGTH 51. MM
LOG DENSITY 1.72 KG/M**3

SPECIMEN NUMBER	ORIENTATION	LOCATION	DENSITY (KG/M**3)	MODULUS OF RUPTURE (MPA) (UNCORRECTED)	FLEXURAL STRENGTH (MPA) (CORRECTED)
3A-51	AX	MLE		31.4	26.1
-52	AX	MLE		31.4	26.1
-54	AX	MLE		31.4	26.1
-55	AX	MLE		31.6	26.3
-56	AX	MLE		31.7	26.3
-59	AX	MLE		27.5	23.6
-60	AX	MLE		27.4	23.5
-61	AX	MLE		29.9	25.2
-62	AX	MLE		29.8	25.1
-63	AX	MLE		32.5	26.8
3B-51	AX	MLE		29.6	24.9
-52	AX	MLE		30.0	25.2
-54	AX	MLE		31.5	26.2
-55	AX	MLE		26.7	23.1
-56	AX	MLE		29.0	24.6
-59	AX	MLE		28.7	24.4
-60	AX	MLE		29.0	24.6
-61	AX	MLE		32.3	26.7
-62	AX	MLE		32.0	26.5
-63	AX	MLE		32.9	27.1
	MEAN			30.3 MPA (4396. PSI)	25.4 MPA (3688. PSI)
	STD. DEV.			1.8 MPA (265. PSI)	1.2 MPA (172. PSI)
3A-72	RAD	MLE		27.3	22.6
-73	RAD	MLE		27.4	22.6
-74	RAD	MLE		26.9	22.4
-75	RAD	MLE		26.2	21.9
-76	RAD	MLE		27.2	22.5
3A-79	RAD	MLE		27.2	22.5
-80	RAD	MLE		27.3	22.6
-81	RAD	MLE		26.6	22.1
-82	RAD	MLE		26.1	21.8
-83	RAD	MLE		27.6	22.8
3B-72	RAD	MLE		30.4	24.4
-73	RAD	MLE		27.6	22.7
-74	RAD	MLE		30.3	24.3
-75	RAD	MLE		26.2	21.9
-76	RAD	MLE		28.3	23.2
-79	RAD	MLE		23.2	19.9
-80	RAD	MLE		26.0	21.7
-81	RAD	MLE		25.1	21.2
-82	RAD	MLE		25.4	21.3
-83	RAD	MLE		22.5	19.4
	MEAN			26.7 MPA (3879. PSI)	22.2 MPA (3220. PSI)
	STD. DEV.			1.9 MPA (276. PSI)	1.2 MPA (172. PSI)

TABLE 11-2 (Continued)

LOT NO. 426 SPEC. DIA. 6.4 MM
LOG NO. 6484-4D SPEC. LENGTH 51. MM
LOG DENSITY 1.72 KG/M**3

SPECIMEN NUMBER	ORIENTATION	LOCATION	DENSITY (KG/M**3)	MODULUS OF RUPTURE (MPA) (UNCORRECTED)	FLEXURAL STRENGTH (MPA) (CORRECTED)
1AC-3	AX	EC		22.3	19.6
-5	AX	EC		26.9	22.8
-6	AX	EC		29.7	24.6
-10	AX	EC		22.7	19.9
-12	AX	EC		28.9	24.1
-13	AX	EC		29.2	24.3
-15	AX	EC		29.9	24.7
-21	AX	EC		29.7	24.6
-22	AX	EC		28.2	23.6
-24	AX	EC		28.5	23.8
1BC-3	AX	EC		27.8	23.4
-5	AX	EC		28.4	23.8
-6	AX	EC		28.5	23.8
-10	AX	EC		28.1	23.6
-12	AX	EC		28.0	23.5
-13	AX	EC		28.5	23.8
-15	AX	EC		30.4	25.0
-21	AX	EC		31.2	25.5
-22	AX	EC		29.9	24.7
-24	AX	EC		30.2	24.9
	MEAN			28.4 MPA (4113. PSI)	23.7 MPA (3436. PSI)
	STD. DEV.			2.3 MPA (327. PSI)	1.5 MPA (218. PSI)
1AC-32	RAD	EC		27.5	22.7
-33	RAD	EC		27.7	22.8
-34	RAD	EC		28.6	23.3
-35	RAD	EC		25.6	21.5
-36	RAD	EC		27.3	22.6
-39	RAD	EC		21.0	18.3
1AC-40	RAD	EC		26.1	21.8
-41	RAD	EC		27.2	22.5
-42	RAD	EC		29.1	23.6
-43	RAD	EC		23.1	19.9
1BC-32	RAD	EC		27.0	22.4
-33	RAD	EC		27.5	22.7
-34	RAD	EC		26.4	22.0
-35	RAD	EC		25.5	21.4
-36	RAD	EC		24.7	20.9
-39	RAD	EC		27.4	22.6
-40	RAD	EC		24.8	21.0
-41	RAD	EC		28.0	23.0
-42	RAD	EC		18.9	16.8
-43	RAD	EC		25.0	21.1
	MEAN			25.9 MPA (3760. PSI)	21.7 MPA (3141. PSI)
	STD. DEV.			2.5 MPA (368. PSI)	1.7 MPA (246. PSI)

TABLE 11-2 (Continued)

LOT NO. 426 SPEC. DIA. 6.4 MM
LOG NO. 6484-40 SPEC. LENGTH 51. MM
LOG DENSITY 1.72 KG/M**3

SPECIMEN NUMBER	ORIENTATION	LOCATION	DENSITY (KG/M**3)	MODULUS OF RUPTURE (MPA) (UNCORRECTED)	FLEXURAL STRENGTH (MPA) (CORRECTED)
1A-51	AX	EE		13.9	12.9
-52	AX	EE		20.3	18.2
-54	AX	EE		15.3	14.2
-55	AX	EE		12.9	12.1
-56	AX	EE		11.6	11.0
-59	AX	EE		14.3	13.3
-60	AX	EE		16.9	15.5
-61	AX	EE		14.7	13.7
-62	AX	EE		15.7	14.5
-63	AX	EE		17.2	15.8
1B-51	AX	EE		24.6	21.5
-52	AX	EE		25.0	21.8
-54	AX	EE		25.2	22.0
-55	AX	EE		24.2	21.3
-56	AX	EE		27.9	23.8
-59	AX	EE		24.4	21.4
1B-60	AX	EE		28.2	24.1
-61	AX	EE		28.8	24.5
-62	AX	EE		25.4	22.1
-63	AX	EE		26.3	22.8
	MEAN			20.6 MPA (2993. PSI)	18.3 MPA (2657. PSI)
	STD. DEV.			5.9 MPA (852. PSI)	4.6 MPA (669. PSI)
1A-72	RAD	EE		26.1	21.8
-73	RAD	EE		25.1	21.2
-74	RAD	EE		23.7	20.3
-75	RAD	EE		27.3	22.6
-76	RAD	EE		25.8	21.6
-79	RAD	EE		25.8	21.6
-80	RAD	EE		27.2	22.5
-81	RAD	EE		26.2	21.9
-82	RAD	EE		25.9	21.7
-83	RAD	EE		28.2	23.1
1B-72	RAD	EE		27.2	22.5
-73	RAD	EE		27.9	23.0
-74	RAD	EE		28.3	23.2
-75	RAD	EE		30.1	24.2
-76	RAD	EE		28.3	23.2
-79	RAD	EE		27.5	22.7
-80	RAD	EE		29.3	23.8
-81	RAD	EE		29.9	24.1
-82	RAD	EE		28.4	23.2
-83	RAD	EE		27.0	22.4
	MEAN			27.3 MPA (3954. PSI)	22.5 MPA (3266. PSI)
	STD. DEV.			1.6 MPA (235. PSI)	1.0 MPA (144. PSI)

TABLE 11-2 (Continued)

LOT NO. 426 SPEC. DIA. 6.4 MM
LOG NO. 6484-41 SPEC. LENGTH 51. MM
LOG DENSITY 1.72 KG/M**3

SPECIMEN NUMBER	ORIENTATION	LOCATION	DENSITY (KG/M**3)	MODULUS OF RUPTURE (MPA) (UNCORRECTED)	FLEXURAL STRENGTH (MPA) (CORRECTED)
3AC-3	AX	MLC		23.1	19.8
-5	AX	MLC		16.9	15.2
-6	AX	MLC		25.9	21.7
-10	AX	MLC		26.3	22.0
-12	AX	MLC		23.0	19.8
-13	AX	MLC		23.0	19.8
-15	AX	MLC		24.2	20.6
-21	AX	MLC		23.0	19.7
-22	AX	MLC		21.9	19.0
-24	AX	MLC		25.3	21.3
3BC-3	AX	MLC		22.8	19.6
-5	AX	MLC		24.6	20.8
-6	AX	MLC		18.3	16.3
-10	AX	MLC		22.5	19.5
-12	AX	MLC		23.9	20.4
-13	AX	MLC		23.4	20.1
-15	AX	MLC		22.5	19.4
-21	AX	MLC		23.7	20.2
-22	AX	MLC		21.7	18.8
-24	AX	MLC		25.9	21.7
	MEAN			23.1 MPA (3349. PSI)	19.8 MPA (2870. PSI)
	STD. DEV.			2.3 MPA (334. PSI)	1.6 MPA (238. PSI)
3AC-32	RAD	MLC		20.7	17.8
3AC-33	RAD	MLC		19.8	17.2
-34	RAD	MLC		18.5	16.2
-35	RAD	MLC		20.1	17.4
-36	RAD	MLC		18.8	16.4
-39	RAD	MLC		22.3	18.9
-40	RAD	MLC		22.4	19.0
-41	RAD	MLC		23.3	19.5
-42	RAD	MLC		19.8	17.2
-43	RAD	MLC		25.5	21.0
3BC-32	RAD	MLC		19.9	17.3
3BC-33	RAD	MLC		19.9	17.3
-34	RAD	MLC		21.9	18.6
-35	RAD	MLC		20.2	17.5
-36	RAD	MLC		22.5	19.0
-39	RAD	MLC		16.6	14.8
-40	RAD	MLC		18.2	16.1
-41	RAD	MLC		22.2	18.8
-42	RAD	MLC		20.5	17.7
-43	RAD	MLC		19.6	17.1
	MEAN			20.6 MPA (2992. PSI)	17.7 MPA (2573. PSI)
	STD. DEV.			2.0 MPA (295. PSI)	1.4 MPA (203. PSI)

TABLE 11-2 (Continued)

LOT NO. 426 SPEC. DIA. 6.4 MM
LOG NO. 6484-41 SPEC. LENGTH 51. MM
LOG DENSITY 1.72 KG/M**3

SPECIMEN NUMBER	ORIENTATION	LOCATION	DENSITY (KG/M**3)	MODULUS OF RUPTURE (MPA) (UNCORRECTED)	FLEXURAL STRENGTH (MPA) (CORRECTED)
3AE-51	AX	MLE		29.1	24.7
-52	AX	MLE		28.9	24.5
-54	AX	MLE		29.7	25.1
-55	AX	MLE		30.8	25.8
-56	AX	MLE		27.3	23.5
-59	AX	MLE		29.7	25.1
-60	AX	MLE		29.7	25.1
3AE-61	AX	MLE		32.2	26.6
-62	AX	MLE		30.8	25.8
-63	AX	MLE		30.1	25.3
3BE-51	AX	MLE		31.4	26.1
-52	AX	MLE		26.3	22.8
-54	AX	MLE		29.4	24.9
-55	AX	MLE		28.8	24.5
-56	AX	MLE		27.5	23.6
-59	AX	MLE		28.7	24.4
-60	AX	MLE		31.4	26.1
3BE-61	AX	MLE		31.9	26.5
-62	AX	MLE		28.6	24.3
-63	AX	MLE		32.5	26.9
	MEAN			29.7 MPA (4314. PSI)	25.1 MPA (3635. PSI)
	STD. DEV.			1.7 MPA (244. PSI)	1.1 MPA (159. PSI)
3AE-72	RAD	MLE		27.0	21.8
-73	RAD	MLE		29.3	23.0
-74	RAD	MLE		27.1	21.9
-75	RAD	MLE		29.7	23.2
-76	RAD	MLE		26.8	21.7
-79	RAD	MLE		25.7	21.0
-80	RAD	MLE		25.7	21.1
-81	RAD	MLE		23.5	19.7
-82	RAD	MLE		25.5	20.9
-83	RAD	MLE		23.5	19.7
3BE-72	RAD	MLE		26.7	21.6
-73	RAD	MLE		28.6	22.6
-74	RAD	MLE		25.2	20.7
-75	RAD	MLE		28.8	22.7
-76	RAD	MLE		28.8	22.7
-79	RAD	MLE		23.8	19.9
-80	RAD	MLE		24.4	20.2
-81	RAD	MLE		22.4	19.0
-82	RAD	MLE		22.7	19.1
-83	RAD	MLE		24.0	20.0
	MEAN			26.0 MPA (3764. PSI)	21.1 MPA (3064. PSI)
	STD. DEV.			2.3 MPA (332. PSI)	1.3 MPA (191. PSI)

TABLE 11-2 (Continued)

LOT NO. 426 SPEC. DIA. 6.4 MM
LOG NO. 6484-41 SPEC. LENGTH 51. MM
LOG DENSITY 1.72 KG/M**3

SPECIMEN NUMBER	ORIENTATION	LOCATION	DENSITY (KG/M**3)	MODULUS OF RUPTURE (MPA) (UNCORRECTED)	FLEXURAL STRENGTH (MPA) (CORRECTED)
1AC-3	AX	EC		19.4	17.1
-5	AX	EC		17.1	15.4
-6	AX	EC		18.5	16.5
-10	AX	EC		21.9	19.0
-12	AX	EC		17.7	15.9
-13	AX	EC		19.4	17.2
-15	AX	EC		18.3	16.3
-21	AX	EC		18.2	16.3
-22	AX	EC		16.5	14.9
-24	AX	EC		20.8	18.2
1BC-3	AX	EC		23.0	19.8
-5	AX	EC		19.3	17.1
-6	AX	EC		17.1	15.4
-10	AX	EC		20.0	17.6
-12	AX	EC		18.6	16.5
-13	AX	EC		17.7	15.9
-15	AX	EC		16.8	15.1
-21	AX	EC		20.2	17.8
-22	AX	EC		18.2	16.3
-24	AX	EC		19.7	17.4
	MEAN			18.9 MPA (2745. PSI)	16.8 MPA (2434. PSI)
	STD. DEV.			1.7 MPA (245. PSI)	1.3 MPA (185. PSI)
1AC-32	RAD	EC		21.9	18.6
1AC-33	RAD	EC		19.0	16.6
-34	RAD	EC		21.0	18.1
-35	RAD	EC		19.6	17.1
-36	RAD	EC		22.1	18.8
-39	RAD	EC		21.2	18.2
-40	RAD	EC		24.3	20.2
-41	RAD	EC		23.6	19.7
-42	RAD	EC		20.4	17.7
-43	RAD	EC		23.6	19.7
1BC-32	RAD	EC		23.6	19.8
1BC-33	RAD	EC		20.8	17.9
-34	RAD	EC		22.9	19.3
-35	RAD	EC		19.9	17.2
-36	RAD	EC		21.9	18.6
-39	RAD	EC		19.0	16.7
-40	RAD	EC		21.6	18.4
-41	RAD	EC		23.2	19.5
-42	RAD	EC		21.3	18.2
-43	RAD	EC		20.0	17.4
	MEAN			21.5 MPA (3124. PSI)	18.4 MPA (2666. PSI)
	STD. DEV.			1.6 MPA (232. PSI)	1.1 MPA (157. PSI)

TABLE 11-2 (Continued)

LOT NO. 426 SPEC. DIA. 6.4 MM
LOG NO. 6484-41 SPEC. LENGTH 51. MM
LOG DENSITY 1.72 KG/M**3

SPECIMEN NUMBER	ORIENTATION	LOCATION	DENSITY (KG/M**3)	MODULUS OF RUPTURE (MPA) (UNCORRECTED)	FLEXURAL STRENGTH (MPA) (CORRECTED)
1AE-51	AX	EE		24.2	20.9
-52	AX	EE		27.0	22.9
-54	AX	EE		25.0	21.5
-55	AX	EE		24.5	21.2
-56	AX	EE		26.2	22.3
-59	AX	EE		27.5	23.2
-60	AX	EE		27.2	23.0
1AE-61	AX	EE		27.8	23.4
-62	AX	EE		25.8	22.1
-63	AX	EE		28.0	23.5
1BE-51	AX	EE		24.0	20.8
-52	AX	EE		26.3	22.4
-54	AX	EE		22.7	19.9
-55	AX	EE		24.0	20.8
-56	AX	EE		29.2	24.2
-59	AX	EE		23.0	20.1
-60	AX	EE		26.4	22.5
1BE-61	AX	EE		27.2	23.0
-62	AX	EE		29.2	24.2
-63	AX	EE		28.6	23.9
	MEAN			26.2 MPA (3799. PSI)	22.3 MPA (3232. PSI)
	STD. DEV.			2.0 MPA (287. PSI)	1.3 MPA (193. PSI)
1AE-72	RAD	EE		22.8	19.2
-73	RAD	EE		26.3	21.4
-74	RAD	EE		26.1	21.3
-75	RAD	EE		26.0	21.2
-76	RAD	EE		23.5	19.7
-79	RAD	EE		22.1	18.8
-80	RAD	EE		26.0	21.2
-81	RAD	EE		26.3	21.4
-82	RAD	EE		24.1	20.1
-83	RAD	EE		21.0	18.0
1BE-72	RAD	EE		27.2	21.9
-73	RAD	EE		27.4	22.0
-74	RAD	EE		25.5	20.9
-75	RAD	EE		22.9	19.3
-76	RAD	EE		22.0	18.7
-79	RAD	EE		20.2	17.5
-80	RAD	EE		20.1	17.4
-81	RAD	EE		21.5	18.4
-82	RAD	EE		19.9	17.2
-83	RAD	EE		19.8	17.2
	MEAN			23.5 MPA (3413. PSI)	19.6 MPA (2849. PSI)
	STD. DEV.			2.6 MPA (382. PSI)	1.7 MPA (243. PSI)

TABLE 11-3
THERMAL CONDUCTIVITY OF H-451 GRAPHITE
GLCC Lot 440, Log 6484-55 (GLCC Log 63), Density = 1.76 Mg/m^3 (g/cm^3)

LOT NUMBER: 440 LOG NUMBER: 6484-55

ORIENTATION	LOCATION	SPECIMEN NUMBER	THERMAL CONDUCTIVITY (W/M-K) AT: 295K (22C)	473K (200C)	673K (400C)	873K (600C)	1073K (800C)
AXIAL	MLC	206-A	138.2	113.2	88.9	74.4	66.4
		206-B	125.6	100.6	82.5	65.5	60.7
		206-C	123.2	119.2	96.2	79.7	71.8
		206-D	125.9	100.8	83.2	68.2	61.6
		206-E	136.2	117.3	97.1	76.9	59.4
		206-F	132.7	120.0	96.9	80.3	69.5
		206-G	145.1	118.9	99.2	81.5	70.2
		206-H	115.3	102.8	87.4	74.2	65.1
		MEAN:	130.3	111.6	91.4	75.1	65.6
		STD. DEV:	9.6	8.7	6.7	5.8	4.7
RADIAL	MLC	244-A	120.8	98.9	79.1	65.9	59.0
		244-B	141.4	115.9	93.8	76.1	63.3
		244-C	136.1	111.5	91.9	75.2	65.0
		244-D	131.2	102.7	85.5	71.1	64.2
		244-E	124.3	108.9	88.5	75.1	61.4
		244-F	121.4	106.2	85.7	68.9	61.3
		244-G	118.7	101.5	83.8	68.7	59.9
		244-H	110.0	99.9	83.1	65.1	62.4
		MEAN:	125.5	105.7	86.4	70.8	62.1
		STD. DEV:	10.2	6.0	4.8	4.3	2.1

TABLE 11-4
FLEXURAL STRENGTH OF H-451 GRAPHITE
GLCC Lot 440, Log 6484-54 (GLCC Log 19), Density = 1.78 Mg/m^3 (g/cm^3)

LOT NO. 440 SPEC. DIA. 6.4 MM
LOG NO. 6484-54 SPEC. LENGTH 51. MM
LOG DENSITY 1.78 KG/M**3

SPECIMEN NUMBER	ORIENTATION	LOCATION	DENSITY (KG/M**3)	MODULUS OF RUPTURE (MPA) (UNCORRECTED)	FLEXURAL STRENGTH (MPA) (CORRECTED)
3A-3	AX	MLC		27.9	24.2
-5	AX	MLC		27.1	23.7
-6	AX	MLC		33.0	27.6
-10	AX	MLC		27.4	23.9
-12	AX	MLC		28.7	24.8
-13	AX	MLC		28.7	24.8
-15	AX	MLC		27.3	23.8
-21	AX	MLC		31.7	26.8
-22	AX	MLC		28.8	24.9
-24	AX	MLC		34.4	28.5
3B-3	AX	MLC		28.8	24.8
-5	AX	MLC		33.7	28.1
-6	AX	MLC		33.6	28.0
-10	AX	MLC		27.7	24.1
3B-12	AX	MLC		32.0	27.0
-13	AX	MLC		32.6	27.4
-15	AX	MLC		31.7	26.8
-21	AX	MLC		29.5	25.3
-22	AX	MLC		28.6	24.7
-24	AX	MLC		30.5	26.0
	MEAN			30.2 MPA (4377. PSI)	25.7 MPA (3734. PSI)
	STD. DEV.			2.4 MPA (352. PSI)	1.6 MPA (236. PSI)
3A-32	RAD	MLC		26.8	22.7
-33	RAD	MLC		20.6	18.3
-34	RAD	MLC		21.5	19.0
3A-35	RAD	MLC		24.6	21.2
-36	RAD	MLC		32.4	26.1
-39	RAD	MLC		19.7	17.6
-40	RAD	MLC		18.2	16.4
-41	RAD	MLC		16.8	15.3
-42	RAD	MLC		12.3	11.5
-43	RAD	MLC		17.6	15.9
3B-32	RAD	MLC		24.3	21.0
-33	RAD	MLC		24.0	20.8
-34	RAD	MLC		16.8	15.3
-35	RAD	MLC		24.5	21.2
-36	RAD	MLC		24.8	21.4
-39	RAD	MLC		15.9	14.6
-40	RAD	MLC		14.6	13.5
-41	RAD	MLC		23.0	20.1
-42	RAD	MLC		22.7	19.9
-43	RAD	MLC		15.9	14.5
	MEAN			20.8 MPA (3024. PSI)	18.3 MPA (2657. PSI)
	STD. DEV.			4.9 MPA (710. PSI)	3.6 MPA (529. PSI)

TABLE 11-4 (Continued)

LOT NO. 440 — SPEC. DIA. 6.4 MM
LOG NO. 6484-54 SPEC. LENGTH 51. MM
LOG DENSITY 1.78 KG/M**3

SPECIMEN NUMBER	ORIENTATION	LOCATION	DENSITY (KG/M**3)	MODULUS OF RUPTURE (MPA) (UNCORRECTED)	FLEXURAL STRENGTH (MPA) (CORRECTED)
3A-51	AX	MLE		33.2	28.2
-52	AX	MLE		33.1	28.1
-54	AX	MLE		38.8	31.7
-55	AX	MLE		37.1	30.7
-56	AX	MLE		30.4	26.3
-59	AX	MLE		33.1	28.1
-60	AX	MLE		31.1	26.8
-61	AX	MLE		30.5	26.4
-62	AX	MLE		33.6	28.5
3A-63	AX	MLE		29.1	25.3
3B-51	AX	MLE		33.7	28.5
-52	AX	MLE		33.0	28.1
-54	AX	MLE		40.4	32.6
-55	AX	MLE		33.8	28.6
-56	AX	MLE		31.9	27.3
-59	AX	MLE		33.3	28.3
-60	AX	MLE		26.3	23.3
-61	AX	MLE		32.6	27.8
-62	AX	MLE		27.5	24.2
-63	AX	MLE		28.9	25.2
	MEAN			32.6 MPA (4723. PSI)	27.7 MPA (4018. PSI)
	STD. DEV.			3.4 MPA (500. PSI)	2.3 MPA (333. PSI)
3A-72	RAD	MLE		29.1	24.2
-73	RAD	MLE		32.0	25.9
-74	RAD	MLE		28.9	24.1
-75	RAD	MLE		31.6	25.7
-76	RAD	MLE		26.7	22.7
-79	RAD	MLE		30.4	25.0
-80	RAD	MLE		27.7	23.3
-81	RAD	MLE		28.9	24.1
-82	RAD	MLE		31.7	25.8
-83	RAD	MLE		30.9	25.3
3B-72	RAD	MLE		23.1	20.2
-73	RAD	MLE		25.5	21.9
-74	RAD	MLE		25.8	22.1
-75	RAD	MLE		19.6	17.5
-76	RAD	MLE		25.8	22.0
3B-79	RAD	MLE		24.0	20.8
-80	RAD	MLE		25.9	22.2
-81	RAD	MLE		22.9	20.0
-82	RAD	MLE		19.0	17.1
-83	RAD	MLE		7.6	7.3
	MEAN			25.9 MPA (3750. PSI)	21.8 MPA (3169. PSI)
	STD. DEV.			5.7 MPA (829. PSI)	4.3 MPA (619. PSI)

TABLE 11-4 (Continued)

LOT NO. 440 — SPEC. DIA. 6.4 MM
LOG NO. 6484-54 — SPEC. LENGTH 51. MM
LOG DENSITY 1.78 KG/M**3

SPECIMEN NUMBER	ORIENTATION	LOCATION	DENSITY (KG/M**3)	MODULUS OF RUPTURE (MPA) (UNCORRECTED)	FLEXURAL STRENGTH (MPA) (CORRECTED)
1A-3	AX	EC		29.6	25.4
-5	AX	EC		29.6	25.4
-6	AX	EC		27.3	23.8
-10	AX	EC		31.2	26.4
-12	AX	EC		25.2	22.2
-13	AX	EC		27.5	23.9
-15	AX	EC		24.4	21.6
-21	AX	EC		23.4	20.8
-22	AX	EC		20.8	18.8
-24	AX	EC		22.8	20.4
1B-3	AX	EC		28.7	24.7
-5	AX	EC		25.0	22.0
-6	AX	EC		31.0	26.3
-10	AX	EC		30.0	25.7
-12	AX	EC		27.5	23.9
-13	AX	EC		29.2	25.1
-15	AX	EC		29.8	25.5
1B-21	AX	EC		21.5	19.4
-22	AX	EC		26.0	22.8
-24	AX	EC		25.7	22.6
	MEAN			26.8 MPA (3886. PSI)	23.3 MPA (3386. PSI)
	STD. DEV.			3.1 MPA (456. PSI)	2.3 MPA (335. PSI)
1A-32	RAD	EC		17.9	16.2
-33	RAD	EC		23.3	20.3
-34	RAD	EC		18.6	16.8
-35	RAD	EC		15.9	14.6
-36	RAD	EC		11.5	10.9
-39	RAD	EC		21.1	18.7
1A-40	RAD	EC		19.8	17.7
-41	RAD	EC		22.1	19.4
-42	RAD	EC		16.4	15.0
-43	RAD	EC		21.3	18.8
1B-32	RAD	EC		30.1	24.8
-33	RAD	EC		22.5	19.7
-34	RAD	EC		26.4	22.5
-35	RAD	EC		29.2	24.3
-36	RAD	EC		27.0	22.8
-39	RAD	EC		24.5	21.2
-40	RAD	EC		31.0	25.4
-41	RAD	EC		26.1	22.2
-42	RAD	EC		22.8	19.9
-43	RAD	EC		28.3	23.7
	MEAN			22.8 MPA (3306. PSI)	19.7 MPA (2863. PSI)
	STD. DEV.			5.2 MPA (750. PSI)	3.8 MPA (553. PSI)

TABLE 11-4 (Continued)

LOT NO. 440 SPEC. DIA. 6.4 MM
LOG NO. 6484-54 SPEC. LENGTH 51. MM
LOG DENSITY 1.78 KG/M**3

SPECIMEN NUMBER	ORIENTATION	LOCATION	DENSITY (KG/M**3)	MODULUS OF RUPTURE (MPA) (UNCORRECTED)	FLEXURAL STRENGTH (MPA) (CORRECTED)
1A-51	AX	EE		34.5	29.1
-52	AX	EE		33.7	28.5
-54	AX	EE		32.0	27.4
-55	AX	EE		24.9	22.2
-56	AX	EE		30.6	26.4
-59	AX	EE		31.2	26.8
-60	AX	EE		35.5	29.7
-61	AX	EE		35.2	29.5
-62	AX	EE		37.3	30.8
-63	AX	EE		34.6	29.1
1B-51	AX	EE		31.8	27.3
-52	AX	EE		37.3	30.8
1B-54	AX	EE		31.5	27.1
-55	AX	EE		34.0	28.7
-56	AX	EE		30.4	26.3
-59	AX	EE		28.2	24.7
-60	AX	EE		31.4	27.0
-61	AX	EE		25.0	22.3
-62	AX	EE		34.2	28.9
-63	AX	EE		26.3	23.3
	MEAN			32.0 MPA (4638. PSI)	27.3 MPA (3959. PSI)
	STD. DEV.			3.7 MPA (531. PSI)	2.5 MPA (369. PSI)
1A-72	RAD	EE		35.2	28.4
1A-73	RAD	EE		28.6	24.4
-74	RAD	EE		31.1	25.9
-75	RAD	EE		28.8	24.4
-76	RAD	EE		30.0	25.2
-79	RAD	EE		26.7	23.0
-80	RAD	EE		26.1	22.6
-81	RAD	EE		20.7	18.6
-82	RAD	EE		28.6	24.3
-83	RAD	EE		30.4	25.5
1B-72	RAD	EE		30.8	25.8
-73	RAD	EE		27.0	23.2
-74	RAD	EE		27.6	23.7
-75	RAD	EE		27.7	23.7
-76	RAD	EE		24.6	21.6
-79	RAD	EE		28.5	24.3
-80	RAD	EE		29.3	24.8
-81	RAD	EE		29.9	25.2
1B-82	RAD	EE		29.3	24.8
-83	RAD	EE		29.2	24.7
	MEAN			28.5 MPA (4135. PSI)	24.2 MPA (3511. PSI)
	STD. DEV.			2.9 MPA (415. PSI)	1.9 MPA (282. PSI)

TABLE 11-5
FLEXURAL STRENGTH OF H-451 GRAPHITE[a]
GLCC Lot 440, Log 6484-55 (GLCC Log 63), Density = 1.76 Mg/m^3 (g/cm^3)

LOT NO. 440 SPEC. DIA. 0.25 IN.
LOG NO. 6484-55 SPEC. LENGTH 2.0 IN.
LOG DENSITY 1.76 G/CC

SPECIMEN NUMBER		ORIENTATION	LOCATION	DENSITY (G/CC)	MODULUS OF RUPTURE (PSI) (UNCORRECTED)	FLEXURAL STRENGTH (PSI) (CORRECTED)
7A	203B	AX	MLC		3262.	2840.
	205A	AX	MLC		3413.	2947.
	205B	AX	MLC		3165.	2769.
	213A	AX	MLC		3915.	3210.
	213B	AX	MLC		3396.	2935.
	219A	AX	MLC		3558.	3047.
	219B	AX	MLC		3081.	2707.
	225A	AX	MLC		2949.	2638.
	225B	AX	MLC		3628.	3094.
	229A	AX	MLC		3597.	3074.
3B	204B	AX	MLC		3773.	3189.
	206A	AX	MLC		3416.	2949.
	206B	AX	MLC		3303.	2869.
	212A	AX	MLC		3494.	3003.
	212B	AX	MLC		3638.	3101.
	222A	AX	MLC		3105.	2724.
	222B	AX	MLC		3885.	3261.
	226A	AX	MLC		3573.	3058.
	226B	AX	MLC		3537.	3033.
	230A	AX	MLC		3971.	3317.
		MEAN			3483.	2990.
		STD. DEV.			284.	197.
3A	235	RAD	MLC		3437.	2874.
	239	RAD	MLC		3488.	2917.
	241	RAD	MLC		3591.	2972.
	245	RAD	MLC		3488.	2907.
	247	RAD	MLC		3422.	2864.
	257	RAD	MLC		3514.	2924.
	259	RAD	MLC		3758.	3070.
	263	RAD	MLC		3899.	3152.
	265	RAD	MLC		3017.	2597.
	269	RAD	MLC		3261.	2760.
3B	236	RAD	MLC		3624.	2992.
	240	RAD	MLC		3586.	2969.
	242	RAD	MLC		3110.	2661.
	246	RAD	MLC		3487.	2907.
	248	RAD	MLC		2960.	2557.
	258	RAD	MLC		3748.	3065.
	260	RAD	MLC		3773.	3079.
	264	RAD	MLC		3545.	2943.
	266	RAD	MLC		3800.	3094.
	270	RAD	MLC		4067.	3241.
		MEAN			3529.	2927.
		STD. DEV.			284.	178.

TABLE 11-5 (Continued)

LOT NO. 440 SPEC. DIA. 0.25 IN.
LOG NO. 6484-55 SPEC. LENGTH 2.0 IN.
LOG DENSITY 1.76 G/CC

SPECIMEN NUMBER		ORIENTATION	LOCATION	DENSITY (G/CC)	MODULUS OF RUPTURE (PSI) (UNCORRECTED)	FLEXURAL STRENGTH (PSI) (CORRECTED)
3A	273A	AX	MLE		4392.	3674.
	273B	AX	MLE		3720.	3225.
	275A	AX	MLE		4819.	3935.
	275B	AX	MLE		4074.	3468.
	279A	AX	MLE		4759.	3900.
	279B	AX	MLE		4128.	3503.
	285A	AX	MLE		4174.	3533.
	285B	AX	MLE		4195.	3547.
	287A	AX	MLE		3377.	2974.
	287B	AX	MLE		2873.	2587.
3B	274A	AX	MLE		4297.	3612.
	274B	AX	MLE		4379.	3665.
	276A	AX	MLE		4821.	3936.
3B	276B	AX	MLE		4418.	3691.
	280A	AX	MLE		4485.	3734.
	280B	AX	MLE		3717.	3223.
	286A	AX	MLE		4001.	3419.
	286B	AX	MLE		4171.	3531.
	288A	AX	MLE		4241.	3576.
	288B	AX	MLE		4174.	3533.
		MEAN			4161.	3513.
		STD. DEV.			471.	323.
3A	295	RAD	MLE		3920.	3227.
	299	RAD	MLE		3803.	3155.
	301	RAD	MLE		4254.	3418.
	305	RAD	MLE		4273.	3428.
	307	RAD	MLE		3700.	3090.
	317	RAD	MLE		4464.	3524.
	319	RAD	MLE		4464.	3524.
	327	RAD	MLE		4280.	3432.
	32	RAD	MLE		4202.	3389.
	329	RAD	MLE		4457.	3521.
3B	296	RAD	MLE		3890.	3209.
	300	RAD	MLE		4027.	3288.
	302	RAD	MLE		3119.	2702.
3B	306	RAD	MLE		3195.	2756.
	308	RAD	MLE		3215.	2770.
	318	RAD	MLE		4726.	3649.
	325	RAD	MLE		4478.	3531.
	324	RAD	MLE		4609.	3595.
	326	RAD	MLE		4708.	3641.
	330	RAD	MLE		3930.	3232.
		MEAN			4086.	3304.
		STD. DEV.			490.	290.

TABLE 11-5 (Continued)

LOT NO. 448 SPEC. DIA. 0.25 IN.
LOG NO. 6484-55 SPEC. LENGTH 2.0 IN.
LOG DENSITY 1.76 G/CC

SPECIMEN NUMBER		ORIENTATION	LOCATION	DENSITY (G/CC)	MODULUS OF RUPTURE (PSI) (UNCORRECTED)	FLEXURAL STRENGTH (PSI) (CORRECTED)
1A	3B	AX	EC		3798.	3224.
	5A	AX	EC		3555.	3061.
	5B	AX	EC		3711.	3167.
	13A	AX	EC		3683.	3148.
	13B	AX	EC		3531.	3044.
	19A	AX	EC		3000.	2657.
	19B	AX	EC		3203.	2808.
	25A	AX	EC		2868.	2556.
	25B	AX	EC		3585.	3082.
	29A	AX	EC		3467.	2999.
1B	4B	AX	EC		3909.	3297.
	6A	AX	EC		4530.	3678.
	6B	AX	EC		3716.	3171.
	12A	AX	EC		3603.	3094.
	12B	AX	EC		4393.	3599.
	22A	AX	EC		2726.	2446.
1B	22B	AX	EC		3856.	3263.
	26A	AX	EC		4021.	3369.
	26B	AX	EC		2943.	2613.
	30A	AX	EC		2824.	2522.
		MEAN			3546.	3040.
		STD. DEV.			499.	346.
1A	35	RAD	EC		3827.	3170.
	39	RAD	EC		4318.	3451.
	41	RAD	EC		4224.	3401.
	45	RAD	EC		3293.	2823.
	47	RAD	EC		3613.	3033.
	57	RAD	EC		3425.	2912.
	59	RAD	EC		3147.	2722.
	63	RAD	EC		2991.	2611.
	65	RAD	EC		3782.	3143.
	69	RAD	EC		3302.	2829.
1B	36	RAD	EC		3205.	2762.
	40	RAD	EC		3835.	3176.
	42	RAD	EC		3835.	3176.
	46	RAD	EC		3450.	2928.
	48	RAD	EC		3670.	3070.
	58	RAD	EC		3109.	2695.
1B	60	RAD	EC		3577.	3010.
	64	RAD	EC		3135.	2713.
	66	RAD	EC		3121.	2704.
	70	RAD	EC		3238.	2786.
		MEAN			3505.	2956.
		STD. DEV.			378.	242.

TABLE 11-5 (Continued)

LOT NO. 440 SPEC. DIA. 0.25 IN.
LOG NO. 6484-55 SPEC. LENGTH 2.0 IN.
LOG DENSITY 1.76 G/CC

SPECIMEN NUMBER	ORIENTATION	LOCATION	DENSITY (G/CC)	MODULUS OF RUPTURE (PSI) (UNCORRECTED)	FLEXURAL STRENGTH (PSI) (CORRECTED)
1A	73A AX	EE		4717.	3858.
	73B AX	EE		4980.	4009.
	75A AX	EE		4606.	3793.
	75B AX	EE		4172.	3519.
	79A AX	EE		3974.	3390.
	79B AX	EE		3596.	3127.
	5A AX	EE		3089.	2749.
	5B AX	EE		4193.	3532.
	7A AX	EE		3574.	3111.
	7B AX	EE		3321.	2925.
1E	74A AX	EE		4331.	3622.
	74B AX	EE		4617.	3800.
	76A AX	EE		4707.	3852.
	76B AX	EE		4903.	3966.
	4A AX	EE		4842.	3930.
	4B AX	EE		4163.	3513.
	6A AX	EE		3899.	3339.
	6B AX	EE		3563.	3103.
	8A AX	EE		4453.	3700.
1E	8B AX	EE		3867.	3276.
	MEAN			4175.	3506.
	STD. DEV.			558.	368.
1A	95 RAD	EE		4274.	3439.
	99 RAD	EE		4322.	3465.
	101 RAD	EE		4723.	3662.
	105 RAD	EE		4144.	3365.
	107 RAD	EE		4007.	3286.
	117 RAD	EE		4529.	3569.
	119 RAD	EE		4249.	3425.
	123 RAD	EE		4509.	3559.
	125 RAD	EE		5056.	3799.
	129 RAD	EE		4524.	3566.
1A	100 RAD	EE		3299.	2833.
	102 RAD	EE		2515.	2254.
	106 RAD	EE		3606.	3035.
	108 RAD	EE		3685.	3087.
	118 RAD	EE		4846.	3715.
	120 RAD	EE		4874.	3727.
	124 RAD	EE		4669.	3637.
	126 RAD	EE		4291.	3448.
	130 RAD	EE		4041.	3306.
1B	96 RAD	EE		4086.	3328.
	MEAN			4212.	3375.
	STD. DEV.			598.	360.

(a) Data obtained prior to conversion to SI units.

TABLE 11-6

FLEXURAL STRENGTH OF H-451 GRAPHITE[a]

GLCC Lot 440, Log 6484-56 (GLCC Log 65), Density = 1.77 Mg/m^3 (g/cm^3)

LOT NO. 440 SPEC. DIA. 0.25 IN.
LOG NO. 6484-56 SPEC. LENGTH 2.0 IN.
LOG DENSITY 1.77 G/CC

SPECIMEN NUMBER		ORIENTATION	LOCATION	DENSITY (G/CC)	MODULUS OF RUPTURE (PSI) (UNCORRECTED)	FLEXURAL STRENGTH (PSI) (CORRECTED)
3A	203B	AX	MLC		3304.	2870.
	205A	AX	MLC		3528.	3027.
	205B	AX	MLC		3240.	2824.
	213A	AX	MLC		3616.	3086.
	213B	AX	MLC		3129.	2743.
	219A	AX	MLC		2732.	2442.
	219B	AX	MLC		3142.	2752.
	225A	AX	MLC		2982.	2633.
	225B	AX	MLC		3226.	2814.
	229A	AX	MLC		3626.	3093.
3E	204B	AX	MLC		3601.	3076.
	206A	AX	MLC		3190.	2798.
	206B	AX	MLC		3160.	2766.
	212A	AX	MLC		3139.	2750.
	212B	AX	MLC		3886.	3262.
	222A	AX	MLC		3696.	3139.
	222B	AX	MLC		3879.	3258.
	226A	AX	MLC		3763.	3183.
	226B	AX	MLC		3922.	3285.
	230A	AX	MLC		3917.	3282.
		MEAN			3434.	2954.
		STD. DEV.			352.	246.
3A	235	RAD	MLC		3174.	2703.
	239	RAD	MLC		3813.	3102.
	241	RAD	MLC		3985.	3199.
	245	RAD	MLC		3411.	2857.
	247	RAD	MLC		3619.	2989.
	257	RAD	MLC		3207.	2725.
	259	RAD	MLC		2768.	2419.
	263	RAD	MLC		2385.	2131.
	265	RAD	MLC		2285.	2053.
	269	RAD	MLC		2737.	2397.
3E	236	RAD	MLC		3302.	2787.
	240	RAD	MLC		2881.	2502.
	242	RAD	MLC		3672.	3020.
	246	RAD	MLC		3780.	3083.
	248	RAD	MLC		2999.	2585.
	258	RAD	MLC		3651.	3008.
	260	RAD	MLC		4082.	3249.
	264	RAD	MLC		3636.	2999.
	266	RAD	MLC		3452.	2884.
	270	RAD	MLC		2210.	1993.
		MEAN			3253.	2734.
		STD. DEV.			561.	380.

TABLE 11-6 (Continued)

LOT NO. 440 SPEC. DIA. 0.25 IN.
LOG NO. 6484-56 SPEC. LENGTH 2.0 IN.
LOG DENSITY 1.77 G/CC

SPECIMEN NUMBER	ORIENTATION	LOCATION	DENSITY (G/CC)	MODULUS OF RUPTURE (PSI) (UNCORRECTED)	FLEXURAL STRENGTH (PSI) (CORRECTED)
3A	273A AX	MLE		3808.	3287.
	273B AX	MLE		3896.	3348.
	275A AX	MLE		4316.	3625.
	275B AX	MLE		3509.	3072.
	279A AX	MLE		3517.	3078.
	279B AX	MLE		3777.	3265.
	285A AX	MLE		4035.	3442.
	285B AX	MLE		4228.	3568.
	287A AX	MLE		4057.	3457.
	287B AX	MLE		3998.	3417.
3B	274A AX	MLE		3653.	3177.
	274B AX	MLE		3738.	3238.
	276A AX	MLE		3402.	2992.
3B	276B AX	MLE		3622.	3154.
	280A AX	MLE		4527.	3761.
	280B AX	MLE		4321.	3628.
	286A AX	MLE		4738.	3888.
	286B AX	MLE		5139.	4115.
	288A AX	MLE		4661.	3843.
	288B AX	MLE		4755.	3898.
	MEAN			4085.	3463.
	STD. DEV.			487.	319.
3A	295 RAD	MLE		4877.	3712.
	299 RAD	MLE		5026.	3771.
	301 RAD	MLE		4865.	3707.
	305 RAD	MLE		4807.	3683.
	307 RAD	MLE		5063.	3784.
	317 RAD	MLE		4187.	3381.
	319 RAD	MLE		4042.	3297.
	323 RAD	MLE		4186.	3380.
	325 RAD	MLE		3818.	3165.
	329 RAD	MLE		2830.	2491.
3B	296 RAD	MLE		4462.	3523.
	300 RAD	MLE		4683.	3630.
	302 RAD	MLE		4703.	3638.
3B	306 RAD	MLE		4594.	3588.
	308 RAD	MLE		4665.	3622.
	318 RAD	MLE		3265.	2804.
	320 RAD	MLE		1904.	1757.
	324 RAD	MLE		3765.	3132.
	326 RAD	MLE		4021.	3285.
	330 RAD	MLE		4087.	3323.
	MEAN			4192.	3334.
	STD. DEV.			796.	498.

TABLE 11-6 (Continued)

LOT NO. 440 SPEC. DIA. 0.25 IN.
LOG NO. 6484-56 SPEC. LENGTH 2.0 IN.
LOG DENSITY 1.77 G/CC

SPECIMEN NUMBER	ORIENTATION	LOCATION	DENSITY (G/CC)	MODULUS OF RUPTURE (PSI) (UNCORRECTED)	FLEXURAL STRENGTH (PSI) (CORRECTED)
1A	3B AX	EC		4195.	3481.
	5A AX	EC		2834.	2530.
	5B AX	EC		3776.	3210.
	13A AX	EC		4128.	3438.
	13B AX	EC		3729.	3179.
	19A AX	EC		3803.	3228.
	19B AX	EC		3462.	2996.
	25A AX	EC		3056.	2698.
	25B AX	EC		3593.	3047.
	29A AX	EC		3144.	2764.
1B	4B AX	EC		4264.	3523.
	6A AX	EC		3304.	2883.
	6B AX	EC		3804.	3229.
	12A AX	EC		4054.	3390.
	12B AX	EC		2384.	2172.
	22A AX	EC		3822.	3240.
1B	22B AX	EC		3946.	3320.
	26A AX	EC		2651.	2396.
	26B AX	EC		4060.	3394.
	30A AX	EC		3619.	3175.
	MEAN			3581.	3063.
	STD. DEV.			531.	379.
1A	35 RAD	EC		3321.	2842.
	39 RAD	EC		2711.	2402.
	41 RAD	EC		3015.	2628.
	45 RAD	EC		3055.	2656.
	47 RAD	EC		3696.	3087.
	57 RAD	EC		3376.	2880.
	59 RAD	EC		3873.	3198.
	63 RAD	EC		3087.	2680.
	65 RAD	EC		3435.	2918.
	69 RAD	EC		3477.	2946.
1B	36 RAD	EC		3364.	2871.
	40 RAD	EC		3470.	2941.
	42 RAD	EC		2814.	2479.
	46 RAD	EC		2763.	2441.
	48 RAD	EC		3667.	3068.
	58 RAD	EC		3704.	3092.
1B	60 RAD	EC		4265.	3424.
	64 RAD	EC		3445.	2925.
	66 RAD	EC		3904.	3217.
	70 RAD	EC		3742.	3117.
	MEAN			3409.	2891.
	STD. DEV.			411.	275.

TABLE 11-6 (Continued)

LOT NO. 440 SPEC. DIA. 0.25 IN.
LOG NO. 6484-56 SPEC. LENGTH 2.0 IN.
LOG DENSITY, 1.77 G/CC

SPECIMEN NUMBER	ORIENTATION	LOCATION	DENSITY (G/CC)	MODULUS OF RUPTURE (PSI) (UNCORRECTED)	FLEXURAL STRENGTH (PSI) (CORRECTED)
1A	73A AX	EE		3561.	3102.
	73B AX	EE		4074.	3485.
	75A AX	EE		3267.	2885.
	75B AX	EE		2576.	2344.
	79A AX	EE		2593.	2358.
	79B AX	EE		3591.	3124.
	85A AX	EE		3532.	3081.
	85B AX	EE		3817.	3263.
	87A AX	EE		3876.	3323.
	87B AX	EE		4171.	3518.
1E	74A AX	EE		3011.	2690.
	74B AX	EE		3935.	3364.
	76A AX	EE		2980.	2666.
	76B AX	EF		3922.	3354.
	82A AX	EE		4704.	3951.
	82B AX	EE		4064.	3449.
	86A AX	EE		4559.	3765.
	86B AX	EE		5078.	4060.
	88A AX	EE		3884.	3329.
1F	88B AX	EE		4662.	3826.
	MEAN			3793.	3241.
	STD. DEV.			681.	474.
1A	95 RAD	EE		4805.	3695.
	99 RAD	EE		4669.	3637.
	101 RAD	EF		4817.	3703.
	105 RAD	EE		4947.	3757.
	107 RAD	EE		4460.	3535.
	117 RAD	EF		4317.	3462.
	119 RAD	EE		4510.	3559.
	123 RAD	EE		3976.	3268.
	125 RAD	EE		3266.	2810.
	129 RAD	EE		4040.	3305.
1C	100 RAD	EE		4365.	3487.
	102 RAD	EE		4570.	3589.
	106 RAD	EE		4561.	3585.
	108 RAD	EE		5023.	3787.
	118 RAD	EF		4216.	3407.
	120 RAD	EE		3231.	2786.
	124 RAD	EE		4407.	3508.
	126 RAD	EF		4001.	3282.
	130 RAD	EF		2967.	2597.
1B	96 RAD	EE		4417.	3513.
	MEAN			4278.	3414.
	STD. DEV.			566.	330.

(a) Data obtained prior to conversion to SI units.

TABLE 11-7
IMPURITY CONTENT OF H-451 GRAPHITE[a]
GLCC Lot 440, Log 6484-57 (GLCC Log 68), Density = 1.77 Mg/m^3 (g/cm^3)

LAB. NO. 41693 REPORT TO: W.R.JOHNSON DATE: 2-26-75
SAMPLE : 6484-57 L211 GRAP MLC PROJECT NO. 3224146005 DILUTION: 1.0000 PLATE NO. 76-11,

ELEMENT	CONCENTRATION, PPM	ELEMENT	CONCENTRATION, PPM	ELEMENT	CONCENTRATION, PPM
AG	< .50	AL	< 1.00	B	1.00
BA	< .50	BE	< .50	BI	< 2.00
CA	< 20.00	CD	< 10.00	CE	< 80.00
CO	< 4.00	CR	< 10.00	CS	< 100.00
CU	< 1.00	DY	< 20.00	ER	< 6.00
EU	< 10.00	FE	< 1.00	GD	< 10.00
HF	< 20.00	HO	< 10.00	IN	< 1.00
K	< 10.00	LA	< 10.00	LI	< 1.00
LU	< .50	MG	1.00	MN	< 1.00
MO	< 1.00	NA	< 10.00	NB	< 6.00
ND	< 200.00	NI	< 4.00	P	< 100.00
PB	< 6.00	PR	< 100.00	RB	< 40.00
SB	< 8.00	SC	< 1.00	SI	60.00
SM	< 100.00	SN	< 6.00	SR	< 40.00
TA	< 40.00	TB	< 40.00	TI	< 1.00
TL	< 20.00	TM	< 4.00	V	< .50
W	< 40.00	YB	< 10.00	ZN	< 20.00
ZR	< .50				

LAB. NO. 41693 REPORT TO: W.R.JOHNSON DATE: 2-26-75
SAMPLE : 6484-57 L216 GRAP MLC PROJECT NO. 3224146005 DILUTION: 1.0000 PLATE NO. 76-11,

ELEMENT	CONCENTRATION, PPM	ELEMENT	CONCENTRATION, PPM	ELEMENT	CONCENTRATION, PPM
AG	< .50	AL	< 1.00	B	1.00
BA	< .50	BE	< .50	BI	< 2.00
CA	< 20.00	CD	< 10.00	CE	< 80.00
CO	< 4.00	CR	< 10.00	CS	< 100.00
CU	< 1.00	DY	< 20.00	ER	< 6.00
EU	< 10.00	FE	< 1.00	GD	< 10.00
HF	< 20.00	HO	< 10.00	IN	< 1.00
K	< 10.00	LA	< 10.00	LI	< 1.00
LU	< .50	MG	< .50	MN	< 1.00
MO	< 1.00	NA	< 10.00	NB	< 6.00
ND	< 200.00	NI	< 4.00	P	< 100.00
PB	< 6.00	PR	< 100.00	RB	< 40.00
SB	< 8.00	SC	< 1.00	SI	40.00
SM	< 100.00	SN	< 6.00	SR	< 40.00
TA	< 40.00	TB	< 40.00	TI	< 1.00
TL	< 20.00	TM	< 4.00	V	< .50
W	< 40.00	YB	< 10.00	ZN	< 20.00
ZR	< .50				

TABLE 11-7 (Continued)

LAB. NO. 41693 REPORT TO: W.R.JOHNSON DATE: 2-26-75
SAMPLE : 6484-57 L273 GRAP MLE PROJECT NO. 3224146005 DILUTION: 1.0000 PLATE NO. 76-11,

ELEMENT	CONCENTRATION, PPM	ELEMENT	CONCENTRATION, PPM	ELEMENT	CONCENTRATION, PPM
AG	< .50	AL	6.00	B	1.00
BA	< .50	BE	< .50	BI	< 2.00
CA	< 20.00	CD	< 10.00	CE	< 80.00
CO	< 4.00	CR	< 10.00	CS	< 100.00
CU	< 1.00	DY	< 20.00	ER	< 6.00
EU	< 10.00	FE	< 1.00	GD	< 10.00
HF	< 20.00	HO	< 10.00	IN	< 1.00
K	< 10.00	LA	< 10.00	LI	< 1.00
LU	< .50	MG	6.00	MN	< 1.00
MO	< 1.00	NA	< 10.00	NB	< 6.00
ND	< 200.00	NI	< 4.00	P	< 100.00
PB	< 6.00	PR	< 100.00	RB	< 40.00
SB	< 8.00	SC	< 1.00	SI	60.00
SM	< 100.00	SN	< 6.00	SR	< 40.00
TA	< 40.00	TB	< 40.00	TI	< 1.00
TL	< 20.00	TM	< 4.00	V	< .50
W	< 40.00	YB	< 10.00	ZN	< 20.00
ZR	< .50				

LAB. NO. 41693 REPORT TO: W.R.JOHNSON DATE: 2-26-75
SAMPLE : 6484-57 L274 GRAP MLE PROJECT NO. 3224146005 DILUTION: 1.0000 PLATE NO. 76-11,

ELEMENT	CONCENTRATION, PPM	ELEMENT	CONCENTRATION, PPM	ELEMENT	CONCENTRATION, PPM
AG	< .50	AL	20.00	B	1.00
BA	< .50	BE	< .50	BI	< 2.00
CA	< 20.00	CD	< 10.00	CE	< 80.00
CO	< 4.00	CR	< 10.00	CS	< 100.00
CU	< 1.00	DY	< 20.00	ER	< 6.00
EU	< 10.00	FE	< 1.00	GD	< 10.00
HF	< 20.00	HO	< 10.00	IN	< 1.00
K	< 10.00	LA	< 10.00	LI	< 1.00
LU	< .50	MG	1.00	MN	< 1.00
MO	< 1.00	NA	< 10.00	NB	< 6.00
ND	< 200.00	NI	< 4.00	P	< 100.00
PB	< 6.00	PR	< 100.00	RB	< 40.00
SB	< 8.00	SC	< 1.00	SI	100.00
SM	< 100.00	SN	< 6.00	SR	< 40.00
TA	< 40.00	TB	< 40.00	TI	< 1.00
TL	< 20.00	TM	< 4.00	V	< .50
W	< 40.00	YB	< 10.00	ZN	< 20.00
ZR	< .50				

TABLE 11-7 (Continued)

LAB. NO. 41693 — REPORT TO: W.R.JOHNSON — DATE: 2-26-75
SAMPLE : 6484-57 L11B GRAP EC — PROJECT NO. 3224146005 — DILUTION: 1.0000 — PLATE NO. 76-11,

ELEMENT	CONCENTRATION, PPM	ELEMENT	CONCENTRATION, PPM	ELEMENT	CONCENTRATION, PPM
AG	< .50	AL	< 1.00	B	2.00
BA	< .50	BE	< .50	BI	< 2.00
CA	< 20.00	CD	< 10.00	CE	< 80.00
CO	< 4.00	CR	< 10.00	CS	< 100.00
CU	6.00	DY	< 20.00	ER	< 6.00
EU	< 10.00	FE	< 1.00	GD	< 10.00
HF	< 20.00	HO	< 10.00	IN	< 1.00
K	< 10.00	LA	< 10.00	LI	< 1.00
LU	< .50	MG	1.00	MN	< 1.00
MO	< 1.00	NA	< 10.00	NB	< 6.00
ND	< 200.00	NI	< 4.00	P	< 100.00
PB	< 6.00	PR	< 100.00	RB	< 40.00
SB	< 8.00	SC	< 1.00	SI	< 10.00
SM	< 100.00	SN	< 6.00	SR	< 40.00
TA	< 40.00	TB	< 40.00	TI	< 1.00
TL	< 20.00	TM	< 4.00	V	< .50
W	< 40.00	YB	< 10.00	ZN	< 20.00
ZR	< .50				

LAB. NO. 41693 — REPORT TO: W.R.JOHNSON — DATE: 2-26-75
SAMPLE : 6484-57 L16B GRAP EC — PROJECT NO. 3224146005 — DILUTION: 1.0000 — PLATE NO. 76-11,

ELEMENT	CONCENTRATION, PPM	ELEMENT	CONCENTRATION, PPM	ELEMENT	CONCENTRATION, PPM
AG	< .50	AL	< 1.00	B	1.00
BA	< .50	BE	< .50	BI	< 2.00
CA	< 20.00	CD	< 10.00	CE	< 80.00
CO	< 4.00	CR	< 10.00	CS	< 100.00
CU	6.00	DY	< 20.00	ER	< 6.00
EU	< 10.00	FE	< 1.00	GD	< 10.00
HF	< 20.00	HO	< 10.00	IN	< 1.00
K	< 10.00	LA	< 10.00	LI	< 1.00
LU	< .50	MG	1.00	MN	< 1.00
MO	< 1.00	NA	< 10.00	NB	< 6.00
ND	< 200.00	NI	< 4.00	P	< 100.00
PB	< 6.00	PR	< 100.00	RB	< 40.00
SB	< 8.00	SC	< 1.00	SI	< 10.00
SM	< 100.00	SN	< 6.00	SR	< 40.00
TA	< 40.00	TB	< 40.00	TI	< 1.00
TL	< 20.00	TM	< 4.00	V	< .50
W	< 40.00	YB	< 10.00	ZN	< 20.00
ZR	< .50				

TABLE 11-7 (Continued)

LAB. NO. 41693 REPORT TO: W.R.JOHNSON DATE: 2-26-75
SAMPLE : 6484-57 L73B CRAP EE PROJECT NO. 3224146005 DILUTION: 1.0000 PLATE NO. 76-11,

ELEMENT	CONCENTRATION, PPM	ELEMENT	CONCENTRATION, PPM	ELEMENT	CONCENTRATION, PPM
AG	< .50	AL	< 1.00	B	1.00
BA	< .50	BE	< .50	BI	< 2.00
CA	< 20.00	CD	< 10.00	CE	< 80.00
CO	< 4.00	CR	< 1.00	CS	< 100.00
CU	< 1.00	DY	< 20.00	ER	< 6.00
EU	< 10.00	FE	< 1.00	GD	< 10.00
HF	< 20.00	HO	< 10.00	IN	< 1.00
K	< 10.00	LA	< 10.00	LI	< 1.00
LU	< .50	MG	1.00	MN	< 1.00
MO	< 1.00	NA	< 10.00	NB	< 6.00
ND	< 200.00	NI	< 4.00	P	< 100.00
PB	< 6.00	PR	< 100.00	RB	< 40.00
SB	< 8.00	SC	< 1.00	SI	100.00
SM	< 100.00	SN	< 6.00	SR	< 40.00
TA	< 40.00	TB	< 40.00	TI	< 1.00
TL	< 20.00	TM	< 4.00	V	< .50
W	< 40.00	YB	< 10.00	ZN	< 20.00
ZR	< .50				

LAB. NO. 41693 REPORT TO: W.R.JOHNSON DATE: 2-26-75
SAMPLE : 6484-57 L74B GRAP EE PROJECT NO. 3224146005 DILUTION: 1.0000 PLATE NO. 76-11,

ELEMENT	CONCENTRATION, PPM	ELEMENT	CONCENTRATION, PPM	ELEMENT	CONCENTRATION, PPM
AG	< .50	AL	< 1.00	B	1.00
BA	< .50	BE	< .50	BI	< 2.00
CA	< 20.00	CD	< 10.00	CE	< 80.00
CO	< 4.00	CR	< 10.00	CS	< 100.00
CU	< 1.00	DY	< 20.00	ER	< 6.00
EU	< 10.00	FE	< 1.00	GD	< 10.00
HF	< 20.00	HO	< 10.00	IN	< 1.00
K	< 10.00	LA	< 10.00	LI	< 1.00
LU	< .50	MG	1.00	MN	< 1.00
MO	< 1.00	NA	< 10.00	NB	< 6.00
ND	< 200.00	NI	< 4.00	P	< 100.00
PB	< 6.00	PR	< 100.00	RB	< 40.00
SB	< 8.00	SC	< 1.00	SI	100.00
SM	< 100.00	SN	< 6.00	SR	< 40.00
TA	< 40.00	TB	< 40.00	TI	< 1.00
TL	< 20.00	TM	< 4.00	V	< .50
W	< 40.00	YB	< 10.00	ZN	< 20.00
ZR	< .50				

(a) CONCENTRATION BASED ON ORGINAL SAMPLE BEFORE DILUTION WITH DILUENT
> MEANS GREATER THAN
< MEANS LESS THAN THE SENSITIVITYOF THE SPECTROGRAPHIC PROCEDURE USED
RESULTS ARE CORRECT WITHIN A FACTOR OF 40% , (ONE STANDARD DEVIATION)

TABLE 11-8
ASH AND SULFUR CONTENT OF H-451 GRAPHITE
GLCC Lot 440, Log 6484-57 (GLCC Log 68),
Density = 1.77 Mg/m^3 (g/cm^3)

	Concentration (ppm)							
	Midlength Center		Midlength Edge		End Center		End Edge	
Element	L211B	L216B	L273B	L274B	L11B	L16B	L73B	L74B
Ash	68	50	106	153	13	13	170	97
Sulfur	<1	<1	<1	<1	<1	4.7	<1	<1
	<1	<1	<1	<1	<1	5.2	<1	<1

TABLE 11-9
THERMAL CONDUCTIVITY OF SO818 GRAPHITE
AS Lot 4B, Log 6484-19 (AS Log 13), Density = 1.74 Mg/m^3 (g/cm^3)

LOT NUMBER: 4-B LOG NUMBER: 6484-19

ORIENTATION	LOCATION	SPECIMEN NUMBER	THERMAL CONDUCTIVITY (W/M-K) AT: 295K (22C)	473K (200C)	673K (400C)	873K (600C)	1073K (800C)
AXIAL	MLC	3A-L3A	134.6	110.2	89.9	74.8	66.8
		3A-L3B	137.7	115.2	98.0	74.9	65.8
		3A-L4A	131.6	115.4	91.8	70.5	71.4
		3A-L4B	142.3	106.5	89.3	72.4	62.5
		3B-L3A	127.5	119.1	93.9	73.2	66.6
		3B-L3B	131.1	111.1	89.9	71.0	68.8
		3B-L4A	135.3	116.9	102.4	84.4	73.4
		3B-L4B	139.4	116.7	103.8	80.7	66.6
		MEAN:	134.9	113.9	94.9	75.3	67.7
		STD. DEV:	4.8	4.2	5.8	4.9	3.4
RADIAL	MLC	3A-L16A	120.1	104.7	84.8	69.6	57.4
		3A-L16B	126.3	112.4	97.7	79.4	64.6
		3A-L22A	129.1	107.7	91.1	72.2	61.4
		3A-L22B	126.4	112.3	94.2	74.8	67.0
		3B-L16A	128.5	111.9	91.3	73.1	65.7
		3B-L16B	119.3	112.3	95.5	79.4	70.5
		3B-L22A	131.1	105.1	86.6	67.9	62.7
		3B-L22B	125.1	112.4	92.0	77.1	63.2
		MEAN:	125.7	109.8	91.6	74.2	64.1
		STD. DEV:	4.2	3.4	4.3	4.3	3.9

TABLE 11-10
FLEXURAL STRENGTH OF SO818 GRAPHITE
AS Lot 4B, Logs 6484-19 and -20 (AS Logs 13 and 16), Density = 1.78 Mg/m^3 (g/cm^3) for Log 6484-19 and 1.74 Mg/m^3 (g/cm^3) for Log 6484-20

LOT NO. 4-B SPEC. DIA. 6.4 MM
LOG NO. 6484-19 SPEC. LENGTH 51. MM
LOG DENSITY 1.74 KG/M**3

SPECIMEN NUMBER	ORIENTATION	LOCATION	DENSITY (KG/M**3)	MODULUS OF RUPTURE (MPA) (UNCORRECTED)	FLEXURAL STRENGTH (MPA) (CORRECTED)
3AC-3	AX	MLC		16.9	15.1
-5	AX	MLC		12.5	11.5
-6	AX	MLC		17.5	15.5
-10	AX	MLC		18.4	16.2
-12	AX	MLC		17.2	15.3
-13	AX	MLC		21.5	18.4
-15	AX	MLC		20.3	17.6
-21	AX	MLC		18.2	16.0
-22	AX	MLC		21.1	18.1
-24	AX	MLC		21.4	18.3
3BC-3	AX	MLC		19.3	16.8
-5	AX	MLC		23.6	19.8
-6	AX	MLC		23.7	19.8
-10	AX	MLC		20.5	17.7
-12	AX	MLC		22.3	18.9
-13	AX	MLC		23.0	19.4
-15	AX	MLC		26.0	21.2
-21	AX	MLC		21.4	18.3
-22	AX	MLC		21.7	18.5
-24	AX	MLC		24.7	20.5
	MEAN			20.6 MPA (2983. PSI)	17.6 MPA (2559. PSI)
	STD. DEV.			3.2 MPA (458. PSI)	2.3 MPA (327. PSI)
3AC-32	RAD	MLC		18.4	16.2
-33	RAD	MLC		18.5	16.3
-34	RAD	MLC		19.0	16.6
-35	RAD	MLC		19.5	17.0
-36	RAD	MLC		20.6	17.8
-39	RAD	MLC		23.9	19.9
-40	RAD	MLC		20.4	17.6
-41	RAD	MLC		19.5	17.0
-42	RAD	MLC		23.1	19.4
-43	RAD	MLC		19.1	16.7
3BC-32	RAD	MLC		19.9	17.3
-33	RAD	MLC		23.2	19.5
-34	RAD	MLC		21.5	18.4
-35	RAD	MLC		20.7	17.8
-36	RAD	MLC		21.4	18.3
-39	RAD	MLC		20.8	17.9
-40	RAD	MLC		25.9	21.2
-41	RAD	MLC		23.5	19.7
-42	RAD	MLC		21.5	18.4
-43	RAD	MLC		22.4	19.0
	MEAN			21.1 MPA (3066. PSI)	18.1 MPA (2625. PSI)
	STD. DEV.			2.0 MPA (291. PSI)	1.4 MPA (196. PSI)

TABLE 11-10 (Continued)

LOT NO. 4-B — SPEC. DIA. 6.4 MM
LOG NO. 6484-19 — SPEC. LENGTH 51. MM
LOG DENSITY 1.74 KG/M**3

SPECIMEN NUMBER	ORIENTATION	LOCATION	DENSITY (KG/M**3)	MODULUS OF RUPTURE (MPA) (UNCORRECTED)	FLEXURAL STRENGTH (MPA) (CORRECTED)
3AE-51	AX	MLE		21.1	18.7
-52	AX	MLE		24.3	21.0
-54	AX	MLE		23.3	20.3
-55	AX	MLE		21.4	18.9
-56	AX	MLE		23.0	20.1
-59	AX	MLE		18.2	16.4
-60	AX	MLE		22.1	19.4
-61	AX	MLE		20.1	17.9
-62	AX	MLE		23.2	20.2
-63	AX	MLE		24.5	21.1
3BE-51	AX	MLE		28.0	23.5
-52	AX	MLE		25.4	21.8
-54	AX	MLE		27.2	23.0
-55	AX	MLE		28.2	23.6
-56	AX	MLE		29.1	24.2
-59	AX	MLE		27.0	22.9
-60	AX	MLE		28.6	23.9
-61	AX	MLE		27.3	23.0
-62	AX	MLE		28.2	23.6
-63	AX	MLE		27.9	23.4
	MEAN			24.9 MPA (3611. PSI)	21.4 MPA (3097. PSI)
	STD. DEV.			3.2 MPA (471. PSI)	2.3 MPA (332. PSI)
3AE-72	RAD	MLE		17.0	15.1
-73	RAD	MLE		15.2	13.7
-74	RAD	MLE		16.6	14.8
-75	RAD	MLE		18.9	16.6
-76	RAD	MLE		15.8	14.2
-79	RAD	MLE		18.0	15.9
3AE-80	RAD	MLE		19.7	17.2
-81	RAD	MLE		17.6	15.6
-82	RAD	MLE		21.1	18.1
-83	RAD	MLE		20.6	17.8
3BE-72	RAD	MLE		19.6	17.1
-73	RAD	MLE		22.3	18.9
-74	RAD	MLE		18.6	16.3
-75	RAD	MLE		23.7	19.8
-76	RAD	MLE		22.0	18.7
-79	RAD	MLE		22.1	18.8
-80	RAD	MLE		24.6	20.4
-81	RAD	MLE		20.5	17.7
-82	RAD	MLE		22.7	19.2
-83	RAD	MLE		23.2	19.5
	MEAN			20.0 MPA (2900. PSI)	17.3 MPA (2503. PSI)
	STD. DEV.			2.7 MPA (398. PSI)	2.0 MPA (283. PSI)

TABLE 11-10 (Continued)

LOT NO. 4-B SPEC. DIA. 6.4 MM
LOG NO. 6484-19 SPEC. LENGTH 51. MM
LOG DENSITY 1.74 KG/M**3

SPECIMEN NUMBER	ORIENTATION	LOCATION	DENSITY (KG/M**3)	MODULUS OF RUPTURE (MPA) (UNCORRECTED)	FLEXURAL STRENGTH (MPA) (CORRECTED)
IAC-3	AX	EC		23.0	19.8
-5	AX	EC		22.5	19.4
-6	AX	EC		24.4	20.7
-10	AX	EC		22.5	19.4
-12	AX	EC		25.3	21.3
-13	AX	EC		24.0	20.4
-15	AX	EC		26.5	22.1
-21	AX	EC		25.9	21.7
-22	AX	EC		22.4	19.4
-24	AX	EC		21.6	18.8
IBC-3	AX	EC		22.6	19.5
-5	AX	EC		24.9	21.1
-6	AX	EC		22.7	19.6
-10	AX	EC		22.0	19.1
-12	AX	EC		23.9	20.4
-13	AX	EC		25.5	21.4
IBC-15	AX	EC		24.6	20.9
-21	AX	EC		18.6	16.5
-22	AX	EC		20.2	17.7
-24	AX	EC		21.9	19.0
	MEAN			23.2 MPA (3371. PSI)	19.9 MPA (2887. PSI)
	STD. DEV.			2.0 MPA (286. PSI)	1.4 MPA (198. PSI)
IAC-32	RAD	EC		25.6	21.0
-33	RAD	EC		19.3	16.9
-34	RAD	EC		22.6	19.1
-35	RAD	EC		23.1	19.4
-36	RAD	EC		21.5	18.4
-39	RAD	EC		22.2	18.8
-40	RAD	EC		23.2	19.5
-41	RAD	EC		23.4	19.6
-42	RAD	EC		23.8	19.9
-43	RAD	EC		21.2	18.2
IBC-32	RAD	EC		21.7	18.5
-33	RAD	EC		18.8	16.5
-34	RAD	EC		20.9	18.0
-35	RAD	EC		19.5	17.0
-36	RAD	EC		20.3	17.6
-39	RAD	EC		22.0	18.7
-40	RAD	EC		21.9	18.6
-41	RAD	EC		27.0	21.8
-42	RAD	EC		23.4	19.6
-43	RAD	EC		26.5	21.5
	MEAN			22.4 MPA (3249. PSI)	18.9 MPA (2746. PSI)
	STD. DEV.			2.2 MPA (322. PSI)	1.4 MPA (209. PSI)

TABLE 11-10 (Continued)

LOT NO. 4-B SPEC. DIA. 6.4 MM
LOG NO. 6484-19 SPEC. LENGTH 51. MM
LOG DENSITY 1.74 KG/M**3

SPECIMEN NUMBER	ORIENTATION	LOCATION	DENSITY (KG/M**3)	MODULUS OF RUPTURE (MPA) (UNCORRECTED)	FLEXURAL STRENGTH (MPA) (CORRECTED)
1AE-51	AX	EE		27.7	23.3
-52	AX	EE		26.5	22.6
-54	AX	EE		24.0	20.8
-55	AX	EE		25.5	21.9
-56	AX	EE		28.3	23.7
-59	AX	EE		19.0	17.1
1AE-60	AX	EE		27.2	23.0
-61	AX	EE		22.0	19.3
-62	AX	EE		26.7	22.7
-63	AX	EE		30.9	25.3
1BE-51	AX	EE		24.9	21.4
-52	AX	EE		26.9	22.8
-54	AX	EE		28.9	24.1
-55	AX	EE		27.1	22.9
-56	AX	EE		20.1	17.9
-59	AX	EE		25.0	21.5
-60	AX	EE		25.6	22.0
-61	AX	EE		27.9	23.4
-62	AX	EE		25.9	22.1
-63	AX	EE		31.5	25.6
	MEAN			26.1 MPA (3782. PSI)	22.2 MPA (3214. PSI)
	STD. DEV.			3.1 MPA (453. PSI)	2.2 MPA (312. PSI)
1AE-72	RAD	EE		21.8	18.6
-73	RAD	EE		22.0	18.7
-74	RAD	EE		20.5	17.7
-75	RAD	EE		20.7	17.9
-76	RAD	EE		22.9	19.3
-79	RAD	EE		22.1	18.8
-80	RAD	EE		23.1	19.4
-81	RAD	EE		16.8	15.0
-82	RAD	EE		21.8	18.6
-83	RAD	EE		19.2	16.8
1BE-72	RAD	EE		17.9	15.8
-73	RAD	EE		25.1	20.7
-74	RAD	EE		21.0	18.0
-75	RAD	EE		24.7	20.5
-76	RAD	EE		21.5	18.4
-79	RAD	EE		22.3	18.9
1BE-80	RAD	EE		21.8	18.6
-81	RAD	EE		23.1	19.4
-82	RAD	EE		22.7	19.2
-83	RAD	EE		23.4	19.6
	MEAN			21.7 MPA (3150. PSI)	18.5 MPA (2681. PSI)
	STD. DEV.			2.0 MPA (294. PSI)	1.4 MPA (203. PSI)

TABLE 11-10 (Continued)

LOT NO. 4-B — SPEC. DIA. 6.4 MM
LOG NO. 6484-20 — SPEC. LENGTH 51. MM
LOG DENSITY 1.76 KG/M**3

SPECIMEN NUMBER	ORIENTATION	LOCATION	DENSITY (KG/M**3)	MODULUS OF RUPTURE (MPA) (UNCORRECTED)	FLEXURAL STRENGTH (MPA) (CORRECTED)
3A-3	AX	MLC		19.6	17.1
-5	AX	MLC		21.4	18.3
-6	AX	MLC		21.0	18.0
-10	AX	MLC		18.8	16.5
-12	AX	MLC		20.9	18.0
-13	AX	MLC		22.2	18.9
-15	AX	MLC		18.8	16.5
-21	AX	MLC		20.8	17.9
-22	AX	MLC		22.0	18.7
-24	AX	MLC		20.4	17.6
3B-3	AX	MLC		28.8	22.7
-5	AX	MLC		24.5	20.3
-6	AX	MLC		25.9	21.2
-10	AX	MLC		22.9	19.3
-12	AX	MLC		21.9	18.6
-13	AX	MLC		22.5	19.0
-15	AX	MLC		21.7	18.5
-21	AX	MLC		18.4	16.2
-22	AX	MLC		21.7	18.5
-24	AX	MLC		22.7	19.2
	MEAN			21.8 MPA (3168. PSI)	18.5 MPA (2690. PSI)
	STD. DEV.			2.5 MPA (356. PSI)	1.6 MPA (228. PSI)
3A-32	RAD	MLC		20.5	17.7
-33	RAD	MLC		17.3	15.4
-34	RAD	MLC		21.5	18.4
-35	RAD	MLC		20.2	17.5
-36	RAD	MLC		19.3	16.8
-39	RAD	MLC		17.6	15.6
3A-40	RAD	MLC		17.9	15.8
-41	RAD	MLC		15.9	14.3
-42	RAD	MLC		18.3	16.1
-43	RAD	MLC		16.4	14.6
3B-32	RAD	MLC		21.7	18.5
3B-33	RAD	MLC		18.1	15.9
-34	RAD	MLC		20.3	17.5
-35	RAD	MLC		20.5	17.7
-36	RAD	MLC		20.7	17.8
-39	RAD	MLC		17.7	15.6
-40	RAD	MLC		19.4	16.9
-41	RAD	MLC		16.7	14.9
-42	RAD	MLC		18.3	16.1
-43	RAD	MLC		17.8	15.7
	MEAN			18.8 MPA (2727. PSI)	16.4 MPA (2385. PSI)
	STD. DEV.			1.7 MPA (249. PSI)	1.3 MPA (182. PSI)

TABLE 11-10 (Continued)

LOT NO. 4-B SPEC. DIA. 6.4 MM
LOG NO. 6484-20 SPEC. LENGTH 51. MM
LOG DENSITY 1.76 KG/M**3

SPECIMEN NUMBER	ORIENTATION	LOCATION	DENSITY (KG/M**3)	MODULUS OF RUPTURE (MPA) (UNCORRECTED)	FLEXURAL STRENGTH (MPA) (CORRECTED)
3A-51	AX	MLE		23.5	20.1
-52	AX	MLE		22.4	19.4
-54	AX	MLE		20.4	17.9
-55	AX	MLE		21.7	18.9
-56	AX	MLE		25.3	21.3
-59	AX	MLE		24.9	21.0
-60	AX	MLE		24.3	20.6
-61	AX	MLE		25.4	21.3
-62	AX	MLE		28.4	23.2
-63	AX	MLE		26.6	22.1
3B-51	AX	MLE		28.4	23.2
-52	AX	MLE		28.6	23.3
-54	AX	MLE		26.2	21.9
-55	AX	MLE		24.7	20.9
-56	AX	MLE		23.4	20.1
-59	AX	MLE		22.7	19.5
-60	AX	MLE		26.5	22.1
3B-61	AX	MLE		26.6	22.1
-62	AX	MLE		24.6	20.9
-63	AX	MLE		30.9	24.6
	MEAN			25.3 MPA (3666. PSI)	21.2 MPA (3080. PSI)
	STD. DEV.			2.6 MPA (377. PSI)	1.7 MPA (242. PSI)
3A-72	RAD	MLE		17.5	15.5
3A-73	RAD	MLE		19.3	16.9
-74	RAD	MLE		19.7	17.1
-75	RAD	MLE		20.8	17.9
-76	RAD	MLE		19.2	16.8
-79	RAD	MLE		20.2	17.5
-80	RAD	MLE		19.3	16.9
-81	RAD	MLE		20.6	17.8
-82	RAD	MLE		19.4	16.9
-83	RAD	MLE		20.2	17.5
3B-72	RAD	MLE		20.4	17.6
-73	RAD	MLE		23.6	19.7
-74	RAD	MLE		23.9	20.0
-75	RAD	MLE		22.3	18.9
-76	RAD	MLE		25.9	21.1
-79	RAD	MLE		20.1	17.4
-80	RAD	MLE		23.2	19.5
-81	RAD	MLE		21.4	18.3
-82	RAD	MLE		19.1	16.7
-83	RAD	MLE		22.9	19.3
	MEAN			20.9 MPA (3038. PSI)	18.0 MPA (2605. PSI)
	STD. DEV.			2.1 MPA (299. PSI)	1.4 MPA (202. PSI)

TABLE 11-10 (Continued)

LOT NO. 4-B SPEC. DIA. 6.4 MM
LOG NO. 6484-20 SPEC. LENGTH 51. MM
LOG DENSITY 1.76 KG/M**3

SPECIMEN NUMBER	ORIENTATION	LOCATION	DENSITY (KG/M**3)	MODULUS OF RUPTURE (MPA) (UNCORRECTED)	FLEXURAL STRENGTH (MPA) (CORRECTED)
1A-3	AX	EC		23.0	20.1
-5	AX	EC		23.8	20.7
-6	AX	EC		23.1	20.1
-10	AX	EC		19.8	17.7
-12	AX	EC		21.5	19.0
-13	AX	EC		23.3	20.3
-15	AX	EC		24.7	21.3
-21	AX	EC		21.0	18.6
-22	AX	EC		23.3	20.3
-24	AX	EC		19.9	17.7
1B-3	AX	EC		24.1	20.9
-5	AX	EC		23.0	20.1
-6	AX	EC		23.8	20.6
-10	AX	EC		22.6	19.8
-12	AX	EC		23.8	20.7
-13	AX	EC		22.9	20.0
-15	AX	EC		25.5	21.8
-21	AX	EC		23.6	20.5
-22	AX	EC		24.0	20.8
-24	AX	EC		25.7	22.0
	MEAN			23.1 MPA (3352. PSI)	20.2 MPA (2923. PSI)
	STD. DEV.			1.6 MPA (228. PSI)	1.2 MPA (167. PSI)
1A-32	RAD	EC		19.4	16.9
-33	RAD	EC		24.1	20.1
-34	RAD	EC		22.3	18.9
-35	RAD	EC		25.7	21.0
-36	RAD	EC		27.6	22.1
-39	RAD	EC		18.2	16.0
1A-40	RAD	EC		19.5	17.0
-41	RAD	EC		21.6	18.5
-42	RAD	EC		23.3	19.6
-43	RAD	EC		23.5	19.7
1B-32	RAD	EC		25.3	20.8
-33	RAD	EC		24.4	20.2
-34	RAD	EC		24.6	20.4
-35	RAD	EC		24.2	20.1
-36	RAD	EC		23.2	19.5
-39	RAD	EC		20.4	17.6
-40	RAD	EC		20.7	17.8
-41	RAD	EC		22.7	19.2
-42	RAD	EC		21.7	18.5
-43	RAD	EC		22.4	19.0
	MEAN			22.7 MPA (3299. PSI)	19.2 MPA (2778. PSI)
	STD. DEV.			2.4 MPA (341. PSI)	1.5 MPA (223. PSI)

TABLE 11-10 (Continued)

LOT NO. 4-B SPEC. DIA. 6.4 MM
LOG NO. 6484-20 SPEC. LENGTH 51. MM
LOG DENSITY 1.76 KG/M**3

SPECIMEN NUMBER	ORIENTATION	LOCATION	DENSITY (KG/M**3)	MODULUS OF RUPTURE (MPA) (UNCORRECTED)	FLEXURAL STRENGTH (MPA) (CORRECTED)
1A-51	AX	EE		23.6	20.5
-52	AX	EE		18.8	16.9
-54	AX	EE		23.1	20.2
-55	AX	EE		23.6	20.6
-56	AX	EE		25.0	21.5
-59	AX	EE		23.1	20.1
1A-60	AX	EE		30.1	24.8
-61	AX	EE		27.5	23.2
-62	AX	EE		27.7	23.3
-63	AX	EE		28.6	23.9
1B-51	AX	EE		29.0	24.2
-52	AX	EE		31.1	25.4
-54	AX	EE		29.3	24.3
-55	AX	EE		30.4	25.0
-56	AX	EE		27.7	23.3
-59	AX	EE		28.7	23.9
-60	AX	EE		29.3	24.3
-61	AX	EE		28.0	23.5
-62	AX	EE		34.4	27.2
-63	AX	EE		32.7	26.3
	MEAN			27.6 MPA (4002. PSI)	23.1 MPA (3354. PSI)
	STD. DEV.			3.7 MPA (542. PSI)	2.5 MPA (359. PSI)
1A-72	RAD	EE		23.8	19.9
-73	RAD	EE		20.7	17.9
-74	RAD	EE		21.8	18.6
-75	RAD	EE		23.9	19.9
-76	RAD	EE		23.6	19.7
-79	RAD	EE		22.6	19.1
-80	RAD	EE		22.6	19.1
-81	RAD	EE		22.0	18.7
-82	RAD	EE		22.4	18.9
-83	RAD	EE		19.9	17.3
1B-72	RAD	EE		22.6	19.1
-73	RAD	EE		27.1	21.9
-74	RAD	EE		22.9	19.3
-75	RAD	EE		24.8	20.5
-76	RAD	EE		24.0	20.0
-79	RAD	EE		24.3	20.2
1B-80	RAD	EE		19.6	17.1
-81	RAD	EE		21.7	18.5
-82	RAD	EE		23.6	19.7
-83	RAD	EE		20.4	17.6
	MEAN			22.7 MPA (3293. PSI)	19.2 MPA (2778. PSI)
	STD. DEV.			1.8 MPA (260. PSI)	1.2 MPA (168. PSI)

TABLE 11-11
IMPURITY CONTENT OF SO818 GRAPHITE(a)
AS Lot 5B, Log 6484-59 (AS Log 118), Density = 1.76 Mg/m^3 (g/cm^3)

LAB. NO. 41692 REPORT TO: W.R.JOHNSON DATE: 2-26-75
SAMPLE : 6484-59 L211 GRAP MLC PROJECT NO. 3224146005 DILUTION: 1.0000 PLATE NO. 76-11,

ELEMENT	CONCENTRATION, PPM	ELEMENT	CONCENTRATION, PPM	ELEMENT	CONCENTRATION, PPM
AG	< .50	AL	< 1.00	B	< .50
BA	< .50	BE	< .50	BI	< 2.00
CA	< 20.00	CD	< 10.00	CE	< 80.00
CO	< 4.00	CR	< 10.00	CS	< 100.00
CU	< 1.00	DY	< 20.00	ER	< 6.00
EU	< 10.00	FE	< 1.00	GD	< 10.00
HF	< 20.00	HO	< 10.00	IN	< 1.00
K	< 10.00	LA	< 10.00	LI	< 1.00
LU	< .50	MG	6.00	MN	< 1.00
MO	< 1.00	NA	< 10.00	NB	< 6.00
ND	< 200.00	NI	< 4.00	P	< 100.00
PB	< 6.00	PR	< 100.00	RB	< 40.00
SB	< 8.00	SC	< 1.00	SI	20.00
SM	< 100.00	SN	< 6.00	SR	< 40.00
TA	< 40.00	TB	< 40.00	TI	< 1.00
TL	< 20.00	TM	< 4.00	V	10.00
W	< 40.00	YB	< 10.00	ZN	< 20.00
ZR	< .50				

LAB. NO. 41692 REPORT TO: W.R.JOHNSON DATE: 2-26-75
SAMPLE : 6484-59 L216 GRAP MLC PROJECT NO. 3224146005 DILUTION: 1.0000 PLATE NO. 76-11,

ELEMENT	CONCENTRATION, PPM	ELEMENT	CONCENTRATION, PPM	ELEMENT	CONCENTRATION, PPM
AG	< .50	AL	40.00	B	< .50
BA	< .50	BE	< .50	BI	< 2.00
CA	< 20.00	CD	< 10.00	CE	< 80.00
CO	< 4.00	CR	< 10.00	CS	< 100.00
CU	< 1.00	DY	< 20.00	ER	< 6.00
EU	< 10.00	FE	< 1.00	GD	< 10.00
HF	< 20.00	HO	< 10.00	IN	< 1.00
K	< 10.00	LA	< 10.00	LI	< 1.00
LU	< .50	MG	4.00	MN	< 1.00
MO	< 1.00	NA	< 10.00	NB	< 6.00
ND	< 200.00	NI	< 4.00	P	< 100.00
PB	< 6.00	PR	< 100.00	RB	< 40.00
SB	< 8.00	SC	< 1.00	SI	10.00
SM	< 100.00	SN	< 6.00	SR	< 40.00
TA	< 40.00	TB	< 40.00	TI	10.00
TL	< 20.00	TM	< 4.00	V	10.00
W	< 40.00	YB	< 10.00	ZN	< 20.00
ZR	< .50				

TABLE 11-11 (Continued)

LAB. NO. 41692 REPORT TO: W.R.JOHNSON DATE: 2-26-75
SAMPLE : 6484-59 L273 GRAP MLE PROJECT NO. 3224146005 DILUTION: 1.0000 PLATE NO. 75-11,

ELEMENT	CONCENTRATION, PPM	ELEMENT	CONCENTRATION, PPM	ELEMENT	CONCENTRATION, PPM
AG	< .50	AL	< 1.00	B	< .50
BA	< .50	BE	< .50	BI	< 2.00
CA	< 20.00	CD	< 10.00	CE	< 80.00
CO	< 4.00	CR	< 10.00	CS	< 100.00
CU	< 1.00	DY	< 20.00	ER	< 6.00
EU	< 10.00	FE	< 1.00	GD	< 10.00
HF	< 20.00	HO	< 10.00	IN	< 1.00
K	< 10.00	LA	< 10.00	LI	< 1.00
LU	< .50	MG	10.00	MN	< 1.00
MO	< 1.00	NA	< 10.00	NB	< 6.00
ND	< 200.00	NI	< 4.00	P	< 100.00
PB	< 6.00	PR	< 100.00	RB	< 40.00
SB	< 8.00	SC	< 1.00	SI	10.00
SM	< 100.00	SN	< 6.00	SR	< 40.00
TA	< 40.00	TB	< 40.00	TI	< 1.00
TL	< 20.00	TM	< 4.00	V	< .50
W	< 40.00	YB	< 10.00	ZN	< 20.00
ZR	< .50				

LAB. NO. 41692 REPORT TO: W.R.JOHNSON DATE: 2-26-75
SAMPLE : 6484-59 L274 GRAP MLE PROJECT NO. 3224146005 DILUTION: 1.0000 PLATE NO. 76-11,

ELEMENT	CONCENTRATION, PPM	ELEMENT	CONCENTRATION, PPM	ELEMENT	CONCENTRATION, PPM
AG	< .50	AL	< 1.00	B	< .50
BA	< .50	BE	< .50	BI	< 2.00
CA	< 20.00	CD	< 10.00	CE	< 80.00
CO	< 4.00	CR	< 10.00	CS	< 100.00
CU	< 1.00	DY	< 20.00	ER	< 6.00
EU	< 10.00	FE	< 1.00	GD	< 10.00
HF	< 20.00	HO	< 10.00	IN	< 1.00
K	< 10.00	LA	< 10.00	LI	< 1.00
LU	< .50	MG	< .50	MN	< 1.00
MO	< 1.00	NA	< 10.00	NB	< 6.00
ND	< 200.00	NI	< 4.00	P	< 100.00
PB	< 6.00	PR	< 100.00	RB	< 40.00
SB	< 8.00	SC	< 1.00	SI	< 10.00
SM	< 100.00	SN	< 6.00	SR	< 40.00
TA	< 40.00	TB	< 40.00	TI	< 1.00
TL	< 20.00	TM	< 4.00	V	< .50
W	< 40.00	YB	< 10.00	ZN	< 20.00
ZR	< .50				

TABLE 11-11 (Continued)

LAB. NO. 41692 REPORT TO: W.R.JOHNSON DATE: 2-26-75
SAMPLE : 6484-59 L11B GRAP EC PROJECT NO. 3224146005 DILUTION: 1.0000 PLATE NO. 76-11,

ELEMENT	CONCENTRATION, PPM	ELEMENT	CONCENTRATION, PPM	ELEMENT	CONCENTRATION, PPM
AG	< .50	AL	< 1.00	B	< .50
BA	< .50	BE	< .50	BI	< 2.00
CA	< 20.00	CD	< 10.00	CE	< 80.00
CO	< 4.00	CR	< 10.00	CS	< 100.00
CU	< 1.00	DY	< 20.00	ER	< 6.00
EU	< 10.00	FE	< 1.00	GD	< 10.00
HF	< 20.00	HO	< 10.00	IN	< 1.00
K	< 10.00	LA	< 10.00	LI	< 1.00
LU	< .50	MG	1.00	MN	< 1.00
MO	< 1.00	NA	< 10.00	NB	< 6.00
ND	< 200.00	NI	< 4.00	P	< 100.00
PB	< 6.00	PR	< 100.00	RB	< 40.00
SB	< 8.00	SC	< 1.00	SI	10.00
SM	< 100.00	SN	< 6.00	SR	< 40.00
TA	< 40.00	TB	< 40.00	TI	< 1.00
TL	< 20.00	TM	< 4.00	V	10.00
W	< 40.00	YB	< 10.00	ZN	< 20.00
ZR	< .50				

LAB. NO. 41692 REPORT TO: W.R.JOHNSON DATE: 2-26-75
SAMPLE : 6484-59 L16B GRAP EC PROJECT NO. 3224146005 DILUTION: 1.0000 PLATE NO. 76-11,

ELEMENT	CONCENTRATION, PPM	ELEMENT	CONCENTRATION, PPM	ELEMENT	CONCENTRATION, PPM
AG	< .50	AL	< 1.00	B	< .50
BA	< .50	BE	< .50	BI	< 2.00
CA	< 20.00	CD	< 10.00	CE	< 80.00
CO	< 4.00	CR	< 10.00	CS	< 100.00
CU	< 1.00	DY	< 20.00	ER	< 6.00
EU	< 10.00	FE	< 1.00	GD	< 10.00
HF	< 20.00	HO	< 10.00	IN	< 1.00
K	< 10.00	LA	< 10.00	LI	< 1.00
LU	< .50	MG	1.00	MN	< 1.00
MO	< 1.00	NA	< 10.00	NB	< 6.00
ND	< 200.00	NI	< 4.00	P	< 100.00
PB	< 6.00	PR	< 100.00	RB	< 40.00
SB	< 8.00	SC	< 1.00	SI	20.00
SM	< 100.00	SN	< 6.00	SR	< 40.00
TA	< 40.00	TB	< 40.00	TI	< 1.00
TL	< 20.00	TM	< 4.00	V	10.00
W	< 40.00	YB	< 10.00	ZN	< 20.00
ZR	< .50				

TABLE 11-11 (Continued)

LAB. NO. 41692 REPORT TO: W.R.JOHNSON DATE: 2-26-75
SAMPLE : 6484-59 L73P GRAP EE PROJECT NO. 3224146005 DILUTION: 1.0000 PLATE NO. 76-11,

ELEMENT	CONCENTRATION, PPM	ELEMENT	CONCENTRATION, PPM	ELEMENT	CONCENTRATION, PPM
AG	< .50	AL	< 1.00	B	< .50
BA	< .50	BE	< .50	BI	< 2.00
CA	< 20.00	CD	< 10.00	CE	< 80.00
CO	< 4.00	CR	< 10.00	CS	< 100.00
CU	< 1.00	DY	< 20.00	ER	< 6.00
EU	< 10.00	FE	< 1.00	GD	< 10.00
HF	< 20.00	HO	< 10.00	IN	< 1.00
K	< 10.00	LA	< 10.00	LI	< 1.00
LU	< .50	MG	2.00	MN	< 1.00
MO	< 1.00	NA	< 10.00	NB	< 6.00
ND	< 200.00	NI	< 4.00	P	< 100.00
PB	< 6.00	PR	< 100.00	RB	< 40.00
SB	< 8.00	SC	< 1.00	SI	20.00
SM	< 100.00	SN	< 6.00	SR	< 40.00
TA	< 40.00	TB	< 40.00	TI	< 1.00
TL	< 20.00	TM	< 4.00	V	< .50
W	< 40.00	YB	< 10.00	ZN	< 20.00
ZR	< .50				

LAB. NO. 41692 REPORT TO: W.R.JOHNSON DATE: 2-26-75
SAMPLE : 6484-59 L74R GRAP EE PROJECT NO. 3224146005 DILUTION: 1.0000 PLATE NO. 76-11,

ELEMENT	CONCENTRATION, PPM	ELEMENT	CONCENTRATION, PPM	ELEMENT	CONCENTRATION, PPM
AG	< .50	AL	< 1.00	B	< .50
BA	< .50	BE	< .50	BI	< 2.00
CA	< 20.00	CD	< 10.00	CE	< 80.00
CO	< 4.00	CR	< 10.00	CS	< 100.00
CU	< 1.00	DY	< 20.00	ER	< 6.00
EU	< 10.00	FE	< 1.00	GD	< 10.00
HF	< 20.00	HO	< 10.00	IN	< 1.00
K	< 10.00	LA	< 10.00	LI	< 1.00
LU	< .50	MG	2.00	MN	< 1.00
MO	< 1.00	NA	< 10.00	NB	< 6.00
ND	< 200.00	NI	< 4.00	P	< 100.00
PB	< 6.00	PR	< 100.00	RB	< 40.00
SB	< 8.00	SC	< 1.00	SI	20.00
SM	< 100.00	SN	< 6.00	SR	< 40.00
TA	< 40.00	TB	< 40.00	TI	< 1.00
TL	< 20.00	TM	< 4.00	V	< .50
W	< 40.00	YB	< 10.00	ZN	< 20.00
ZR	< .50				

(a) CONCENTRATION BASED ON ORGINAL SAMPLE BEFORE DILUTION WITH DILUENT
> MEANS GREATER THAN
< MEANS LESS THAN THE SENSITIVITYOF THE SPECTROGRAPHIC PROCEDURE USED
RESULTS ARE CORRECT WITHIN A FACTOR OF 40% , (ONE STANDARD DEVIATION)

TABLE 11-12
IMPURITY CONTENT OF S0818 GRAPHITE[a]
AS Lot 5B, Log 6484-60 (AS Log 113), Density = 1.75 Mg/m^3 (g/cm^3)

LAB. NO. 41691 — REPORT TO: W.R.JOHNSON — DATE: 2-26-75
SAMPLE : 6484-60 L211 GRAP MLC — PROJECT NO. 3224146005 — DILUTION: 1.0000 — PLATE NO. 76-11,

ELEMENT	CONCENTRATION, PPM	ELEMENT	CONCENTRATION, PPM	ELEMENT	CONCENTRATION, PPM
AG	< .50	AL	< 1.00	B	< .50
BA	< .50	BE	< .50	BI	< 2.00
CA	< 20.00	CD	< 10.00	CE	< 80.00
CO	< 4.00	CR	< 10.00	CS	< 100.00
CU	< 1.00	DY	< 20.00	ER	< 6.00
EU	< 10.00	FE	< 1.00	GD	< 10.00
HF	< 20.00	HO	< 10.00	IN	< 1.00
K	< 10.00	LA	< 10.00	LI	< 1.00
LU	< .50	MG	< .50	MN	10.00
MO	< 1.00	NA	< 10.00	NB	< 6.00
ND	< 200.00	NI	< 4.00	P	< 100.00
PB	< 6.00	PR	< 100.00	RB	< 40.00
SB	< 8.00	SC	< 1.00	SI	10.00
SM	< 100.00	SN	< 6.00	SR	< 40.00
TA	< 40.00	TB	< 40.00	TI	< 1.00
TL	< 20.00	TM	< 4.00	V	10.00
W	< 40.00	YB	< 10.00	ZN	< 20.00
ZR	< .50				

LAB. NO. 41691 — REPORT TO: W.R.JOHNSON — DATE: 2-26-75
SAMPLE : 6484-60 L216 GRAP MLC — PROJECT NO. 3224146005 — DILUTION: 1.0000 — PLATE NO. 76-11,

ELEMENT	CONCENTRATION, PPM	ELEMENT	CONCENTRATION, PPM	ELEMENT	CONCENTRATION, PPM
AG	< .50	AL	< 1.00	B	< .50
BA	< .50	BE	< .50	BI	< 2.00
CA	< 20.00	CD	< 10.00	CE	< 80.00
CO	< 4.00	CR	< 10.00	CS	< 100.00
CU	< 1.00	DY	< 20.00	ER	< 6.00
EU	< 10.00	FE	> 1000.00	GD	< 10.00
HF	< 20.00	HO	< 10.00	IN	< 1.00
K	< 10.00	LA	< 10.00	LI	< 1.00
LU	< .50	MG	< .50	MN	6.00
MO	< 1.00	NA	< 10.00	NB	< 6.00
ND	< 200.00	NI	20.00	P	< 100.00
PB	400.00	PR	< 100.00	RB	< 40.00
SB	100.00	SC	< 1.00	SI	60.00
SM	< 100.00	SN	10.00	SR	< 40.00
TA	< 40.00	TB	< 40.00	TI	20.00
TL	< 20.00	TM	< 4.00	V	400.00
W	< 40.00	YB	< 10.00	ZN	< 20.00
ZR	< .50				

TABLE 11-12 (Continued)

LAB. NO. 41691 REPORT TO: W.R.JOHNSON DATE: 2-26-75
SAMPLE : 6484-60 L273 GRAP MLE PROJECT NO. 3224146005 DILUTION: 1.0000 PLATE NO. 76-11,

ELEMENT	CONCENTRATION, PPM	ELEMENT	CONCENTRATION, PPM	ELEMENT	CONCENTRATION, PPM
AC	< .50	AL	< 1.00	B	< .50
BA	< .50	BE	< .50	BI	< 2.00
CA	< 20.00	CD	< 10.00	CE	< 80.00
CO	< 4.00	CR	< 10.00	CS	< 100.00
CU	< 1.00	DY	< 20.00	ER	< 6.00
EU	< 10.00	FE	< 1.00	GD	< 10.00
HF	< 20.00	HO	< 10.00	IN	< 1.00
K	< 10.00	LA	< 10.00	LI	< 1.00
LU	< .50	MG	10.00	MN	< 1.00
MO	< 1.00	NA	< 10.00	NB	< 6.00
ND	< 200.00	NI	< 4.00	P	< 100.00
PB	< 6.00	PR	< 100.00	RB	< 40.00
SB	< 8.00	SC	< 1.00	SI	20.00
SM	< 100.00	SN	< 6.00	SR	< 40.00
TA	< 40.00	TB	< 40.00	TI	< 1.00
TL	< 20.00	TM	< 4.00	V	< .50
W	< 40.00	YB	< 10.00	ZN	< 20.00
ZR	< .50				

LAB. NO. 41691 REPORT TO: W.R.JOHNSON DATE: 2-26-75
SAMPLE : 6484-60 L274 GRAP MLE PROJECT NO. 3224146005 DILUTION: 1.0000 PLATE NO. 76-11,

ELEMENT	CONCENTRATION, PPM	ELEMENT	CONCENTRATION, PPM	ELEMENT	CONCENTRATION, PPM
AG	< .50	AL	< 1.00	B	< .50
BA	< .50	BE	< .50	BI	< 2.00
CA	< 20.00	CD	< 10.00	CE	< 80.00
CO	< 4.00	CR	< 10.00	CS	< 100.00
CU	< 1.00	DY	< 20.00	ER	< 6.00
EU	< 10.00	FE	10.00	GD	< 10.00
HF	< 20.00	HO	< 10.00	IN	< 1.00
K	< 10.00	LA	< 10.00	LI	< 1.00
LU	< .50	MG	6.00	MN	< 1.00
MO	< 1.00	NA	< 10.00	NB	< 6.00
ND	< 200.00	NI	< 4.00	P	< 100.00
PB	< 6.00	PR	< 100.00	RB	< 40.00
SB	< 8.00	SC	< 1.00	SI	10.00
SM	< 100.00	SN	< 6.00	SR	< 40.00
TA	< 40.00	TB	< 40.00	TI	< 1.00
TL	< 20.00	TM	< 4.00	V	< .50
W	< 40.00	YB	< 10.00	ZN	< 20.00
ZR	< .50				

TABLE 11-12 (Continued)

LAB. NO. 41691 — REPORT TO: W.R.JOHNSON — DATE: 2-26-75
SAMPLE : 6484-60 L11B GRAP EC — PROJECT NO. 3224146005 — DILUTION: [illegible] — PLATE NO. 76-11,

ELEMENT	CONCENTRATION, PPM	ELEMENT	CONCENTRATION, PPM	ELEMENT	CONCENTRATION, PPM
AG	< .50	AL	< 1.00	B	< .50
BA	< .50	BE	< .50	BI	< 2.00
CA	< 20.00	CD	< 10.00	CE	< 80.00
CO	< 4.00	CR	< 10.00	CS	< 100.00
CU	< 1.00	DY	< 20.00	ER	< 6.00
EU	< 10.00	FE	400.00	GD	< 10.00
HF	< 20.00	HO	< 10.00	IN	< 1.00
K	< 10.00	LA	< 10.00	LI	< 1.00
LU	< .50	MG	< .50	MN	2.00
MO	< 1.00	NA	< 10.00	NB	< 6.00
ND	< 200.00	NI	10.00	P	< 100.00
PB	< 6.00	PR	< 100.00	RB	< 40.00
SB	< 8.00	SC	< 1.00	SI	10.00
SM	< 100.00	SN	< 6.00	SR	< 40.00
TA	< 40.00	TB	< 40.00	TI	10.00
TL	< 20.00	TM	< 4.00	V	100.00
W	< 40.00	YB	< 10.00	ZN	< 20.00
ZR	< .50				

LAB. NO. 41691 — REPORT TO: W.R.JOHNSON — DATE: 2-26-75
SAMPLE : 6484-60 L16B GRAP EC — PROJECT NO. 3224146005 — DILUTION: 1.0000 — PLATE NO. 76-11,

ELEMENT	CONCENTRATION, PPM	ELEMENT	CONCENTRATION, PPM	ELEMENT	CONCENTRATION, PPM
AG	< .50	AL	< 1.00	B	< .50
BA	< .50	BE	< .50	BI	4.00
CA	< 20.00	CD	< 10.00	CE	< 80.00
CO	< 4.00	CR	< 10.00	CS	< 100.00
CU	< 1.00	DY	< 20.00	ER	< 6.00
EU	< 10.00	FE	> 1000.00	GD	< 10.00
HF	< 20.00	HO	< 10.00	IN	< 1.00
K	< 10.00	LA	< 10.00	LI	< 1.00
LU	< .50	MG	10.00	MN	< 1.00
MO	4.00	NA	< 10.00	NB	< 6.00
ND	< 200.00	NI	20.00	P	< 100.00
PB	800.00	PR	< 100.00	RB	< 40.00
SB	100.00	SC	< 1.00	SI	40.00
SM	< 100.00	SN	20.00	SR	< 40.00
TA	< 40.00	TB	< 40.00	TH	80.00
TI	20.00	TL	< 20.00	TM	< 4.00
V	100.00	W	< 40.00	YB	< 10.00
ZN	< 20.00	ZR	< .50		

TABLE 11-12 (Continued)

LAB. NO. 41691 — REPORT TO: W.R.JOHNSON — DATE: 2-26-75
SAMPLE : 6484-60 L73B GRAP EE — PROJECT NO. 3224146005 — DILUTION: 1.0000 — PLATE NO. 76-11,

ELEMENT	CONCENTRATION, PPM	ELEMENT	CONCENTRATION, PPM	ELEMENT	CONCENTRATION, PPM
AG	< .50	AL	< 1.00	B	< .50
BA	< .50	BE	< .50	BI	< 2.00
CA	< 20.00	CD	< 10.00	CE	< 80.00
CO	< 4.00	CR	< 10.00	CS	< 100.00
CU	< 1.00	DY	< 20.00	ER	< 6.00
EU	< 10.00	FE	< 1.00	GD	< 10.00
HF	< 20.00	HO	< 10.00	IN	< 1.00
K	< 10.00	LA	< 10.00	LI	< 1.00
LU	< .50	MG	6.00	MN	< 1.00
MO	< 1.00	NA	< 10.00	NB	< 6.00
ND	< 200.00	NI	< 4.00	P	< 100.00
PB	< 6.00	PR	< 100.00	RB	< 40.00
SB	< 6.00	SC	< 1.00	SI	10.00
SM	< 100.00	SN	< 6.00	SR	< 40.00
TA	< 40.00	TB	< 40.00	TI	< 1.00
TL	< 20.00	TM	< 4.00	V	< .50
W	< 40.00	YB	< 10.00	ZN	< 20.00
ZR	< .50				

LAB. NO. 41691 — REPORT TO: W.R.JOHNSON — DATE: 2-26-75
SAMPLE : 6484-60 L74B GRAP EE — PROJECT NO. 3224146005 — DILUTION: 1.0000 — PLATE NO. 76-11,

ELEMENT	CONCENTRATION, PPM	ELEMENT	CONCENTRATION, PPM	ELEMENT	CONCENTRATION, PPM
AG	2.00	AL	< 1.00	B	< .50
BA	< .50	BE	< .50	BI	< 2.00
CA	< 20.00	CD	< 10.00	CE	< 80.00
CO	< 4.00	CR	< 10.00	CS	< 100.00
CU	< 1.00	DY	< 20.00	ER	< 6.00
EU	< 10.00	FE	< 1.00	GD	< 10.00
HF	< 20.00	HO	< 10.00	IN	< 1.00
K	< 10.00	LA	< 10.00	LI	< 1.00
LU	< .50	MG	10.00	MN	< 1.00
MO	< 1.00	NA	< 10.00	NB	< 6.00
ND	< 200.00	NI	< 4.00	P	< 100.00
PB	< 6.00	PR	< 100.00	RB	< 40.00
SB	< 8.00	SC	< 1.00	SI	20.00
SM	< 100.00	SN	< 6.00	SR	< 40.00
TA	< 40.00	TB	< 40.00	TI	< 1.00
TL	< 20.00	TM	< 4.00	V	< .50
W	< 40.00	YB	< 10.00	ZN	< 20.00
ZR	< .50				

(a) CONCENTRATION BASED ON ORGINAL SAMPLE BEFORE DILUTION WITH DILUENT
> MEANS GREATER THAN
< MEANS LESS THAN THE SENSITIVITYOF THE SPECTROGRAPHIC PROCEDURE USED
RESULTS ARE CORRECT WITHIN A FACTOR OF 40% , (ONE STANDARD DEVIATION)

TABLE 11-13
IMPURITY CONTENT OF SO818 GRAPHITE[a]
AS Lot 5B, Log 6484-61 (AS Log 144), Density = 1.75 Mg/m^3 (g/cm^3)

LAB. NO. 41890 — REPORT TO: W.R.JOHNSON — DATE: 2-26-75
SAMPLE : 6484-61 L211 GRAP MLC — PROJECT NO. 3224146005 — DILUTION: 1.0000 — PLATE NO. 76-11,

ELEMENT	CONCENTRATION, PPM	ELEMENT	CONCENTRATION, PPM	ELEMENT	CONCENTRATION, PPM
AG	< .50	AL	< 1.00	B	< .50
BA	< .50	BE	< .50	BI	< 2.00
CA	< 20.00	CD	< 10.00	CE	< 80.00
CO	< 4.00	CR	< 10.00	CS	< 100.00
CU	< 1.00	DY	< 20.00	ER	< 6.00
EU	< 10.00	FE	< 1.00	GD	< 10.00
HF	< 20.00	HO	< 10.00	IN	< 1.00
K	< 10.00	LA	< 10.00	LI	< 1.00
LU	< .50	MG	1.00	MN	< 1.00
MO	< 1.00	NA	< 10.00	NB	< 6.00
ND	< 200.00	NI	< 4.00	P	< 100.00
PB	< 6.00	PR	< 100.00	RB	< 40.00
SB	< 8.00	SC	< 1.00	SI	20.00
SM	< 100.00	SN	< 6.00	SR	< 40.00
TA	< 40.00	TB	< 40.00	TI	< 1.00
TL	< 20.00	TM	< 4.00	V	< .50
W	< 40.00	YB	< 10.00	ZN	< 20.00
ZR	< .50				

LAB. NO. 41890 — REPORT TO: W.R.JOHNSON — DATE: 2-26-75
SAMPLE : 6484-61 L216 GRAP MLC — PROJECT NO. 3224146005 — DILUTION: 1.0000 — PLATE NO. 76-11,

ELEMENT	CONCENTRATION, PPM	ELEMENT	CONCENTRATION, PPM	ELEMENT	CONCENTRATION, PPM
AG	< .50	AL	< 1.00	B	< .50
BA	< .50	BE	< .50	BI	< 2.00
CA	< 20.00	CD	< 10.00	CE	< 80.00
CO	< 4.00	CR	< 10.00	CS	< 100.00
CU	< 1.00	DY	< 20.00	ER	< 6.00
EU	< 10.00	FE	< 1.00	GD	< 10.00
HF	< 20.00	HO	< 10.00	IN	< 1.00
K	< 10.00	LA	< 10.00	LI	< 1.00
LU	< .50	MG	1.00	MN	< 1.00
MO	< 1.00	NA	< 10.00	NB	< 6.00
ND	< 200.00	NI	< 4.00	P	< 100.00
PB	< 6.00	PR	< 100.00	RB	< 40.00
SB	< 8.00	SC	< 1.00	SI	20.00
SM	< 100.00	SN	< 6.00	SR	< 40.00
TA	< 40.00	TB	< 40.00	TI	< 1.00
TL	< 20.00	TM	< 4.00	V	< .50
W	< 40.00	YB	< 10.00	ZN	< 20.00
ZR	< .50				

TABLE 11-13 (Continued)

LAB. NO. 41890 REPORT TO: W.R.JOHNSON DATE: 2-26-75
SAMPLE : 6484-61 L273 GRAP MLE PROJECT NO. 3224146005 DILUTION: 1.0000 PLATE NO. 76-11,

ELEMENT	CONCENTRATION, PPM	ELEMENT	CONCENTRATION, PPM	ELEMENT	CONCENTRATION, PPM
AG	< .50	AL	< 1.00	B	< .50
BA	< .50	BE	< .50	BI	< 2.00
CA	< 20.00	CD	< 10.00	CE	< 80.00
CO	< 4.00	CR	< 10.00	CS	< 100.00
CU	< 1.00	DY	< 20.00	ER	< 6.00
EU	< 10.00	FE	< 1.00	GD	< 10.00
HF	< 20.00	HO	< 10.00	IN	< 1.00
K	< 10.00	LA	< 10.00	LI	< 1.00
LU	< .50	MG	1.00	MN	< 1.00
MO	< 1.00	NA	< 10.00	NB	< 6.00
ND	< 200.00	NI	< 4.00	P	< 100.00
PB	< 6.00	PR	< 100.00	RB	< 40.00
SB	< 8.00	SC	< 1.00	SI	20.00
SM	< 100.00	SN	< 6.00	SR	< 40.00
TA	< 40.00	TB	< 40.00	TI	< 1.00
TL	< 20.00	TM	< 4.00	V	< .50
W	< 40.00	YB	< 10.00	ZN	< 20.00
ZR	< .50				

LAB. NO. 41890 REPORT TO: W.R.JOHNSON DATE: 2-26-75
SAMPLE : 6484-61 L274 GRAP MLE PROJECT NO. 3224146005 DILUTION: 1.0000 PLATE NO. 76-11,

ELEMENT	CONCENTRATION, PPM	ELEMENT	CONCENTRATION, PPM	ELEMENT	CONCENTRATION, PPM
AG	< .50	AL	< 1.00	B	< .50
BA	< .50	BE	< .50	BI	< 2.00
CA	< 20.00	CD	< 10.00	CE	< 80.00
CO	< 4.00	CR	< 10.00	CS	< 100.00
CU	< 1.00	DY	< 20.00	ER	< 6.00
EU	< 10.00	FE	< 1.00	GD	< 10.00
HF	< 20.00	HO	< 10.00	IN	< 1.00
K	< 10.00	LA	< 10.00	LI	< 1.00
LU	< .50	MG	1.00	MN	< 1.00
MO	< 1.00	NA	< 10.00	NB	< 6.00
ND	< 200.00	NI	< 4.00	P	< 100.00
PB	< 6.00	PR	< 100.00	RB	< 40.00
SB	< 8.00	SC	< 1.00	SI	20.00
SM	< 100.00	SN	< 6.00	SR	< 40.00
TA	< 40.00	TB	< 40.00	TI	< 1.00
TL	< 20.00	TM	< 4.00	V	< .50
W	< 40.00	YB	< 10.00	ZN	< 20.00
ZR	< .50				

TABLE 11-13 (Continued)

LAB. NO. 4189C — REPORT TO: W.R.JOHNSON — DATE: 2-26-75
SAMPLE : 6484-61 L11 GRAP EC — PROJECT NO. 322414C05 — DILUTION: 1.0000 — PLATE NO. 76-11,

ELEMENT	CONCENTRATION, PPM	ELEMENT	CONCENTRATION, PPM	ELEMENT	CONCENTRATION, PPM
AG	< .50	AL	6.00	B	< .50
BA	< .50	BE	< .50	BI	< 2.00
CA	< 20.00	CD	< 10.00	CE	< 80.00
CO	< 4.00	CR	< 10.00	CS	< 100.00
CU	< 1.00	DY	< 20.00	ER	< 6.00
EU	< 10.00	FE	6.00	GD	< 10.00
HF	< 20.00	HO	< 10.00	IN	< 1.00
K	< 10.00	LA	< 10.00	LI	< 1.00
LU	< .50	MG	< .50	MN	< 1.00
MO	< 1.00	NA	< 10.00	NB	< 6.00
ND	< 200.00	NI	< 4.00	P	< 100.00
PB	< 6.00	PR	< 100.00	RB	< 40.00
SB	< 8.00	SC	< 1.00	SI	< 10.00
SM	< 100.00	SN	< 6.00	SR	< 40.00
TA	< 40.00	TB	< 40.00	TI	< 1.00
TL	< 20.00	TM	< 4.00	V	10.00
W	< 40.00	YB	< 10.00	ZN	< 20.00
ZR	< .50				

LAB. NO. 4189C — REPORT TO: W.R.JOHNSON — DATE: 2-26-76
SAMPLE : 6484-61- L16 GRAP EC — PROJECT NO. 322414C05 — DILUTION: 1.0000 — PLATE NO. 76-11,

ELEMENT	CONCENTRATION, PPM	ELEMENT	CONCENTRATION, PPM	ELEMENT	CONCENTRATION, PPM
AG	< .50	AL	< 1.00	B	< .50
BA	< .50	BE	< .50	BI	< 2.00
CA	< 20.00	CD	< 10.00	CE	< 80.00
CO	< 4.00	CR	< 10.00	CS	< 100.00
CU	< 1.00	DY	< 20.00	ER	< 6.00
EU	< 10.00	FE	40.00	GD	< 10.00
HF	< 20.00	HO	< 10.00	IN	< 1.00
K	< 10.00	LA	< 10.00	LI	< 1.00
LU	< .50	MG	1.00	MN	< 1.00
MO	< 1.00	NA	< 10.00	NB	< 6.00
ND	< 200.00	NI	< 4.00	P	< 100.00
PB	< 6.00	PR	< 100.00	RB	< 40.00
SB	< 8.00	SC	< 1.00	SI	10.00
SM	< 100.00	SN	< 6.00	SR	< 40.00
TA	< 40.00	TB	< 40.00	TI	< 1.00
TL	< 20.00	TM	< 4.00	V	40.00
W	< 40.00	YB	< 10.00	ZN	< 20.00
ZR	< .50				

TABLE 11-13 (Continued)

LAB. NO. 41890 REPORT TO: W.P.JOHNSON DATE: 2-26-75
SAMPLE : 6484-61 L73 GRAP EE PROJECT NO. 3224146005 DILUTION: .0033 PLATE NO. 76-11,

ELEMENT	CONCENTRATION, PPM	ELEMENT	CONCENTRATION, PPM	ELEMENT	CONCENTRATION, PPM
AG	< .50	AL	< 1.00	B	< .50
BA	< .50	BE	< .50	BI	< 2.00
CA	< 20.00	CD	< 10.00	CE	< 80.00
CO	< 4.00	CR	< 10.00	CS	< 100.00
CU	< 1.00	DY	< 20.00	ER	< 6.00
EU	< 10.00	FE	< 1.00	GD	< 10.00
HF	< 20.00	HO	< 10.00	IN	< 1.00
K	< 10.00	LA	< 10.00	LI	< 1.00
LU	< .50	MG	< .50	MN	< 1.00
MO	< 1.00	NA	< 10.00	NB	< 6.00
ND	< 200.00	NI	< 4.00	P	< 100.00
PB	< 6.00	PR	< 100.00	RB	< 40.00
SB	< 8.00	SC	< 1.00	SI	10.00
SM	< 100.00	SN	< 6.00	SR	< 40.00
TA	< 40.00	TB	< 40.00	TI	< 1.00
TL	< 20.00	TM	< 4.00	V	< .50
W	< 40.00	YB	< 10.00	ZN	< 20.00
ZR	< .50				

LAB. NO. 41890 REPORT TO: W.P.JOHNSON DATE: 2-26-75
SAMPLE : 6484-61 L74 GRAP EE PROJECT NO. 3224146005 DILUTION: 1.0000 PLATE NO. 76-11,

ELEMENT	CONCENTRATION, PPM	ELEMENT	CONCENTRATION, PPM	ELEMENT	CONCENTRATION, PPM
AG	< .50	AL	< 1.00	B	< .50
BA	< .50	BE	< .50	BI	< 2.00
CA	< 20.00	CD	< 10.00	CE	< 80.00
CO	< 4.00	CR	< 10.00	CS	< 100.00
CU	< 1.00	DY	< 20.00	ER	< 6.00
EU	< 10.00	FE	< 1.00	GD	< 10.00
HF	< 20.00	HO	< 10.00	IN	< 1.00
K	< 10.00	LA	< 10.00	LI	< 1.00
LU	< .50	MG	1.00	MN	< 1.00
MO	< 1.00	NA	< 10.00	NB	< 6.00
ND	< 200.00	NI	< 4.00	P	< 100.00
PB	< 6.00	PR	< 100.00	RB	< 40.00
SB	< 8.00	SC	< 1.00	SI	10.00
SM	< 100.00	SN	< 6.00	SR	< 40.00
TA	< 40.00	TB	< 40.00	TI	< 1.00
TL	< 20.00	TM	< 4.00	V	< .50
W	< 40.00	YB	< 10.00	ZN	< 20.00
ZR	< .50				

(a) CONCENTRATION BASED ON ORGINAL SAMPLE BEFORE DILUTION WITH DILUENT

> MEANS GREATER THAN

< MEANS LESS THAN THE SENSITIVITYOF THE SPECTROGRAPHIC PROCEDURE USED

RESULTS ARE CORRECT WITHIN A FACTOR OF 40% , (ONE STANDARD DEVIATION)

TABLE 11-14
IMPURITY CONTENT OF SO818 GRAPHITE[a]
AS Lot 5B, Log 6484-62 (AS Log 161), Density = 1.77 Mg/m^3 (g/cm^3)

LAB. NO. 41889 REPORT TO: W.R.JOHNSON DATE: 2-26-75
SAMPLE : 6484-62 L211 GRAP MLC PROJECT NO. 3224146005 DILUTION: 1.0000 PLATE NO. 76-11,

ELEMENT	CONCENTRATION, PPM	ELEMENT	CONCENTRATION, PPM	ELEMENT	CONCENTRATION, PPM
AG	< .50	AL	< 1.00	B	< .50
BA	< .50	BE	< .50	BI	< 2.00
CA	< 20.00	CD	< 10.00	CE	< 80.00
CO	< 4.00	CR	< 10.00	CS	< 100.00
CU	< 1.00	DY	< 20.00	ER	< 6.00
EU	< 10.00	FE	< 1.00	GD	< 10.00
HF	< 20.00	HO	< 10.00	IN	< 1.00
K	< 10.00	LA	< 10.00	LI	< 1.00
LU	< .50	MG	1.00	MN	< 1.00
MO	< 1.00	NA	< 10.00	NB	< 6.00
ND	< 200.00	NI	< 4.00	P	< 100.00
PB	< 6.00	PR	< 100.00	RB	< 40.00
SB	< 8.00	SC	< 1.00	SI	< 10.00
SM	< 100.00	SN	< 6.00	SR	< 40.00
TA	< 40.00	TB	< 40.00	TI	< 1.00
TL	< 20.00	TM	< 4.00	V	< .50
W	< 40.00	YB	< 10.00	ZN	< 20.00
ZR	< .50				

LAB. NO. 41889 REPORT TO: W.R.JOHNSON DATE: 2-26-75
SAMPLE : 6484-62 L216 GRAP MLC PROJECT NO. 3224146005 DILUTION: 1.0000 PLATE NO. 76-11,

ELEMENT	CONCENTRATION, PPM	ELEMENT	CONCENTRATION, PPM	ELEMENT	CONCENTRATION, PPM
AG	< .50	AL	< 1.00	B	< .50
BA	< .50	BE	< .50	BI	< 2.00
CA	< 20.00	CD	< 10.00	CE	< 80.00
CO	< 4.00	CR	< 10.00	CS	< 100.00
CU	< 1.00	DY	< 20.00	ER	< 6.00
EU	< 10.00	FE	20.00	GD	< 10.00
HF	< 20.00	HO	< 10.00	IN	< 1.00
K	< 10.00	LA	< 10.00	LI	< 1.00
LU	< .50	MG	1.00	MN	< 1.00
MO	< 1.00	NA	< 10.00	NB	< 6.00
ND	< 200.00	NI	10.00	P	< 100.00
PB	< 6.00	PR	< 100.00	RB	< 40.00
SB	< 8.00	SC	< 1.00	SI	10.00
SM	< 100.00	SN	< 6.00	SR	< 40.00
TA	< 40.00	TB	< 40.00	TI	< 1.00
TL	< 20.00	TM	< 4.00	V	20.00
W	< 40.00	YB	< 10.00	ZN	< 20.00
ZR	< .50				

TABLE 11-14 (Continued)

LAB. NO. 41889 REPORT TO: W.R.JOHNSON DATE: 2-26-75
SAMPLE : 6484-62 L273 GRAP MLE PROJECT NO. 3224146005 DILUTION: 1.0000 PLATE NO. 76-11,

ELEMENT	CONCENTRATION, PPM	ELEMENT	CONCENTRATION, PPM	ELEMENT	CONCENTRATION, PPM
AC	< .50	AL	< 1.00	B	< .50
BA	< .50	BE	< .50	BI	< 2.00
CA	< 20.00	CD	< 10.00	CE	< 80.00
CO	< 4.00	CR	< 10.00	CS	< 100.00
CU	< 1.00	DY	< 20.00	EP	< 6.00
EU	< 10.00	FE	< 1.00	GD	< 10.00
HF	< 20.00	HO	< 10.00	IN	< 1.00
K	< 10.00	LA	< 10.00	LI	< 1.00
LU	< .50	MG	1.00	MN	< 1.00
MO	< 1.00	NA	< 10.00	NB	< 6.00
ND	< 200.00	NI	< 4.00	P	< 100.00
PB	< 6.00	PR	< 100.00	RB	< 40.00
SB	< 8.00	SC	< 1.00	SI	20.00
SM	< 100.00	SN	< 6.00	SR	< 40.00
TA	< 40.00	TB	< 40.00	TI	< 1.00
TL	< 20.00	TM	< 4.00	V	< .50
W	< 40.00	YB	< 10.00	ZN	< 20.00
ZR	< .50				

LAB. NO. 41889 REPORT TO: W.R.JOHNSON DATE: 2-26-75
SAMPLE : 6484-62 L274 GRAP MLE PROJECT NO. 3224146005 DILUTION: 1.0000 PLATE NO. 76-11,

ELEMENT	CONCENTRATION, PPM	ELEMENT	CONCENTRATION, PPM	ELEMENT	CONCENTRATION, PPM
AG	< .50	AL	< 1.00	B	< .50
BA	< .50	BE	< .50	BI	< 2.00
CA	< 20.00	CD	< 10.00	CE	< 80.00
CO	< 4.00	CR	< 10.00	CS	< 100.00
CU	< 1.00	DY	< 20.00	ER	< 6.00
EU	< 10.00	FE	< 1.00	GD	< 10.00
HF	< 20.00	HO	< 10.00	IN	< 1.00
K	< 10.00	LA	< 10.00	LI	< 1.00
LU	< .50	MG	1.00	MN	< 1.00
MO	< 1.00	NA	< 10.00	NB	< 6.00
ND	< 200.00	NI	< 4.00	P	< 100.00
PB	< 6.00	PR	< 100.00	RB	< 40.00
SB	< 8.00	SC	< 1.00	SI	< 10.00
SM	< 100.00	SN	< 6.00	SR	< 40.00
TA	< 40.00	TB	< 40.00	TI	< 1.00
TL	< 20.00	TM	< 4.00	V	< .50
W	< 40.00	YB	< 10.00	ZN	< 20.00
ZR	< .50				

TABLE 11-14 (Continued)

LAB. NO. 41889 REPORT TO: W.R.JOHNSON DATE: 2-26-75
SAMPLE : 6484-62 L11 GRAP EC PROJECT NO. 3224146005 DILUTION: 1.0000 PLATE NO. 76-11,

ELEMENT	CONCENTRATION, PPM	ELEMENT	CONCENTRATION, PPM	ELEMENT	CONCENTRATION, PPM
AG	< .50	AL	< 1.00	B	< .50
BA	< .50	BE	< .50	BI	< 2.00
CA	< 20.00	CD	< 10.00	CE	< 80.00
CO	< 4.00	CR	< 10.00	CS	< 100.00
CU	< 1.00	DY	< 20.00	ER	< 6.00
EU	< 10.00	FE	< 1.00	GD	< 10.00
HF	< 20.00	HO	< 10.00	IN	< 1.00
K	< 10.00	LA	< 10.00	LI	< 1.00
LU	< .50	MG	2.00	MN	< 1.00
MO	< 1.00	NA	< 10.00	NB	< 6.00
ND	< 200.00	NI	< 4.00	P	< 100.00
PB	< 6.00	PR	< 100.00	RB	< 40.00
SB	< 8.00	SC	< 1.00	SI	< 10.00
SM	< 100.00	SN	< 6.00	SR	< 40.00
TA	< 40.00	TB	< 40.00	TI	< 1.00
TL	< 20.00	TM	< 4.00	V	4.00
W	< 40.00	YB	< 10.00	ZN	< 20.00
ZR	< .50				

LAB. NO. 41889 REPORT TO: W.R.JOHNSON DATE: 2-26-75
SAMPLE : 6484-62 L16 GRAP EC PROJECT NO. 3224146005 DILUTION: 1.0000 PLATE NO. 76-11,

ELEMENT	CONCENTRATION, PPM	ELEMENT	CONCENTRATION, PPM	ELEMENT	CONCENTRATION, PPM
AG	< .50	AL	< 1.00	B	< .50
BA	< .50	BE	< .50	BI	< 2.00
CA	< 20.00	CD	< 10.00	CE	< 80.00
CO	< 4.00	CR	< 10.00	CS	< 100.00
CU	< 1.00	DY	< 20.00	ER	< 6.00
EU	< 10.00	FE	< 1.00	GD	< 10.00
HF	< 20.00	HO	< 10.00	IN	< 1.00
K	< 10.00	LA	< 10.00	LI	< 1.00
LU	< .50	MG	2.00	MN	< 1.00
MO	< 1.00	NA	< 10.00	NB	< 6.00
ND	< 200.00	NI	< 4.00	P	< 100.00
PB	< 6.00	PR	< 100.00	RB	< 40.00
SB	< 8.00	SC	< 1.00	SI	< 10.00
SM	< 100.00	SN	< 6.00	SR	< 40.00
TA	< 40.00	TB	< 40.00	TI	< 1.00
TL	< 20.00	TM	< 4.00	V	4.00
W	< 40.00	YB	< 10.00	ZN	< 20.00
ZR	< .50				

TABLE 11-14 (Continued)

LAB. NO. 41889 REPORT TO: W R JOHNSON DATE: 2-26-75
SAMPLE : 6484-62 L7 GRAP EE PROJECT NO. 3224146005 DILUTION: 1.0000 PLATE NO. 76-11

ELEMENT	CONCENTRATION, PPM	ELEMENT	CONCENTRATION, PPM	ELEMENT	CONCENTRATION, PPM
AG	< .50	AL	< 1.00	B	< .50
BA	< .50	BE	< .50	BI	< 2.00
CA	< 20.00	CD	< 10.00	CE	< 80.00
CO	< 4.00	CR	< 10.00	CS	< 100.00
CU	< 1.00	DY	< 20.00	EP	< 6.00
EU	< 10.00	FE	< 1.00	GD	< 10.00
HF	< 20.00	HO	< 10.00	IN	< 1.00
K	< 10.00	LA	< 10.00	LI	< 1.00
LU	< .50	MG	1.00	MN	< 1.00
MO	< 1.00	NA	< 10.00	NB	< 6.00
ND	< 200.00	NI	< 4.00	P	< 100.00
PB	< 6.00	PR	< 100.00	RB	< 40.00
SB	< 8.00	SC	< 1.00	SI	10.00
SM	< 100.00	SN	< 6.00	SR	< 40.00
TA	< 40.00	TB	< 40.00	TI	< 1.00
TL	< 20.00	TM	< 4.00	V	< .50
W	< 40.00	YB	< 10.00	ZN	< 20.00
ZR	< .50				

LAB. NO. 41889 REPORT TO: W.R.JOHNSON DATE: 2-26-75
SAMPLE : 6484-62 L74 GRAP EE PROJECT NO. 3224146005 DILUTION: 1.0000 PLATE NO. 76-11,

ELEMENT	CONCENTRATION, PPM	ELEMENT	CONCENTRATION, PPM	ELEMENT	CONCENTRATION, PP
AG	< .50	AL	< 1.00	B	< .50
BA	< .50	BE	< .50	BI	< 2.00
CA	< 20.00	CD	< 10.00	CE	< 80.00
CO	< 4.00	CR	< 10.00	CS	< 100.00
CU	< 1.00	DY	< 20.00	ER	< 6.00
EU	< 10.00	FE	< 1.00	GD	< 10.00
HF	< 20.00	HO	< 10.00	IN	< 1.00
K	< 10.00	LA	< 10.00	LI	< 1.00
LU	< .50	MG	2.00	MN	< 1.00
MO	< 1.00	NA	< 10.00	NB	< 6.00
ND	< 200.00	NI	< 4.00	P	< 100.00
PB	< 6.00	PR	< 100.00	RB	< 40.00
SB	< 8.00	SC	< 1.00	SI	< 10.00
SM	< 100.00	SN	< 6.00	SR	< 40.00
TA	< 40.00	TB	< 40.00	TI	< 1.00
TL	< 20.00	TM	< 4.00	V	< .50
W	< 40.00	YB	< 10.00	ZN	< 20.00
ZR	< .50				

(a) CONCENTRATION BASED ON ORGINAL SAMPLE BEFORE DILUTION WITH DILUENT
> MEANS GREATER THAN
< MEANS LESS THAN THE SENSITIVITYOF THE SPECTROGRAPHIC PROCEDURE USED
RESULTS ARE CORRECT WITHIN A FACTOR OF 40% , (ONE STANDARD DEVIATION)

TABLE 11-15
ASH AND SULFUR CONTENT OF SO818 GRAPHITE, AS LOT 5B

Element	Concentration (ppm)							
	Midlength Center		Midlength Edge		End Center		End Edge	
	L211B	L216B	L273B	L279B	L11B	L16B	L73B	L74B
	Log 6484-59 (AS Log 118), Density = 1.77 Mg/m^3 (g/cm^3)							
Ash	42	64	21	26	8	58	24	24
Sulfur	<1	<1	<1	<1	<1	<1	<1	<1
	<1	<1	<1	<1	<1	<1	<1	<1
	Log 6484-60 (AS Log 113), Density = 1.75 Mg/m^3 (g/cm^3)							
Ash	111	384	38	27	696	5112	21	47
Sulfur	3.1	14.0	<1	<1	<1	15.3	<1	2.8
	2.2	13.3	<1	<1	<1	17.5	<1	2.5
	Log 6484-61 (AS Log 144), Density = 1.75 Mg/m^3 (g/cm^3)							
Ash	15	9	18	3	52	101	2	2
Sulfur	<1	<1	<1	<1	<1	<1	<1	<1
	<1	<1	<1	<1	<1	<1	<1	<1
	Log 6484-62 (AS Log 161), Density = 1.77 Mg/m^3 (g/cm^3)							
Ash	2	126	33	8	8	2	28	2
Sulfur	<1	<1	<1	<1	<1	<1	<1	<1
	<1	<1	<1	<1	<1	<1	<1	<1

TABLE 11-16
SUMMARY OF STATISTICAL STUDY OF THE STRENGTH OF H-451 GRAPHITE
Log 5651-90 (GLCC Log 48), Slab 1 (End of Parent Log)

Orientation	Location in Parent Log	Type of Specimen	No. of Replicate Specimens	Strength				Strength Ratio	
				Mean (MPa)	Standard Deviation (MPa)	Coefficient of Variation (%)	Weibull Modulus, m	Small Tensile / Large Tensile	Flexural / Small Tensile
Axial	End edge	Small tensile	48	16.4	2.0	12.2	9.4	1.03	1.51
		Large tensile	47	15.9	2.2	13.5	8.1		
		Flexural[a]	48	24.7	1.5	6.3	19.7		
	End center	Small tensile	40	15.9	2.4	15.4	7.5	1.04	1.48
		Large tensile	31	15.3	1.8	11.7	8.9		
		Flexural[a]	25	23.6	2.4	10.2	11.1		
Radial	End edge	Small tensile	47	13.0	1.9	14.7	7.2	1.07	1.56
		Large tensile	48	12.1	2.5	20.3	5.3		
		Flexural[a]	46	20.3	2.7	13.2	8.0		
	End center	Small tensile	38	12.2	2.3	18.8	6.2	1.14	1.66
		Large tensile	36	10.7	1.7	15.9	7.2		
		Flexural[a]	38	20.3	1.9	9.4	13.1		

[a] Corrected for nonlinear stress-strain relationship.

TABLE 11-17
SUMMARY OF STATISTICAL STUDY OF THE STRENGTH OF H-451 GRAPHITE
Log 5651-90 (GLCC Log 48), Slab 2 (Midlength of Parent Log)

Orientation	Location in Parent Log	Type of Specimen	No. of Replicate Specimens	Strength				Strength Ratio	
				Mean (MPa)	Standard Deviation (MPa)	Coefficient of Variation (%)	Weibull Modulus, m	Small Tensile / Large Tensile	Flexural / Small Tensile
Axial	Midlength edge	Small tensile	46	18.2	1.7	9.4	12.6	1.03	1.36
		Large tensile	48	17.6	1.7	9.9	11.8		
		Flexural[a]	48	24.8	2.1	8.3	14.5		
	Midlength center	Small tensile	38	15.0	1.3	8.6	13.4	1.02	1.51
		Large tensile	32	14.7	1.1	7.3	15.2		
		Flexural[a]	40	22.6	1.2	5.1	22.9		
Radial	Midlength edge	Small tensile	48	15.2	1.8	11.9	9.7	1.09	1.40
		Large tensile	48	13.9	2.0	14.5	8.0		
		Flexural[a]	48	21.3	1.8	8.3	14.9		
	Midlength center	Small tensile	38	12.3	2.8	22.6	4.6	1.04	1.62
		Large tensile	35	11.8	1.1	9.6	12.4		
		Flexural[a]	38	19.9	1.9	9.6	12.3		

[a] Corrected for nonlinear stress-strain relationship.

TABLE 11-18
SUMMARY OF STATISTICAL STUDY OF THE STRENGTH OF H-451 GRAPHITE
Log 5651-90 (GLCC Log 48), Slab 3 (Midlength of Parent Log)

Orientation	Location in Parent Log	Type of Specimen	No. of Replicate Specimens	Strength				Strength Ratio	
				Mean (MPa)	Standard Deviation (MPa)	Coefficient of Variation (%)	Weibull Modulus, m	Small Tensile / Large Tensile	Flexural / Small Tensile
Axial	Midlength edge	Small tensile	48	17.0	1.9	11.4	10.0	1.00	1.52
		Large tensile	48	17.0	1.7	9.9	11.9		
		Flexural[a]	48	25.8	2.2	8.4	14.1		
	Midlength center	Small tensile	40	13.7	2.0	14.4	6.8	1.05	1.66
		Large tensile	31	13.3	1.1	8.0	14.4		
		Flexural[a]	40	22.8	1.6	6.8	17.1		
Radial	Midlength edge	Small tensile	47	14.1	2.1	15.2	6.8	1.01	1.62
		Large tensile	24	14.0	1.3	9.5	12.1		
		Flexural[a]	48	22.8	1.6	7.0	17.0		
	Midlength center	Small tensile	37	13.0	1.8	13.6	8.3	1.13	1.62
		Large tensile	36	11.5	1.4	12.1	9.1		
		Flexural[a]	40	21.1	1.6	7.5	15.7		

[a] Corrected for nonlinear stress-strain relationship.

TABLE 11-19
SUMMARY OF STATISTICAL STUDY OF THE STRENGTH OF H-451 GRAPHITE
Log 5651-90 (GLCC Log 48), Slab 4 (End of Parent Log)

Orientation	Location in Parent Log	Type of Specimen	No. of Replicate Specimens	Strength				Strength Ratio	
				Mean (MPa)	Standard Deviation (MPa)	Coefficient of Variation (%)	Weibull Modulus, m	Small Tensile / Large Tensile	Flexural / Small Tensile
Axial	End edge	Small tensile	48	16.8	2.0	11.8	10.0	1.01	1.48
		Large tensile	48	16.7	1.5	9.2	12.9		
		Flexural[a]	48	24.8	2.0	7.9	14.9		
	End center	Small tensile	40	14.1	2.0	14.1	8.2	1.08	1.61
		Large tensile	32	13.1	1.5	11.6	10.0		
		Flexural[a]	39	22.7	2.3	9.9	11.7		
Radial	End edge	Small tensile	48	15.7	1.8	11.7	9.9	1.08	1.39
		Large tensile	48	14.6	1.9	12.7	9.2		
		Flexural[a]	48	21.9	1.9	8.8	12.9		
	End center	Small tensile	40	14.0	2.2	15.6	7.2	1.04	1.55
		Large tensile	36	13.4	2.3	16.9	6.2		
		Flexural[a]	40	21.7	1.7	7.8	15.0		

[a] Corrected for nonlinear stress-strain relationship.

TABLE 11-20
FATIGUE TESTS ON H-451 GRAPHITE
GLCC Lot 408, Log 5651-90 (GLCC Log 48)

LOT NO: 408 LOG NO: 5651-90
ORIENTATION: AXIAL LOCATION: QUARTER-LENGTH EDGE

CONTROL TENSILE TESTS

SPECIMEN NO.	DIAMETER (MM)	FRACTURE LOAD (KN)	TENSILE STRENGTH (MPA)
3-A	12.70	2.66	21.0
4-A	12.70	2.56	20.2
5-A	12.69	2.36	18.6
6-A	12.71	2.22	17.5
8-A	12.70	2.25	17.8
9-A	12.68	2.44	19.3
10-A	12.70	1.96	15.4
11-A	12.70	2.57	20.3
12-A	12.70	2.79	22.0
13-A	12.70	2.09	16.5
14-A	12.70	2.31	18.2
15-A	12.70	2.31	18.2
16-A	12.70	2.66	21.0
17-A	12.70	2.57	20.3
25-A	12.70	2.79	22.0
26-A	12.70	1.98	15.6
27-A	12.70	2.20	17.3
28-A	12.70	2.52	19.9
29-A	12.65	2.36	18.8
30-A	12.71	2.57	20.3
31-A	12.70	2.74	21.6
32-A	12.70	2.49	19.7
34-A	12.70	2.47	19.5
35-A	12.71	2.28	18.0
36-A	12.70	2.15	16.9
37-A	12.70	2.20	17.3
38-A	12.70	2.25	17.8
39-A	12.70	2.36	18.6
		MEAN:	18.9 MPA (2745.PSI)
		STD. DEV:	1.8 MPA (263.PSI)

TABLE 11-21
FATIQUE TESTS ON H-451 GRAPHITE
GLCC Lot 408, Log 5651-90 (GLCC Log 48)

LOT NO: 408 LOG NO: 5651-90
ORIENTATION: AXIAL LOCATION: QUARTER-LENGTH EDGE

STRESS RATIO, R (MIN. STRESS / MAX. STRESS): -1.0

SPECIMEN NO.	MAX. STRESS (MPA)	MIN. STRESS (MPA)	CYCLES TO FAILURE	
3-C	10.2	-10.2	13100	
16-E	10.2	-10.2	4500	
10-D	10.2	-10.2	≥ 121200	(RUNOUT)
22-C	10.6	-10.2	> 103000	(RUNOUT)
32-D	10.6	-10.6	> 119000	(RUNOUT)
34-B	11.6	-11.6	39300	
42-B	11.7	-12.9	17900	
21-A	11.8	-12.7	12400	
38-B	12.1	-12.3	> 115100	(RUNOUT)
20-A	12.3	-12.3	3851	
39-B	12.3	-12.7	7600	
41-B	12.3	-12.7	465	
37-B	12.5	-12.5	200	
36-B	12.5	-12.5	> 121200	(RUNOUT)
35-B	12.5	-12.5	> 100000	(RUNOUT)
22-B	13.1	-13.1	7000	
23-B	13.5	-13.5	7768	
31-B	13.5	-14.0	59	
27-B	13.6	-14.0	6	
29-B	13.6	-13.6	56	
32-B	13.8	-13.8	117	
26-B	14.0	-13.6	577	
25-B	14.0	-13.6	351	
28-B	14.0	-13.6	137	
30-B	14.0	-13.6	115	
20-B	14.8	-14.8	2	
18-B	14.8	-14.8	3	
21-B	14.8	-15.7	162	
8-B	14.8	-15.7	162	
17-B	15.2	-15.2	87	
9-B	15.3	-14.8	< 1	(FIRST CYCLE)
5-B	15.3	-14.9	24	
19-B	15.3	-15.3	36	
6-B	15.7	-14.8	3	
14-B	16.1	-11.9	< 1	(FIRST CYCLE)
10-B	16.6	-18.3	34	
11-B	16.9	-16.9	5200	
7-B	17.0	-17.8	115	
3-B	17.1	-16.7	10	
12-B	17.1	-17.1	45	
45-B	17.2	-19.1	< 1	(FIRST CYCLE)
46-B	17.2	-19.5	< 1	(FIRST CYCLE)
16-B	17.4	-16.1	832	
15-B	17.6	-16.5	16	
13-B	17.6	-16.5	40	
47-B	17.8	-18.6	< 1	(FIRST CYCLE)
48-B	18.6	-19.0	< 1	(FIRST CYCLE)
18-A	19.0	-19.0	< 1	(FIRST CYCLE)
19-A	19.1	-19.1	< 1	(FIRST CYCLE)
43-B	19.7	-19.7	5	
44-B	19.7	-19.9	3	

TABLE 11-22
FATIGUE TESTS ON H-451 GRAPHITE
GLCC Lot 408, Log 5651-90 (GLCC Log 48)

LOT NO: 408 LOG NO: 5651-90
ORIENTATION: AXIAL LOCATION: QUARTER-LENGTH EDGE

STRESS RATIO, R (MIN. STRESS / MAX. STRESS): -.5

SPECIMEN NO.	MAX. STRESS (MPA)	MIN. STRESS (MPA)	CYCLES TO FAILURE	
38-C	10.0	-5.4	16900	
37-C	10.0	-5.4	> 186000	(RUNOUT)
35-C	10.0	-5.4	3100	
41-C	10.0	-5.4	1700	
42-C	10.0	-5.4	> 100000	(RUNOUT)
39-C	10.0	-5.4	> 196000	(RUNOUT)
36-C	10.0	-5.4	> 102000	(RUNOUT)
31-C	12.5	-7.1	> 114000	(RUNOUT)
30-C	12.9	-6.7	> 100000	(RUNOUT)
26-C	12.9	-6.7	31500	
28-C	12.9	-6.7	30	
27-C	12.9	-6.7	10800	
34-C	12.9	-6.7	> 194300	(RUNOUT)
29-C	12.9	-6.7	1756	
4-C	14.3	-7.9	1033	
9-C	14.5	-7.1	100	
6-C	14.5	-7.5	122	
5-C	14.5	-7.5	139	
10-C	14.6	-7.1	37	
8-C	14.7	-7.1	412	
7-C	14.7	-7.1	50	
43-C	15.0	-7.1	176	
44-C	15.0	-7.1	210	
45-C	15.0	-7.1	3000	
48-C	16.2	-8.3	96	
47-C	16.2	-8.3	13	
46-C	16.2	-8.3	28	
11-C	16.6	-8.7	193	
17-C	16.6	-8.3	258	
13-C	16.6	-8.7	105	
16-C	17.0	-8.3	748	
12-C	17.0	-8.3	302	
14-C	17.0	-8.3	49	
15-C	17.0	-8.3	1	
23-C	17.8	-9.5	1	(FIRST CYCLE)
20-C	19.1	-10.0	85	
22-C	19.1	-9.5	1	(FIRST CYCLE)
25-C	19.1	-10.0	5	
18-C	19.5	-9.5	51	
21-C	19.5	-9.5	9	
19-C	19.6	-9.6	55	

TABLE 11-23
FATIGUE TESTS ON H-451 GRAPHITE
GLCC Lot 408, Log 5651-90 (GLCC Log 48)

LOT NO: 408 LOG NO: 5651-90
ORIENTATION: AXIAL LOCATION: QUARTER-LENGTH EDGE

STRESS RATIO, R (MIN. STRESS / MAX. STRESS): .0

SPECIMEN NO.	MAX. STRESS (MPA)	MIN. STRESS (MPA)	CYCLES TO FAILURE	
34-D	10.0	.0	> 207400	(RUNOUT)
38-D	10.4	.0	> 532600	(RUNOUT)
32-D	10.4	.0	> 120400	(RUNOUT)
35-D	10.4	.0	> 100000	(RUNOUT)
39-D	10.4	.0	> 103000	(RUNOUT)
37-D	10.4	.0	> 118000	(RUNOUT)
36-D	10.5	.0	> 252900	(RUNOUT)
30-D	12.4	.0	5800	
25-D	12.4	.0	> 105500	(RUNOUT)
26-D	12.6	.0	> 203800	(RUNOUT)
31-D	12.6	.0	> 242000	(RUNOUT)
28-D	12.6	.0	> 100000	(RUNOUT)
29-D	12.7	.0	11800	
27-D	13.0	.0	2388	
18-D	14.7	.0	756	
21-D	14.7	.0	3359	
17-D	14.7	.0	835	
19-D	14.7	.0	6666	
20-D	15.1	.0	55	
23-D	15.5	.0	189	
22-D	15.9	.0	198	
8-D	16.7	.0	< 1	(FIRST CYCLE)
9-D	16.7	.0	< 1	(FIRST CYCLE)
23-E	16.8	.0	< 1	(FIRST CYCLE)
15-D	16.8	.0	1	
12-D	16.8	.0	1232	
41-D	16.8	.0	< 1	(FIRST CYCLE)
14-D	16.8	.0	1	
13-D	16.8	.0	48	
11-D	17.2	.0	313	
16-D	17.2	.0	93	
43-D	17.6	.0	67	
42-D	17.7	.0	50	
44-D	17.7	.0	15	
10-D	17.7	.0	< 1	(FIRST CYCLE)
3-D	17.7	.0	< 1	(FIRST CYCLE)
6-D	18.1	.0	< 1	(FIRST CYCLE)
5-D	18.1	.0	< 1	(FIRST CYCLE)
7-D	18.4	.0	< 1	(FIRST CYCLE)
45-D	18.7	.0	< 1	(FIRST CYCLE)
4-D	19.0	.0	< 1	(FIRST CYCLE)

TABLE 11-24
FATIGUE TESTS ON H-451 GRAPHITE
GLCC Lot 408, Log 5651-90 (GLCC Log 48)

LOT NO: 408 LOG NO: 5651-90
ORIENTATION: AXIAL LOCATION: QUARTER-LENGTH EDGE

STRESS RATIO, R (MIN. STRESS / MAX. STRESS): .5

SPECIMEN NO.	MAX. STRESS (MPA)	MIN. STRESS (MPA)	CYCLES TO FAILURE
4-E	10.0	5.0	> 139800 (RUNOUT)
5-E	10.0	5.0	> 293300 (RUNOUT)
32-E	14.1	7.1	> 100000 (RUNOUT)
34-E	14.1	7.1	> 119300 (RUNOUT)
30-E	14.1	7.1	> 101300 (RUNOUT)
28-E	14.1	7.1	> 103200 (RUNOUT)
46-C	14.1	7.1	> 220200 (RUNOUT)
35-E	14.1	7.1	> 305300 (RUNOUT)
48-C	14.1	7.1	> 116300 (RUNOUT)
36-E	14.1	7.1	> 109200 (RUNOUT)
47-C	14.1	7.1	> 104100 (RUNOUT)
29-E	14.3	7.1	382
43-A	14.9	7.5	> 104400 (RUNOUT)
15-E	15.0	8.3	< 1 (FIRST CYCLE)
45-A	15.0	7.5	725
46-A	15.0	7.5	4
47-A	15.0	7.5	2530
42-A	15.0	7.5	> 100000 (RUNOUT)
48-A	15.0	7.5	1759
44-A	15.0	7.5	455
46-E	15.8	8.7	< 1 (FIRST CYCLE)
22-E	16.6	8.3	56
12-E	16.6	8.3	> 248800 (RUNOUT)
27-E	16.6	8.3	4844
23-E	16.6	8.3	900
26-E	16.6	8.3	621
14-E	16.6	8.3	380
44-E	16.8	8.7	< 1 (FIRST CYCLE)
41-E	17.1	9.6	< 1 (FIRST CYCLE)
45-E	17.1	8.7	< 1 (FIRST CYCLE)
37-E	17.2	9.6	< 1 (FIRST CYCLE)
6-E	17.4	9.5	< 1 (FIRST CYCLE)
43-E	17.5	8.7	39
42-E	17.5	8.7	464
9-E	17.5	9.6	< 1 (FIRST CYCLE)
47-E	17.5	8.7	423
38-E	17.5	9.6	< 1 (FIRST CYCLE)
48-E	17.5	8.7	3
11-E	18.7	9.1	1367
8-E	19.1	9.5	94
7-E	19.1	9.6	175

TABLE 11-25
DATA FOR AXIAL POSITION 23[a]

Power Day	Fluence x 10^{-25} (n/m^2)	Heat Generation (MW/m^3)		Conductivity ($W/m \cdot K$)		Conductance ($W/m^2 \cdot K$) Sleeve-Graphite	Gap Length, Fuel-Graphite (mm)	Coolant Temp (K)	Film Coeff. ($W/m^2 \cdot K$)
		Fuel	Sleeve or Graphite	Fuel	Sleeve or Graphite				
276	0	469,051	9,875	10.38	55.59	2518.9	0.1295	925	1166.7
333	0.163	446,236	9,395	10.05	49.03	2360.5	0.1524	911	1158.7
388	0.320	498,236	10,490	9.75	41.63	2383.7	0.1727	947	1211.5
435	0.465	428,755	9,027	9.50	39.24	2187.3	0.1880	899	1132.1
581	0.885	466,006	9,811	8.82	30.73	2141.3	0.2184	886	1186.0
662	1.117	505,194	10,636	8.48	29.23	2212.3	0.2311	907	1216.6
713	1.282	503,191	10,594	8.27	29.23	2205.4	0.2388	897	1227.4
812	1.6	538,619	11,340	7.89	29.01	2302.5	0.2489	884	1225.7

[a] From Ref. 11-9.

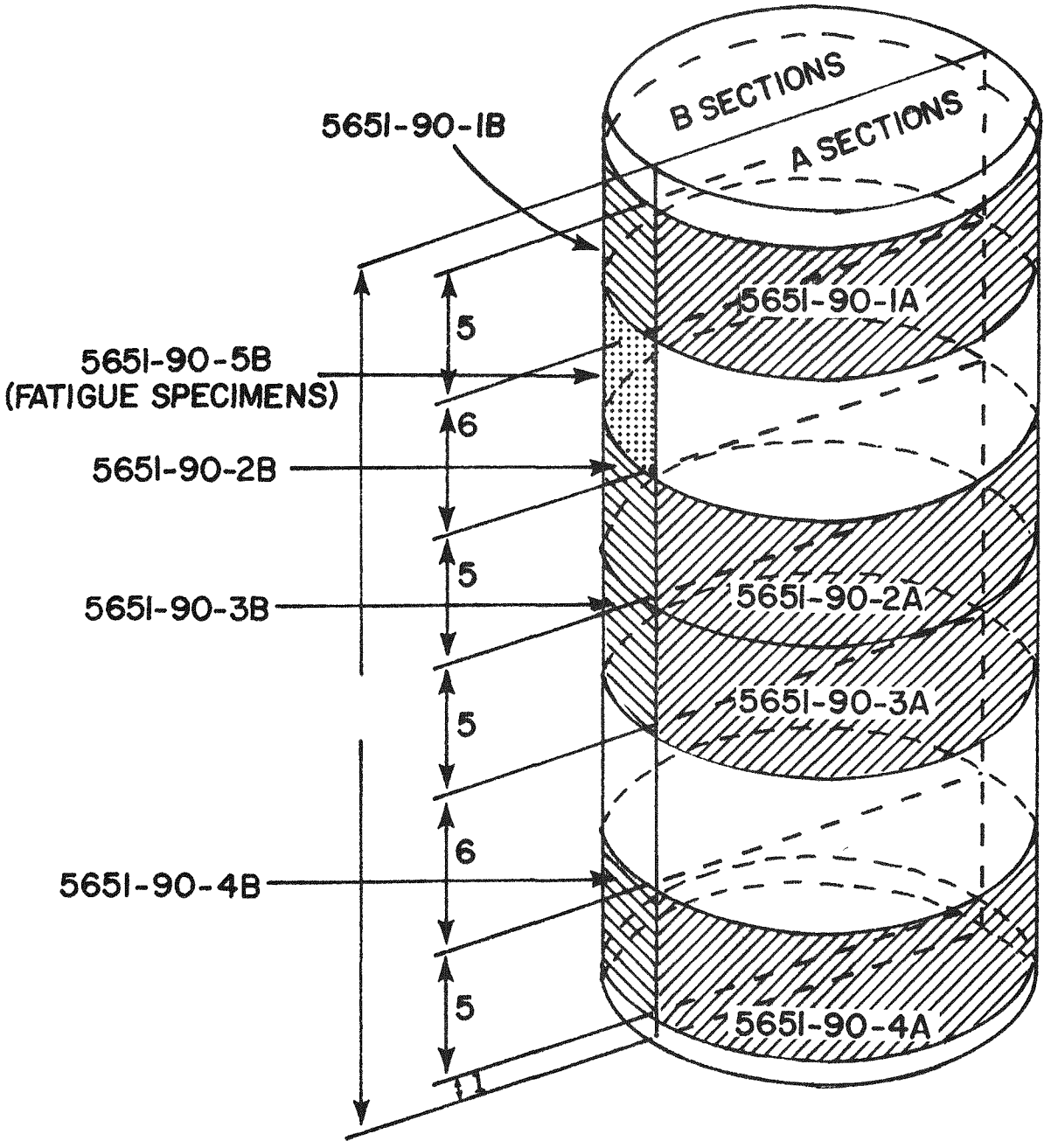

Fig. 11-1. Log 5651-90 of H-451 graphite showing locations of slabs used in statistical strength study (shaded) and fatigue study (dotted)

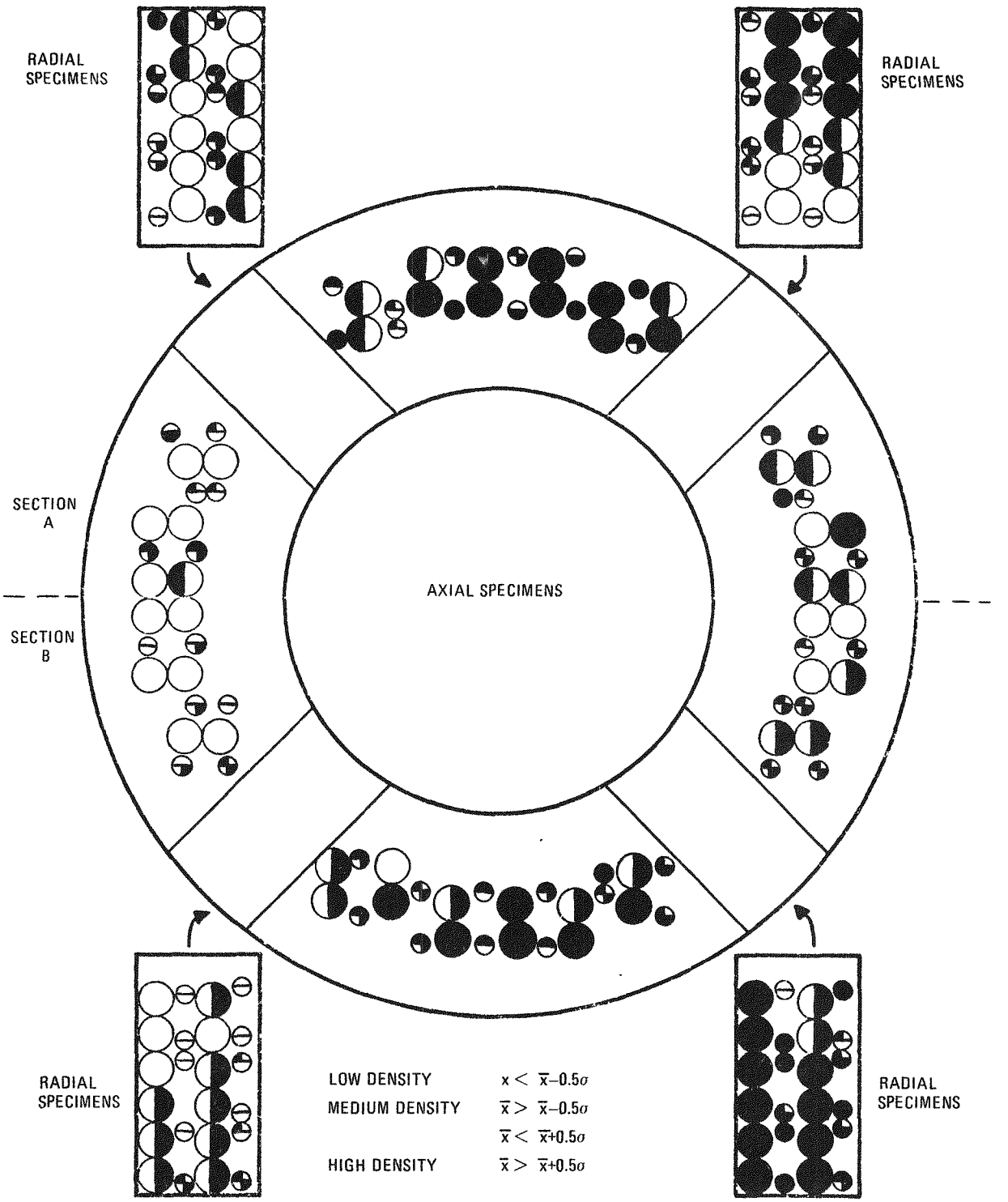

Fig. 11-2. Map of local variations in density in edge zone of slab 1

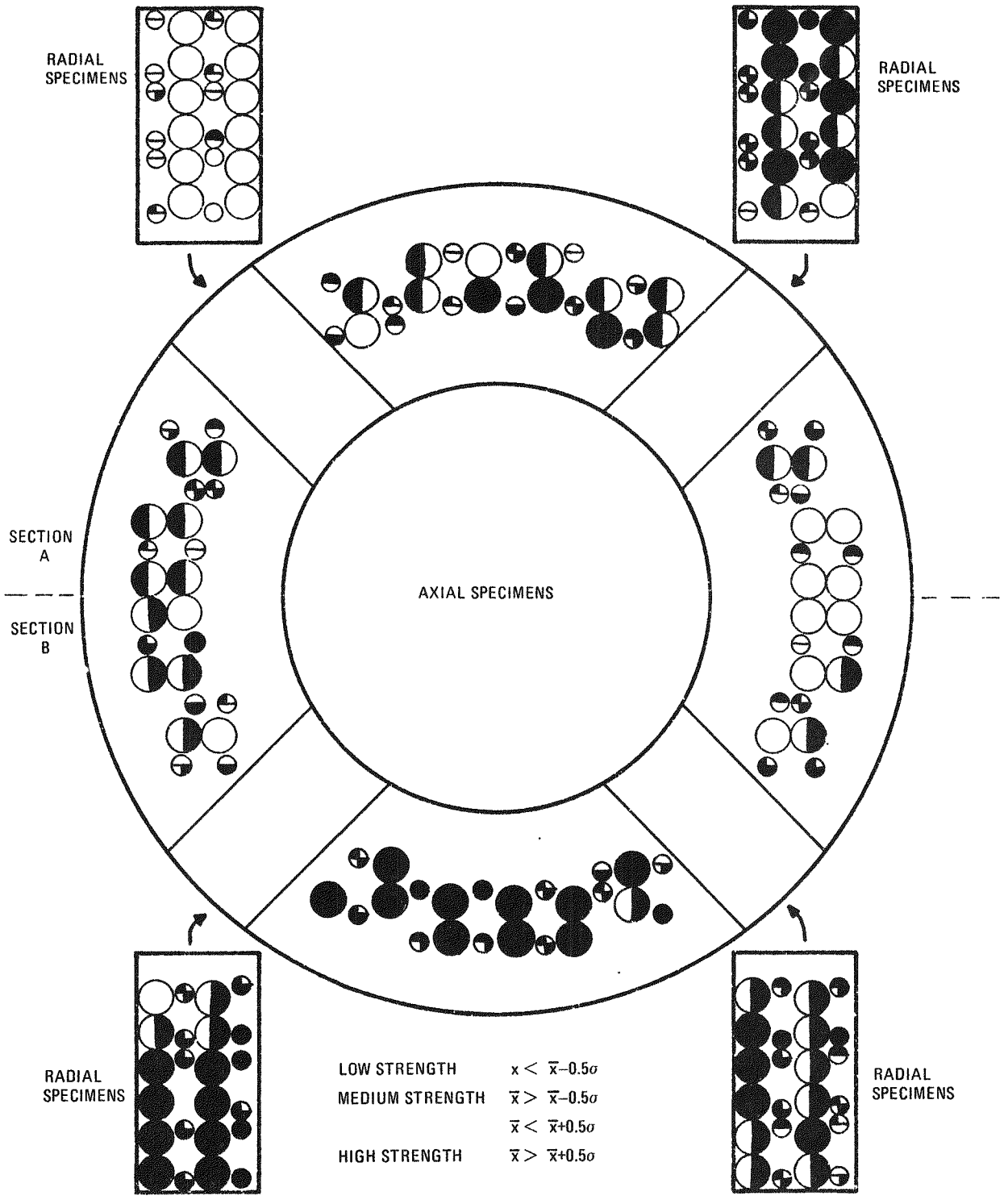

Fig. 11-3. Map of local variations in strength in edge zone of slab 1

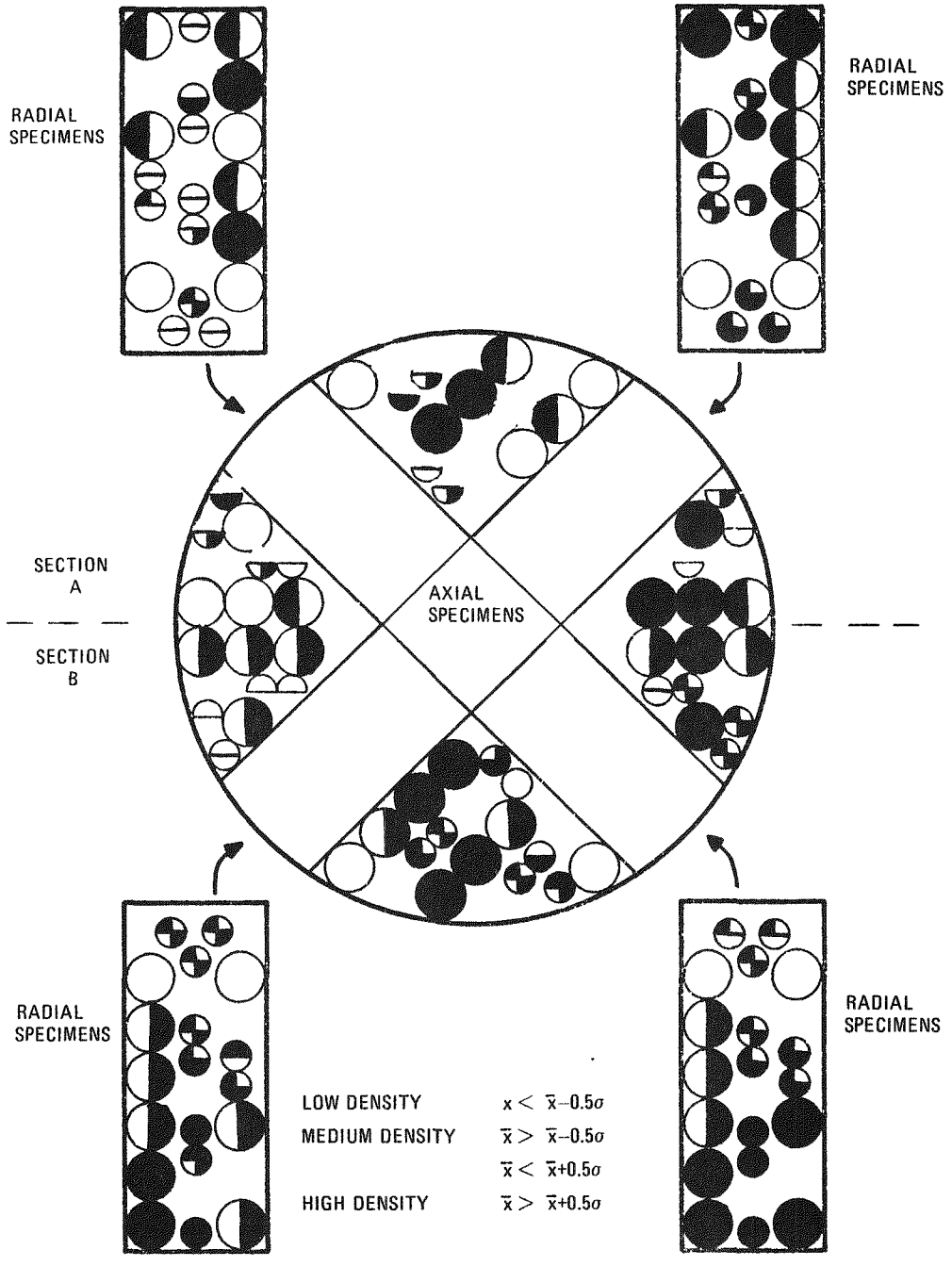

Fig. 11-4. Map of local variations in density in center zone of slab 1

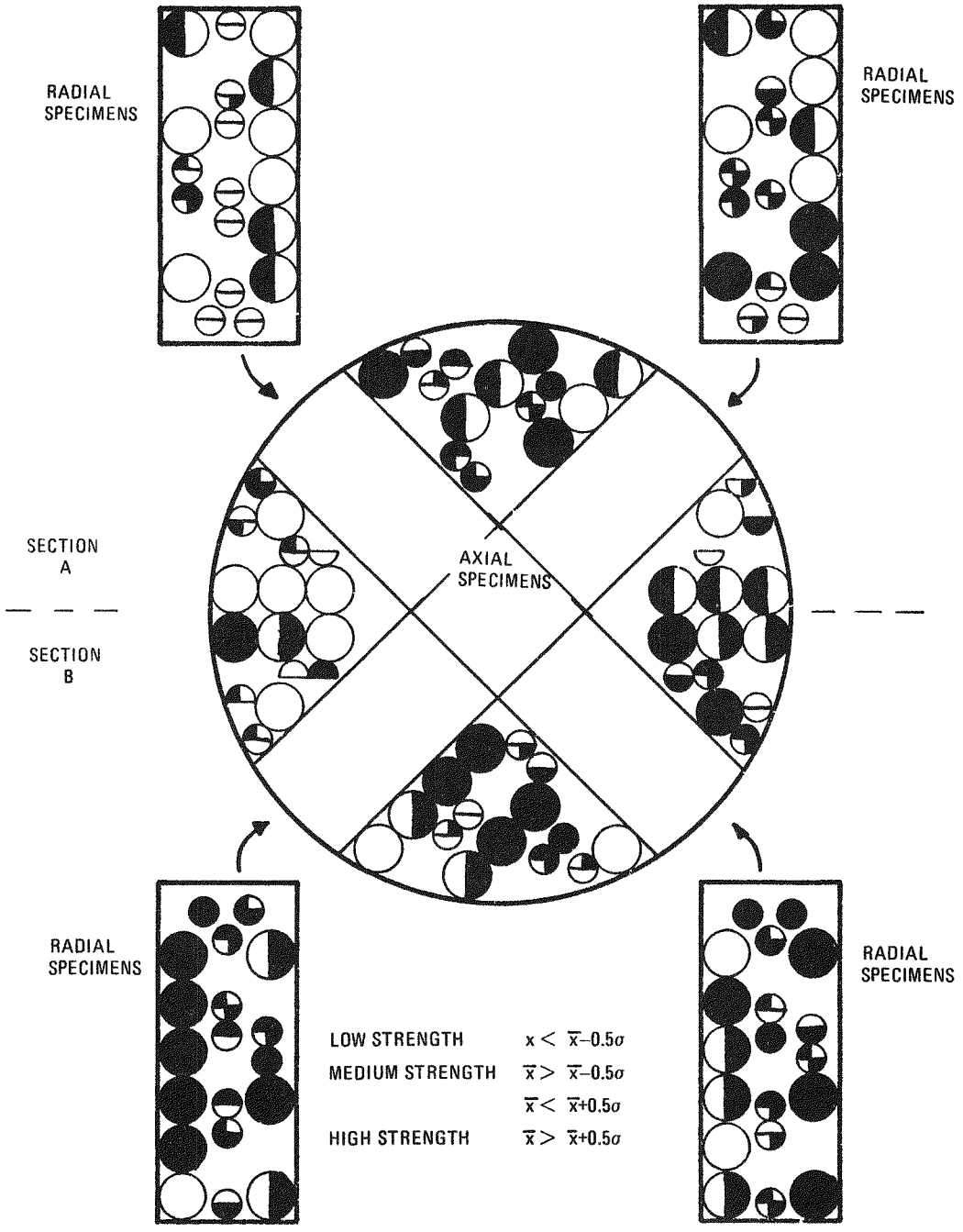

Fig. 11-5. Map of local variations in strength in center zone of slab 1

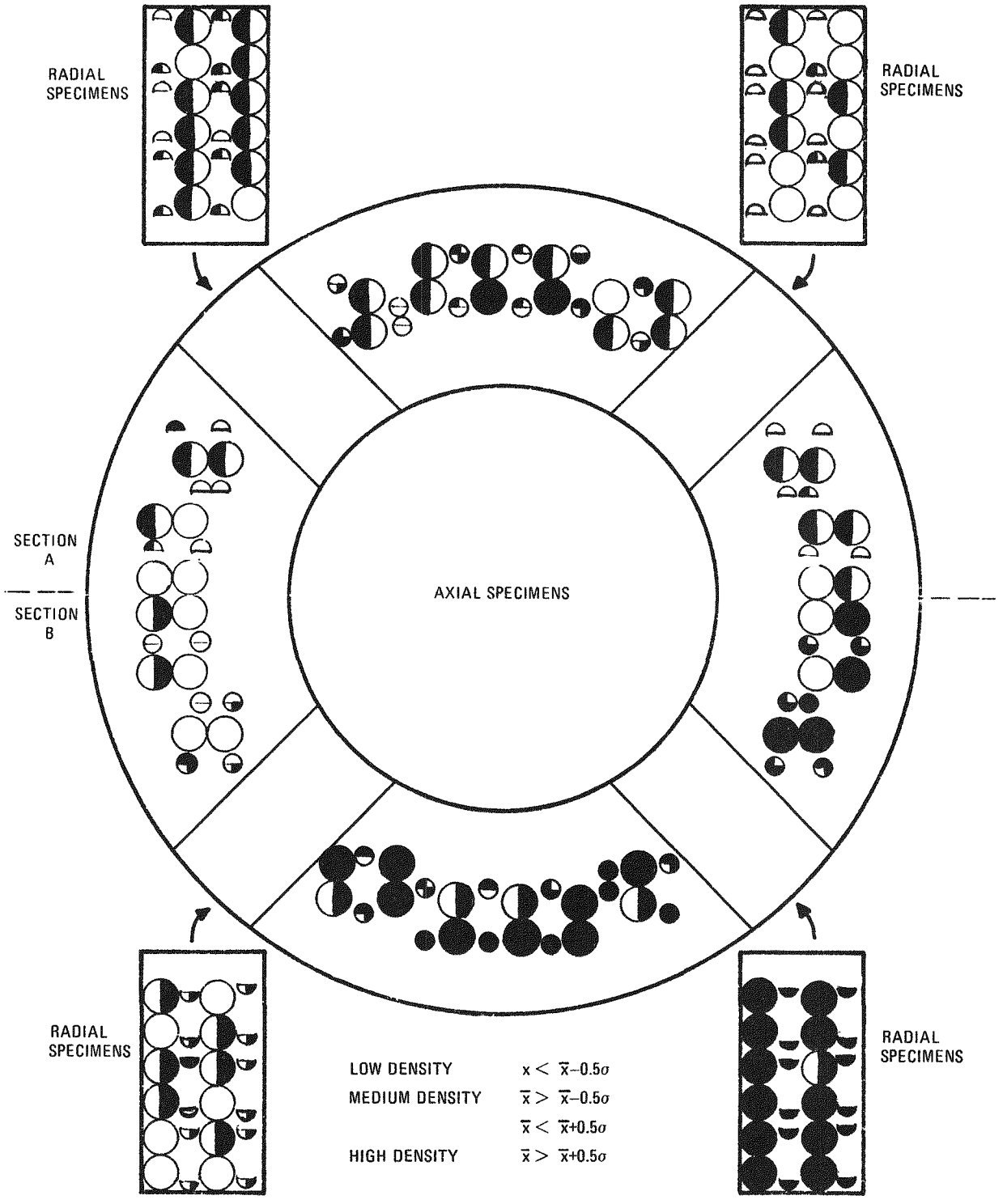

Fig. 11-6. Map of local variations in density in edge zone of slab 2

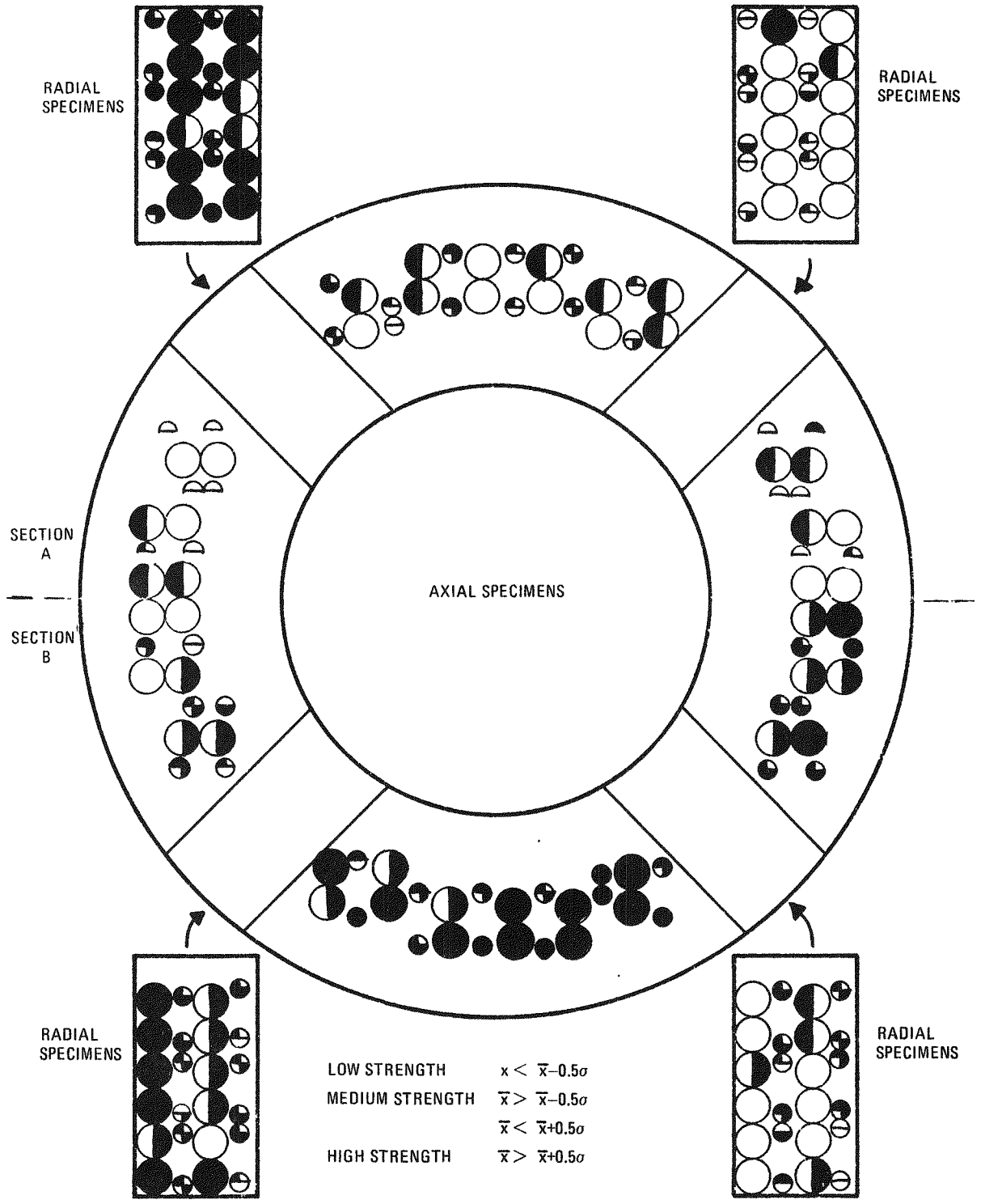

Fig. 11-7. Map of local variations in strength in edge zone of slab 2

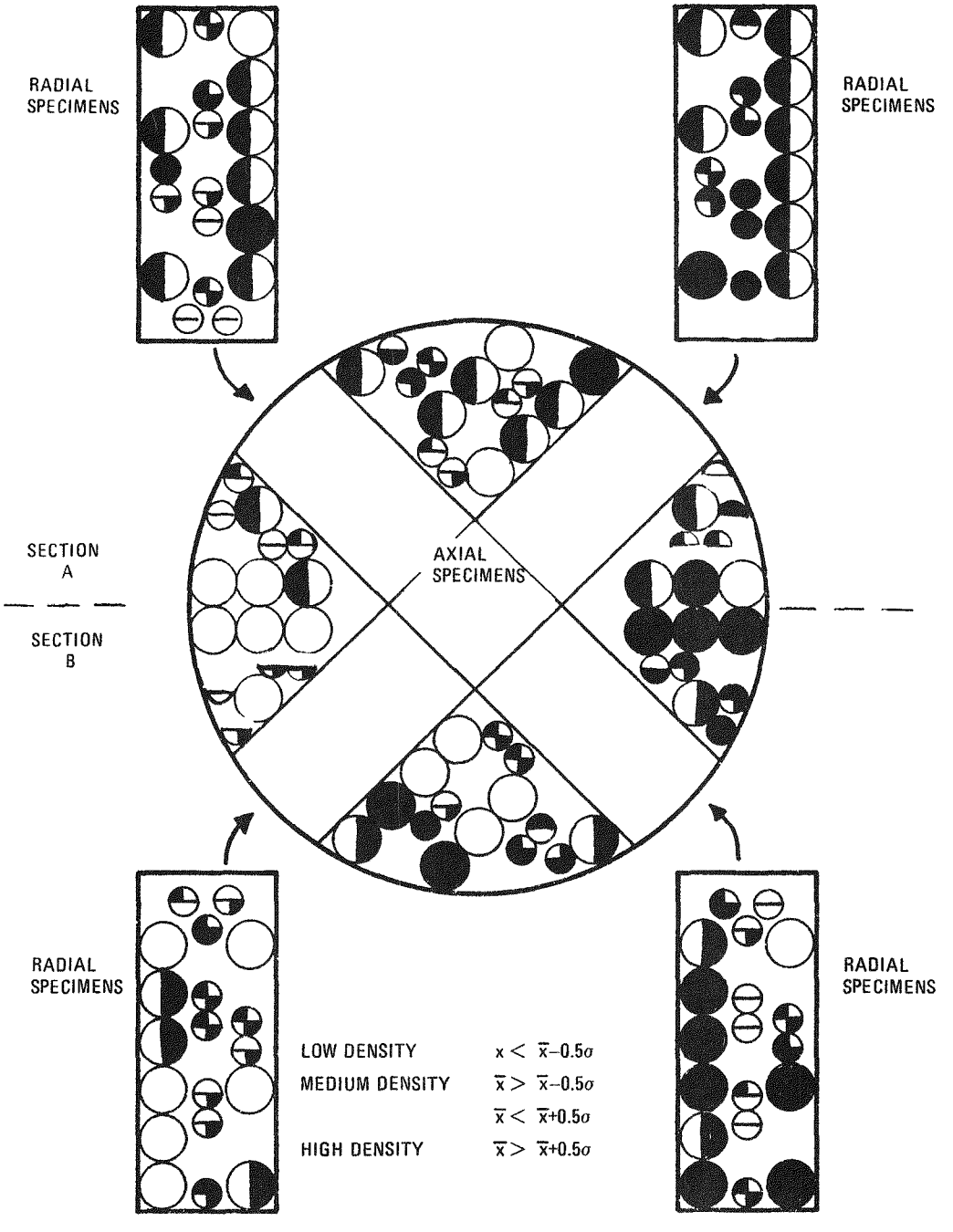

Fig. 11-8. Map of local variations in density in center zone of slab 2

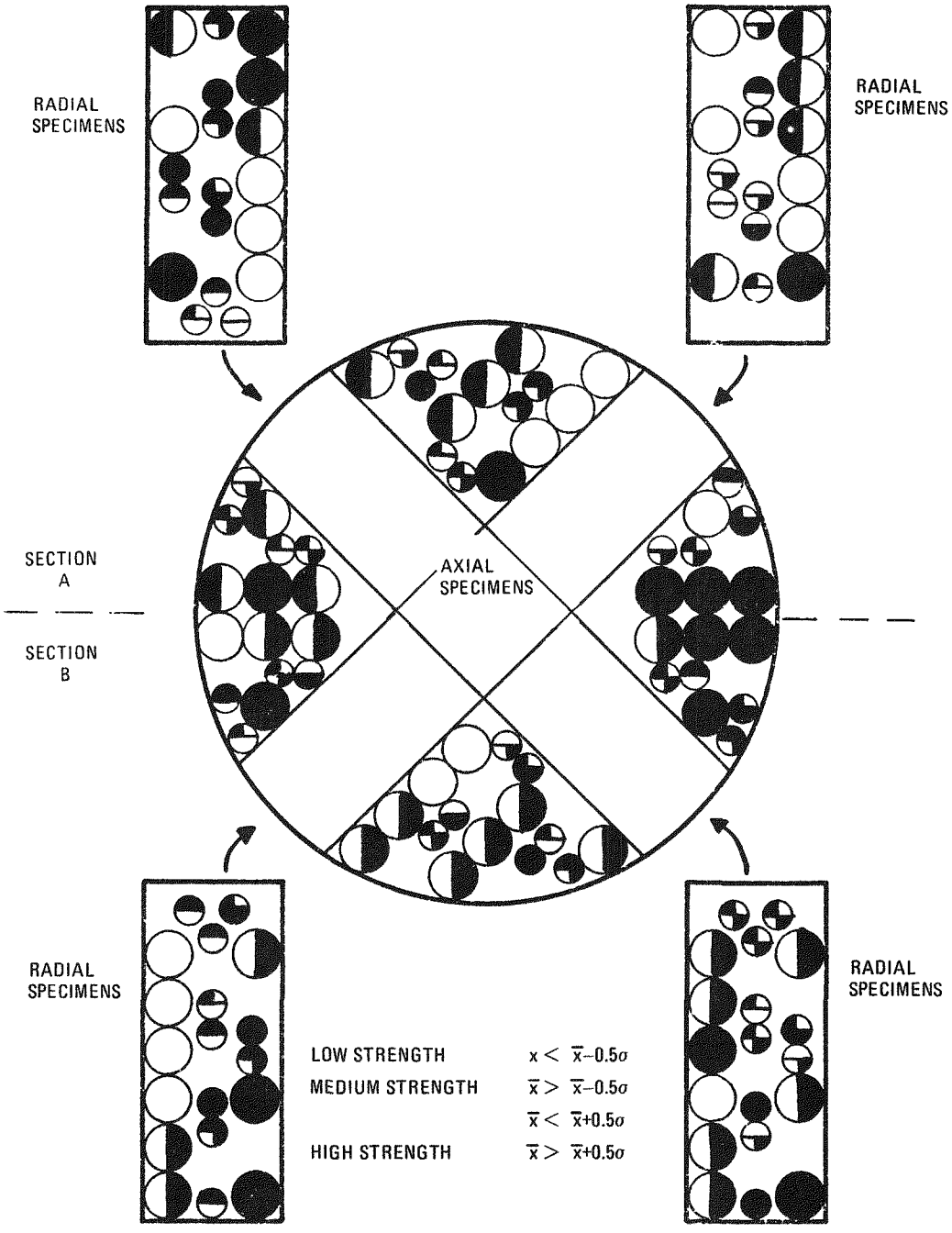

Fig. 11-9. Map of local variations in strength in center zone of slab 2

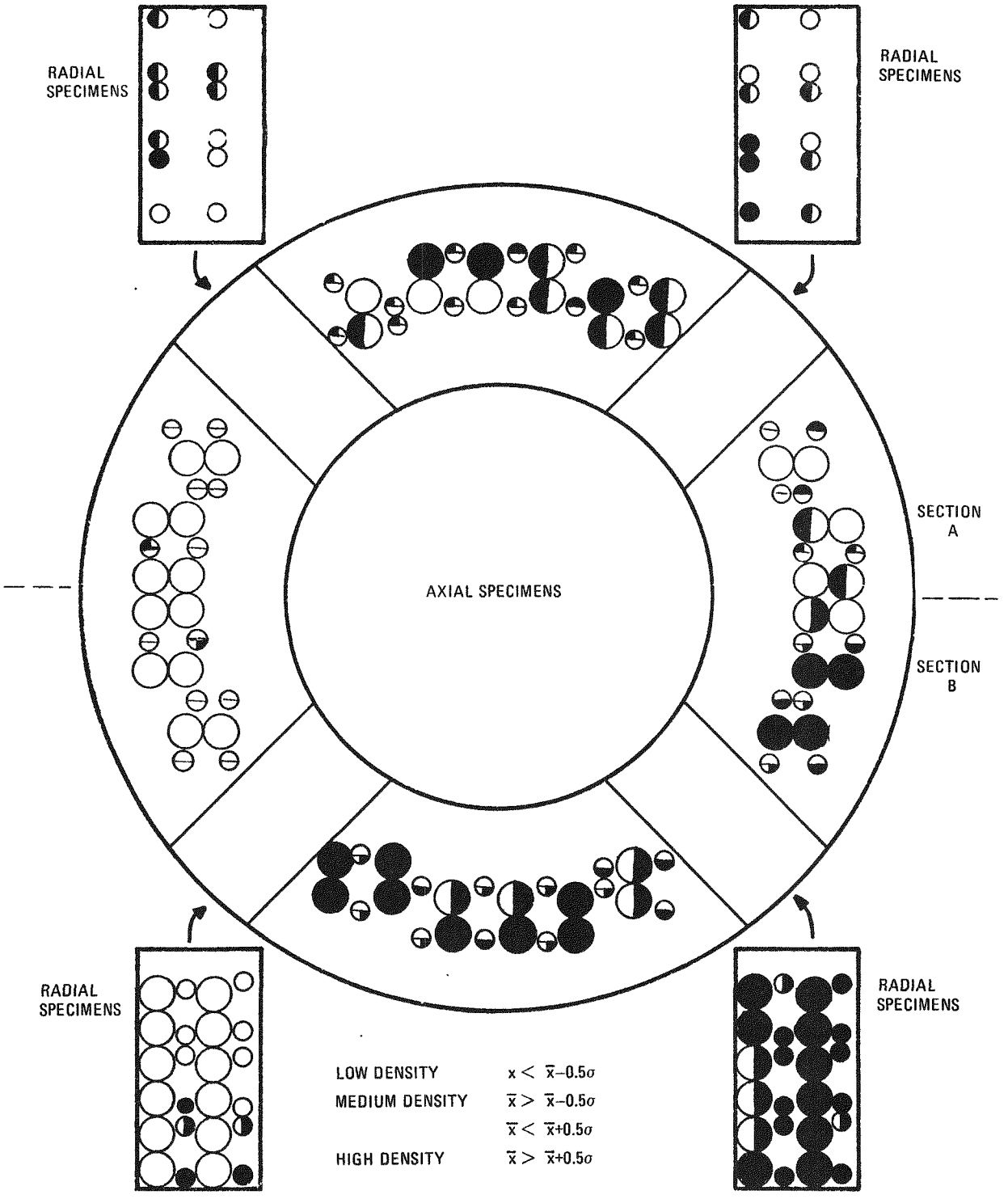

Fig. 11-10. Map of local variations in density in edge zone of slab 3

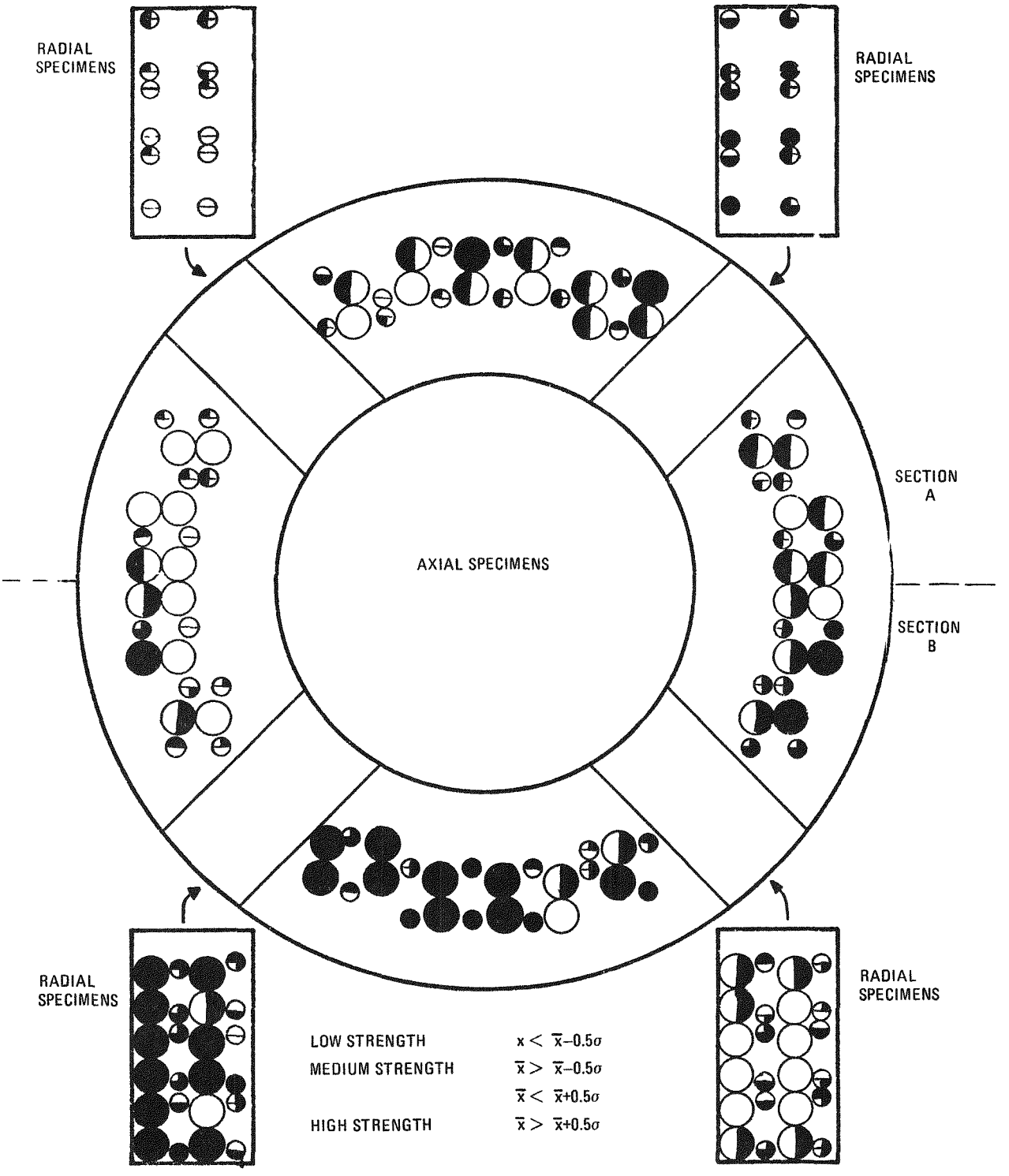

Fig. 11-11. Map of local variations in strength in edge zone of slab 3

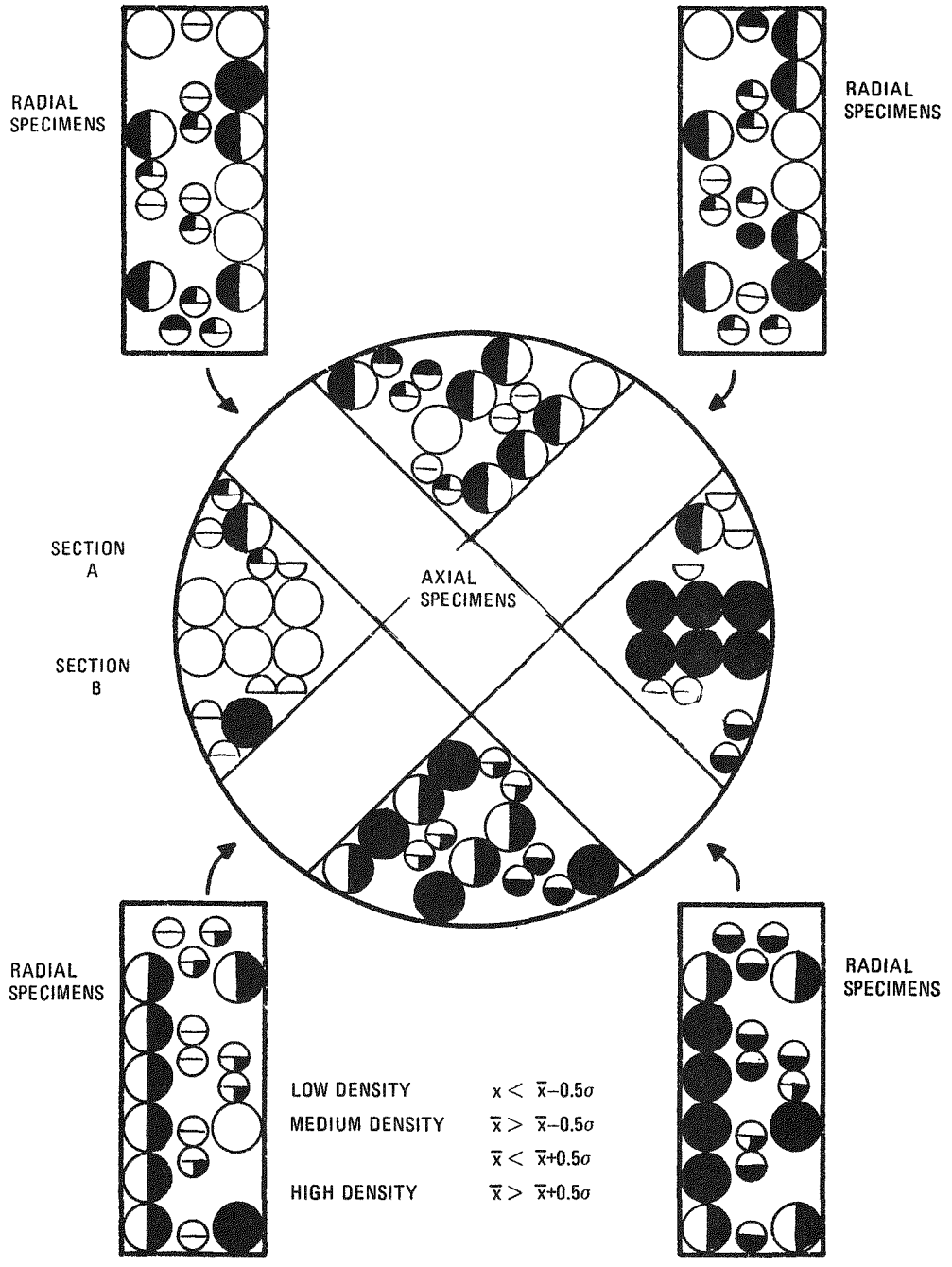

Fig. 11-12. Map of local variations in density in center zone of slab 3

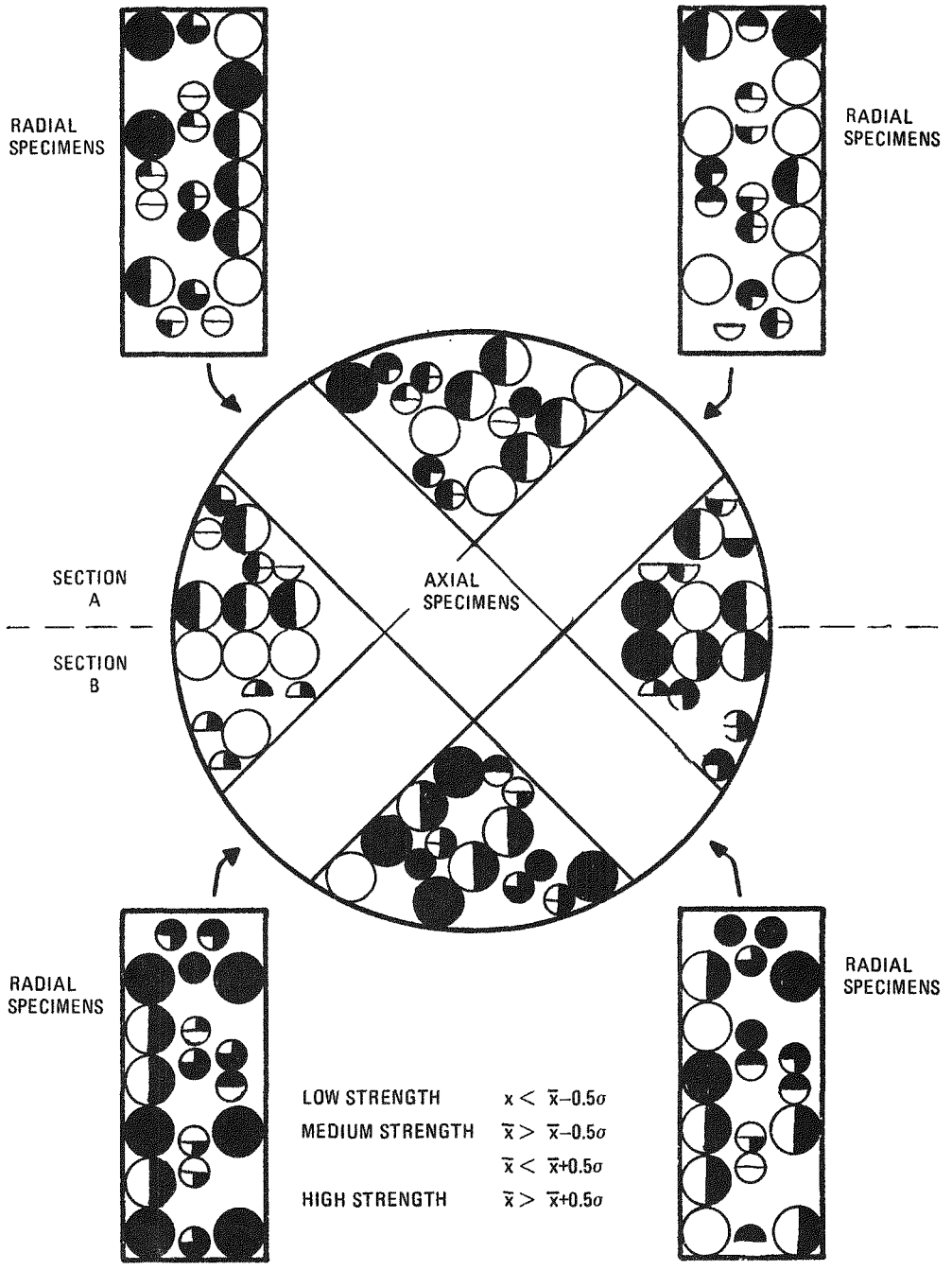

Fig. 11-13. Map of local variations in strength in center zone of slab 3

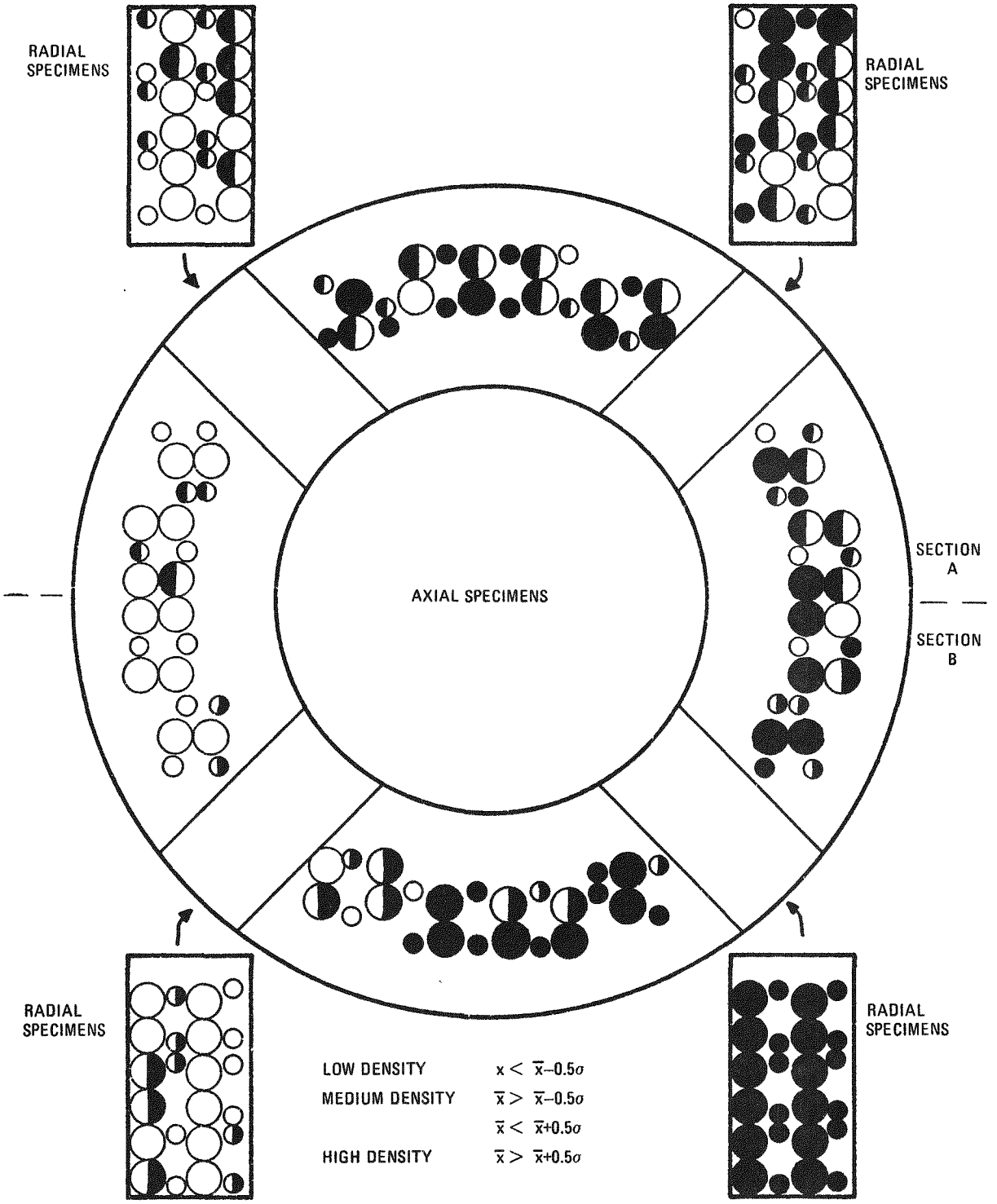

Fig. 11-14. Map of local variations in density in edge zone of slab 4

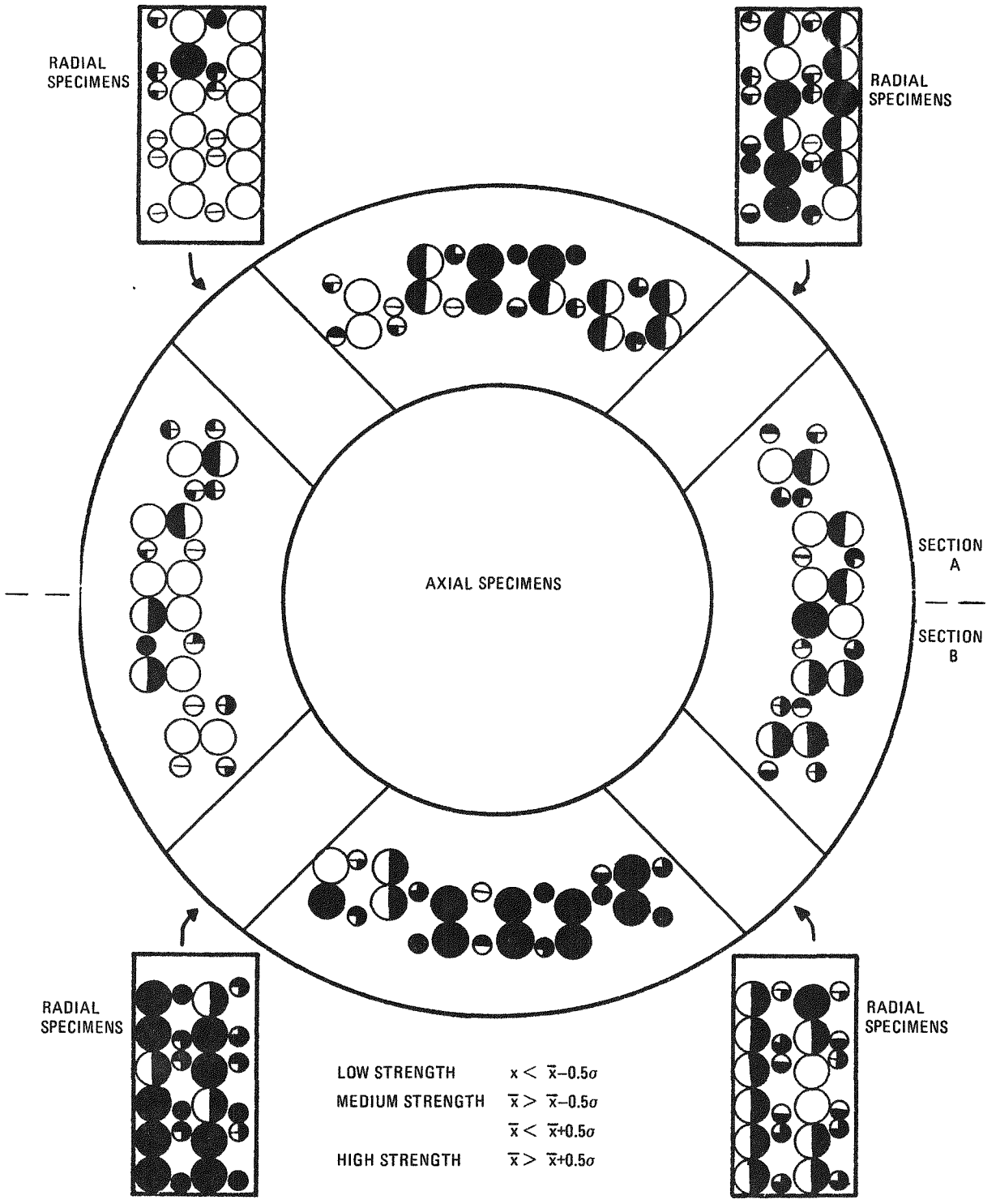

Fig. 11-15. Map of local variations in strength in edge zone of slab 4

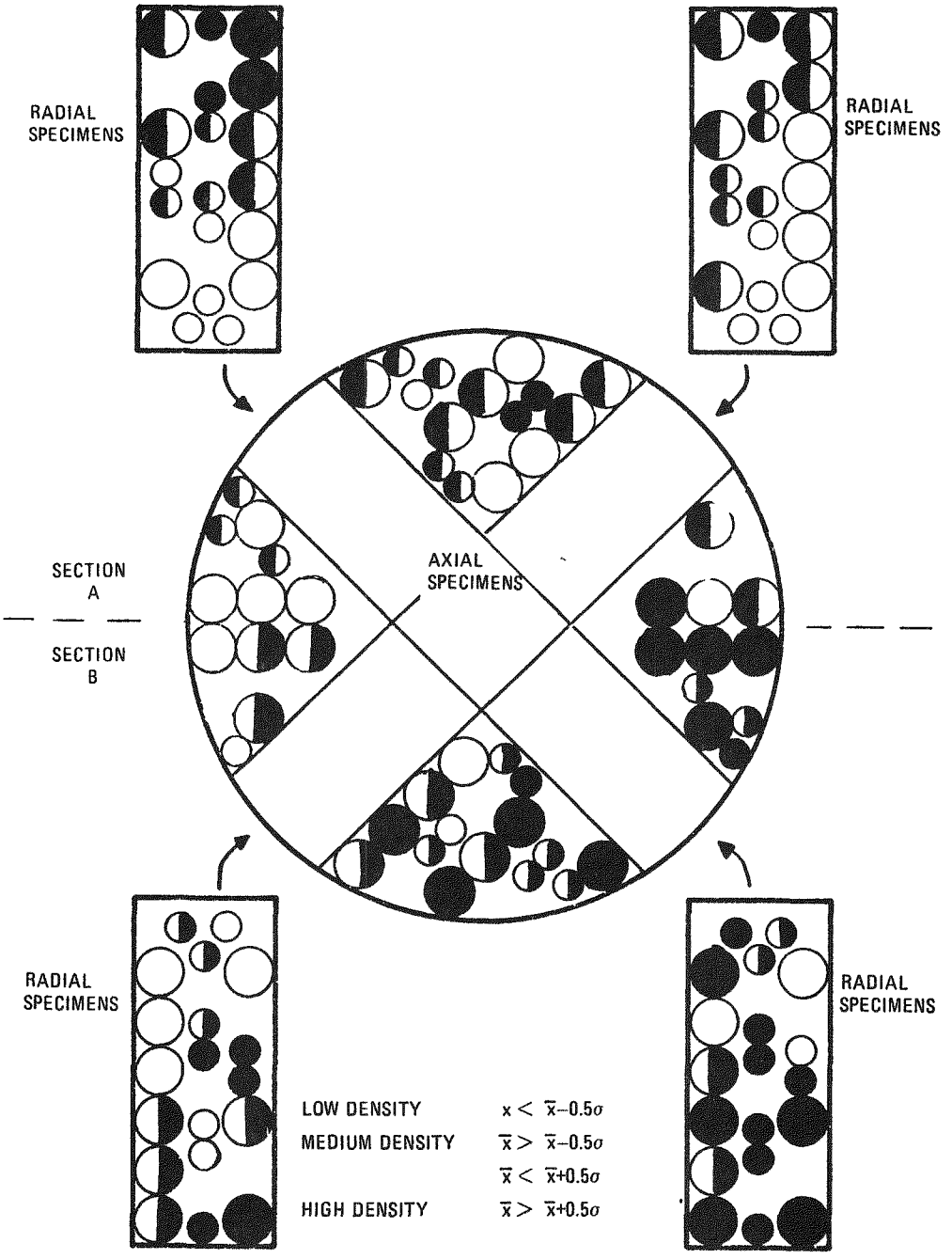

Fig. 11-16. Map of local variations in density in center zone of slab 4

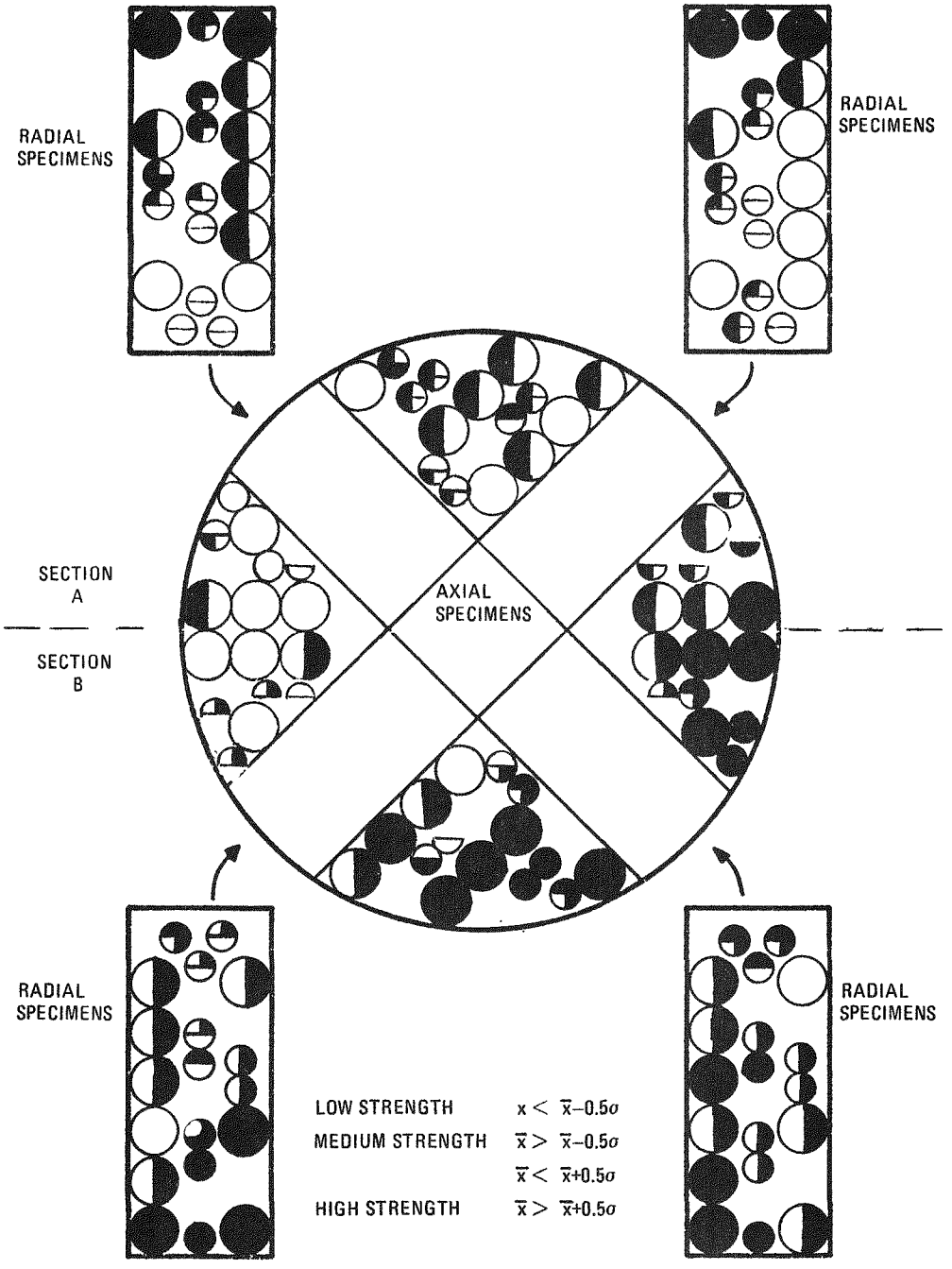

Fig. 11-17. Map of local variations in strength in center zone of slab 4

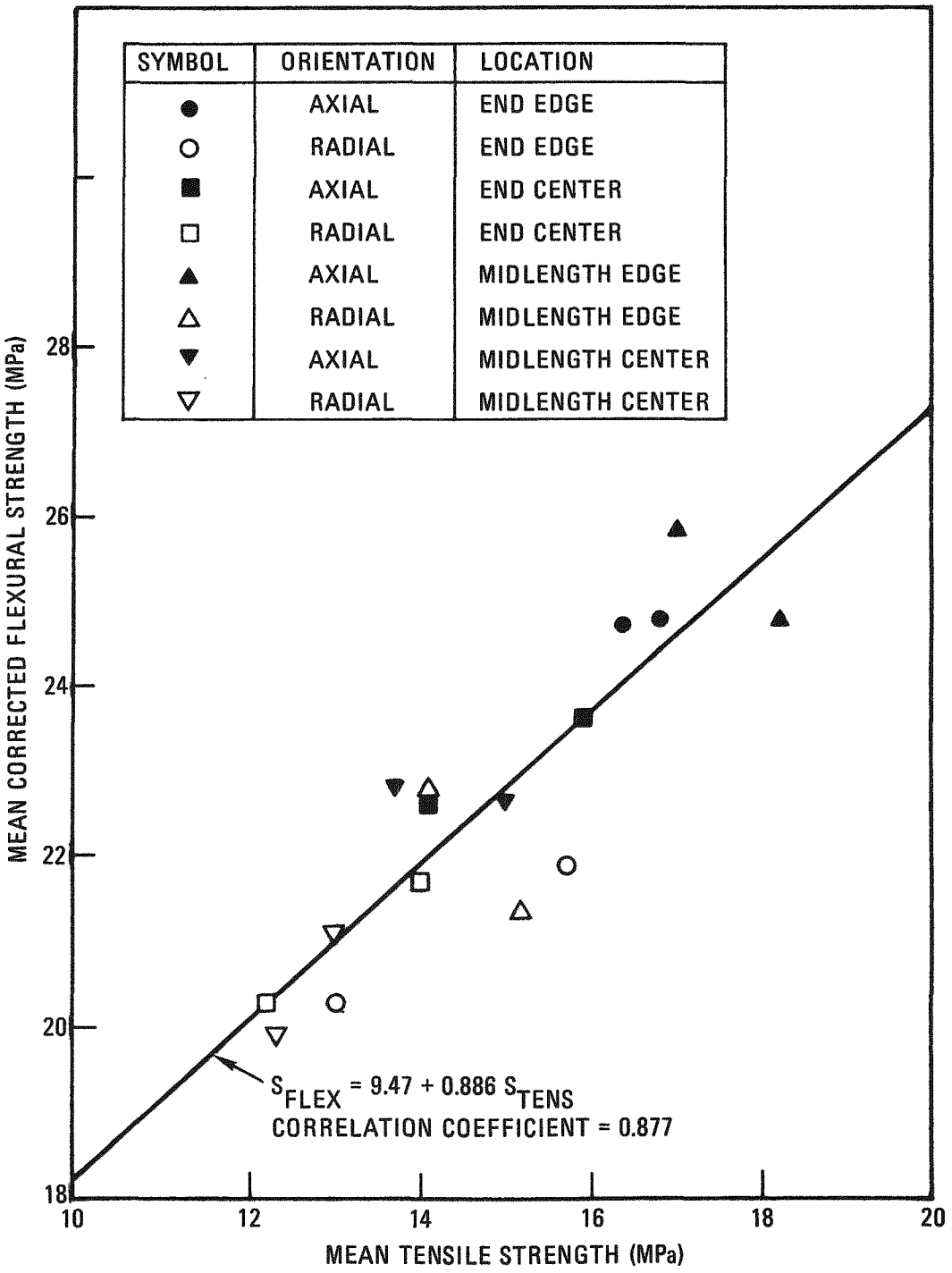

Fig. 11-18. Mean flexural strength of 6.4-mm-diameter specimens (corrected for nonlinearity of the stress-strain curve) versus mean tensile strength of 6.4-mm-diameter companion specimens. Each point represents the mean for one orientation, slab, and zone (center or edge).

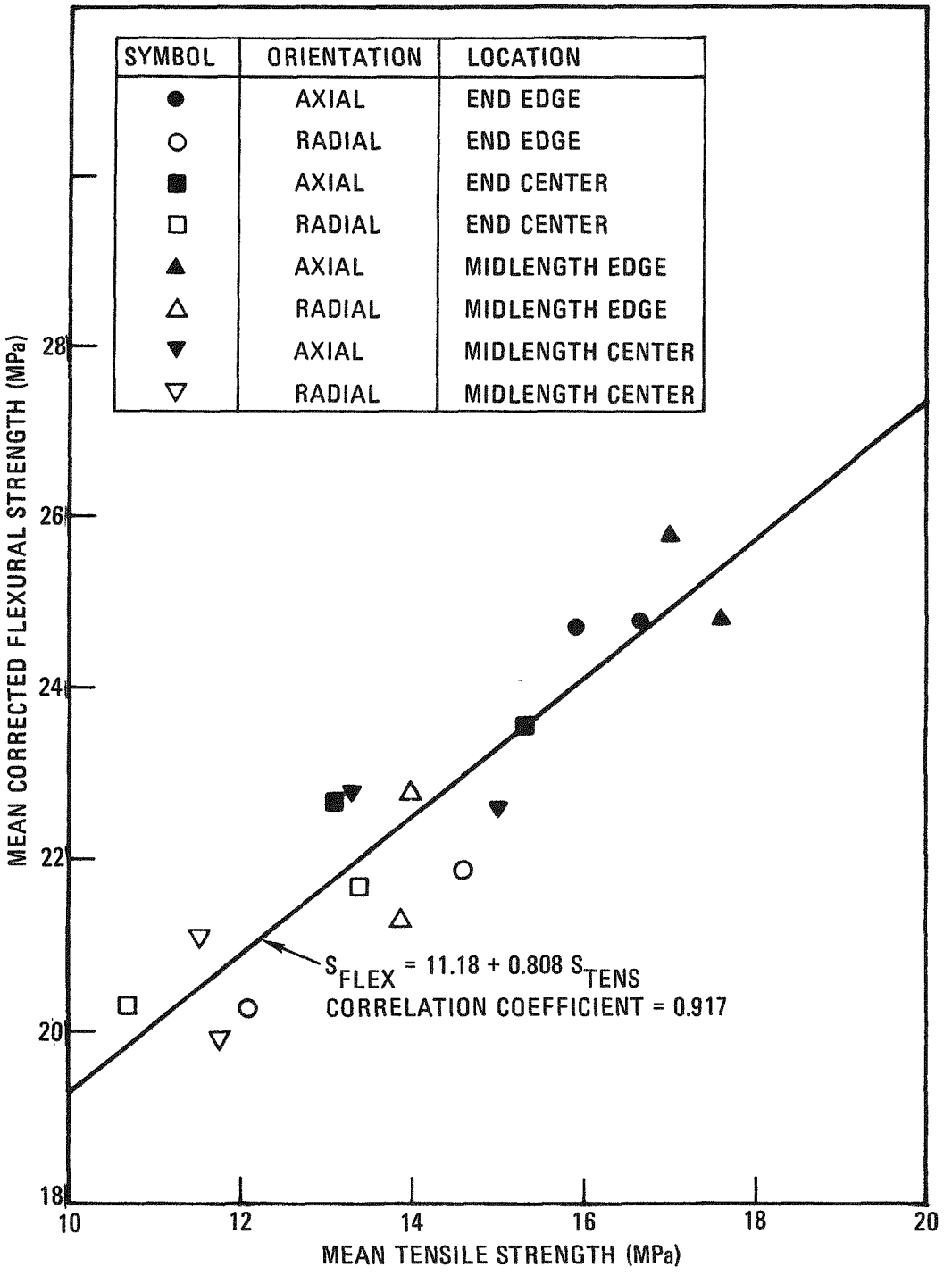

Fig. 11-19. Mean flexural strength of 6.4-mm-diameter specimens (corrected for nonlinearity of the stress-strain curve) versus mean tensile strength of 12.8-mm-diameter companion specimens. Each point represents the mean for one orientation, slab, and zone (center or edge).

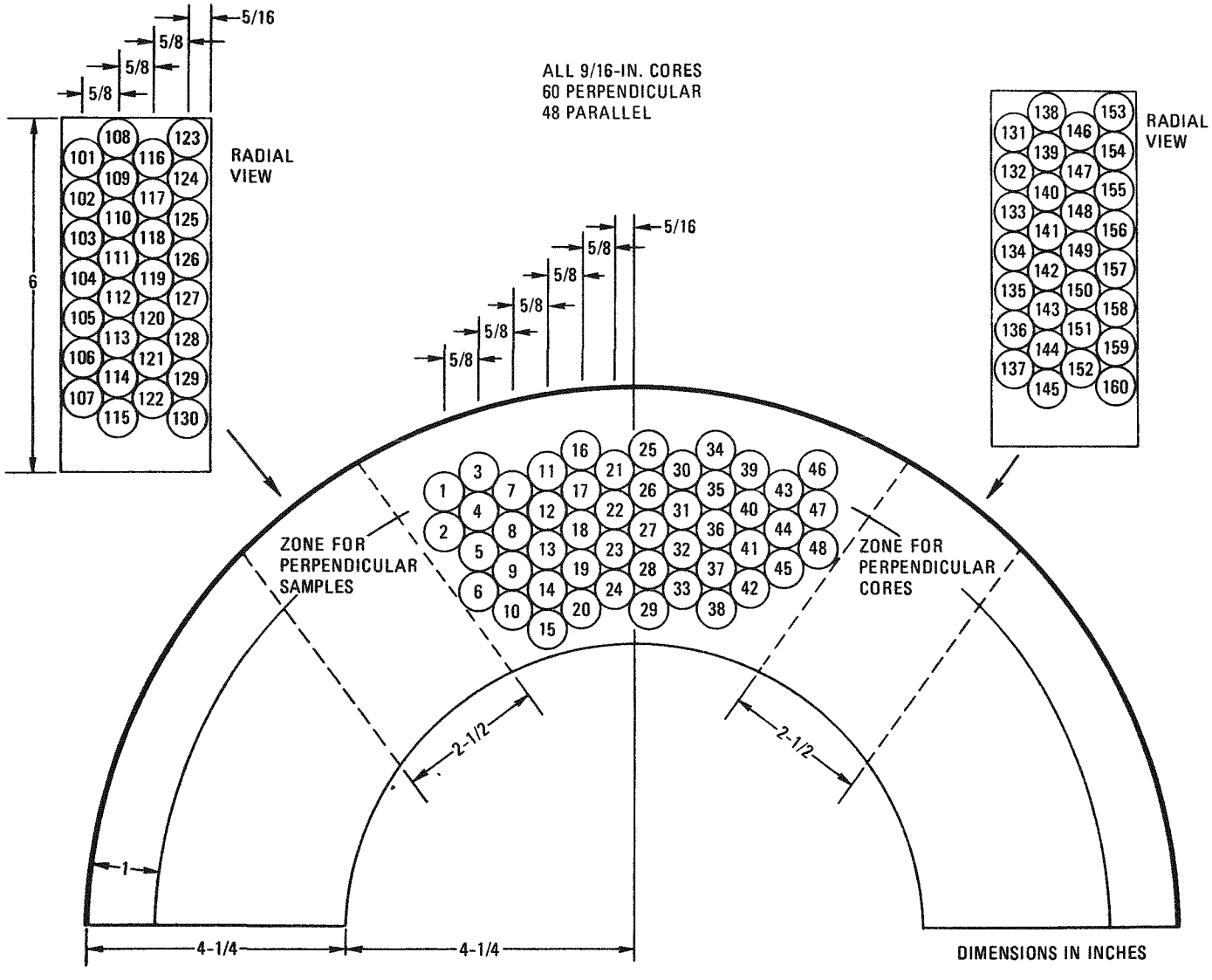

Fig. 11-20. Location of the cores for fatigue specimens in slab 5B

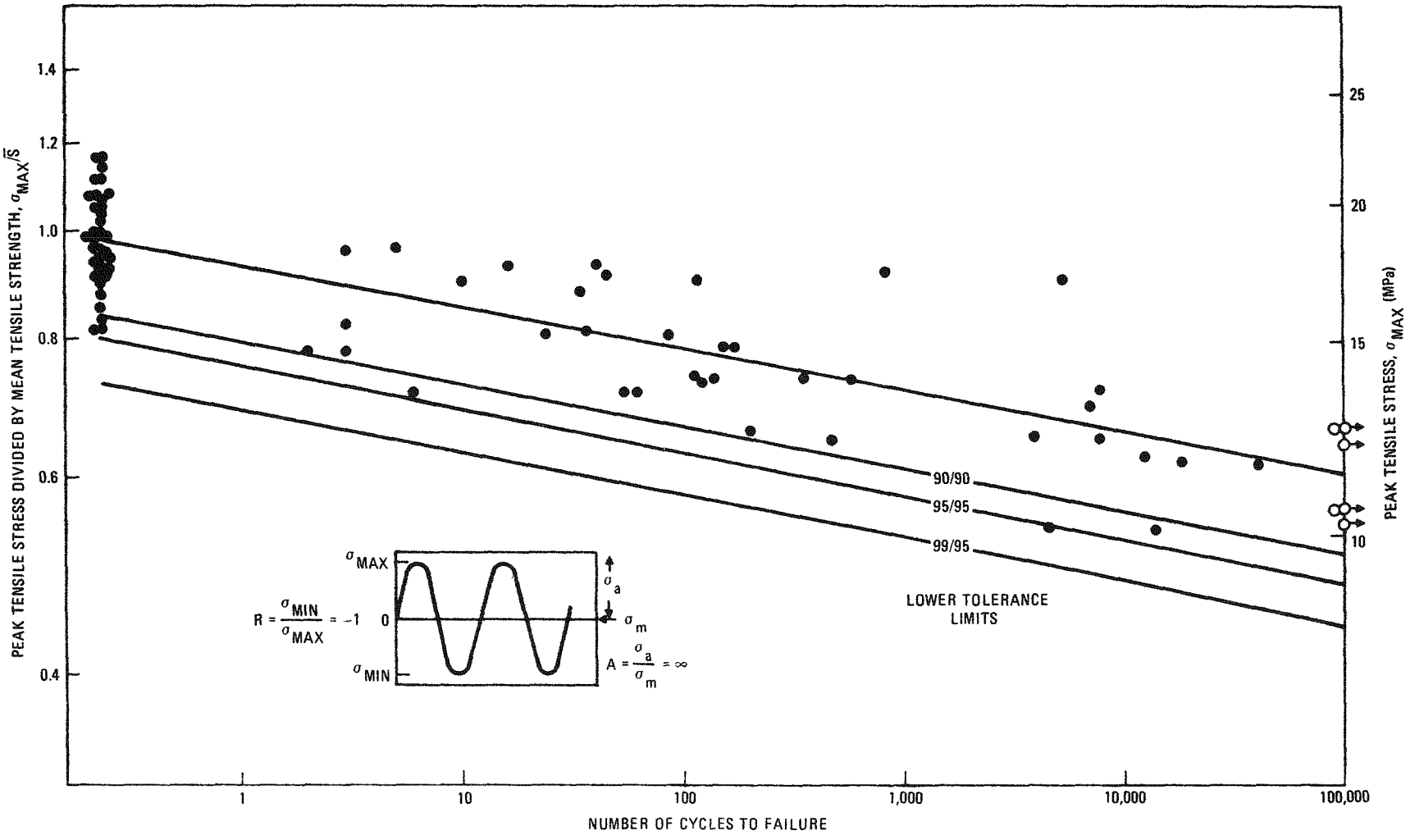

Fig. 11-21. Fatigue test data on H-451 graphite, axial orientation, quarter-length edge location, in air at ambient temperature. Log-log plot of normalized maximum stress versus number of cycles to failure with R = -1. Lower x/y tolerance limits represent the limits above which at least x% of the data fall, with y% confidence.

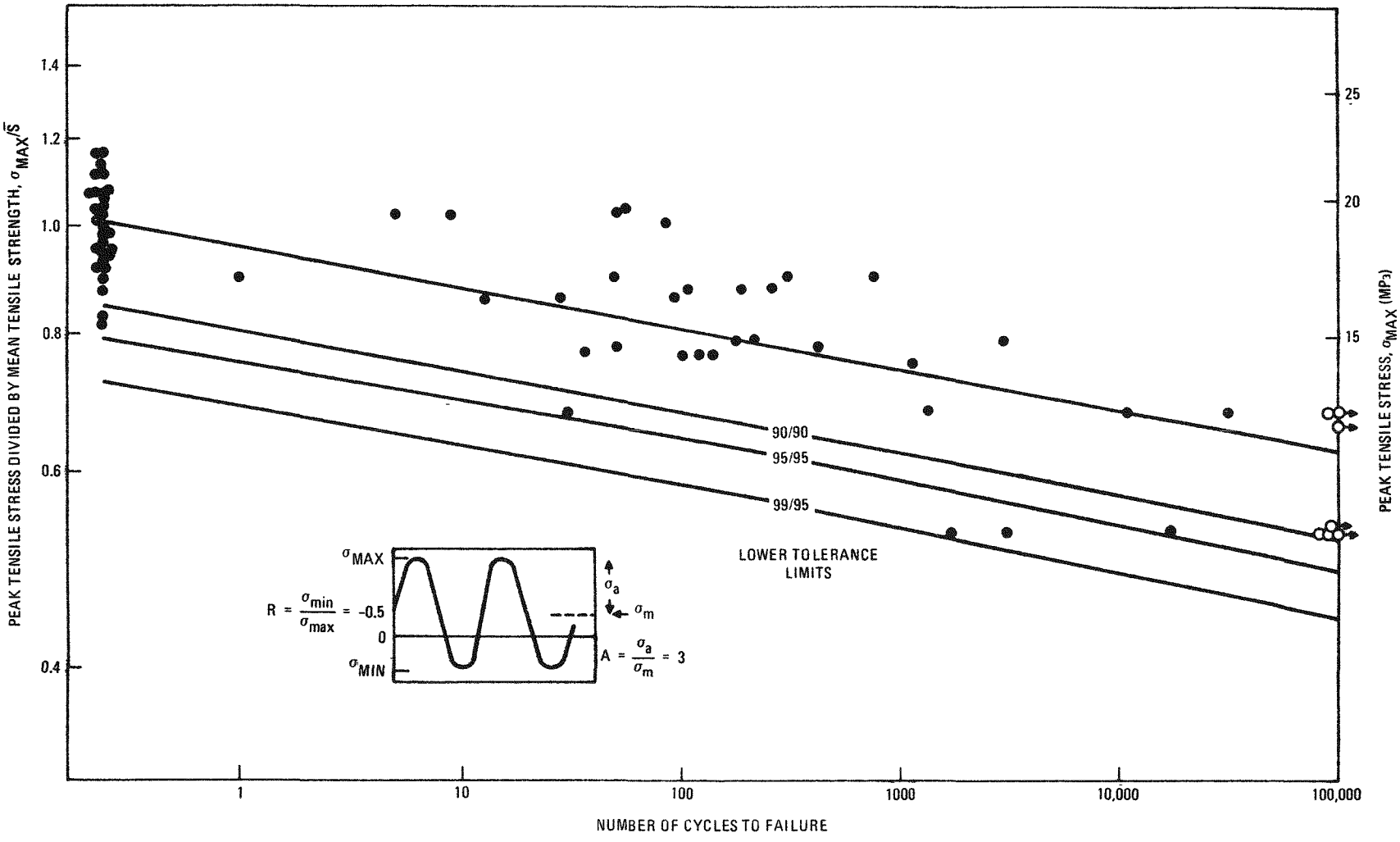

Fig. 11-22. Fatigue test data on H-451 graphite, axial orientation, quarter-length edge location, in air at ambient temperature. Log-log plot of normalized maximum stress versus number of cycles to failure with R = -0.5. Lower x/y tolerance limits represent the limits above which at least x% of the data fall, with y% confidence.

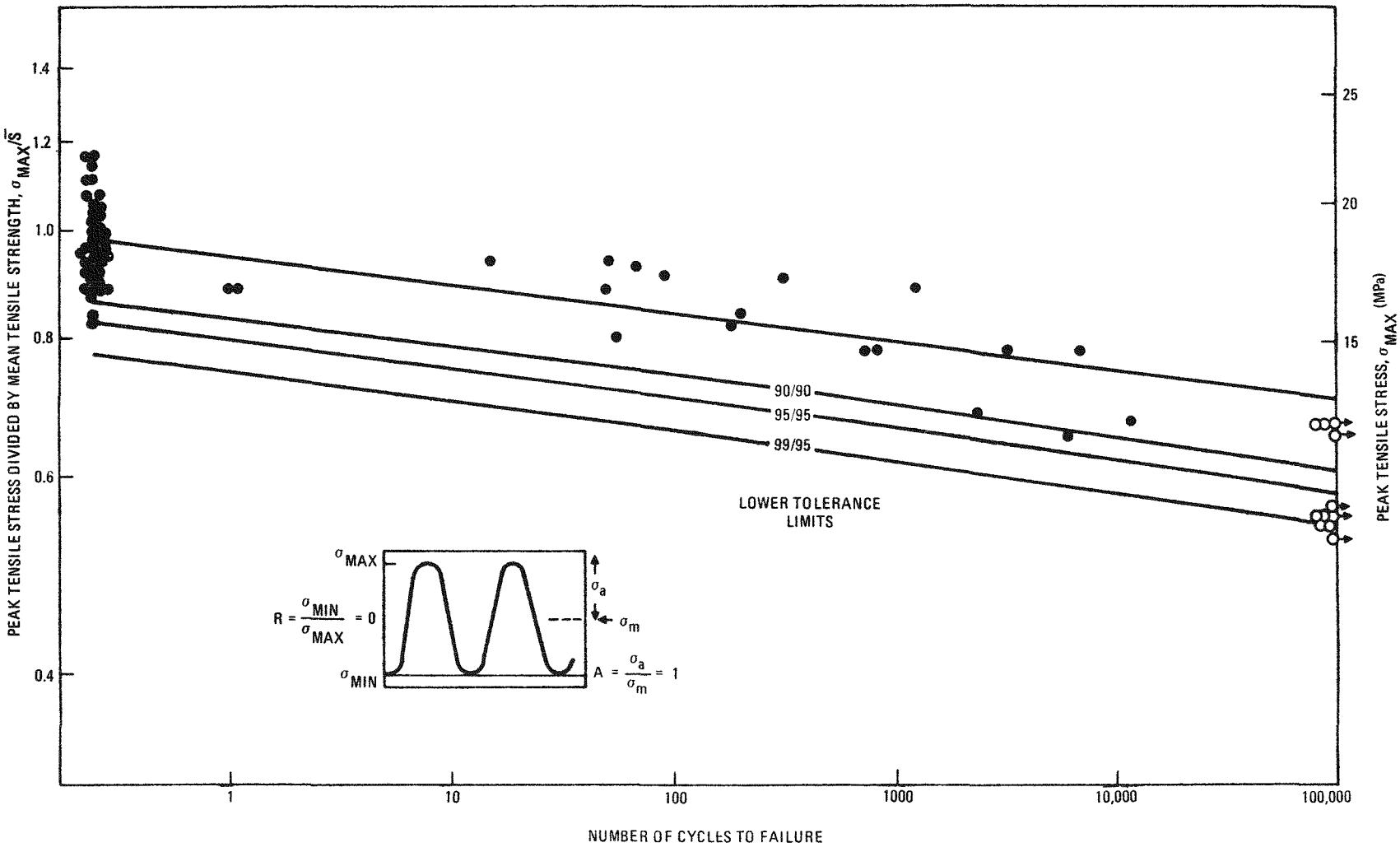

Fig. 11-23. Fatigue test data on H-451 graphite, axial orientation, quarter-length edge location, in air at ambient temperature. Log-log plot of normalized maximum stress versus number of cycles to failure with R = 0. Lower x/y tolerance limits represent the limits above which at least x% of the data fall, with y% confidence.

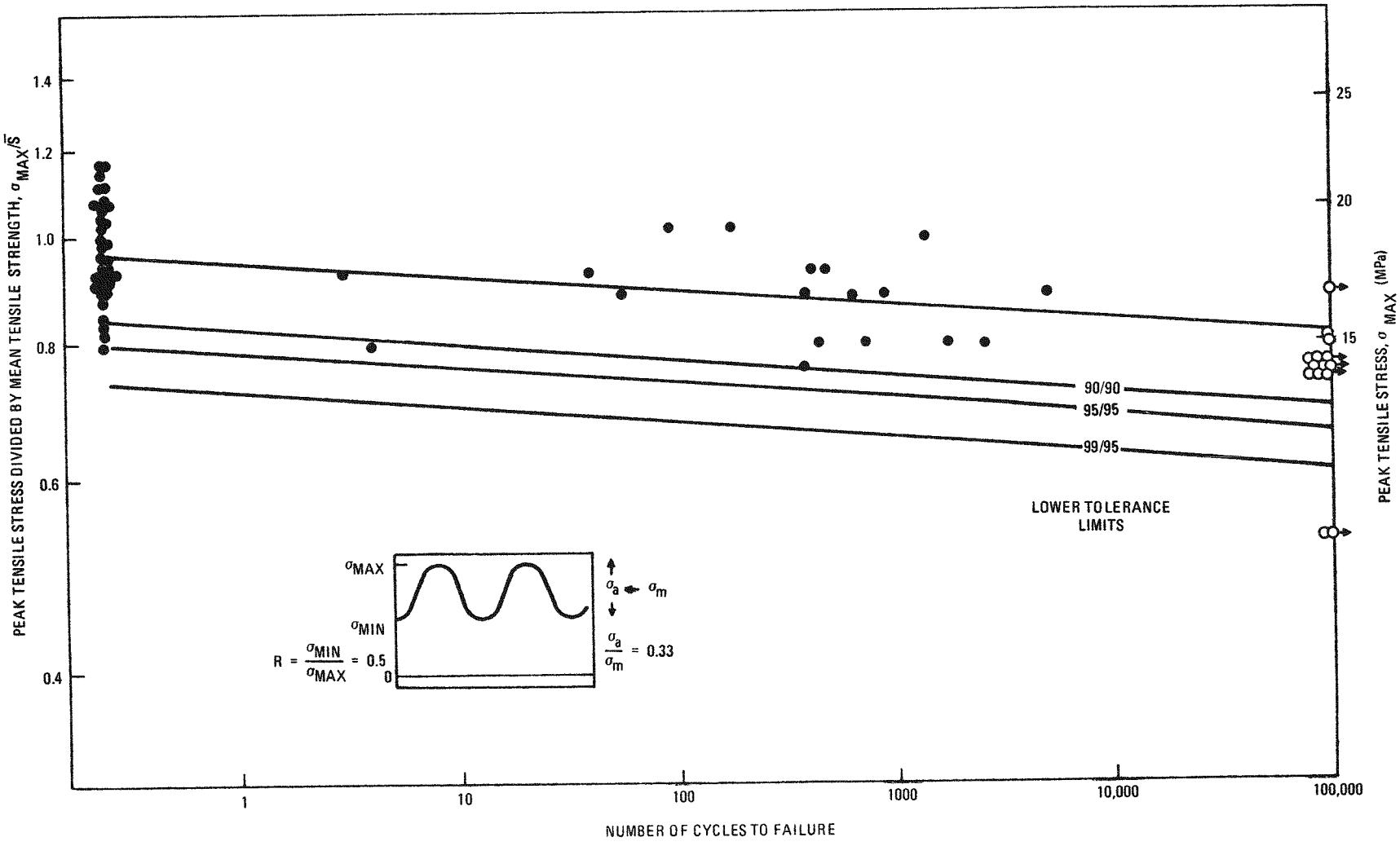

Fig. 11-24. Fatigue test data on H-451 graphite, axial orientation, quarter-length edge location, in air at ambient temperature. Log-log plot of normalized maximum stress versus number of cycles to failure with R = 0.5. Lower x/y tolerance limits represent the limits above which at least x% of the data fall, with y% confidence.

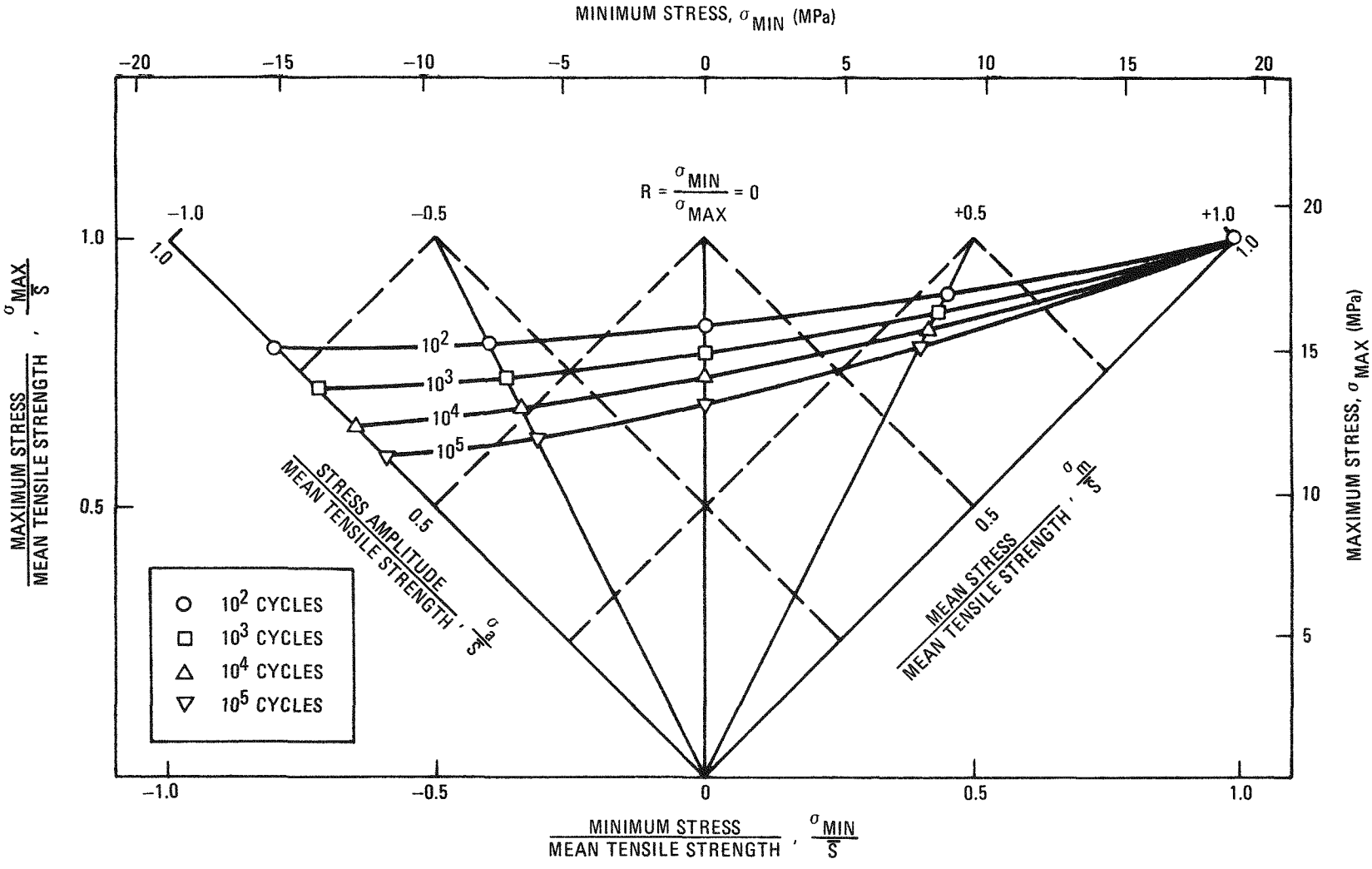

Fig. 11-25. Constant life fatigue diagram (Goodman diagram) for H-451 graphite, axial orientation, tested in air at ambient temperature

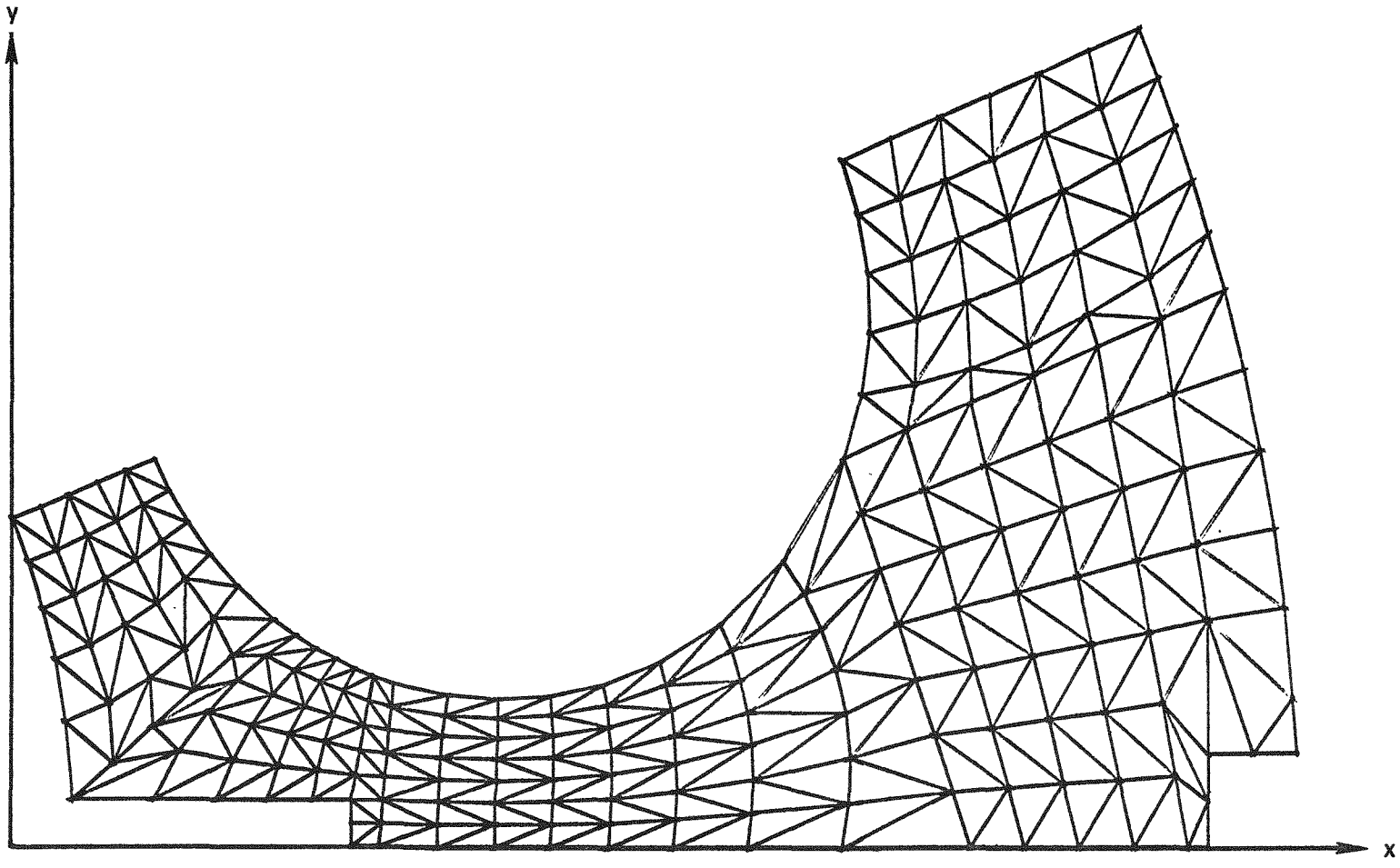

Fig. 11-26. Finite element model for residual stress analysis

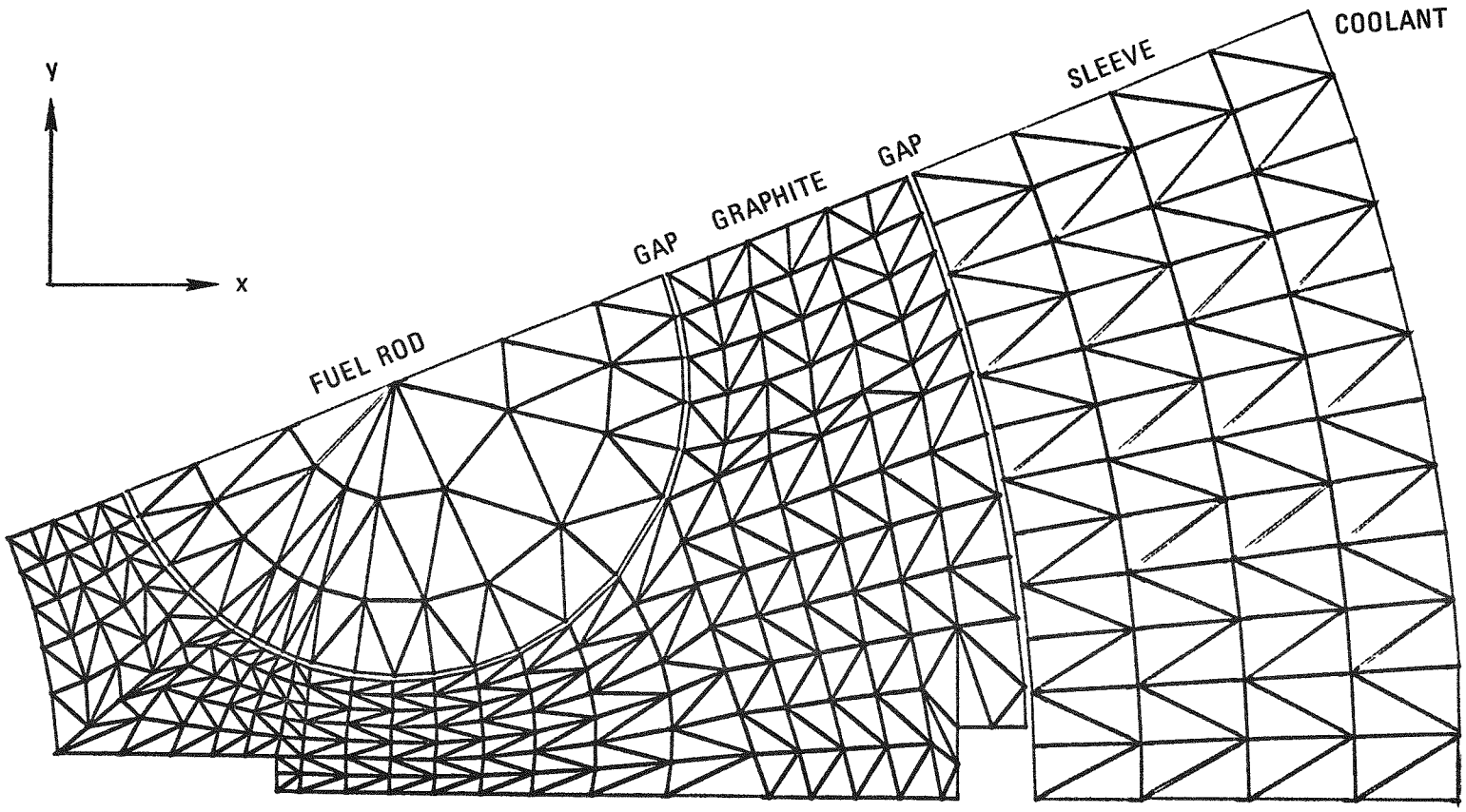

Fig. 11-27. Finite element model for thermal analysis

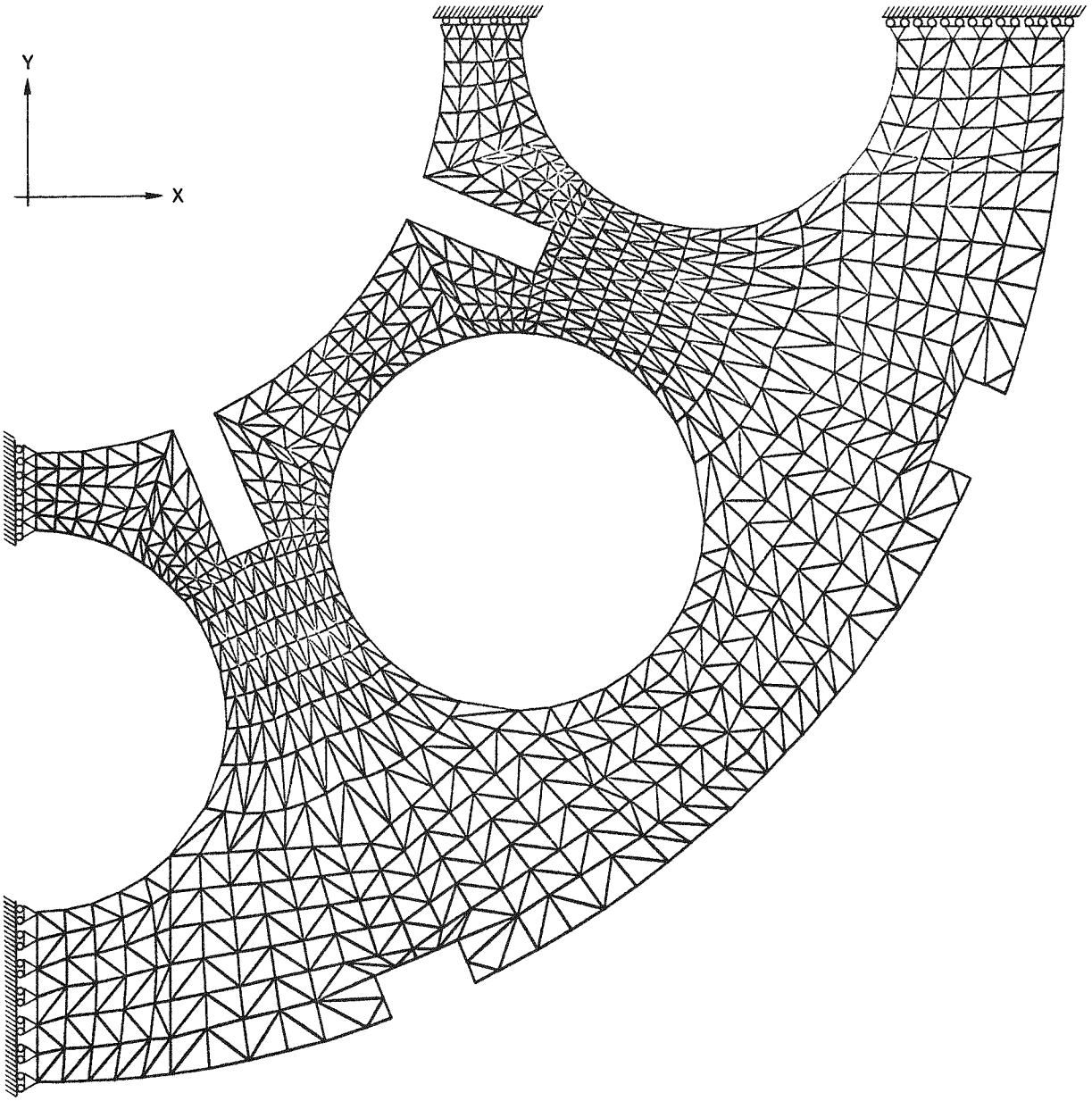

Fig. 11-28. Finite element model for primary loading analysis

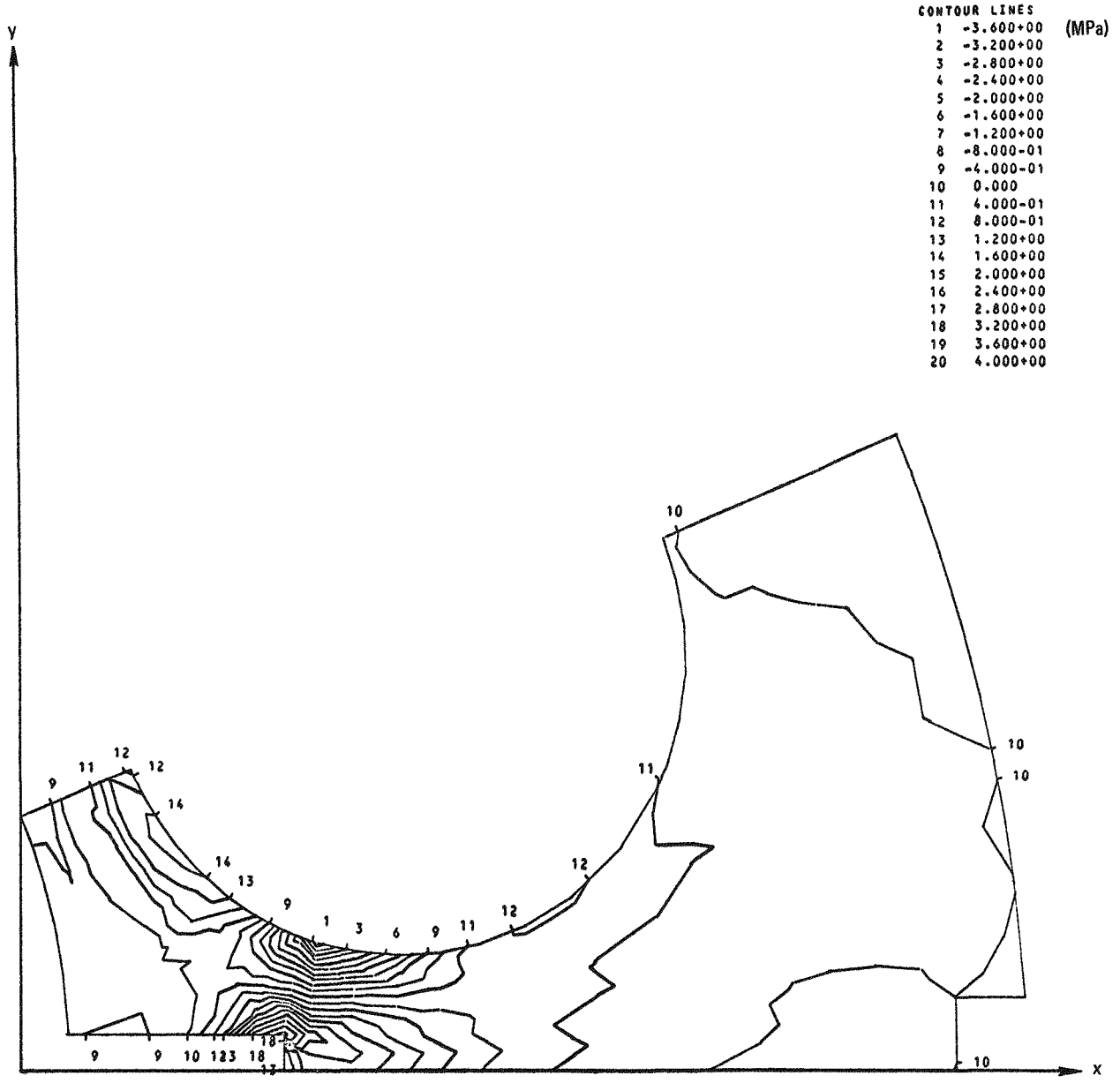

Fig. 11-29. Residual stress, σ_{max}, for FTE-4 at axial position 23

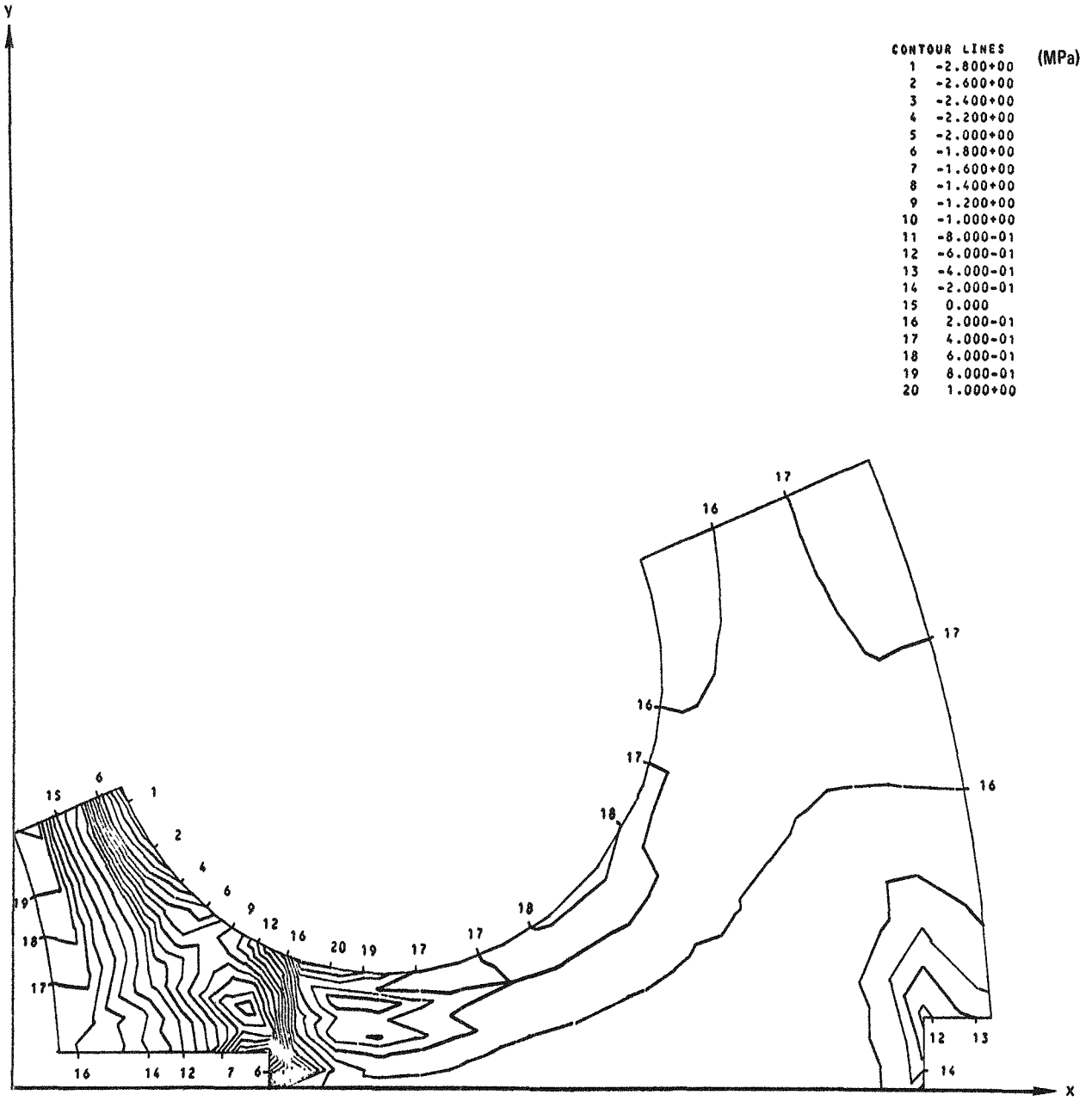

Fig. 11-30. Residual stress, σ_{xy}, for FTE-4 at axial position 23

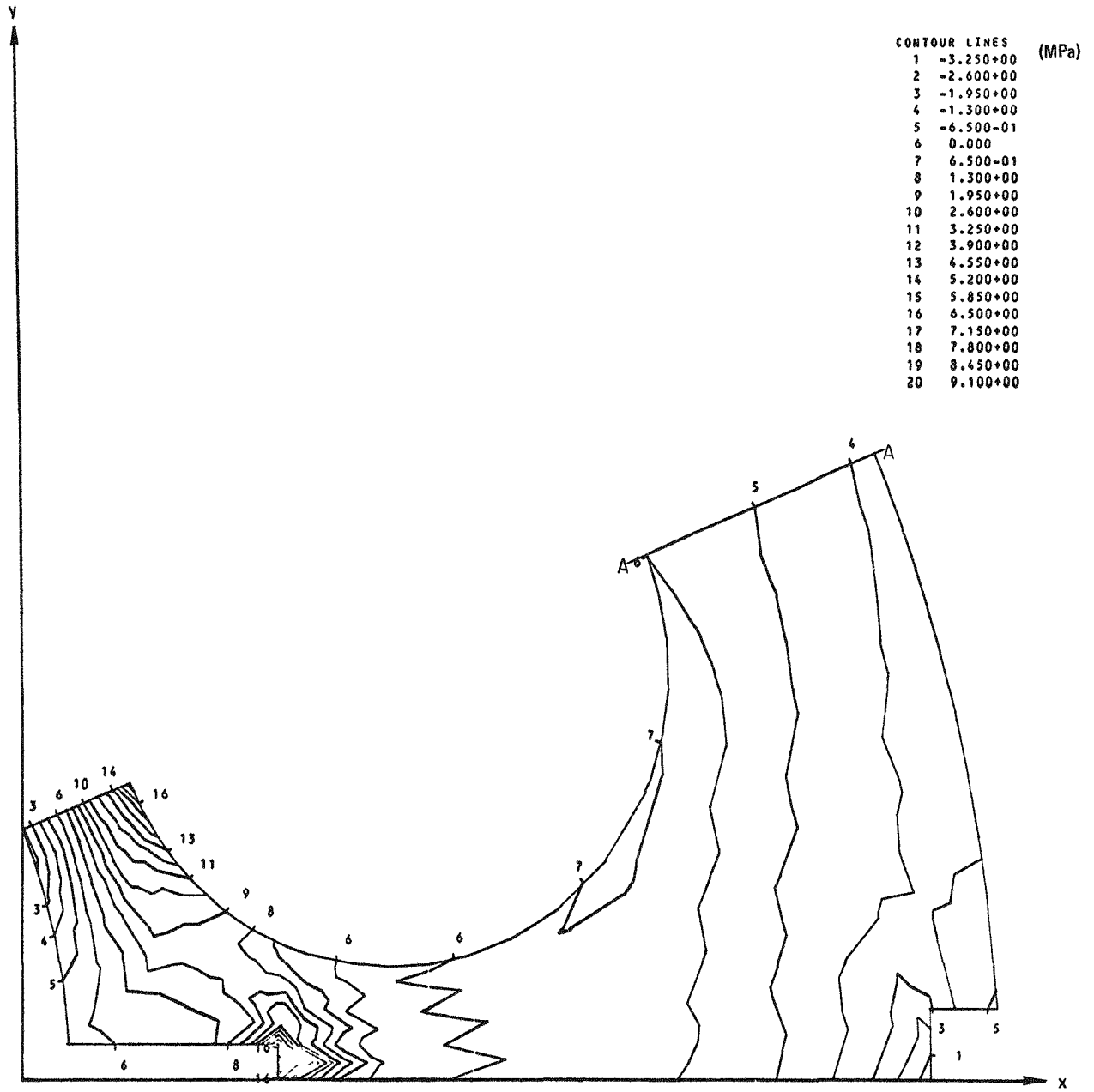

Fig. 11-31. Residual stress, σ_{yy}, for FTE-4 at axial position 23

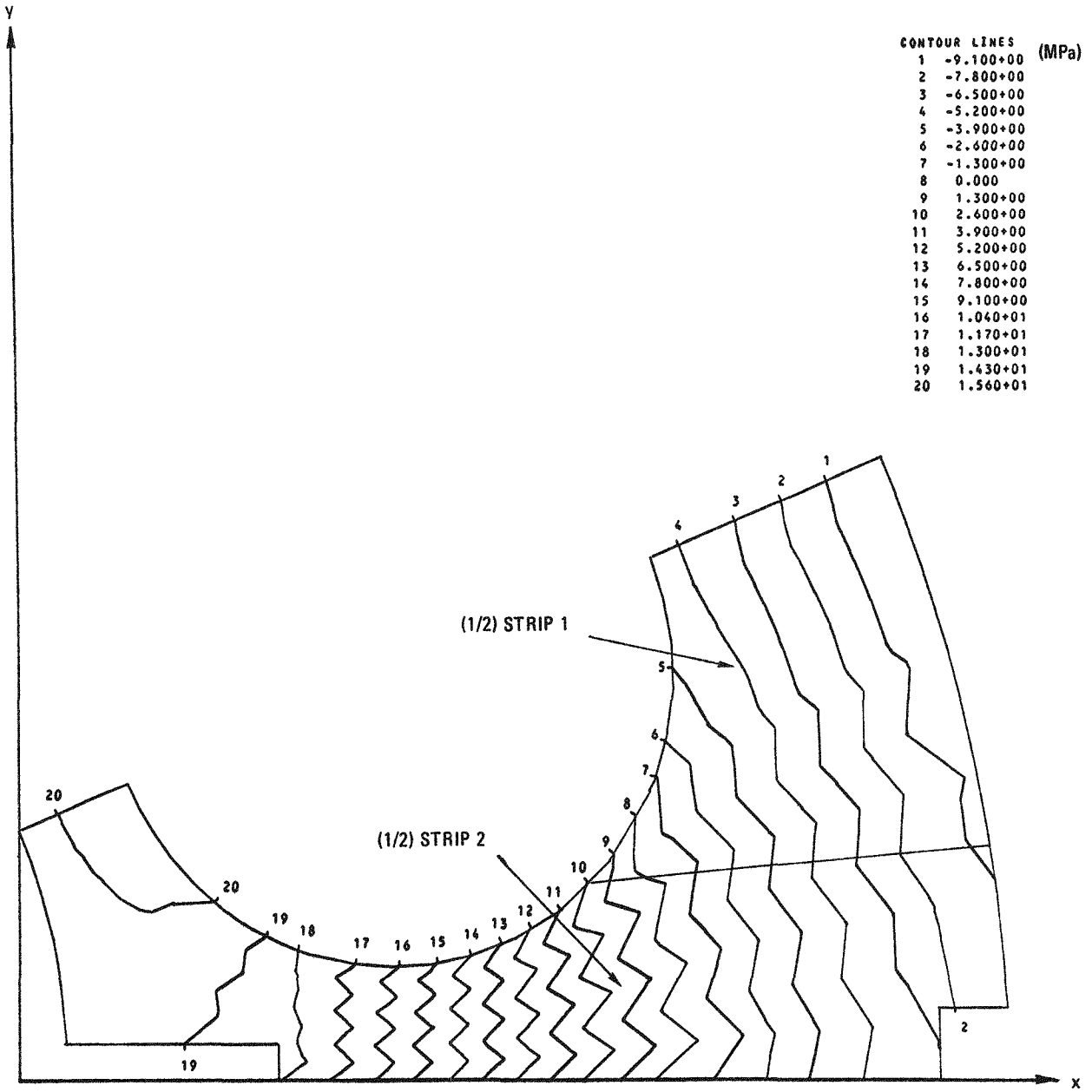

Fig. 11-32. Residual stress, σ_{zz}, for FTE-4 at axial position 23

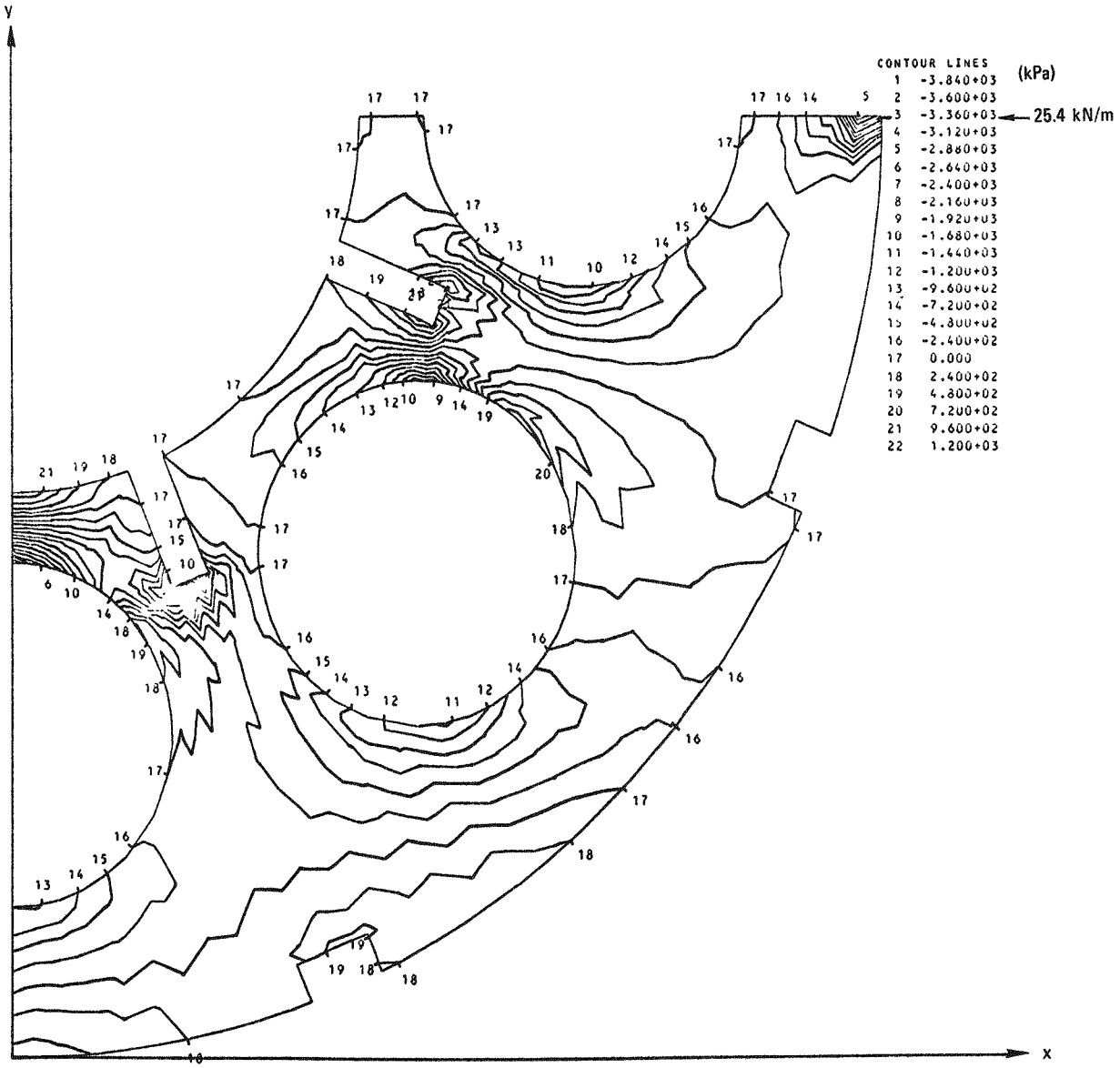

Fig. 11-33. x-stress contour under 25.4 kN/m compression load

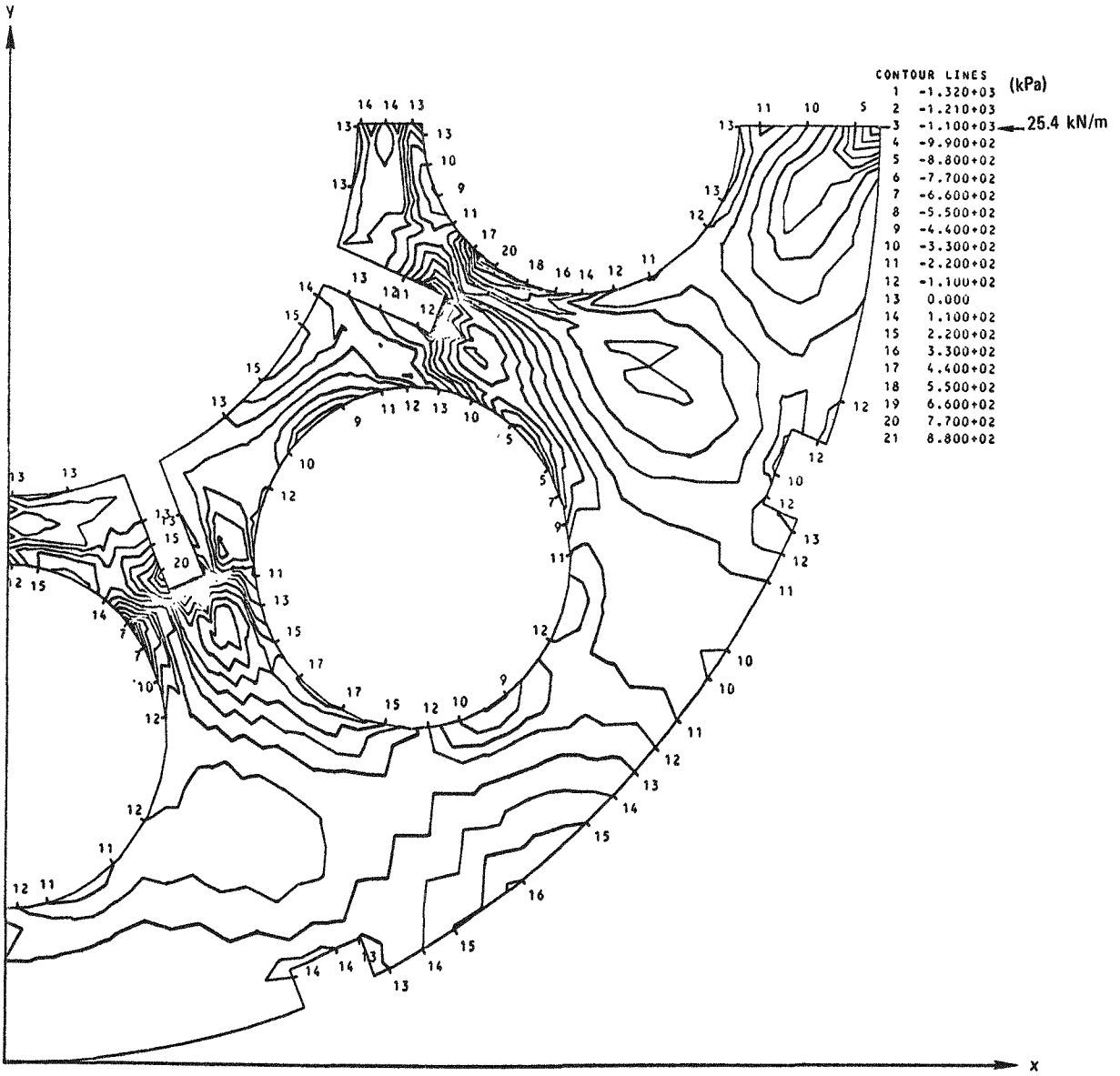

Fig. 11-34. xy-stress contour under 25.4 kN/m compression load

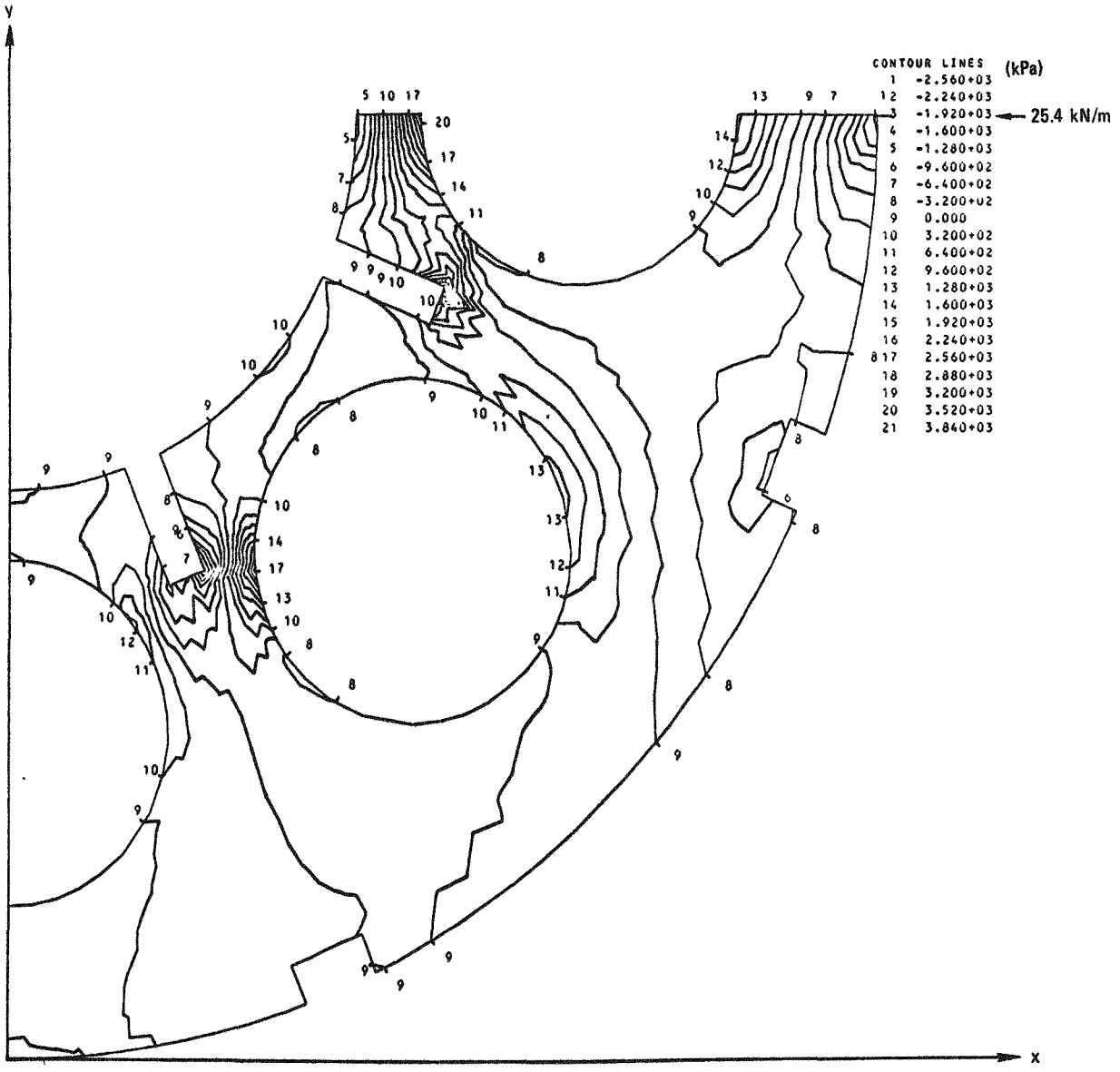

Fig. 11-35. y-stress contour under 25.4 kN/m compression load

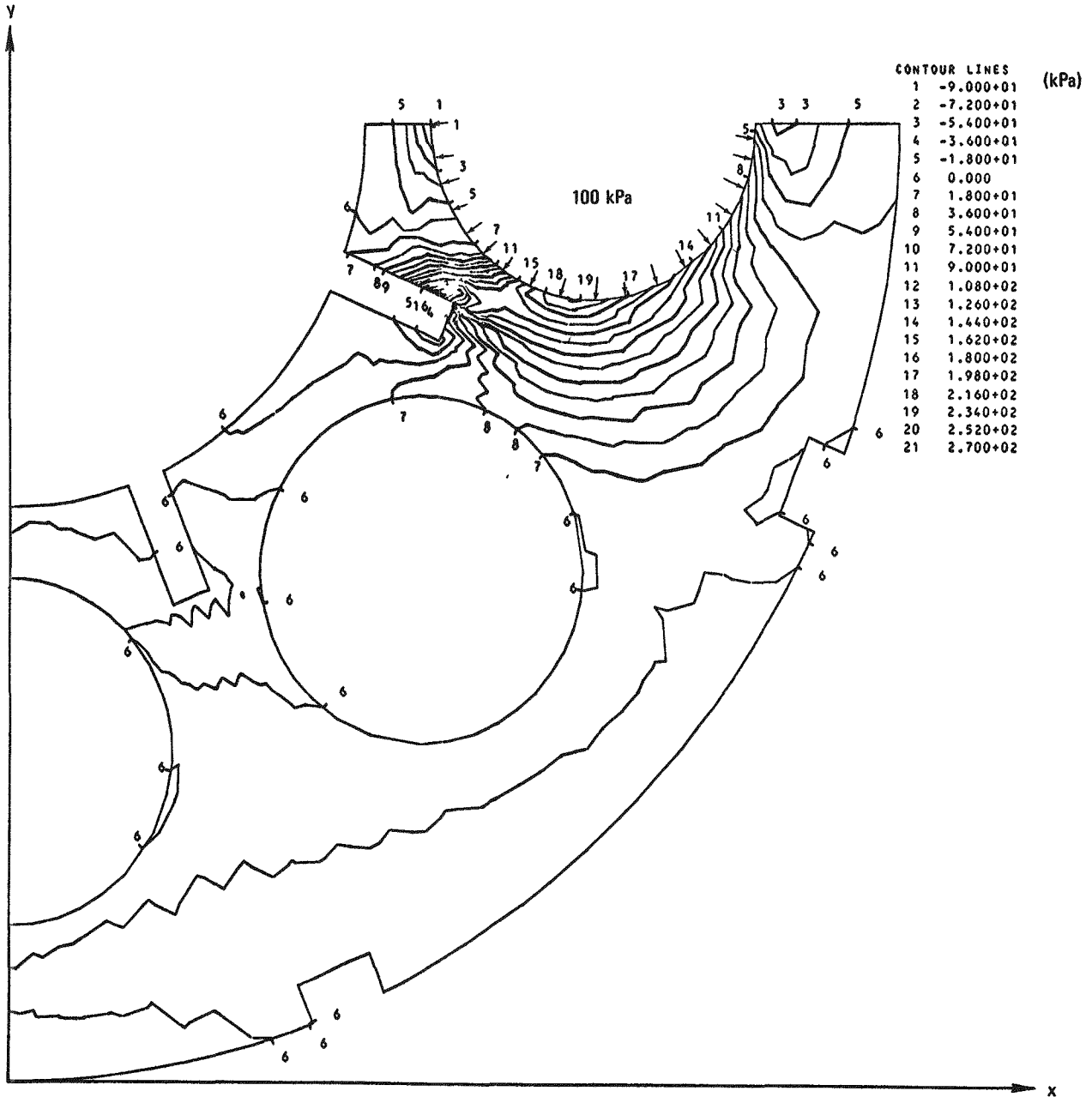

Fig. 11-36. x-stress contour under 100 kPa pressure load

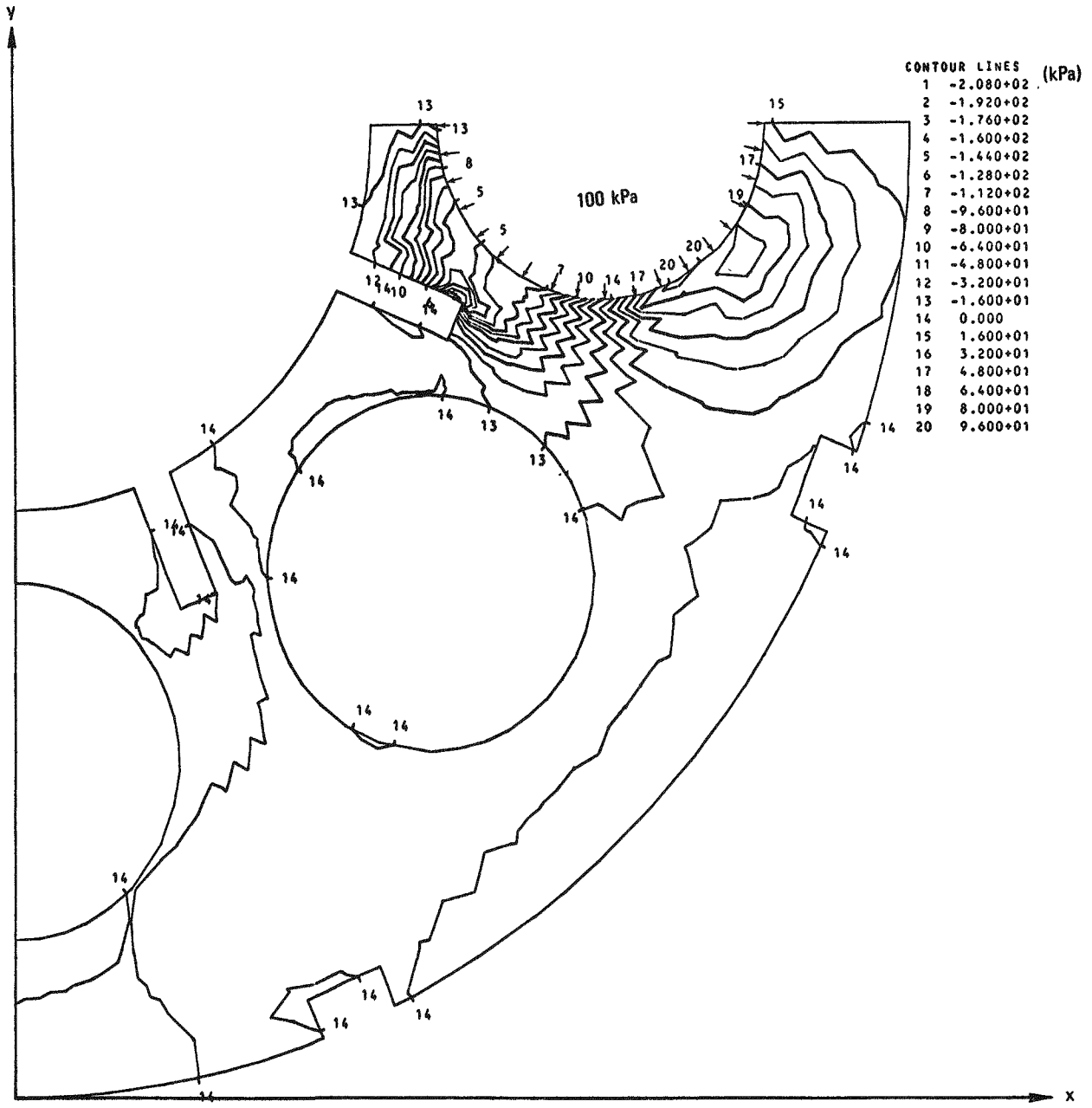

Fig. 11-37. xy-stress contour under 100 kPa pressure load

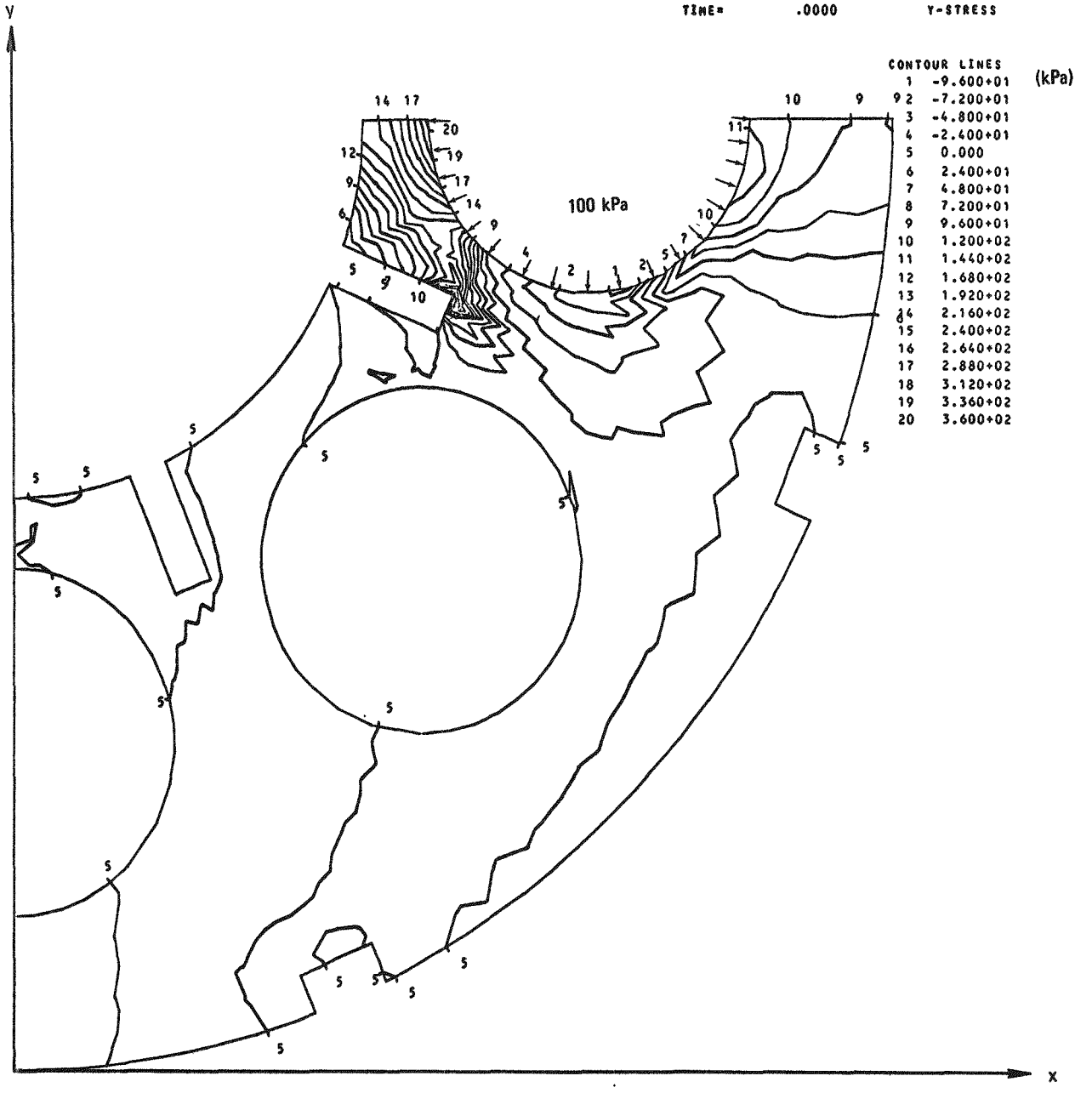

Fig. 11-38. y-stress contour under 100 kPa pressure load

APPENDIX
TOPICAL REPORTS PUBLISHED DURING THE QUARTER

Lane, R. K., and L. Yang, "HTGR Fuel Development Plans for Alternate Fuel Systems," ERDA Report GA-A13879, April 19, 1976.